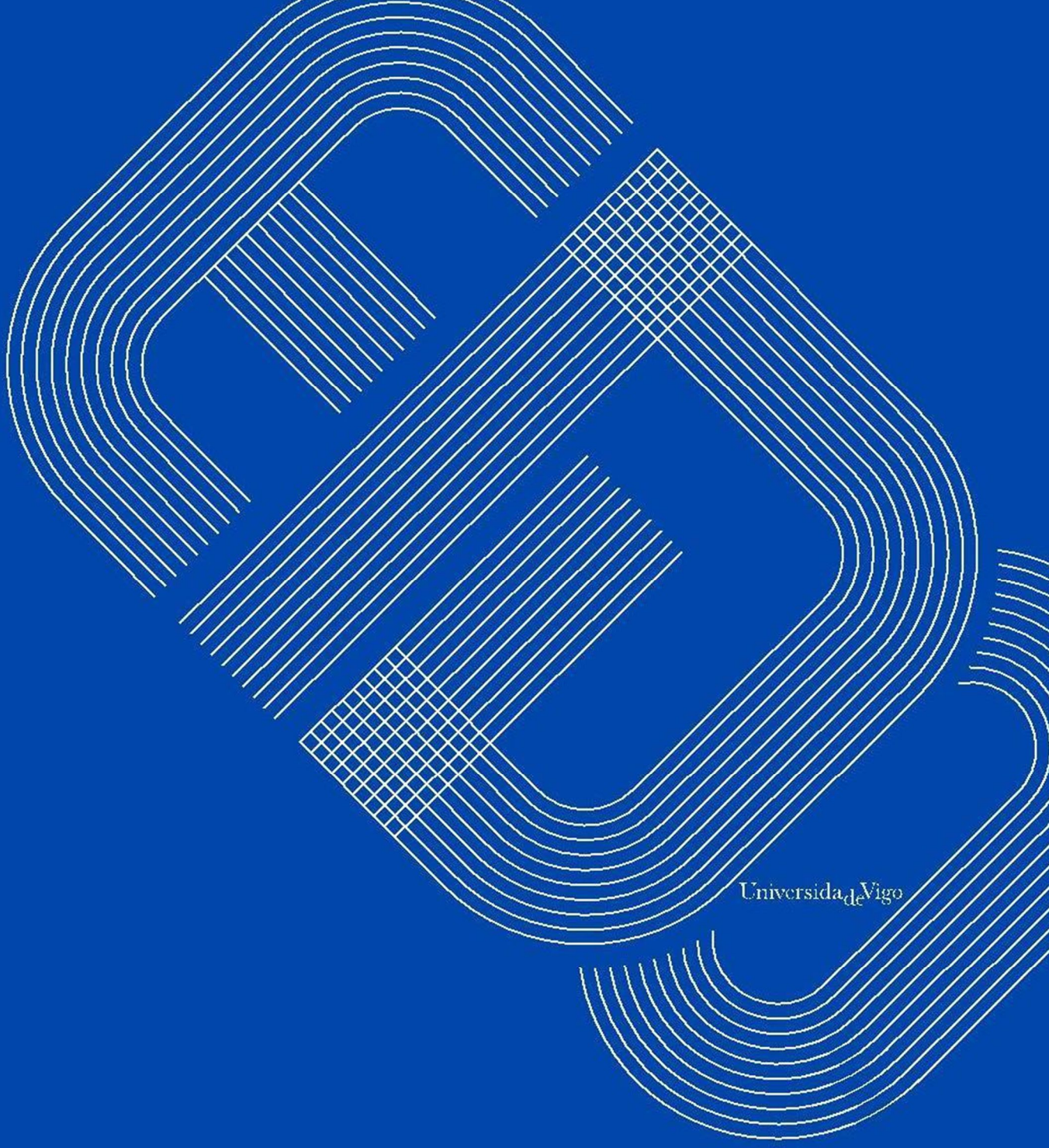

Universidade Vigo

Universidade Vigo

EIDO
Escola Internacional
de Doutoramento

DOCTORAL DISSERTATION

Elemental and molecular characterization and bioavailability of dissolved organic matter in the Mediterranean Sea

Alba María Martínez Pérez

2018

Universidade Vigo

International Doctoral School

Alba María Martínez Pérez

DOCTORAL DISERTATION

ELEMENTAL AND MOLECULAR CHARACTERIZATION AND BIOAVAILABILITY OF DISSOLVED ORGANIC MATTER IN THE MEDITERRANEAN SEA

Supervised by:

Dr. Xosé Antón Álvarez Salgado

Dr. María del Mar Nieto Cid

2018

Universidade Vigo

International Doctoral School

Dr. Xosé Antón Álvarez Salgado and Dr. María del Mar Nieto Cid

DECLARE that the present work, entitled "**ELEMENTAL AND MOLECULAR CHARACTERIZATION AND BIOAVAILABILITY OF DISSOLVED ORGANIC MATTER IN THE MEDITERRANEAN SEA**", submitted by **Alba María Martínez Pérez** to obtain the title of Doctor, was carried out under their supervision in the PhD programme "Marine Science, Technology And Management". This is a joint PhD programme integrating the following Universities: University of Santiago de Compostela, University of Vigo; University of Aveiro (Portugal), University of Trás–os–Montes e Alto Douro (Portugal) and University of Minho (Portugal).

Vigo, 20 February 2018

The supervisors,

Dr. Xosé Antón Álvarez Salgado

Dr. María del Mar Nieto Cid

Memoria de Tesis presentada por la Licenciada en Química, Alba María Martínez Pérez, para optar al título de Doctora por la Universidad de Vigo.

Esta Tesis Doctoral fue llevada a cabo en el Laboratorio de Geoquímica Orgánica (LGO), Departamento de Oceanografía del Instituto de Investigaciones Marinas (IIM) perteneciente al Consejo Superior de Investigaciones Científicas (CSIC) en Vigo. Los trabajos de investigación incluidos en esta Tesis fueron financiados por el proyecto "Zonas de mezcla y frentes en el océano oscuro como "hot-spots" de biodiversidad y flujos biogeoquímicos a través del Mar Mediterráneo y Atlántico Nordeste (HOTMIX)" (referencia CTM2011–30010–C02–02–MAR), cofinanciado con fondos FEDER. A.M. Martínez–Pérez estuvo financiada por una beca predoctoral (referencia BES–2012–056175) del Ministerio de Economía, Industria y Competitividad y por el proyecto MODMED del CSIC (PIE, 201730E020). Además, a lo largo de esta Tesis también se realizaron dos estancias de investigación en el grupo "Research Group for Marine Geochemistry" perteneciente al Institute for Chemistry and Biology of the Marine Environment (ICBM) de la Universidad de Oldenburg y al Max Planck Institute (MPI) financiadas por el Ministerio de Economía, Industria y Competitividad (referencias EEBB–I–14–08926 y EEBB–I–16–10902).

En Vigo, a 20 de febrero de 2018

A mi madre y a Andrés

Agradecimientos

En primer lugar quiero dar las gracias a mis directores de tesis, Pepe y Mar. Pepe, gracias por darme la oportunidad de trabajar en tu grupo, de formar parte del proyecto Hotmix, por transmitirme esa pasión por la ciencia, por hacer fáciles las cosas difíciles, por tu paciencia infinita y en definitiva por todo el apoyo, tanto profesional como personal, que me has dado durante estos años de tesis. Si como científico no hay duda de que eres excelente, como persona lo eres aún más. Mar, gracias por transmitirme la meticulosidad del trabajo de laboratorio, por todo lo que he aprendido contigo y por el apoyo que me has dado durante estos años. Me siento muy afortunada de teneros como directores y sin lugar a dudas sin vosotros está tesis no habría sido posible. Gracias!

Gracias a los coautores de los trabajos, X. A. Álvarez–Salgado, M. Nieto–Cid, M. Álvarez, J. Otero, T. Dittmar, H. Osterholz, J. Arístegui, T. Catalá, I. Reche, M. Emelianov, por vuestra dedicación.

Gracias Marta Álvarez y Eva Teira por formar parte de mi Comisión de Seguimiento Do*Mar y por los buenos consejos durante los PAI.

Gracias a los demás miembros del grupo de LGO: Vanesa, María, Jaime, Isabel Fuentes, Bieito, y Seve por estar siempre dispuestos a echar una mano en lo que haga falta y por el buen ambiente que hay siempre en el laboratorio. En especial, gracias María por tu apoyo en todo lo que he necesitado y por estar siempre disponible para ayudar. Isabel F. y Jaime gracias por vuestra ayuda con R. También me gustaría agradecer a todos los miembros del grupo de oceanoloxía: Fernando, Jesús, Trini, Rosa, Susana, Paco, Miguel, Fiz, Des, Carmen, Isabel Teixeira, Merche, Nico, Belén, María, Diana, Susa, Sara, Toni, Antón y en especial a mis compis de oficina, Dani, Marcos y Bieito, gracias por hacer los días de trabajo más agradables! También quiero dar las gracias a nuestras compañeras Aida y Eva, siempre os recordaré! Gracias a las niñas CSIC, Maribel, Clara, Noe, Alba Marina, Eva, Elisa, Bea, Lidia, que aunque estéis desperdigadas por el mundo, siempre estáis dispuestas a ayudar y sois un apoyo importante. Gracias a todos los miembros de la campaña Hotmix por hacer agradable la vida y el trabajo a bordo. Gracias Lorena por tu ayuda con el papeleo del depósito.

Gracias Thorsten Dittmar por acogerme en tu laboratorio y a todos los miembros de tu grupo por hacer muy agradables y productivas mis estancias en Oldenburg, en especial gracias Helena Osterholz por tu ayuda en el laboratorio.

Gracias Andrea, Jeny, Chus, Yago y Ana por estar siempre ahí.

Gracias Santiago y Jesusa por todo vuestro apoyo y el cariño que me habéis dado siempre.

Gracias mamá por el amor y el apoyo incondicional que me has dado siempre y perdón por no haberte dedicado todo el tiempo que me gustaría y te mereces. Siempre te estaré agradecida.

Y por último pero no menos importante, gracias Andrés por todo tu amor, paciencia y por ser mi gran apoyo.

INDEX

List of relevant acronyms

*a*254	Absorption coefficient at 254 nm
AdDW	Adriatic Deep Water
AdMW	Adriatic Middle Water
AI_{mod}	Aromaticity Index modified
AOU	Apparent Oxygen Utilization
AW	Atlantic Water
BC	Black Carbon
BIX	Biological IndeX
C:N:P	Carbon to Nitrogen to Phosphorous ratio
CDOM	Chromophoric Dissolved Organic Matter
CF	Concentration Factor
Chl *a*	Chlorophyll *a*
CHO	Molecular formulae with C, H and O atoms
CHON	Molecular formulae with C, H, O and N atoms
CHONS	Molecular formulae with C, H, O, N and S atoms
CHOP	Molecular formulae with C, H, O and P atoms
CHOS	Molecular formulae with C, H, O and S atoms
CHOSP	Molecular formulae with C, H, O, S and P atoms
CIW	Cretan Intermediate Water
CRAM	Carboxyl–Rich Alicyclic Molecules
DBE	Double Bond Equivalent
DCM	Deep Chlorophyll Maximum
DFAA	Dissolved Free Amino Acids
DOC	Dissolved Organic Carbon
DOM	Dissolved Organic Matter
DON	Dissolved Organic Nitrogen
DOP	Dissolved Organic Phosphorous
EastMed	Eastern Mediterranean Sea
EEM	Excitation–Emission Matrix
EIW	Eastern Intermediate Water (found in the Western basin)
EMDW	Eastern Mediterranean Deep Water
EMT	Eastern Mediterranean Transient
ESI	ElectroSpray Ionization
FDOM	Fluorescent Dissolved Organic Matter
FT–ICR–MS	Fourier Transform Ion Cyclotron Resonance Mass Spectrometry
GAMs	Generalized Additive Models
H/C	Hydrogen to Carbon ratio
HIX	Humification IndeX
HMW	High Molecular Weight (>1KDa)
HU	Highly Unsaturated compounds
Ideg	Index of degradation
LDOM	Labile Dissolved Organic Matter
LIW	Levantine Intermediate Water
LMW	Low Molecular Weight (<1KDa)
LSW	Levantine Surface Water
m/z	mass to charge ratio
MAW	Modified Atlantic Water
MCP	Microbial Carbon Pump
MedSea	Mediterranean Sea

MW	Molecular Weight
NELHA	Natural Energy Laboratory of Hawaii Authority
NEqPIW	North Equatorial Pacific Intermediate Water
NFlIU	Normalized Fluorescence Intensity Units
NMR	Nuclear Magnetic Resonance
O_2	Dissolved Oxygen
O/C	Oxygen to Carbon ratio
OML	oxygen Minimum Layer
OMP	Optimum MultiParametric Analysis
PARAFAC	PARAllel FACtor Analysis
PCoA	Principal Coordinates Analysis
PHA	Prokaryotic Heterotrophic Abundance
Polip	Polyphenols
POM	Particulate Organic Matter
RDOM	Refractory Dissolved Organic Matter
RO/ED	Reverse Osmosis ElectroDialysis
RU	Raman Units
S	Salinity
$S_{275–295}$	Spectral Slope between 275–295 nm
$S_{350–400}$	Spectral Slope between 350–400 nm
Sat FA	Saturated Fatty Acids
SLDOM	Semi Labil Dissolved Organic Matter
SPE	Solid Phase Extraction
SPE–DOC	Solid Phase Extracted DOC
SR	Spectral Ratio between 275–295 nm and 350–400 nm
SRC	Size Reactivity Continuum hypothesis
SRDOM	Semi Refractory Dissolved Organic Matter
TDN	Total Dissolved Nitrogen
TDP	Total Dissolved Phosphorous
THAA	Total Hydrolysable Amino Acids
UA	Unsaturated Aliphatic compounds
UDOM	Ultrafiltered Dissolved Organic Matter
URDOM	Ultrarefractory Dissolved Organic Matter
WestMed	Western Mediterranean Sea
WIW	Winter Intermediate Water
WMDW	Western Mediterranean Deep Water
WMT	Western Mediterranean Transition
θ	Potential Temperature
Φ340	Fluorescence quantum yield at 340 nm

Abstract/Resumo/Resúmenes

Abstract

The chemical composition and bioavailability of dissolved organic matter (DOM) in the dark ocean is still enigmatic. To better understand the role played by DOM in the global ocean carbon cycle, it is crucial to decipher its composition and mechanisms of production and degradation. Knowing how DOM persists for hundreds to thousands years in the ocean is also pivotal. Within this framework, the main purpose of this PhD thesis is to shed light on the elemental and molecular composition of DOM, identify the environmental drivers of DOM variability and gain knowledge about DOM bioavailability.

This PhD thesis is framed in the trans–Mediterranean cruise HOTMIX 2014. The Mediterranean Sea (MedSea) is an oligotrophic semi–enclosed basin suitable to study the DOM dynamics as it comprises water mass formation areas with its own thermohaline circulation. The smaller size and faster ventilation rates of the MedSea compared to the global ocean allow DOM changes to be observed in shorter spatial and temporal scales. Further, the high temperature of the deep waters stimulates DOM mineralization in the dark MedSea.

The variability of dissolved organic carbon (DOC) and the absorption coefficient of colored DOM (CDOM) at 254 nm (*a*254) in the epipelagic layer of the MedSea was mostly explained by the apparent oxygen utilization (AOU). In the deep layer, water mass mixing and basin–scale mineralization processes contributed more substantially to explicate their variability. Further, considering the eastern and western basins separately, DOC contributed to 66 ± 10% of the oxygen demand in the eastern basin and to 24 ± 4% in the western basin. These results indicate that local mineralization processes of DOC and CDOM play a more relevant role in the eastern than the western MedSea. In addition, we identified 4 fluorophores in the MedSea: three humic–like and one protein–like. In the epipelagic layer, the distribution of marine humic–like substances was mainly driven by AOU suggesting that those compounds are by–products of mineralization processes. On the contrary, protein–like fluorescence was mainly driven by prokaryotic heterotrophic abundance. Again, in the deep layer mixing processes exhibited more influence on FDOM variability in the eastern than in the western basin.

The molecular composition of DOM in the MedSea was also studied and water mass origin and DOM biodegradation were identified as the main drivers. Deep waters in the eastern basin exhibited significant molecular differences linked to their formation site, Adriatic *versus* Aegean Sea, and their formation time. Exploring the link between optical and molecular properties of DOM, it was found that 52% of the molecular formulae were correlated with one or more optical parameter. Furthermore, multiple linear regressions models to estimate molecular indices from optical indices were established for the first time.

Finally, we assessed the reactivity of DOM transported by the intermediate waters of the MedSea by following *in situ* the evolution of two size–fractionated fractions (high and low molecular weight). Larger molecules were the only responsible for the oxygen consumption, resulting more reactive than the smaller counterpart and, therefore, verifying the size reactivity continuum hypothesis on the field. Further, in parallel to this DOC consumption, a decline of the protein–like substances together with a production of humic–like substances occurred in both size fractions, also corroborating the microbial carbon pump model.

Resumo

A composición química e biodispoñibilidade da materia orgánica disolta (DOM) no océano profundo é aínda un enigma. Para entender mellor o papel que xoga a DOM no ciclo do carbono do océano global, é crucial dilucidar a súa composición e os seus mecanismos de producción e degradación. Coñecer cómo a DOM é capaz de persistir durante centos e miles de anos no océano é tamén esencial. Dentro deste marco, o obxectivo principal desta tese doutoral é arroxar luz na composición elemental e molecular da DOM, identificar os factores ambientais que influen na súa variabilidade e aumentar o coñecemento sobre a súa biodispoñibilidade.

Esta tese doutoral está enmarcada na campaña oceanográfica transmediterránea HOTMIX 2014. O mar Mediterráneo (MedSea) é unha cunca oligotrófica semi–pechada adecuada para o estudo da DOM xa que é unha zona de formación de masas de auga coa súa propia circulación termohalina. O seu pequeno tamaño e as súas rápidas taxas de ventilación comparadas co océano global permiten observa–los cambios na DOM en escalas espaciais e temporais menores.

A variabilidade do carbono orgánico disolto (DOC) e o coeficiente de absorción da DOM coloreada (CDOM) a 254 nm (a254) na capa epipeláxica do MedSea foi maiormente explicada pola utilización aparente de osíxeno (AOU). Nas capas profundas, os procesos de mestura das masas de auga e a mineralización a gran escala contribuíron máis substancialmente a explica–la súa variabilidade. Ademais, considerando as cuncas oriental e occidental por separado, o DOC contribuíu nun 66 ± 10% á demanda de osíxeno na cunca oriental e nun 24 ± 4% na occidental. Estes resultados indican que os procesos locais de mineralización do DOC e CDOM teñen maior influencia na cunca oriental. Adicionalmente, identificáronse 4 fluoróforos no MedSea: 3 húmicos e 1 proteico. Na capa epipeláxica, a distribución das sustancias húmicas foi modulada principalmente pola AOU, suxerindo que estas sustancias son subproduto de procesos de mineralización. Pola contra, a fluorescencia proteica foi afectada principalmente pola abundancia de procariotas heterotróficos. Nas capas profundas os procesos de mestura amosaron máis influencia na variabilidade da fluorescencia da DOM na cunca oriental.

Tamén se estudou a composición da DOM no MedSea e se identificaron os principais factores que a gobernan: a orixe das masas de auga e a biodegradación da DOM. As augas profundas da cunca oriental amosaron diferenzas moleculares significativas asociadas ó seu lugar de formación, mar Adriático vs Exeo, e ó seu tempo de formación. Analizando a relación entre as propiedades ópticas e moleculares da DOM atopouse que o 52% das fórmulas moleculares estiveron correlacionadas con un ou máis parámetros ópticos. Ademais, establecéronse, por vez primeira, modelos de regresión múltiple para estimar índices moleculares a partir de índices ópticos.

Finalmente, estudouse a reactividade da DOM transportada polas augas intermedias do MedSea, seguindo a evolución *in situ* de dúas fraccións separadas por tamaño (alto e baixo peso molecular). As moléculas máis grandes foron as únicas responsables do consumo de osíxeno, resultando ser máis reactivas que as pequenas e verificando a hipótese do continuo tamaño–reactividade no campo. Ademais, en paralelo a este consumo de osíxeno, observouse un descenso das sustancias proteicas xunto cunha produción de sustancias húmicas nas dúas fraccións corroborando tamén o modelo da bomba microbiana de carbono.

Resumen

La composición química y biodisponibilidad de la materia orgánica disuelta (DOM) en el océano profundo es todavía un enigma. Para entender mejor el papel que juega la DOM en el ciclo del carbono del océano global es crucial dilucidar su composición y sus mecanismos de producción y degradación. Conocer cómo la DOM es capaz de persistir de cientos a miles de años en el océano es también esencial. En este marco, el objetivo de esta tesis doctoral es arrojar luz en la composición elemental y molecular de la DOM, identificar los factores ambientales que influyen en su variabilidad y aumentar el conocimiento sobre su biodisponibilidad.

Esta tesis doctoral está enmarcada en la campaña oceanográfica trans–mediterránea HOTMIX 2014. El mar Mediterráneo (MedSea) es una cuenca oligotrófica semi–cerrada adecuada para el estudio de la DOM ya que es una zona de formación de masas de agua con su propia circulación termohalina. Su pequeño tamaño y rápidas tasas de ventilación permiten observar cambios en la DOM en escalas espacio–temporales menores que en el océano global.

La variabilidad del carbono orgánico disuelto (DOC) y el coeficiente de absorción de la DOM coloreada (CDOM) a 254 nm (a254) en la capa epipelágica del MedSea se explica mayoritariamente por la utilización aparente de oxígeno (AOU). En las capas profundas, los procesos de mezcla de masas de agua y la mineralización a gran escala contribuyeron más substancialmente a explicar su variabilidad. Además, considerando las cuencas oriental y occidental por separado, el DOC contribuyó en un 66 ± 10% a la demanda de oxígeno en la cuenca oriental y en un 24 ± 4% en la cuenca occidental. Estos resultados indican que los procesos locales de mineralización del DOC y CDOM tienen mayor influencia en la cuenca oriental. Adicionalmente, se identificaron 4 fluoróforos en el MedSea: 3 de tipo húmico y 1 de tipo proteico. En la capa epipelágica, la distribución de las sustancias húmicas fue modulada principalmente por la AOU sugiriendo que estas sustancias son subproducto de procesos de mineralización. Por el contrario, la fluorescencia proteica fue influenciada primordialmente por la abundancia de procariotas heterotróficos. En las capas profundas los procesos de mezcla mostraron más influencia en la variabilidad de la fluorescencia de la DOM en la cuenca oriental.

También se estudió la composición de la DOM en el MedSea y se identificaron los principales factores que la gobiernan: el origen de las masas de agua y la biodegradación de la DOM. Las aguas profundas de la cuenca oriental mostraron diferencias moleculares significativas asociadas a su lugar, mar Adriático vs Egeo, y su tiempo de formación. Analizando la relación entre las propiedades ópticas y moleculares de la DOM se encontró que el 52% de las fórmulas moleculares estuvieron correlacionadas con uno o más parámetros ópticos. Además, se establecieron, por primera vez, modelos de regresión múltiple para estimar índices moleculares a partir de índices ópticos.

Finalmente, se estudió la reactividad de la DOM transportada por las aguas intermedias del MedSea, siguiendo la evolución *in situ* de dos fracciones separadas por tamaño (alto y bajo peso molecular). Las moléculas más grandes fueron las únicas responsables del consumo de oxígeno, resultando ser más reactivas que las pequeñas y verificando la hipótesis del continuo tamaño–reactividad en el campo. Además, en paralelo a este consumo de oxígeno, se observó un descenso de las sustancias proteicas junto con una producción de sustancias húmicas en las dos fracciones corroborando también el modelo de la bomba microbiana de carbono.

Resumen largo en castellano

Introducción

Materia orgánica disuelta en el océano

La materia orgánica en el océano está formada por una compleja mezcla de compuestos que abarcan un amplio rango de tamaños. Para facilitar su estudio la materia orgánica ha sido operacionalmente dividida en dos grandes grupos: materia orgánica particulada (POM) y materia orgánica disuelta (DOM). La POM se define como la fracción físicamente retenida por filtros de tamaño de poro de 0.2–0.7 μm, mientras que la DOM se define como la fracción que pasa dichos filtros. La DOM forma un continuo de tamaños y es a su vez clasificada como DOM verdaderamente disuelta o de bajo peso molecular (LMW) y DOM coloidal o de alto peso molecular (HMW).

La DOM constituye el mayor reservorio de carbono orgánico reducido en el océano y, sin embargo, es el menos estudiado. Con 662 Pg C (1 Pg = 10^{15} g), la DOM representa el 96% del carbono orgánico total en los océanos (Hansell et al., 2009; Hansell, 2013). A pesar de su enorme cantidad global, la DOM existe en el océano abierto en concentraciones extremadamente bajas, generalmente entre 34 y 80 μmol C kg^{-1} (Hansell et al., 2009). La DOM se produce principalmente en la capa epipelágica del océano (0–150 m de profundidad) como resultado de la fotosíntesis del fitoplancton y las subsecuentes interacciones dentro de la red trófica microbiana y la cadena trófica clásica (Carlson, 2002). La mayoría de esta DOM recientemente producida es lábil y por lo tanto presenta tiempos de vida cortos, siendo rápidamente respirada a CO_2. Sin embargo, existe una pequeña fracción que no se mineraliza rápidamente porque, o bien, es originalmente resistente a la degradación o es transformada mediante procesos bióticos o abióticos en materia resistente, acumulándose en la capa superficial del océano para finalmente ser exportada al océano profundo (>150 m de profundidad).

La mayoría de los 662 Pg C de DOM acumulados en el océano son resistentes a la degradación microbiana y por lo tanto, se almacenan en él durante cientos o miles de años (Hansell et al., 2009; Hansell, 2013). Los mecanismos capaces de explicar este almacenamiento de carbono en el interior del océano todavía son inciertos (Dittmar, 2015) pero se han postulado diversas hipótesis para explicarlo: 1) la bomba microbiana de carbono (Ogawa et al., 2001; Jiao et al., 2010); 2) la teoría del continuo reactividad (Amon and Benner, 1996; Benner and Amon, 2015); 3) la hipótesis de la dilución extrema (Arrieta et al., 2015; Dittmar, 2015); 4)

la estabilidad intrínseca de la DOM (Dittmar, 2015); y 5) condiciones ambientales adversas como ocurre en zonas anóxicas u oligotróficas (Dittmar, 2015). Existen evidencias a favor de todas estas hipótesis, y la razón de la estabilidad de la DOM en el océano es probablemente debida a la combinación de todas o la mayoría de ellas (Dittmar, 2015).

Caracterización química de la DOM

La caracterización química de la DOM es limitada ya que es difícil de estudiar debido a que la DOM en agua de mar está formada por una compleja mezcla de cientos de miles de compuestos en donde cada compuesto individual está presente en extremadamente bajas concentraciones en medio de enormes cantidades de sal. De hecho cada litro de agua de mar tiene 30–40 g de sal y solo 0.5–1.0 mg de C (Repeta, 2015), por lo que su estudio supone todo un reto analítico y ha sido abordado desde diferentes aproximaciones, como por ejemplo, cálculo de ratios elementales de carbono, nitrógeno y fósforo, determinación de concentraciones de grupos moleculares (proteínas, carbohidratos, lípidos), propiedades ópticas y a nivel de fórmulas moleculares (Benner et al., 1992, 1997; Bauer, 2002; Benner, 2002; Hertkorn et al., 2006; Dittmar and Stubbins, 2014; Beaupré, 2015; Stedmon and Nelson, 2015; Hertkorn et al., 2016). Una pequeña fracción de la DOM absorve luz UV y visible, se denomina DOM cromofórica (CDOM) y está presente ubicuamente en el océano (Nelson and Siegel, 2013). A su vez entre el 3–21% de la CDOM emite parte de la luz absorbida a longitudes de onda mayores y se conoce como DOM fluorescente (FDOM). El estudio de las caracteristicas ópticas de la DOM han permitido estudiar las dinámicas de la DOM y conocer rasgos moleculares como el tamaño molecular, aromaticidad, grado de humificación, además de identificar determinados tipos de compuestos (húmicos, proteicos, aromáticos, etc) en el reservorio de la CDOM (Dahlén et al., 199, Weishaar et al., 2003, Engelhaupt et al., 2003, Coble 2007, Helms et al., 2008). Las primeras investigaciones sobre la composición molecular de la DOM fueron realizadas usando resonancia magnética nuclear (RMN) de DOM ultrafiltrada (Benner et al., 1992; Aluwihare et al., 1997; McCarthy et al., 1997; Clark et al., 1998; Hertkorn et al., 2006). Estos estudios pioneros revelaron que la DOM estaba formada principalmente por carbohidratos, amino ácidos, lípidos, proteinas y una fracción de naturaleza refractaria compuesta por moléculas alicíclicas ricas en grupos carboxílicos. Hoy en día, la espectrometría de masas de resonancia ciclotrónica iónica por transformada de Fourier acoplada con ionización por electrospray (ESI–FT–ICR–MS, por sus siglas en inglés) es una de las técnicas más poderosas para el estudio de la composición molecular de la DOM. ESI–FT–ICR–MS es capaz de distinguir cientos de miles de masas moleculares y a partir de ellas asignar miles de fórmulas moleculares (Kujawinski, 2002; Koch et al., 2005; Hertkorn et al., 2006, 2008, 2013, 2016;

Dittmar and Paeng, 2009; D'Andrilli et al., 2010). Características estructurales de la DOM, como el estado de saturación y oxigenación, aromaticidad, número de dobles enlaces equivalentes, el índice de degradación pueden ser calculados a partir de los datos de las fórmulas moleculares (Hertkorn et al., 2006; Koch and Dittmar, 2006, Flerus et al., 2012, Osterholz et al., 2014). Sin embargo, a partir de los análisis de FT–ICR–MS no se puede obtener una información estructural completa puesto que cada formula molecular puede presentar miles de isómeros (Hertkorn et al., 2008).

El mar Mediterráneo

El área de estudio de esta tesis doctoral es el mar Mediterráneo (MedSea), una cuenca semicerrada que está abierta al océano Atlántico a través del estrecho de Gibraltar. Está formado por dos cuencas de tamaño similar, la oriental y la occidental conectadas entre sí por el estrecho de Sicilia. Su baja concentración en nutrientes hace que se clasifique al MedSea como una región oligotrófica, en donde la circulación anti–estuarina produce un desequilibrio entre el flujo de agua rica en nutrientes, que sale por profundidad del MedSea y el flujo de agua pobre en nutrientes, que entra por superficie desde el océano Atlántico (Huertas et al., 2012). La circulación del MedSea está limitada por su topografía, el estrecho de Sicilia impide el intercambio de aguas profundas entre las dos cuencas, permitiendo solo el paso superficial. La circulación termohalina en el MedSea está definida por una celda superficial longitudinal abierta que comprende toda la cuenca y dos celdas meridionales cerradas limitadas en las subcuencas occidental y oriental. La celda termohalina abierta comprende el agua atlántica (AW) desplazándose por superficie desde el estrecho de Gibraltar hasta la cuenca oriental. Sin embargo, las celdas meridionales cerradas implican fundamentalmente a las masas de agua profundas (Skliris, 2014). Las principales masas de agua en el MedSea son en la capa epipelágica, el AW, en la capa mesopelágica el agua intermedia Levantina (LIW) que se encuentra en la cuenca oriental y el agua intermedia del este (EIW) en la cuenca occidental, y en las capas batipelágicas el agua profunda del este (EMDW) y del oeste (WMDW).

El MedSea ha sido utilizado como un laboratorio natural para estudiar procesos de circulación oceánica y procesos físicos y biogeoquímicos en el océano debido a que presenta las siguientes características que lo hacen especialmente adecuado: 1) presenta su propia circulación termohalina; 2) es una zona de formación de masas de agua; 3) presenta tasas de ventilación y tiempos de residencia rápidos en comparación con el océano global; 4) la temperatura de las aguas profundas es alrededor de 10°C más elevada que en el océano global; 5) la respiración y mineralización de la DOM está estimulada; y 6) tiene un fácil acceso.

Motivación, hipótesis, objetivos y estructura de esta tesis doctoral

En respuesta a la laguna de conocimiento que existía sobre la caracterización química de la DOM y su reactividad en el océano abierto del MedSea cuando esta tesis doctoral fue propuesta, las preguntas científicas e hipótesis de trabajo que nos planteamos fueron las siguientes: ¿Cuáles son los factores medioambientales que regulan los gradientes de concentración, la estequiometria, las propiedades ópticas y la composición molecular de la DOM en el océano abierto del mar Mediterráneo? ¿Están estos factores regulados principalmente por la mezcla de masas de agua? ¿O en cambio, están regulados por procesos biogeoquímicos de degradación? ¿O por ambos? Para ser capaces de responder a estas preguntas hemos fijado los siguientes objetivos específicos de esta tesis doctoral:

1. Estudiar la composición elemental y las propiedades ópticas de la DOM y evaluar los factores físicos y biogeoquímicos que influyen en su distribución a lo largo del MedSea.
2. Caracterizar la composición molecular de la DOM en las principales masas de agua del MedSea.
3. Relacionar las propiedades ópticas y moleculares de la DOM en las principales masas de agua del MedSea.
4. Relacionar el tamaño molecular y la biodisponibilidad de la DOM en las aguas intermedias del MedSea.

Para abordar estos objetivos esta tesis doctoral se dividió en 8 capítulos, el primero de ellos contiene una introducción general que explica los aspectos más relevantes sobre la DOM en el océano y el mar Mediterráneo como área de estudio. El capítulo 2 describe los principales factores ambientales que influyen en la distribución del DOC y el CDOM usando modelos aditivos generalizados (GAMs) para la capa superficial y un modelo multiparamétrico óptimo de análisis de masas de agua (OMP) para las capas intermedias y profundas. El capítulo 3 utiliza las mismas aproximaciones metodológicas que el capítulo 2 (GAMs y OMP) para abordar el estudio de los principales factores ambientales que modulan la distribución del FDOM. El capítulo 4 examina la composición molecular de la DOM en las principales masas de agua del MedSea y la compara con la composición de la DOM en el océano Atlántico adyacente utilizando ESI–FT–ICR–MS. En el capítulo 5 se relacionan las propiedades ópticas de la DOM con su composición molecular y se establecen por primera vez correlaciones múltiples que permiten obtener datos moleculares a partir de medidas ópticas. El capítulo 6 se centra en el estudio de la biodisponibilidad de la DOM y muestra la relevancia del tamaño molecular

para explicarla validando la teoría del continuo tamaño reactividad en el campo. El capítulo 7 contiene una discusión general en donde se abordan cuestiones tanto conceptuales como metodológicas que fueron surgiendo en el transcurso de la realización de esta tesis doctoral y que involucran a todos los capítulos anteriores. Por último el capítulo 8 expone las conclusiones obtenidas en esta tesis doctoral.

Resultados y discusión

En esta tesis doctoral se han utilizado casi 400 muestras recolectadas en perfiles verticales completos (hasta 15 niveles) a lo largo de las 29 estaciones muestreadas en el MedSea y el Atlántico norte adyacente durante la campaña oceanográfica trans–Mediterránea HOTMIX en el año 2014, a bordo del buque oceanográfico Sarmiento de Gamboa. En todas estas muestras se ha determinado la salinidad (S), temperatura potencial (θ), concentración de oxígeno disuelto, utilización aparente de oxígeno (AOU), abundancia de biomasa microbiana (PHA), intensidad de fluorescencia de la clorofila *a* (Chl *a*), nutrientes inorgánicos y carbono orgánico disuelto. Además se ha medido su absorbancia y calculado los coeficientes de absorción y parámetros espectrales de la CDOM (por ejemplo, a254, a325, $S_{275–295}$, $S_{350–400}$, SR) y medido la intensidad de fluorescencia (por ejemplo, pico M, pico T, pico E). El elevado número de muestras recolectadas ha permitido llevar a cabo un análisis estadístico de masas de agua e interceptar 19 masas de agua, un número considerablemente elevado teniendo en cuenta el pequeño tamaño que presenta el MedSea. De las 19 masas de agua encontradas, 10 de ellas se corresponden con aguas profundas distintas debido a eventos climáticos extremos conocidos como transición del Mediterráneo Este y Oeste (EMT y WMT, respectivamente) que cambiaron la estructura y propiedades de las capas profundas de las dos cuencas del MedSea (Roether et al., 2007; Schroeder et al., 2016) dando lugar a masas de agua con características hidrológicas bien diferenciadas. A lo largo de la campaña recogimos además 30 muestras en 9 estaciones específicas atendiendo a sus propiedades físico–químicas, como el máximo profundo de clorofila, el mínimo de oxígeno, el máximo de salinidad o las aguas profundas, para su caracterización molecular y su fraccionamiento por tamaño y estudiar así la relación entre el tamaño molecular y la reactividad.

DOC y propiedades ópticas de la DOM en el mar Mediterráneo

En los capítulos 2 y 3 se muestran las distribuciones a nivel de cuenca y en profundidad del DOC, CDOM y FDOM. La cuenca oriental mostró en superficie mayor DOC que la cuenca occidental debido a la mayor oligotrofía de esta cuenca que produce un desacoplamiento entre la producción y el consumo de DOC. La distribución de *a*254 fue muy similar a la del DOC

correlacionando muy significativamente, lo que confirmó que el coeficiente *a*254 es un buen trazador de DOC. En cuanto a los fluoróforos, se aplicó un análisis estadístico PARAFAC a las matrices de excitación–emisión obtenidas con las medidas de fluorescencia para identificar los principales fluoróforos presentes en el MedSea. Se Identificaron 4 fluoróforos, 3 de ellos de naturaleza húmica (pico C, pico M y pico E) y el otro de origen proteico (pico T). La intensidad de fluorescencia del pico M fue menor en superficie y mayor en profundidad debido a que estos compuestos son sensibles a la fotodegradación. A nivel de cuencas su intensidad fue mayor en la cuenca occidental puesto que estas sustancias son un subproducto de la degradación microbiana y la cuenca occidental presenta mayor actividad heterotrófica y enzimática (Luna et al., 2012). Por el contrario el pico T presentó mayores intensidades en superficie que en profundidad ya que estos compuestos se producen durante la fotosíntesis en la capa fótica, son resistentes a la fotodegradación y en profundidad son consumidos por los microbios gracias a su naturaleza lábil. En la capa epipelágica la mayor parte de la variabilidad de DOC, *a*254, pico M es explicada por la AOU, lo que indica una dominancia de la respiración microbiana neta acumulada. Por el contrario, el pico T fue mayoritariamente explicado por la biomasa bacteriana. En el estudio de las capas intermedias y profundas el análisis OMP facilitó diferenciar el impacto de la mezcla de masas de agua y la mineralización a gran escala de los procesos biogeoquímicos producidos a escala local. Los resultados del OMP indican que los procesos de mezcla de las masas de agua explicaron la mayor parte de la variabilidad del DOC, a254, pico M y pico T. Analizando las dos cuencas por separado se observó que los procesos de mezcla tuvieron una mayor influencia en la cuenca oriental debido a su ultraoligotrofía. El añadir al modelo de mezcla una variable biogeoquímica como es la AOU permitió determinar la parte de la variación debida a los procesos de mineralización a escala local. En este sentido determinamos que los procesos de degradación a escala local del DOC fueron responsables del 31 ± 4% del consumo de oxígeno en el MedSea y que esta contribución fue mucho mayor en la cuenca oriental (66 ± 10%) que en la occidental (24± 4%).

Composición molecular de la DOM en el mar Mediterráneo

Para el estudio de la composición molecular de la DOM, primero aislamos la DOM por extracción en fase sólida con resinas poliméricas (PPL) y posteriormente estos extractos (SPE–DOM) los caracterizamos por espectrometría de masas (ESI–FT–ICR–MS). Se detectaron un total de 6057 masas moleculares de compuestos en las 32 muestras analizadas (29 en el MedSea y 3 en el Atlántico norte adyacente) en el rango de masas de 154–817 Da. De todas estas masas se identificaron 3689 formulas moleculares en el rango de masas de 157–736 Da. A partir de las fórmulas moleculares se calcularon una serie de parámetros como por ejemplo,

el ratio H/C, el ratio O/C, el número de dobles enlaces equivalentes, el peso molecular medio, el índice de aromaticidad y el índice de degradación. Además también clasificamos las fórmulas en grupos de compuestos moleculares como polifenoles, compuestos altamente insaturados o compuestos insaturados alifáticos. Todos estos parámetros moleculares permitieron observar la heterogeneidad que existe en la composición molecular de la DOM entre cuencas y masas de agua del MedSea a pesar de su relativamente pequeño tamaño y sus cortos tiempos de residencia. En esta tesis doctoral se ha determinado que los factores que más influyen en esta heterogeneidad de composición son la zona de formación de las masas de agua y los procesos de mineralización de la DOM. Aprovechando que el MedSea tiene su propia circulación oceánica, se ha seguido la evolución de la SPE–DOM transportada por las aguas intermedias que se forman en la cuenca levantina y circulan longitudinalmente a través de todo el MedSea hasta salir por el estrecho de Gibraltar. Como resultado se ha observado que a medida que la SPE–DOM se va degradando se produce una disminución de la concentración de DOC, y a su vez el DOC que permanece está más degradado. En este sentido, se ha observado una disminución del ratio H/C y una menor proporción de compuestos insaturados alifáticos (de naturaleza lábil) junto con un aumento del peso molecular medio, de oxigenación, del estado de degradación y un enriquecimiento en compuestos altamente insaturados (de naturaleza refractaria). También se analizó si la composición de esta SPE–DOM que sale hacia el océano Atlántico por profundidad a través del estrecho de Gibraltar es diferente a la SPE–DOM que entra por superficie desde el Atlántico, observándose que esta última presenta una composición menos degradada, como demuestra su menor índice de degradación y dobles enlaces equivalentes y mayor proporción de compuestos insaturados alifáticos. Con respecto a las aguas profundas, en la cuenca occidental su composición está modulada por su momento de formación (las aguas más viejas muestran una SPE–DOM más degradada que las añadas más jóvenes), sin embargo en la cuenca oriental la composición está más influenciada por el área de formación de las masas de agua, mar Adriático *versus* mar Egeo. Las aguas más viejas, formadas en el mar Adriático, presentaron una SPE–DOM menos degradada que las aguas más jóvenes, formadas en el mar Egeo, lo que indica que el origen de las masas de agua tiene más peso que su edad en la cuenca oriental del MedSea.

Relación de la composición molecular de la DOM con sus propiedades ópticas

Una vez estudiadas las propiedades ópticas y moleculares de la DOM en el MedSea se estudió si estas propiedades estarían relacionadas entre sí. Para ello se aplicaron correlaciones de Spearman entre las 3689 fórmulas moleculares identificadas con el análisis de espectrometría de masas y los coeficientes de absorción, las intensidades de fluorescencia y

los índices de fluorescencia. Este análisis estadístico indicó que el 52% de las 3689 fórmulas correlacionaron, positiva o negativamente, con uno o más parámetros ópticos. Estas fórmulas suponen el 70% de la intensidad total del espectro de masas lo que indica que las intensidades de absorbancia y fluorescencia covarian con una fracción mayoritaria de la SPE–DOM y no sólo con la fracción fluorescente, que es minoritaria. Además conviene recordar que una correlación estadística entre las fórmulas moleculares y las propiedades ópticas no implica necesariamente que los compuestos que correlacionan presenten en su estructura grupos cromóforos o fluoróforos, sino que indica que tienen un comportamiento biogeoquímico similar (Kellerman et al., 2015). El número de fórmulas moleculares que correlacionaron positivamente con la intensidad de fluorescencia de las sustancias húmicas fueron menores comparados con las correlaciones negativas, sin embargo representaron un mayor porcentaje de las intensidades relativas del espectro de masas. Al contrario, el número de moléculas positivamente correlacionadas con la intensidad de fluorescencia de las sustancias proteicas fueron mucho mayores que el número de correlaciones negativas, pero representaron a un porcentaje de intensidad menor del espectro de masas. Las sustancias húmicas (de carácter refractario) correlacionaron positivamente con fórmulas moleculares de mayor peso molecular (más degradadas), y las proteicas (carácter lábil) con fórmulas de menor peso molecular (menos degradadas). Una vez verificada la existencia de correlaciones significativas entre las fórmulas moleculares y las propiedades ópticas, se aplicaron regresiones lineales múltiples (Pearson) para estimar parámetros moleculares a partir de medidas de absorbancia y fluorescencia. Los modelos obtenidos a partir de 29 muestras con parámetros moleculares medidos permitieron estimar la distribución de dichos parámetros moleculares en todo el mar Mediterráneo, en donde sólo se realizaron medidas de absorbancia y fluorescencia, con un error relativamente bajo. Por lo tanto, por primera vez en el océano abierto, estimamos propiedades moleculares a partir de medidas ópticas, las cuales son mucho más fáciles, rápidas y económicas de obtener.

Estudio de la reactividad de la DOM en el mar Mediterráneo

Finalmente, estudiamos la reactividad de la DOM de estas mismas 29 muestras caracterizadas molecularmente. Para ello se fraccionó la DOM utilizando una célula de ultrafiltración con un filtro de tamaño de poro de 1 KDa lo que permitió obtener dos fracciones de DOM, una de alto peso molecular (>1 KDa) y otra de bajo peso molecular (<1 KDa). Se analizó este fraccionamiento de la DOM y la AOU en las muestras de la capa intermedia (máximo de salinidad) por ser la única que cruza todo el MedSea, con el objetivo de comprobar si se cumple la teoría del continuo reactividad (Amon and Benner, 1996). Esto permitió

observar cambios en el fraccionamiento por tamaño de la DOM a medida que las aguas intermedias se van envejeciendo en su recorrido desde la cuenca levantina hacia el océano Atlántico. Durante este recorrido el agua intermedia experimenta una disminución de la concentración de DOC con el aumento de AOU tanto en la fracción total de DOC como en la de alto peso molecular, sin embargo la fracción de bajo peso molecular no experimenta esta disminución. Estos resultados revelan que los compuestos de alto peso molecular son preferiblemente consumidos durante los procesos de mineralización, lo que valida la teoría del continuo de reactividad. Además, el fraccionamiento del DOC en alto y bajo peso molecular permitió establecer, por primera vez, la contribución de cada fracción a la mineralización total. También se estudiaron las fracciones coloreadas, observándose que, en paralelo al consumo de DOC, las sustancias tipo húmicas aumentaban tanto en la fracción de alto peso molecular como en la de bajo peso molecular, verificando así la hipótesis de la bomba microbiana de carbono que establece que la DOM refractaria es producida durante la mineralización de materia orgánica lábil (Jiao et al., 2010). Por lo tanto, se ha comprobado *in situ* la teoría del continuo reactividad y la hipótesis de la bomba microbiana utilizando el mar Mediterráneo como un incubador natural.

Conclusiones

Las conclusiones específicas de esta tesis doctoral son las siguientes:

1) En la capa epipelágica del mar Mediterráneo la variabilidad en la distribución del DOC, el coeficiente de absorción medido a 254 nm (a254) de la materia orgánica disuelta coloreada (CDOM), la fluorescencia de las sustancias húmicas marinas y los índices de fluorescencia (índice biológico, índice de humificación y el rendimiento cuántico de fluorescencia medido a 340 nm) a escala de cuenca se explica principalmente por la respiración acumulada neta de la comunidad (utilización aparente de oxígeno). Por el contrario, mientras la variabilidad del coeficiente de absorción de la CDOM medido a 325 nm (a325) es controlado principalmente por la temperatura potencial, la fluorescencia de las sustancias proteicas y fúlvicas de origen terrestre están influenciadas mayoritariamente por la abundancia de procariotas heterotróficos.
2) Las distribuciones a escala de cuenca del DOC y la DOM fluorescente (FDOM) en las capas meso– y batipelágicas del mar Mediterráneo están controladas principalmente por la mezcla de masas de agua y los procesos de mineralización a gran escala. Considerando las cuencas oriental y occidental por separado, la primera está más

afectada por los procesos de mezcla de masas de agua lo cual está relacionado directamente con su ultra–oligotrofía.

3) Los procesos de mineralización del DOC a escala local contribuyen en un 66 ± 10% a la demanda de oxígeno en la cuenca oriental y solamente en un 24 ± 4% en la cuenca occidental del mar Mediterráneo.
4) La composición molecular de la DOM en el mar Mediterráneo está controlada principalmente por dos factores, el lugar de formación de las masas de agua y la mineralización de la DOM usando la utilización aparente de oxígeno como una variable canónica. Específicamente, el agua que sale del mar Mediterráneo hacia el océano Atlántico presenta una composición molecular diferente a la DOM presente en el agua que entra por superficie en el mar Mediterráneo procedente del océano Atlántico.
5) En el océano abierto del mar Mediterráneo se encontró una relación entre las propiedades ópticas y moleculares de la DOM, corroborando así resultados previos obtenidos en zonas costeras, estuarios y ecosistemas de agua dulce.
6) Siguiendo la degradación microbiana de la DOM a lo largo del máximo de salinidad característico de las aguas intermedias del mar Mediterráneo y aplicando, por primera vez, una aproximación de estudio *in situ*, demostramos que la fracción de alto peso molecular de la DOM es la responsable en exclusiva del consumo de oxígeno en las aguas intermedias, validando de este modo la teoría del continuo tamaño–reactividad en el campo.
7) El tiempo de renovación de las aguas intermedias del mar Mediterráneo es de 13 años y la tasa neta de consumo del DOC en estas aguas es de 0.92 µM por año.
8) A lo largo de esta tesis hemos encontrado evidencias que avalan las hipótesis del continuo tamaño–reactividad y la de la bomba microbiana de carbono a través de los resultados obtenidos de los análisis ópticos, moleculares y del fraccionamiento por tamaños de la DOM.

Chapter 1
Introduction

1.1 What is dissolved organic matter?

Globally, organic matter in seawater is made of a complex mixture of compounds in a wide range of sizes. To facilitate its study, organic matter has been operationally divided into particulate organic matter (POM) and dissolved organic matter (DOM). Thus, POM is defined as the fraction physically retained by filters with pore sizes of approximately 0.2 to 0.7 µm, whereas DOM is the portion of organic material that pass through such filter. DOM forms a continuum, and it is further classified as truly dissolved or low molecular weight (LMW) DOM (<200 nm or <1 KDa) and colloidal or high molecular weight (HMW) DOM (>200–700 nm or >1 KDa) fractions (Figure 1.1).

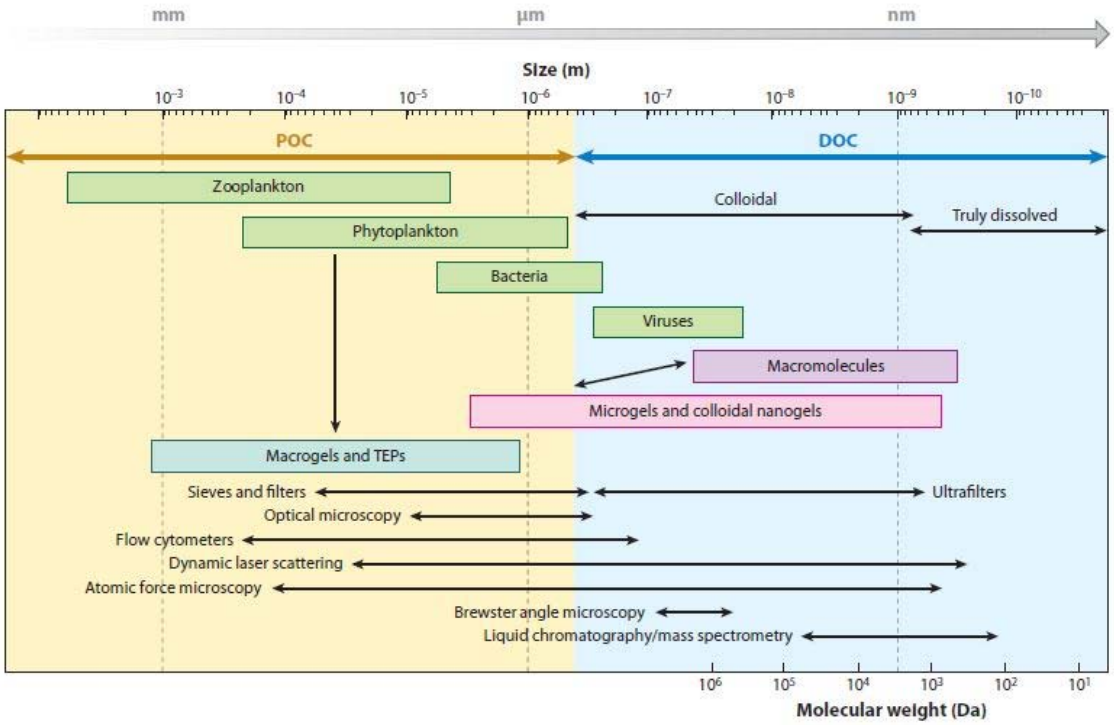

Figure 1.1: *Operational classification of organic matter in seawater based on size ranges. Green boxes represent living organic matter, blue and pinkish boxes depict non–living organic matter. On the bottom of the figure are summarized the main methods used to measure each size fraction. Taken from Verdugo (2012).*

Marine DOM is one of the largest and least understood reservoirs of reduced carbon on the Earth's surface. At 662 Pg C (1 Pg = 1015 g), DOM represents 96% of the total organic carbon in the oceans (Hansell et al., 2009; Hansell, 2013). Despite its large global inventory, DOM exists in the open ocean at extremely low concentrations, generally ranging from 34 to 80 µmol C kg–1 (Hansell et al., 2009). DOM is produced mainly in the ocean epipelagic layer (0–150 m depth) as a result of phytoplankton photosynthesis and subsequent microbial and classic food web interactions (Carlson, 2002; Latasa et al., 2005; Gutiérrez–Rodriguez et al.,

2010). Most of this recently produced DOM is labile and thus has short lifetimes, being quickly respired back to CO_2. However, a small fraction escapes rapid mineralization because it is originally resistant or it is transformed into resistant materials through biotic or abiotic processes, being accumulated in the surface layer for eventual export to the dark ocean (>150 m depth) by convective overturning and vertical mixing. Accordingly, Hansell (2013) classified the DOM into the following five fractions based on their reactivity or lifetime (Figure 1.2): labile DOM (LDOM), semi–labil DOM (SLDOM), semi–refractory DOM (SRDOM), refractory DOM (RDOM) and ultra–refractory DOM (URDOM) with decreasing reactivity, respectively. The LDOM represents a small fraction of the DOM pool as it is rapidly consumed by marine microorganisms in time scales of hours to days, supporting the bacterial carbon and nutrient demand at the surface waters. This fraction contains monomers and oligomers including dissolved free neutral sugars, dissolved free amino acids, organic sulphur and phosphorous compounds and hydrolysable HMW compounds (Carlson and Hansell, 2015). The SLDOM fraction is more resistant to microbial degradation than LDOM and turns over on time scales of months to years. Therefore, it is accumulated in the surface water, being the most important exportable DOM fraction to the mesopelagic layer (Figure 1.2). This fraction is made partly of polysaccharides, dissolved combined neutral sugar and amino acids. The SRDOM fraction shows turnover times of decades and it comprises compounds of intermediate reactivity. This fraction accumulates in the surface and then it is exported to the mesopelagic layer playing a potential role into C–sequestration. The RDOM is the most resistant fraction to microbial degradation and, therefore, persists into the ocean interior for centuries to millennia. It is ubiquitous in the water column and represents the largest fraction of accumulated DOM playing a key role on C–sequestration. It is mainly formed by LMW DOM (Amon and Benner, 1994, 1996). Finally, the URDOM is a small fraction of RDOM that comprises thermogenic black carbon and it can persist in the ocean for 2500–13900 ^{14}C–years (Ziolkowski and Druffel, 2010).

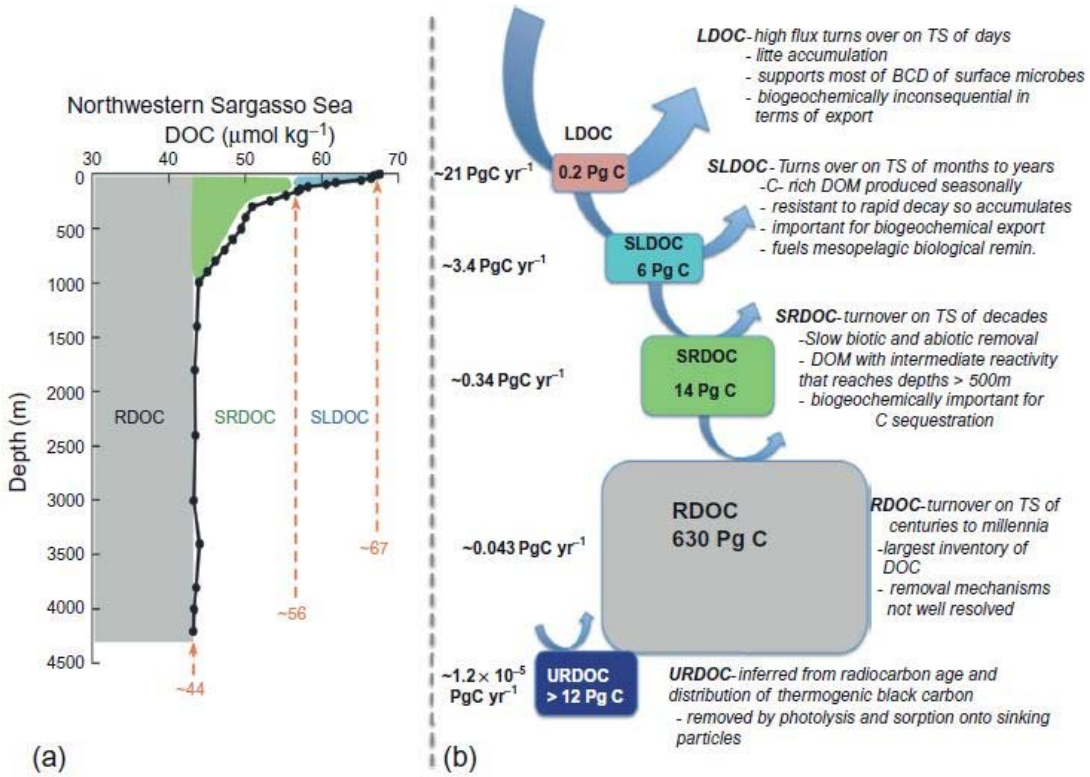

Figure 1.2: *Classification of dissolved organic carbon (DOC) fractions based on its reactivity.TC = time scale, BCD = bacterial carbon demand. Taken from Carlson and Hansell (2015).*

1.2 Which roles does DOM play in marine ecosystems?

DOM delivers key services to marine ecosystems since it is 1) the primary substrate for the food web and provides the nutrients and energy for heterotrophic growth (Cuss and Guéguen, 2015), contributing significantly to both the coastal and open ocean recycled and new production (Bronk et al., 1994; Hansell et al., 2009); 2) regulates sunlight absorption protecting living organisms from the potentially harmful UV radiation (Fichot et al., 2008; Nelson and Siegel, 2013); and 3) acts as a trace metal ligand reducing toxicity and avoiding the adsorption loss of bioactive dissolved metal ions to sinking particles (Hirose, 2007). In addition, DOM 4) contributes to the total alkalinity of seawater (Kim and Lee, 2009); 5) participates in the air–sea exchange of volatile organic carbon (Dachs et al., 2005) and decreases the surface tension of the water altering air–sea gas exchange rates (Moore et al., 2008); and 6) presents antioxidant activity, minimizing the negative effects of free radicals in aquatic organisms (Romera–Castillo and Jaffé, 2015) among other relevant functions.

1.3 Global distribution of DOM

The distribution of DOM, referred as the distribution of dissolved organic carbon (DOC), in the world ocean has been studied over the last two decades and has been summarized in Figure 1.3. Higher concentrations (70–80 µmol C kg^{-1}) are found at the surface in the tropical

and subtropical biogeographic provinces (40°N to 40°S), because the ultimate source of DOM is from phytoplankton photosynthesis in the euphotic zone, together with the vertical stratification in these regions, which favours DOM accumulation. Lower concentrations (40–60 µmol C kg^{-1}) are found at the surface of equatorial regions, in subpolar seas and in the Southern Ocean, where DOM–depleted deep ocean waters upwell to the surface. Deep waters of the Pacific Ocean are especially depleted in DOM due to the subsequent decay of these materials through the thermohaline circulation (Hansell et al., 2009; Hansell, 2013).

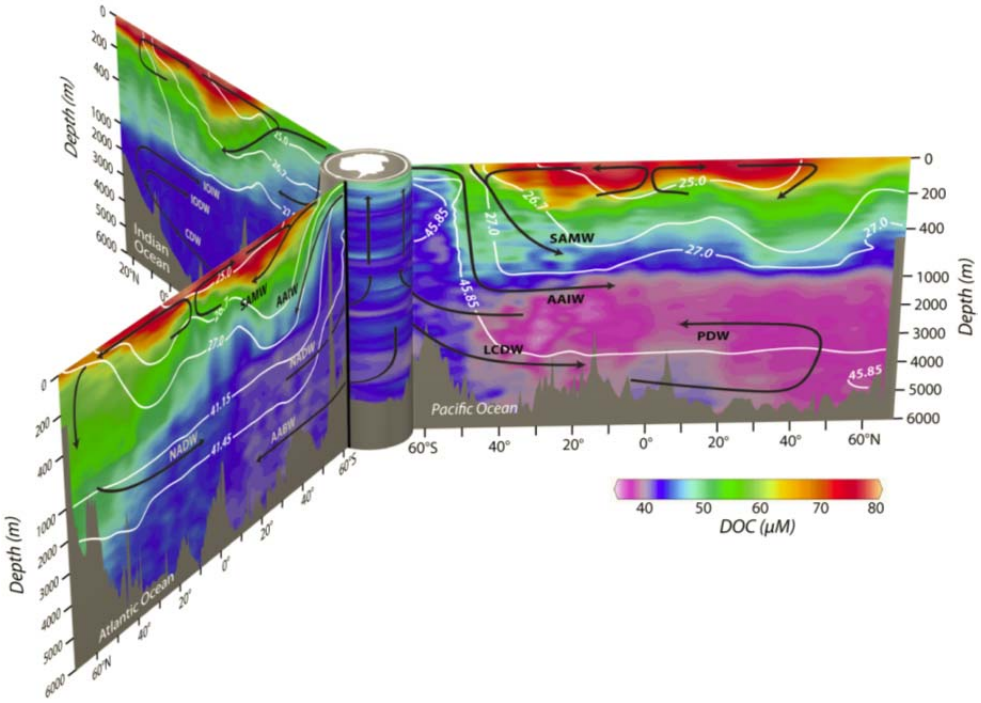

Figure 1.3: *Dissolved organic carbon (DOC) distributions in the global oceans (µmol kg^{-1}). Black arrows represent the main water masses and white lines depict isopycnal surfaces. Taken from Hansell et al. (2009).*

The fraction of the DOM containing nitrogen, dissolved organic nitrogen (DON), has been also studied in the last decades (Antia et al., 1991; Bronk, 2002; Berman and Bronk, 2003; Aluwihare and Meador, 2008; McCarthy and Bronk, 2008). Surface global concentrations of DON ranged from 2 to 7 µmol N Kg^{-1}, with a mean concentration of 4.4 ± 0.5 µmol N Kg^{-1} (Letscher et al., 2013). Higher concentrations of DON (>5 µmol N Kg^{-1}) are found in regions either adjacent to or immediately downstream of eastern boundaries and equatorial upwelling zones (Letscher et al., 2013). On the contrary, lower concentrations are observed polewards and westwards of upwelling regions, whereas subtropical gyres are sinks for DON due to biological consumption (Sipler and Bronk, 2015). DON concentrations decrease with depth, in the deep ocean concentrations generally ranging from 2 to 3 µmol N L^{-1} (Torres–Valdés et al., 2009; Sipler and Bronk, 2015). DON is mainly removed by vertical mixing and subsequent

remineralization by microbes below the mixed layer (Letscher et al., 2013). Deep–ocean DON determinations are especially uncertain due to the low concentration of DON together with the high NO_3^- concentrations present in the deep waters. Note that DON is determined by the difference between total dissolved nitrogen (TDN) and inorganic nitrogen (NO_3^-, NO_2^- and NH_4^+).

The global dissolved organic phosphorous (DOP) distributions show almost exclusively elevated values in the upper 100 m of the water column (Karl and Björkman, 2015). DOP is often reported as the percentage of total dissolved phosphorous (TDP) pool which includes dissolved inorganic and organic P. Global ocean DOP at the surface (<100 m) range between 40–60% of TDP, decreasing to 18–38% of TDP in the intermediate waters and to 8–18% of TDP in deep waters (>500 m) (Karl and Björkman, 2015).

1.4 Biological and microbial carbon pumps: long–term storage of DOM in the ocean

The main biological mechanism of organic matter export into the ocean interior involves the biological carbon pump, which comprises the production of organic matter and biominerals in the epipelagic layer, the sinking of POM together with the vertical diffusion (turbulent and convective mixing) of DOM into the meso– and bathypelagic layers and its decomposition in the ocean interior (De La Rocha, 2006). It is estimated that ~50 Pg C yr^{-1} is fixed by photosynthesis in the global ocean (Carr et al., 2006; Chavez et al., 2010). Most of this fixed carbon is converted straight back into CO_2 by zooplankton and bacteria in the euphotic zone and ~20% escapes rapid remineralization in the surface and sinks to the ocean interior mostly in the form of particulate material (~8 Pg C yr^{-1}), whereas only 2 Pg C yr^{-1} enters the ocean interior as DOM (Hansell, 2009). Further, about 1–6% of the POM export production reaches the seafloor (Dunne et al., 2007). Most of the 662 Pg C of DOM accumulated in the oceans is resistant to microbial degradation (RDOM, Figure 1.2) and, therefore, stored for hundreds to thousands of years (Hansell et al., 2009; Hansell, 2013). The mechanisms behind this long–term storage of carbon are still poorly understood (Dittmar, 2015). The microbial carbon pump (MCP) concept has emerged in recent years as one of the most plausible mechanisms to explain this storage. Within the MCP framework, refractory DOM is originated as a by–product of the microbial mineralization of bioavailable organic matter (Ogawa et al., 2001; Jiao et al., 2010).

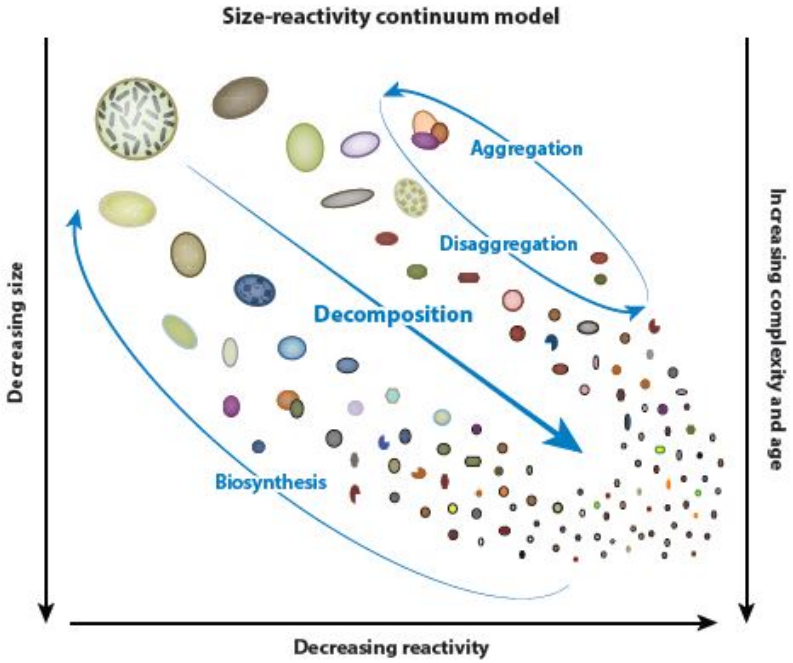

Figure 1.4: *Graphical representation of the size reactivity continuum (SRC) model showing a net flow of organic carbon from larger to smaller molecules. With increasing decomposition the chemical complexity of organic matter increases, biological reactivity declines, and the radiocarbon ages increase. Biosynthesis transforms organic carbon from small into larger molecules* (Benner and Amon, 2015).

Closely related with the MCP concept is the size–reactivity continuum (SRC) hypothesis (Figure 1.4) to explain marine DOM reactivity (Amon and Benner, 1996; Benner and Amon, 2015). According to this assumption, larger molecules are preferentially degraded by microbes leading to smaller complex structures, which present lower reactivity and more age. More recently, a dissolved organic matter size–age–composition relationship was reported supporting the SRC model (Walker et al., 2011, 2016a, 2016b). In addition, these studies suggest microbial degradation as the primary source of recalcitrant DOM to the deep ocean, in agreement with the MCP conceptual model.

Another feasible explanation of the DOM persistence in the ocean is the dilution hypothesis (Arrieta et al., 2015; Dittmar, 2015). As DOM is made up of a complex mixture of hundred thousands of compounds, if concentrations of individual DOM compounds are too low, the viable uptake of DOM by prokaryotes is unfavourable (Jannasch, 1994), as these organisms can utilize substrates only above a certain concentration. This threshold concentration prevents an energy–efficient uptake of DOM and leads to low DOM turnover rates due to the limited encounters between bacteria and substrate. This hypothesis, contrary to the SRC, considers all compounds as potentially labile and its apparent refractory nature would mask their diluted concentrations (Kattner et al., 2011).

The intrinsic stability of chemical structures of deep sea DOM could further explain the refractory nature of this material. It is possible that heterotrophs lack enzymatic pathways to decompose certain molecular structures and therefore they are accumulated in the ocean interior (Dittmar, 2015). As an example, highly oxygenated molecules could be thought as instable molecules per se, however e.g. carboxyl–rich alicyclic molecules (considered refractory due to the highly degree of oxygenation; Hertkorn et al., 2006) present a high polarity and, therefore, they could need specific and energy–efficient uptake systems (Kattner et al., 2011). Following this hypothesis, the less reactive fraction of DOM would prevail in the oldest water masses of the deep ocean (Hansell, 2013).

Another plausible reason explaining the long–term DOM storage could be adverse environmental conditions, as it happens in anoxic or oligotrophic areas where the lack of oxygen and/or inorganic nutrients prevent the degradation of DOM stimulating its accumulation (Dittmar, 2015).

Photochemistry presents a dual role in the context of the DOM stability. On the one hand, it can produce refractory molecular structures in the surface layer, as experiments have demonstrate that photochemically modified DOM resisted microbial degradation over months (Kieber et al., 1997; Benner and Biddanda, 1998; Ortega–Retuerta et al., 2010a; Rossel et al., 2013). On the other hand, when refractory compounds from the deep sea reach the surface again through upwelling or the meridional overturning circulation, they are decomposed and returned back into active cycles by photochemical reactions (Moran and Zepp, 1997; Beaupré and Druffel, 2012; Gonsior et al., 2014).

Although there are evidences in favour of all these hypotheses, up to date none of them is conclusive. The reason of the DOM stability in the ocean is likely due to a combination of the different mechanisms exposed above (Dittmar, 2015).

1.5 DOM in an ocean under global change

Evidences of the effects of global change in the oceans have been reported, including significant shifts in seawater temperature, pH, sea level, circulation patters, oxygen content and eutrophication (Church et al., 2013; Rhein et al., 2013). Nowadays, it is known that oligotrophic subtropical gyres are areas where DOM is accumulated and exported (Carlson et al., 1994; Church et al., 2002). Future scenarios predict an extension of those areas, and hence an increase of the net oceanic DOM accumulation. Experiments simulating ocean acidification conditions show different results, from DOM accumulation (Paul et al., 2015; Zark et al., 2017)

to no effect on the DOM concentration (Zark et al., 2015; Aparicio et al., 2016; Maugendre et al., 2017), but also enhancement of bacterial DOM consumption (Engel et al., 2014; Endres et al., 2014) and a reduction of the formation of colloids and microgels (Chen et al., 2015). Therefore, the effects of climate change on DOM dynamics or chemical composition are still unclear (Moran et al., 2016). A side effect of ocean acidification on the role of DOM is the decline of the DOM–trace metal interaction, consequence of the preferential free form of the trace metals at lower pH of the seawater. A key element in the ocean DOM cycle is the dissolved oxygen (O_2), which is prone to undergo a decline under rising temperatures (Keeling et al., 2010). This O_2 decline is linked to the lower O_2 solubility (up to 15%), but most importantly due to the ocean stratification, associate to the higher temperatures, that preclude ocean ventilation and the transport of O_2 from surface to subsurface waters (Helm et al., 2011). Besides, in the deep ocean, higher temperatures would promote POM and DOM decomposition, which consequently would produce a further decline in the O_2 concentrations. In addition, anthropogenic nutrients fertilization would also produce a decline of O_2 concentrations due to high rates of primary production that lead to high rates of oxygen consumption in subsurface waters (Keeling et al., 2010). Further, eutrophication is suggested to produce changes in both quantity and quality of DOM (Aparicio et al., 2016). These authors observed an increase of the DOC concentration in nutrient amended treatment of mesocosms experiments as compared to the control. Further, the higher humification degree and average molecular weight found in the nutrient enriched experiment suggest changes on the DOM quality under eutrophication conditions. Another direct effect of stratified waters is the lower concentration of the UV–protective CDOM in the surface due to higher CDOM photodegradation and lower inputs of CDOM from deep waters enhancing the UV radiation penetration into the ocean (Zepp et al., 2011).

1.6 Chemical characterisation of DOM

As DOM is made of a complex mixture of compounds, the study of its composition have been approached from a wide variety of characteristics, e.g. from elemental ratios of carbon, nitrogen and phosphorous, optical signatures, stable and radio–isotopic content, inventory of dissolved compounds (amino acids, carbohydrates, lipids) to molecular level characterization (Benner et al., 1992, 1997; Bauer, 2002; Benner, 2002; Hertkorn et al., 2006; Dittmar and Stubbins, 2014; Beaupré, 2015; Stedmon and Nelson, 2015; Hertkorn et al., 2016).

The DOM pool is mainly composed by C, H, O, N and P. The stoichiometry of the elemental ratios of the bulk DOM is different in surface and deep ocean waters (Benner, 2002;

Hopkinson Jr. and Vallino, 2005). Hopkinson Jr. and Vallino, (2005) found C:N:P ratios of 374:27:1 and 3511:202:1 for surface and deep waters, respectively. These results show that DOM in surface waters is depleted in N and P compared to the average marine phytoplankton composition (Redfield ratio of 106:16:1; Redfield et al., 1963) and this depletion is still more acute for deep waters. Those ratios are larger than the production/decomposition ratio of the DOM pool, with average values of 199:20:1 (Hopkinson Jr. and Vallino, 2005; Lønborg and Álvarez–Salgado, 2012) or 225:19:1 (Letscher et al., 2015). These results show that DOM is degraded with a C:N:P ratio remarkably lower than the bulk DOM but higher than the Redfield ratio. In addition, these results also suggest that DOC is exported downwards more efficiently than DON and DOP linked to the fact that compounds containing C, N and P are more bioavailable than compounds containing only C and N, which are in turn more bioavailable than those hosting only C (Lønborg et al., 2017). In this regard, Letscher et al. (2015) reported export efficiencies of 55.0%, 33.0% and 17.5% below 100 m for DOC, DON and DOP, respectively.

1.6.1 Optical characterisation of DOM

A small fraction of the total DOM pool absorbs light in the UV and visible ranges of the light spectrum. It is referred to as chromophoric DOM (CDOM) and it is a ubiquitous component in the coastal and open ocean. In seawater, the components that contribute to the total light absorption are pure seawater, living phytoplankton, detrital particulates and CDOM. For wavelengths <440 nm (UV and blue region) CDOM is by far the most important component regulating the total absorption in the surface open ocean (Figure 1.5) and can contribute to about 50% of the light absorption at 400 nm and >70% at 300 nm (Nelson and Siegel, 2013; Pérez et al., 2016). This contribution can increase up to almost 100% below the deep chlorophyll maximum (DCM; Bricaud et al., 2010). At 440 nm, which is the wavelength used by satellites to estimate the ocean chlorophyll *a* (Siegel et al., 2002), phytoplankton and CDOM contribute in the same proportion to the total light absorption (Figure 1.5) accounting by about 30% each (Bricaud et al., 2010, Nelson and Siegel, 2013).

This control of light penetration into the ocean has ecological implications as CDOM can limit the light available for photosynthesis and also absorbs harmful UVB and UVA radiation, weakening the negative impacts of high UV exposure on plankton populations (Arrigo and Brown, 1996).

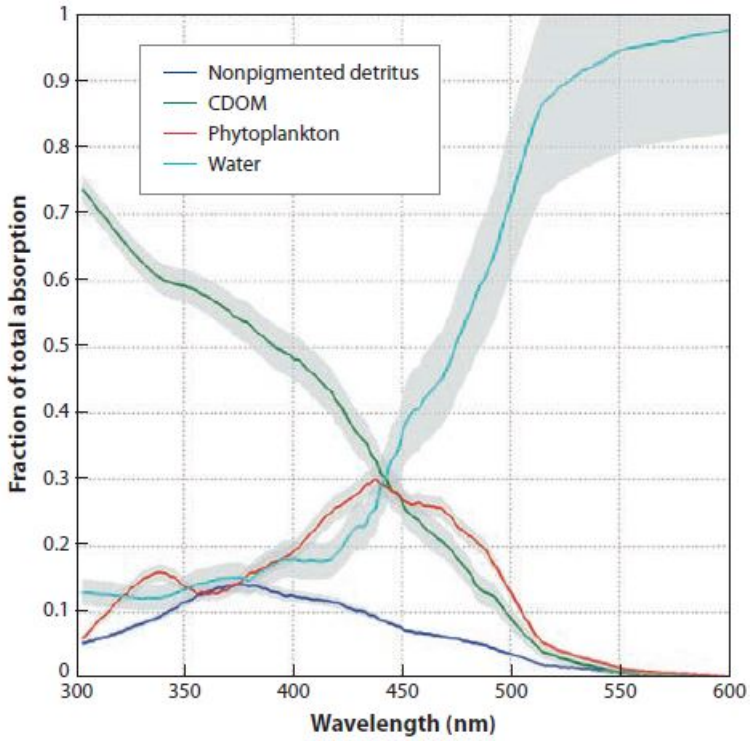

Figure 1.5: Estimated mean relative contributions of CDOM and other components to the total absorption at wavelength of 300–600 nm. Taken from Nelson and Siegel (2013).

Operationally, CDOM measurements have been used to estimate DOC concentrations (Fichot et al., 2013; Lønborg and Alvarez–Salgado, 2014), as well as to distinguish DOM derived from terrestrial material to that originated by aquatic organisms (Stedmon and Nelson, 2015). As the chemical composition of CDOM is largely unknown, CDOM cannot be quantified in moles per litre. Instead, these chromophoric compounds are counted by the strength of their optical signals. Absorption coefficients at specific wavelengths, absorption coefficient ratios, and spectral slopes over defined wavelength ranges have been used to trace changes in CDOM composition driven by water masses transport and mixing, microbial production and photochemical decomposition processes (Nelson et al., 2007). Absorption coefficients at a specific wavelength are commonly used to quantify different CDOM fractions and the spectral slopes offer insight regarding the source, processing, molecular weight and chemistry of DOM (Coble, 2007; Helms et al., 2008; Catalá et al., 2015a). An example of the use of UV and visible absorption in the field is presented in Figure 1.6 where contrasting CDOM spectra evidences the optical and therefore chemical differences along the water column of the Catalan Sea. Note that absorption increase exponentially toward shorter wavelengths. The ratio of the absorption coefficients at 254 and 365 nm, $a(254/365)$, is an indicator of the average molecular weight of the coloured fraction of DOC; the higher the ratio, the lower the average molecular weight (Dahlén et al., 1996; Engelhaupt et al., 2003). The ratio between spectral

slopes at 275–295 nm and 350–400 nm (SR) presents a good correlation with the origin (terrestrial vs marine) and the aromaticity of CDOM; ratios below 1 are characteristic of highly aromatic materials of terrestrial origin (Helms et al., 2008). The C–specific absorption coefficient at 254 nm is used as an indicator of aromaticity (Weishaar et al., 2003).

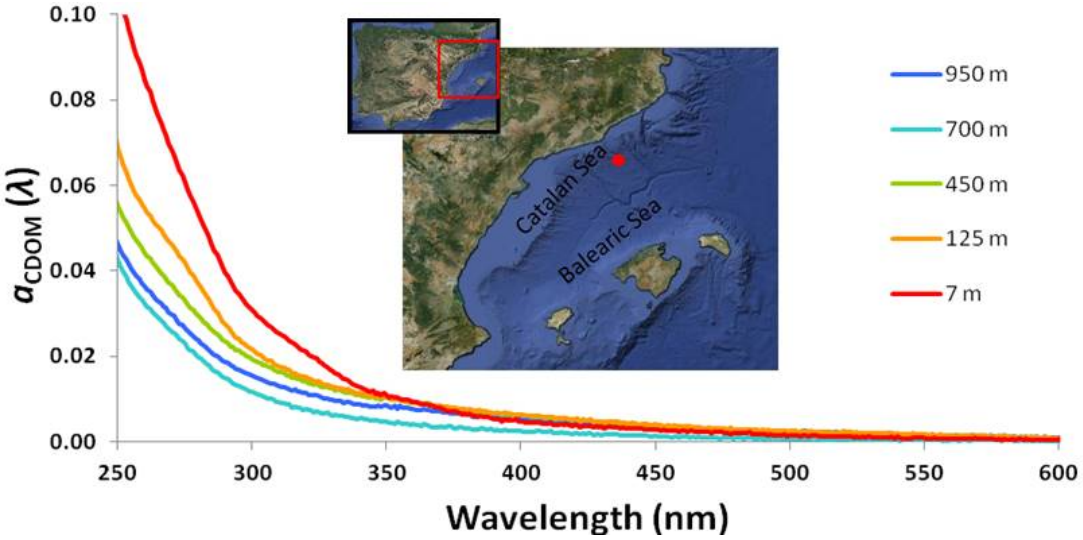

Figure 1.6: *Example of absorption spectra of CDOM, $a_{CDOM}(\lambda)$, for the water samples collected through the water column in the Catalan Sea in October 2013. Red dot in the map represent the station where the samples were collected.*

The distribution of CDOM in the oceans has been obtained from field observations (Yamashita and Tanoue, 2009; Bricaud et al., 2010; Ortega–Retuerta et al., 2010a; Lønborg and Álvarez–Salgado, 2014; Catalá et al., 2015a) and by satellite estimates (Siegel et al., 2002; Mannino et al., 2008; Nelson et al., 2010; Ortega–Retuerta et al., 2010b; Bricaud et al., 2012; Nelson and Siegel, 2013). Higher CDOM levels are found in coastal regions, over continental shelves and estuaries where inputs of terrigenous DOM are significant. Although CDOM has been historically under–sampled in the open ocean, the global ocean distribution of coloured DOM has been recently reported (Nelson et al., 2010; Nelson and Siegel, 2013; Catalá et al., 2015a). The highest abundances are found at high latitudes and in upwelling regions, indicating a connection to both productivity and CDOM–rich deep waters (Stedmon and Nelson, 2015). The lowest concentrations are observed in the subtropical gyres due to the low productivity, high stratification and large photochemical removal (Figure 1.7). In the bottom layers of the major basins (Figure 1.7) CDOM at 325 nm showed less variability, suggesting that, like DOC, abyssal CDOM is biorefractory. In the Pacific and Indian Oceans CDOM (a325) correlated with AOU, suggesting that CDOM is produced as a by–product of microbial respiration (Nelson et al., 2010; Catalá et al., 2015a). However, this correlation was not found in the Atlantic Ocean probably because of water mass ventilation rates, larger in the Atlantic

Ocean than in the Pacific and Indian Oceans, would exceed the production rates of CDOM in the ocean interior masking the CDOM–AOU correlation (Nelson et al., 2010).

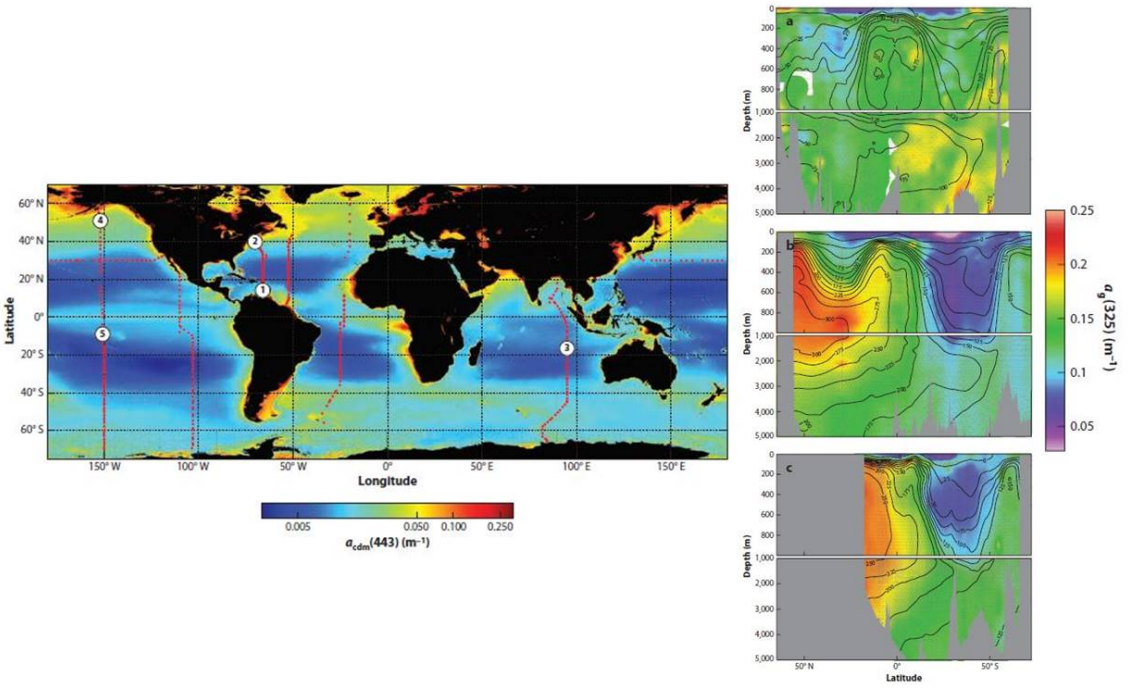

Figure 1.7: The left panel represent the global surface ocean distribution of CDOM plus detrital particle absorption at 443 nm derived from satellite data (1997–2010). Red dots represent field samples. Right panel represent the absorption coefficient at 325 nm across the (a) Atlantic, (b) Pacific and (c) Indian Ocean basins. Adapted from Nelson and Siegel (2013).

Thus, the distribution of CDOM in the major ocean basins is controlled by a balance between microbial production in the mesopelagic layer, surface photochemical removal and water mass mixing (Coble, 2007; Yamashita and Tanoue, 2009; Nelson et al., 2010; Álvarez–Salgado et al., 2013). The main source of autochthonous CDOM appears to be the microbial degradation of organic matter (Nelson et al., 1998; Nieto–Cid et al., 2006; Jörgensen et al., 2011) and the main sink in the ocean is thought to be solar bleaching (Nelson and Siegel, 2013).

A small fraction (3–15%) of the CDOM pool is able to emit the light absorbed in the UV range of the spectrum in the form of blue fluorescence, constituting the fluorescent dissolved organic matter (FDOM) pool. The fluorescence and absorbance properties of DOM are connected by the quantum yield of fluorescence (QY(λ)). QY(λ) is the amount of absorbed light at λ nm that is reemitted at longer wavelengths in form of fluorescence (Green and Blough, 1994). In the ocean, the quantum yield of fluorescence of the humic–like substances, QY(340), presents values <3% (Catalá et al., 2015a; Wünsch et al., 2015). The quantum yield is higher for tyrosine and tryptophan (13–14%), one order of magnitude higher than for phenylalanine, 3%

(Chen, 1967; Yamashita and Tanoue, 2003). Natural fluorescence properties of seawater and its usefulness to trace freshwater inputs in coastal zones were firstly recognized in 1949 (Kalle, 1949). However, from relatively recent years (almost two decades ago) methodological improvements (e.g. the approach of collecting data as excitation–emission matrices, EEMs) in fluorescence measurements and interpretation have allowed the extensive use of fluorescence properties to study DOM composition and dynamics in the ocean (Coble et al., 1990). EEMs consist in a number of fluorescence emission scans at different excitation wavelengths that are compiled into a matrix (Figure 1.8). EEMs contain a huge amount of information and often are presented as the intensities of individual excitation–emission pairs or peaks associated with different compound classes (Coble, 2007). The most common peaks assignments are those summarized in Table 1.1 and defined by Coble (1996) and Stedmon et al. (2003). FDOM are classically classify in two groups of aromatic compounds: 1) protein–like substances, related mainly to the aromatic amino–acids, which absorb at <300 nm; and 2) humic–like substances related to terrestrial and marine humic acids and aquatic fulvic acids, which absorb at >300 nm (Coble, 2007; Nelson and Siegel, 2013; Stedmon and Nelson, 2015).

Table 1.1: Classical defined peaks and locations in the excitation/emission matrices (EEMs) obtained for marine FDOM in water samples. [a]Coble, 1996, 2007; [b]Stedmon et al. (2003). Adapted from Coble, 2014.

Peak	Excitation max (nm)	Emission max (nm)	Description
T	275	340	Tryptophan–like, amino acid–like, autochthonous [a]
B	275	305	Tryptophan–like, amino acid–like, autochthonous [a]
–	260	282	Tryptophan–like, amino acid–like, autochthonous [a]
A	260	400–460	Humic–like, terrestrial [a]
C	320–360	420–460	Humic–like, terrestrial [a]
M	290–310	370–410	Humic–like, marine [a]
E	455	521	Humic–like, soil fulvic acid [b]

The protein–like substances group is associated with the fluorescence intensity of tryptophan (peak T, Coble, 1996), tyrosine (peak B, Coble, 1996) and phenylalanine (Jørgensen et al., 2011), which typically present maximum fluorescence at excitation (Ex)/emission (Em) wavelengths of Ex/Em 280 nm/350 nm, 275 nm/305 nm and 260 nm/282 nm, respectively. In this PhD thesis we will focus on the fluorescence evolution of peak T because peak B is strongly affected by the Raman scattering band of water leading to unreliably low fluorescence signal/noise ratio and phenylalanine is often quenched by tryptophan. The humic–like substances are classically divided into 4 main groups, peak A (Ex/Em 250 nm/435 nm, Coble, 1996) due to general humic substances, peak C (Ex/Em 340 nm/440 nm, Coble, 1996) representing the terrestrial humic substances, peak M (Ex/Em 320 nm/410 nm, Coble, 1996)

due to marine humic compounds and peak E (Ex/Em 450 nm/520 nm, Stedmon and al., 2003) due to soil fulvic acids.

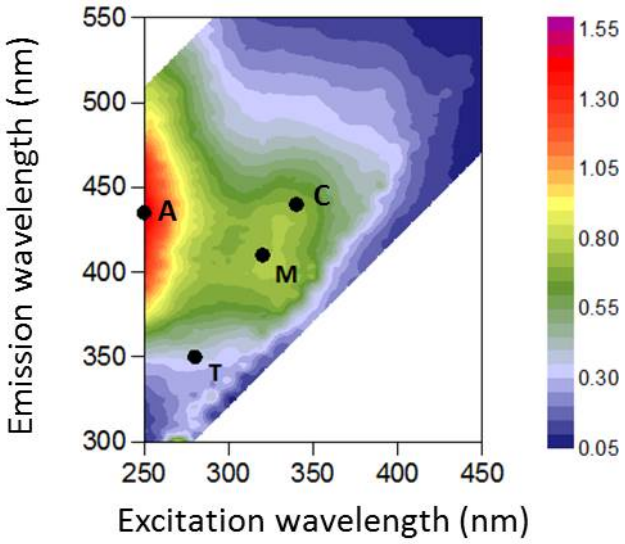

Figure 1.8: *Excitation–emission matrix of a deep ocean sample from the HOTMIX cruise.*

Since EEMs produce a huge amount of data, in the last decade parallel factor analysis (PARAFAC) has been applied to process this data. PARAFAC is a multivariate statistical technique that decompose the combined fluorescence signal into individual and independent components as it is shown in Figure 1.9 (Bro, 1997; Stedmon and Bro, 2008; Murphy et al., 2010). For the case of fluorescence EEMs, a three–way arrays dataset (sample x excitation wavelength x emission wavelength; Figure 1.9) is decomposed by PARAFAC into a set of trilinear terms and a residual array:

$$x_{ijk} = \sum_{f=1}^{F} a_{if} b_{jf} c_{kf} + e_{ijk}$$

Where, i = 1, …, I represents the sample; j = 1, …, J represents the emission wavelength; k = 1, …, K represents the excitation wavelength; x_{ijk} is the fluorescence intensity of the sample i measured at the emission wavelength j and at the excitation wavelength k (measured data); e_{ijk} is the residual due to the unexplained variability (e.g un–modeled variation, scatter and instrument noise); f correspond to a PARAFAC component and finally parameters a, b and c are the outcomes of the model and represent concentration, emission spectra and excitation spectra of the underlying fluorophores, respectively.

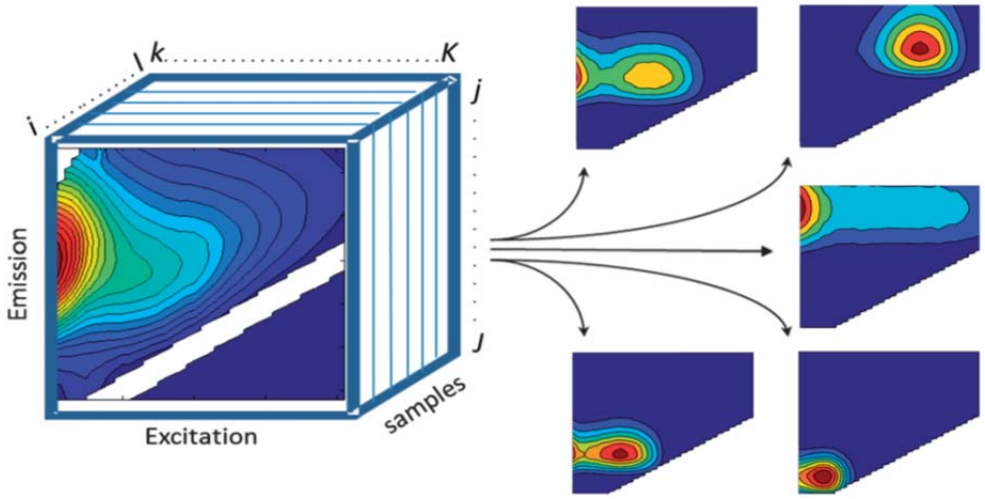

Figure 1.9: *Parafac applied to an EEM dataset arranged in a multi–way (three–way) structure and decomposed into five PARAFAC components. Taken from Murphy et al. (2013).*

The chemical interpretation of a PARAFAC model relies on the right number of components being specified by the user and in 3 main assumptions for successfully decomposing a multi–way dataset (Murphy et al., 2013, Stedmon and Bro, 2008):

1. Variability: two fluorophores cannot present the same fluorescence intensity or identical spectra (same excitation and emission wavelengths).
2. Trilinearity: the same number of components underlies the chemical variation in each dimension of the dataset. This means that emission spectra are invariant across excitation wavelengths, excitation spectra are invariant across emission wavelengths, and fluorescence intensity increases approximately linearly with concentration (Lambert–Beer Law).
3. Additivity: the total fluorescence intensity is due to the linear superposition of a fixed number of components chemically isolated (chemical reactions, quenching, inner filters effects, interactions between fluorophores, changes in the electronic environment of the fluorophores (with pH) are considered to be minimal).

In the open ocean, global distributions (Figure 1.10) of humic–like fluorophores showed general patterns of lower humic–like fluorescence in the surface mainly because of photochemical removal, increasing with depth due to production in these layers by microbial activity (Yamashita and Tanoue, 2008; Jørgensen et al., 2011; Lønborg and Álvarez–Salgado, 2014; Catalá et al., 2015b; Nelson and Gauglitz, 2016) and almost constant values at depth. Besides, this microbial origin was also demonstrated by culture experiments (Nieto–Cid et al., 2006; Lønborg et al., 2009; Jørgensen et al., 2014; Aparicio et al., 2015; Goto et al., 2017; Kinsey et al., 2018). Protein–like fluorescence showed opposite trends with highest

fluorescence intensities at the surface because those compounds are by–products of the photosynthesis and are photoresistant, decreasing with depth because of their consumption through mineralization processes (Jørgensen et al., 2011; Catalá et al., 2015b; 2016; Nelson and Gauglitz, 2016).

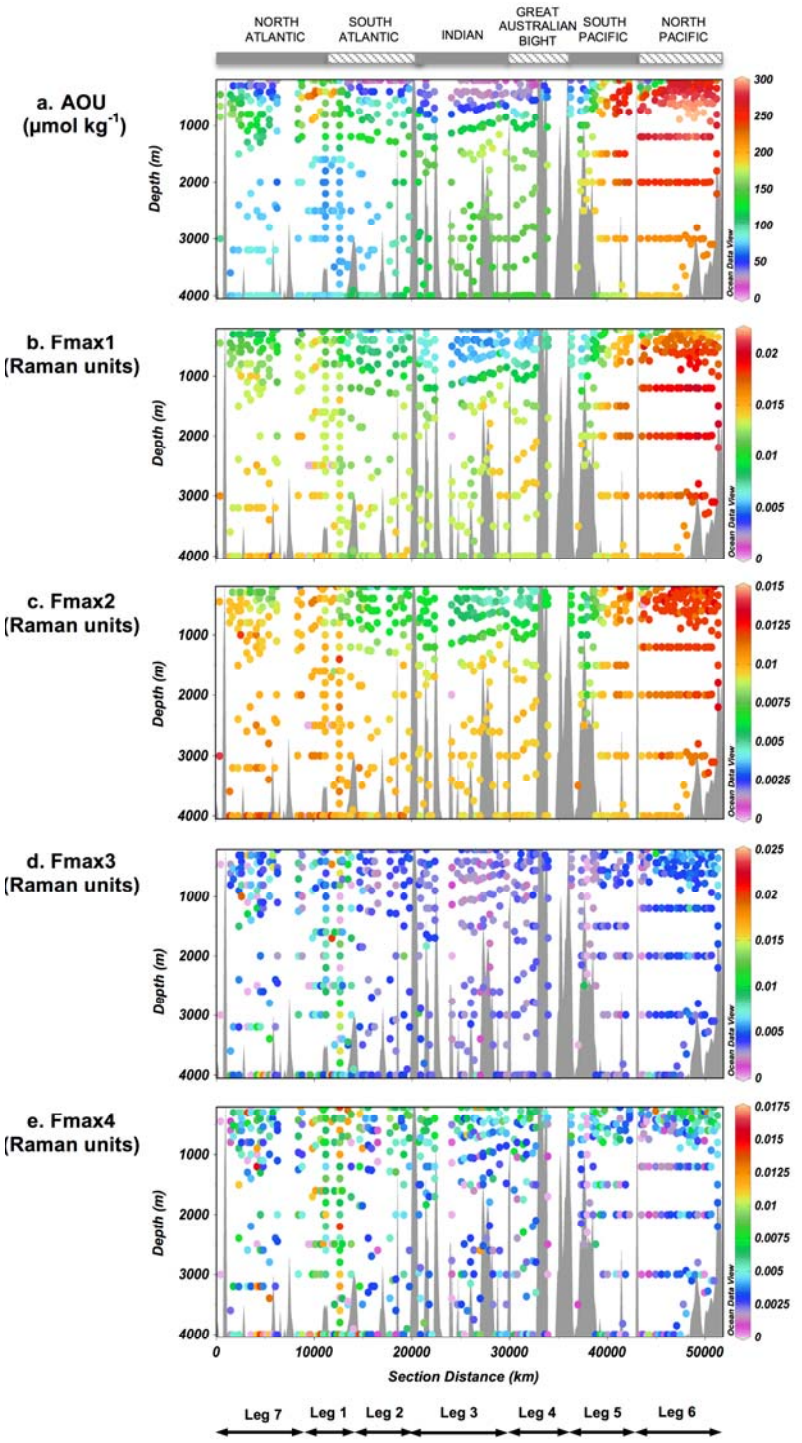

***Figure 1.10**: Global distribution of the (a) apparent oxygen utilization (AOU) and the fluorescence intensity at the excitation–emission maxima of the four components (b) Fmax1 (peaks A+C), (c) Fmax2 (peak M), (d) Fmax3 (peak T) and (e) Fmax4 (peak B) discriminated by the PARAFAC analysis in the global ocean data set of Malaspina 2010 Expedition. Taken from Catalá et al. (2015b).*

1.6.2 Molecular characterization of DOM

Until recent years DOM molecular composition has been approached studying the inventories of some specific groups of compounds, also called molecular building blocks, such as carbohydrates, amino acids, proteins or lipids (McCarthy et al., 1996; Benner and Kaiser, 2003; Yamashita and Tanoue, 2003; Panagiotopoulos and Sempéré, 2005). From this point of view, less than 10% of the DOM has been characterized (Kaiser and Benner, 2012; Repeta, 2015). However, nowadays cutting–edge–techniques, such as Fourier–Transform Ion–Cyclotron Resonance Mass Spectrometry (FT–ICR–MS) and Nuclear Magnetic Resonance spectroscopy (NMR) have characterized molecular features of major C, N or P functional groups and major classes of compounds of DOM. From this point of view, between 60–70% of the DOM has been "characterized" (Repeta, 2015). These two state–of–the–art techniques for the structural characterization of DOM are non–targeted organic structural spectroscopy that aims to unselectively characterize the entire carbon pool present in DOM samples (Hertkorn et al., 2013).

The molecular characterization would help to better understand sources, fates and the turnover time of DOM in the ocean. However, up to date DOM molecular characterization is still scarce and tough to elucidate because natural DOM comprises a complex mixture of hundreds thousands of compounds, extremely low concentrations of each individual compound and a large number of potential isomers for each molecular mass or formula (Hertkorn et al., 2008). This huge structural diversity, together with the large amount of salts in the seawater matrix (note that every litre of seawater host 35–40 g of salts and only 0.5–1.0 mg of C, Repeta (2015)) leads to a challenge to modern analytical tools deciphering DOM molecular structures.

FT–ICR–MS and NMR techniques require salt–free samples with high DOM concentrations. Therefore, prior to the analyses, it is necessary to concentrate and desalt the samples. There are three methods that have been used to isolate and desalt marine samples (Minor et al., 2014): i) tangential–flow ultrafiltration with a 0.5–1 kDa cut–off is able to isolate up to 30% of marine DOM (Benner et al., 1992; Guo et al., 1996; Benner et al., 1997), ii) solid–phase extraction (SPE) using styrene divinyl benzene polymer (PPL) cartridges has more recently been introduced as an efficient method for isolating more than 60% of marine DOM (Dittmar et al., 2008; Green et al., 2014) and iii) reverse osmosis coupled with electrodialysis (RO/ED) isolate more than 64% of marine DOM (Vetter et al., 2007; Koprivnjak et al., 2009; Helms et al., 2015). The ultrafiltration method leads to isolates that still contain large amounts

of salts, being necessary a desalting step prior the DOM molecular analysis. The RO/ED is more expensive and time consuming than SPE, and SPE method produces salt–free extracts that are accessible to modern DOM molecular analysis, it is easy to handle and can be performed in the field. SPE was the one chosen to perform the samples of this PhD thesis. All the three isolation methods described above recover just a fraction of the DOM, thus the results obtained in this thesis are only valid for solid phase extractable DOM (SPE–DOM).

First insights on the molecular composition of deep ocean DOM were obtained from NMR spectroscopy analyses of ultrafiltered materials (UDOM). NMR provides detailed information about atomic bonds and the relative quantities of different functional groups within the bulk sample using stable isotopes of ^{1}H, ^{13}C, ^{15}N and ^{31}P (Benner et al., 1992; Aluwihare et al., 1997; McCarthy et al., 1997; Clark et al., 1998; Hertkorn et al., 2006). These initial studies have reported at least two major components of UDOM: i) a heteropolysaccharide fraction and ii) carboxyl–rich alicyclic molecules (CRAM). The former includes carbohydrates, amino acids, lipids and proteins and it is considered as a rapidly cycling component of DOM, whereas the latter is thought to be refractory. CRAM is considered the major component of UDOM in the deep ocean, accounting for about 8% of the DOC, distributed throughout the water column and their core structures are similar to sterols and hopanoids (Figure 1.11), suggesting that they may be released from the membranes of marine microbes (Hertkorn et al., 2006).

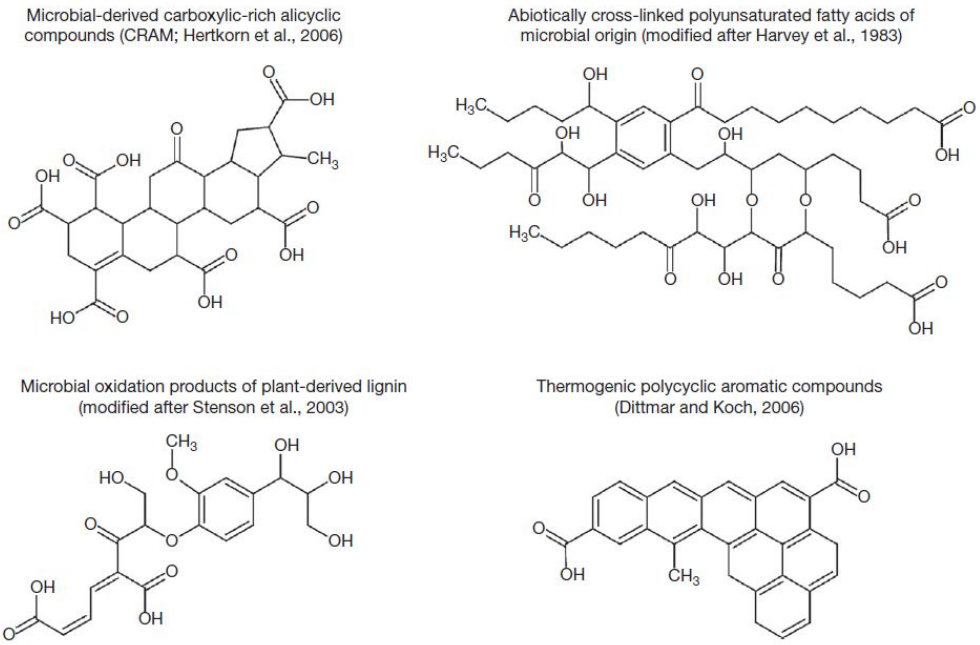

Figure 1.11: Examples of refractory DOM molecular structures. Taken from Dittmar and Stubbins, (2014).

^{1}H and ^{13}C NMR analysis of UDOM showed carbohydrates as a major constituent of the UDOM pool accounting for more than 54% of ultrafiltered dissolved organic carbon (UDOC) in surface waters and decreasing through the water column (Benner et al., 1992; Aluwihare et al., 1997; Sannigrahi et al., 2005). Thus, the abundance of carbohydrates is maxima in surface waters and decrease sharply with depth, indicative of rapidly cycling component of UDOM in the upper layers. In addition, those studies reported as other minor biochemical components of UDOM amino acids, acetate and lipids. Dissolved free amino acids (DFAA) and total hydrolysable amino acids (THAA) followed a similar pattern with higher and more variable concentrations in surface waters and lower and more stable values below the euphotic zone (Yamashita and Tanoue, 2003; Kaiser and Benner, 2009). Regarding the relative abundance of aromatic carbons, a threefold lower value was found in surface than deep UDOM samples, accounting for surface samples less than 1% of the total carbon and at any depth less than 5% (Benner et al., 1992; Aluwihare et al., 1997; Repeta, 2015). Accordingly, ^{1}H and ^{13}C NMR analysis in SPE–DOM Atlantic Ocean samples revealed that aromatic carbons were also less abundant that olefinic carbons (Hertkorn et al., 2013). More recently, Arakawa et al. (2017) used ^{1}H and ^{13}C NMR analysis in SPE–DOM samples and reported carotenoids (a type of isoprenoids) as a key precursor to a significant component of refractory DOM. These authors showed that 4% of total DOC is derived from carotenoid degradation products.

The chemical composition of the DON pool is largely unknown. Globally, as DOC, DON is made of a refractory (large) and a labile (small) pool. Up to date, compound classes classified within the DON fraction include urea, amino acids, nucleic acids and humic and fulvic substances (Sipler and Bronk, 2015). Total hydrolysable amino acids (THAA) contribute a larger portion (1.4–11%) of DON (Repeta, 2015). Further, ^{15}N NMR measurements allowed McCarthy et al. (1997) to show amide as the main constituent of DON in UDOM samples. Later, Aluwihare et al. (2005) identified two distinct pools of DON in UDOM samples, i) N–acetyl amino polysaccharides, present in 50% of HMW–DON in surface waters and of labile nature, and ii) amide nitrogen present in almost all deep–sea HMW–DON and resistant to chemical hydrolysis and biological decomposition. Regarding DOP, ^{31}P NMR analysis revealed phosphorus esters (75% of HMW–DOP) and phosphonates (25% of HMW–DOP) as the dominant components of HMW–DOP, remaining constant throughout the water column (Clark et al., 1998; Kolowith et al., 2001; Repeta et al., 2016).

Lam and Simpson (2008) applied direct ^{1}H NMR to DOM samples (without pre–treatment) by means of a water suppression technique to obtain a NMR spectrum as close as possible to the natural state. These authors demonstrated that DOM concentration, isolation

and extraction techniques did not affect to the NMR profiles, as both spectra obtained, the direct and the ultrafiltered, were dominated by the carbohydrate signal. These results were consistent with previous works reported carbohydrates as major constituents of UDOM (Benner et al., 1992; Aluwihare et al., 1997) and demonstrated that UDOM samples are representative of bulk DOM in its natural state.

NMR presents the advantage that can be applied to any molecular size of organic molecules and can be performed on liquid or solid DOM samples (Simpson et al., 2011) but despite detailed molecular level information has been reveal by means of NMR, the original molecular structures of the DOM compounds remain unknown because the structural features cannot be assigned to individual molecules.

FT–ICR–MS coupled to electrospray ionization (ESI) has emerged as one of the most powerful technique for the DOM molecular characterization because it is able to distinguish thousands of molecular formulae constituting the DOM pool (Kujawinski, 2002; Koch et al., 2005; Hertkorn et al., 2006, 2008, 2013, 2016; Dittmar and Paeng, 2009; D'Andrilli et al., 2010). Its resolution power and mass accuracy are better than 0.1 mDa which is less than the mass of a single electron, 0.5 mDa (Dittmar and Stubbins, 2014). This high mass accuracy allows to assign molecular formulae to the detected masses utilizing the mass defect within an error of <1 ppm (Stenson et al., 2003; Koch et al., 2005). If the mass of a molecule is known, molecular formulae can be calculated simply by mathematically combining the exact masses of the elements to the mass of the molecule assuming some pre–established restrictions (Dittmar and Stubbins, 2014). Figure 1.12 revealed that SPE–DOM molecules occupy a small mass range mainly from 250 to 550 Da, indicative that they are mainly composed of microbial metabolites (Dittmar and Stubbins, 2014). DOM FT–ICR–MS analyses have reported that SPE–DOM is composed mainly by atoms of C, H, N, and, in a lesser extent, by S and P (Hertkorn et al., 2006; Chen et al., 2016).

A very common graphical tool to observe the large amount of molecular data obtained by FT–ICR–MS is the Van Krevelen diagram (Kim et al., 2003). It consists in plotting the hydrogen–to–carbon–ratio (H/C) of every detected molecular formula against its oxygen–to–carbon–ratio (O/C). Different areas in the van Krevelen diagram can be assigned to different compound classes (e. g. proteins, carbohydrates, lipids, CRAM) according to their saturation and oxidation state (Figure 1.13). In addition, Kim et al. (2003) proposed further interpretation of the Van Krevelen plots with the identification of possible chemical reaction pathways, such

as methylation/demethylation, hydrogenation/dehydrogenation, condensation or oxidation/reduction (yellow lines in Figure 1.13).

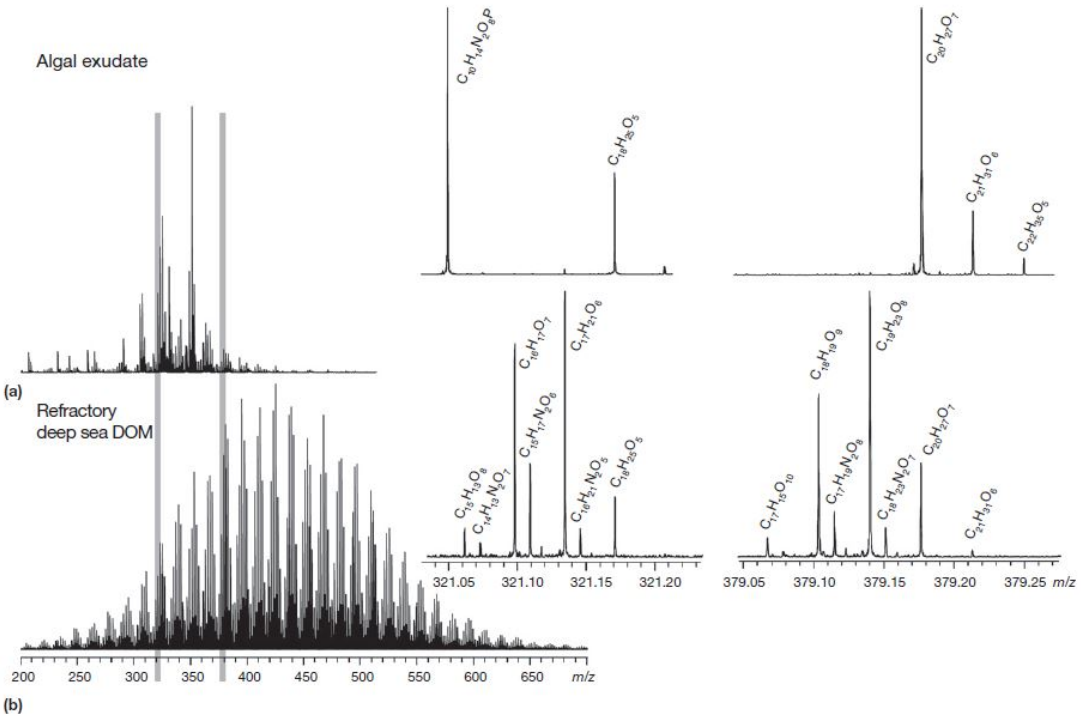

Figure 1.12: *Ultra–high resolution FT–ICR mass spectra of (a) labile DOM from an algal exudate and (b) refractory DOM from a deep sea sample. The whole mass spectra and two exemplary masses (m/z = 321 and 379 Da) are shown where each peak represents a singly charged intact molecule. The high mass accuracy allows assigning molecular formulae to the detected masses. Note that while refractory DOM is characterized by a high molecular diversity, the labile DOM is less diverse. Taken from Dittmar and Stubbins (2014).*

Molecular parameters calculated from the molecular formula obtained from the FT–ICR–MS data are used to infer structural features of DOM (Hertkorn et al., 2006; Osterholz et al., 2014). Saturation and oxygenation state (H/C ratio and O/C ratio, respectively), aromaticity index (AI_{mod}) and number of double bond equivalents (DBE) give structural information about the compound groups present in the SPE–DOM of the sample (Koch and Dittmar, 2006, 2016, Hertkorn et al., 2006). Further, the degradation index (Ideg) is used as a simple proxy to assess the relative degradation state of the SPE–DOM (Flerus et al., 2012). Table 1.2 summarises relevant information about theses indices.

Although FT–ICR–MS analysis does not allow to assign individual molecular structures because each molecular formula can consist of millions of structural isomers, basic structural features, molecular diversity, abundance patterns and DOM cycling pathways can be obtained for each specific mass (Dittmar and Stubbins, 2014).

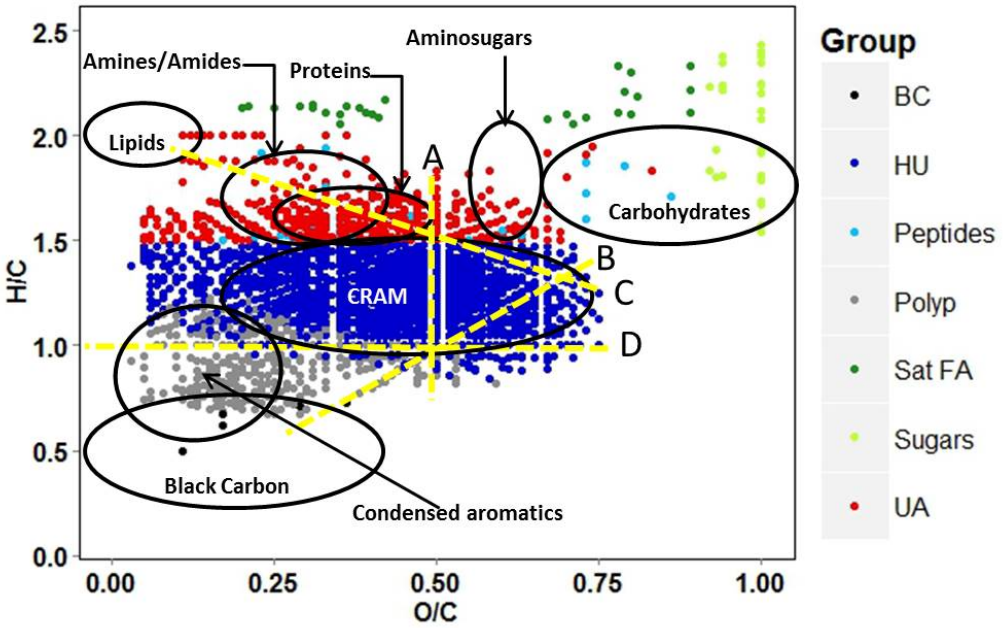

Figure 1.13: Example of a van Krevelen diagram illustrating the molecular composition of DOM from a deep MedSea sample by elemental H/C and O/C ratios. Each dot represents a molecular formula that was assigned to a mass detected by FT–ICR–MS. The colour code represents the compound groups used to classify all the molecular formula detected. BC = black carbon, HU = highly unsaturated compounds, polyp = polyphenols, Sat FA = saturated fatty acids, UA = unsaturated aliphatic compounds. Yellow lines represent chemical reactions previously defined by Kim et al. (2003): A = hydrogenation / dehydrogenation, B = hydration / condensation, C = methylation / demethylation and D = oxidation / reduction. Black circles indicate specific compounds classes with H/C and O/C ratios identified in previous works (Kim et al., 2003, Hertkorn et al., 2008).

Table 1.2: Calculation of the most relevant molecular indices obtained from the FT–ICR–MS data. H/C = hydrogen to carbon ratio; O/C = oxygen to carbon ratio; DBE = double bond equivalent; AI_{mod} = aromaticity index modified; Ideg = degradation index; C, H, O, N, S, P are the number of carbon, hydrogen, oxygen, nitrogen, sulphur and phosphorous atoms, respectively in a given molecular formula. Flerus et al. (2012) used for the Ideg calculation 10 molecular formulae highly correlated with their SPE–DOC radiocarbon age data, 5 of them negatively correlated (NEG_{Ideg}; $C_{12}H_{26}O_4$, $C_{17}H_{20}O_9$, $C_{19}H_{22}O_{10}$, $C_{20}H_{22}O10$ and $C_{20}H_{24}O_{11}$) and 5 of them positively correlated (POS_{Ideg};$C_{13}H_{18}O_7$, $C_{14}H_{20}O_7$, $C_{15}H_{22}O_7$, $C_{15}H_{22}O_8$ and $C_{16}H_{24}O_8$).

Molecular Index	Calculation	Proxy	Reference
H/C	H/C	↑saturation	Hertkorn et al., 2006
O/C	O/C	↑oxygenation	Hertkorn et al., 2006
DBE	$\frac{(1 + C - \frac{1}{2}O - S - \frac{1}{2}H - \frac{1}{2}N - \frac{1}{2}P)}{(C - \frac{1}{2}O - S - N - P)}$	↑unsaturation	Koch and Dittmar, 2006
AI_{mod}	1 + ½ (2 C – H + N +P)	↑aromaticity	Koch and Dittmar, 2016
Ideg	$\frac{\sum magnitudes\ NEG_{Ideg}}{\sum(magnitudes\ (NEG_{Ideg} + POS_{Ideg})}$	↑degradation state	Flerus et al., 2012

1.7 The Mediterranean Sea

1.7.1 Oceanography

The Mediterranean Sea (MedSea) is a semi–enclosed basin open to the Atlantic Ocean through the narrow Strait of Gibraltar (about 13 km wide and 300 m deep) and to the Black Sea by the Strait of Dardanelles/Marmara Sea/Strait of Bosphorus system (Figure 1.14). The surface area and the water volume of the MedSea is about 2.5 x 10^6 km^2 and 3.75 x 10^6 km^3 (0.7% of the surface area and 0.25% volume of the world's oceans), the average depth is about 1500 m reaching the deepest point at 5267 m in the Ionian Sea (Santinelli, 2015). It is constituted by two basins of similar size, the western and the eastern, connected by the Strait of Sicily (about 35 km wide and 300 m deep). Both basins present a number of sub–basins characterized by a rugged topography, especially within the eastern part (Bergamasco and Malanotte–Rizzoli, 2010). Recently, Reygondeau et al. (2017) have proposed biogeochemical regions in the MedSea based on the Longhurst's biogeochemical provinces approach (Longhurst, 2007). These authors used a set of environmental parameters resolved in horizontal and vertical dimensions to catch the biogeochemical complexity of the basin. They have reported 12 regions for the epipelagic, 12 for the mesopelagic, 13 for the bathypelagic and 26 for the seafloor (Figure 1.15).

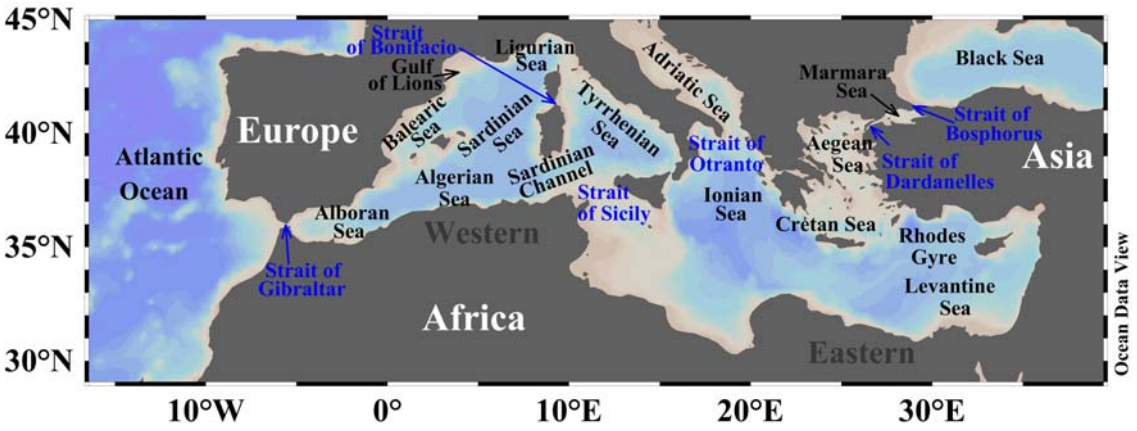

Figure 1.14: *Map of the MedSea with the main seas and areas identified. Figure created using ODV software (Schlitzer, 2016).*

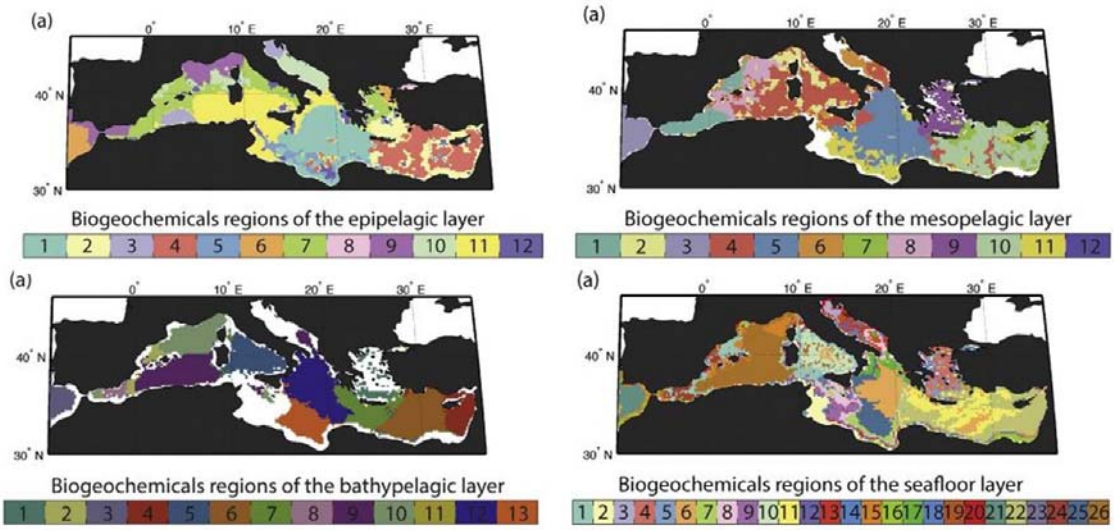

Figure 1.15: *Biogeochemical regions of the MedSea for the epipelagic, mesopelagic, bathypelagic and seafloor layers. Modified from Reygondeau et al. (2017).*

Evaporation exceeds precipitation and continental runoff in the MedSea (Salat et al., 2010). Further, according to its low inorganic nutrient concentrations it is classified as an oligotrophic system. This is due to the anti–estuarine circulation that lead to an imbalance between the bottom outflow of nutrient–rich Mediterranean Water and the surface inflow of nutrient–poor Atlantic water at the Strait of Gibraltar (Huertas et al., 2012). High oxygen concentrations in the deep layers are a consequence of the recent formation of the Mediterranean deep waters (Cruzado, 1985). Relatively small in size, resembling the global conveyor belt and its easier accessibility, the MedSea has been used as a test basin for general ocean circulation studies (Béthoux et al., 1998; Bergamasco and Malanotte–Rizzoli, 2010). The time scale of the Mediterranean Sea meridional overturning circulation is about 42 and 150 years for the western and eastern basin, respectively (Powley et al., 2016), compared to about 350 years for the world ocean (Laruelle et al., 2009).

To better understand the results presented in this PhD thesis, it is essential to be familiarized with the circulation and mixing of the MedSea. First insights on the MedSea circulation were provided by Nielsen (1912) who produced the first overall scheme of the MedSea circulation. Later, Wüst (1961) studied the water mass formation areas and proposed the open thermohaline cell of the MedSea. The Mediterranean thermohaline circulation (Figure 1.16) is strongly affected by the Strait of Gibraltar and the Strait of Sicily, which constraint the water mass circulation along the basin. The Mediterranean thermohaline circulation is typically defined by an open longitudinal cell comprising the whole basin and two closed meridional cells bounded within the western and eastern sub–basins, respectively. The

open thermohaline cell involves the Atlantic Water (AW) spreading in the surface layer from the Strait of Gibraltar to the eastern Mediterranean and also its return westward as Levantine intermediate water (LIW) in depth. However, the closed meridional cells evolve mainly the deep water masses (Skliris, 2014).

The main water masses of the MedSea are the AW in the epipelagic layer, the Levantine Intermediate water (LIW) in the mesopelagic layer and the Eastern (EMDW) and Western (WMDW) Mediterranean Deep waters in the bathypelagic layer. The Atlantic inflow enters the Strait of Gibraltar as a surface current at a rate of about 1 Sv (1 Sv = 10^6 m^3 s^{-1}) with salinity around 36.5, being slightly modified particularly due to the strong evaporation and through mixing with the outflowing Mediterranean waters, leading to the Modified Atlantic Water (MAW). This MAW moves towards the East through a thermohaline cell that involves the whole basin and leads to the formation of LIW. Its salinity gradually increases from about 36.2 at the Strait of Gibraltar to about of 37.5 at the Strait of Sicily and exceeds 38.6 at the eastern part of the Levantine basin (Skliris 2014).

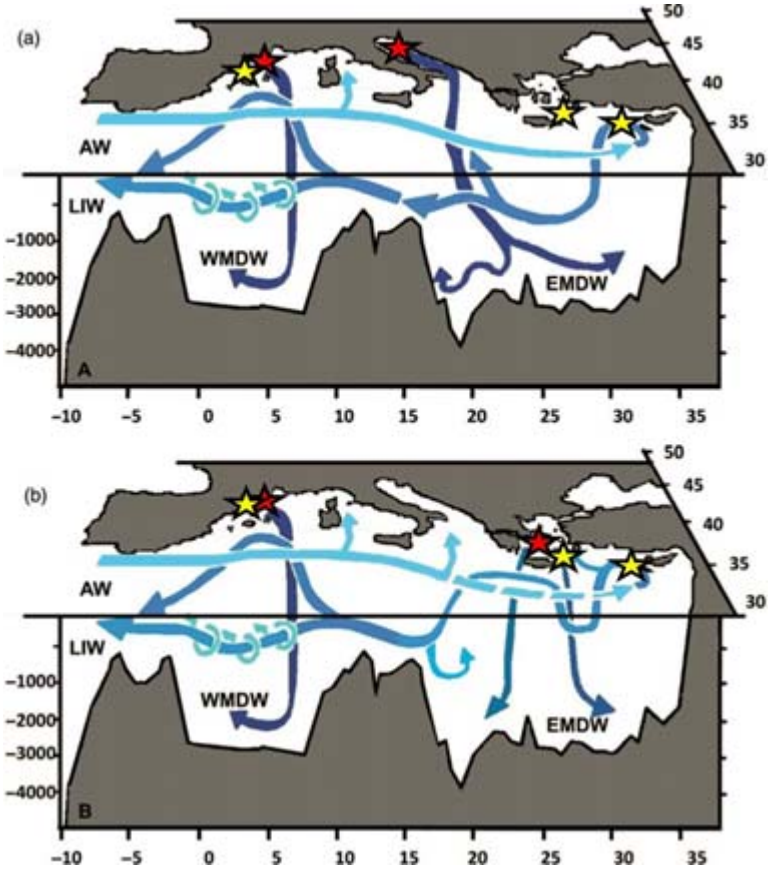

Figure 1.16: *Mediterranean thermohaline circulation. Dark blue arrows represent the meridional circulation of the deep waters and light blue arrows depict the open thermohaline circulation. Panel (a) represent the scheme circulation during the pre— and post— Eastern Mediterranean Transient (EMT) and panel (b) represent circulation during EMT. Red and yellow stars depict deep and intermediate water mass formation areas, respectively. Modified from Bergamasco and Malanotte–Rizzoli, 2010.*

The LIW is formed by convection in the northern part of the Levantine sub–basin (Figure 1.16), mainly at the area of the cyclonic Rhodes Gyre, where the high salinity surface water (MAW) is cooled in winter becoming dense enough to sink. LIW is the largest volume formed in the Mediterranean basin, about 1 Sv, in the same order than the AW entering the MedSea. LIW is easily detected as a subsurface salinity maximum along the whole MedSea at a depth range between 200–600 m depth (Tsimplis et al., 2006) and presents the maximum salinity (absolute, around 39) and temperature (relative, around 15.5°C) of the Mediterranean water masses (Lascaratos, 1993; Emelianov et al., 2006). LIW spreads westwards along a complex route mixing with surrounding water masses (e. g. Cretan intermediate water (CIW) and EMDW) to become the Eastern intermediate water (EIW) once passed the Strait of Sicily in the WestMed (Millot, 2013). Then, EIW continues westwards to exit through the Strait of Gibraltar (Millot, 2013). Apart from the LIW, dense water formation at intermediate layers is also observed in the Cretan Sea (Southern Aegean) where CIW is formed, as well as in the western basin where the Western Intermediate Water (WIW) is formed in the continental shelf of the Gulf of Lions and the Balearic Sea (Millot, 1999).

Concerning the deep waters, the EMDW is formed in the Southern Adriatic when very dense water, so–called Adriatic Deep Water (AdDW) plunges down through the Otranto Strait at a rate of about 0.3 Sv. It occupies the water column below the LIW in the Eastern Mediterranean basin and presents temperatures >13.3°C and salinities >38.66 (Wu et al., 2000). For a short period of time, in the early nineties, during the Eastern Mediterranean Transient (EMT), due to an abrupt shift in the climate and hydrography in this area, the main deep–water formation area was the Aegean Sea, providing a warmer, more saline and denser deep–water mass than the previously existing EMDW of Adriatic origin (Roether et al., 1996; Robinson et al., 2001; Tsimplis et al., 2006). The EMT is the strongest signal of climatic variability ever observed, and it is suggested to be related with many different dynamical aspects of the circulation, water mass formation, and air–sea interaction (Skliris, 2014). Consequently, large deep–water formation in the Aegean Sea is linked with anomalous air–sea heat and freshwater fluxes.

The WMDW is formed in winter in the Gulf of Lions (Gascard, 1978) and occupies the water column below the EIW in the western Mediterranean basin with temperatures between 12.75 and 12.80°C and salinities between 38.44 and 38.46 (Millot, 1999). Deep–water formation processes in the Gulf of Lions were extensively investigated for the first time by the MEDOC group during several cruises conducted in the area in the late 1960s (MEDOC Group 1970). Deep–water formation processes occur during strong persistent northerly winds

(Mistral) in winter, which provoke excessive heat loss (Skliris, 2014). WMDW formation rate is estimated to be about 0.3 Sv (Lascaratos, 1993). Apart from the air–sea heat/freshwater fluxes, the LIW layer, which extends over the whole MedSea, was found to play and important role both in the western (Gulf of Lions) and the eastern (Adriatic Sea) deep–water formation sites, influencing the formation process (Robinson et al., 2001; Skliris, 2014). Parallel to the EMT but in the western basin, recent observational studies suggested a Western Mediterranean transition (WMT) due to an abrupt warming and salinity increase in the bottom layer of the western basin (López-Jurado et al., 2005).

The sill at the Strait of Sicily preclude the exchange of deep waters, therefore deep waters found in both sub–basins do not mix directly (Santinelli, 2015).

The features that make the MedSea especially suitable to study physical and biogeochemical processes in the ocean are:

1. It hosts its own thermohaline circulation.
2. It is a water mass formation area.
3. Fast ventilation rates and residence times compared to the Global Ocean.
4. Deep–water temperatures are about 10°C higher than the Global Ocean.
5. Enhanced respiration and DOC mineralization.
6. Easy accessibility.

1.7.2 DOM in the MedSea

Oligotrophic areas, as the MedSea, exhibit the highest open ocean DOC concentrations, since nutrients shortage limits the microbial degradation of DOM (Thingstad et al., 1997; Hansell et al., 2009; Romera–Castillo et al., 2016). In the epipelagic MedSea, in parallel to the rising oligotrophy from West to East (Moutin and Raimbault, 2002; Reygondeau et al., 2017), the expected increase in the concentration of DOC is observed (Santinelli et al., 2012b, 2013). The distribution of DOC in the meso– and bathypelagic MedSea is also well–known (Santinelli et al., 2010; Santinelli, 2015 and references therein). The general trend of higher concentrations at surface and lower at depth is observed. DOC concentrations in the deep waters are in the order of those found in the world's oceans (36–42 μmol L^{-1}; Santinelli, 2015 and literature therein). It is remarkable the large contribution of DOC to the oxygen demand of the mesopelagic MedSea (30–50%; Santinelli et al., 2010; 2012b) as compared with the open world ocean, where accounted for less than half of the MedSea (Arístegui et al., 2002). Furthermore, in the deep MedSea, the DOC mineralization rates are estimated in 1.4–14.4 μM C yr^{-1} (Santinelli et al., 2010; Hansell et al., 2012), which are substantially higher than the

largest values reported for the open ocean (0.1–0.9 µM C yr^{-1}; Carlson et al., 2010). In this regard, carbon isotopic data ($\Delta^{14}C$ and $\delta^{13}C$) support the idea that up to 45% of the refractory DOC transported by the AW is removed in the deep MedSea in less than 126 yr (Santinelli et al., 2015). In the MedSea DON concentrations ranges between 3.5–6.3, 2.1–5.4 and 2.1–4.3 for the first 250 m, intermediate and deep layers, respectively (Pujo–Pay et al., 2011). Regarding DOP, extremely low concentrations were found in the P–limited MedSea, ranging between 0.01–0.10 µM, 0–0.07 µM and 0–0.07 µM for the first 250 m, intermediate and deep layers, respectively (Pujo–Pay et al., 2011). Previous studies applying ^{1}H NMR, amino acid and neutral sugar analysis of UDOM revealed that carbohydrates are main constituents of this material at the sea surface of the MedSea (Jones et al., 2013).

CDOM dynamics in the open MedSea is scarcely documented. Only few works have been developed, based in coastal areas (Para et al., 2010; Romera–Castillo et al., 2013; Sempéré et al., 2015; Pitta et al., 2017), offshore (Bracchini et al., 2010; Organelli et al., 2014) and just one in the open MedSea (Xing et al., 2014). Xing et al. (2014) investigated the spatial and seasonal CDOM dynamics and their drivers from surface to 400 m using two Bio–Argo floats, one for each basin. These authors reported slightly higher $a412$ values for the western (0.00 to 0.08 m^{-1}) than for the eastern basin (0.00 to 0.06 m^{-1}). In addition, a high seasonality, with strong photobleaching processes in summer and water mass mixing in winter, was shown. Regarding FDOM, only very few works have been reported FDOM measurements in coastal zones of the MedSea (Para et al., 2010; Romera–Castillo et al., 2013; Zeri et al., 2014; Aparicio et al., 2017; Pitta et al., 2017). In the Dardanelles outflow of the Aegean Sea Pitta et al. (2017) used PARAFAC analysis to identify the main fluorophores in this area. They have reported the presence of 3 humic–like (of terrestrial and marine origin) and one protein–like (tryptophan) fluorophores. However, Zeri et al. (2014) showed 3 PARAFAC components in the Marmara Sea and Dardanelles outflow of the Aegean Sea including a humic–like component resembling the traditional mixture of peak A and C defined by Coble (1996) and two protein–like component representing quinone–like (peak N) and tyrosine–like (peak B) fluorophores also previously defined by Coble (1996).

The MedSea is especially vulnerable to global change effects (Giorgi, 2006). Several studies have shown sea surface temperatures increasing at 2–3 times larger than in the global ocean average over the last two decades (Belkin, 2009; Skliris et al., 2012; Skliris, 2014; Marbà et al., 2015). Further, rising temperatures is expected to change the thermohaline circulation of both basins of the MedSea, although forecasts range from a weakening to a strengthening of the thermohaline circulation (Adloff et al., 2015). Recently, Powley et al. (2016) have

reported a future decline in oxygen concentrations but their model predicts an unlikely severe oxygen depletion of the deep waters of the MedSea due to climate–driven changes in the thermohaline circulation based on predictions for timescales of 100 and 1000 years. This is important because changes in the oxygenation can induce variations in the SRDOC and RDOC pools (Ridgwell and Arndt, 2015). The MedSea as a hot–spot of climate change response appears to be a suitable study area for studying the climate change effects and very useful to test the likely climate effects on the global ocean.

1.8 Objectives and structure of this thesis

In response to the gap of knowledge on DOM chemical characterization and reactivity in deep ocean waters at the time when this PhD thesis was proposed, the overall question that we posed was: What are the environmental drivers of the concentration gradients, stoichiometry, optical properties and molecular composition of DOM in the open MedSea? Are they mainly driven by water mass mixing? Or by biogeochemical re–working processes? Or are both important? To answer these questions, we defined the following specific objectives:

1. To study the elemental composition and optical properties of DOM and assess the physical and biogeochemical drivers of their distribution along the MedSea.
2. To characterize the molecular composition of DOM in the main water masses of the MedSea.
3. To link optical and molecular properties of DOM in the main water masses of the MedSea.
4. To relate the molecular size and the bioavailability of DOM in the intermediate waters of the MedSea.

This PhD thesis is structured as follow:

Chapter 1 provides a general introduction about DOM in aquatic ecosystems and the Mediterranean Sea as a suitable study area for DOM.

Chapter 2 describes the main environmental drivers of the CDOM distribution in the MedSea using generalized additive models and optimum multiparametric water mass analysis.

Chapter 3 focuses on the main environmental drivers of the FDOM distribution in the MedSea using the same approaches than in chapter 2. For chapters 2 and 3 we used almost 400 samples collected along the cruise track, which allow us to run a statistically significant water mass analysis.

Chapter 4 examines the DOM molecular composition in the main water masses of the MedSea and compares its composition with the adjacent Atlantic Ocean by means of ultrahigh resolution Fourier transform ion cyclotron resonance mass spectrometry. In this chapter we used 29 samples collected at key locations attending to their physical–chemical properties, i.e. deep chlorophyll maximum, salinity maximum, oxygen minimum and deep waters at 1000 and 2000 m. Logistic and analytical constrictions precluded collected and processing a larger sample set.

Chapter 5 links the optical features and molecular composition of DOM and proposes a useful tool to infer molecular data from optical measurements. In this chapter we used the same sample set as in chapter 4.

Chapter 6 focuses on the DOM bioavailability and show the relevance of the molecular–size to support the SRC hypothesis in the field. In this chapter we used the same sample set as in chapters 4 and 5.

Chapter 7 contains a general discussion. As every chapter of this PhD thesis host its own discussion section, in this chapter we discuss both technical and conceptual issues involving and linking all chapters.

Chapter 8 presents the general conclusions achieved in this PhD thesis.

References contains the references cited in this PhD thesis.

Annex contains three published papers associated to this PhD thesis.

Chapter 2
Dissolved organic matter (DOM) and its optical properties in the open Mediterranean Sea: basin–wide distribution and drivers of chromophoric DOM

The research work presented in this chapter is also a contribution to the paper submitted to Progress in Oceanography:

Catalá, T.S., Martínez–Pérez, A.M., Nieto–Cid, M., Álvarez, M., Otero, J., Emelianov, M., Reche, I., Arístegui, J., Álvarez–Salgado, X.A. 2018. Optical properties of Dissolved Organic Matter (DOM) in the open Mediterranean Sea: basin wide distribution and drivers of chromophoric DOM.

Abstract

Chromophoric dissolved organic matter (CDOM) in the open Mediterranean Sea (MedSea) is barely documented, remaining the basin–wide patterns in intermediate and deep waters still enigmatic. Here, full–depth distributions of CDOM absorption coefficients and spectral slopes recorded during the HOTMIX 2014 cruise are presented and their respective environmental drivers resolved. General Additive Models (GAMs) in surface waters and Optimum MultiParameter (OMP) water mass analysis in deep waters were applied. In the surface, apparent oxygen utilisation (AOU), a proxy to cumulative net community respiration, explained most of the variability of dissolved organic carbon (DOC) and the absorption coefficient at 254 nm (a_{254}), whereas the absorption coefficient at 325 nm (a_{325}), and the spectral slopes were mostly explained by potential temperature, a proxy to stratification and solar radiation, indicating that both water column stability and photobleaching may drive the variability of the UV–A absorbing CDOM components. In deep waters, the effect of water mass mixing and basin–scale mineralization were discerned from local mineralization processes. Water mass mixing and basin–scale mineralization contributed more substantially to explain the variability of DOC, a_{254} and a_{325} (82–91%) than the variability of the spectral slopes (35–64%). Local mineralization processes indicate that DOC and CDOM play a more relevant role in the carbon cycle in the eastern (EastMed) than in the western (WestMed) Mediterranean: whereas DOC contributed to 66 ± 10% of the oxygen demand in the EastMed, it represented only 24 ± 4% in the WestMed. Independently of basins and layers, a_{254} revealed as an excellent proxy to the concentration of DOC in the MedSea. Also, the unexpected inverse relationship of a_{325} with AOU indicates that the consumption of the UV–A absorbing CDOM fraction prevails over their production.

1 Introduction

The Mediterranean Sea, hereafter MedSea, is considered a laboratory basin for physical, chemical and biological ocean processes occurring on shorter temporal and spatial scales compared to the world ocean (see details in chapter 1). In the epipelagic MedSea, an increase in the concentration of dissolved organic carbon (DOC) from West to East has been observed (Santinelli et al., 2012b; 2013) associated to the rising oligotrophy of the nutrient–poor Atlantic water (AW) flowing eastwards (Moutin and Raimbault, 2002; Reygondeau et al., 2017). This accumulation of DOC is characteristic of oligotrophic areas since nutrient limitation constraints the microbial degradation of dissolved organic matter (DOM) (Thingstad et al., 1997; Hansell et al., 2009; Romera–Castillo et al., 2016). The distribution of DOC in the meso– and bathypelagic MedSea has been widely studied (Santinelli et al., 2010; 2012b; Santinelli, 2015). DOC concentrations in the eastern and western Mediterranean deep waters, (EMDW and WMDW, respectively) present minimum values comparable to those in the deep Atlantic and Pacific Oceans (36–42 μmol L^{-1}; Santinelli, 2015 and literature therein), which is unexpected given the short renewal time of the MedSea (20–126 years; Andrie and Merlivat, 1988; Schlitzer et al., 1991) and the terrestrial inputs of carbon (Mladenov et al., 2011; Santinelli, 2015). Besides DOC presents a key contribution to the oxygen demand of the LIW (up to 50%; Santinelli et al., 2010; 2012b) as compared with the open world ocean (up to 20%; Arístegui et al., 2002).

Contrary to DOC, the dynamics of the chromophoric fraction of DOM (CDOM) is barely documented in the MedSea. Although CDOM is a small fraction of the total DOM pool in the open ocean (Nelson et al., 1998; Nelson and Siegel, 2002; Siegel et al., 2002; Nelson et al., 2010), it plays important roles in the carbon cycle (Mopper and Kieber, 2002) and in the optical properties of seawater (Organelli et al., 2014). In the MedSea, CDOM values from the upper layers have been reported only very recently (Xing et al., 2012; Organelli et al., 2014; Xing et al., 2014; Pérez et al., 2016; Pitta et al., 2017). However, basin–wide patterns of CDOM in the intermediate and deep Mediterranean waters are currently unknown, likely due to technical constrains of the standard spectrophotometric procedures because of their extremely low signal intensities.

In this context, the aim of this study is to disclose the full–depth distributions of CDOM across the open MedSea and to determine the physical and biogeochemical drivers responsible for those distributions. Since the hydrographic properties are not conservative in the surface layer because of mass and heat exchange with the atmosphere, we used General

Additive Models (GAMs) to resolve the key environmental drivers of CDOM variability in the epipelagic layer. On the contrary, the conservativeness of the hydrographic properties in the meso– and bathypelagic layers allowed us to use an Optimum MultiParameter (OMP) water mass analysis to differentiate the impact of water mass mixing and basin–scale mineralization from the local biogeochemical processes on the distributions of CDOM.

2 Materials and Methods

2.1 General sampling strategy and analytical methods

During the HOTMIX 2014 cruise, on board the R/V Sarmiento de Gamboa (Heraklion, Crete, 27 April 2014 – Las Palmas, Canary Islands, 29 May 2014), 24 hydrographic stations were occupied along the whole Mediterranean Sea (Figure 2.1).

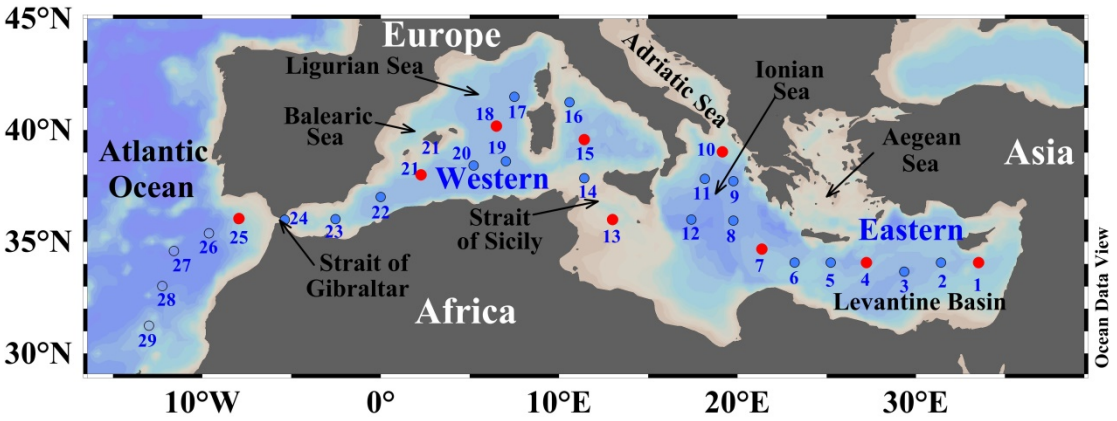

Figure 2.1: *Map of the study area with the HOTMIX cruise transect and sampling stations superposed. The circles depict all the cruise stations. Red circles represent the stations where samples were taken for the molecular characterization and size fractionation of DOM (chapters 4, 5 and 6, respectively). Red and blue circles represent the stations where samples were collected for DOC and DOM fluorescence and absorption characterization (chapters 2 and 3). Figure created using Ocean Data View (R. Schlitzer, 2016. http://odv.awi.de).*

2.1.1 Determination of the explanatory variables: salinity, inorganic nutrients, dissolved oxygen, chlorophyll a and bacterial biomass

Samples for salinity (S) were measured with a Guildline Portasal salinometer Model 8410A. Conductivity measurements were converted into practical salinity scale values (UNESCO, 1985). Samples for dissolved oxygen (O_2) determination were collected in flared neck iodine calibrated flasks and measured using a Winkler potentiometric method adapted from Langdon (2010). The apparent oxygen utilization was calculated as AOU = O_2sat – O_2 (Benson and Krause, UNESCO, 1986), where O_2sat is the oxygen saturation. Chlorophyll *a* (Chl *a)* measurements were performed by filtering 500 mL of water through a Whatman GF/F

filter and stored frozen until analysis on board. Chl *a* pigments were extracted in cold acetone (90% v/v) for 24 h and analysed with a 10 AU Turner Designs bench fluorometer, previously calibrated with pure Chl *a* (Sigma Aldrich) (Holm–Hansen et al., 1965). Samples for inorganic nutrient analysis were collected in 50 mL polyethylene bottles and kept in the dark at 4°C until analysis on board. Nitrate, phosphate and silicate concentrations were determined using a Skalar segmented flow autoanalyzer SAN++ following the colorimetric methods of Grasshoff et al. (1999).

The prokaryote heterotrophic abundance (PHA) was estimated by flow cytometry. Samples (1.6 mL) were preserved with paraformaldehyde (2% final concentration), left 15 min at 4°C in the dark to fix, deep frozen in liquid nitrogen and stored at –80°C until analysed. The day after, subsamples (400 µL) were stained with the fluorochrome SYBR Green I, Molecular Probes (final concentration 1000x dilution of the commercial product) at room temperature before analyses at low speed (<20 µL min^{-1}) with a BD FACSCalibur cytometer, fitted with a 15 mW laser emitting at 488 nm. Cells were identified in bivariate plots of side scatter (SSC–H) versus green fluorescence (FL1–H). A suspension of yellow–green 1 µm latex beads (~10^6 beads mL^{-1}) was added as an internal standard (Polysciences, Inc.)

2.1.2 Determination of the response variables: DOC and CDOM

Seawater samples for the determination of DOC and CDOM were collected in 0.25 L acid–cleaned glass bottles and stored in the dark. Surface samples (<200 m) were filtered through precombusted (450°C, 4 h) Whatman GF/F filters with an acid–cleaned all–glass filtration system under positive pressure of high–purity N_2, previously rinsed with about 50 mL of the sample. Deep ocean samples (>200 m) were not filtered because light absorption due to pigments and detrital particles contribute only to a minor fraction of the deep open ocean CDOM absorption (Nelson et al., 1998; Nelson et al., 2007).

Aliquots of 10 mL were collected for DOC determination in precombusted (450°C, 12 h) glass ampoules. These samples were acidified to pH < 2 and the ampoules were heat–sealed and stored in the dark at 4°C until analysis in the base laboratory. DOC concentration was determined with a Shimadzu TOC–V organic carbon analyser by high temperature catalytic oxidation. Potassium hydrogen phthalate (99.95–100.05%, p.a., Merck) was used to calibrate the system daily. The precision of the equipment was ±1 µmol L^{-1}. The accuracy was checked daily with the DOC reference materials provided by D. A. Hansell (University of Miami, USA).

The UV–Visible–NIR absorption spectra of CDOM was measured from 178 nm to 879

nm at 0.38 nm intervals by using a 100 cm path length liquid waveguide capillary cell (LWCC) from World Precision Instruments (model LPC100CM), a Deuterium–Halogen Light Sources for the UV–Vis (Ocean Optics model DH2000BAC) and a miniature spectrometer (Ocean Optics model USB2000+UV–VIS). Finally, two 600 μm fibber optic cables (Ocean Optics model QP600–1–SR–BX) connected the LWCC with the light source and the spectrometer (Figure 2.2). The LWCC is made of quartz capillary tubing coated with a low refractive index polymer. Therefore, these cells are designed to minimize absorbance biases due to changes in the refractive index between samples of different salinity and the waveguide. In the particular case of our LWCC, 10% and 50% dilutions of filtered (0.2 μm) natural seawater of salinity 35.9 yielded average differences of 0.005 $\pm$ 0.005 m^{-1} at any wavelength between the measured and the expected concentration according to the sample dilution. This result prevented us to make any further correction of the refractive index in our measurements. Prior to measuring, the reference (Milli–Q water) and the samples were acclimatized at room temperature to minimize temperature effects. Each sample was measured twice and the average of the two spectra was reported. Only the absorbances (Abs) from 250 nm and 700 nm were logged. Finally, absorbances were converted into naeperian absorption coefficients (a_λ) multiplying by 2.303 and dividing by the light pathlength, which was of 99.89 cm as certified by World Precision Instruments.

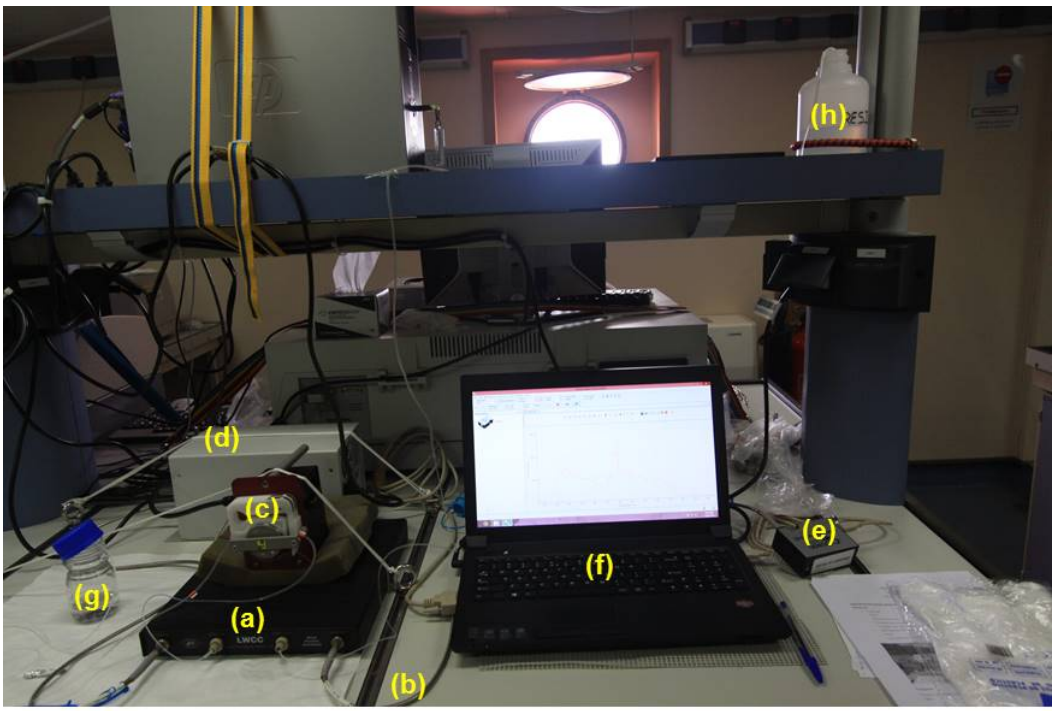

Figure 2.2: Equipment for the CDOM measurements: (a) liquid waveguide capillary cell (LWCC), (b) fibber optic cables, (c) peristaltic pumps, (d) light source, (e) miniature spectrometer, (f) laptop, (g) sample and (h) waste. Picture from M. Nieto–Cid.

In this study, we will focus on the absorption coefficients at wavelengths at 254 nm, a_{254}, and at 325 nm, a_{325}, and the spectral slopes for the wavelength bands 275–295 nm, $S_{275–295}$, and 350–400 nm, and $S_{350–400}$ (Helms et al., 2008). These spectral slopes were calculated from the linear regression of the log–transformed absorption spectra. Only those $S_{275–295}$ with $R^2 > 0.95$ and those $S_{350–400}$ with $R^2 > 0.85$ were retained. Finally, the slope ratio (S_R) was calculated as the ratio of the slope of the shorter wavelength band (275–295 nm) to that of the longer wavelength band (350–400 nm). a_{254} is proportional to the abundance of conjugated carbon double bonds and it has been suggested as a proxy for the concentration of DOC (e.g. Lønborg and Álvarez–Salgado, 2014), whereas a_{325} is an indicator of the presence of aromatic substances (Nelson et al., 2004; Catalá et al., 2015a). The slopes of the 275–295 nm region and S_R have been related to DOM molecular weight and to its corresponding photochemically induced shifts (Helms et al., 2008).

2.2 Generalized additive models (GAMs)

To assess the effect of the environmental conditions on the basin–wide variability of DOC and CDOM in the epipelagic layer of the MedSea we used generalized additive models (GAMs, (Wood, 2006)). We examined the influence of the environmental explanatory variables described above on the response variables DOC, a_{254}, a_{325}, $S_{275–295}$ and S_R. Before model fitting, covariability among predictors was examined using variance inflation factors (VIFs, Table 2.1). GAMs were formulated as follows:

$$Y_{i,l} = \alpha + \sum_j g_j\left(X^j{}_{i,l}\right) + \in_{i,l} \qquad (2.1)$$

where *Y* is DOC, a_{254}, a_{325}, $S_{275–295}$ or S_R measured at a station *i* and depth level *l*, α is an intercept, *X* is a vector of predictor variables where the superscript *j* identifies each covariate, *g* is a non–parametric smoothing function specifying the effect of each covariates on the response variables and $\in_{i,l}$ is the error term assumed to be normally distributed. Smoothing functions were fit by penalized cubic regression splines restricted to a maximum of three knots. The smoothness of the functions was estimated by minimizing the generalized cross validation criterion. Results from the GAM analysis of DOC and CDOM variables are summarised in Table 2.6. All models were fitted in R 3.2.3 software (R Development Core Team, 2014) and using the 'mgcv 1.8–16' package (Wood, 2006).

Table 2.1: Variance Inflation Factor (VIF) for each explanatory variable considered in the GAM models. We began with all explanatory variables (2nd column) and estimated successive VIFs once dropped collinear covariates one at a time (3rd to 5th column) until all VIFs values were below 5.

Covariate	VIF	VIF	VIF	VIF
θ	4.60	4.56	4.52	4.55
AOU	16.87	10.11	7.76	4.49
NO_3^-	32.07			
PO_4^{2-}	7.78	4.41	3.86	
SiO_2	11.93	8.31		
Chl *a*	2.13	2.04	1.91	1.60
PHA	2.75	2.63	2.33	2.08

2.3 Optimum MultiParameter (OMP) water mass analysis

The cornerstone of an OMP water mass analysis is the identification and quantification of the water types that contribute to the water samples collected in a certain study area. In this regard, a water type (WT) is a unique combination of potential temperature (θ), S and other tracer values used to unambiguously define a given water mass (Tomczak, 1999). Particularly, the variables used to define the water types in our OMP analysis are θ, S, the conservative chemical parameter NO ($NO = O_2 + R_N \times NO_3$, Broecker, 1974) and silicate (SiO_4). R_N is the stoichiometric ratio of dissolved oxygen consumption to nitrate production during the mineralization of biogenic organic matter in the ocean, which has been fixed at 9.3 mol O_2 mol NO_3^{-1} (Anderson, 1995).

Despite having a relatively small area, the MedSea contains a wide variety of surface, intermediate and deep water masses (e.g., Schroeder et al., 2012), which makes setting and solving an OMP analysis particularly difficult. Extreme climate events have changed the structure and properties of the deep layers in the western and eastern MedSea during the Eastern Mediterranean Transient (EMT) and Western Mediterranean Transition (WMT) events (Roether et al., 2007; Schroeder et al., 2016). This is the reason behind the relatively large number of deep water types proposed in this study, a total of 10. Five of them correspond to different varieties of Eastern Mediterranean Deep Water (Table 2.2a) and the other five to different varieties of Western Mediterranean Deep Water (Table 2.2b). The oceanographic setting found during the HOTMIX 2014 cruise can be effectively explained with the array of water types described in Table 2.2. Note that the eastern (Table 2.2a) and western (Table 2.2b) basins are considered separately. The physical properties of these water types (Table 2.3) were extracted from the literature and corresponded to the θ and S of the

water types in their formation area or when they enter a given MedSea basin. The θ–S pairs of the water types should envelope the θ–S diagrams of the CTD profiles collected during the cruise, as shown in Figure 2.3 and 2.4

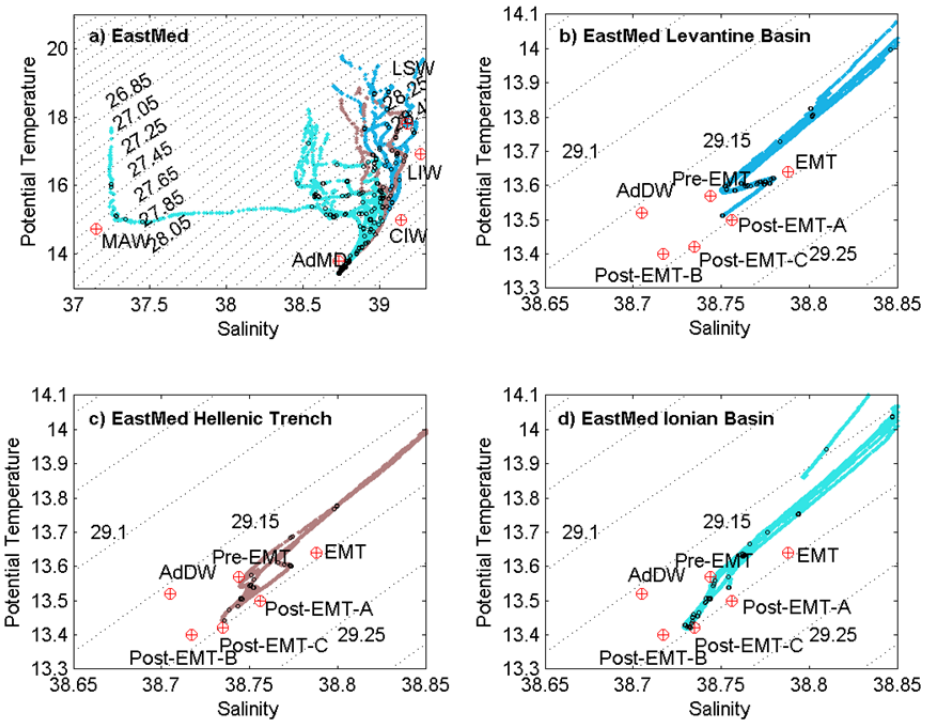

Figure 2.3: *Potential temperature (°C) vs. salinity diagrams for the EastMed CTD (lines) and discrete bottle data (points) in the a) upper water samples, b) deep water in the Levantine basin (stations 1 – 4), c) deep waters in the Hellenic Trench (stations 5 – 7), and d) deep waters in the Ionian basin (stations 8–13).* σ_θ *isolines are included. The coloured lines correspond to CTD data, dark blue for the Levantine basin, light blue for the Ionian basin and brown for the Hellenic Trench. Red dots indicate the potential temperature and salinity of the water types. Water types physical characteristics and acronyms as in Table 2.2 are shown*.

The chemical properties of each water type were estimated from a linear regression analysis of NO and SiO_4 with S or θ within the realm of that water type (Álvarez et al., 2014). Following Poole and Tomczak (1999), the standard error of these regression equations have been used to compute the uncertainty of the estimation of the water type characteristics (Table 2.3). Samples collected in the upper layer cannot be included in the OMP analysis because θ, S and NO do not behave conservatively due to the air–sea exchange of heat, water and gases and SiO_4 is affected by biological utilization.

Table 2.2a. Summary of the main water masses in the Eastern Mediterranean Sea with a brief description of their characteristics and some references (Ref) where more information about their origin and circulation can be found. The Water Types (WT) used to model them are also shown.

Name	Source	Characteristics	Acronym & WT	Ref
Modified Atlantic water	Atlantic Ocean	MAW derives from the Atlantic Water entering the MedSea at the Strait of Gibraltar, in the way to the Strait of Sicily it mixes, evaporates and loses nutrients. MAW enters the EastMED crossing the Strait of Sicily in the surface layer following a cyclonic path. In this work it is identified by a minimum of salinity.	MAW	a, b, c
Levantine Surface Water	Levantine Basin	Highly modified Atlantic Water, detected by a surface maximum of salinity (S > 39) and temperature (θ > 17°C).	LSW	d, e
Levantine Intermediate Water	Rhodes Gyre (~30°E)	Formed by the combined effects of evaporation, increasing salinity in summer, and relatively deep vertical mixing caused by intense dry northerly winds in winter. It flows at mid depths (200–500 m) in the EastMED. Typically presents S = 38.74–39.20 and θ= 15–17°C in the Levantine Basin.	LIW	e, f, g, h
Cretan Intermediate Water	Cretan Sea	Outflowing water from the Cretan Sea into the EastMed through the Cretan Arc straits. It is colder, less saline and denser than LIW, so it is found between LIW and EMDW. It moves westward along the Cretan continental slope towards the Ionian and Adriatic seas.	CIW	i, j, k, l
Middle Adriatic Water	Adriatic Sea	Operative water type defined from data in the Adriatic Pit taken from the M84/3 cruise in 2011. This WT is influenced by Adriatic Surface Water with a low S and θ, around 400 m, and detected in the eastern Ionian Sea.	AdMW	k, m
Adriatic Deep Water	Adriatic Sea	Formed in the Southern Adriatic Pit where a cyclonic gyre is nearly permanently present, produced by open ocean deep convection from water preconditioned by LIW and CIW. This water spills over the Ionian Sea following the western part.	AdDW	n, ñ
Eastern Mediterranean Deep Water (EMDW)	Adriatic Sea	The Adriatic Sea was the source of deep waters to the EastMed prior to the eastern Mediterranean transient (EMT) event (1987–1995). This water is less saline, warmer and denser than EMDW produced during the post–EMT phase.	Pre–EMT	o, p,
	Aegean Sea	EMDW produced in the Cretan / Aegean Sea during the EMT event (1995–1999). This denser water compared to Pre–EMT caused an uplifting of the bottom isopycnals. The EMDW with Aegean Sea origin produced during the EMT event is warmer, more saline and less oxygenated than the Pre–EMT water of Adriatic origin.	EMT	o, p, q, r
	Adriatic Sea	After the EMT event, the Adriatic Sea started to produce again EastMed deep waters. This Post–EMT EMDW is mainly found in the Levantine basin from 2007s. This water is colder and less saline than the EMT water type.	Post–EMT–A	s, t, u
	Adriatic Sea	After 2003s Adriatic Deep Water became warmer and saltier than that previously produced. This water is still found in the Ionian basin in 2011.	Post–EMT–B	ñ, v, w
	Adriatic Sea	After 2007s Adriatic Deep Water spilling is still getting saltier and warmer and found over the bottom of the Ionian Sea. This newer deep water is also detected by high oxygen values.	Post–EMT–C	ñ, v, x

Table 2.2b. Summary of the main water masses in the Western Mediterranean Sea with a brief description of their characteristics and some references where more information about their origin and circulation can be found. The Water Types (WT) used to model them are also shown.

Name	Source	Characteristics	Acronym & WT	Ref
Atlantic Water (AW)	Atlantic Ocean	Surface Atlantic Water entering the MedSea at the Strait of Gibraltar flows anticlockwise suffering continuous modifications by mixing and evaporation. It is identified by a minimum in salinity in the upper surface layer and it contains very low nutrients.	AW	b, y
Eastern Intermediate Water	Strait of Sicily	Recently named by Millot (2013). High salinity intermediate waters from the EastMed (i.e. LIW and CIW) flow into the WestMed also mixing with transitional EMDW. Recognized in the WestMed by its maximum in temperature and salinity, contains relatively more nutrients than LIW.	EIW	g, i, z, aa
Western Intermediate Water	NW basin	The WIW is formed in the continental shelf of the Gulf of Lions and the Balearic Sea through severe winter convection. Recognized by relative minimum in temperature between the surface AW and WMDW.	WIW	b, ab, ac
Western Mediterranean Deep Water (WMDW)	NW basin	The oldest resident WMDW water in the WestMed formed prior to the western Mediterranean transition (WMT) (before 2004/5) by deep convection in the Gulf of Lions. Nowadays detected as a deep relative minimum in θ and S. We use the nomenclature as in (k) to name the different vintages of WMDW.	A	ad, ae, af
	NW basin	Originated during the extreme forcing conditions in winter 2004/5 by open sea convection, mainly in the Gulf of Lions, as preconditioned with saltier and warmer CIW and LIW. This WMDW is warmer and saltier than the previous resident one, A.	B	af, ag
	NW basin	Originated during the extreme forcing conditions in winter 2004/5 but with a higher influence of coastal shelf waters. It is fresher, colder and more oxygenated than B.	C	af, ah
	NW basin	Each winter since 2009/10, but especially in 2011/12, warmer, saltier and denser deep water is produced, uplifting the older deep waters near the bottom. We operationally call the more recent WestMed types found in 2011 and 2014 as D11 and D14, clearly distinguished in the temperature–salinity diagrams.	D	ah, ai, aj

Note:Letters in the references column depict: a: Manzella and La Violette (1990), b: Millot (1999), c: Lermusiaux and Robinson (2001), d: Theocaris et al. (1993), e: Özturgut (1976), f: Wüst (1961), g: Millot (2013), h: Lascaratos et al. (1993), i: Astraldi et al. (1999), j: Theocharis et al. (1999), k: Velaoras et al. (2014), l: Schlitzer et al. (1991), m: Vilibić and Orlić (2002), n: Artegiani et al. (1993), ñ: Rubino and Hainbucher (2007), o: Roether et al. (1996), p: Lascaratos et al. (1999), q: Roether et al., (2007), r: Klein et al. (1999), s: Manca et al. (2003), t: Sparnocchia et al. (2011), u: Kovačević et al. (2012), v: Hainbucher et al. (2006), w: Cardin et al. (2015), x: Bensi et al. (2013); y: Huertas et al. (2012), z: Gasparini et al. (2005), aa: Astraldi et al. (2002), ab: Salat and Font (1987), ac: Sparnocchia et al. (1999) , ad: Bethoux and Tailliez, (1994), ae: MEDOC Group (1970), af: Schroeder et al. (2006), ag: López–Jurado et al. (2005), ah: Puig et al. (2013), ai: Schroeder et al. (2016), aj: Houpert et al. (2016).

Table 2.3: Thermohaline and chemical characteristics (average value ± uncertainty) of the water types defined to model the mixing of Mediterranean water masses along the HOTMIX cruise, separating eastern and western basins. R^2 = determination coefficient, SE = standard error of the residuals from the regression between measured and back–calculated variables and N = number of data. Only data below 200 m are considered.

Acronym	θ_i (°C)	S_i	SiO_{4i} (µmol kg^{-1})	NO_i (µmol kg^{-1})
EASTERN MEDITERRANEAN BASIN				
MAW	14.740 ± 0.002	37.150 ± 0.005	0.6 ± 0.3	250 ± 5
LSW	17.800 ± 0.002	39.180 ± 0.005	0.7 ± 0.3	221 ± 5
LIW	16.910 ± 0.002	39.270 ± 0.005	0.9 ± 0.3	219 ± 5
CIW	15.000 ± 0.002	39.140 ± 0.005	4.0 ± 0.3	234 ± 5
AdMW	13.790 ± 0.002	38.732 ± 0.005	1.1 ± 0.3	250 ± 5
AdDW	13.520 ± 0.002	38.705 ± 0.005	3.1 ± 0.3	250 ± 5
Pre–EMT	13.570 ± 0.002	38.744 ± 0.005	9.1 ± 0.3	228 ± 5
EMT	13.640 ± 0.002	38.788 ± 0.005	7.8 ± 0.3	229 ± 5
Post–EMT–A	13.500 ± 0.002	38.756 ± 0.005	7.2 ± 0.3	237 ± 5
Post–EMT–B	13.400 ± 0.002	38.717 ± 0.005	6.3 ± 0.3	240 ± 5
Post–EMT–C	13.420 ± 0.002	38.735 ± 0.005	6.3 ± 0.3	238 ± 5
R^2	0.9984	0.9989	0.9987	0.72
SE	0.014	0.005	0.10	2.7
N	100	100	100	100
WESTERN MEDITERRANEAN BASIN				
AW	14.800 ± 0.002	37.000 ± 0.005	0.9 ± 0.3	254 ± 5
EIW	14.220 ± 0.002	38.840 ± 0.005	5.9 ± 0.3	226 ± 5
WIW	12.934 ± 0.002	38.259 ± 0.005	1.6 ± 0.3	262 ± 5
A	12.840 ± 0.002	38.460 ± 0.005	9.3 ± 0.3	268 ± 5
B	12.910 ± 0.002	38.480 ± 0.005	7.8 ± 0.3	271 ± 5
C	12.881 ± 0.002	38.477 ± 0.005	8.4 ± 0.3	275 ± 5
D11	12.902 ± 0.002	38.486 ± 0.005	7.7 ± 0.3	280 ± 5
D14	12.913 ± 0.002	38.492 ± 0.005	9.5 ± 0.3	283 ± 5
R^2	0.9987	0.9967	0.9859	0.95
SE	0.013	0.005	0.21	3.2
N	75	75	75	75

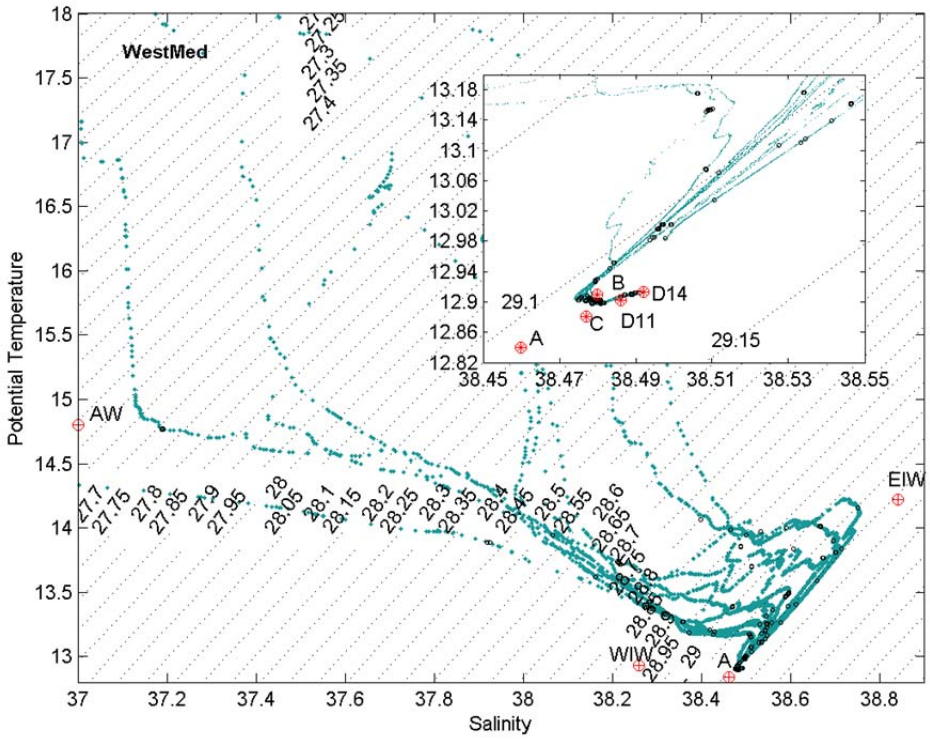

Figure 2.4: *Potential temperature (°C) vs. salinity diagrams for the WestMed CTD (lines) and discrete bottle data (points), σ_ϑ isolines are included. The inset shows the deepest water column. Red dots indicate the potential temperature and salinity of the water types. Water types physical characteristics and acronyms as in Table 2.2 are shown.*

The mass balance equations involved in our OMP analysis are:

$$\sum_i x_{ij} \cdot \theta_i = \theta_j + \mathrm{R}\theta\mathrm{j}$$

$$\sum_i x_{ij} \cdot S_i = S_j + \mathrm{RSj}$$

$$\sum_i x_{ij} \cdot NO_i = NO_j + \mathrm{RNOj} \qquad (2.2)$$

$$\sum_i x_{ij} \cdot (SiO_4)_i = (SiO_4)_j + \mathrm{RSiO4j}$$

$$\sum_i x_{ij} = 1 + \mathrm{R}\sum$$

where x_{ij} is the proportion of water type i in sample j; θ_i, S_i, NO_i and SiO_{4i} are the values of θ, S, NO and SiO_4 of water type i shown in Table 2.3; θ_j, S_j, NO_j and SiO_{4j} are the values of θ, S, NO and SiO_4 in sample j; and $R\theta_j$, RS_j, RNO_j, $RSiO_{4j}$ and $R\sum$ are the residuals of the mass balance equations of θ, S, NO, SiO_4 and mass conservation for sample j. A restriction to this

system of equations is that the values of x_{ij} have to be $\geq$ 0% (a negative proportion has no physical sense). The linear mixing equations are normalized and weighted. The normalization is done using the mean and standard deviation values of the four parameters in Table 2.3. Equations are weighted taking into account the measurement error of each parameter in relation with its variability in the study area and its relative conservative nature. Weights of 8, 8, 1 and 2 were assigned to θ, S, NO and SiO_4, respectively. Lower weights were assigned to the chemical variables as they are partially affected by non–conservative processes. NO uses a constant R_N ratio and, therefore, introduces more uncertainty in the OMP analysis (Álvarez et al., 2014) and SiO_4 is influenced by silica dissolution. A weight of 100 was assigned to the mass balance equation of volume to ensure that it is stringently conserved.

Our OMP solves the mixing of 19 water types, 11 in the EastMed (Table 2.2a) and 8 in the WestMed (Table 2.2b). However, given that only 5 mass balance equations are available (Eq. 2.2), the mixing of up to 5 water types can be solved simultaneously. Previous OMP analysis of the MedSea defined a limited number of water types or a larger number of tracers and/or were constrained to one sub–basin (e.g., Manca et al., 2006; Cardin et al., 2011; Kovačević et al., 2012; Hassoun et al., 2015). A recent work by Jullion et al. (2017) applies a parametric OMP to a similar basin–wide section in the MedSea, with the aim of separating non– and conservative processes on the dissolved barium dynamics. Their simple parametric OMP parameterizes the mixing fractions as a function of position and uses much less water types, even no LIW is included in the EastMed. We avoid the lack of conservation of water masses as in previous OMP (Hainbucher et al., 2014) and also constrain the distributions of water types to avoid discontinuities or unrealistic distributions. We constrained our OMP by defining oceanographically consistent mixing groups where a maximum of 5 water types are allowed to mix simultaneously following the procedure proposed in Álvarez et al. (2014).

Therefore, in order to solve the OMP it is crucial to define mixing groups, this is, which water masses mix and in which basin, maintaining the horizontal and vertical connection or continuity between basins. Mixing groups were defined on the basis of reasonable vertical and geographical constraints to water mass mixing, taking into account recent changes in the properties, structure and circulation of the water masses of the MedSea (Table 2.4). Within each basin, EastMed and WestMed, water mass conservation is stringently maintained. The only common water masses between the EastMed and WestMed correspond to those involved in the shallow open overturning cell (see Figure 1.16 in chapter 1), the low salinity Atlantic surface water (MAW and AW in the EastMed and WestMed, respectively) and the salinity

maximum intermediate Mediterranean water (LIW and EIW in the EastMed and WestMed, respectively) (e.g., Tsimplis et al., 2006). Resolving how AW transforms into MAW and how LIW transforms into EIW is beyond the scope of this work.

Table 2.4: Mixing groups proposed to solve the OMP model for the HOTMIX cruise. The number of samples comprised within each group (N) is shown.

Basin	Water Types comprised	Area – layer	N
EastMed	LIW – LSW – MAW	EastMed – upper	15
	AdMW – CIW – LIW – MAW	EastMed – intermediate	49
	Pre–EMT – EMT – AdMW – CIW	Levantine basin & Hellenic Trench – intermediate	16
	Pre–EMT – EMT – Post–EMT–A – Post–EMT–B	Levantine basin – deep & bottom	16
	Pre–EMT – EMT – Post–EMT–A – Post–EMT–C	Hellenic Trench – deep & bottom	11
	Pre–EMT – AdDW – AdMW – CIW – EMT	Ionian Basin – intermediate	12
	Pre–EMT – AdDW – Post–EMT–B – Post–EMT–C – Post–EMT–A	Northern Ionian Basin – deep & bottom	18
	Pre–EMT – EMT – Post–EMT–A	Ionian basin – deep & bottom	1
WestMed	WIW – EIW – AW	WestMed – upper	37
	A – B – WIW – EIW	WestMed – intermediate	41
	A – B – C – D11 – D14	WestMed – deep & bottom	28
		Total	244

Starting at the EastMed (comprises HOTMIX stations 1 to 13, Figure 2.1), upper waters are resolved using the warm and saline LSW, the colder and fresher MAW and the intermediate LIW (Figure 2.3a, Table 2.2a). Note in the θ–S diagrams (Figure 2.3a) that the HOTMIX station 1 (Figure 2.1) crosses the permanent Cyprus eddy and the scorpion tail θ–S signal associated with LIW is first encountered. The strongest signal for MAW is evident at station 13 in the eastern part of the Strait of Sicily. Intermediate waters in the EastMed are solved using AdMW, CIW, LIW and MAW. High salinity intermediate waters coming out from the Cretan arc straits (CIW) are mostly noticed in stations 4 and 5 south of Crete while the low salinity intermediate waters coming out from the Adriatic Sea (AdMW) are noticed in the Northern Ionian basin (station 10) (Figure 2.3a) where waters with $14.5 < \theta < 15.0$ deviate to lower salinities (Figure 2.5a).

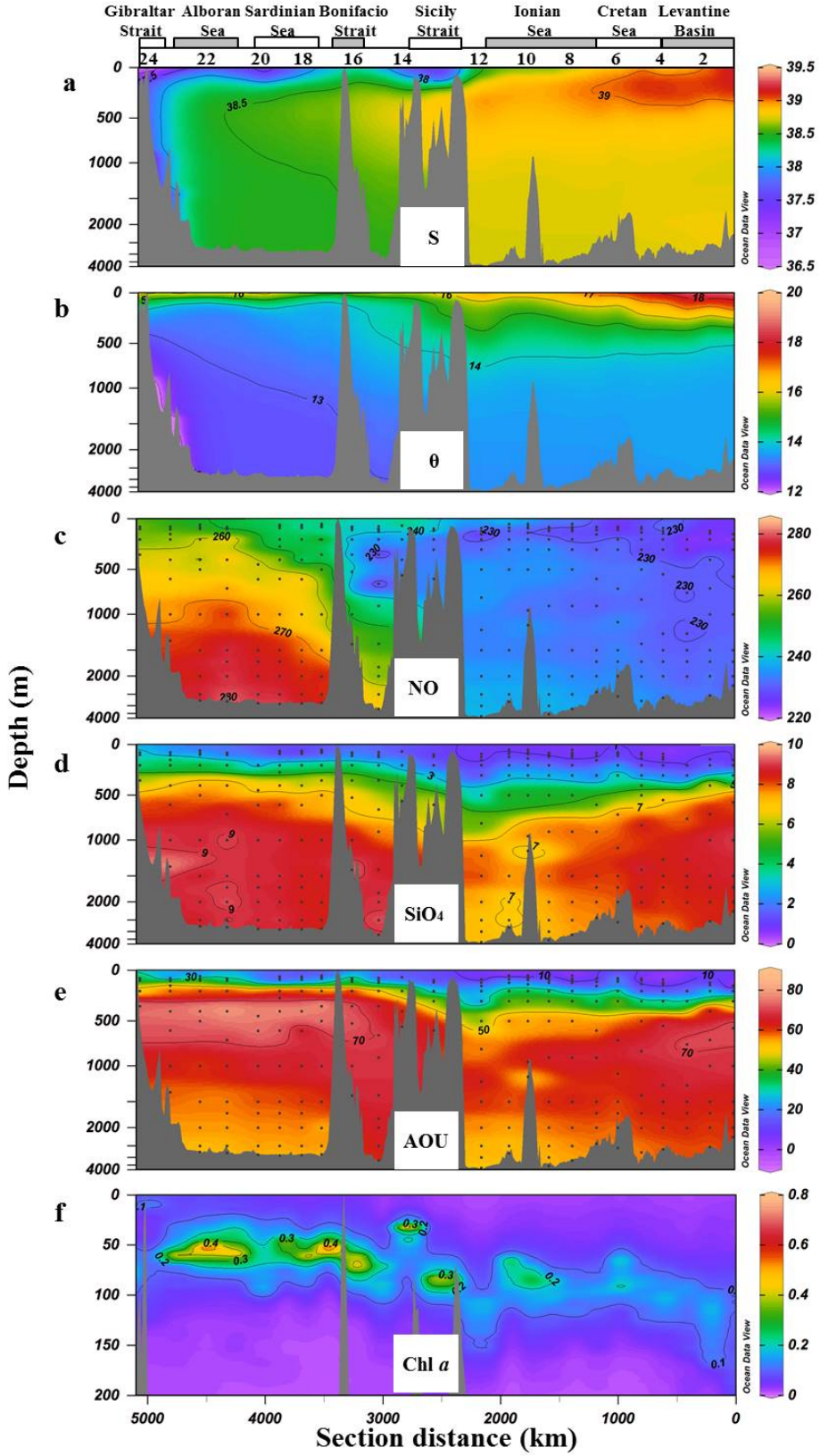

Figure 2.5: *Distribution of the variables used to run the OMP analysis: (a) potential temperature (ϑ, °C), (b) salinity (S), (c) NO (µmol kg^{-1}), (d) silicate (SiO_4, µmol kg^{-1}). Besides (e) apparent oxygen utilization (AOU, µmol kg^{-1}) and (f) fluorescence of chlorophyll a (Chl a, fluorescence units) are represented. Note that the depth of panels a–e are displayed on a not linear scale. Numbers located on the top of the figure indicate the sample stations, which are depicted in Figure 2.1 (page 58). Figure produced with Ocean Data View (Schlitzer, 2017).*

The proposed groups to solve the mixing of EastMed deep and bottom waters maintain the continuity of the different water masses in the EastMed, this is, none of the water types disappears suddenly. In the Levantine basin (stations 1 to 4, East of the Eastern Mediterranean Ridge south of Crete, the hook–like signal in the deep waters θ–S diagrams (Figure 2.3b) associated with Aegean EMT waters is clear. Below them, Post–EMT waters with Adriatic Sea origin are also detected with higher salinity and temperature in the Levantine basin (Figure 2.3b) than the more recent ones found in the Hellenic Trench (Figure 2.3c) and the Ionian basin (Figure 2.3d). In the Levantine basin (station 1–4), East of the Hellenic Trench, the oxygen content below 1000 m is lower than in the Hellenic Trench and Ionian basin. Here and in the near bottom of station 5 the influence of more recently ventilated waters coming from the Adriatic is noticed (Figure 2.5e). In the bottom of the Levantine basin the most recent water type coming out from the Adriatic Sea is not allowed, Post–EMT–C (Figure 2.3b). West of the Eastern Mediterranean Ridge mixing of the different varieties of Post–EMT coming out from the Adriatic Sea since 2000s occurs (Figure 2.3c, d). A larger influence of AdDW is noticed only in the northern Ionian Sea close to the Strait of Otranto, mainly by the high oxygen and low silicate signal (Figure 2.5d, e), but not clear in the θ–S diagram (Figure 2.3d).

The mixing groups in the WestMed (Table 2.4, Figure 2.4) are somehow simpler. Upper waters are solved using AW entering at the Strait of Gibraltar, the much saltier EIW entering the basin at the Strait of Sicily and WIW. EIW is a mixture of intermediate waters from the EastMed, CIW and LIW, along with EMDW at the Strait of Sicily (Figure 2.4). Atlantic Water flowing at the surface eastwards from the Strait of Gibraltar and the intermediate high salinity water flowing in the opposite direction define the open–cell overturning circulation in the MedSea (see figure 1.16 in chapter 1). The pairs AW–EIW and MAW–LIW model this cell in each basin. The resident WMDW type called A by Schröder et al. (2006) along with the younger vintages B, C and D solve deep and bottom waters in the WestMed (inset in Figure 2.4).

The reliability of our OMP model is mostly dependent on the characteristics of the water types proposed (Table 2.3) and the mixing constraints used (Table 2.4). The high correlation between the input measured variables and those predicted or back–calculated from the OMP using the water type proportions gives confidence to our calculations. Only data below 200 m less affected by seasonal variability is considered in calculating the R^2 and SE of the linear regression between the measured and back–calculated values for the input variables, S, θ, NO and SiO_4 and the distribution of the total and individual residuals from the system of mass balance equations (2.2) showed in Table 2.3. The back–calculated fields are obtained multiplying the OMP water mass proportions (x_{ij}) by the water type values of S, θ, NO and SiO_4.

Except in the EastMed where the R^2 and SE of the NO tracer is lower (Table 2.3) as expected due to the non Redfieldian behaviour, the other R^2 are very high and the SE values comparable to the measurement error.

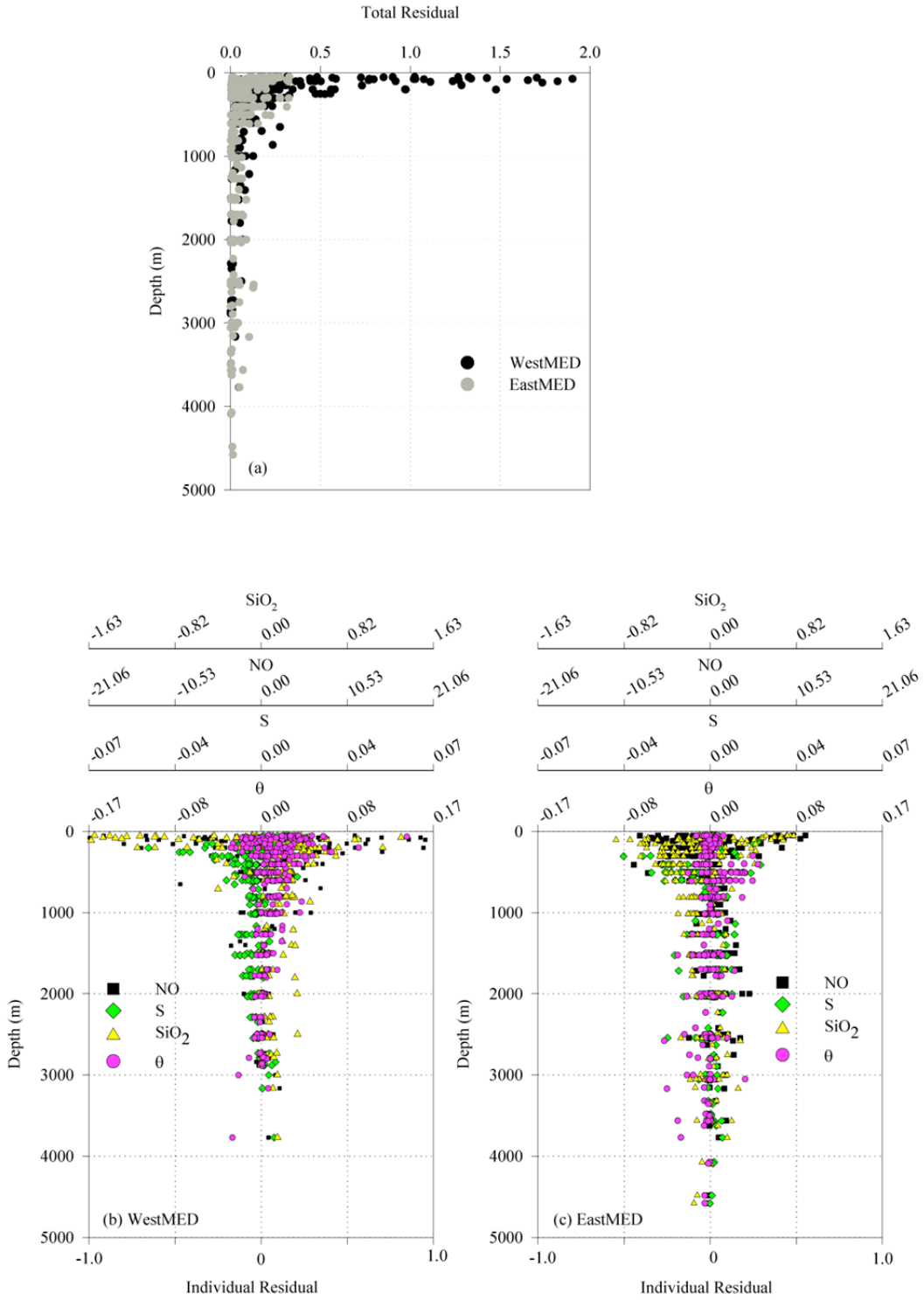

Figure 2.6: *(a) Total Residual from the mixing model and (b, c) Individual Residuals (dimensionless and weighted) from each equation introduced in the mixing analysis. The upper axes in (b, c) show the residuals with real units: potential temperature (θ, °C), salinity (S), silicate (SiO_4, µmol kg^{-1}) and NO (µmol kg^{-1}).*

In addition, the vertical distributions for the EastMed and WestMed of the total and individual residuals from Eq. 2.2 are shown in Figure 2.6. Except for the upper 200 m where the total residual is higher, in both basin the total residual from the OMP analysis is very low, as are the individual contribution from the different input equations, and no trend is discerned with pressure or basin, assuring the reliability of our proposed mixing model.

Following Álvarez et al. (2014), the water proportions showed in this work are the mean values of the 100 solutions obtained after 100 random perturbations were applied to the water type input characteristics around their respective uncertainties.

2.4 Assessing the impact of water mass mixing and biogeochemistry in the distribution of the explanatory and response variables

2.4.1 Water mass mixing weighted–average values

The water mass mixing weighted–average value, hereinafter archetype value, of any variable (N) in a given water mass can be obtained as:

$$\langle N_i \rangle = \frac{\sum_j x_{ij} \cdot N_j}{\sum_j x_{ij}} \quad (2.3)$$

where $\langle N_i \rangle$ is the archetype value of N in water mass *i*; N_j is the value of N in sample j; and x_{ij} is the proportion of water mass *i* in sample j. The standard deviation (SD) of the archetype value of N is calculated as:

$$SDN_i = \frac{\sqrt{\sum_j x_{ij} \cdot (N_j - \langle N_i \rangle)^2}}{\sum_j x_{ij}} \quad (2.4)$$

Application of Eq. (2.3) to the longitude, latitude and depth of the samples allowed the calculation of the centre of mass or barycentre of each water mass.

Finally, the proportion of the total volume of the samples occupied by a given water mass ($\%VOL_i$) was calculated as:

$$\langle \%VOL_i \rangle = 100 \cdot \frac{\sum_j x_{ij}}{n} \quad (2.5)$$

where n = 244, is the number of samples included in the OMP analysis.

2.4.2 Mixing model of DOC and CDOM

The fraction of the total variability of parameter N due to water mass mixing can be calculated from the multiple linear regression of N_j with the previously obtained x_{ij} values. A system of n linear equations (one per sample) with m coefficients (one per WT) has to be solved for each chemical variable:

$$N_j = \sum_j x_{ij} \cdot \alpha_i \qquad (2.6)$$

where α_i is the linear fitting parameter of WT i for parameter N. The determination coefficient (R^2) and the standard deviation of the residuals (SD res) of this regression define the goodness of the fit.

2.4.3 Mixing–biogeochemical model of DOC and CDOM

The distribution of any chemical variable depends on (i) the conservative mixing of water masses with contrasting initial values of that chemical variable and (ii) the non–conservative biogeochemical processes occurring during that mixing. The non–conservative processes can be classified in two types: those that correlate with the water mass proportions and those that are independent of the water mass proportions.

The non–conservative processes that correlate with the water mass proportions represent the mineralization occurring from the formation area of each water mass to the study area. Therefore, the multiple linear regressions with the water type proportions (Eq. 2.6) do not retain only the variability due to mixing of water masses of contrasting origins and initial concentrations of the chemical properties. They retain also the variability associated with the biogeochemical processes occurring at the basin–scale (Perez et al., 1993; Álvarez–Salgado et al., 2013; Álvarez et al., 2014). By contrast, the non–conservative processes independent of the water mass proportions retain the variability associated with samples with the same water mass composition but different biogeochemical history, i.e. experiencing different processes or the same processes but with different intensity.

Simultaneous modelling of the impact of both mixing and biogeochemical processes on the distribution of DOC and CDOM implies the addition to Eq. 2.6 of a term that models the non–conservative processes independent of the water type proportions. To do that, an explanatory chemical variable (N_2) is introduced to improve our explanation of the response variable (N_1) as follows:

$$N_{1j} - \sum_j x_{ij} \cdot \alpha_{1i} = \beta \cdot \left(N_{2j} - \sum_j x_{ij} \cdot \alpha_{2i} \right) \quad (2.7)$$

Note that the term in the left represents the residuals of Eq. 2.6 for the response variable and the term in parenthesis in the right are the residuals of Eq. 2.6 for the explanatory variable. β is the fitting parameter of the relationship between N_1 and N_2, independent of the mixing, assuming that such a relationship is linear and homogeneous (i.e., β does not vary) in all the study area. This equation can be rearranged as follows:

$$N_{1j} = \sum_j x_{ij} \cdot (\alpha_{1i} - \beta \cdot \alpha_{2i}) + \beta \cdot N_{2j} \quad (2.8)$$

Therefore, a system of n linear equations (one per sample) with m+1 unknowns (one per water type, $\alpha_{1i} - \beta \cdot \alpha_{2i}$, and the coefficient β) has to be solved. As for the case of Eq. 2.6, the goodness of this linear mixing–biogeochemical model was tested using the determination coefficient (R^2) and the standard deviation of the residuals of the least squares analysis (SD res).

3 Results

3.1 Distribution of the main MedSea water masses during the HOTMIX cruise

The distributions of salinity, potential temperature, NO and silicate (Figure 2.5), i.e. the input parameters of the OMP analysis (section 2.3), are our prime tracers of water mass mixing in the MedSea.

Salinity in the upper layers mainly reflects the shallow overturning cell of the MedSea with the low salinity surface Atlantic Water (AW) displacing from West to East, centred at 88 ± 14 m in the WestMed and 125 ± 26 m in the EastMed (Table 2.5; Figure 2.7). Note that in the EastMed the AW is introduced in the OMP Analysis as modified Atlantic Water (MAW) (Table 2.2a). In the Levantine basin, the MAW mixes with the Levantine Surface Water (LSW), centred at 116 ± 21 m (Table 2.5; Figure 2.7). These shallow water masses represent all together 8.7% of the total volume sampled during the cruise (Table 2.5). The counterpart of this low salinity eastward surface flow is the high salinity Levantine Intermediate Water (LIW) that returns at depth towards the Atlantic. Maximum salinity was found around 200 m in the EastMed (Figure 2.5a). LIW is centred at 149 ± 13 m in the EastMed, where it represents 12.2% of the total volume of water sampled during the cruise (Table 2.5). In the WestMed, a modified LIW, named as Eastern Intermediate Water (EIW) is introduced in the OMP analysis (Table 2.2b).

Note that the EIW is a mixture of the LIW that enters the WestMed through the Sicily Strait, with WIW and the Ionian deep water (Table 2.2b). EIW is centred at 364 ± 79 m and represents 11.4% of the volume sampled (Table 2.5). In the EastMed, where the LIW is shallower, it is also important the volume of Cretan Intermediate Water (CIW), 6.6% of the volume sampled, that forms in the Cretan Sea and spreads below the LIW at 379 ± 56 m (Table 2.5; Figure 2.7). Conversely, in the WestMed, where the EIW is deeper, the layer above this water mass is occupied by the Winter Intermediate Water (WIW), formed in the Western Mediterranean basin, centred at 170 ± 33 m and representing 6.9% of the total volume sampled (Figure 2.7).

Similarly to salinity, θ presented its maximum in the upper layers of the EastMed (Figure 2.5b), reaching a θ_i of 17.8°C (Table 2.3) for the LSW. In the EastMed, the average ± SD of θ in the surface layer was 16.17 ± 0.78°C, whereas in the WestMed the value was lower, 13.99 ± 0.35°C. In the deep layers, different varieties of EMDW, with initial salinites ranging from 38.717 to 38.788 and initial temperatures from 13.40 to 13.64°C, were found (Table 2.3). They were more saline and warmer than the varieties of WMDW found in the WestMed, which ranged from 38.460 to 38.492 and 12.840 to 12.913°C (Table 2.3). The Pre–EMT water type is the most abundant EMDW sampled during the cruise, with 14.3% of the total volume and it is located at 1462 ± 125 m depth (Table 2.5; Figure 2.7); the EMT water type is present in the Levantine basin just below the Pre–EMT water at a depth of 1702 ± 135 m (Figure 2.7). The Post–EMT, with three different varieties (A, B, C), is the most recent EMDW water mass produced in the Adriatic Sea after the EMT event. The Post–EMT–A was intercepted in the Levantine basin just below Pre–EMT, at 1903 ± 180 m, representing 3.3% of the total volume. The Post–EMT–B and Post–EMT–C were intercepted in the Ionian Sea, i.e. much closer to their formation area, at depths >2000 m near Crete, covering a lower volume extent (2.3 and 1.8% of the total volume, respectively). These youngest water masses are replacing and uplifting the old water masses present in this basin. In the deep WestMed, WMDW is formed in winter in the Gulf of Lions (Gascard, 1978) and occupies the water column below the EIW (Figure 2.7). Here, five different varieties of WMDW have been intercepted. The variety A is the oldest and the most abundant deep WT of the WestMed, with 9.3% of the total sampling volume; the varieties B and C were originated in winter 2004/5 but they presented different θ–S properties, implying a larger contribution of LIW to B and of AW to C (Schröder et al., 2006). The most recent varieties, D11 and D14, were found in 2011 and 2014 and correspond to the saltiest and densest WMDW (Puig et al., 2013; Schroeder et al., 2016; Houpert et al., 2016).

Table 2.5: Archetypal depth (Z_i), apparent oxygen utilization (AOU_i), dissolved organic carbon (DOC_i), absorption coefficient at 254 nm (a_{254i}) and 325 nm (a_{325i}), slope between 275–295 nm ($S_{275–295i}$), slope between 350–400 nm ($S_{350–400i}$), ratio of the slope between 275–295 nm divided by the slope between 350–400 nm (S_{Ri}), and the prokaryotic heterotrophic abundance (PHA_i) of the water masses intercepted during the HOTMIX cruise. The percentage of the total volume of water sampled corresponding to each water type (VOL_i) is also reported.

	Acronym	VOL_i (%)	Z_i (m)	AOU_i (µmol kg^{-1})	DOC_i (µmol L^{-1})	a_{254i} (m^{-1})	a_{325i} (10^3 m^{-1})	$S_{275–295i}$ (µm^{-1})	S_{Ri}	PHA_i (10^{-3} cells ml^{-1})
EastMed	MAW	3.2	125±26	13±5	57±3	1.16±0.05	18.1±1.4	33.3±–1.4	2.2±0.1	348±53
	LSW	1.8	116±21	3±3	59±2	1.18±0.06	15.3±0.8	37.3±–1.5	2.5±0.2	331±50
	LIW	12.2	149±13	15±2	59±1	1.08±0.03	15.0±0.5	35.8±–0.5	2.4±0.1	260±18
	CIW	6.6	379±56	47±3	48±2	0.86±0.03	12.6±0.6	33.4±–0.8	2.6±0.1	122±15
	AdMW	5.8	273±55	34±5	54±2	0.94±0.05	13.7±0.9	33.9±–0.9	2.4±0.1	179±27
	AdDW	0.5	1425±403	59±4	41±1	0.65±0.02	9.5±0.6	30.7±–3.6	2.3±0.3	42±8
	Pre–EMT	14.3	1462±125	62±1	39±1	0.66±0.01	9.6±0.3	32.3±–0.5	2.5±0.1	41±4
	EMT	4.3	1702±135	62±1	37±1	0.62±0.01	8.6±0.3	33.6±–1.1	2.5±0.1	30±3
	Post–EMT–A	3.3	1903±180	58±1	40±1	0.65±0.01	9.3±0.3	32.5±–1.2	2.4±0.1	32±3
	Post–EMT–B	2.3	2892±227	55±1	41±1	0.66±0.01	9.8±0.3	31.6±–1.0	2.2±0.1	31±3
	Post–EMT–C	1.8	2414±235	56±1	41±1	0.66±0.01	9.9±0.3	31.1±–1.3	2.3±0.1	30±4
WestMed	AW	3.7	88±14	23±5	56±2	1.11±0.03	19.3±0.9	30.7±–0.4	2.1±0.0	550±60
	EIW	11.4	364±79	51±5	50±1	0.89±0.03	15.1±0.7	30.3±–0.2	2.3±0.0	308±45
	WIW	6.9	170±33	45±5	53±1	0.99±0.03	17.2±0.8	30.0±–0.3	2.3±0.0	414±53
	A	9.3	1210±156	67±1	42±1	0.69±0.01	11.2±0.3	28.9±–0.3	2.4±0.0	86±13
	B	5.8	1632±222	61±2	43±1	0.69±0.01	10.9±0.3	29.0±–0.3	2.5±0.1	77±12
	C	0.7	2012±300	56±1	42±2	0.67±0.01	10.4±0.5	29.5±–1.1	2.5±0.2	51±3
	D11	0.7	2476±357	55±1	42±2	0.69±0.01	10.8±0.4	29.2±–1.2	2.4±0.2	55±4
	D14	5.4	2134±160	56±1	42±1	0.68±0.00	10.7±0.2	28.9±–0.5	2.4±0.1	56±2

NOTE: MAW: Modified Atlantic Water, LSW: Levantine Surface Water, LIW: Eastern Levantine Intermediate Water, CIW: Cretan Intermediate Water, AdMW: Adriatic Middle Water, AdDW: Adriatic Deep Water, Pre–EMT: Eastern Mediterranean Deep Water (EMDW) previous to the EMT, EMT: EMDW during the EMT, Post–EMT–A: EMDW after the EMT found in the Levantine basin, Post–EMT–B: EMDW formed after the year 2003, Post–EMT–C: EMDW formed after the year 2007, AW: Atlantic Water, EIW: Eastern Intermediate Water formed in the Levantine Basin and found in the western basin, WIW: Winter Intermediate Water, A: Western Mediterranean Deep Water (WMDW) formed prior to the year 2005, B: WMDW formed in winter 2004/5 in the Gulf of Lions, C: WMDW originated in winter 2004/5 with high influence of coastal shelf waters, D11: WMDW formed prior to the year 2011, D14: WMDW formed prior to the year 2014.

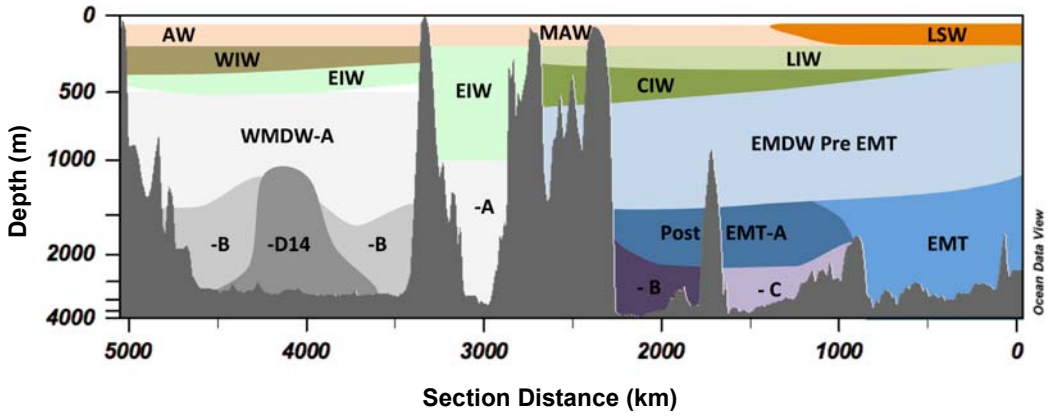

Figure 2.7: *Distribution of the water masses in the MedSea. See Table 2.2 for detailed information of the water masses nomenclature.*

NO ranged between 220 and 300 µmol kg^{-1} and its maximum was found in the deep waters of the WestMed (Figure 2.5c) indicating the presence of the newest variety of the WMDW (WMDW–D) which is characterized by the maximum initial NO value of 280 ± 5 µmol kg^{-1} (Table 2.3). SiO_4 ranged between 0.6 to 9.6 µmol kg^{-1} (Figure 2.5d). The highest SiO_4 concentrations were found in the deep waters of the WestMed, with SiO_{4i} values around 9.5 µmol kg^{-1} (Table 2.3). In the EastMed, the highest SiO_4 concentrations were found at about 1000 m in the Levantine basin, where the Pre–EMT with an initial SiO_4 of 9.1 µmol kg^{-1} (Table 2.3) is found. In the upper ocean, low SiO_4 concentrations of around 2 µmol kg^{-1} covered a thick depth range in the EastMed up to 400 m, whereas in the WestMed higher SiO_4 values for the same depths were observed as a result of the AW inflow (Figure 2.5d).

3.2 Distribution of the explanatory variables: AOU and Chl a

The distribution of AOU in the MedSea during the HOTMIX cruise (Figure 2.5e) reflects the differential ageing of the 19 water types intercepted during the navigation, i.e. the cumulative oxygen consumption from the formation area of each water mass to the study section. The lowest AOU levels were recorded in the epipelagic layer (<150 m) with a significant decrease towards the East (Figure 2.5e). Whereas the AW of the WestMed had an archetype AOU of 23 ± 5 µmol kg^{-1}, the LSW formed in the Levantine basin was characterized by an archetype AOU of just 3 ± 3 µmol kg^{-1} (Table 2.5). AOU values were maxima in the mesopelagic layer (150–1000 m) all along the MedSea. The LIW was characterized by an archetype AOU of 15 ± 2 µmol kg^{-1} whereas this value was 51 ± 5 µmol kg^{-1} for the EIW. The other intermediate waters of the WestMed (WIW) and EastMed (CIW) had the same archetype AOU of 45–47 µmol kg^{-1} (Table 2.5). Furthermore, the AOU maximum layer was shallower in the WestMed, between 350 to 400 m, concurring with the archetype depth of the EIW (364 ±

79 m) (Table 2.5; Figure 2.5e) as was previously observed (Tanhua et al., 2013; Álvarez et al., 2014). Note that although the AOU maximum in the WestMed reached up to 80 μmol kg^{-1}, the archetype AOU of the EIW was 51 ± 5 μmol kg^{-1} because it is a water mass proportion weighted average of all samples containing LIW and not just those from the AOU maximum. In the EastMed, the AOU maximum was found deeper, between 600 and 700 m, in between the LIW, centred at 149 ± 13 m and the Pre–EMT, centred at 1462 ± 125 m (Table 2.5). Finally, in the bathypelagic layer (>1000 m) the older EMDW varieties, present in the Levantine basin, had a higher archetype AOU of 62 ± 1 μmol kg^{-1}. In contrast, the younger EMDW branches, found in the Ionian Sea, had a lower AOU of 55–58 μmol kg^{-1}. In the western basin, the oldest WMDW–A presented the highest archetype AOU of 67 ± 1 μmol kg^{-1} whereas the youngest varieties (WMDW–B, C, D) had a lower AOU of 55–61 μmol kg^{-1} (Table 2.5).

Apart from the AOU, which is a key parameter to understand the distribution of any biogeochemical variable throughout the entire water column, Chl *a* is also a major environmental driver in the epipelagic layer of the ocean. In the MedSea, as in any other oligotrophic region, Chl *a* levels are very low and concentrated around a deep chlorophyll maximum (DCM). This DCM was shallower and with higher Chl *a* concentrations in the oligotrophic WestMed than in the ultraoligothropic EastMed (Figure 2.5f). In the EastMed, the DCM was situated at 93 ± 11 m with a mean ± SD concentration of 0.22 ± 0.08 mg m^{-3} and in the WestMed was at 53 ± 18 m with 0.46 ± 0.17 mg m^{-3}.

3.3 Distributions of the response variables: DOC and CDOM

In the epipelagic layer, the EastMed showed higher DOC concentrations than the WestMed (Figure 2.8a), with mean ± SD values of 60 ± 1 and 56 ± 1 μmol L^{-1}, respectively. In fact, the water mass with the highest archetype DOC concentration was the LSW with 59 ± 2 μmol L^{-1} (Table 2.5). In the mesopelagic layer, a marked westward decrease of DOC was observed with the LIW presenting an archetype DOC of 59 ± 1 μmol L^{-1}, whereas the EIW presented 50 ± 1 μmol L^{-1}. Accordingly, DOC removal occurs when this water mass moves westwards. Unlike the epi– and mesopelagic layers, DOC concentrations in the bathypelagic layer (>1000 m) were much lower and homogeneous. Most of the deep water masses of the EastMed and WestMed present archetype concentrations of 39–41 and 42–43 μmol L^{-1}, respectively (Table 2.5). It is remarkable the low archetype DOC of the EMDW formed during the EMT (37 ± 1 μmol kg^{-1}).

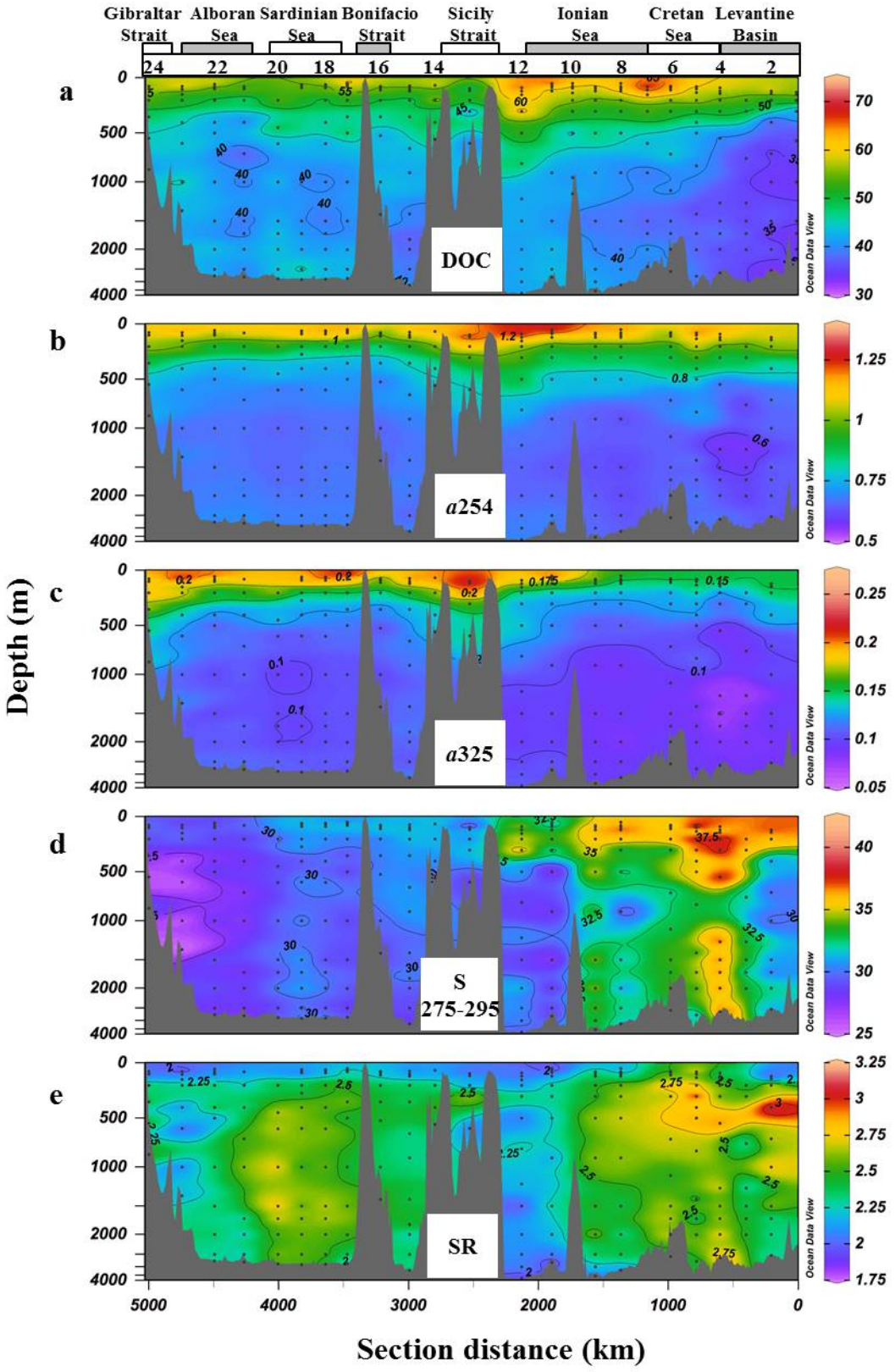

Figure 2.8: *Distribution of (a) DOC (µmol C L^{-1}), (b) absorption coefficient at 254 nm (a_{254}, m^{-1}), (c) absorption coefficient at 325 nm (a_{325}, m^{-1}), spectral slope between 275–295 nm ($S_{275–295}$, 10^{-3} m^{-1}), and (d) slope ratio (S_R, unitless). Numbers located on the top of the figure indicate the sample stations, which are depicted in Figure 2.1 (page 58). Figure produced with Ocean Data View (Schlitzer, 2017).*

a_{254} values ranged between 0.56 to 1.34 m^{-1} and maximum values were found in the epipelagic layer, particularly in the Ionian Sea (Figure 2.8b). As for the case of DOC, the LSW presented the maximum archetype a_{254} value of 1.18 ± 0.06 m^{-1}, followed by the MAW with 1.16 ± 0.05 m^{-1} (Table 2.5). The lowest values were found around 1500 m in the EastMed and the minimum archetype a_{254} was attributed to the EMT (0.62 ± 0.01 m^{-1}). Overall, the distribution of a_{254} (Figure 2.8b) was parallel to the distribution of DOC (Figure 2.8a); the direct linear regression of both variables was highly significant (DOC = 9 (±1) + 46 (±1) a_{254}; R^2 = 0.87, $p < 0.001$, n = 273; Figure 2.9).

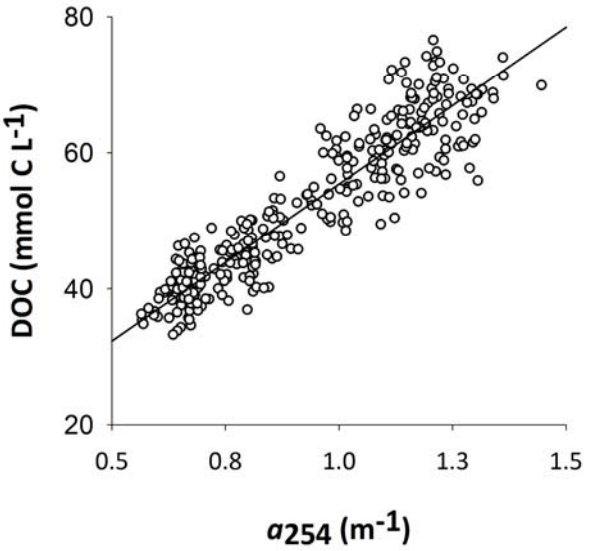

Figure 2.9: *Relationship of DOC (µmol C L^{-1}) with a_{254} (m^{-1}).*

For a_{325}, minimum values were also found in the deep waters of the EastMed (Figure 2.8c), and the lowest archetype a_{325} was attributed again to the EMT with 8.6 ± 0.3 x 10^3 m^{-1} (Table 2.5). In the epipelagic layer, a_{325} decreased from West to East, from archetype values of 19.3 ± 0.9 x 10^3 m^{-1} for the AW to 15.3 ± 0.8 x 10^3 m^{-1} for the LSW (Table 2.5). Considering the $S_{275–295}$ and the S_R ratio, the largest values were found in the EastMed at around 500 m depth (Figure 2.8d and e). The LSW features the highest archetype $S_{275–295}$ of 37.3 ± 1.5 μm^{-1} and the CIW the highest S_{Ri} of 2.6 ± 0.1 (Table 2.5). Whereas the lowest $S_{275–295}$ values were found in the WestMed between 500 and 1500 m (Figure 2.8d) with minimum archetype $S_{275–295}$ for the five WMDW varieties, the S_R values were more spread over the WestMed surface and the deep layer of the Ionian Sea (Figure 2.8e). The lowest ratio was found in AW with a value of 2.1 ± 0.1.

3.4 Drivers of DOC and CDOM parameters in epipelagic waters

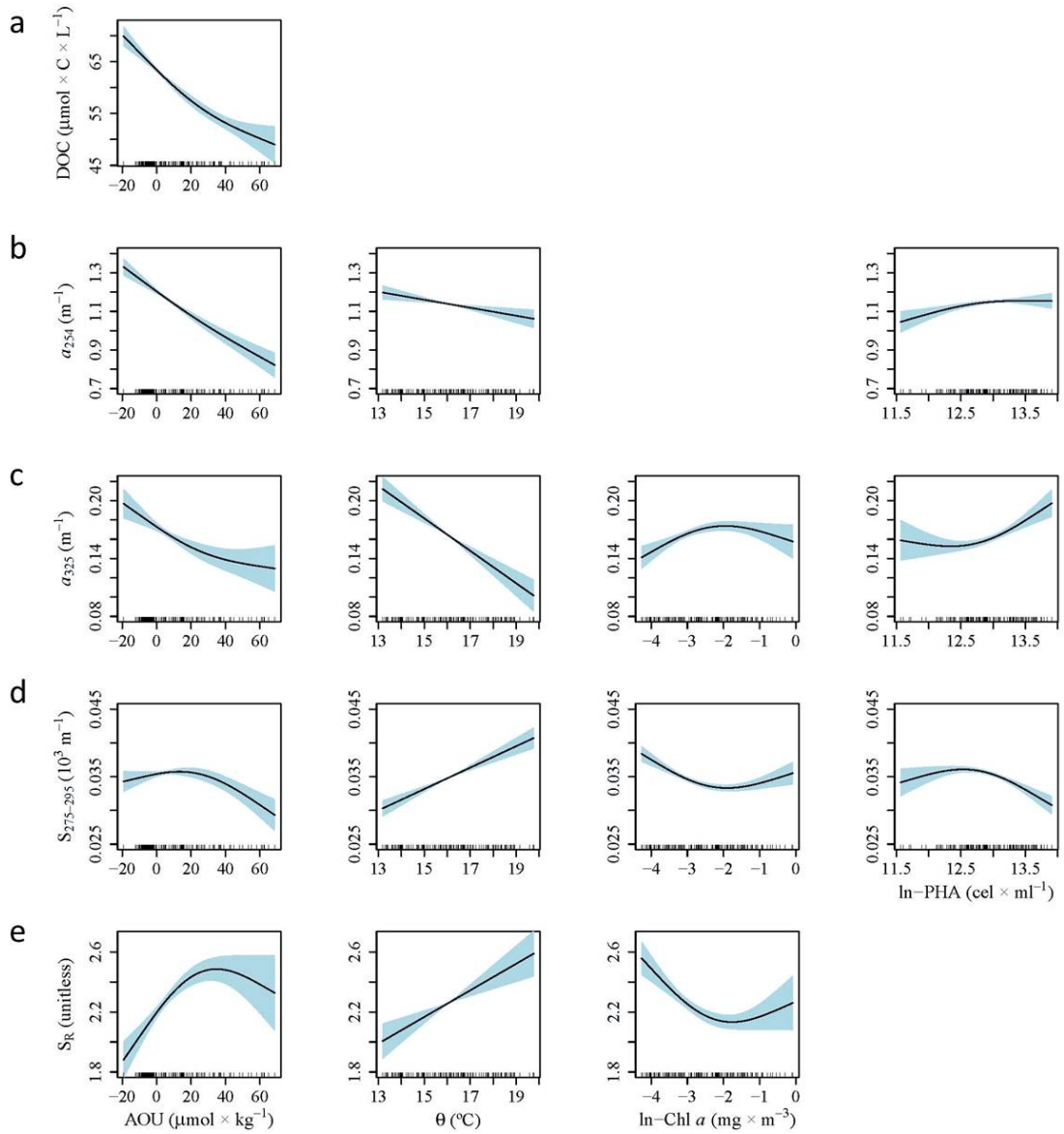

Figure 2.10: *Partial plots of the additive effects of the physical, chemical and biological covariates on the DOC and CDOM parameters after fitting Generalized Additive Models. (a) DOC, (b) a_{254}, (c) a_{325}, (d) $S_{275–295}$. (e) S_R. Rugs on x–axis indicate the distribution of the data.*

We used GAMs for exploring non–linear relationships between CDOM parameters and selected environmental factors (Figure 2.10). The variable that exhibited the largest effect on DOC was AOU (F–value = 86.02; Table 2.6) with a negative power–law relationship (Figure 2.10a) and a percentage of the variance explained of 76.2%. Likewise, a_{254} had AOU as the most significant explanatory variable (F–value = 52.56; Table 2.6) with a negative linear relationship (Figure 2.10b). For a given AOU, any increase in θ has a negative effect on a_{254} (F–value = 10.68; Table 2.6; Figure 2.10b). However, a_{254} responded positively to PHA until reaching a concentration of approximately e^{13} (= 4.4 x 10^5 cell mL^{-1}; F–value = 4.94; Table 2.6).

All these three variables together represented a deviance explained (DE) of 76.2% (Table 2.6).

Contrary to a_{254}, a_{325} was mainly controlled by θ (F–value = 56.79; Table 2.6), decreasing its value linearly with increasing temperature (Figure 2.10c). For a given θ, a_{325} presented a negative power–law response to AOU (F–value = 11.22) with a plateau at around 20 µmol kg^{-1} (Figure 2.10c). Unlike a_{254}, PHA presented a positive linear relationship with a_{325} from values of $e^{12.7}$ (= 3.3 x 10^5) cell mL^{-1} onwards (F–value = 11.83). In this case, Chl *a* contributed significantly to explain a_{325} in contrast with a_{254} (F–value = 8.60), being positive until becoming constant at a value of e^{-2} (= 0.14) mg m^{-3}. These four variables contributed to explain 72.6% of the total variance of a_{325}. Similarly, $S_{275–295}$ was explained by the same variables than a_{325} at a DE = 83% (Table 2.6). In addition, it was mostly explained by θ (F–value = 56.88), through a positive linear relationship (Figure 2.10d). Here, Chl *a* and bacterial abundance contributed more substantially to explain the variability of this parameter than those of the absorption coefficients, with F–values of 20.11 and 19.32, respectively (Table 2.6). At a given θ, bacterial abundance and AOU exert negatively at values higher than approximately $e^{12.7}$ (= 3.3 x 10^5) cell mL^{-1} and 20 µmol kg^{-1}, respectively. The explained variance for S_R (43.5%) was substantially lower than those of the absorption coefficients and $S_{275–295}$ (Table 2.6). S_R variability was controlled by θ, AOU and Chl *a* with F–values of 18.74, 20.02 and 15.23 (Table 2.6). Whereas the relationship with θ was positive and linear, the relationships with AOU and Chl *a* were not, shifting from positive to negative at AOU of around 30 µmol kg^{-1} and from negative to positive for Chl *a* at around e^{-2} (= 0.14) mg m^{-3} (Figure 2.10e).

3.5 Drivers of DOC and CDOM parameters in meso– and bathypelagic waters

The mixing model (Eq. 2.6), which includes the effect of water mass mixing and basin–scale mineralization, explained 83% of the variability of DOC in the meso– and bathypelagic MedSea (Table 2.7). The addition of AOU produces a mixing–biogeochemical model (Eq. 2.7) that increased the explained variability to 86%, accompanied by a reduction of the SD of the residuals by 10.3% (Table 2.7). The water mass mixing independent DOC/AOU slope for the entire MedSea was –0.22 ± 0.03 mol C mol O_2^{-1}, which translates into a DOC/AOU–Ceq ratio of 31 ± 4% assuming a $–O_2$/C mineralization ratio of 1.4 (Anderson and Sarmiento, 1994; Anderson, 1995). In the EastMed, the mixing model explained 86% of the variability of DOC, which increased to 90% when AOU is included in the mixing–biogeochemical model and the SD of the residuals reduced by 15.2% (Table 2.7). For this basin, the slope DOC/AOU slope was –0.47 ± 0.07 mol C mol O_2^{-1}, i.e. a DOC/AOU–Ceq ratio of 66 ± 10%. Conversely, in the WestMed, the mixing model explained much less variability (only 74%), which increased to

80% when AOU is included and the resultant DOC/AOU slope was –0.17 ± 0.03 mol C mol O_2^{-1}, which translates into a DOC/AOU–Ceq ratio of 24 ± 4%. For the case of $a_{254,}$ the mixing model explained 91% of its variance in the entire MedSea. Inclusion of AOU derives in a mixing–biogeochemical model that increased the explained variance of a_{254} to 95% with a substantial reduction of the SD of the residuals by 26.3%. In the WestMed, the SD of the residuals reduction was even higher (i.e. 38.4%, Table 2.7). The water mass mixing independent a_{254}/AOU ratio was significantly higher in the EastMed (–8 ± 1 m^2 mol O_2^{-1}) than in the WestMed (–4.3 ± 0.4 m^2 mol O_2^{-1}).

Table 2.6: Results of the Generalized Additive Models (GAMs) fitted to the dissolved organic carbon (DOC) and the absorbance variables data in the epipelagic layer. Note that only statistically significant covariates were retained in the final formulations. SE = Standard Error; EDF = Estimated Degrees of Freedom; DE = Deviance Explained. Note that Chl *a* and PHA were ln–transformed.

Variable	Parameter	Estimate (±SE)	EDF	t–value	F–value	P–value
DOC	Intercept	60.88 (0.39)		154.6		<0.0001
N = 159	AOU		1.82		86.02	<0.0001
DE = 76.2%						
a_{254}	Intercept	1.14 (0.005)		213.9		<0.0001
N = 142	θ		1.00		10.68	<0.0014
DE = 76.2%	AOU		1.65		52.56	<0.0001
	PHA		1.81		4.94	<0.0056
a_{325}	Intercept	0.16 (0.002)		94.67		<0.0001
N = 142	θ		1.00		56.79	<0.0001
DE = 72.6%	AOU		1.73		11.22	<0.0001
	Chl *a*		1.96		8.60	<0.0004
	PHA		1.92		11.83	<0.0001
$S_{275–295}$	Intercept	0.035 (0.0002)		214.1		<0.0001
N = 142	θ		1.00		56.88	<0.0001
DE = 83%	AOU		1.99		13.29	<0.0001
	Chl *a*		1.99		20.11	<0.0001
	PHA		1.99		19.32	<0.0001
S_R	Intercept	2.26 (0.02)		122.8		<0.0001
N = 142	θ		1.00		18.74	<0.0001
DE = 43.5%	AOU		1.95		20.02	<0.0001
	Chl *a*		1.94		15.23	<0.0001

Table 2.7: Parameters of the linear mixing (Eq. 2.6) and mixing–biogeochemical (Eq. 2.7) models. R^2, determination coefficient; SD res, standard deviation of the residuals of the estimation; % SD reduction, percentage of reduction of the SD res of the mixing biogeochemical as compared with the corresponding mixing model; β, fitting parameter of the relationship between N_1 and N_2 independent of the mixing; SE(β), standard error of the estimation of b; *p*, significance level of the estimation of β. Results are presented for all samples and for the EastMed and WestMed, separately.

N_1	N_2	R^2	SD res	%SD reduction	β	SE(β)	*p*	n
MedSea								
AOU		0.88	7.8					233
PHA		0.78	88518					240
TOC		0.83	3.8					233
a_{254}		0.91	0.06					209
a_{325}		0.82	0.02					209
$S_{275–295}$		0.64	0.002					209
S_R		0.35	0.2					149
TOC	AOU	0.86	3.4	10.3%	–0.22	0.03	0.0000	226
a_{254}	AOU	0.95	0.05	26.3%	–0.0048	0.0004	0.0000	203
a_{325}	AOU	0.88	0.01	17.8%	–0.0010	0.0001	0.0000	203
$S_{275–295}$	AOU	0.64	0.002	–0.5%			n.s.	203
S_R	AOU	0.37	0.2	2.1%	0.006	0.002	0.0012	203
EastMed								
AOU		0.96	4.4					130
PHA		0.85	51696					134
TOC		0.86	3.9					131
a_{254}		0.92	0.06					105
a_{325}		0.84	0.01					105
$S_{275–295}$		0.46	0.002					105
S_R		0.34	0.2					105
TOC	AOU	0.90	3.3	15.2%	–0.47	0.07	0.0000	126
a_{254}	AOU	0.95	0.05	21.0%	–0.008	0.001	0.0000	101
a_{325}	AOU	0.85	0.01	7.4%	–0.0007	0.0003	0.0270	101
$S_{275–295}$	AOU	0.43	0.002	–1.3%			n.s.	101
S_R	AOU	0.36	0.2	2.8%	0.017	0.006	0.0056	101
WestMed								
AOU		0.72	10.6					103
PHA		0.73	119600					106
TOC		0.74	3.6					102
a_{254}		0.90	0.06					104
a_{325}		0.80	0.02					104
$S_{275–295}$		0.31	0.001					104
S_R		0.35	0.2					104
TOC	AOU	0.80	3.2	10.9%	–0.17	0.03	0.0000	99
a_{254}	AOU	0.96	0.04	38.4%	–0.0043	0.0004	0.0000	101
a_{325}	AOU	0.89	0.01	25.5%	–0.0010	0.0001	0.0000	101
$S_{275–295}$	AOU	0.31	0.001	0.8%			n.s.	101
S_R	AOU	0.41	0.2	3.6%	0.005	0.002	0.00705	101

The mixing model explained 82% of the variability of a_{325}, increasing to 88% when adding the AOU as explanatory variable in the mixing–biogeochemical model. Furthermore, a reduction of 17.8% of the SD of the residuals was observed. In this case, a maximum SD of the residuals reduction of 25.5% was observed in the WestMed (Table 2.7). Unexpectedly, a_{325} decreased with basin scale mineralization; the water mass mixing independent a_{325}/AOU slope was negative, –1.0 ± 0.1 m^2 mol O_2^{-1}, for the entire MedSea, with no significant differences among basins. Water mass mixing explained much less variance of $S_{275–295}$ (64%) and there was not any improvement when considering the mixing–biogeochemical model (Table 2.7).

Finally, S_R was the CDOM parameter with less percentage of explained variance by the linear mixing model with 35% (Table 2.7). Consideration of the mixing–biogeochemical model contributed scarcely to increase the explained variance, even for the two basins separately (Table 2.7). Interestingly, the water mass mixing independent S_R/AOU ratio was positive, 6 ± 2 m^3 mol O_2^{-1}, being higher in the EastMed, 17 ± 6 m^3 mol O_2^{-1}.

Only for a_{254} and a_{325}, the simultaneous inclusion of AOU and PHA in the mixing–biogeochemical model improved the explained variance and reduced the SD of the residuals (not shown). In the entire MedSea, for a_{254}, the explained variance increased to 96% and the SD of the residuals reduced by 27.3% compared with the mixing model. For a_{325}, the explained variance and SD of the residuals reduction were 89% and 21.4%, respectively. In the WestMed, the reduction of the SD of the residuals was even higher, reaching 41.2% and 29.1% for a_{254} and a_{325}, respectively. In the EastMed, no improvement with the addition of PHA was detected. It is noteworthy to underscore the positive relationship of PHA with both absorption coefficients, contrary to the negative relationship recorded with AOU.

4 Discussion

4.1 DOM, a major player in the carbon cycle of the Mediterranean Sea

Despite the relatively small size of the MedSea and the short renewal times of the western (42 years) and eastern (150 years) Mediterranean deep waters (Powley et al., 2016), DOC concentrations in the deep MedSea expand over the range found in the deep waters of the World Ocean, from 34 to 45 µmol L^{-1} (Table 2.5; Figure 2.8a). Whereas the average DOC concentration of the WMDW varieties is around 42–43 µmol L^{-1}, it drops to 37–41 µmol L^{-1} in the less ventilated EMDW varieties. Particularly, the archetype DOC concentration of the EMT, 37 ± 1 µmol L^{-1}, is similar to the concentration found in the North Pacific Intermediate Water (NPIW), which is among the less ventilated water masses of the world ocean (Hansell et al.,

2009; Hansell et al., 2012). Note that the EMT is an old water mass, but not the oldest of the EastMed, which is the Pre–EMT with an archetype DOC of 39 ± 1 μmol L^{-1}. Given that the archetype AOU of both water masses is the same, 62 ± 1 μmol kg^{-1} (Table 2.5), the 2 μmol L^{-1} difference in archetype DOC should be due to the different initial DOC concentrations of these water masses at their respective formation site in the Aegean Sea (during the EMT) or in the Adriatic Sea (before the EMT).

The DOC distribution obtained in our study is consistent with previous ones in the MedSea (Santinelli, 2015; Santinelli et al., 2010). The novelty of this work has been the application of a water mass analysis that allowed us to obtain water mass proportion weighted–average DOC concentrations for each of the 19 water types identified during the HOTMIX cruise.

An additional advantage of the water mass analysis is the possibility of estimating the contribution of DOC to the dissolved oxygen demand of the dark MedSea independent of water mass mixing. The values of parameter β in the DOC–AOU mixing biogeochemical model (Table 2.7), indicate that 66 ± 10% of the oxygen demand of the dark eastern basin and 24 ± 4% in the dark western basin is due to DOC consumption. For the whole dark MedSea, the contribution of DOC is 31 ± 4%. Previous estimates by Santinelli et al. (2010, 2012b) for the core of the LIW indicated a contribution of around 49 ± 4% during its route across the Ionian and Tyrrhenian Sea and 32 ± 4% when the whole MedSea is considered. Therefore, when considering the whole meso– and bathypelagic EastMed, the contribution of DOC to the oxygen demand is much higher than when considering only the core of the LIW. This excess consumption is likely due to the injection of bioavailable DOC accumulated in the surface layer (<50 m) into the winter mixed layer (<150 m) all along the EastMed, as described by Carlson et al. (1994) for the Sargasso Sea.

As indicated above, our results also show an accumulation of DOC in the surface layer of the EastMed in agreement with previous studies (Pujo–Pay et al., 2011; Santinelli, 2015). The explanation behind this accumulation is that ultraoligotrophy decreases heterotrophic activity, resulting in a decoupling between DOC production and consumption (Thingstad et al., 1997; Pujo–Pay and Conan, 2003; Luna et al., 2012). DOC removal occurs after winter mixing through the winter mixed layer (<150 m) and as the recently formed LIW (>200 m) moves westwards, indicating DOC consumption as nutrients become more available.

4.2.1 a254 as a proxy for DOC

As in Lønborg and Álvarez–Salgado (2014) for the Northeast Atlantic Ocean, the highly significant linear regression of DOC with a_{254} in the MedSea (Figure 2.9) confirms that a_{254} could be used as a proxy for the concentration of DOC. The intercept of this relationship indicates that 9 µmol L^{-1} of DOC varies independently of a_{254}, whereas the remaining variability would be dependent on a_{254}. However, the regression obtained in Lønborg and Álvarez–Salgado (2014) in the Northeast Atlantic Ocean (DOC = 10 (±1) + 40 (±1) a_{254}; R^2 = 0.80; n = 233) presented a lower slope and the same intercept than that obtained in this work in the MedSea (Figure 2.9 in page 81). These results suggest that this relationship is not universal for the open ocean and that in the MedSea.

4.2.2 The counterintuitive behaviour of a325 in the MedSea

Unlike other studies, an unexpected relationship between a_{325} and water mass ageing emerges in the MedSea. Whereas positive relationships between a_{325} and AOU have been observed in the global ocean, particularly in the Indian and Pacific oceans (Nelson et al., 2010; Catalá et al., 2015a), here a_{325} decreases with increasing AOU both in the epipelagic (Figure 2.10c) and in the dark MedSea (Table 2.7). A positive relationship between a_{325} and AOU has been interpreted as a production of aromatic humic–like substances during microbial degradation of organic matter in the dark ocean (Nelson et al., 2010; Jørgensen et al., 2011; Catalá et al., 2015a; 2016). Therefore, the negative a_{325}/AOU slope obtained in the MedSea would suggest the prevalence of the consumption of the bulk CDOM absorbing at this wavelength over the microbial production of the fluorescent fraction of this CDOM. Accordingly, the positive S_R/AOU slope is also contrary to what was observed in the global tropical and subtropical ocean (Catalá et al., 2015a). We hypothesize that the dominance of CDOM consumption in the MedSea could be attributed to its oligotrophy, which would divert microbial heterotrophs towards a specialization in the consumption of colored compounds of more recalcitrant nature. However, as it will be further discussed in chapter 3, the humic–like fluorescent fraction of the materials absorbing at 325 nm shows the expected increase with AOU.

5 Conclusions

In the epipelagic MedSea, AOU explained most of the variability of DOC and a_{254}, suggesting that the cumulative net community respiration is driving these two variables. However, the variability of a_{325}, $S_{275–295}$ and S_R was mostly explained by θ, a proxy to thermal

stratification and solar radiation, indicating that apart from microbial activity, water column stability and photobleaching also drive the variability of CDOM.

For the meso– and bathypelagic MedSea, water mass mixing and basin–scale mineralization processes contributed more substantially to explain the variability of DOC, a_{254} and a_{325} (82–91%) than the variability of $S_{275–295}$ and S_R (35–64%). The addition of local mineralization processes only contributed to improve the explained variance of the absorption coefficients. Local mineralization processes also indicate that DOC and CDOM play a more relevant role in the carbon cycle of the EastMed than the WestMed: whereas DOC contributed to 66 ± 10% of the oxygen demand of the EastMed, it represented only 24 ± 4% in the WestMed.

a_{254} has been revealed as an excellent proxy to the concentration of DOC in the MedSea and the overall negative relationship of a_{325} with AOU indicates that, contrary to expected, the consumption of colored substances absorbing at 325 nm prevails over their production.

Chapter 3

Dissolved organic matter (DOM) and its optical properties in the open Mediterranean Sea: basin–wide distribution and drivers of fluorescent DOM

The research work presented in this chapter is also a contribution to the paper submitted to Progress in Oceanography:

Martínez–Pérez, A.M., Catalá, T.S., Nieto–Cid, M., Otero, J., Álvarez, M., Emelianov, M., Reche, I., Álvarez–Salgado, X.A , Arístegui, J. 2018. Optical properties of Dissolved Organic Matter (DOM) in the open Mediterranean Sea: basin wide distribution and drivers of fluorescent DOM.

Abstract

Fluorescent dissolved organic matter (FDOM) in the Mediterranean Sea was analyzed by excitation–emission matrix (EEM) spectroscopy and parallel factor (PARAFAC) analysis during the cruise HOTMIX 2014. A 4–component model, including 3 humic–like and 1 protein–like compounds, was obtained. Humification (HIX) and biological (BIX) indices and the fluorescence quantum yield at 340 nm (QY(340)) were also considered. To decipher the environmental factors that dictate the distributions of these components and indices, we run generalized additive models (GAMs) in the epipelagic layer (<200 m) and an optimum multiparametric (OMP) water masses analysis in the meso– and bathypelagic layers. In the epipelagic layer, apparent oxygen utilization (AOU) presented the most significant effect on the variability of the marine humic–like peak M fluorescence, HIX and QY(340), suggesting that their distributions were controlled by the net community respiration of organic matter. On the contrary, the variability of the soil humic–like peak E and the protein–like peak T fluorescence was explained mainly by the prokaryotic heterotrophic abundance, which decreased eastwards. In the meso– and bathypelagic layers, water mass mixing and basin–scale mineralization processes explained more than 72% and 63% of the humic–like and protein–like fluorescence variability, respectively. When analysing the two basins separately, the OMP model offered a better explanation of the distribution of fluorescence in the eastern Mediterranean Sea, as expected from the reduced biological activity in this ultra–oligotrophic basin. Furthermore, while western Mediterranean deep waters display the usual trend in the global ocean (increase of humic–like fluorescence and decrease of protein–like fluorescence with higher AOU values), the eastern Mediterranean deep waters presented an opposite trend. Different initial fluorescence intensities of the water masses that mix in the eastern basin, with Adriatic and Aegean origins, seem to be behind this contrasting pattern. The analysis of the local–scale mineralization processes corroborate this hypothesis, suggesting a production of humic–like and a consumption of protein–like fluorescence in parallel with water mass ageing. Remarkably, the local–scale variability of the chromophoric dissolved organic matter (CDOM) absorbing at the excitation wavelength of the humic–like peak M indicates an unexpected loss with increasing AOU, which suggests that the consumption of the non–fluorescent fraction of CDOM absorbing at that wavelength exceeded the production of the fluorescent fraction observed here.

1 Introduction

The bulk dissolved organic carbon (DOC) and the chromophoric fraction of DOM (CDOM) in the Mediterranean Sea (MedSea) have been studied in chapter 2 with the data collected during the HOTMIX 2014 cruise. The physical and biogeochemical drivers that dictate the distributions of DOC, CDOM absorption coefficients at specific wavelengths and the CDOM spectral slopes in epi–, meso–, and bathypelagic waters of the MedSea have been assessed.

Chapter 3 will be focused on the small fraction of the CDOM pool that is able to emit the light absorbed in the UV–VIS range of the spectrum in the form of blue fluorescence, constituting the fluorescent dissolved organic matter (FDOM) pool. FDOM consist basically on two groups of aromatic compounds: protein–like substances, related mainly to the aromatic amino–acids tyrosine and tryptophan, which absorb at <300 nm; and humic–like substances, related to terrestrial and marine humic and fulvic acids, which absorb at >300 nm (Coble, 2007; Nelson and Siegel, 2013; Stedmon and Nelson, 2015). FDOM is reliably, fast and easily determined by fluorescence spectroscopy, being widely used over the last decade to gain fundamental knowledge on the impact of ocean circulation, mixing and biogeochemical processes on DOM cycling in open ocean waters (Yamashita and Tanoue, 2008; Jørgensen et al., 2011; Catalá et al., 2015b; Nelson and Gauglitz, 2016; Yamashita et al., 2017). The particular hydrography and circulation of the MedSea with its large variety of water masses despite their small size (see chapter 1 and 2), its reduced renewal times of decades *versus* centuries for the global ocean (Laruelle et al., 2009; Schneider et al., 2014; Powley et al., 2016), and its relatively high deep water temperatures of about 13°C *versus* <3°C in the global ocean (Dickson and Brown, 1994) makes this “miniature ocean” very suitable for studying the fluorescent fraction of CDOM.

Following chapter 2, chapter 3 deals with the environmental drivers, physical *versus* biogeochemical, autotrophic *versus* heterotrophic, that dictates the distribution of FDOM in the MedSea. Parallel factor (PARAFAC) analysis (Stedmon and Bro, 2008) is used to identify the main fluorophores present in the MedSea. Classical fluorescence indicators such as the humification (HIX; Zsolnay et al., 1999) or biological (BIX; Huguet et al., 2009) indices are calculated too and confronted to the fluorophores. Furthermore, to link the CDOM study of chapter 2 to the FDOM study of chapter 3, the quantum yield of fluorescence, i.e. the proportion of the light absorbed that is reemitted as blue fluorescence (Green and Blough, 1994) is introduced. We performed the same methodological approaches than in chapter 2. That is, general additive models (GAMs) and an optimum multiparameter (OMP) water mass

analysis. GAMs are used to explore the environmental drivers of the different FDOM fluorophores and indices in the epipelagic layer. The OMP water mass analysis is used to differentiate the effect of water mass mixing from the biogeochemical processes occurring during this mixing, on the variability of FDOM in the meso– and bathypelagic layers. Furthermore, the OMP analysis also allowed us to conduct a census of the main fluorophores and FDOM indices in all the water masses intercepted during the HOTMIX 2014 cruise.

2 Materials and methods

Twenty–four hydrographic stations were sampled across the entire MedSea during the HOTMIX 2014 cruise (see Figure 2.1 in page 58), on board the R/V Sarmiento de Gamboa (Heraklion, Crete, 27 April 2014 – Las Palmas, Canary Islands, 29 May 2014). A detailed description of the sampling strategy, core measurements, GAMs and OMP water mass analysis is included in chapter 2. Here we present a brief description.

Full–depth water samples (max. 15 levels) were collected using a SBE 38 rosette sampler, equipped with 24 (12 L) Niskin bottles. Discrete sampling depths were decided according to the values of the continuous profiles of potential temperature (θ), salinity (S), dissolved oxygen (O_2) and fluorescence of chlorophyll a (Chl *a*).

Seawater samples for the determination of dissolved organic carbon (DOC), and chromophoric (CDOM) and fluorescent dissolved organic matter (FDOM) were collected in 0.5–litres acid–cleaned glass bottles. Surface samples (<200 m) were filtered through precombusted (450°C, 4 h) Whatman GF/F filters with an acid–cleaned all–glass filtration system under positive pressure of high–purity N_2, previously rinsing with about 50 mL of the sample. Dark ocean samples (>200 m) were not filtered. FDOM aliquots were kept in the dark until analysis on board by fluorescence spectroscopy within two hours of collection.

2.1 Determination of FDOM, PARAFAC processing and fluorescence indices calculation

Fluorescence excitation–emission matrices (EEMs) were collected with a JY–Horiba Spex Fluoromax–4 spectrofluorometer at room temperature (around 20°C) using 5 nm excitation and emission slit widths, an integration time of 0.25 s, an excitation range of 240–450 nm at 10 nm increments and an emission range of 300–560 nm at 2 nm increments. To correct for lamp spectral properties and to compare results with those reported in other studies, spectra were collected in signal–to–reference (S:R) mode with instrument–specific excitation and emission

corrections applied during collection, and EEMs were normalized to the Raman area (RA). In our case, the RA and its baseline correction were performed with the emission scan at 350 nm of the Milli–Q water blanks and the area was calculated following the trapezoidal rule of integration (Murphy et al., 2010). Rayleigh scatter bands were removed mathematically from the EEMs.

To track the variability of the instrument in the Raman, protein– and humic–like regions of the spectrum and to assess gradual spectral bias during the 33 working days of the cruise, three standards were run daily: (1) a p–terphenyl block (Starna) that fluoresces in the protein region, between 310 and 600 nm exciting at 295 nm; (2) a tetraphenyl butadiene block (Starna) that fluoresces in the humic region, between 365 and 600 nm exciting at 348 nm; and (3) a sealed Milli–Q cuvette (Perkin Elmer) scanned between 365 and 450 nm exciting at 350 nm. Figure 3.1a shows that the time evolution of the RA of the Milli–Q water produced on board and the reference p–terphenyl and tetraphenyl butadiene materials were parallel, only a slight decay on the signal intensity was observed (0.29%, 0.56% and 0.05% for the Milli–Q water, p–terphenyl and tetraphenyl butadiene, respectively), which confirms that the Raman normalization was successful in both the protein– and the humic–like regions of the EEMs. Therefore, no additional drift corrections were necessary. In addition, sealed Milli–Q reference cuvette and daily Milli–Q water produced on board showed similar pattern of evolution during the cruise, indicative of a good quality of the Milli–Q water produced in the ship (Figure 3.1b). Furthermore, two scans of the reference sealed Milli–Q water were measured at the beginning (sMQ1) and at the end (sMQ2) of each session, which reveals a slight decrease of the fluorescence intensities along each working day (Figure 3.1c). The initial and final sMQ spectra were separated about 8 hours of continuous work of the spectrofluorometer. We found that the difference between sMQ1 and sMQ2 was only 0.69%. Raman–normalized Milli–Q blanks were subtracted to remove the Raman scattering signal (Stedmon et al., 2003; Murphy et al., 2010). RA normalization, blank subtraction and generation of EEMs were performed using Matlab (version R2014B).

A Parallel factor analysis (PARAFAC) was then applied to decompose the fluorescence signal of the EEMs into the underlying individual fluorescent components (Bro, 1997). The PARAFAC was based on 406 corrected EEMs and was performed using the DOMFluor 1_7 Toolbox8 (Stedmon and Bro, 2008) run in Matlab (version R2014B). Before validating the model, only 3 outliers were withdrawn from the database. A 4–component model was obtained (Figure 3.2) after split–half validation and random initialization steps (Stedmon and Bro, 2008; Murphy et al., 2013).

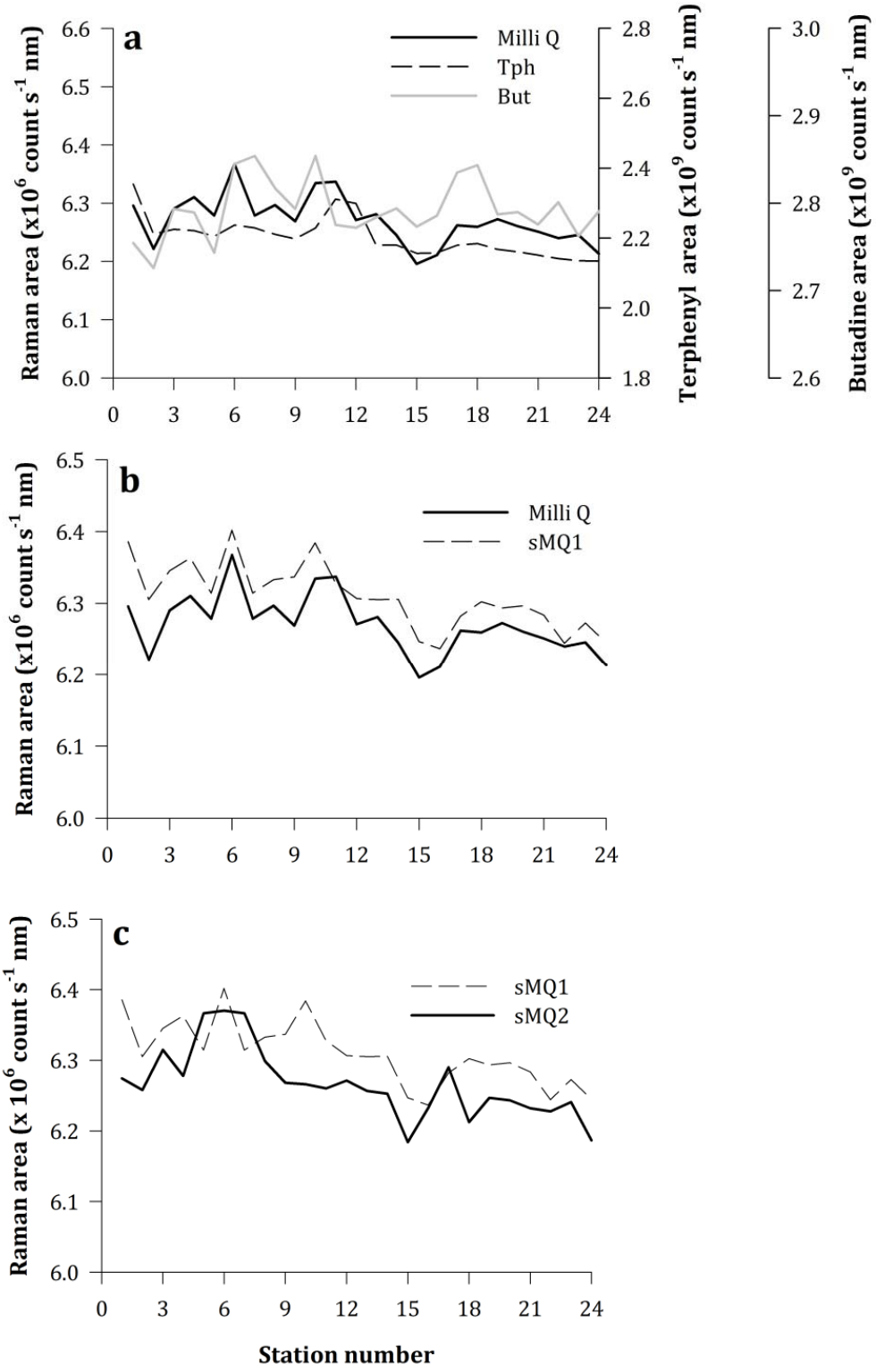

***Figure 3.1**: Checking the reliability of the fluorescence measurements during the HOTMIX 2014 cruise. Evolution of the fluorescence intensities of (a) p–Terphenyl (Tph, dotted line), Tetraphenyl butadiene (But, grey line) and R/V Sarmiento de Gamboa Milli–Q water (black line); (b) R/V Sarmiento de Gamboa Milli–Q water (black line) and sealed initial Milli–Q (sMQ1, dotted line); (c) initial (sMQ1) and final (sMQ2) sealed Milli–Q water along the HOTMIX cruise.*

Furthermore, from these EEMs we picked up specific values at selected excitation–emission wavelength pairs previously defined by Coble (1996) and Stedmon et al. (2003). The selected Ex/Em wavelength pairs were 250 nm/435 nm (peak A) due to general humic substances; 340 nm/440 nm (peak C) due to humic substances of terrestrial origin; 320 nm/410 nm (peak M) due to humic substances of marine origin; 450 nm/520 nm (peak E) due to soil fulvic acids; and 280 nm/350 nm (peak T) and 270 nm/304 nm (peak B) due to protein–like substances, tryptophan and tyrosine–like respectively. Fluorescence intensities of these peaks are reported in Raman units (RU) (Stedmon and Bro, 2008; Stubbins et al., 2014).

We also calculated fluorescence–based indices such as the biological index (BIX) determined as the ratio of the emission at 380 nm and 430 nm when excited at 310 nm (Huguet et al., 2009). BIX is indicative of the organic matter recently produced from biological activity (Coble et al., 2014). The humification index (HIX), calculated as the ratio between the integrated emission spectra at 435–480 nm and 300–345 nm when excited at 260 nm (Zsolnay et al., 1999), is a proxy of the degree of humification (Zsolnay et al., 1999; Fellman et al., 2010;).

Finally, we calculated the fluorescence quantum yield at 340 nm, QY(340), which is the proportion of the light absorbed at 340 nm that is reemitted as fluorescent light between 360 and 560 nm and was determined as in Green and Blough (1994). The analysis of the CDOM data to calculate this index is described in chapter 2. The QY(340) is used as a proxy of aromaticity.

2.2 Generalized additive models (GAMs)

To test for the effect of the environmental parameters (inorganic nutrients, O_2, AOU, Chl *a* and bacterial biomass) on the distribution of the FDOM fluorophores and indices in the epipelagic layer of the MedSea we have used generalized additive models (GAMs, Wood, 2006). As described in detail in chapter 2, a GAM is a nonparametric regression technique that allows inspecting the relationship between a response variable and one (or more) continuous explanatory variable(s) without the need to choose a particular parametric form for describing the shape of the relationship(s). In this study, the explanatory variables are the environmental parameters and the response variables are the FDOM fluorophores and indices. Before model fitting, covariability among all potential predictors was examined using pairwise correlations and calculating variance inflation factors (VIFs, Table 2.1 in chapter 2). Smoothing functions were fit by penalized cubic regression splines restricted to a maximum of three knots. The

smoothness of the functions was estimated by minimizing the generalized cross validation criterion. All models were fitted in R 3.2.3 software (R Development Core Team, 2016) and using the 'mgcv 1.8–16' package (Wood, 2006).

2.3 Optimum multiparameter (OMP) water mass analysis

In brief, a total of 19 water types were identified along the HOTMIX 2014 cruise track (see chapter 2). Our OMP allows computing the optimum contribution of each water type to every water parcel/sample by solving over–determined systems of linear mixing equations for volume, θ, S, SiO_4 and NO and silicate in a non–negative less–squares sense.

Using the values of any measured variable (N) and the proportions of the 19 water masses identified in chapter 2 (x_{ij}), the water mass proportion–weighted average concentration of N in each water type, N_i, herein after archetype value of N, can be calculated using equation 2.3 (page 73).

To determine the fraction of the total variability of variable N that is due to water mass mixing, a multiple linear regression of N_j with the previously obtained x_{ij} values is performed. A system of n linear equations (one per sample) with m coefficients (one per water type) has to be solved for each variable N, using the equation 2.6 (page 74).

Finally, to consider simultaneously the effect of mixing and biogeochemical processes on the distribution of FDOM variables, a term is added to equation 2.6 that models the non–conservative processes independent of the water type proportions. To do that, an additional explanatory chemical variable (N_2) is introduced to model the distribution of the response variable (N_1) as in equation 2.8 (page 75). Therefore, a system of n linear equations (one per sample) with m+1 unknowns (one per water type, $\alpha_{1i} - \beta \cdot \alpha_{2i}$, and the coefficient β) has to be solved. For further details please see materials and methods section of chapter 2.

3 Results

3.1 Fluorescent DOM components in the deep Mediterranean Sea

A 4–component model was obtained from the PARAFAC analysis (Figure 3.2). Components 1, 2 and 4 have been already classified as humic–like (Coble, 1996; Stedmon et al., 2003). Component 1 corresponds to a mixture of Coble's (1996) peaks A (shorter excitation wavelength associated with general humic substances) and C (longer excitation wavelength linked to terrestrial humic substances) and component 2 to Coble's (1996) peak M, related

with marine humic substances. Component 4 is close to Stedmon's et al. (2003) peak E, which has been associated with soil fulvic acids. This component was previously found in coastal areas (Stedmon et al., 2003; Stedmon and Markager, 2005) but not in the open ocean (e.g. Jørgensen et al., 2011; Kowalczuk et al., 2013; Catalá et al., 2015b).

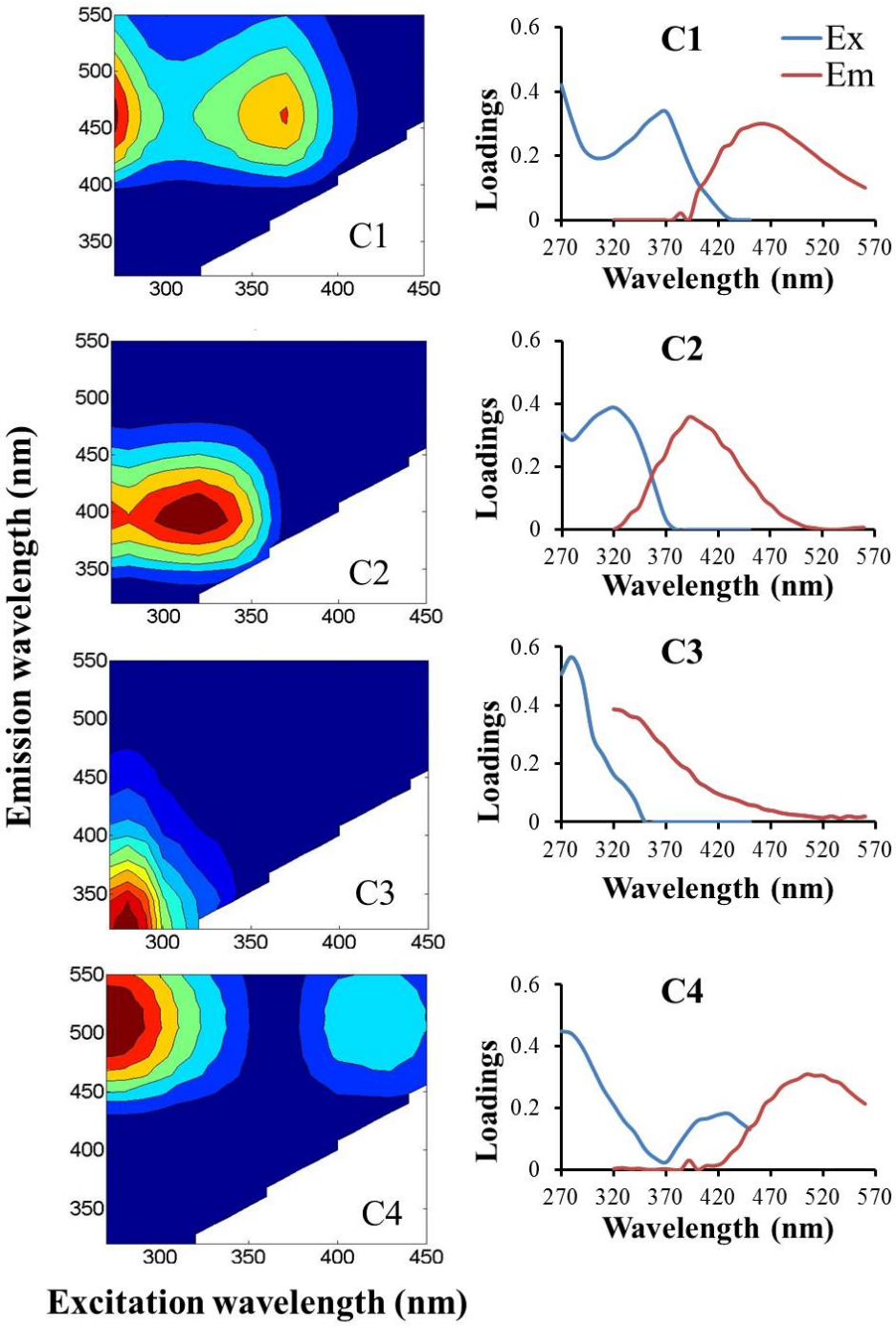

Figure 3.2: *Fluorescence matrices of the four identified PARAFAC components. C1 represents a combination of Coble's (1996) peaks A and C, C2 represents peak M, C3 corresponds to a mixture of peak T and peak B and C4 represents Stedmon's et al. (2003) peak E. The right panels represent the excitation (blue lines) and the emission (red lines) fluorescence intensities of the four PARAFAC components. Figure created using the software Matlab (version R2014B; MathWorks, USA).*

In the Mediterranean Sea it was already found in the mixing zone of the Dardanelles Strait and the North Aegean Sea, which is an area of strong terrestrial influences due to river discharge into the Black Sea (Pitta et al., 2017). The fact that we observed this component also in the open MedSea points to the impact of continental runoff in the distal zone of this relatively small and enclosed basin. On the contrary, component 3 has been classified as protein–like, exhibiting its maximum fluorescence at the Ex/Em wavelength pair of 280/320 nm, which is in between Coble's (1996) peaks T and B. Therefore, this component represents a mixture of tryptophan– and tyrosine–like compounds.

Given that the PARAFAC components roughly match the classical fluorescence peak intensities at the Ex/Em wavelength pairs previously established by Coble (1996) and Stedmon et al. (2003) we decided to use the latter in order to allow direct comparison with previous studies.

3.2 Distribution of fluorescent DOM in the deep Mediterranean Sea

3.2.1 Distribution of humic– and protein–like substances

The three major humic–like peaks (A, C and M) presented very strong positive correlations among them (peak A *vs* peak M, $R^2 = 0.91$, $p < 0.0001$, n = 317, peak A *vs* peak C, $R^2 = 0.91$, $p < 0.0001$, n = 317 and peak C *vs* peak M $R^2 = 0.97$, $p < 0.0001$, n = 317). Thus, for simplicity, we will report only peak M results. Although peak E also exhibited positive correlations with the other humic–like peaks, they were much weaker (peak E *vs* peak A, $R^2 = 0.44$, $p < 0.0001$, n = 314, peak E *vs* peak C, $R^2 = 0.55$, $p < 0.0001$, n = 314 and peak E *vs* peak M $R^2 = 0.43$, $p < 0.0001$, n = 314). Therefore, we will present the results of peak E apart.

Fluorescence intensities of peak M ranged from 2 to 11 x 10^{-3} RU. Lower values were found at the surface layer with mean values (upper 100 m) of 4 ± 2 x 10^{-3} and 7 ± 2 x 10^{-3} RU for the EastMed and WestMed, respectively. Concerning water masses, in the EastMed the lowest intensities of peak M corresponded with LSW (archetype depth of 116 ± 21 m) with an archetype intensity of 5.5 ± 0.3 x 10^{-3} RU. On the other hand, the highest intensities were attributed to the intermediate waters, characterized by maximum archetype values of 8.0 ± 0.2 x 10^{-3} RU. In the Levantine basin and the eastern part of the Aegean Sea, peak M increased with depth up to about 750 m and then decreased into the deep waters until reaching the bottom where it raised again. In the western part of the Aegean Sea and in the Ionian Sea, peak M showed higher intensities than in the Levantine basin, increasing down to the intermediate waters and maintaining almost constant through the water column below this

depth (Figure 3.3a). In the WestMed, peak M fluorescence increased from surface to intermediate waters where maximum intensities were recorded (red branch in Figure 3.3a) and then decreased monotonically with depth. In this basin, maximum values were found in EIW and WIW (archetype depths of 364 ± 79 m and 170 ± 33 m, respectively) with archetype values of 8.8 ± 0.1 x 10^{-3} RU and 9.1 ± 0.1 x 10^{-3} RU, respectively (Table 3.1).

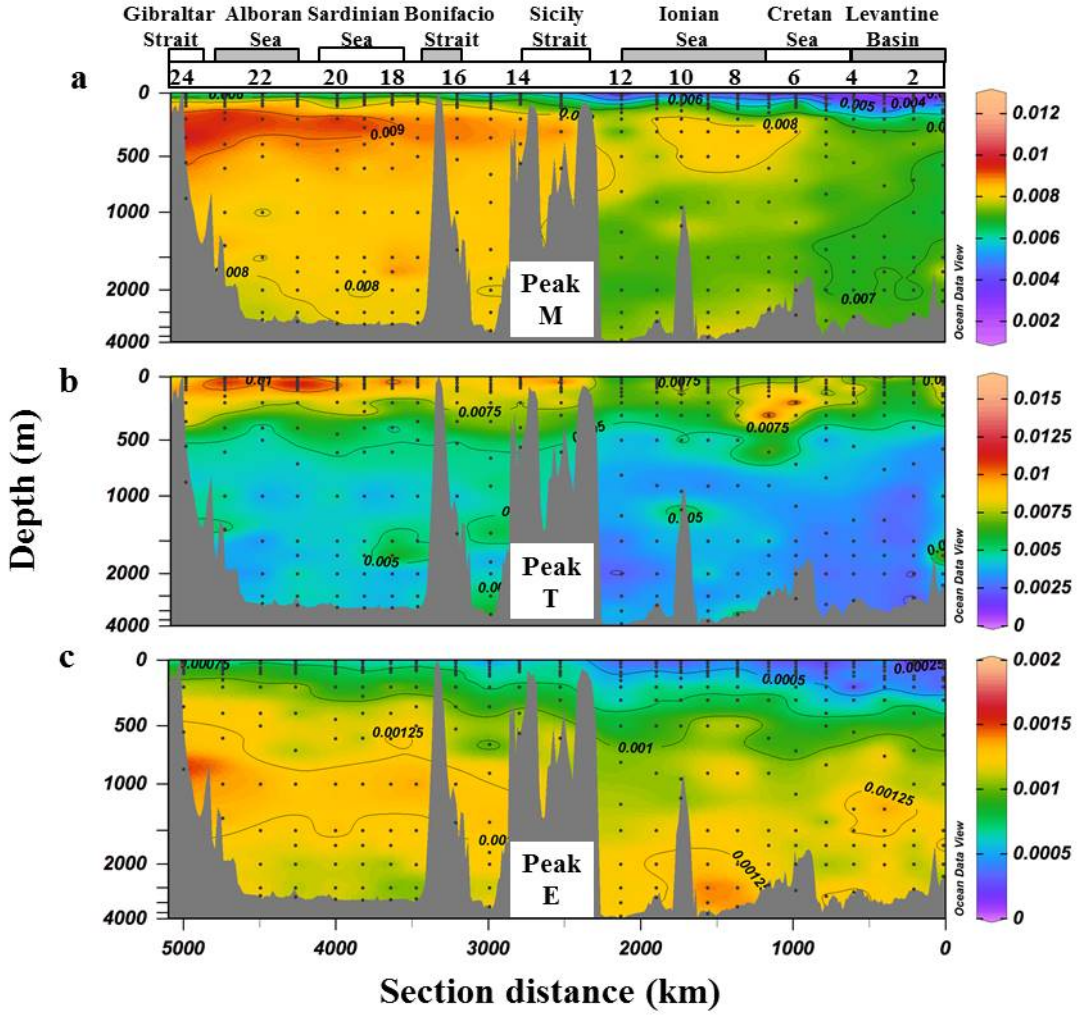

Figure 3.3: *Distribution of the fluorescence peaks: (a) peak M (RU), (b) peak T (RU) and (c) peak E (RU) along the Mediterranean Sea. Numbers located on the top of the figure indicate the sample stations, which are depicted in Figure 2.1 in page 58. Figure created using ODV software (Schlitzer, 2017).*

The basin–wide variability of protein–like substances will be described on basis of peak T measurements, characteristic of tryptophan, because measurements at peak B, characteristic of tyrosine, are strongly affected by the Raman scattering band of water leading to unreliably low fluorescence signal/noise ratio in many of the samples. Protein–like fluorescence ranged between 2 and 15 x 10^{-3} RU and, similarly to peak M fluorescence, exhibited higher intensities in the WestMed (Figure 3.3b). Contrary to peak M, peak T showed higher intensities at the surface with mean values in the upper 100 m of 7 ± 2 x 10^{-3} and 10 ± 2 x 10^{-3} RU for the

EastMed and WestMed, respectively. Peak T decreased through the water column, achieving minimum values at the bottom in both basins. In the EastMed, MAW and LSW presented an archetype intensity of 7.4 ± 0.6 x 10^{-3} and 7.6 ± 0.8 x 10^{-3} RU, respectively, significantly lower than AW in the WestMed, 9.2 ± 0.1 x 10^{-3} RU. These basin–wide differences in the upper layer can be easily recognised in Figure 3.3b. In the intermediate layer of the EastMed, LIW presented significantly higher archetype peak T intensity than CIW (7.5 ± 0.3 x 10^{-3} RU and 6.0 ± 0.7 x 10^{-3} RU, respectively). Analogously, in the WestMed, WIW presented slightly higher archetype peak T intensity than EIW (8.1 ± 0.4 x 10^{-3} RU and 7.1 ± 0.4 x 10^{-3} RU, respectively). Comparison between the water masses of the intermediate layers in both basins at similar depths yielded no differences in the archetype intensities of peak T (Table 3.1). Regarding the deep waters, the mean archetype intensity of all EMDW varieties was 3.5 ± 0.2 x 10^{-3} RU, significantly lower than WMDW average value (4.4 ± 0.3 x 10^{-3} RU). The archetype intensities of peak T in the different deep water varieties were homogeneous inside each basin (Table 3.1) although in Figure 3.3b some local differences can be seen. Specifically, deep waters of the WestMed at station 22 (2500 and 2700 m) displayed a relative maximum of peak T. These two samples corresponded with the highest proportion of WMDW–D14 (i.e., the most recent WMDW variety, found in 2014). On the contrary, shallower samples collected at station 22 (1000 and 1500 m) presented minimum values and higher water mass proportions of WMDW–C and –B, respectively. WMDW–B and –C were formed during the western Mediterranean transition in winter 2004/2005 as detailed in Table 2.2 of chapter 2.

Fluorescence intensities of peak E ranged from 1 to 15 x 10^{-4} RU, that is an order of magnitude lower than peaks M and T. Lower intensities were found at the surface layer (upper 100 m) with mean values of 4 ± 2 x 10^{-4} and 7 ± 2 x 10^{-4} RU for the EastMed and WestMed, respectively. In the epipelagic layer MAW presented significantly lower archetypal value (5.5 ± 0.7 x 10^{-4} RU) than AW (8.3 ± 0.4 x 10^{-4} RU). In the intermediate layer LIW exhibited a significantly lower archetypal value (4.9 ± 0.4 x 10^{-4} RU) than EIW (9.8 ± 0.4 x 10^{-4} RU). In the bathypelagic layer, basin–scale differences were not evident (Figure 3.3c), exhibiting mean archetype values of 12 ± 1 and 12.0 ± 0.4 x 10^{-4} RU, for the EastMed and WestMed, respectively (Table 3.1). Considering the deep water varieties of the EastMed, Post–EMT–C (newest deep water mass) presented the highest archetypal value of peak E (13.1 ± 0.5 x 10^{-4} RU).

Table 3.1: Archetypal depth (Z_i, m), apparent oxygen utilization (AOU_i, µmol kg^{-1}), Peak A_i (10^{-3} RU), Peak C_i (10^{-3} RU), Peak M_i (10^{-3} RU), Peak T_i (10^{-3} RU), Peak E_i (10^{-4} RU), BIX_i, HIX_i and $QY(340)_i$ (%), of the water mass intercepted during the HOTMIX cruise. VOL_i, (%) represents the percentage of the total volume of water sampled that corresponded to each water mass.

	Acronym	VOL_i	Z_i	AOU_i	Peak A_i	Peak C_i	Peak M_i	Peak T_i	Peak E_i	BIX_i	HIX_i	$QY(340)_i$
EastMED	MAW	3.2	125 ± 26	13 ± 5	14.0 ± 0.7	5.4 ± 0.3	7.1 ± 0.4	7.4 ± 0.6	5.5 ± 0.7	1.00 ± 0.01	2.0 ± 0.2	0.8 ± 0.1
	LSW	1.8	116 ± 21	3 ± 3	11.3 ± 0.6	4.3 ± 0.3	5.5 ± 0.3	7.6 ± 0.8	3.9 ± 0.5	1.02 ± 0.01	1.8 ± 0.3	0.7 ± 0.1
	LIW	12.2	149 ± 13	15 ± 2	13.6 ± 0.4	5.3 ± 0.2	6.9 ± 0.2	7.5 ± 0.3	4.9 ± 0.4	1.01 ± 0.01	2.1 ± 0.1	0.94 ± 0.04
	CIW	6.6	379 ± 56	47 ± 3	15.4 ± 0.4	6.4 ± 0.1	8.0 ± 0.2	6 .0 ± 0.7	8.2 ± 0.5	0.92 ± 0.01	3.2 ± 0.3	1.4 ± 0.1
	AdMW	5.8	273 ± 55	34 ± 5	15.6 ± 0.4	6.2 ± 0.2	7.9 ± 0.2	6.7 ± 0.6	6.8 ± 0.7	0.96 ± 0.02	2.7 ± 0.3	1.2 ± 0.1
	AdDW	0.5	1425 ± 403	59 ± 4	14.5 ± 0.5	6.1 ± 0.2	7.3 ± 0.2	3.7 ± 0.8	11.5 ± 0.7	0.84 ± 0.02	4.3 ± 0.9	1.6 ± 0.1
	Pre–EMT	14.3	1462 ± 125	62 ± 1	14.2 ± 0.2	6.1 ± 0.1	7.3 ± 0.1	3.6 ± 0.2	11.5 ± 0.2	0.828 ± 0.005	4.6 ± 0.2	1.62 ± 0.04
	EMT	4.3	1702 ± 135	62 ± 1	14.0 ± 0.3	6.0 ± 0.1	7.1 ± 0.1	3.3 ± 0.5	11.7 ± 0.4	0.82 ± 0.01	4.5 ± 0.6	1.7 ± 0.1
	Post–EMT–A	3.3	1903 ± 180	58 ± 1	14.5 ± 0.3	6.2 ± 0.1	7.3 ± 0.1	3.5 ± 0.4	12.1 ± 0.4	0.82 ± 0.01	4.8 ± 0.5	1.7 ± 0.1
	Post–EMT–B	2.3	2892 ± 227	55 ± 1	15.1 ± 0.2	6.4 ± 0.1	7.6 ± 0.1	3.8 ± 0.4	12.1 ± 0.4	0.81 ± 0.01	4.8 ± 0.5	1.7 ± 0.1
	Post–EMT–C	1.8	2414 ± 235	56 ± 1	14.8 ± 0.4	6.5 ± 0.2	7.5 ± 0.1	3.5 ± 0.3	13.1 ± 0.5	0.83 ± 0.01	5.0 ± 0.6	1.7 ± 0.1
WestMED	AW	3.7	88 ± 14	23 ± 5	16.7 ± 0.5	6.8 ± 0.2	8.6 ± 0.2	9.2 ± 0.5	8.3 ± 0.4	0.98 ± 0.01	2.0 ± 0.1	0.9 ± 0.1
	EIW	11.4	364 ± 79	51 ± 5	17.0 ± 0.2	7.1 ± 0.1	8.8 ± 0.1	7.1 ± 0.4	9.8 ± 0.4	0.92 ± 0.01	2.9 ± 0.2	1.3 ± 0.1
	WIW	6.9	170 ± 33	45 ± 5	17.6 ± 0.3	7.3 ± 0.1	9.1 ± 0.1	8.1 ± 0.4	9.6 ± 0.4	0.95 ± 0.01	2.4 ± 0.2	1.1 ± 0.1
	A	9.3	1210 ± 156	67 ± 1	16.9 ± 0.2	7.0 ± 0.1	8.4 ± 0.1	4.8 ± 0.2	12.3 ± 0.2	0.85 ± 0.01	4.0 ± 0.2	1.63 ± 0.03
	B	5.8	1632 ± 222	61 ± 2	16.5 ± 0.3	6.9 ± 0.2	8.3 ± 0.1	4.6 ± 0.4	11.8 ± 0.3	0.86 ± 0.01	3.9 ± 0.3	1.67 ± 0.04
	C	0.7	2012 ± 300	56 ± 1	16.3 ± 0.6	6.6 ± 0.3	8.1 ± 0.3	4.2 ± 0.7	11.6 ± 0.8	0.85 ± 0.01	3.9 ± 0.5	1.7 ± 0.1
	D11	0.7	2476 ± 357	55 ± 1	16.0 ± 0.5	6.5 ± 0.2	8.0 ± 0.2	4.2 ± 0.4	11.3 ± 0.6	0.86 ± 0.02	4.2 ± 0.7	1.6 ± 0.1
	D14	5.4	2134 ± 160	56 ± 1	16.3 ± 0.2	6.6 ± 0.1	8.1 ± 0.1	4.3 ± 0.2	11.6 ± 0.3	0.86 ± 0.01	4.1 ± 0.2	1.61 ± 0.04

NOTE: MAW: Modified Atlantic Water, LSW: Levantine Surface Water, LIW: Eastern Levantine Intermediate Water, CIW: Cretan Intermediate Water, AdMW: Adriatic Middle Water, AdDW: Adriatic Deep Water, Pre–EMT: Eastern Mediterranean Deep Water (EMDW) previous to the EMT, EMT: EMDW during the EMT, Post–EMT–A: EMDW after the EMT found in the Levantine basin, Post–EMT–B: EMDW formed after the year 2003, Post–EMT–C: EMDW formed after the year 2007, AW: Atlantic Water, EIW: Eastern Intermediate Water formed in the Levantine Basin and found in the western basin, WIW: Winter Intermediate Water, A: Western Mediterranean Deep Water (WMDW) formed prior to the year 2005, B: WMDW formed in winter 2004/5 in the Gulf of Lions, C: WMDW originated in winter 2004/5 with high influence of coastal shelf waters, D11: WMDW formed prior to the year 2011, D14: WMDW formed prior to the year 2014.

3.2.2 Distribution of fluorescence indices

BIX ranged between 0.77 and 1.24, showing significantly higher values at the surface layer (upper 100 m) of 1.01 ± 0.06 (Figure 3.4a). Archetype BIX decreased significantly from the epipelagic (1.00 ± 0.01, 1.02 ± 0.01 and 0.98 ± 0.01 for MAW, LSW and AW, respectively) to the mesopelagic (ranged between 0.92 and 1.01 for LIW, CIW and AdMW and between 0.92 and 0.95 for EIW and WIW) and the bathypelagic water masses (0.82 ± 0.01 and 0.86 ± 0.01 for the EastMed and WestMed, respectively). The different varieties of the deep water masses in both basins did not present significantly different archetype values of this index (Table 3.1).

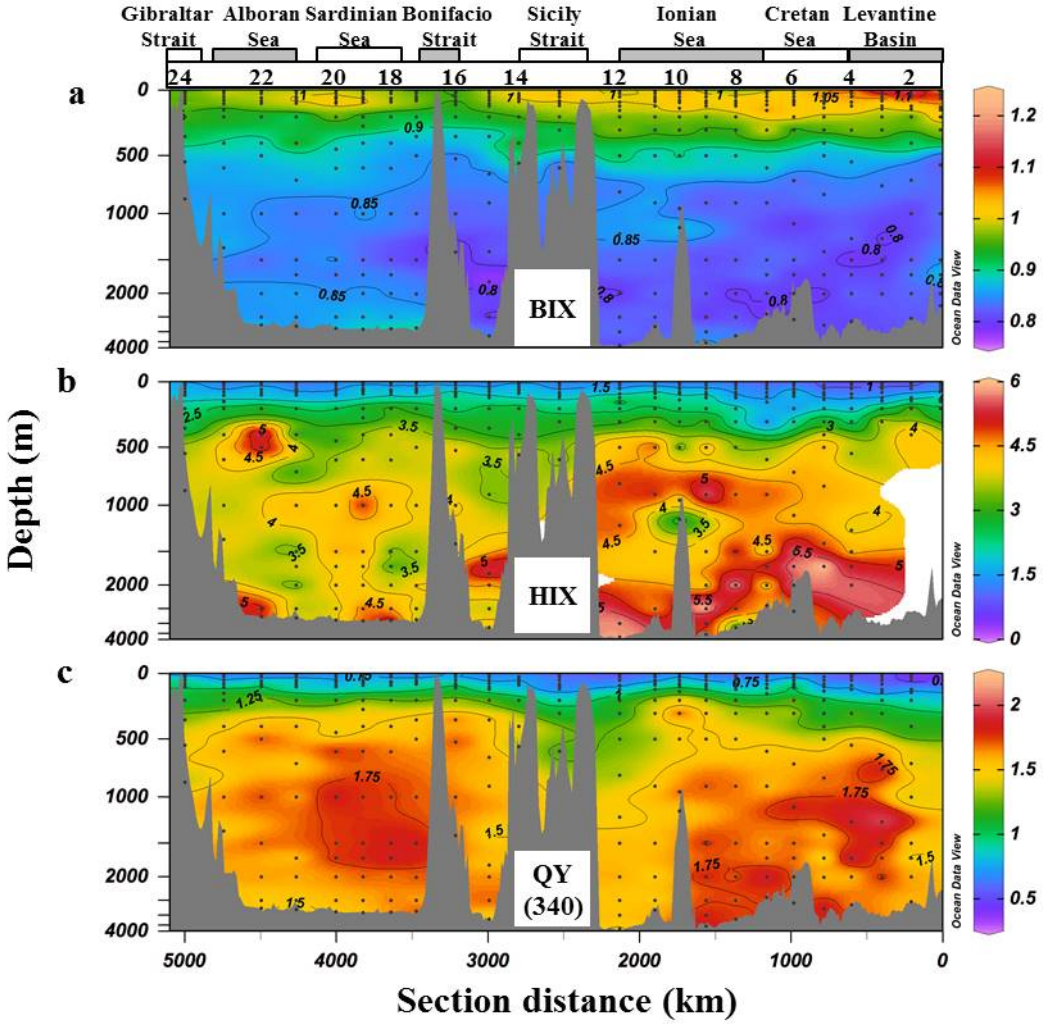

Figure 3.4: *Distribution of the fluorescence indices: (a) BIX, (b) HIX, and (c) QY(340) in % along the Mediterranean Sea. Numbers located on the top of the figure indicate the sample stations, which are depicted in Figure 2.1 in page 58. Figure created using ODV software (Schlitzer, 2017).*

HIX values ranged between 0.56 and 6.4 and showed a marked increase with depth (Figure 3.4b). Note that the HIX of the deep waters at stations 1 to 3 are not displayed (Figure 3.4b) because those samples presented estimation errors >25% for this index, then we decided

to discard them. HIX values in the upper layers were not significantly different between basins. The mean HIX in the upper 100 m were 1.3 ± 0.5 and 1.6 ± 0.4 for the eastern and western basins, respectively. The water masses with lower HIX were MAW, LSW and LIW with archetype values of 2.0 ± 0.2, 1.8 ± 0.3 and 2.1 ± 0.1, respectively (Table 3.1). Highest values of HIX were found mainly in the EastMed (Figure 3.4b), particularly in EMDW below 1500 m. The mean archetype value for the deep waters of the EastMed was significantly higher (4.7 ± 0.2) than in the western basin (4.0 ± 0.1).

QY(340) showed a distribution parallel to HIX, with lower values at the surface and a monotonic increase with depth (Figure 3.4c). QY(340) ranged between 0.3 and 2.2%. The mean value in the epipelagic layer was similar in both basins (0.7 to 0.8 ± 0.2%) and lower than in the deep layers (range between 1.3–2.1%). In the EastMed LSW presented similar archetype value (0.7 ± 0.1%) than AW in the WestMed (0.9 ± 0.1%). However, LIW displayed significantly lower archetype value (0.94 ± 0.04%) than EIW (1.3 ± 0.1%). At station 10 between 300 and 400 m a relative maximum QY(340) value (Figure 3.4c) corresponded with two samples that presented the highest proportion of CIW and AdMW. Regarding the deep water masses, all varieties of both basins presented similar archetype QY(340) values with a mean value of 1.67 ± 0.03% and 1.64 ± 0.04% for the EastMed and WestMed, respectively (Table 3.1).

3.2.3 Drivers of fluorescent DOM in the epipelagic Mediterranean Sea

To assess the drivers that dictate the distribution of the fluorescence peaks and indices in the epipelagic layer of the MedSea we performed a GAM analysis. Before model fitting, the environmental explanatory variables were inspected for covariability resulting in that the VIF analysis selected the following variables: θ, AOU, Chl *a* and PHA (Table 2.1 in chapter 2). Additionally, we included in the model the absorption coefficients at 254 nm (a_{254}), 325 nm (a_{325}) and 340 nm (a_{340}). We chose these absorption coefficients for two reasons: i) because they allow to link the variability of the fluorescent fraction of coloured DOM (FDOM) with the variability of the bulk CDOM, as described in chapter 2 and ii) because these wavelengths are very close to those where the fluorophores used in this study absorb light.

The model results indicated that 90.6% of the variability of peak M was explained by a combination of θ, AOU, a_{325}, Chl *a* and PHA. The main explanatory variables were AOU, Chl *a* and θ (Table 3.2), showing a positive linear relationship with AOU and Chl *a* and an inverse relationship with θ (Figure 3.5a). The absorption coefficient that contributed better to explain the distribution of peak M was a_{325} with a positive linear relationship (Figure 3.5a). Additionally, the model results for peaks A and C are presented in the appendix A (Figure 3.A1

and Table3. A1). Regarding peak T, the total variance explained was significantly lower (31%) than for the humic–like peak M (Table 3.2). PHA and θ were the only two variables that contributed to explain the observed variability. PHA had a strong influence on the distribution of peak T (F–value = 30.12) with a shift from an inverse to a direct linear relationship at around $e^{12.5}$ (= 2.7 x 10^5) cell mL^{-1} (Figure 3.5b). The explanatory power of θ was lower (F–value = 3.95) and showed a negative linear relationship with peak T. Concerning peak E, the model explained 74% of the total variability, with θ, AOU and PHA as selected explanatory variables (Figure 3.5c and Table 3.2). PHA was the better predictor of the variability of peak E (F–value = 30.34) with a shift from an inverse to a direct linear relationship, similar to that observed for peak T (Figure 3.5b). Peak E showed a positive linear relationship with AOU, similar to that observed with peak M (Figure 3.5a), nevertheless it showed an inverse relationship with θ.

Likewise peak T, BIX was the fluorescence index explained worst by the models, with only 30.8% of the explained variance. The selected explanatory variables were θ, AOU, Chl *a* and PHA. AOU and PHA were the variables that better explained BIX with a negative relationship. θ and Chl *a* showed a nonlinear and positive relationship, respectively (Figure 3.6a and Table 3.2). Concerning HIX, the variables that explained the variability (74.2%) of this index were AOU, Chl *a*, θ and PHA, being AOU the best explanatory variable (F–value = 45.76) with a positive linear relationship (Figure 3.6b and Table 3.2). The explained variance of QY(340) (63.4%) was mainly retained by AOU (F–value = 15.40) with a positive linear relationship. PHA had a non–linear effect on this index and θ described a power–law relationship (Figure 3.6c and Table 3.2).

In summary, while AOU is the major explanatory variable of the peak M, peaks E and T were mostly explained by PHA. Regarding the fluorescent indices, although AOU had a large effect on the variability of all these indices, PHA, Chl *a* and θ also had remarkable effects on BIX, HIX and QY(340), respectively.

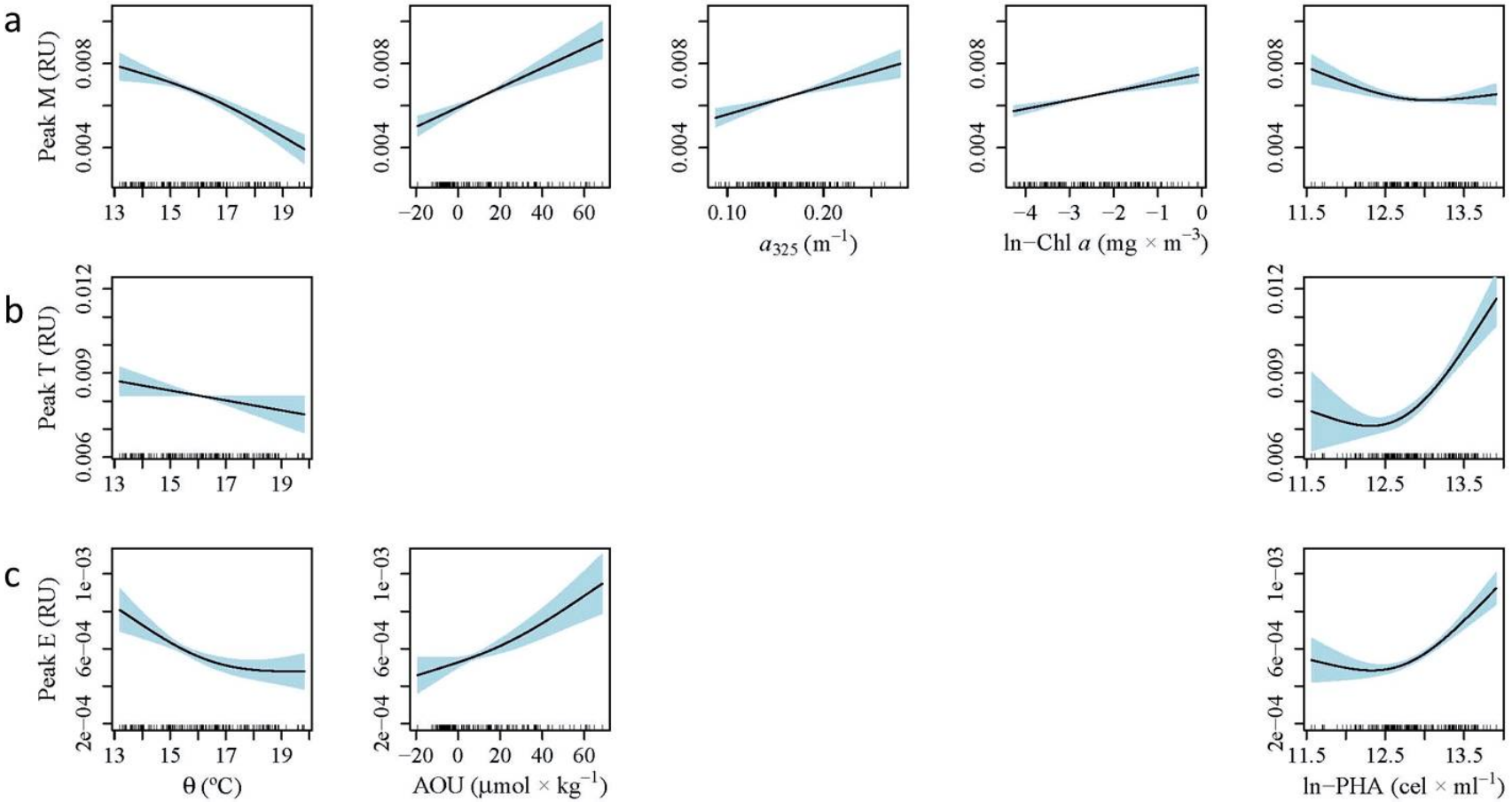

Figure 3.5: *Partial plots of the additive effects of the physical, chemical and biological covariates on the FDOM parameters after fitting Generalized Additive Models. (a) Peak M, (b) Peak T and (c) peak E. Rugs on x–axis indicate the distribution of the data.*

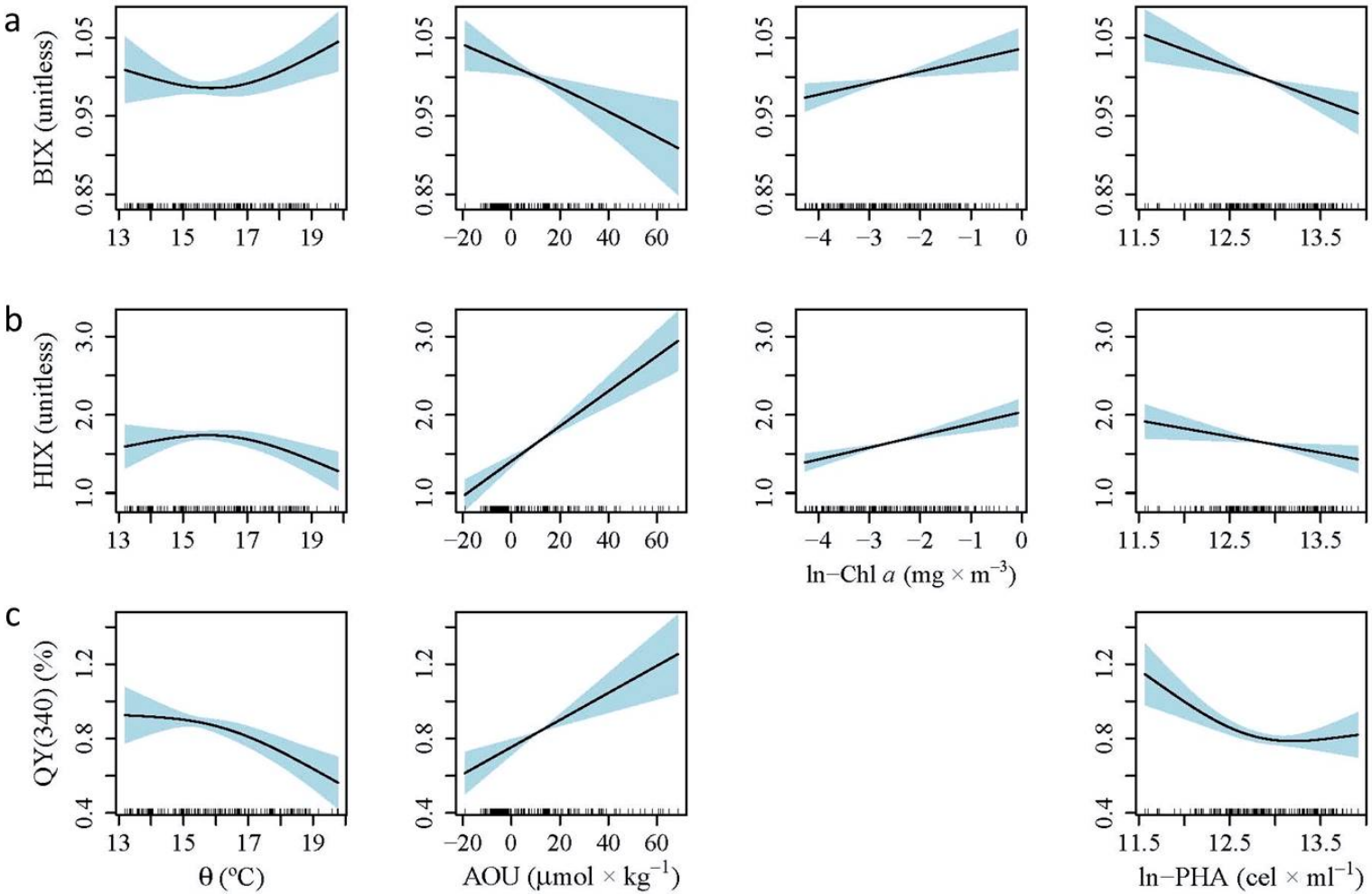

Figure 3.6: *Partial plots of the additive effects of the physical, chemical and biological covariates on the FDOM parameters after fitting Generalized Additive Models. (a) BIX, (b) HIX and (c) QY(340). Rugs on x–axis indicate the distribution of the data.*

Table 3.2: Results of the Generalized Additive Models (GAMs) fitted to the fluorescence variables. Note that only statistically significant covariates were retained in the final formulations. SE = Standard Error; EDF = Estimated Degrees of Freedom; DE = Deviance Explained; N = number of data. See the main text for the variables and parameters descriptions. Note that Chl *a* fluorescence and prokaryotic heterotrophic abundance (PHA) were ln–transformed.

Variable	Parameter	Estimate (±SE)	EDF	t–value	F–value	P–value
Peak M	Intercept	6.45e−03 (6.14e−05)		105		<0.0001
N = 141	θ		1.77		22.62	<0.0001
DE = 90.6%	AOU		1.00		35.79	<0.0001
	a_{325}		1.00		21.38	<0.0001
	Chl *a*		1.00		27.40	<0.0001
	PHA		1.87		6.82	0.0011
Peak T	Intercept	0.008 (0.0002)		53.82		<0.0001
N = 165	θ		1.00		3.95	<0.0486
DE = 31%	PHA		1.91		30.12	<0.0001
Peak E	Intercept	5.86e−04 (1.07e−05)		54.95		<0.0001
N = 159	θ		1.92		7.78	<0.0007
DE = 74.1%	AOU		1.73		8.63	<0.0002
	PHA		1.95		30.34	<0.0001
BIX	Intercept	1.00 (0.004)		254.3		<0.0001
N = 158	θ		1.87		4.85	<0.0084
DE = 30.8%	AOU		1.19		5.65	<0.0082
	Chl *a*		1.00		7.76	<0.006
	PHA		1.00		11.37	<0.0009
HIX	Intercept	1.64 (0.03)		63.15		<0.0001
N = 153	θ		1.88		6.30	<0.0021
DE = 74.2%	AOU		1.00		45.76	<0.0001
	Chl *a*		1.00		20.46	<0.0001
	PHA		1.00		6.18	<0.0140
QY(340)	Intercept	0.84 (0.016)		54.01		<0.0001
N = 152	θ		1.73		6.50	<0.0013
DE = 63.4%	AOU		1.00		15.40	<0.0001
	PHA		1.87		6.43	<0.0014

3.2.4 Drivers of fluorescent DOM in the meso– and bathypelagic Mediterranean Sea

Fluorescence peaks and indices presented strong linear correlations with water mass mixing proportions ($R^2 > 0.62$) (Table 3.3). Specifically, 73% of the variability of the intensity of peak M is explained by water mass mixing. It should be kept in mind that this multiple linear regression model with water type proportions retains not only the variability due to different initial concentrations at the formation area of each water type, but also the large scale mineralization from the formation area to the study section (Álvarez–Salgado et al., 2013). Inclusion of a biogeochemical parameter as AOU in the multiple regression model improves the explained variance to 76%. In addition the SD of the residuals of the estimation improved by 5.8%. More importantly, a water mass mixing independent peak M/AOU ratio of 2.1 (± 0.4) x 10^{-5} RU µmol O_2^{-1} kg was obtained (Table 3.3), suggesting a production of marine humic–like substances in parallel to water mass ageing. For the case of the protein–like peak T the variability explained by the water mass mixing model was slightly lower (62%) and the mixing–biogeochemical model barely reduced the SD of the residuals, but a significant ($p < 0.05$) water mass mixing independent peak T/AOU ratio of –3.7 (± 1.3) x 10^{-5} RU µmol O_2^{-1} kg was obtained (Table 3.3). Contrary to the humic–like peak M, peak T/AOU ratio was negative, suggesting a decay of this fluorophore in parallel with water mass ageing. For peak E the mixing model explained 83% of its variability. The explained variance and the SD of the residuals did not improve when the mixing–biogeochemical model is applied but a significant ($p < 0.0001$) water mass mixing independent peak E/AOU ratio of 3 (± 1) x 10^{-6} RU µmol O_2^{-1} kg (Table 3.3) is obtained.

The linear mixing model for BIX and HIX explained the 87 and 64% of their variability, respectively. The mixing–biogeochemical model barely reduced the SD of the residuals of the estimation by about 2.0 and 1.4% for BIX and HIX, respectively. However it produces significant water mass mixing independent BIX/AOU and HIX/AOU ratios of –6 (± 2) x 10^{-4} and 17 (± 7) x 10^{-3} µmol O_2^{-1} kg, respectively, indicative of decreasing BIX and increasing HIX with ageing (Table 3.3). Finally, water mass mixing explained 79% of the variability of QY(340) in the dark MedSea. Inclusion of AOU increases the explained variability of this parameter to 82% and reduces, by about 8%, the SD of the estimation. The water mass mixing independent QY(340)/AOU ratio, 7 (± 1) x 10^{-3} µmol O_2^{-1} kg, (Table 3.3) indicates an increase of the quantum yield of the humic substances with ageing.

Table 3.3: Parameters of the linear mixing (Eq. 2.6; page 74) and mixing–biogeochemical (Eq. 2.7; page 75) models. R^2, determination coefficient; SD res, standard deviation of the residuals of the estimation; % SD reduction, percentage of reduction of the SD res of the mixing biogeochemical as compared with the corresponding mixing model; β, fitting parameter of the relationship between N_1 and N_2 independent of the mixing; SE(β), standard error of the estimation of β; *p*, significance level of the estimation of β. Results are presented for all samples and for the EastMed and WestMed separately.

N_1	N_2	R^2	SD res	%SD reduction	β	SE(β)	*p*	n
MedSea								
AOU		0.88	7.8					233
PHA		0.78	88518					240
Peak A		0.72	0.001					240
Peak C		0.77	0.0004					240
Peak M		0.73	0.00052					240
Peak T		0.62	0.00149					240
Peak E		0.83	0.00012					237
BIX		0.86	0.029					238
HIX		0.64	0.79					210
QY (340)		0.79	0.168					226
Peak A	AOU	0.74	0.00097	4.9%	0.000033	0.000009	0.0001	233
Peak C	AOU	0.79	0.0004	7.1%	0.000019	0.000003	0.0000	233
Peak M	AOU	0.76	0.00049	5.8%	0.000021	0.000004	0.0000	233
Peak T	AOU	0.63	0.00148	0.7%	–0.000037	0.000013	0.05	233
Peak E	AOU	0.83	0.00012	–	0.000003	0.000001	0.0001	231
BIX	AOU	0.87	0.028	2.3%	–0.0006	0.0002	0.016	231
HIX	AOU	0.66	0.79	1.4%	0.017	0.007	0.014	203
QY (340)	AOU	0.82	0.155	7.7%	0.007	0.001	0.0000	220
EastMed								
AOU		0.96	4.4					130
PHA		0.85	51696					134
Peak A		0.64	0.001					134
Peak C		0.69	0.00043					134
Peak M		0.59	0.00058					134
Peak T		0.55	0.00167					134
Peak E		0.86	0.00012					131
BIX		0.90	0.029					133
HIX		0.66	0.881					108
QY (340)		0.79	0.1835					121
Peak A	AOU	0.64	0.001	–	–	–	Ns	130
Peak C	AOU	0.73	0.00040	7%	0.00004	0.00001	0.0000	130
Peak M	AOU	0.64	0.00055	5.2%	0.00005	0.00001	0.0001	130
Peak T	AOU	0.56	0.00164	1.8%	–0.00008	0.00003	0.02	130
Peak E	AOU	0.86	0.00012	–	0.000005	0.000003	0.0001	128
BIX	AOU	0.91	0.027	4.8%	–0.001	0.0005	0.002	129
HIX	AOU	0.68	0.854	3.1%	0.045	0.019	0.016	104
QY (340)	AOU	0.79	0.1794	2.2%	0.007	0.004	0.1(ns)	118

N_1	N_2	R^2	SD res	%SD reduction	β	SE(β)	*p*	n
WestMed								
AOU		0.72	10.6					103
PHA		0.73	119700					106
Peak A		0.26	0.001					106
Peak C		0.40	0.0004					106
Peak M		0.50	0.00042					106
Peak T		0.71	0.00124					106
Peak E		0.64	0.00012					106
BIX		0.77	0.029					105
HIX		0.62	0.683					102
QY (340)		0.80	0.15					105
Peak A	AOU	0.36	0.001	–	0.00004	0.00001	0.0001	103
Peak C	AOU	0.51	0.00035	12.5%	0.000015	0.000003	0.0000	103
Peak M	AOU	0.59	0.00037	9.5%	0.000016	0.000004	0.0000	103
Peak T	AOU	0.72	0.00123	0.8%	–0.000027	0.000012	0.02	103
Peak E	AOU	0.63	0.00012	–	0.000002	0.000001	0.0001	103
HIX	AOU	0.63	0.682	–	0.011	0.007	0.09	99
QY (340)	AOU	0.87	0.123	18%	0.008	0.001	0.0000	102

Considering the two basins independently, the variance explained of the fluorescence peaks and indices using the mixing model was significantly lower in the western basin than in the eastern basin, except for peak T (Table 3.3). Regarding the mixing–biogeochemical model, the EastMed presented significantly higher water mass mixing–independent peak M/AOU and HIX/AOU ratios of 5 (± 1) x 10^{-5} and 45 (± 19) x 10^{-3} µmol O_2^{-1} kg, respectively compared to the WestMed of 1.6 (± 0.4) x 10^{-5} and 11 (± 4) x 10^{-3} µmol O_2^{-1} kg, respectively. The water mass mixing independent peak T/AOU in the EastMed, –8 (± 3) x 10^{-5} µmol O_2^{-1} kg, was more negative than in the WestMed, –2.7 (±1.2) x 10^{-5} µmol O_2^{-1} kg, due to the oligotrophy of the EastMed. QY(340) was the variable that showed the highest reduction of the SD of the residuals in the WestMed when considering the mixing–biogeochemical model, with a decrease by 18% (Table 3.3). However, the water mass mixing independent QY340/AOU ratio was similar in both basins.

4 Discussion

4.1 Fluorescence peaks *vs* fluorescence indices

Only a few works have dealt with the dynamics of FDOM in coastal areas (Para et al., 2010; Romera–Castillo et al., 2013) and local seas (Zeri et al., 2014; Gonnelli et al., 2016; Cyr et al., 2017; Pitta et al., 2017) of the MedSea. Here, we show the distribution of fluorescence

peaks and indices along a transect crossing the entire open MedSea and assess the drivers controlling their dynamics in the epi–, meso– and bathypelagic layers.

Overall, humic–like substances presented the typical vertical profile found in other regions of the ocean (e.g. Yamashita and Tanoue, 2008; Gueguen and Kowalczuk, 2014; Catalá et al., 2015b; Nelson and Gauglitz, 2016). This is, lower values are recorded at the surface layer, they increase monotonically until the intermediate layers and, from there to the bottom, they remain roughly constant. Peaks A, C and M presented higher intensities in the WestMed (Figure 3.3a). This fact is related to the association of these peaks with microbial respiration processes (Kramer and Herndl, 2004; Jørgensen et al., 2011; Zhao et al., 2017). In this regard, the ultra–oligotrophic EastMed presents lower heterotrophic production and enzymatic activities (Luna et al., 2012). The lowest values of peaks A, C and M corresponded with LSW and AW in the EastMed and WestMed, respectively. This is likely due to photobleaching (Kouassi and Zika, 1992; Moran et al., 2000; Mopper et al., 2015), because these substances containing aromatic structures that are prone to undergo decomposition into colourless smaller molecules. On the contrary, protein–like fluorescence was higher at the euphotic zone and declined with depth in agreement with Jørgensen et al. (2011), who suggested a labile or semilabile nature of these compounds linked to primary production in the surface layer. In the epipelagic layer, protein–like fluorescence presented lower intensity in the EastMed despite DOC concentrations were higher there (chapter 2). This combination of higher DOC but lower protein–like fluorescence intensity is likely associated to the ultra–oligotrophy of the EastMed that could preclude a regular functioning of the microbial loop (Thingstad et al., 1997). Following these authors, we propose that in the eastern basin phytoplankton exude organic matter depleted in nitrogen or structurally different than that formed in the western basin. In addition, we also propose that prokaryotes are not able to decompose DOM because of the extremely low values of nutrients in these surface waters (0.1 ± 0.3 and 1.0 ± 0.5 µmol kg^{-1} NO_3^- and 0.01 ± 0.01 and 0.04 ± 0.07 µmol kg^{-1} HPO_4^{-2} for the first 100 m of the EastMed and WestMed, respectively). Note that this fact does not mean that the accumulated compounds are refractory, but just that the microbial communities somehow are not able to use them. Conversely, in the WestMed the higher nutrient concentrations, transported by the surface AW entering from the Atlantic Ocean through the Strait of Gibraltar, stimulate the primary production and the accumulation of protein–like compounds by means of phytoplanktonic exudation processes. Peak E, associated with soil fulvic acids (Stedmon et al., 2003), presented lower fluorescence intensities than the other peaks, either humic– or protein–like, in agreement with Pitta et al. (2017). The distribution of peak E showed minimum intensities in

the surface layer, which was previously related with photodegradation processes (Pitta et al., 2017). In addition, the intensity was lower at the surface of the EastMed as the shallower water mass (MAW) results from the photodegradation processes underwent by AW after entering the MedSea through the Strait of Gibraltar and completing its route towards the Levantine basin. No significant differences were observed between basins in meso– and bathypelagic layers (Figure 3.3c).

Fluorescence indices, HIX and BIX, are based on ratios of fluorescence intensities at different wavelengths or wavelength ranges and were designed to provide information about the source, degree of humification and microbial influence in marine DOM (Fellman et al., 2010; Coble et al., 2014). The interpretation of these indices depends on the organic matter source, matrix and environmental conditions (Coble et al., 2014). Studies using fluorescence indices were mainly focused in fresh and coastal waters (Fellman et al., 2010; Para et al., 2010; Lavonen et al., 2015). Only few works have reported these indices in the open ocean (e.g. Kowalczuk et al., 2013; Zhao et al., 2013; Loginova et al., 2016). In the MedSea only a couple of papers, one in each basin, reported values of fluorescence indices but in surface coastal waters (Para et al., 2010; Pitta et al., 2017). Increasing values of HIX with depth suggest a higher humification at the intermediate and deep waters as DOM aged. The values reported here are in the range of those found in the Atlantic Ocean by Kowalczuk et al. (2013) and in the East China Sea by Zhao et al. (2013). BIX values obtained in the surface layer of the open MedSea are in the range of those found in Marseille Bay by Para et al. (2010) and are indicative of the predominantly autochthonous origin of DOM in the upper layer. QY(340) measurements of marine DOM are scarce in the literature (Green and Blough, 1994; Romera–Castillo et al., 2011a; Andrew et al., 2013; Catalá et al., 2015a; Wünsch et al., 2015; Zhao et al., 2017). In our samples QY(340), a proxy to aromaticity, increased with depth and with DOM ageing as suggested by Catalá et al. (2015a) for the global ocean. QY(340) values in the epipelagic layer are in agreement with the apparent quantum yields reported by Wünsch et al. (2015) for the Norwegian Sea, Romera–Castillo et al. (2011a) in the Ría de Vigo (NE Atlantic Ocean) and Andrew et al. (2013) in the Equatorial Atlantic Ocean. Zhao et al. (2017) have recently reported apparent QY(340) for picocyanobacteria, marine and terrestrially derived FDOM from solid–phase extracted samples. Their QY(340) values for the surface waters are higher than the values reported in this study, however our results are not directly comparable since our samples host the whole FDOM pool, and the values reported by Zhao et al. (2017) correspond only to the solid phase extractable FDOM fraction.

We also examined the relationship between Peak C and HIX because the emission wavelength is the same in both parameters, and we found a significant positive linear relationship between them up to peak C intensities of about 6–8 10^{-3} RU. At those intensities, while peak C remains constant, HIX can vary from 3 to 6 units (Figure 3.7a). Conversely, HIX was negatively correlated with peak T (Figure 3.7b). Furthermore, a strong linear correlation of HIX with the peak C/peak T ratio was observed (Figure 3.7c; HIX = (1.17 ± 0.03) peak C/peak T – (0.23 ± 0.07); R^2 = 0.87, p < 0.001, n = 286). This relationship was maintained when both basins were considered separately. In summary, while HIX presented not robust correlations with peak C and peak T, the correlation was stronger with the peak C/peak T ratio because HIX works really as a humic/protein like fluorescence ratio.

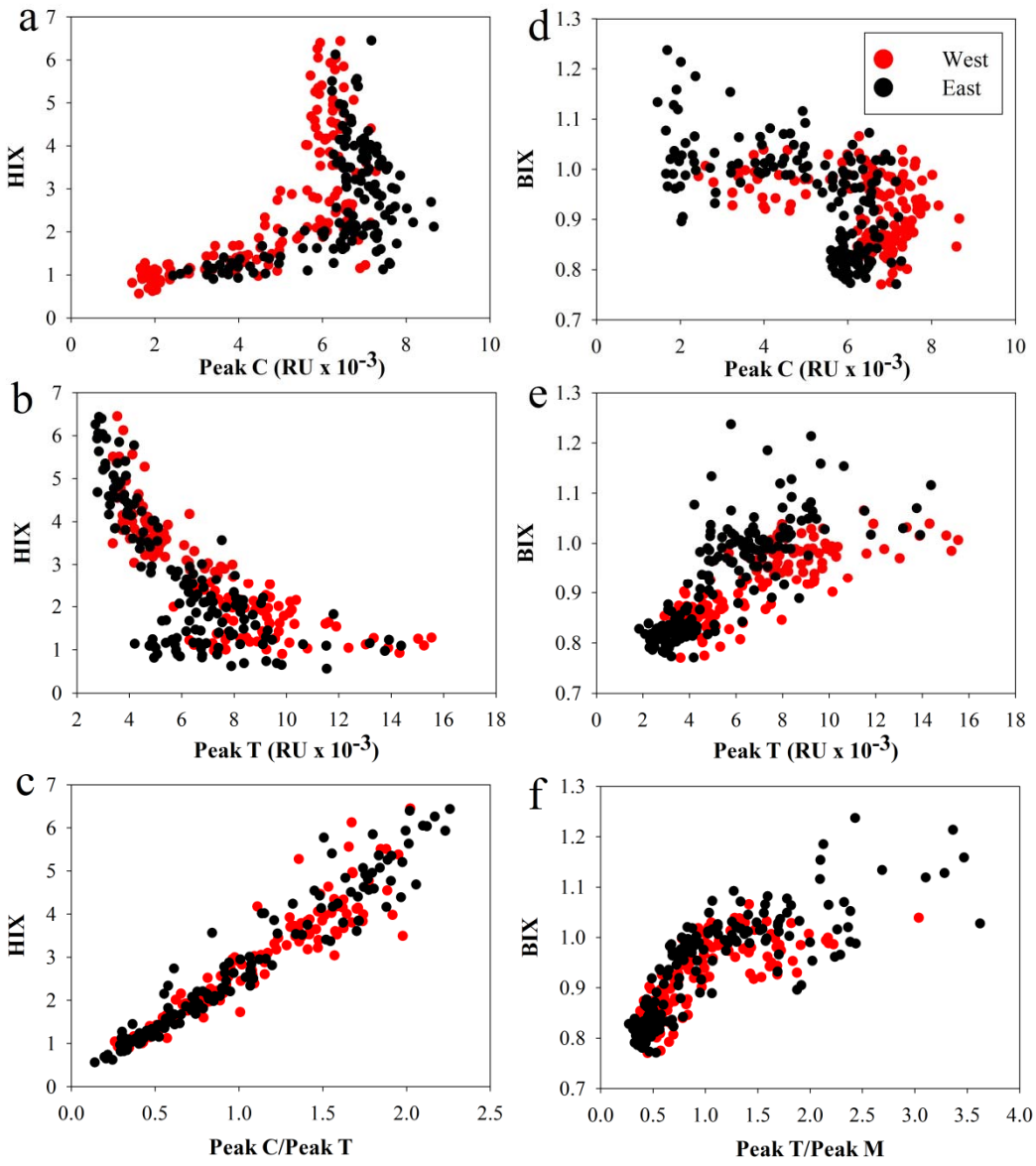

Figure 3.7: *Relationships between the fluorescence indices: HIX with (a) peak C, (b) peak T and (c) peakC/peakT ratio and BIX with (d) peak C, (e) peak T and (f) peakT/peakM ratio. Red and black circles correspond with samples from the WestMed and EastMed, respectively.*

While BIX did not show a significant correlation with peak C (Figure 3.7d), it was positively correlated with peak T (Figure 3.7e; BIX = (23.5 ± 1.3) peak T + (0.78 ± 0.01); R^2 = 0.52, p < 0.01, n = 310). Considering both basins separately, the EastMed (BIX = (32 ± 2) peak T + (0.75 ± 0.01); R^2 = 0.62, p < 0.0001, n = 172) presented a higher BIX/peak T slope than the WestMed (BIX = (19 ± 1) peak T + (0.78 ± 0.01); R^2 = 0.63, p < 0.0001, n = 138). BIX and peak T did not correlate stronger because they are not directly comparable. While peak T is measured at Ex/Em 280/350 nm representing protein–like compounds, BIX is measured as the ratio of the emission at 380 nm and 430 nm when excited at 310 nm (Huguet et al., 2009). Consequently, BIX measurements are influenced also by the humic–like fluorescence signal and it would match better the peak T/peak M ratio. In fact, the determination coefficient of the correlation between BIX and the peak T/peak M ratio (Figure 3.7f; BIX = (0.946 ± 0.003) (peak T/peak M) $^{(0.138 \pm 0.005)}$; R^2 = 0.71, p < 0.01, n= 310) was better than with just peak T. Therefore, although fluorescence peaks and indices are correlated, they provide complementary information and therefore it is convenient to obtain and interpret both.

4.2 FDOM drivers in oligotrophic epipelagic waters

GAM analysis showed that in the epipelagic layer the distribution of peak M fluorescence were addressed mainly by 4 variables (Figure 3.5a): i) AOU, which is a proxy of the net community respiration (i.e. the community respiration minus the autotrophic oxygen production) integrated over the time elapsed since the water was last in contact with the atmosphere, ii) Chl *a* concentration, which is indicative of autotrophic biomass and it is in agreement with the findings of marine humic–like substances generated by phytoplankton (Romera–Castillo et al., 2010; Fukuzaki et al., 2014), iii) θ, which apart from being related to stratification, can be partly considered as a proxy to solar irradiation, and therefore linked to photodegradation processes; and iv) a_{325} that is the absorption coefficient at around the excitation wavelength of peak M (320 nm). Peak T was mainly controlled by PHA (Figure 3.5b and table 3.2). To a lesser extent, θ also controlled the distribution of peak T. In this case, it should not be related with photodegradation processes since peak T is mainly resistant to photobleaching. However, it could be due to the enhancement of biological processes with increasing temperatures. The distribution of peak E was driven mainly by PHA and to a lesser extent by AOU and θ. In this case, contrary to peak T, θ is mainly related with photodegradation processes. In agreement with peak T and based on the GAMs results, BIX was mainly driven by PHA (Figure 3.6a and table 3.2). Conversely, HIX and QY(340) were driven by AOU, suggesting the control of net community respiration in the humification and DOM

aromaticity increase. Note that although AOU is negative at the surface layer because autothrophic oxygen production exceeds community respiration, there was not any change in the shape of the relationship of any FDOM peak or index (peak M, peak T, peak E, HIX, BIX and QY(340)) and AOU when this variable changes from net community production (AOU < 0) to net community respiration (AOU > 0) (Figure 3.5 and 3.6). Therefore, it was not necessary to analyse both set of samples separately.

4.3 FDOM drivers in meso– and bathypelagic waters

Maximum fluorescence intensities of peak M were found in the intermediate layers, corresponding with CIW in the EastMed and with WIW and EIW in the WestMed matching with the highest archetype AOU values. These results are in agreement with the hypothesis of humic–like compounds being produced by microbes as by–products during bioavailable organic matter mineralization (Nieto–Cid et al., 2006; Yamashita and Tanoue, 2008; Jørgensen et al., 2011; Catalá et al., 2015b). Regarding the deep water masses, they presented different behaviour depending on the basin. While deep waters of the WestMed showed the expected positive trend between peak M and AOU (red circles in Figure 3.8a), deep waters of the EastMed showed a negative relationship between both variables (white circles in Figure 3.8a). In the WestMed, deep water mass varieties presented different ages but the same area of formation and, therefore, equivalent peak M intensities at the formation time. However, deep water masses of the EastMed presented different peak M values at their formation time depending on the formation site. In this case, we hypothesized that the area of formation have a larger influence than the subsequent alteration due to biogeochemical processes in the final intensity of peak M. Specifically, fluorescence intensity of peak M was higher in Post–EMT–B and –C water masses (archetype AOU = 55 ± 1 and 56 ± 1 μmol kg^{-1}, respectively) than in the water masses formed during the EMT (archetype AOU = 62 ± 1 μmol kg^{-1}) in spite of being formed earlier and presenting lower archetype AOU. While Post–EMT–B and –C water masses were formed in the Adriatic Sea, EMT was originated in the Aegean Sea (Roether et al., 1996). On the other hand, in the deep waters of the WestMed, the water mass WMDW–A (archetype AOU, 67 ± 1 μmol kg^{-1}) presented significantly higher peak M fluorescence than WMDW–D11 and WMDW–D14 varieties (archetype AOU, = 55 ± 1 and 56 ± 1 μmol kg^{-1}), as WMDW–A was the oldest WMDW in this basin, formed prior to WMT (before 2004/5; (López-Jurado et al., 2005; Schroeder et al., 2016). The HIX index presented a decreasing trend with AOU in the Eastern Mediterranean deep waters (white circles in Figure 3.8d) parallel to peak M decrease with AOU (Figure 3.8a).

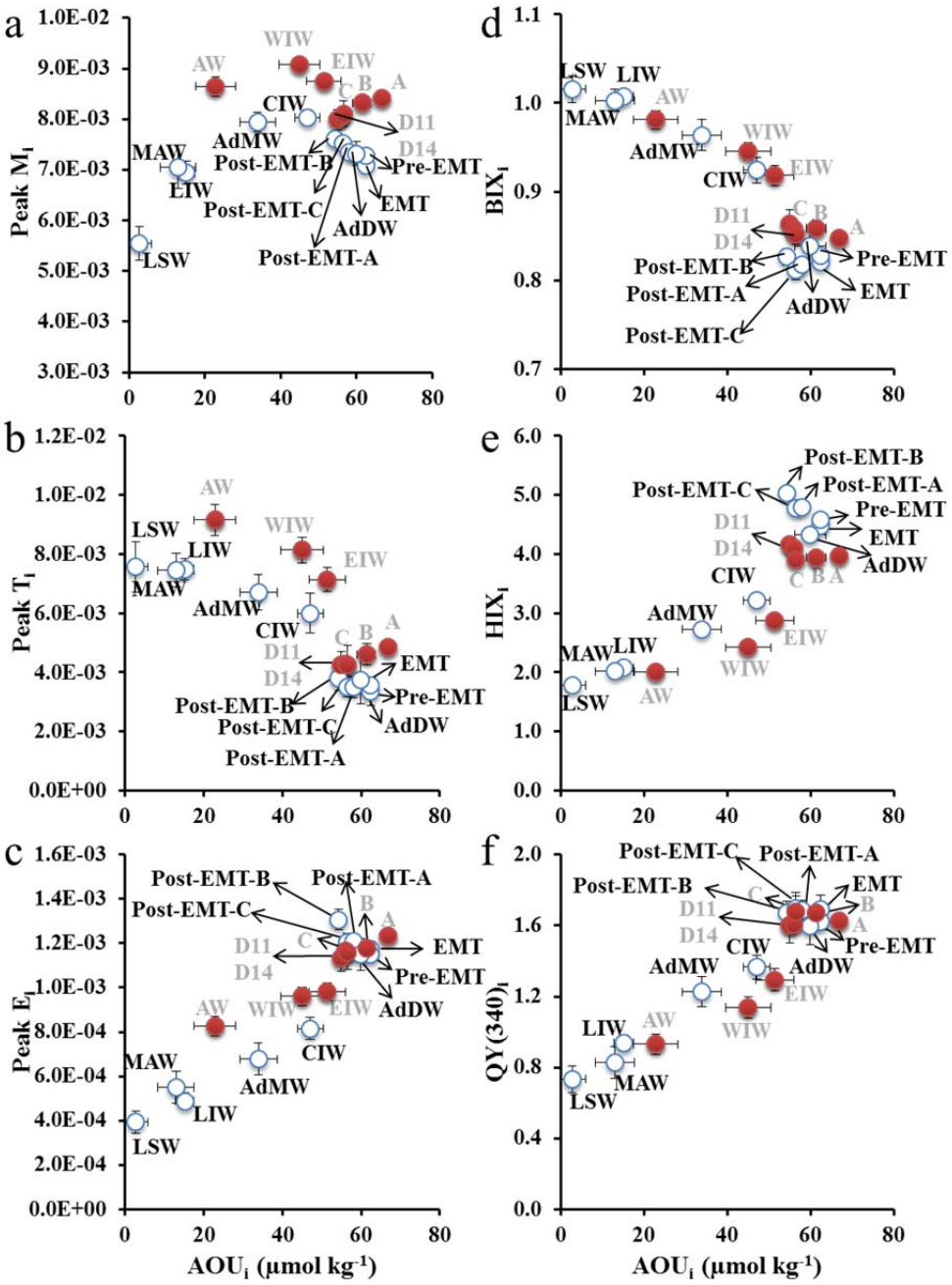

Figure 3.8: *Relationships of archetype fluorescence peaks and indices with archetype apparent oxygen utilization (AOU). (a) archetype peak M (peak M_i, RU), (b) archetype peak T (peak T_i), (c) archetype peak E (peak E_i), (d) archetype BIX (BIX_i), (e) archetype HIX (HIX_i) and (f) archetype QY(340) ($QY(340)_i$)(versus archetype apparent oxygen utilization (AOU_i, µmol kg^{-1}). Error bars represent the standard deviation of the estimated archetypal values. Red and white circles represent samples of the WestMed and EastMed basins, respectively. The acronyms of the water masses are explained in Table 2.2 in chapter 2.*

Regarding peak T in the EastMed, LIW presented the highest intensity of the water masses that coexist in the mesopelagic layer, probably because it is the shallowest and youngest intermediate water of the EastMed. The archetype fluorescence intensity of LIW was similar to MAW and LSW, which are centred at similar archetype depths. In addition, when considering deep water masses, all varieties hosted similar peak T intensities. Conversely, in

the WestMed, AW was the water mass with the highest peak T intensity due to its shallowness and, therefore, proximity to the primary production layer. Down in the mesopelagic layer, WIW presented higher intensity than EIW because the former was more recently formed in the Gulf of Lions and the Balearic Sea. However, EIW was originated in the Levantine basin and mixed with the surrounding water masses in its route westwards (EMDW, CIW and WIW, the later is present in the western part of the Strait of Sicily) and then, once in the WestMed, EIW was further mixed with WIW and WMDW (chapter 2). Regarding the WMDW varieties they presented an unexpected positive relationship between peak T and AOU (four red circles in bottom right Figure 3.8b). Specifically, WMDW–A variety showed significantly higher peak T fluorescence intensity than WMDW–D14. This is an unexpected result since WMDW–A is the oldest WMDW in the western basin and WMDW–D14 is the youngest WMDW. Conversely, the archetype BIX showed an opposite trend with archetype AOU in WMDW (Figure 8.3d). This indicates that peak T is not directly comparable with BIX, because the former is a proxy to the total amount of fluorescent amino acids and the latter is closer to a ratio of protein to humic–like substances. The susceptibility of peak T of being affected by humic–like compounds and small organic acids fluorescing near the peak T region (Stubbins et al., 2014) is another feasible reason that may cause those differences.

Peak E showed a different distribution and behaviour compared to peak M (Figure 3.3a, c and Figure 3.8a, c). While peak M presented significant differences between the eastern and western basins, peak E was homogeneously distributed.

Regarding the mixing model and considering both basins independently, the variance explained of fluorescence peaks and indices were significantly lower in the WestMed than in the EastMed. This result indicates that the water mass mixing processes were more influential in the eastern basin because of its ultra–oligotrophy. In addition, when considering the mixing–biogeochemical model the water mass mixing independent peak M/AOU ratio and peak E/AOU ratio were 2.1 (± 0.4) x 10^{-5} and 3 (± 1) x 10^{-6} RU µmol O_2^{-1} kg, respectively suggesting a production of peak M and peak E fluorescence in parallel to cumulative microbial respiration. However, as peak E has been associated with soil fulvic acids (Stedmon et al., 2003), the production of this terrestrial material in the deep MedSea as a by–product of respiration processes is unexpected. Likely, the explanation to this positive relationship between peak E and AOU could be the enhancement of the fluorescence intensity of the existing terrestrial source material (soil fulvic acid) by further chemical or microbial transformations (Andrew et al., 2013) rather than its autochtonous production.

Finally, in this work we have reported a positive relationship between peak M and AOU. However, in chapter 2 was observed a negative relationship between a_{325} and AOU, indicating a consumption of these coloured compounds. Since peak M absorb at a_{325}, it should be expected that both peak M and a_{325} had parallel trends with AOU as it was already observed for the global ocean (Catalá et al., 2015a; 2015b). However, the trends of peak M and a_{325} were opposite in the MedSea. These results suggest that in the oligotrophic MedSea the CDOM fraction absorbing at a_{325} nm but not emitting fluorescence is consumed at a higher rate than the production of the fluorescent fraction, resulting in an unexpected net inverse relationship.

5 Conclusions

In the epipelagic layer of the MedSea, AOU explained most of the variability of the humic–like fluorescence, suggesting a dominant influence of net microbial respiration in the distribution of these compounds. On the contrary, the variability of protein–like fluorescence was largely explained by PHA. Likewise, AOU explained largely the variability of HIX and QY(340) whereas BIX was better explained by PHA. In the meso– and bathypelagic layers, the combination of water mass mixing and basin scale mineralization explained better the variability of peaks E and M, BIX and QY(340) (73, 86 and 79%, respectively) than the variability of peak T and HIX (62 and 64%, respectively). Considering both basins independently, the explained variance was better in the EastMed due to its extreme oligotrophy. Regarding the deep water masses, while FDOM peaks dynamics in the WestMed was mostly driven by ageing, in the EastMed knowledge of EMDW formation areas, in the Adriatic or the Aegean Sea, was relevant to explain the distributions. Estimation of water mass independent ratios of peak M with AOU (peak M/AOU ratio) revealed the production of peak M with the net microbial respiration. Furthermore, the fact that contrary to the peak M/AOU ratio, the a_{325}/AOU ratio was negative (chapter 2), indicates that in the particular case of the MedSea the consumption of the non fluorescent fraction of CDOM that absorbs at 325 nm exceeds the production of the fluorescent fraction represented by peak M.

Appendix

Chapter 3

Appendix 3.A

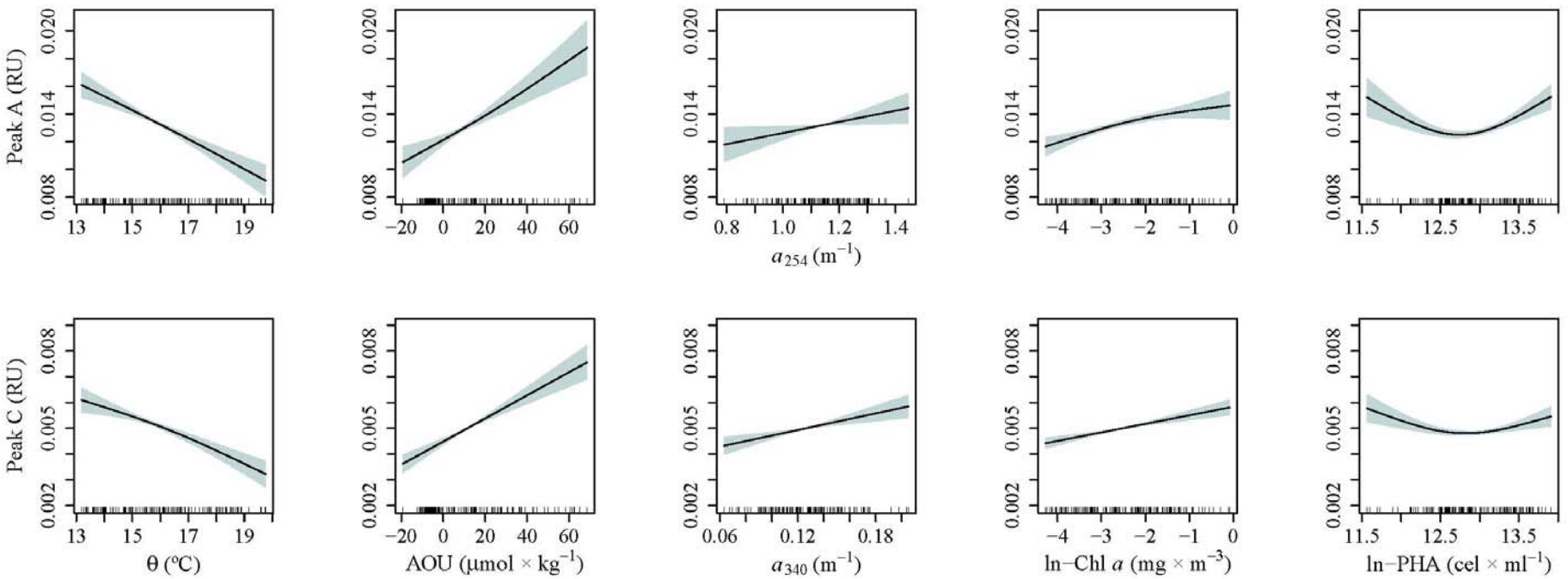

Figure 3.A1: Partial plots of the additive effects of the physical, chemical and biological covariates on the FDOM parameters after fitting Generalized Additive Models. (a) Peak A, (b) Peak C. Rugs on x–axis indicate the distribution of the data.

Table 3.A1: Results of the Generalized Additive Models (GAMs) fitted to the fluorescence indices. Note that only statistically significant covariates were retained in the final formulations. SE = Standard Error; EDF = Estimated Degrees of Freedom; DE = Deviance Explained. See the main text for the variables and parameters descriptions. Note that Chl *a* fluorescence and prokaryotic heterotrophic abundance (PHA) were ln–transformed.

Fluorescence Index	Parameter	Estimate (±SE)	EDF	t–value	F–value	P–value
Peak A	Intercept	0.013 (0.0001)		118.9		<0.0001
N = 140	θ		1.16		30.74	<0.0001
DE = 88.3%	AOU		1.40		16.34	<0.0001
	a_{254}		1.00		5.00	0.027
	Chl *a*		1.64		13.56	<0.0001
	PHA		1.99		17.01	<0.0001
Peak C	Intercept	4.99e−03 (4.71e−05)		105.9		<0.0001
N = 141	θ		1.61		18.67	<0.0001
DE = 91.7%	AOU		1.00		59.54	<0.0001
	a_{340}		1.00		15.01	0.0002
	Chl *a*		1.00		29.38	<0.0001
	PHA		1.95		8.56	0.0003

Chapter 4
Molecular composition of dissolved organic matter in the Mediterranean Sea

The research work presented in this chapter is also a contribution to the paper:

Martínez–Pérez, A. M., Osterholz, H., Nieto–Cid, M., Álvarez, M., Dittmar, T. and Álvarez–Salgado, X. A., 2017. Molecular composition of dissolved organic matter in the Mediterranean Sea. Limnol. Oceanogr. 62, 2699–2712. doi: 10.1002/lno.10600.

Abstract

The molecular composition of marine dissolved organic matter (DOM) is still poorly understood, particularly in the Mediterranean Sea (MedSea). In this work, DOM from the open MedSea and the adjacent Northeast Atlantic Ocean was isolated by solid–phase extraction (SPE–DOM) and molecularly characterized using Fourier–Transform Ion Cyclotron Resonance Mass Spectrometry (FT–ICR–MS). We assessed the gradual reworking of the SPE–DOM transported by the shallow overturning circulation of the Mediterranean Sea by following the increase in molecular weight (+20 Da), oxygenation (+5%), degradation index (Ideg +22%) and the proportional decrease of unsaturated aliphatic compounds (+34%) along the Levantine Intermediate Water (LIW). This reworked SPE–DOM that leaves the MedSea through the Strait of Gibraltar strongly contrasts with the fresh material transported by the inflow of Atlantic water (Ideg –25%). In the deep eastern and western overturning cells the molecular composition of the deep waters varied according to their area and/or time of formation. SPE–DOM of the waters formed in the Aegean Sea during the Eastern Mediterranean Transient (EMT) was more processed than the DOM in pre–EMT waters formed in the Adriatic Sea (molecular weight and the proportion of unsaturated aliphatic compounds were increased by 5 Da and 9%, respectively). Furthermore, pre–EMT waters contain more reworked SPE–DOM (Ideg +7%) than post–EMT waters formed also in the Adriatic Sea. In summary, our study shows that the MedSea constitutes a laboratory basin where degradation processes and diagenetic transformations of DOM can be observed on close spatial and temporal scales.

1 Introduction

To achieve a better understanding of the fate of DOM in the Mediterranean Sea (MedSea), identifying the molecular composition and structure of this material is essential. Previous studies applying ^{1}H nuclear magnetic resonance (NMR), amino acid and neutral sugar analysis of ultrafiltered DOM (UDOM) revealed that carbohydrates are main constituents of this material at the sea surface of the MedSea (Jones et al., 2013). This pool decreases with depth indicating DOM biodegradation. In addition, a strong correlation between amino acid concentration, apparent oxygen utilization (AOU) and picoplankton activity has been observed (Meador et al., 2010; Jones et al., 2013).

Molecular characterisation of marine DOM compels previous isolation of the samples (chapter 1). In this regard, solid–phase extraction (SPE) using styrene divinyl benzene polymer (PPL) cartridges has recently been introduced as an efficient method for isolating more than 60% of marine DOM (Dittmar et al., 2008; Green et al., 2014). The salt–free extracts are accessible by modern, non–targeted ultrahigh–resolution analytical techniques such as Fourier–Transform Ion Cyclotron Resonance Mass Spectrometry (FT–ICR–MS) for a comprehensive characterization. Nowadays, FT–ICR–MS is a widely used technique to distinguish thousands of molecular formulae constituting the DOM pool. Previous studies on the molecular composition of DOM by FT–ICR–MS showed molecular level differences between terrestrial and marine DOM (Koch et al., 2005), open ocean and coastal DOM (Koprivnjak et al., 2009) as well as surface and deep water DOM in the North Pacific (Medeiros et al., 2015) and North Atlantic (Hansman et al., 2015) oceans. Furthermore, the effect of degradation on the molecular composition of DOM was investigated along the eastern Atlantic and Southern Oceans combining FT–ICR–MS with radiocarbon analysis (Flerus et al., 2012; Lechtenfeld et al., 2014). Hertkorn et al. (2006) combined multidimensional NMR with FT–ICR–MS on ultrafiltered DOM, reporting carboxylic–rich alicyclic molecules (CRAM) as a likely major component of the DOM (8% of the whole DOM pool). More studies exist on the molecular characterization of open ocean DOM by FT–ICR–MS (Hertkorn et al., 2006; Chen et al., 2014; Hansman et al., 2015; Medeiros et al., 2015), but DOM composition in the enclosed MedSea has not been studied in this detail yet.

During the HOTMIX 2014 cruise we collected samples at selected depths along a longitudinal transect from the Levantine Sea to the Northeast Atlantic Ocean to characterize the molecular composition of solid–phase extractable DOM (SPE–DOM) through the water column *via* FT–ICR–MS. The specific objectives of our study are to 1) determine the overall

molecular composition of the SPE–DOM in the MedSea; 2) compare the molecular composition between the inflow of Atlantic surface water entering the Mediterranean Sea and the overflow of Mediterranean water into the Atlantic Ocean; and 3) explore the main drivers controlling the DOM transformations through changes in the molecular characteristics of SPE–DOM in relation to the "oceanographic model system" of the MedSea.

2 Materials and methods

2.1 Sampling and determination of core parameters

Water samples were collected during the trans–Mediterranean cruise HOTMIX 2014 aboard R/V Sarmiento de Gamboa in spring (Heraklion, Crete, 27 April – Las Palmas, Canary Islands, 29 May). The transect consisted of 24 stations (stn) crossing the MedSea from the Levantine Basin to the Strait of Gibraltar and 5 stations in the adjacent Northeast Atlantic Ocean (Figure 2.1; page 58).

2.2 Collection of SPE–DOM samples

At nine stations (red dots in Figure 2.1; page 58) water samples were collected for the solid phase extraction of DOM (SPE–DOM) to perform FT–ICR–MS analysis. Four to five depths were sampled depending on the bathymetry of the stations (Figure 4.1), except for the site at the Strait of Sicily (stn 13) where only Levantine intermediate water (LIW) was sampled due to its shallowness. The deep chlorophyll maximum (DCM) was sampled according to the maximum fluorescence intensity, the LIW was sampled at the absolute maximum of the salinity profile at each station, the oxygen minimum layer (OML) was established on basis of the absolute minimum of the dissolved oxygen profile, and the deep waters were sampled according to the salinity and temperature characteristic of the bathypelagic zone of the EastMed and WestMed (Figure 4.1).

The sampling strategy was restricted by time constraints during the cruise, which limited the number of collected samples, especially in the bathypelagic layer where different varieties of deep waters were found. Unfortunately, we were not able to sample any station in the Ionian Sea, so we missed the youngest variety of the EMDW. Note that although the hydrographic properties of the OML sample at stn 4 are reported in Table 4.1, this sample was rejected from the FT–ICR–MS analysis due to a contamination problem.

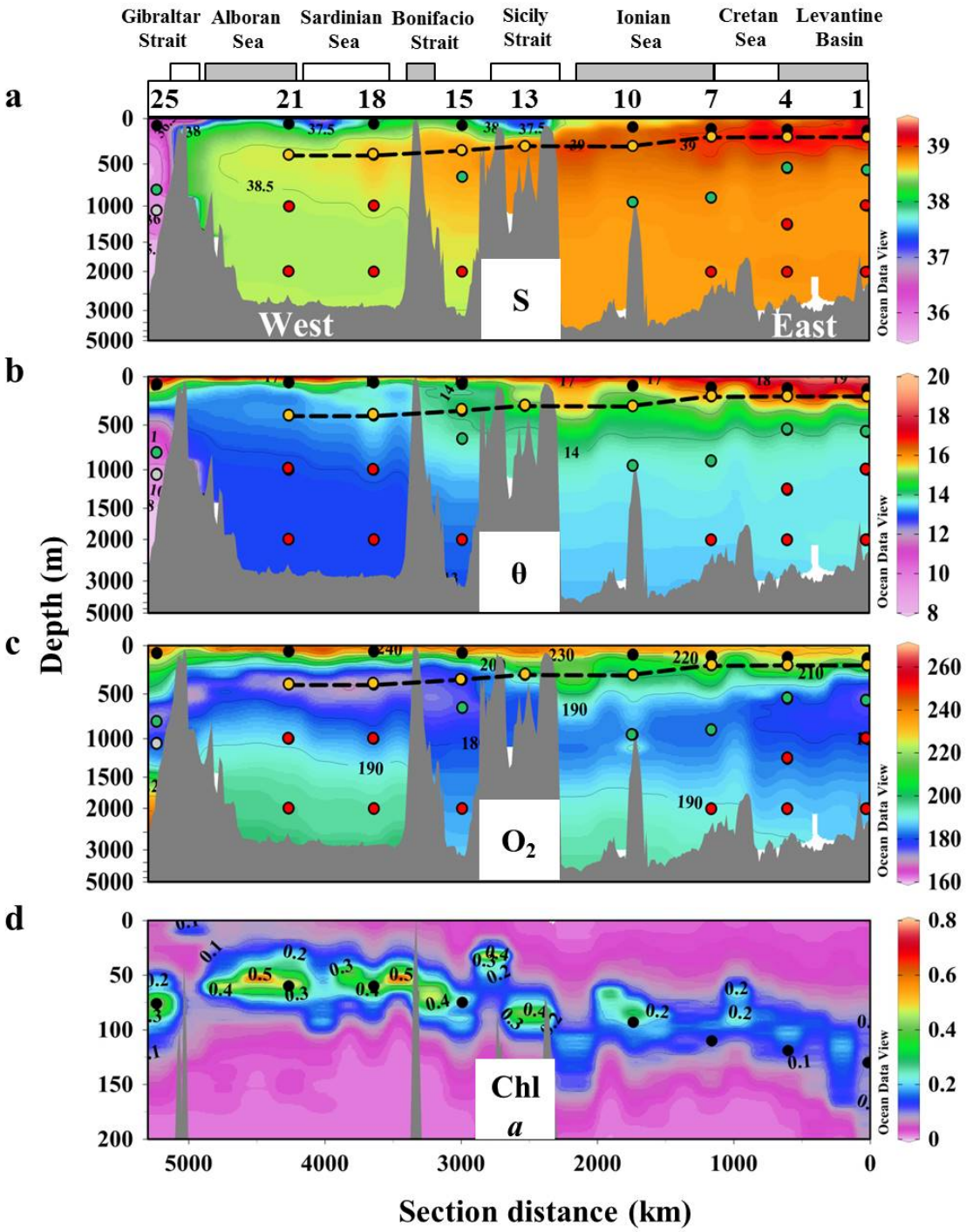

Figure 4.1: *Distribution of (a) salinity (S), (b) potential temperature (ϑ) in °C, (c) dissolved oxygen (O_2) in µmol/kg and (d) fluorescence of chlorophyll a (Chl a) in mg m^{-3} obtained from the sensors attached to the rosette sampler along the Mediterranean Sea. Black, yellow, green and red dots represent samples taken in the epipelagic layer (DCM), Levantine Intermediate Water (LIW), oxygen minimum layer and deep waters, respectively. The dashed black line represents the route of the LIW along the transect. Note that the depth is displayed on a non–linear scale. Values from all stations were used to show these distributions. Numbers located on the top of the figure indicate the sample stations, which are depicted in Figure 2.1 in page 58. Figure created using ODV software (Schlitzer, 2016).*

Water samples were collected in 5–litres acid–cleaned polycarbonate carboys, and then stored in the dark at 13°C until filtration within 5 hours. Filtration was performed through precombusted (450°C, 4 h) Whatman GF/F filters in an acid–clean all–glass filtration system under positive pressure with low flow of high purity N_2. Two–litres aliquots of the filtrate were collected in acid–cleaned PTFE bottles for SPE–DOM. Approximately 10 mL of the filtrate were collected for initial DOC determination in precombusted (450°C, 12 h) glass ampoules (see page 59 in chapter 2 for details on the DOC determination).

For SPE–DOM isolation, the filtered sea water sample (2 L) was acidified to pH 2 with HCl (37%, p.a., Merck) and the DOM was extracted on board with commercially available modified styrene divinyl benzene polymer cartridges (PPL, Agilent) as described in Dittmar et al. (2008). After extraction, cartridges were rinsed with acidified ultrapure water (pH 2, HCl 37%, p.a., Merck) to remove remaining salts and frozen at –20°C. Once in the base lab, the cartridges were dried by flushing with high purity N_2 and eluted with 6 mL of methanol (HPLC–grade, Sigma–Aldrich). Extracts were stored in amber vials at –20°C. DOC concentrations in the extracts were measured after complete evaporation of an aliquot and re–dissolution in ultrapure water. The extraction efficiency is the ratio of SPE–DOC to initial DOC concentrations. The mean extraction efficiency was 47.3 ± 3.9% on a carbon basis. Some of the epipelagic water samples showed slightly lower extraction efficiencies, likely due to the fact that PPL cartridges do not efficiently elute/retain the larger molecules (Chen et al., 2016; Raeke et al., 2016; also see the discussion section of this thesis, page 208), which can be a significant fraction of DOM in the surface mixed layer.

Table 4.1: Physical–chemical properties and solid–phase extraction efficiency (Ext effic) of DOM on a carbon basis. SD = standard deviation from duplicate analyses of DOC concentration.

Stn	Sample	Depth	S	θ	O_2	AOU	DOC		Ext effic
		m		°C	µmol kg^{-1}	µmol kg^{-1}	µM	SD	%
01	Deep	2000	38.78	13.62	186.7	61.3	39.7	1.1	50.5
01	Deep	1000	38.75	13.60	180.0	68.2	43.9	2.8	45.8
01	OML	575	38.80	13.82	174.4	72.6	45.7	5.4	37.3
01	LIW	201	39.17	16.87	214.3	18.1	60.2	0.9	47.7
01	DCM	130	39.22	17.63	224.9	4.0	68.8	0.9	42.2
04	Deep	2000	38.77	13.60	187.6	60.5	43.1	5.2	46.9
04	Deep	1250	38.76	13.61	183.0	65.1	43.9	2.8	48.1
04	OML	551	38.85	14.00	176.9	69.1	45.7	2.1	–
04	LIW	201	39.13	16.17	220.4	15.1	59.2	0.4	44.1
04	DCM	119	39.03	16.59	230.6	3.1	65.9	2.2	42.7
07	Deep	2001	38.75	13.51	190.6	58.0	44.9	0.8	50.7
07	OML	900	38.80	13.77	182.3	65.0	45.7	8.5	49.1
07	LIW	201	39.02	15.95	220.3	16.4	59.7	0.7	51.5
07	DCM	110	38.97	16.52	228.8	5.4	64.5	0.1	50.9
10	OML	951	38.76	13.63	184.3	63.7	42.3	1.8	51.0
10	LIW	300	38.90	14.52	201.6	38.0	58.6	0.2	44.3
10	DCM	93	38.70	15.08	230.2	10.9	60.8	6.5	43.9
13	LIW	301	38.87	14.81	196.1	46.1	54.8	0.4	46.7
15	Deep	2001	38.53	13.11	184.7	66.3	47.1	7.1	49.9
15	OML	651	38.71	13.83	174.5	72.6	49.6	6.4	44.6
15	LIW	351	38.75	14.16	176.6	68.9	46.2	1.2	51.5
15	DCM	75	38.32	14.33	242.7	2.7	64.3	5.2	41.7
18	Deep	2000	38.48	12.90	195.0	57.2	42.7	0.6	52.8
18	Deep	1000	38.53	13.11	183.0	68.1	42.7	5.4	50.1
18	LIW	401	38.67	13.77	171.3	76.2	47.4	0.7	48.4
18	DCM	60	37.96	14.23	242.8	3.7	61.0	0.2	49.2
21	Deep	2000	38.48	12.90	196.3	55.9	44.4	5.4	50.9
21	Deep	1000	38.48	12.94	189.0	63.0	42.5	5.4	51.1
21	LIW	401	38.53	13.25	169.9	80.5	47.4	0.7	48.2
21	DCM	60	37.63	14.75	243.1	1.4	65.2	1.6	42.0
25	MW	1050	35.89	9.80	181.0	93.0	45.7	0.6	51.1
25	OML	800	35.80	10.42	174.3	96.3	49.8	5.1	49.1
25	DCM	76	36.30	16.12	230.5	9.8	69.0	1.0	41.1

2.3 FT–ICR–MS analysis

SPE–DOM methanol extracts were diluted with ultrapure water and methanol (MS grade) to yield a DOC concentration of 15 mg C L^{-1} and a methanol–to–water ratio of 1:1 (v/v). Duplicates of each sample were prepared for analysis by ultrahigh–resolution mass spectrometry using a Solarix FT–ICR–MS (Bruker Daltonik GmbH) connected to a 15 Tesla superconducting magnet (Bruker Biospin). Samples were infused at a flow rate of 120 µL h^{-1} into the electrospray source (ESI; Apollo II ion source, Bruker Daltonik GmbH) with the capillary voltage set to 4 kV in negative mode. Ions were accumulated in the hexapole for 0.3 s prior to transfer into the ICR cell. Data acquisition was done in broadband mode with a scanning range of 150–2000 Da. For each mass spectrum, 500 scans were accumulated. The spectra were mass calibrated (linear) using the Bruker Daltonics Data Analysis software package with an internal calibration list consisting of 51 known $C_xH_yO_z$ molecular formulae over the mass range of the samples. With this calibration procedure, a mass error of <0.1 ppm was achieved. SPE–DOM from the North Equatorial Pacific Intermediate Water (NEqPIW) collected at a depth of 670 m at the Natural Energy Laboratory of Hawaii Authority (NELHA) in Kona, Hawaii (Green et al., 2014) was used as an internal reference sample to assess instrument variability over time (Osterholz et al., 2014; Hansman et al., 2015). Molecular formulae were assigned to peaks considering a maximum mass error of 0.5 ppm and in the mass range between 150 and 850 Da by applying the following restrictions: $^{12}C_{1–130}{}^{1}H_{1–200}\,O_{1–50}{}^{14}N_{0–4}S_{0–2}P_{0–2}$ as described in Seidel et al. (2014). Only compounds with a signal–to–noise (S/N) ratio of 4 and higher were used for further analysis. Moreover, compounds present in less than 20% of samples with a maximum S/N less than 20 were removed, as well as the molecules containing the following heteroatom combinations: NSP, N_2S, N_3S, N_4S, N_2P, N_3P, N_4P, NS_2, N_2S_2, N_3S_2, N_4S_2 and S_2P as these are less likely to occur in nature and, furthermore, to be more conservative in assigning molecular formulae to a given *m/z*. The FT–ICR–MS signal intensity of each identified molecular formula was normalized to the sum of all molecular formula intensities with S/N higher than 5 in each sample. We assumed that the inorganic (and organic) matrix is approximately the same for all the samples, so the intensity of each molecular mass is only affected by its concentration. Further, Seidel et al. (2015) incrementally mixed Amazon DOM with open Atlantic Ocean DOM showing that the response signal of ESI–FT–ICR–MS was linear to the mixing ratio. Therefore, we interpret the FT–ICR–MS data semi–quantitatively (Seidel et al., 2015; Hawkes et al., 2016). The analytical window of the FT–ICR–MS was restricted by both the SPE method and electrospray ionization efficiency. The former, using PPL cartridges, allows to concentrate from the most apolar DOM species through to highly polar molecules, but not the smallest polar

molecules (i.e. short chain organic acids and free amino acids) and colloidal aggregates (Chen et al., 2016; Hawkes et al., 2016; Raeke et al., 2016). ESI is a low–fragmentation technique that preferentially ionizes polar functional groups (Kujawinski, 2002), therefore carbohydrates are likely less efficiently ionized by ESI than organic acids as it was suggested by Stubbins et al. (2010).

The aromaticity and the degree of unsaturation of a compound were assessed based on its molecular formula and were expressed as the modified aromaticity index (AI_{mod}) and double bond equivalents (DBE), (Koch and Dittmar, 2006, 2016; see calculation in Table 1.2, page 44). Higher aromaticity index and DBE are indicative of higher presence of aromatic or even condensed aromatic molecules (Koch and Dittmar, 2006), which have been suggested to be resistant to biodegradation (Stubbins et al., 2010; Rossel et al., 2013). The degradation index (Ideg) was calculated using the formula proposed by Flerus et al. (2012) ranging between 0 and 1 (see calculation in Table 1.2 in page 44). It is used as a simple proxy to assess the relative degradation state of the SPE–DOM, and Flerus et al. (2012) suggested that a higher Ideg points towards a more reworked DOM. The intensity–weighted averages of molecular weight, number of elemental atoms (C, H, O), number of heteroatoms (N, S, P), molar ratios (H/C, O/C and C/N), AI_{mod} and DBE were calculated for each sample by taking into account the FT–ICR–MS signal intensity of each assigned molecular formula. We sorted the assigned formulae into groups of formulae containing the following atoms: CHO, CHON, CHOS, CHOP, CHONS and CHOSP. In addition, we assigned the identified molecular formula to compound groups based on established molar ratios, AI_{mod}, DBE and heteroatoms contents (Seidel et al., 2014). The compound groups used in this work were: i) polyphenols ($0.5 < AI_{mod} < 0.666$) which are highly aromatic compounds, ii) highly unsaturated compounds ($AI_{mod} < 0.5$, $H/C < 1.5$ and $O/C < 0.9$), iii) unsaturated aliphatic ($1.5 < H/C < 2$, $O/C < 0.9$ and $N = 0$) and iv) carboxyl–rich alicyclic molecules (CRAM, $0.3 < DBE/C < 0.68$, $0.2 < DBE/H < 0.95$ and $0.77 < DBE/O < 1.75$) as described by Hertkorn et al. (2006). Note that 94% of the molecular formulae assigned to CRAM were also classified as highly unsaturated compounds. As this grouping includes a mixture of structural isomers and does not imply the presence of a structural entity in the sample (Seidel et al., 2014), we emphasize that this categorization is not unambiguous and alternative structures may exist for a given molecular formula. However, this classification is a useful tool to identify likely structures behind an identified molecular formula. All molecular parameters of each sample were calculated as averages of the duplicates.

2.4 Statistical analysis

Bray–Curtis dissimilarity matrices (Bray and Curtis, 1957) were computed based on relative signal average intensities. Principal Coordinates Analysis (PCoA) was then used for graphical representation of the DOM variability on the first two major axes of compositional change. Environmental and calculated parameters were correlated to the PCoA factors and graphed accordingly (Pearson's product moment correlation). The analyses were performed in R (version 3.1.1, R Development Core Team 2012, [http://cran.r–project.org/]) and using the package vegan (Oksanen et al., 2016).

Multiple linear regressions were performed using R. Moreover, the Student's t–test was used for determining the significant differences between sample means (Table 4.3).

3 Results

3.1 Hydrography and bulk dissolved organic carbon background

Discrete sampling depths were chosen on basis of the vertical profiles of S, θ, O_2 and Chl *a* (Figure 4.1). The DCM (black dots in Figure 4.1) was deeper in the EastMed than in the WestMed (Table 4.1), showing higher O_2 and Chl *a* in the western basin. Regarding the intermediate waters, the salinity maximum (yellow dots in Figure 4.1) was found between 200–300 m in the eastern basin, accompanied by a relative maximum of θ and DO. In the WestMed the salinity maximum was located deeper (between 350–400 m) concurring with a relative maximum of θ and a minimum of DO. In general, the S, θ and O_2 along the core of the intermediate waters were lower in the WestMed than in the EastMed (Table 4.1, Figure 4.1a–c). The oxygen minimum layer (green dots in Figure 4.1a–c) was found at 744 ± 211 m (n = 4) in the EastMed. It coincided with the depth of the intermediate waters in the western basin (layer dominated by the eastern intermediate water (EIW) Table 4.2). Regarding the bathypelagic layer (red dots in Figure 4.1), the eastern basin was dominated by the different varieties of EMDW, mainly by the pre–eastern Mediterranean transient (pre–EMT) and EMT varieties (Table 2.2 and Figure 2.7 in chapter 2 and Table 4.2), which were saltier and warmer than the analogous waters in the western basin, dominated by the WMDW–A, –B and –D14 varieties (Table 2.2 and Figure 2.7 in chapter 2 and Table 4.2). O_2 values were similar in both basins.

Table 4.2: Water mass proportion (%) in each sample. Only water masses with proportions ≥10% are shown. Acronyms as in table 2.2 in chapter 2.

			WM							EMDW							WMDW			
Stn	Sample	Depth		MAW	LSW	LIW	CIW	AdMW	AdDW	Pre	EMT	Post–A	Post–C	AW	EIW	WIW	A	B	C	D14
01	Deep	2000								44	55									
01	Deep	1000								94										
01	OML	575					16			81										
01	LIW	201				88														
01	DCM	130			80	20														
04	Deep	2000								24	59	16								
04	Deep	1250								59	36									
04	OML	551					28			65										
04	LIW	201				75		21												
04	DCM	119		10		86														
07	Deep	2001								42		25	31							
07	OML	900					12			64	18									
07	LIW	201				42	21	35												
07	DCM	110		13		83														
10	OML	951							19	76										
10	LIW	300					57	39												
10	DCM	93		15		37		47												
13	LIW	301		10			67	19												
15	Deep	2001													20		80			
15	OML	651													72		25			
15	LIW	351													90					
15	DCM	75												27	65					
18	Deep	2000															13	55	10	18
18	Deep	1000													17		55	27		
18	LIW	401													65	16	12			
18	DCM	60												42	37	22				
21	Deep	2000															18			73
21	Deep	1000															17	23		60
21	LIW	401													24		31	36		
21	DCM	60												45	38	17				

DOC concentrations (Figure 4.2 and Table 4.1) showed the maximum values of the sampling depths at the DCM (>60 µmol L^{-1}), decreasing to a minimum of 43–44 µmol L^{-1} in the deep waters. Note that these values are slightly higher than those reported in chapter 2. It is due to in chapter 2 DOC samples (vertical profile in all stations) were immediately stored into fire–sealed glass ampoules after sampling, however in this chapter DOC samples (4–5 depths at 8 stations) were filtered into a 0.5–litre glass bottles within 5 hours after collection and then stored into fire–sealed glass ampoules. During this sample treatment some DOC contamination could occur. We performed a linear regression (model II) between the DOC from chapter 2 and those reported here and the relationship $DOC_{chap\ 4}$ = 1.05 (±0.12) DOC_{chap2} 3.0 (±4.8) was found. This relationship indicates that both DOC measurements varied similarly (slope near 1), but also suggests an average contamination of about 7.7 ± 5.1 µM C along samples of this chapter due to the additional treatment underwent. In the epipelagic layer an inverse relationship between Chl *a* and DOC concentration was observed (Figure 4.1d and 4.2a).

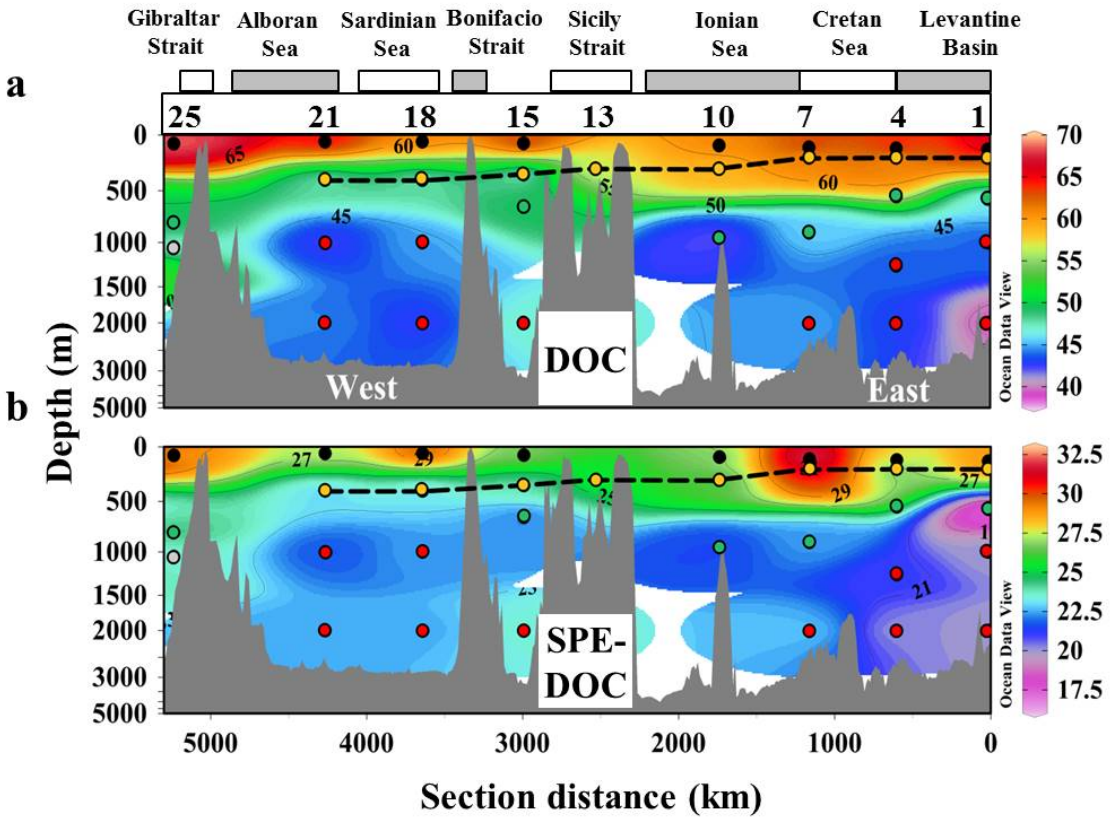

Figure 4.2: *(a) DOC and (b) SPE–DOC distribution in the Mediterranean Sea and Northeast Atlantic Ocean in µmol/L. The dashed black line represents the route of the LIW along the transect. Black, yellow, green and red dots represent samples collected at the DCM, LIW, OML and deep layers, respectively. Note that the depth is displayed on a non–linear scale. Numbers located on the top of the figure indicate the sample stations, which are depicted in Figure 2.1 in page 58. Figure created using ODV software (Schlitzer, 2016).*

Table 4.3: Comparison between the average molecular composition of SPE–DOM from the Mediterranean Sea and the NEqPIW. All values are calculated from FT–ICR–MS data (average ± standard deviation). The letters represent the significant differences based on the Student's t–test for each variable ($p<0.05$). Values sharing the same letter are statistically equal. MF = molecular formula, Nr = Number.

	Units	Average Mediterranean Sea n = 29	NEqPIW n = 13
General			
Number of peaks	Nr	4940 ± 338 [a]	4562 ± 112 [b]
Number of assigned MF	Nr	3105 ± 189 [a]	3142 ± 51 [a]
% of masses with MF	%	63 ± 1 [a]	69 ± 1 [b]
Weighted average mass	Da	375.3 ± 5.8 [a]	425.6 ± 1.9 [b]
Elemental composition			
C	Nr	18.82 ± 0.23 [a]	20.23 ± 0.06 [b]
H	Nr	24.52 ± 0.20 [a]	25.66 ± 0.12 [b]
O	Nr	7.40 ± 0.19 [a]	9.40 ± 0.12 [b]
N	Nr	0.36 ± 0.02 [a]	0.37 ± 0.01 [a]
S	Nr	0.07 ± 0.01 [a]	0.06 ± 0.01 [b]
P	Nr	0.01 ± 0.01 [a]	0.02 ± 0.00 [b]
H/C	at H/at C	1.30 ± 0.01 [a]	1.27 ± 0.00 [b]
O/C	at O/at C	0.39 ± 0.01 [a]	0.47 ± 0.01 [b]
C/N	at C/at N	52.39 ± 1.96 [a]	55.20 ± 2.30 [b]
Molecular indices			
AI_{mod}	Nr	0.25 ± 0.00 [a]	0.23 ± 0.00 [b]
DBE	Nr	7.74 ± 0.14 [a]	8.59 ± 0.04 [b]
Ideg	Unitless	0.59 ± 0.06 [a]	0.86 ± 0.01 [b]
Molecular diversity			
CHO	%	72.3 ± 0.6 [a]	70.8 ± 0.4 [b]
CHON	%	21.4 ± 0.7 [a]	22.3 ± 0.2 [b]
CHOS	%	5.0 ± 0.5 [a]	4.4 ± 0.6 [b]
CHOP	%	0.9 ± 0.4 [a]	2.2 ± 0.3 [b]
CHONS	%	0.2 ± 0.0 [a]	0.3 ± 0.0 [b]
CHOSP	%	0.2 ± 0.1 [a]	0.1 ± 0.0 [b]
Polyphenols	%	4.8 ± 0.3 [a]	2.6 ± 0.2 [b]
Highly unsaturated	%	83.9 ± 1.6 [a]	91.9 ± 0.5 [b]
Unsaturated aliphatics	%	9.7 ± 1.4 [a]	4.8 ± 0.3 [b]
CRAM	%	51.9 ± 1.0 [a]	48.6 ± 0.5 [b]

It is remarkable that in the intermediate waters the DOC decreased significantly from 60.2 ± 0.9 μmol L^{-1} in the easternmost station (stn 1; LIW) to 47.4 ± 0.7 μmol L^{-1} in the western basin (stn 18; EIW) (Figure 4.2). Atlantic samples showed similar DOC concentrations as the MedSea samples (Figure 4.2).

The NEqPIW sample repeatedly analysed as a reference sample to control the instrument variation over time also let us compare the molecular composition of the SPE–DOM in the MedSea with one of the oldest water masses of the world ocean: NEqPIW (Table 4.3). As expected, we observe that the MedSea contains significantly less reworked DOM (lower molecular weight, O/C, DBE and Ideg) than the NEqPIW.

The Atlantic water entering the MedSea through the Strait of Gibraltar (represented by the DCM sample at stn 25; black dot in Figure 4.3) exhibited a significantly different molecular composition than the overflow of Mediterranean water (represented by the LIW at stn 18, yellow dot in Figure 4.3; really it is EIW as in chapter 2, however for simplicity in Figure 4.3 we refer for the intermediate waters as LIW regardless the basin where they are found). Specifically, the SPE–DOM found in the Atlantic water inflow displayed lower molecular weight, O/C ratio, DBE, Ideg, CRAM and highly unsaturated compounds contribution, as well as a higher proportion of unsaturated aliphatic compounds and an increased H/C ratio (Figure 4.3 and Table 4.4). A principal coordinates analysis (PCoA) to link molecular composition to environmental parameters that includes all samples (Figure 4.4) also reveals the molecular dissimilarity between the Atlantic inflow and the Mediterranean overflow. While the Atlantic sample was found in the negative part of both axes, the LIW sample was found in the positive. Note that the first 2 coordinates of the PCoA comprised 72% of the SPE–DOM molecular variability. The differences between the inflow and outflow at the Strait of Gibraltar were also explored using a differential mass spectrum (Figure 4.5a), subtracting the normalized peak intensities of the LIW at stn 18 from the normalized peak intensities of the DCM at stn 25. Positive differences of intensity showed peaks of higher relative intensities in the Atlantic inflow with an average molecular weight of 349 Da. Negative signals indicated peaks of higher relative intensities in the Mediterranean overflow enriched in compounds of an average molecular weight of 432 Da. Note that LIW at stn 18 was chosen to represent the Mediterranean water overflow as LIW at stn 21, close to Strait of Gibraltar, is influenced by the mixing with WMDW (up to 67%, Table 4.2) as it is located close to the deep waters in the θ/S diagram (Figure 4.6c) and apart from the LIW at stns 15 and 18 in the PCoA (Figure 4.4).

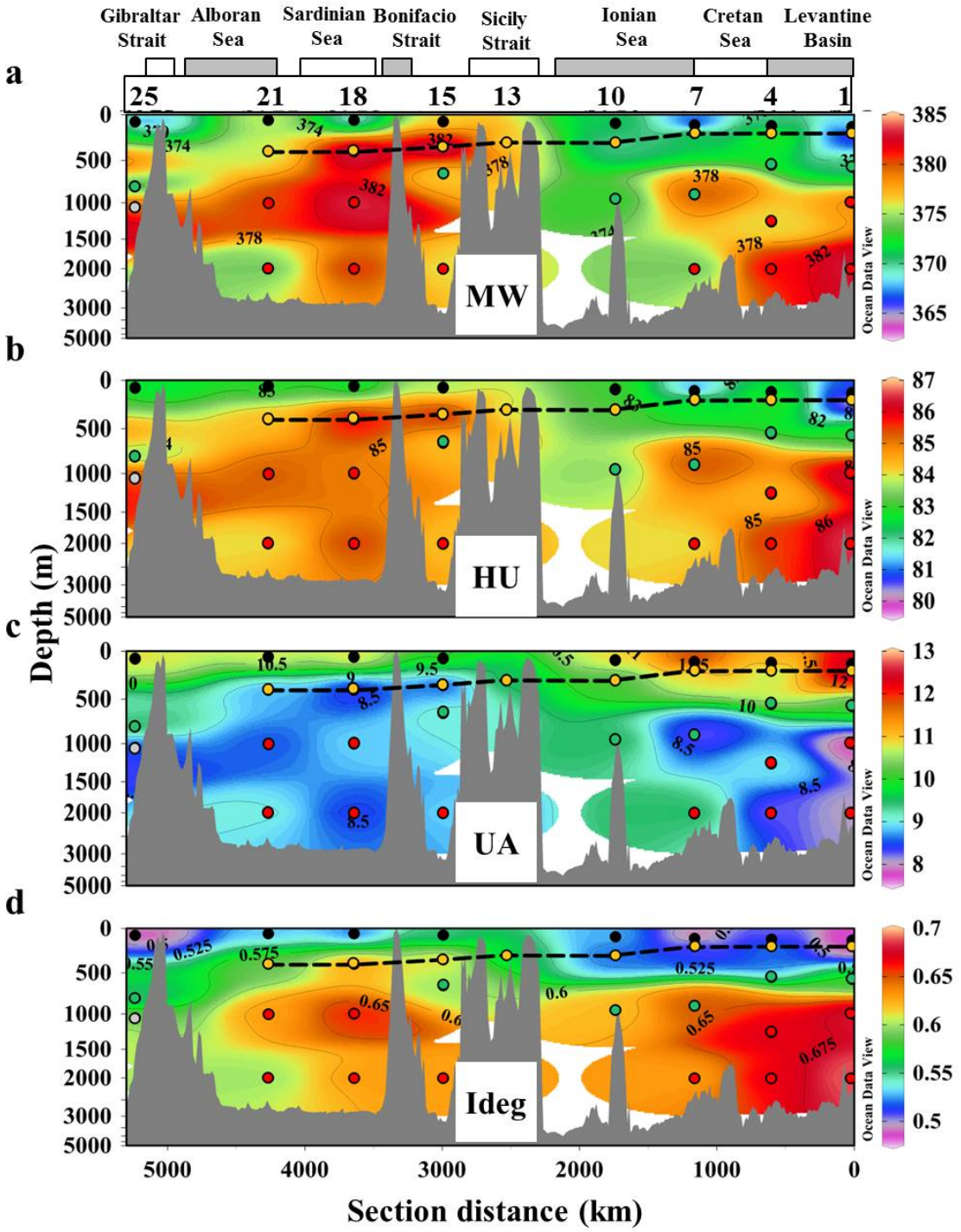

Figure 4.3: *Distributions of (a) MW = molecular weight in Dalton, (b) HU = highly unsaturated compounds in %, (c) UA = unsaturated aliphatic compounds in % and (d) Ideg = degradation index (range between 0 and 1, unitless) using averages of duplicates in the Mediterranean Sea and Northeast Atlantic Ocean. The dashed black line represents the route of the LIW along the transect. Black, yellow, green and red dots represent samples collected at the DCM, LIW, OML and deep layers, respectively. Note that the depth is displayed on a non–linear scale. Numbers located on the top of the figure indicate the sample stations, which are depicted in Figure 2.1 in page 58. Figure created using ODV software (Schlitzer, 2016).*

To study the DOM degradation along the shallow overturning circulation cell of the MedSea we followed the compositional changes of SPE–DOM collected in the core–of–flow of the LIW. The molecular characteristics of the LIW samples were uneven and the samples were split in the PCoA (Figure 4.4): while the eastern basin samples were found in the negative part of the first coordinate, the western basin samples were located in the positive. In addition, a constrained analysis of principal coordinates (CAP) based on Bray–Curtis dissimilarities revealed significant molecular differences between both basins ($p < 0.05$, $n = 8$). Specifically, as the LIW flowed westwards we observed a raise of molecular size (Figure 4.3a), O/C ratio, DBE and AImod. Moreover, we observed an increase of the Ideg and the proportion of highly unsaturated molecules, as well as a decrease of the proportion of unsaturated aliphatic molecules (Figure 4.3b–d and Table 4.4). Again, these differences were examined in more detail using a differential spectrum (Figure 4.5b), subtracting the normalized peak intensities of the LIW at stn 18 (western basin, more reworked DOM) from the normalized peak intensities of the LIW at stn 1 (eastern basin, fresher DOM). Positive differences of intensity showed peaks with higher relative intensities in the LIW at stn 1, where this sample presented an enrichment of molecules with an average molecular weight of 335 Da. Negative signals indicated peaks with higher relative intensities in the LIW at stn 18, sample enriched in molecules of an average molecular weight of 427 Da.

Concerning the deep waters, in the eastern basin samples collected at 2000 m depth at stns 1 and 4 (EMT was the dominant water mass, Table 4.2) fell closely together in the PCoA analysis (Figure 4.4). However, the samples collected at 1000 m at stns 1 and 4 (pre–EMT was the dominant water mass, Table 4.2) and at 2000 m at stn 7 (post–EMT–A and –C were dominant accounting for 56%, Table 4.2) grouped in our ordination and were separated from the EMT samples. Comparing the molecular composition of SPE–DOM in these water masses, the deep water at stn 7 showed a less degraded SPE–DOM signature (lower molecular weight, oxygen, DBE, Ideg, highly unsaturated and higher contribution of unsaturated aliphatic compounds; Figure 4.3 and Table 4.4).

Table 4.4: Intensity–weighted averages (average ± standard deviation) of molecular parameters from the FT–ICR–MS duplicate analysis of SPE–DOM. mw = molecular weight in Dalton, AI_{mod} = modified aromaticity index (Koch and Dittmar, 2006, 2016), DBE = double bond equivalent (Koch and Dittmar, 2006), Ideg = degradation index (Flerus et al., 2012), Poly = polyphenols, HU = highly unsaturated compounds, UA = unsaturated aliphatic compounds, CRAM = carboxyl–rich alicyclic molecules (Hertkorn et al., 2006), at = atoms. Note that sample St 7 Deep was analysed only once.

St	Sample	Depth	mw	H/C	O/C	AI_{mod}	DBE	Ideg	Poly	HU	UA	CRAM
		m	Da	at H/at C	at O/at C	–	–	–	%	%	%	%
01	Deep	2000	382.9 ± 1.3	1.296 ± 0.001	0.400 ± 0.001	0.248 ± 0.000	7.93 ± 0.03	0.685 ± 0.002	4.1 ± 0.1	86.5 ± 0.3	8.1 ± 0.1	53.88 ± 0.01
01	Deep	1000	378.3 ± 1.6	1.294 ± 0.001	0.395 ± 0.003	0.252 ± 0.001	7.90 ± 0.02	0.68 ± 0.01	4.5 ± 0.2	86.3 ± 0.5	7.8 ± 0.2	54.0 ± 0.5
01	OML	575	374.1 ± 0.6	1.307 ± 0.006	0.387 ± 0.002	0.250 ± 0.002	7.77 ± 0.01	0.64 ± 0.01	4.7 ± 0.1	84.2 ± 0.2	9.0 ± 0.1	52.5 ± 0.2
01	LIW	201	363.8 ± 0.5	1.326 ± 0.001	0.383 ± 0.001	0.244 ± 0.001	7.410 ± 0.002	0.49 ± 0.01	5.0 ± 0.1	79.81 ± 0.04	12.61 ± 0.01	49.7 ± 0.2
01	DCM	130	370.3 ± 2.4	1.316± 0.001	0.391 ± 0.003	0.243 ± 0.002	7.56 ± 0.02	0.482 ± 0.003	4.9 ± 0.4	81.2 ± 0.4	12.24 ± 0.03	50.7 ± 0.3
04	Deep	2000	381.7 ± 1.6	1.298 ± 0.000	0.396 ± 0.001	0.249 ± 0.001	7.90 ± 0.02	0.67 ± 0.01	4.6 ± 0.3	85.6 ± 0.4	8.2 ± 0.0	52.9 ± 0.1
04	Deep	1250	376.3 ± 0.9	1.302 ± 0.000	0.392 ± 0.003	0.250 ± 0.001	7.812 ± 0.003	0.665 ± 0.001	4.8 ± 0.4	84.5 ± 0.5	9.0 ± 0.2	52.4 ± 0.4
04	OML	551	–	–	–	–	–	–	–	–	–	–
04	LIW	201	374.5 ± 0.5	1.307 ± 0.001	0.397 ± 0.000	0.244 ± 0.001	7.68 ± 0.01	0.526 ± 0.001	4.8 ± 0.2	83.2 ± 0.1	10.4 ± 0.1	51.5 ± 0.3
04	DCM	119	368.9 ± 0.6	1.310 ± 0.001	0.394 ± 0.004	0.244 ± 0.000	7.57 ± 0.01	0.501 ± 0.004	4.8 ± 0.2	82.4 ± 0.6	11.3 ± 0.3	50.8 ± 0.7
07	Deep	2001	374.1	1.305	0.391	0.249	7.76	0.63	4.74	84.0	9.5	52.1
07	OML	900	379.9 ± 0.1	1.296 ± 0.000	0.396 ± 0.000	0.250 ± 0.000	7.887 ± 0.004	0.646 ± 0.002	4.82 ± 0.03	85.37 ± 0.02	8.27 ± 0.03	52.38 ± 0.02
07	LIW	201	373.6 ± 1.1	1.306 ± 0.000	0.398 ± 0.000	0.245 ± 0.000	7.67 ± 0.02	0.516 ± 0.000	4.75 ± 0.02	83.4 ± 0.1	10.33 ± 0.02	51.39 ± 0.01
07	DCM	110	363.9 ± 0.8	1.317 ± 0.001	0.385 ± 0.003	0.246 ± 0.000	7.46 ± 0.01	0.48 ± 0.01	5.3 ± 0.1	80.3 ± 0.4	12.5 ± 0.2	49.5 ± 0.6
10	OML	951	372.7 ± 1.9	1.305 ± 0.002	0.383 ± 0.013	0.252 ± 0.001	7.75 ± 0.04	0.621 ± 0.004	5.1 ± 0.1	83.6 ± 0.5	9.5 ± 0.3	51.8 ± 0.5
10	LIW	300	370.0 ± 2.4	1.305 ± 0.004	0.387 ± 0.005	0.251 ± 0.000	7.67 ± 0.05	0.52 ± 0.01	5.2 ± 0.3	83.2 ± 1.1	10.0 ± 0.5	51.6 ± 0.9
10	DCM	93	371.3 ± 0.1	1.310 ± 0.002	0.398 ± 0.001	0.243 ± 0.000	7.61 ± 0.01	0.534 ± 0.001	4.5 ± 0.2	83.1 ± 0.1	10.9 ± 0.1	51.4 ± 0.1
13	LIW	301	376.2 ± 1.5	1.306 ± 0.000	0.395 ± 0.001	0.246 ± 0.001	7.73 ± 0.02	0.555 ± 0.000	4.7 ± 0.1	83.9 ± 0.2	9.6 ± 0.1	52.0 ± 0.1
15	Deep	2001	376.1 ± 0.2	1.301 ± 0.000	0.389 ± 0.000	0.252 ± 0.000	7.81 ± 0.01	0.628 ± 0.005	5.02 ± 0.03	84.3 ± 0.1	8.9 ± 0.1	52.45 ± 0.03
15	OML	651	376.3 ± 0.8	1.301 ± 0.001	0.392 ± 0.002	0.250 ± 0.000	7.80 ± 0.02	0.60 ± 0.01	5.02 ± 0.03	84.3 ± 0.1	9.08 ± 0.04	52.2 ± 0.3
15	LIW	351	385.0 ± 3.6	1.298 ± 0.001	0.407 ± 0.004	0.244 ± 0.002	7.90 ± 0.05	0.62 ± 0.02	4.31 ± 0.4	85.9 ± 0.6	8.4 ± 0.1	52.7 ± 0.1
15	DCM	75	376.3 ± 1.3	1.306 ± 0.004	0.401 ± 0.002	0.243 ± 0.000	7.70 ± 0.05	0.55 ± 0.01	4.64 ± 0.04	83.7 ± 0.6	10.1 ± 0.3	51.3 ± 0.3

St	Sample	Depth	mw	H/C	O/C	AI_{mod}	DBE	Ideg	Poly	HU	UA	CRAM
		m	Da	at H/at C	at O/at C	–	–	–	%	%	%	%
18	Deep	2000	380.8 ± 0.6	1.298 ± 0.001	0.400 ± 0.002	0.248 ± 0.000	7.87 ± 0.02	0.633 ± 0.002	4.6 ± 0.1	85.5 ± 0.3	8.4 ± 0.2	52.8 ± 0.4
18	Deep	1000	383.4 ± 3.0	1.301 ± 0.002	0.402 ± 0.006	0.244 ± 0.001	7.87 ± 0.05	0.66 ± 0.01	4.5 ± 0.2	85.0 ± 0.7	8.9 ± 0.4	52.2 ± 0.7
18	LIW	401	384.1 ± 1.2	1.296 ± 0.001	0.404 ± 0.001	0.246 ± 0.000	7.92 ± 0.03	0.633 ± 0.002	4.4 ± 0.1	86.0 ± 0.2	8.28 ± 0.02	52.6 ± 0.1
18	DCM	60	368.4 ± 3.1	1.309 ± 0.005	0.394 ± 0.004	0.246 ± 0.005	7.58 ± 0.03	0.52 ± 0.02	5.1 ± 0.6	82.6 ± 0.7	10.9 ± 0.3	51.0 ± 0.3
21	Deep	2000	374.1 ± 0.9	1.302 ± 0.001	0.388 ± 0.002	0.252 ± 0.000	7.78 ± 0.01	0.602 ± 0.002	5.20 ± 0.04	84.1 ± 0.2	9.0 ± 0.1	51.7 ± 0.4
21	Deep	1000	380.4 ± 2.4	1.299 ± 0.001	0.396 ± 0.003	0.248 ± 0.001	7.87 ± 0.04	0.63 ± 0.01	4.7 ±0.2	85.3 ± 0.6	8.5 ± 0.2	52.7 ± 0.4
21	LIW	401	375.5 ± 1.1	1.302 ± 0.001	0.392 ± 0.003	0.251 ± 0.001	7.78 ± 0.01	0.59 ± 0.01	5.08 ± 0.18	84.3 ± 0.5	8.8 ± 0.3	52.0 ± 0.6
21	DCM	60	375.7 ± 3.8	1.310 ± 0.001	0.400 ± 0.006	0.242 ± 0.002	7.66 ± 0.05	0.53 ± 0.01	4.7 ± 0.3	82.9 ± 0.5	10.8 ± 0.3	51.0 ± 0.3
25	MW	1050	379.5 ± 1.9	1.297 ± 0.000	0.401 ± 0.002	0.247 ± 0.002	7.85 ± 0.02	0.59 ± 0.01	4.7 ± 0.2	85.5 ± 0.2	8.5 ± 0.1	52.4 ± 0.1
25	OML	800	372.6 ± 1.2	1.304 ± 0.000	0.389 ± 0.003	0.250 ± 0.001	7.72 ± 0.01	0.551 ± 0.001	5.2 ± 0.1	83.4 ± 0.2	9.6 ± 0.1	51.1 ± 0.2
25	DCM	76	364.9 ± 0.8	1.309 ± 0.000	0.388 ± 0.001	0.249 ± 0.001	7.56 ± 0.01	0.477 ± 0.002	5.3 ± 0.2	82.2 ± 0.4	10.87 ± 0.03	50.5 ± 0.1

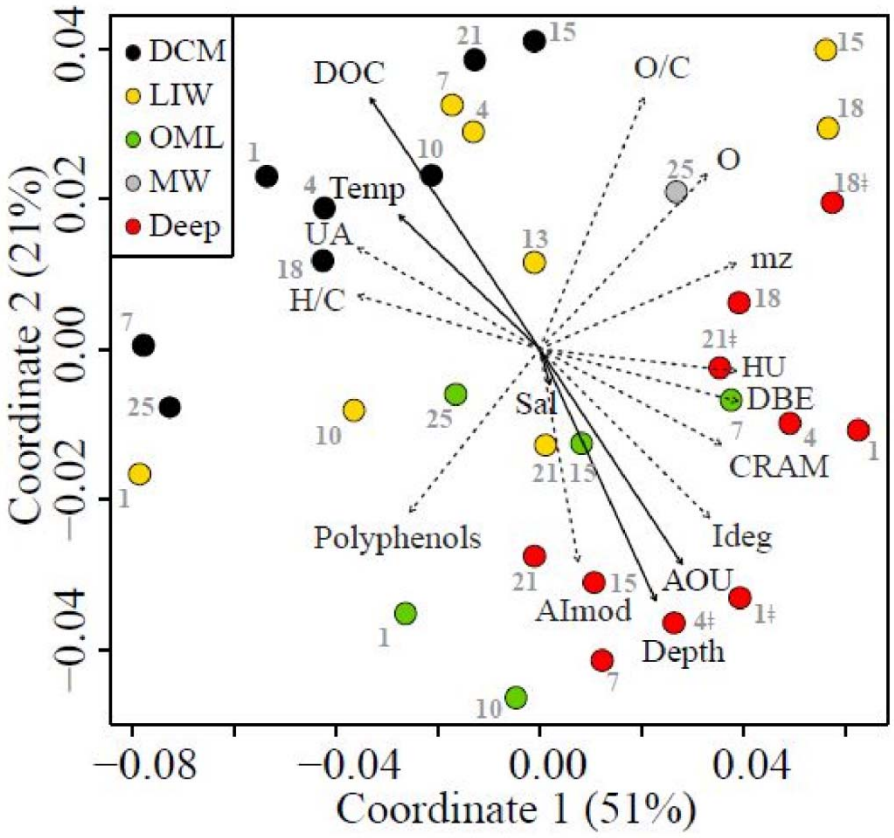

Figure 4.4: *Principal coordinates analysis (PCoA) of all detected molecular formulae and their normalized FT–ICR–MS signal intensities (averages of duplicates), based on Bray–Curtis dissimilarity of all samples, colour coded by waters dominating in each layer. Environmental and calculated parameters fitted to the PCoA factors are shown with black bold and dashed arrows, respectively. HU = highly unsaturated compounds, UA = unsaturated aliphatic compounds, Sal = Salinity, Temp = Temperature. The symbol ǂ represents samples collected at 1000 m.*

Globally, the PCoA revealed a clear separation of the samples by water layers. Along both PCoA axes, less reworked DOM was clearly separated from more degraded DOM. Samples collected at the DCM (recently formed) were characterized by less reworked DOM (higher proportion of unsaturated aliphatic compounds, higher H/C ratio and DOC concentration). Highly unsaturated molecules, likely susceptible to photochemical processes, and photoresistant unsaturated aliphatic molecules comprised the largest fraction of the SPE–DOM (>90%) in all samples (Table 4.4). Since abundances are expressed as relative contributions (percentages), the increase of one kind of compounds entails the decrease of the others. Thus, the lower percentage of highly unsaturated compounds in the epipelagic layer (Figure 4.3b) could be due to the photochemical removal of this type of molecules in the photic layer.

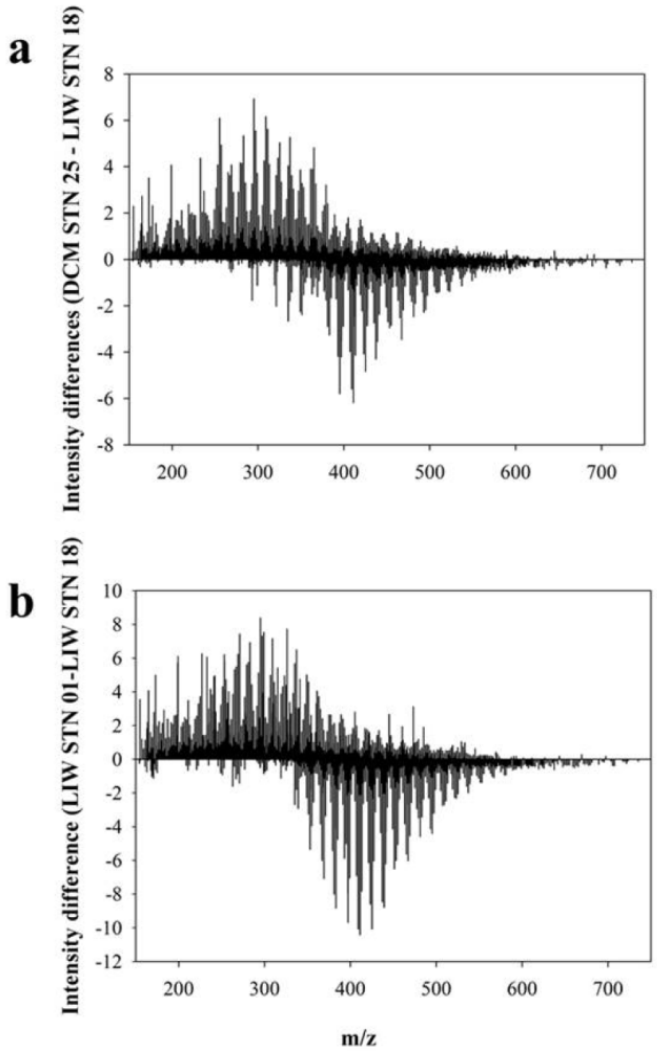

Figure 4.5: *Differences of FT–ICR–MS normalized signal intensities of SPE–DOM along a molecular mass scale (m/z) between a) the inflow of Atlantic water collected at the DCM in stn 25 and the overflow of Mediterranean water represented by the LIW at stn 18, b) LIW collected at stn 01 (near formation site) and LIW at stn 18 in the western basin. Positive differences correspond to higher relative intensities of DCM at stn 25 and LIW at stn 01 DOM, while negative differences correspond to higher relative intensities in the LIW stn 18 DOM, respectively for a and b panels. The weighted average molecular mass of these differential spectra was calculated taking into account absolute peak heights of positive and negative peaks.*

4 Discussion

Despite the relatively small size and short residence times of the MedSea, a PCoA analysis revealed that the molecular composition of DOM was found to be heterogeneous among basins and water layers. We show that this heterogeneity is mainly caused by three different factors that control the DOM molecular composition in the MedSea: water mass origin, biodegradation and photobleaching.

4.1 Water mass origin as a driver of SPE–DOM composition

We found that the overall molecular composition of the MedSea was significantly less reworked than the NEqPIW (Table 4.3). This water mass acts a reference for refractory DOM, as it is one of the oldest, least ventilated, water masses of the global ocean (Stuiver et al., 1983; Osterholz et al., 2015). This result demonstrates the noticeable molecular differences between the MedSea DOM and the NEqPIW DOM in spite of presenting similar radiocarbon ages as recently reported by Santinelli et al. (2015).

The exchange across the Strait of Gibraltar results in the Atlantic inflow transporting relatively fresh, nutrient–poor (Huertas et al., 2012), and less degraded DOC–rich surface Atlantic waters into the MedSea. On the other hand, the Mediterranean outflow transports salty, nutrient–rich and reworked DOC–poor intermediate Mediterranean water into the Atlantic. Accordingly, Ideg and DBE of the SPE–DOC in the Mediterranean overflow increased by 25% and 5%, respectively and the proportion of unsaturated aliphatic compounds decreased by 24% compared to the Atlantic inflow. Given that the Atlantic water that enters the MedSea is part of the shallow overturning cell of the Mediterranean intermediate waters that constitute the Gibraltar overflow (Schneider et al., 2014), it is expected that the difference in composition is implemented during completion of that overturning circulation within the MedSea basin. When the LIW is formed (stn 1) the DOM molecular composition is similar to the DOM Atlantic inflow (DCM in stn 25) (stn 25– black dot and stn 1–yellow dot in Figure 4.4). However, once the LIW flows in the shallow overturning circulation across the MedSea this water mass transports more degraded DOM as will be discussed in the next section.

Deep waters in the EastMed exhibited significant molecular differences related to their formation site (Aegean *versus* Adriatic) or time (pre– *versus* post–EMT). Samples collected at 2000 m depth at stns 1 and 4 presented more degraded DOM (molecular weight increased by 5 Da, the proportion of polyphenols by 6% and the proportion of unsaturated aliphatic compounds decreased by 9%) than samples collected at 1000 m at the same stations (Figure 4.3, 4.4, Table 4.4). These molecular changes were attributed to the fact that samples collected at 2000 m were formed in the Aegean Sea during the EMT (according to their thermohaline properties and oxygen concentrations; Figure 4.6d and Table 4.1 and according to the water mass analysis that reported a higher proportion of EMT water in these samples, Table 4.2; chapter 2). However, samples collected at 1000 m were formed in the Adriatic Sea in the pre–EMT (water mass analysis revealed a dominant proportion of pre–EMT water accounting for 94% and 59% at stations 1 and 4, respectively; Table 4.2) which showed lower S and O_2

concentration than the deep waters of Aegean origin (chapter 2). These results support the idea that water mass origin drives the DOM molecular composition. Regarding the formation time of these deep waters it would be plausible that the oldest (pre–EMT) would host most degraded DOM, however the results show the opposite. It seems that water mass origin has a higher impact on DOM molecular composition than water mass age in the deep waters of the EastMed. On the other hand, samples collected at 2000 m at stn 7 (post–EMT–C was the water mass dominant, Table 4.2) presented less degraded DOM (lower molecular weight (–5 Da), Ideg (–7%), DBE (–2%) and an about 9% higher proportion of unsaturated aliphatic compounds) than the sample collected at stn 1 at 1000 m (pre–EMT). In this case, although both water masses were formed in the Adriatic Sea, their formation times were different according to their thermohaline properties and O_2 concentrations (Figure 4.6d and Table 4.1), which lead to dissimilar DOM molecular signatures.

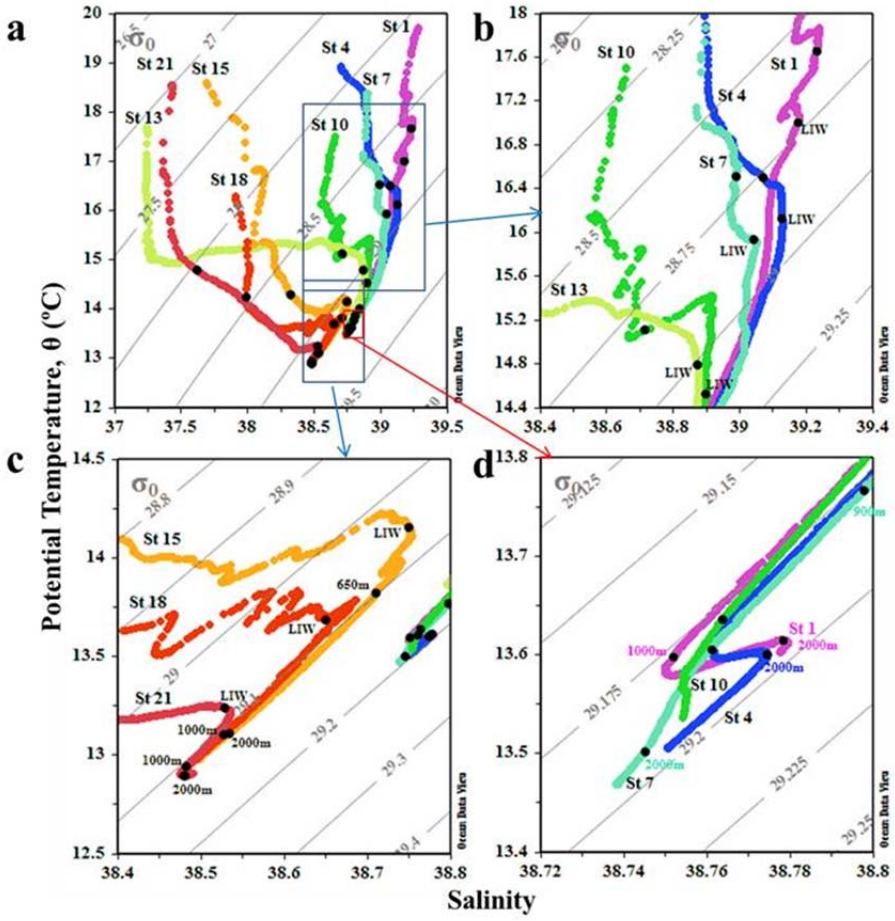

Figure 4.6: *ϑ–S diagrams of the Mediterranean stations considered for the SPE–DOM molecular characterisation. Black dots represent the 29 samples collected for this study in (a) the full range diagram and the zoom areas for (b) the intermediate waters in the eastern basin, (c) the intermediate and deep waters in the western basin and (d) the deep waters in the eastern basin. For a more detailed description of the ϑ–S diagrams, please see Figures 2.3 and 2.4 in pages 63 and 67, respectively).*

4.2 Diagenetic transformations of SPE–DOM through the Mediterranean Sea

Microbial oxidation leads to decreasing DOC concentrations along the overturning cell (Figure 4.2a) and the remaining DOC is, indeed, more reworked. In this regard, in agreement with Hansman et al. (2015), we found a positive relationship between the Ideg and AOU for all collected samples: Ideg = (0.0019 ± 0.0002) AOU + (0.50 ± 0.01) (R^2 = 0.71, $p < 0.0001$). The obtained regression slope suggests that the degradation ratio per oxygen consumption unit is faster in the MedSea than in the Atlantic Ocean, given that it is significantly higher ($p < 0.0001$) than the regression slope obtained by Hansman et al. (2015) in the Atlantic Ocean (slope = 0.00073 ± 0.00003, R^2 = 0.64, $p < 0.001$). This more efficient degradation could also be related to the above mentioned warmer deep water temperatures in the MedSea. As a consequence, the rate of microbial processes would be about 2–fold higher in the MedSea than in the Atlantic Ocean, according to the Arrhenius law. To assess the role of water mass mixing in this relationship we performed a multiple linear regression of Ideg with θ, S and AOU (R^2 = 0.80; $p < 0.003$, Ideg/AOU slope = 0.0011 ± 0.0003). Whereas the standard deviation of Ideg (SD_{Ideg} = 0.065) retains the variability due to both water mass mixing and biogeochemical processes in the MedSea, the standard deviation of the residuals of the multiple linear regression of Ideg with θ and S ($SD_{\Delta Ideg}$ = 0.035) retains only the variability due to biogeochemical processes. Therefore, from the ratio of both SD, it can be inferred that 54% of the observed variability of Ideg could be explained by processes not associated to water mass mixing. Note that in this chapter we could not applied the mixing–biogeochemical model to remove the effect of water mixing (equation 2.8 in chapter 2) due to the low number of samples (29) and the high number of water masses (19) would lead to a not significant fit into the model. We could presume that the mixing of LIW, with EMDW in the eastern basin and of EIW with WMDW in the western basin, can be partly responsible for the different molecular composition observed in the LIW of stns 1 and 18. However, in the western basin, mixing cannot be the only process affecting the EIW, since this water mass with the highest AOU is surrounded by water bodies (the DCM on top and the WMDW underneath) which present lower AOU values (Table 4.1). Concomitantly, part of the observed changes in the molecular composition of SPE–DOM could be due to the production/consumption of higher/lower molecular weight compounds as the LIW becomes older (more degraded) in its route westwards. A parallel increase in molecular weight (Figure 4.5b) and oxygenation (5%) and a decrease of the H/C ratio (Table 4.4) were found to be indicators of degraded organic matter (Flerus et al., 2012; Hertkorn et al., 2013; Chen et al., 2014), in accordance with an increase of the Ideg (22%). A higher DBE and AI_{mod} are indicative of an increasing degree of aromaticity and unsaturation (Koch and Dittmar, 2006, 2016). In

addition, a higher proportion of highly unsaturated compounds (7%) is also indicative of reworked DOM, as these compounds are considered refractory and produced during the remineralisation processes in the meso– and bathypelagic layers (Seidel et al., 2015). Conversely, unsaturated aliphatic compounds are considered bio–labile molecules, as they comprise a major fraction of phytoplankton exudates (Medeiros et al., 2015). We observed a decrease by 34% of the proportion of unsaturated aliphatic compounds in the LIW along its route westwards.

4.3 Photodegradation versus biodegradation in the epipelagic layer

Photochemical processes have been proposed as an abiotic pathway for DOC degradation in the surface ocean (Mopper et al., 2015). The Ideg is used to assess the degradation state of the SPE–DOM. Since photodegradation can produce bio–labile aliphatic and peptide–like compounds (Stubbins et al., 2010; Stubbins and Dittmar, 2015), we hypothesize that this process could lead to a lower Ideg. We observed an increasing trend of Ideg with depth (Figure 4.3d), likely indicating a synergy between an increasing contribution of prokaryote DOM degradation with depth, and the potential photodegradation and new production in the photic layer. However both processes, new production and photodegradation, cannot be deciphered by applying the Ideg. Therefore, we do not find conclusive evidence for the effect of photodegradation in the MedSea, probably due to the great depth of the shallowest level that we sampled (DCM). In addition, the cruise was conducted in April–May, i.e. after winter mixing and when solar radiation is not at the summer maximum. Further studies/experiments should be performed to clarify the role of photochemical processing on the DOM composition in the MedSea.

5 Conclusions

Despite the small size and relatively short residence time of the MedSea, water mass origin and mineralization processes lead to contrasting molecular composition of SPE–DOM with depth and basin. SPE–DOM in the MedSea was remarkably different from the SPE–DOM in the Atlantic Ocean inflow. Considering the shallow overturning cell of the MedSea, the evolution of the molecular composition of SPE–DOM from the Levantine basin to the Strait of Gibraltar evidences the transformation of these materials since LIW is formed. As a result, a westward decrease of DOC concentrations and a lower proportion of unsaturated aliphatic compounds are observed, as well as an increase in average molecular weight and enrichment in unsaturation, oxygenation, state of degradation and highly unsaturated compounds as the

SPE–DOM is degraded. We found that the water mass origin and the formation time lead to distinct DOM molecular properties. Thus, pre–EMT deep waters formed in the Adriatic Sea presented less degraded DOM than deep waters formed in the Aegean Sea during the EMT. In addition, different varieties of deep waters formed in the Adriatic Sea (pre– and post–EMT–A, –B and –C) presented different DOM molecular composition in spite of being formed in the same area. Consequently, the MedSea constitutes a suitable model basin for future DOM studies as water bodies of different molecular composition can be observed in closest proximity. Taking advantages of forthcoming hydrographic cruises, it would be worthwhile to study the molecular composition of DOM in the Mediterranean waters at their formation sites and help to complete the picture of DOM molecular composition and turnover in the MedSea.

Chapter 5
Linking optical and molecular signatures of dissolved organic matter in the Mediterranean Sea

The research work presented in this chapter is also a contribution to the paper:

Martínez–Pérez, A.M., Nieto–Cid, M., Osterholz, H., Catalá, T.S., Reche, I., Dittmar, T., Álvarez–Salgado, X.A., 2017. Linking optical and molecular signatures of dissolved organic matter in the Mediterranean Sea. Sci. Rep. 7, 3436. doi: 10.1038/s41598–017–03735–4.

ABSTRACT

Dissolved organic matter (DOM) experiences changes in molecular composition as it undergoes processing. In the semi–closed basins of the oligotrophic Mediterranean Sea, these gradual molecular modifications can be observed in close proximity. In order to extend the spatial resolution of information on DOM molecular composition available from ultrahigh resolution mass spectrometry in this area, we relate this data to optical (fluorescence and absorption spectroscopy) measurements. Covariance between molecular formulae signal intensities and carbon–specific fluorescence intensities was examined by means of Spearman's rank correlations. Fifty two per cent of the assigned molecular formulae were associated with at least one optical parameter, accounting for 70% of the total mass spectrum signal intensity. Furthermore, we obtained significant multiple linear regressions between optical and intensity–weighted molecular indices. The statistical linkages between DOM molecular and optical properties illustrate that the simple, rapid and cost–efficient optical spectroscopic measurements provide valuable proxy information on the molecular composition of open ocean marine DOM.

1 INTRODUCTION

Marine dissolved organic matter (DOM) comprises a complex mixture of molecules essentially uncharacterized and present at very low concentrations (Benner, 2002; Repeta et al., 2015). Fourier Transform Ion Cyclotron Resonance Mass Spectrometry (FT–ICR–MS) is a widely used technique nowadays to distinguish thousands of molecular formulae constituting the DOM pool. Although this technique does not unambiguously reveal the structure of DOM compounds, it offers new possibilities for the characterization of individual formulae or classes of molecules. A small fraction of these molecular formulae absorbs light in the UV and visible range of the spectrum; it is called colored DOM (CDOM) and it is present in the ocean ubiquitously (Nelson and Siegel, 2013). Furthermore, a fraction of CDOM emits fluorescence; it is called fluorescent DOM (FDOM) and it is widely used to trace the reactivity, composition (Nieto–Cid et al., 2006; Yamashita et al., 2010; Jørgensen et al., 2011; Catalá et al., 2015b), sources and chemical structure of DOM (Weishaar et al., 2003; Yamashita and Tanoue, 2003; Helms et al., 2008; Fellman et al., 2010; Romera–Castillo et al., 2011a).

The linkage between molecular and optical properties of DOM in natural waters is a subject of rising interest among aquatic biogeochemists (Osburn and Bianchi, 2016). Recent studies have combined FT–ICR–MS and optical measurements to better understand the composition of DOM in natural waters (Gonsior et al., 2011; Gonsior et al., 2013) but few of them have directly related optical and molecular signatures (Herzsprung et al., 2012; Stubbins et al., 2014; Kellerman et al., 2015; Lavonen et al., 2015; Timko et al., 2015; Wagner et al., 2015). These studies, mainly focused on freshwater and coastal systems, have reported significant relationships between optical indices and molecular formulae. However, DOM of terrestrial and marine origin is characterized by contrasting molecular size and composition, as well as absorption and fluorescence spectral properties (Nelson and Siegel, 2013; Osburn et al., 2014). Therefore, the results obtained in previous studies conducted in freshwater and coastal systems should not be directly generalized to open ocean waters.

In this study, we link the fluorescence and absorption of DOM with the molecular signatures obtained from the FT–ICR–MS data of 29 samples from the open epi–, meso– and bathypelagic waters of the Mediterranean Sea (MedSea) during the HOTMIX 2014 cruise (chapter 4). Our main objective is to determine the covariance between optical and molecular signatures in this low–CDOM ocean system and examine similarities and differences with the relationships found in high–CDOM freshwater and coastal systems.

2 MATERIAL AND METHODS

The 29 samples used in this study were the same than in chapter 4, collected during the trans–Mediterranean cruise HOTMIX 2014. The cruise track with the nine sampling points is shown in chapter 2 (Figure 2.1; page 58), and the sample collection is described in chapter 4 (section 2.2; page 132). The distributions of salinity, potential temperature, dissolved oxygen and chlorophyll *a* for the 29 samples are summarized in Figure 4.1 (page 133). We used these profiles to sample the deep chlorophyll maximum, the salinity maximum, the oxygen minimum layer and the deep waters, as explained in chapter 4. Seawater samples were collected in 5–litres acid–cleaned polycarbonate carboys for the determination of dissolved organic carbon (DOC), optical properties and molecular formulae. Prior to filtration (within 5 hours), samples were stored in the dark at 13°C and then filtered through precombusted (450°C, 4 h) Whatman GF/F filters. Two–liter aliquots of the filtrate were collected in acid–cleaned PTFE bottles for solid phase extraction of DOM (SPE–DOM).

2.1 Dissolved organic carbon and optical measurements

Aliquots of 10 mL of the filtrate were collected for DOC quantification in precombusted (450°C, 12 h) glass ampoules. These samples were acidified with H_3PO_4 (85%, p.a., Merck) to pH < 2 and the ampoules were flame sealed and stored in the dark at 4°C until analysis in the base laboratory. A detailed description about DOC concentration determination can be consulted in chapter 2 (page 59).

CDOM was measured on board using a double beam Perkin Elmer lambda 850 spectrophotometer equipped with 10 cm path length quartz cuvettes for sample and reference (ultrapure water, Milli–Q, Millipore Advantage A10). Spectral scans were collected from 250 nm to 750 nm at 1 nm intervals and constant room temperature. The absorbance was converted into Naeperian absorption coefficient (m^{-1}) (Green and Blough, 1994). The carbon–specific absorption coefficient at 254 nm (a254*; L m^{-1} mg^{-1} C) was calculated.

FDOM was determined on board with a Perkin Elmer LS55 luminescence spectrometer. Slit widths were 10 nm for both excitation and emission wavelengths. Measurements were performed at room temperature in a 1 cm quartz fluorescence cell and Milli–Q was used as a reference blank. The spectrofluorometer was tested daily: intensity of the Raman peak was analyzed with a sealed Milli–Q water cell (Perkin Elmer) while p–terphenyl and tetraphenylbutadiene methacrylate blocks (Starna) were used to check the instrument signal intensity at the excitation–emission wavelengths characteristic of the aromatic amino acids

and humic–like substances, respectively. Excitation (Ex)–emission (Em) matrices (EEMs) were generated by combining 22 fluorescence emission spectra from 300 to 560 nm at excitation wavelengths ranging from 240 to 450 nm at 10 nm intervals. Rayleigh scatter bands were removed mathematically from the EEMs. Parallel factor analysis (PARAFAC) was used to decompose the fluorescence signal of the 108 EEMs into the underlying individual fluorescent components (Bro, 1997). Data analyses were performed using the DOMFluor 1_7 Toolbox8 and conducted in Matlab R2014B (MathWorks, USA). A four–component (4–C) model with the most common fluorescent peaks of aquatic environments was obtained (Figure 5.1), two of them (C1 and C2) of humic–like nature, compatible with peaks A+C (at Ex/Em < 270–350/470 nm) and M (at Ex/Em 330/402 nm) and two of amino acid–like nature (C3 and C4), attributed to tryptophan and tyrosine at Ex/Em 280/374 nm and 270/306 nm, respectively. Model validation was performed by split–half diagnostics and random initialization (Stedmon and Bro, 2008; Murphy et al., 2013).

Note that for time optimization during the cruise, as for the case of the absorbance measurements, the spectrofluorometer used in this chapter was different than the oneused in chapter 2. Therefore, we have obtained two PARAFAC models from measurements of two different spectrometers with different settings. The PARAFAC obtained in this chapter corresponded with a subset of samples (36) of the PARAFAC run in chapter 3 (406). While the classical humic–like components (C1 and C2) were found at the same wavelengths in both PARAFAC models, the fluorescent signal attributed to tryptophan and tyrosine was a bit different. In the PARAFAC model including all samples (chapter 3) tryptophan and tyrosine peaks were found together in the same component (C3), however in this chapter tryptophan was found in a separate component (C3) than tyrosine (C4). Further, in chapter 3 a new component appeared, related to peak E, due to soil fulvic acids. The dissimilarities between both PARAFAC models are likely due to the different spectrometer settings and the number of samples used to run the PARAFAC modeling. The Fluoromax spectrofluorometer (chapter 3) was set to 5 nm excitation emission slit widths because of its higher sensitivity (signal/noise ratio at the Raman peak, 5000); however the Perkin–Elmer spectrofluorometer was set to 10 nm, because of its lower sensitivity (signal/noise ratio at the Raman peak, 500). The higher sensibility of the Fluoromax allowed detection of peak E, which presented fluorescence intensity about an order of magnitude below than the other fluorophores (chapter 3). However, peak T and B fell together in chapter 3 as those fluorophores span a smaller area in the EEM together with the fact that peak B is strongly affected by the water Raman scattering

band. This effect is also shown in the PARAFAC model of this chapter where C4 is a residual fluorescence of peak B.

Given that the PARAFAC components (Figure 5.1) match the classical fluorescence peak intensities at selected Ex/Em wavelength pairs previously established (Coble, 1996), we decided to use the latter to allow direct comparison with previous studies. The selected Ex/Em wavelengths were 250/435 nm (peak A) due to general humic substances; 340/440 nm (peak C) due to humic substances of terrestrial origin; 320/410 nm (peak M) due to humic substances of marine origin; and 280/350 nm (peak T) and 270/304 nm (peak B) due to protein–like substances. The fluorescence of each peak was determined by subtracting the Milli–Q blank peak height from the sample average peak height. All the samples were normalized using a solution of quinine sulphate dihydrate (≥99.0%, purum for fluorescence, Fluka) and tryptophan (≥99.0%, Fluka) standards in H_2SO_4 0.05M (95–97%, p.a., Merck) allowing to express fluorescence in Normalized Fluorescence Intensity Units (NFIU; Nieto–Cid et al., 2005) which are more adequate and precise for pick peaking measurements than the Raman units as they normalize each peak using the calibration curve in the Ex/Em wavelength where every peak is measured (see chapter 7 page 203). The fluorescence of each peak was then calculated as the mean of 4 individual measurements, which presented a coefficient of variation of <6 ± 2% (n = 30) for all the peaks. Carbon–specific fluorescence of humic–like (peaks A*, C* and M*) and protein–like (peak T*) substances were calculated dividing the fluorescence intensity by the DOC concentration (in NFIU L mg^{-1} C). Humic–/protein–like and terrestrial/marine fluorescence ratios (A/T, C/T, M/T and C/M) were also calculated. In addition, we calculated fluorescence–based indices such as the fluorescence (FI; Cory and McKnight, 2005), freshness (FrI; Wilson and Xenopoulos, 2009; Wagner et al., 2015), biological (BIX; Huguet et al., 2009) and humification (HIX; Zsolnay et al., 1999) indices (see material and methods of chapter 3 for wavelength ranges; page 99).

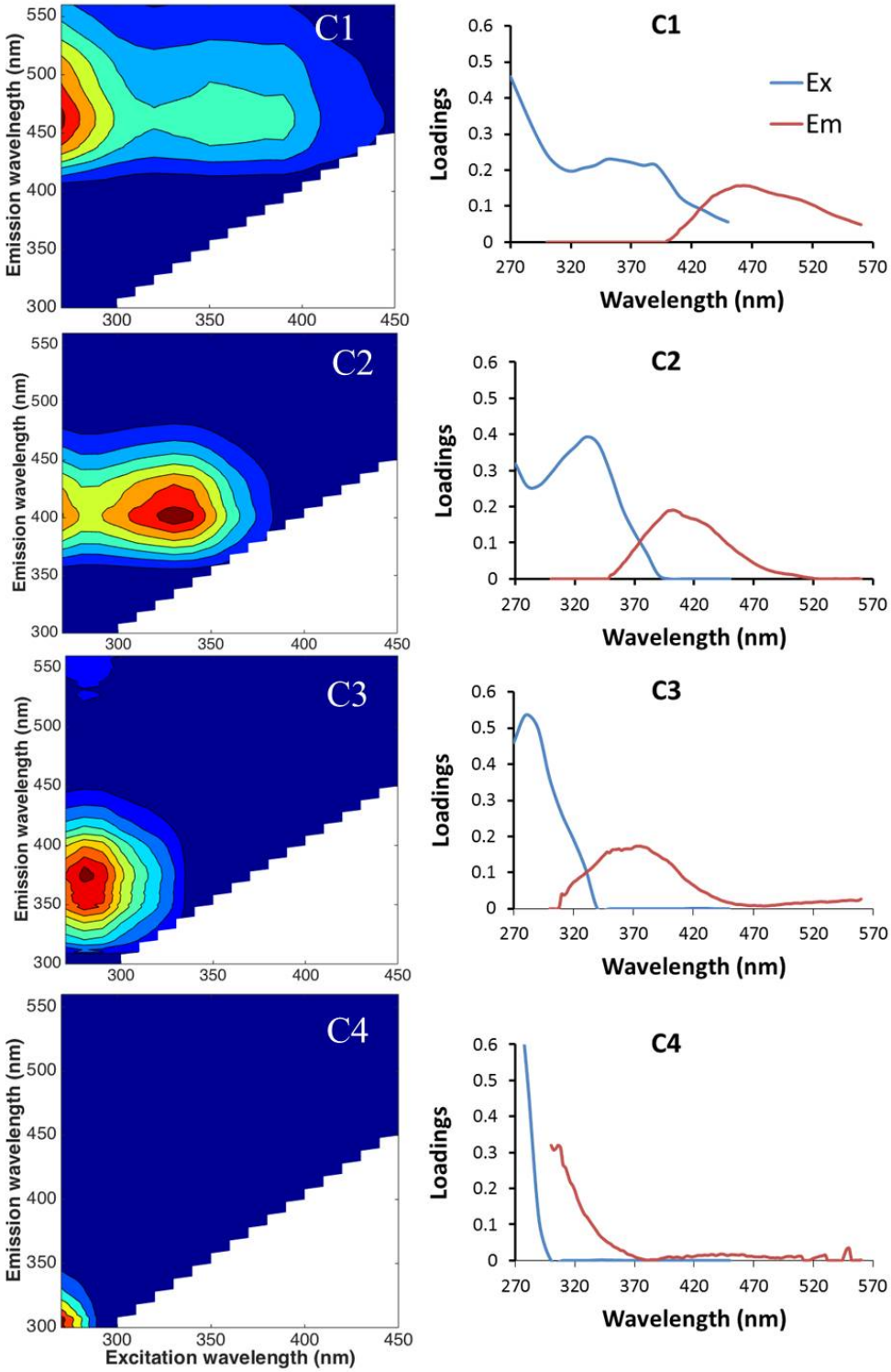

Figure 5.1: *Fluorescence matrices of the four identified PARAFAC components. C1 represents a combination of classical defined peak A and C, C2 tracks classical defined peak M, C3 corresponds to peak T and C4 falls near peak B. The right panels represent the excitation (blue lines) and the emission (red lines) fluorescence intensities of the four PARAFAC components. Figure created using the software Matlab (version R2014B; MathWorks, USA).*

2.2 Statistical analyses and graphical tools

Carbon–specific fluorescence peak intensities, fluorescence ratios, a254*, FI, FrI, HIX and BIX were correlated with all assigned molecular formulae applying Spearman's rank correlations. Each individual optical parameter was correlated with each individual molecule. Spearman's rank correlation coefficients (R) greater than 0.43 were considered significant at the 99% confidence limit (Student's t–test for a set of 29 samples). Therefore, all molecular formulae correlating with R > 0.43 with a given optical index were assigned to that optical index. A similar approach was applied in previous studies (Herzsprung et al., 2012; Stubbins et al., 2014; Wagner et al., 2015). In addition, multiple linear regression models between molecular parameters and optical indices were calculated using Pearson's regressions. To determine if our sample size allows to detect significant differences we performed a power analysis for n = 29. We found that the power was higher than 0.72 for all variables. We therefore assume that the sample size n = 29 is appropriate to detect significant differences. To validate our models we performed a cross validation exercise. We used 80% of the samples to obtain the models and then validated them with the remaining 20% of the samples. The subsets to obtain and validate the models were chosen randomly and repeated 1000 times. Then, we calculated the error of the estimation for the 1000 runs and obtained mean errors. All the statistical analyses were performed in R (version 3.1.1, 2014–07–10, http://cran.r–project.org/).

3 RESULTS AND DISCUSSION

3.1 Carbon stock and optical characterization of DOM in the Mediterranean Sea

As already described in chapter 4, DOC concentrations of the collected samples showed the characteristic exponential decay profile with depth found in the open ocean. Considering the sampling depths, maximum concentrations higher than 60 μmol C L^{-1} were observed at the deep chlorophyll maximum (DCM) and minimum concentrations of about 42 μmol C L^{-1} were found in the deep waters (Figure 5.2a). The vertical distribution of the C–specific fluorescence of humic–like substances (peak C*) increased with depth although leveling off from about 750 m to the bottom (Figure 5.2b). The increase of peak C* with depth was likely caused by the production of humic–like materials during microbial respiration processes in meso– and bathypelagic layers (Meador et al., 2010; Santinelli et al., 2010; Yamashita et al., 2010; Dainard and Guéguen, 2013) and its accumulation due to the refractory nature (centennial turnover

times) of this material (Yamashita et al., 2008; Catalá et al., 2015b). The peak C* minimum at the DCM can also be attributed to the vulnerability of humic–like substances to photobleaching in the upper mixed layer (Nieto–Cid et al., 2006; Catalá et al., 2016). Conversely, the vertical profile of the carbon–specific fluorescence of protein–like substances (peak T*) was opposite to peak C* (Figure 5.2c). The maximum value for peak T* at the sampling depths was found at the DCM and attributed to the accumulation of semi–labile materials, such as amino acids from phytoplankton exudation, cell autolysis and microzooplankton grazing (Biddanda and Benner, 1997; Nagata, 2008). In addition, those substances are much less vulnerable to photodegradation than humic–like substances (Stedmon and Cory, 2014), which leads to their accumulation in this layer. The observed decrease of peak T* with depth likely resulted from the bio–labile nature of these compounds, as it was suggested in a previous study (Lønborg et al., 2010), who found a strong relationship between protein–like fluorescence and biodegradable DOC. In our study, the peak T* profile was also similar to the DOC profile, showing a similar pattern to other ocean areas (Jørgensen et al., 2011). This finding indicates that peak T* at the DCM accumulates at a higher rate than the bulk DOM and it would be consumed faster in the deep ocean. The carbon–specific absorption coefficient at 254 nm (a254*), used as an aromaticity index (Weishaar et al., 2003), showed a decreasing profile with depth, although it remained constant from about 750 m to the bottom (Figure 5.2d), similar to the DOC and peak T* profiles (Figure 5.2a, c).

The FI reveals information about DOM origin, terrestrial versus microbial (McKnight et al., 2001), and ranged between 1.8 and 2.2. This result indicates that FDOM in the Mediterranean Sea presented a predominantly microbial origin (Fellman et al., 2010). FrI and BIX, both indicators of recent biological activity (Huguet et al., 2009; Wilson and Xenopoulos, 2009), ranged between 0.8 and 1.0 (alike in chapter 3 for all samples). HIX, a proxy to the DOM humification degree, ranged between 0.9 and 7.6, slightly higher than in chapter 3 due to the different treatment of the samples discussed in chapter 4, page 140). The values of these indices are indicative of weak humic character and important recent autochthonous sources of DOM (Huguet et al., 2009) as showed and discussed in chapter 3. FI, FrI and BIX showed a vertical profile similar to a254*, DOC and peak T*. However HIX was, as expected, more similar to the profile of peak C*.

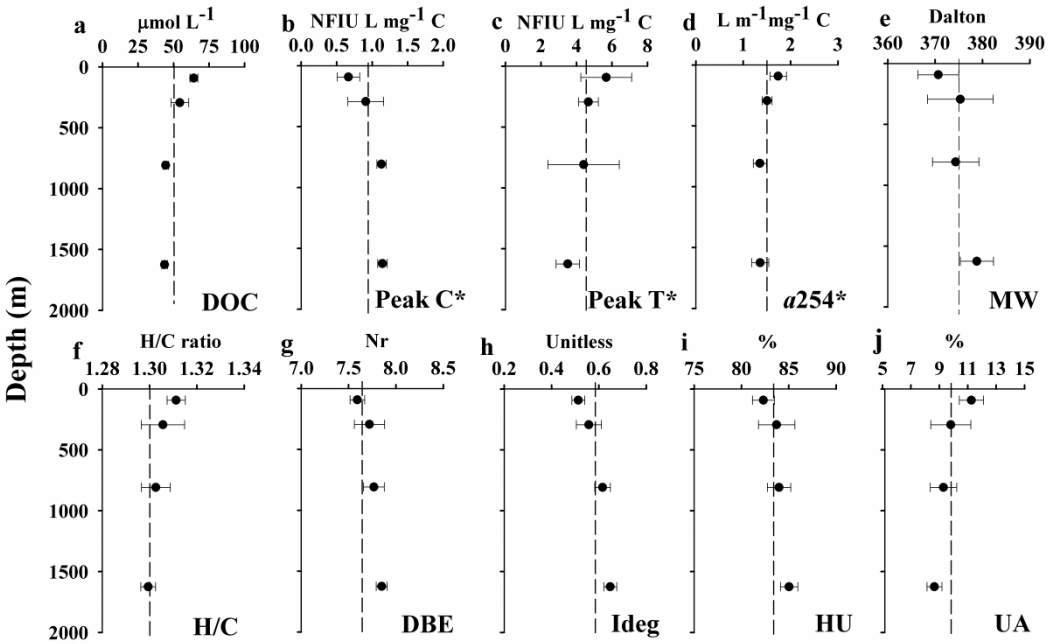

Figure 5.2: *Vertical profiles of DOC, optical and molecular parameters averaged by water layer (a) DOC, (b) carbon–specific fluorescence intensity of humic–like substances (peak C*), (c) carbon–specific fluorescence intensity of protein–like substances (peak T*), (d) carbon–specific absorption coefficient at 254 nm (a254*), (e) average molecular weight (MW), (f) H/C ratio, (g) double bond equivalent (DBE), (h) degradation index (Ideg), (i) relative abundance of the highly unsaturated (HU) and (j) relative abundance of unsaturated aliphatic (UA) compounds. Error bars are standard deviation and the dashed lines represent the mean value for each variable.*

3.2 Molecular level DOM characterization in the Med Sea

As described in detail in chapter 4, a total of 6057 resolved molecular masses of singly charged compounds were detected in the FT–ICR–MS spectra covering a mass range of 154–817 Da. We assigned 3689 molecular formulae in the mass range of 157–736 Da, not considering ^{13}C isotopologues. The vertical profile of the molecular parameters calculated from the mass spectra (Figure 5.2e–j) showed that DOM compounds were more unsaturated and of higher molecular weight with depth. The most abundant group of molecules, in terms of number of formulae, was represented by the highly unsaturated compounds (HU; 70.4 ± 0.6%), followed by unsaturated aliphatics (UA; 13.7 ± 0.7%), polyphenols (Polip; 11.8 ± 0.2%), peptides (2.5 ± 0.1%), saturated fatty acids with heteroatoms (Sat FA; 0.78 ± 0.05%) and sugars with heteroatoms (0.6 ± 0.1%). Carboxyl–rich alicyclic molecules (CRAM; Hertkorn et al. 2006) accounted for 21.9 ± 0.6% of the total number of molecular formulae. Note that 94% of the molecular formulae assigned to CRAM were also classified as highly unsaturated compounds. All assigned molecular formulae were represented in a van Krevelen diagram (Figure 5.3) grouped by compound classes.

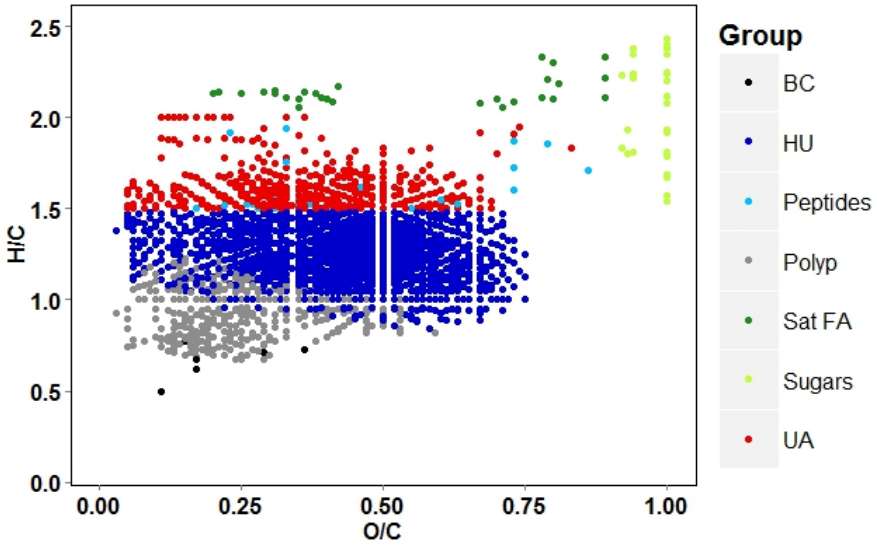

Figure 5.3: *Van Krevelen diagram (O/C, oxygen to carbon and H/C, hydrogen to carbon ratios) for all formulae detected by the FT–ICR–MS sorted by compound groups. BC = Black carbon, Polyp = polyphenols, HU = highly unsaturated compounds, UA = unsaturated aliphatic compounds, peptides, sugars, Sat FA = saturated fatty acids. Note that CRAM were not included in the van Krevelen plot because of the overlap with the highly unsaturated compounds.*

2.3 Linking optical and molecular properties of SPE–DOM

We explored the covariability of each one of the 3689 molecular formulae identified from the FT–ICR–MS analysis with the C–specific fluorescence intensities, fluorescence indices and absorption coefficients described in the Material and Methods section by means of Spearman's rank correlations (99% confidence limit). Our statistical analysis indicated that 52% of the 3689 assigned molecular formulae were correlated, either positively or negatively, with one or more optical parameter. These molecular formulae accounted for 70% of the mass spectrum peak intensities. Considering only the positive correlations ($R > 0.43$), 46% of the molecular formulae (65% of the spectra signal intensity) correlated with one or more optical parameter (Table 5.1). These percentages were slightly higher than those found in Canadian boreal rivers (Stubbins et al., 2014), but lower than in the Florida Everglades (Wagner et al., 2015). Note that the number of molecular formulae not correlating (NC) with any optical parameter was different for the positive and negative correlations (Table 5.1 and Table 5.2, respectively). This result is due to the fact that a molecular formulae that correlated positively with one or more optical parameters but did not correlate negatively with any optical parameter will count in the no correlation group in Table 5.2 (negative correlations) but not in Table 5.1 (positive correlations). The majority of the formulae correlated significantly with more than one optical parameter (Table 5.3). These results indicate that fluorescence and absorption measurements covary with a substantial fraction of the SPE–DOM and not only

with the minor fraction of fluorescent molecular formulae. Note that the fractions of DOM captured by both techniques are different, and both techniques have specific analytical windows. For optical measurements only the colored/fluorescent pools of DOM are considered. Furthermore, FDOM can be affected by quenching processes, which depend on the sample matrix (Sharpless and Blough, 2014). FT–ICR–MS analysis, on the other hand, provides information on the solid–phase extractable and ionizable fraction. In this regard, SPE–DOM comprises a wide range of the most apolar DOM molecules to highly polar molecules, but not the smallest ionic molecules (i.e. short chain organic acids and free amino acids) and colloidal aggregates (Hawkes et al., 2016). ESI is a soft ionization technique that preferentially ionizes polar functional groups that renders DOM molecules their water solubility (Kujawinski, 2002).

A statistical linkage between molecular formulae and optical properties does not necessarily imply that compounds with a given molecular formula contain fluorophores or chromophores, but it indicates similar biogeochemical behavior in an aquatic system (Kellerman et al., 2015).

The number of positive correlations ($R > 0.43$) between the molecular formulae and humic–like compounds and fluorescence ratios (peak A/T, C/T and M/T) were fewer compared to the negative correlations ($R < –0.43$), however they accounted for higher relative spectrum intensities (Table 5.1 and 5.2). On the contrary, the number of molecules positively correlated with peak T*, *a*254*, FrI and BIX was much higher than the number of negative correlations but they accounted for relatively lower spectrum intensities. Plotting the significant correlations into Van Krevelen diagrams (Figure 5.4), where the color scale represents the molecular weight of each formula, we can distinguish the molecular families associated with each optical parameter. For the range of materials isolated with our SPE methodology, which excludes free amino acids and colloidal aggregates (see above), we observed that peak C* correlated positively with higher average MW formulae and peak T* correlated with lower average MW formulae. *a*254* and BIX correlated positively with formulae similarly to peak T* whereas HIX was related to peak C* (Figure 5.4). Van Krevelen diagrams representing the negative correlations for the same variables (Figure 5.5) showed the opposite trend, peak C* and HIX correlated with lower average MW molecules and peak T*, *a*254* and BIX were related to higher average MW molecules.

Table 5.1: Positive correlations between the total assigned molecular formulae as well as the different type of molecular groups and the optical parameters; carbon–specific fluorescence intensity in NFIU L mg^{-1} C of general humic–like substances (peak A*), terrestrial humic–like substances (peak C*), marine humic–like substances (peak M*), protein–like substances (peak T*), fluorescence ratios (peak A/T, C/T and M/T ratios), carbon–specific absorption coefficient at 254 nm (a254*; L m^{-1} mg^{-1} C), fluorescence index (FI), freshness index (FrI), biological index (BIX) and the humification index (HIX). NC = no correlation. MW= intensity–weighted average molecular weight, Nr = number. Numbers in parentheses correspond to the signal intensity percentage from the spectra.

	All	NC	Peak A*	Peak C*	Peak M*	Peak T*	A/T	C/T	M/T	C/M	a254*	FI	FrI	BIX	HIX
Nr total formulae	3689	1995	408	511	432	704	396	447	429	72	718	441	825	843	298
	(100)	(35)	(27)	(30)	(25)	(19)	(27)	(29)	(28)	(2)	(20)	(12)	(22)	(23)	(22)
MW (Da)	375	366	426	430	433	315	420	421	422	350	317	289	313	314	398
Nr formulae with N	1456	756	135	156	133	328	140	161	153	35	324	222	389	390	112
	(100)	(52)	(10)	(10)	(8)	(24)	(11)	(12)	(11)	(4)	(24)	(16)	(28)	(29)	(12)
Black Carbon (Nr)	8	3	0	0	0	3	0	0	0	0	2	3	4	0	3
	(100)	(23)	(0)	(0)	(0)	(45)	(0)	(0)	(0)	(0)	(32)	(47)	(62)	(0)	(0)
Polyphenols (Nr)	433	220	32	36	30	93	35	39	37	7	93	74	124	121	46
	(100)	(47)	(16)	(16)	(11)	(13)	(17)	(18)	(18)	(2)	(14)	(12)	(19)	(19)	(23)
Highly unsaturated (Nr)	2594	1460	293	279	317	448	288	316	305	56	454	271	509	523	193
	(100)	(35)	(29)	(32)	(27)	(17)	(29)	(32)	(31)	(2)	(18)	(11)	(20)	(21)	(22)
Unsaturated aliphatic (Nr)	507	238	73	83	75	122	70	76	73	5	133	74	144	152	51
	(100)	(30)	(29)	(30)	(28)	(23)	(27)	(28)	(27)	(4)	(24)	(15)	(26)	(28)	(23)
Saturated fatty acids (Nr)	28	10	0	1	0	13	0	0	0	0	13	7	16	17	0
	(100)	(11)	(0)	(1)	(0)	(62)	(0)	(0)	(0)	(0)	(62)	(38)	(66)	(88)	(0)
Sugars (Nr)	30	20	3	3	3	2	4	6	6	0	2	2	3	3	2
	(100)	(32)	(35)	(35)	(35)	(8)	(23)	(52)	(52)	(0)	(8)	(8)	(11)	(11)	(18)
Peptides (Nr)	89	44	7	9	7	23	7	10	8	4	21	10	25	24	6
	(100)	(33)	(15)	(17)	(15)	(30)	(15)	(17)	(16)	(4)	(29)	(9)	(42)	(42)	(6)

Table 5.2: Negative correlations between the total assigned molecular formulae as well as the different type of molecular groups and the optical parameters. Abbreviations equal to Table 5.1.

	All	NC	Peak A*	Peak C*	Peak M*	Peak T*	A/T	C/T	M/T	C/M	*a*254*	FI	FrI	BIX	HIX
Nr total formulae	3689	2071	772	816	801	154	877	872	880	65	251	388	453	406	172
	(100)	(37)	(21)	(23)	(23)	(13)	(24)	(24)	(24)	(1)	(19)	(26)	(31)	(28)	(4)
MW (Da)	375	373	309	309	309	416	314	315	315	422	417	421	419	422	321
Nr formulae with N	1457	673	363	384	378	50	411	408	410	19	80	134	159	140	71
	(100)	(45)	(27)	(28)	(28)	(6)	(29)	(29)	(29)	(1)	(8)	(11)	(13)	(11)	(4)
Black Carbon (Nr)	8	3	3	3	3	0	4	4	4	1	0	0	0	0	0
	(100)	(23)	(50)	(50)	(50)	(0)	(62)	(62)	(62)	(13)	(0)	(0)	(0)	(0)	(0)
Polyphenols (Nr)	433	195	119	125	122	5	134	135	138	3	17	29	41	34	27
	(100)	(41)	(19)	(23)	(20)	(2)	(22)	(23)	(24)	(0)	(6)	(14)	(19)	(15)	(3)
Highly unsaturated (Nr)	2594	1288	474	499	490	110	544	537	542	57	163	292	318	281	102
	(100)	(30)	(19)	(20)	(20)	(14)	(22)	(21)	(22)	(1)	(20)	(29)	(33)	(29)	(4)
Unsaturated aliphatic (Nr)	507	210	134	141	142	39	150	151	150	4	67	50	81	80	28
	(100)	(25)	(26)	(29)	(29)	(18)	(28)	(28)	(28)	(0)	(25)	(20)	(31)	(30)	(6)
Saturated fatty acids (Nr)	28	9	17	17	17	0	17	17	17	0	1	1	0	0	7
	(100)	(8)	(88)	(88)	(88)	(0)	(88)	(88)	(88)	(0)	(3)	(1)	(0)	(0)	(21)
Sugars (Nr)	30	18	2	2	2	0	2	2	2	0	1	7	4	3	0
	(100)	(28)	(8)	(8)	(8)	(0)	(8)	(8)	(8)	(0)	(3)	(56)	(40)	(20)	(0)
Peptides (Nr)	89	40	23	25	25	0	26	26	27	0	2	9	9	8	8
	(100)	(32)	(41)	(41)	(41)	(0)	(42)	(42)	(43)	(0)	(2)	(17)	(17)	(16)	(19)

Table 5.3: Total number of molecular formulae with shared correlations (positive and negative) between each optical variable.

	Peak A*	Peak C*	Peak M*	Peak T*	a254*	BIX	HIX
Peak A*	1180						
Peak C*	1159	1327					
Peak M*	1140	1233	1233				
Peak T*	743	743	734	858			
a254*	817	817	808	796	969		
BIX	1053	1068	1041	819	922	1249	
HIX	319	312	299	272	302	357	470

We also studied the correlations between different groups of molecules and the optical indices (Table 5.1). We observed that about 59% of the spectrum intensity assigned to polyphenols correlated with one or more optical parameter. These compounds were negatively correlated with peak M*, fluorescence ratios A/T, C/T and M/T and BIX and positively with peak T*, *a*254* and HIX. These findings are in agreement with the fact that some polyphenols fluoresce in an area relatively close to the protein–like substances region (Yamashita et al., 2008; Bianchi et al., 2014). Furthermore, it was suggested that hydrocarbons are detected in the peak T* region (Stubbins et al., 2014).

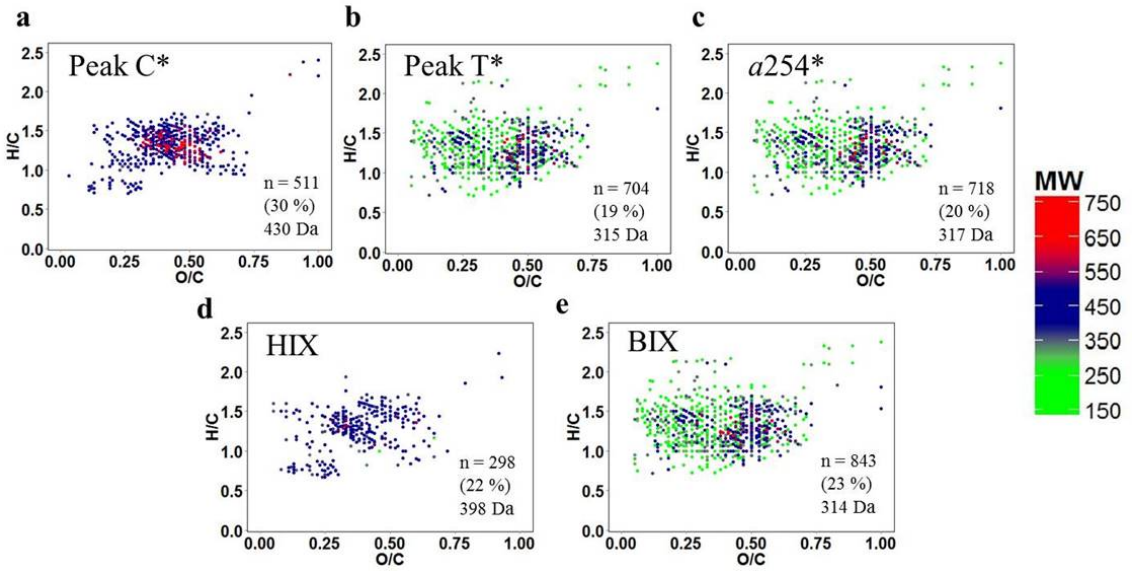

Figure 5.4: *Van Krevelen diagrams. Molecular formulae positively correlated with (a) peak C*, (b) peak T*, (c) a254*, (d) HIX and (e) BIX. Color scale represents the molecular weight. In the right–bottom corner of each panel is summarized the number of molecular formulae correlating, the percentage of peak intensity and the average molecular weight.*

About 70% of the mass spectrum intensity of highly unsaturated compounds, the most abundant group in our samples (Figure 5.6a), correlated both positively and negatively with all the optical parameters (Table 5.1 and Table 5.2). The unsaturated aliphatic compounds were the group that accounted the most to the correlations with the optical properties (about 75% of their mass spectrum intensity). Almost the same percentage of these compounds correlated positively and negatively with peaks A*, C*, M* and the fluorescence ratios A/T, C/T and M/T (Table 5.1, Table 5.2). However, the positive correlations were greater compared with the negative for peak T*, likely due to the labile nature of these compounds as it was suggested in previous studies (Nieto–Cid et al., 2006; Lønborg et al., 2010; Romera–Castillo et al., 2011b), and for some of the fluorescence indices (FI, FrI and BIX) which are proxies for recent biologic activity.

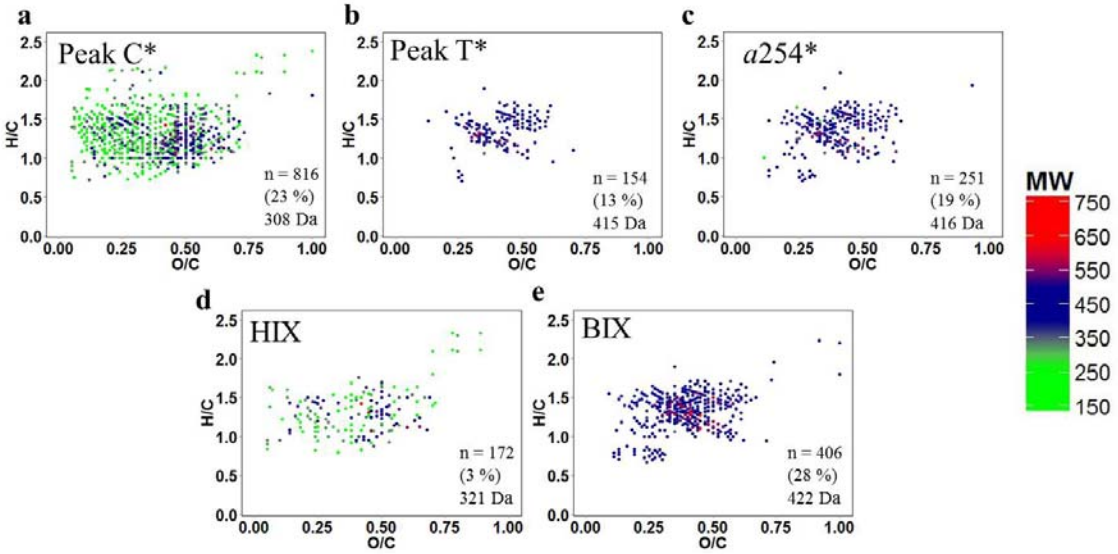

Figure 5.5: *Van Krevelen diagrams showing the molecular formulae negatively correlated with: (a) peak C*, (b) peak T*, (c) a254*, (d) HIX and (e) BIX. Color scale represents the molecular weight. In the left corner of each panel is summarized the molecular formulae number correlating, the percentage of peak intensity and the intensity–weighted average molecular weight.*

The saturated fatty acids correlated only negatively with peak A*, C* and M*, the ratios A/T, C/T and M/T and HIX and positively with peak T*, *a*254*, FI, FrI and BIX. Similarly, peptides correlated negatively with peak A*, C*, M*, the ratios A/T, C/T, M/T and HIX, but only positively with peak T* and *a*254*. These results are in agreement with the fact that saturated fatty acids are presumably bioavailable molecules (Kieber et al., 1997).

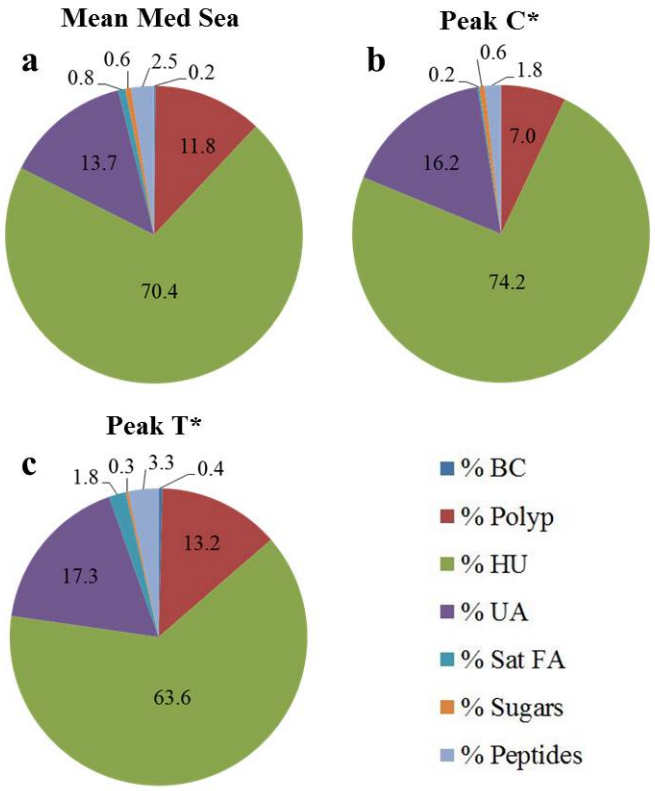

Figure 5.6: *Pie charts showing the mean percentage distribution of the different groups of molecules (BC = Black carbon, Polyp = polyphenols, HU = highly unsaturated compounds, UA = unsaturated aliphatic compounds, peptides, sugars, Sat FA = saturated fatty acids) from the FT–ICR–MS analysis in (a) the Mediterranean Sea (Med Sea) and the distribution of the positively correlated molecular groups percentage according to the Spearman's rank correlations for (b) the carbon–specific fluorescence intensity of humic–like substances (peak C*) and (c) protein–like substances (peak T*).*

The distribution of all the molecules positively correlated with peak C* and peak T* are graphically shown in Figure 5.6b and c. Compared with the mean compound group distribution of SPE–DOM in the Mediterranean Sea (Figure 5.6a), molecules correlating with peak C* were enriched in highly unsaturated compounds and impoverished in polyphenols. Conversely, molecules correlating with peak T* were enriched in unsaturated aliphatic molecules but impoverished in highly unsaturated molecules. In addition, peak T* showed an enrichment in polyphenols compared to peak C*.

3.4 Inferring DOM molecular indices from optical properties

Once we have verified the existence of significant correlations between DOM molecular formulae and optical properties, we propose using multiple linear regressions to estimate molecular indices from optical indices. First, a correlation matrix including salinity (S), potential temperature (θ), peak C*, peak T* and *a*254* was obtained (data not shown) to check for covariance between these variables. On basis of this analysis, Peak C* and peak T* along with θ were chosen for performing the multiple regressions. These regression models were fitted

using the 29 samples for which we have peak C* and peak T* measurements together with FT–ICR–MS molecular parameters. The cross validation exercise of the multiple regression of each molecular index with peak C*, peak T* and θ (see Materials and Methods) yielded estimated mean errors of 1, 5, 7 and 1% for DBE, Ideg, UA and CRAM, respectively. Therefore, the models were able to estimate molecular parameters from optical indices with a relatively low error. Then, we calculated the mean and standard deviation of the regression coefficients obtained after the 1000 times that each regression model was run to perform the cross validation exercise. These mean regression coefficients (Table 5.4) were not significantly different from the regression coefficients obtained with the individual multiple linear regressions of the molecular indices with peak C*, peak T* and θ for the 29 samples. The regression coefficients showed that peak C* was positively correlated with DBE, Ideg and CRAM, but negatively with unsaturated aliphatic compounds. Opposite results were obtained with peak T*. Regarding the normalized regression coefficients (beta), they were higher for peak C* than for peak T* for all the regressions (Table 5.4). The relative weight of peak T* increases when modeling Ideg and CRAM.

Table 5.4: Multiple linear regressions (Pearson) between the intensity–weighted average molecular parameters from FT–ICR–MS analysis of the SPE–DOM (DBE = double bond equivalent, Ideg = degradation index, unsaturated aliphatic compounds (UA) and CRAM = carboxyl rich alicyclic molecules) and potential temperature and the optical properties of the DOM (carbon–specific fluorescence intensity of the humic–like compounds (peak C*) and the protein–like compounds (peak T*) in NFIU L mg^{-1} C. Normalized regression coefficients (beta) are given in parentheses.

	Peak C*	Peak T*	R^2	p– value
DBE	0.31 ± 0.14 (*beta* = 0.55)	–0.02 ± 0.01 (*beta* = –0.22)	0.76	<0.0001
Ideg	0.13 ± 0.05 (*beta* = 0.50)	–0.015 ± 0.004 (*beta* = –0.30)	0.87	<0.0001
UA	–2.4 ± 1.2 (*beta* = –0.44)	0.23 ± 0.10 (*beta* = 0.22)	0.82	<0.0001
CRAM	1.7 ± 1.2 (*beta* = 0.43)	–0.23 ± 0.09 (*beta* = –0.30)	0.68	<0.0001

4 Conclusions

Overall, in this work we have shown that DOM optical and molecular properties correlated significantly in the Mediterranean Sea. In detail, we have observed relationships between different SPE–DOM groups of molecules and specific DOM fluorescence or absorption parameters. Specifically, the 52% of the assigned molecular formulae were correlated with one or more optical parameter, which accounted for 70% of the spectral signal intensity. FDOM and CDOM covary with a substantial fraction of SPE–DOM and not only with fluorescent molecular formulae. While peak C* correlated positively with higher average molecular weight formulae (more reworked DOM according with chapter 4), peak T* correlated positively with lower average molecular weight (less reworked DOM). Furthermore, we have established, for the first time, empirical multiple regression models to estimate molecular parameters from optical measurements in open ocean waters.

Chapter 6
Deep–ocean dissolved organic matter reactivity along the Mediterranean Sea: does size matter?

The research work presented in this chapter is also a contribution to the paper:

Martínez–Pérez, A.M., Álvarez–Salgado, X.A., Arístegui, J., Nieto–Cid, M., 2017. Deep–ocean dissolved organic matter reactivity along the Mediterranean Sea: does size matter? Sci. Rep. 7, 5687. doi: 10.1038/s41598–017–05941–6.

Abstract

Despite of the major role ascribed to marine dissolved organic matter (DOM) in the global carbon cycle, the reactivity of this pool in the dark ocean is still poorly understood. Present hypotheses, posed within the size–reactivity continuum (SRC) and the microbial carbon pump (MCP) conceptual frameworks, need further empirical support. Here, we provide field evidence of the soundness of the SRC model. We sampled the high salinity core–of–flow of the Levantine Intermediate Water along its westward route through the entire Mediterranean Sea. At selected sites, DOM was size–fractionated in apparent high (aHMW) and low (aLMW) molecular weight fractions using an efficient ultrafiltration cell. A percentage decline of the aHMW DOM from 68–76% to 40–55% was observed from the Levantine Sea to the Strait of Gibraltar in parallel with increasing apparent oxygen utilization (AOU). DOM mineralization accounted for 30 ± 3% of the AOU, being the aHMW fraction solely responsible for this consumption, verifying the SRC model in the field. We also demonstrate that, in parallel to this aHMW DOM consumption, fluorescent humic–like substances accumulate in both fractions and protein–like substances decline in the aLMW fraction, thus indicating that not only size matters and providing field support to the MCP model.

1 Introduction

Most of the 662 Pg C of dissolved organic matter (DOM) accumulated in the oceans is resistant to microbial degradation and, therefore, stored for hundreds to thousands of years (Hansell et al., 2009; Hansell, 2013). The mechanisms behind this long–term storage of carbon are still poorly understood (Dittmar, 2015). The microbial carbon pump (MCP) concept is suggested to explain this storage, as it postulates that microbial degradation of bio–labile DOM produces bio–refractory DOM (Ogawa et al., 2001; Jiao et al., 2010).

Closely related with the MCP concept is the size–reactivity continuum (SRC) hypothesis to explain marine DOM reactivity (Benner and Amon, 2015). According to this assumption, initially based on microbial degradation experiments (Amon and Benner, 1994; Amon and Benner, 1996), changes in the bioavailability of DOM would be explained by varying proportions of more labile high molecular weight (HMW) DOM compared with slower degrading low molecular weight (LMW) DOM. Earlier works showing patterns, compositions and concentrations of major DOM biochemical compounds (carbohydrates and amino acids) in the ocean provided independent validation of the relative reactivity of different size classes of organic matter (Benner et al., 1992; Aluwihare et al., 1997; McCarthy et al., 1997). Posterior field studies supported the SRC hypothesis as they found higher $\Delta^{14}C$ values in the HMW DOC fraction compared to the LMW DOC fraction (Guo et al., 1996; Loh et al., 2004). Lastly, it has been recently reported a significant dissolved organic matter size–age–composition relationship that is also consistent with the SRC model (Walker et al., 2011; Walker et al., 2016a, 2016b). These studies suggest microbial degradation as the primary source of recalcitrant DOM to the deep ocean, in agreement with the MCP conceptual model. Nevertheless, other works based on bacterial degradation experiments have found discrepancies with the SRC model (Covert and Moran, 2001; Khodse and Bhosle, 2011), as they observed that LMW DOM is biologically more reactive than HMW DOM.

Focusing only on the colored fraction of DOM (CDOM) a different picture may arise, facing the SRC hypothesis. It is well established that fluorescence spectroscopy measurements at specific wavelength pairs are due to refractory humic–like substances and to bioavailable protein–like compounds (Coble, 1996; Stedmon and Nelson, 2015). Microbial cultures have demonstrated consumption of the protein–like and production of the humic–like DOM in a daily to yearly basis (Nieto–Cid et al., 2006; Lønborg et al., 2010; Jørgensen et al., 2011; Aparicio et al., 2015). The generation of humic–like substances implies the formation of structurally complex molecules that, apparently, challenges the SRC postulates.

Here, we assess the validity of the SRC model *in situ,* by following the course of two size fractions of DOM along the shallow overturning circulation cell of the Mediterranean Sea (MedSea) (Chapter 2). We chose this region because its high temperatures boost biogeochemical rates, resulting in shorter spatial and time scales, acting as a natural laboratory to explore processes happening at a global extent. The shallow branch of the Mediterranean overturning circulation drives the Levantine intermediate water (LIW), which is formed by convection in the northern part of the Levantine basin. LIW is found along the whole MedSea between 200 m depth in the eastern and 500 m depth in the western basin (as Eastern Intermediate Water (EIW)), displaying the maximum salinity of all Mediterranean water masses (Emelianov et al., 2006). According to the SRC hypothesis, the LIW in the Levantine basin (close to its formation site) should transport a higher concentration of DOM with a higher average molecular weight. This DOM would be progressively consumed within the overturning cell in such a way that the EIW leaving the Strait of Gibraltar would transport less DOM with a lower average molecular weight. Regarding the optical properties of DOM, at the formation site we would expect enrichment in bioavailable protein–like substances and depletion in refractory humic–like compounds. Conversely, as the LIW displaces westwards, the proportions of protein– and humic–like substances should reverse.

2 Material and methods

2.1 Study area and sampling

Water samples were collected at the nine reference stations already treated in chapters 4 and 5 (red dots in Figure 2.1 page 58) during the trans–Mediterranean cruise HOTMIX 2014. Four to five depths were sampled depending on the bathymetry of the stations, except for the station at the Strait of Sicily (stn 13) where only LIW was sampled due to its shallowness. As already explained in chapter 4, deep chlorophyll maximum (DCM) samples were distinguish according to the maximum fluorescence intensity, the LIW and EIW were sampled at the absolute maximum of the salinity profile of each station, the oxygen minimum layer (OML) was established on basis of the absolute minimum of the dissolved oxygen profile, and the deep waters were sampled according to the salinity and temperature characteristic of the bathypelagic zone of the eastern and western Mediterranean basins (See Figure 4.1 in page 133).

2.2 DOM size–fractionation

DOM water samples were collected in 5–litres acid–cleaned polycarbonate carboys and stored in the dark at 13°C until filtration within 5 hours. Filtration was performed through precombusted (450°C, 4 h) Whatman GF/F filters in an acid–clean all–glass filtration system under positive pressure with low flow of high purity N_2. Two–litre aliquots of the filtrate were collected in acid–cleaned PTFE bottles for DOM size–fractionation using an ultrafiltration cell (Millipore, 2000) equipped with a cut–off membrane of 1000 Da (Millipore, PLAC 150 mm). A pressure of 55 psi, using high purity N_2, was maintained during the fractionation splitting the DOM into an apparent high molecular weight (aHMW, >1000 Da; 0.5 L) and an apparent low molecular weight (aLMW, <1000 Da; 1.5 L) fractions. The ultrafiltration cell was cleaned between samples by passing 0.3 L of NaOH through the membrane filter, followed by three rinses with 1 L of MQ water. The efficiency of the ultrafiltration cell (>90%) was checked using a solution of vitamin B12 (1355 Da; Sigma, 50 mg L^{-1}). For large–volume ultrafiltration systems, previous works (Guo et al., 1996; Guo et al., 2000) reported lower efficiency rates (about 80%) using the same solution of vitamin B12. This fact was due to the general decrease of the retention rate with increasing concentration factors (CF). In our case, the CF (sample volume/ retentate volume) was 4. We used a low CF for two main reasons: i) the ultrafiltration time increased with higher CF, so we keep it low in order to processes a significant number of samples, and ii) to ensure a pure aLMW fraction, which is much less studied compared to the aHMW fraction. Note that due to this CF and the ultrafiltration cell system used in this study, up to 25% of the aHMW fraction may correspond with low molecular weight molecules. In this system the sample is not recirculated, but it is being forced to a continuous and vigorous stirring inside the ultrafiltration cell. Then, the bulk DOM and aLMW fraction are pure treatments, but the aHMW fraction presents all the high molecular weight molecules (100%) plus a portion of the low molecular weight molecules (up to 25% of the aHMW fraction) due to the retention of aLMW–DOM during ultrafiltration. Taking into account that the %aHMW ranged between 76 to 55% and that in our ultrafiltration system the retentate was 0.5 L and the permeate 1.5 L, applying a simple system of 2 linear equations with 2 unknowns, the lower molecular weight molecules in the aHMW fraction varied between 8 and 15%, respectively.

2.3 Dissolved organic carbon (DOC) and fluorescence spectroscopy (FDOM)

Approximately 100 mL of the DOM filtrate, and the HMW and LMW fractions were collected for DOC and FDOM analyses. Aliquots of 10 mL were collected in precombusted (450°C, 12 h) glass ampoules for DOC determination. These samples were acidified with H_3PO_4

(85%, p.a., Merck) to pH <2 and the ampoules were heat–sealed and stored in the dark at 4°C until analysis in the base laboratory with a Shimadzu TOC–V organic carbon analyser (see chapter 2; page 59). FDOM was determined on board with a Perkin Elmer LS55 luminescence spectrometer. Slit widths were 10.0 nm for both excitation and emission wavelengths. Measurements were performed at constant room temperature (25°C) in a 1 cm quartz fluorescence cell and Milli–Q water was used as a reference blank. Measurements were performed at the classical fluorescence peaks (Coble, 1996) selecting Ex/Em wavelengths of 340 /440 nm (peak C), due to humic substances and 280/350 nm (peak T), due to protein–like substances. The fluorescence of each peak was determined by subtracting the Milli–Q blank peak height from the sample average peak height. As explained in chapter 5 (page 161), all the samples were normalized using a solution of quinine sulphate dihydrate (≥99.0%, purum for fluorescence, Fluka) and tryptophan (≥99.0%, Fluka) standards in H_2SO_4 0.05M (95–97%, p.a., Merck) allowing to express fluorescence in normalized fluorescence intensity units (NFIU).

3 Results and discussion

The 30 samples collected along the MedSea were size–fractionated using a 1 kDa cut–off membrane (Millipore, PLAC 150 mm), and the DOC and fluorescence intensity of all fractions were determined. On a carbon basis, the mass balance for the size–fractionation process presented an overall error lower than 10%. The high recovery of our low–volume ultrafiltration cell (50–80%) was mainly due to the low concentration factor (CF) of just 4 used in this study. This cell allowed us to separate the size fractions in less than 5 hours in such a way that several samples can be processed within the same day. On the contrary, standard ultrafiltration methodologies for large sample volumes, isolate about 30–55% of the marine DOM (Guo et al., 1995; Guo and Santschi, 1996), applying CFs ranging from about 12 to about 500, depending on the purpose of the ultrafiltration (%HMW quantification (Guo et al., 1995; Cai and Guo, 2009) *versus* isolation (Benner et al., 1992; Guo et al., 1996)). Ultrafiltration using higher CFs is more time consuming, which is not compatible with our oceanographic approach. Given that our separation method is not comparable with the classical approaches in using ultrafiltration methods, we refer hereinafter to the fraction <1 kDa as apparent LMW DOM (aLMW DOM) and the fraction >1 kDa as apparent HMW DOM (aHMW DOM). Furthermore, due to the ultrafiltration system and the CF used in this study, our aHMW fraction may include up to 25% of low molecular weight molecules (see DOM size–fractionation in the Material and Methods section).

3.1 Testing the size–reactivity continuum hypothesis

DOC and the carbon–specific fluorescence of humic–like (peak C*) and protein–like (peak T*) substances for the different sampling depths are represented against the apparent oxygen utilisation (AOU) in Figure 6.1. DCM or deep water samples showed narrow AOU variations through the cruise track (mean ± SD; 4.5 ± 3.1 and 64.4 ± 5.2 µmol kg^{-1}, respectively; blue rectangle boxes in Figure 6.1). Recently ventilated DCM waters presented very low AOU values, whereas aged deep waters exhibited significantly higher values. Instead, samples collected at the intermediate salinity maximum layer displayed a wide AOU range (mean ± SD; 50.2 ± 30.3 µmol kg^{-1}; red rectangle boxes in Figure 6.1) revealing an increasing trend from the Levantine basin (water mass formation area) to the Strait of Gibraltar (Figure 2.5e in chapter 2 and Figure 6.1).

The corresponding SD values translated into carbon equivalents using the canonical Redfield $-O_2/C$ ratio of 1.4, AOU–Ceq, were 2.2, 21.6 and 3.7 µmol–C kg^{-1} for DCM, LIW and deep waters, respectively. Therefore, the core–of–flow of the LIW is the layer that presents the largest variability of AOU–Ceq, an order of magnitude above the DCM and deep layers.

At the DCM there is not a clear relationship between AOU and the bulk (DOM), aHMW and aLMW fractions of dissolved organic matter. This is an expected result given the narrow ranges of variability of AOU–Ceq and DOC. In this regard, DOC at the DCM was 64.3 ± 2.8, 41.9 ± 5.5 and 23.0 ± 5.3 µmol–C L^{-1} for bulk DOM, aHMW and aLMW fractions, respectively (circles in Figure 6.1a, b, c). It is noticeable too that the SD of DOC, 2.8 µmol–C L^{-1}, was larger than the SD of AOU–Ceq, 2.2 µmol–C kg^{-1} suggesting that this behaviour could be related to the primary production processes dominating in this layer, which lead to lower AOU and higher DOC values.

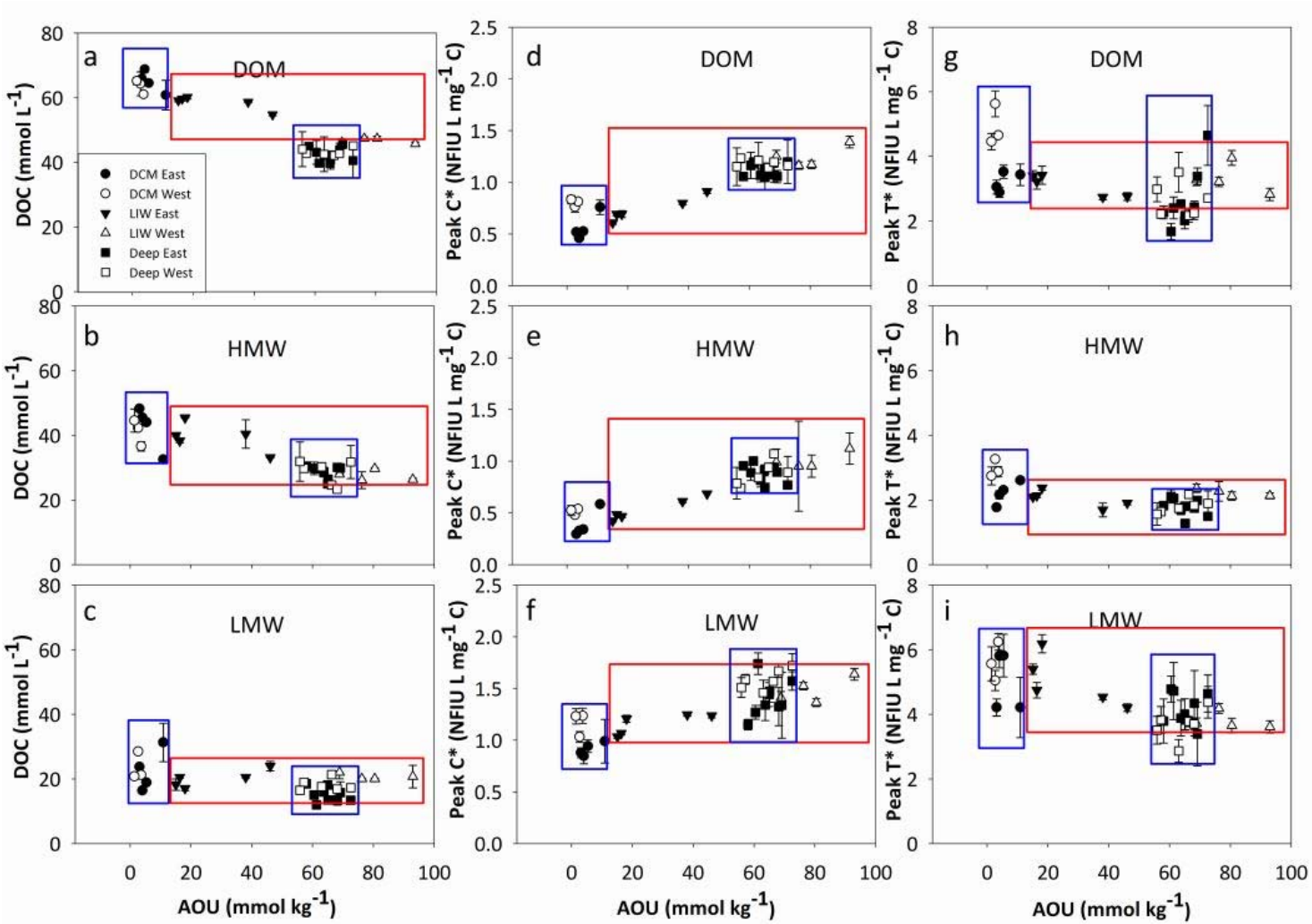

Figure 6.1: *Range of variability of DOC and FDOM in DOM, apparent low molecular weight (LMW) DOM and apparent high molecular weight (HMW) DOM with respect to AOU for all collected samples. (a–c) DOC, (d–f) humic–like fluorescence of the peak C per carbon unit (peak C*) and (g–i) protein–like fluorescence of the peak T per carbon unit (peak T*). Black filled circles, black circles, black filled triangles, black triangles, black filled squares and black squares represent samples collected at the DCM in the East, DCM in the West, LIW in the East, LIW in the West (EIW), deep samples in the East and deep samples in the West, respectively. The blue rectangles cover the DCM and deep samples and the red ones the LIW samples. Error bars represent standard errors.*

In the deep waters (squares in Figure 6.1a, b, c) mean ± SD concentrations of DOC were 42.6 ± 1.9, 28.7 ± 2.7 and 16.3 ± 2.5 µmol–C L^{-1}, for bulk DOM, aHMW and aLMW fractions, respectively. This range is also quite narrow considering that we are merging all samples from more than 1000 m in either the eastern and western basin. In this case, the SD of AOU–Ceq for the deep waters, 3.7 µmol–C kg^{-1}, was about 50% larger than the SD of DOC, indicating that DOC should be a major contributor to the oxygen demand of the deep water from their respective formation site to the study zone.

The samples collected at the salinity maximum, corresponding to the higher proportion of intermediate waters (e. g. LIW and EIW) (triangles in Figure 6.1a, b, c), presented the highest AOU variability, with lower values at the stations located near the formation area (Levantine basin) and higher in the western basin. Moreover, these intermediate waters presented wide DOC changes, (mean ± SD) except for the LMW fraction, (53.2 ± 6.4, 34.1 ± 7.1 and 20.4 ± 2.0. µmol–C L^{-1} for bulk DOM, aHMW and aLMW, respectively) associated with the DOM mineralization processes taking place in this layer along its route westwards (AOU increment).

This size–fractionation pattern is also observed when plotting AOU against the optical properties of DOM. Peak C* (Figure 6.1d, e, f), considered as a proxy to microbial degradation processes (Nieto–Cid et al., 2006; Lønborg et al., 2010), showed higher fluorescence intensity per carbon unit for the aLMW fraction for all samples collected at different depths (DCM, Deep and LIW). In addition, in general terms this fluorescence intensity was significantly higher (p–value < 0.001) in the western basin, due to the higher heterotrophic and enzimatic activity in this area (Luna et al., 2012). Specifically, in the deep waters a slight increase of peak C* with the AOU was observed for the aLMW fraction (Figure 6.1f), indicative of the generation of humic–like substances in this fraction. However, it was not observed for the bulk DOM, which means that the rate of peak C production in the LMW fraction is higher than the DOC consumption rate. Analogously, Peak T* (Figure 6.1g, h, i), considered as a proxy for bioavailable substances, showed the same trend of higher fluorescence intensity per carbon unit for the LMW fraction.

For the interest of our study, we focused on samples with the highest proportion of intermediate waters (LIW and EIW), which is the single water mass crossing the entire MedSea. This allowed us to observe changes in DOM size–fractionation, as this intermediate water was ageing along their westward route from the Levantine basin to the Atlantic Ocean (Tsimplis et al., 2006).

The DOM size–fractionation at the intermediate level is illustrated in more detail in Figures 6.2 and 6.3. A significant decrease of DOC with increasing AOU was detected for the bulk DOM and the aHMW fraction (Figure 6.2a), revealing that larger organic compounds are preferably consumed during mineralization processes. However, the aLMW DOC concentration showed a slight increase with AOU, although it was not significant. Note that although up to 25% of the aHMW fraction corresponds with low molecular weight molecules, the changes observed cannot be due to this smaller DOM since, as observed in Figure 6.2a, the LMW fraction did not undergo any decay with AOU. Thus, we can infer that larger molecules are more bioreactive. Taking into account the slopes of the linear regressions (Figure 6.2a, Table 6.1) and converting them into carbon equivalents using the canonical Redfield $-O_2/C$ ratio of 1.4 (Redfield et al., 1963) we obtained that 30 ± 3% of the oxygen utilization at the intermediate level was due to DOM decomposition. To assess the effect of water mass mixing on the DOC/AOU relationship we should apply the mixing–biogeochemical model using equation 2.8 in chapter 2, however, as discussed in chapter 4, it is not possible due to in this chapter we deal with just 30 samples and we have intercepted 19 water masses (chapter 2). Therefore the statistical analysis would not be significant. A simpler way to minimize the effect of water mass mixing on the DOC/AOU relationship is to perform a multiple linear regression of DOC with θ, S and AOU. Doing this the slope changed to –0.31 ± 0.08, which, converted into oxygen equivalents as above, resulted in a 43 ± 11% of the oxygen consumption due to prokaryotic oxidation of DOC. Note that this number is not significantly different from the previously obtained with the simple linear regression. Further, comparing these results (only intermediate layer samples, n = 9) to that obtained in chapter 2 for the whole dark MedSea (31 ± 4%) by means of the water mass analysis including all samples (n= 226), we observed that they were very similar. Therefore intermediate waters not necessarily present the higher slope in the DOC/AOU relationship in spite of exhibiting the highest AOU variability.

This result is in agreement with the value reported for the intermediate and deep waters of the Eastern Mediterranean Sea (27 ± 18%) (Meador et al., 2010), but slightly lower than the 38% reported for the LIW (Santinelli et al., 2010). Our values are higher than those found in the global ocean (10–20%; Arístegui et al., 2002) and highlight the relevance of the DOC pool for oxygen consumption in the mesopelagic layers of the MedSea.

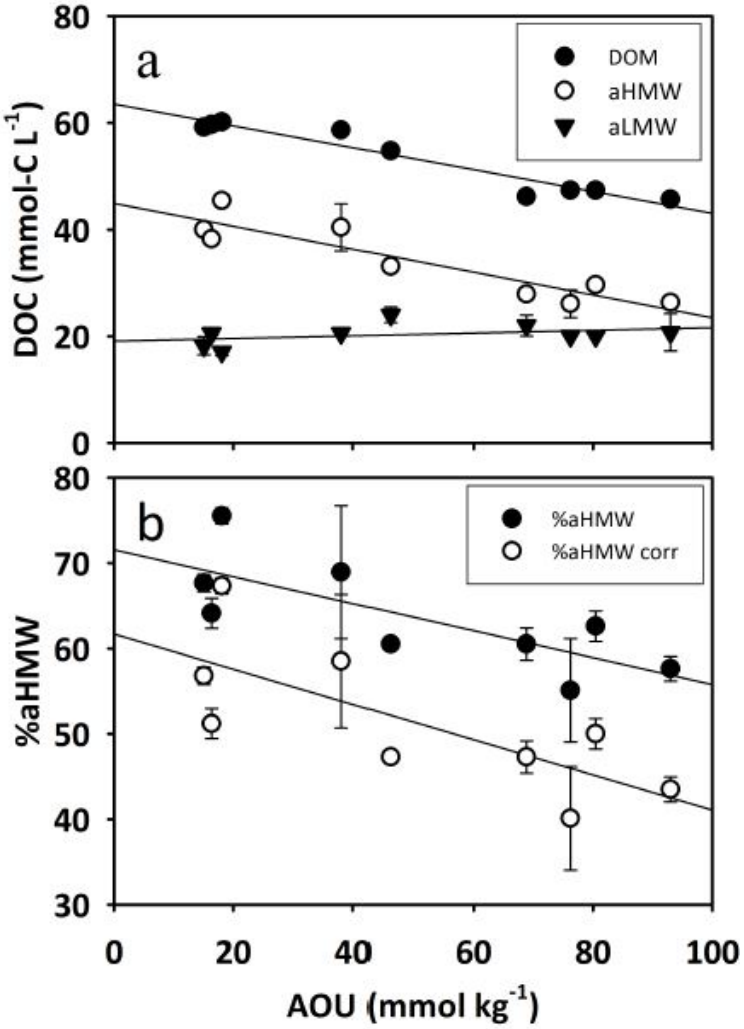

Figure 6.2: *DOM size–fractionation with apparent oxygen utilization on a carbon basis. (A) size–fractionated DOC where DOM (solid black circles), aHMW (open circles) and aLMW (solid black triangles) represent the bulk DOC, the apparent high molecular weight fraction and the apparent low molecular weight fraction, respectively. (B) aHMW percentage (solid black circles) and corrected aHMW percentage (open circles) with respect to apparent oxygen utilization (AOU) of samples collected along the core–of–flow of the Levantine Intermediate Water. Error bars represent standard errors.*

Warmer deep water temperatures in the MedSea (>13°C *versus* <5°C; Dickson and Brown, 1994), which stimulate the prokaryotic degradation processes, and the higher exportation of DOM compared to POC in the MedSea (Guyennon et al., 2015), are the likely reasons behind this difference. In addition, the partition of DOC into aHMW and aLMW allowed establishing, for the first time, the contribution of each apparent fraction to the overall mineralization. As observed in Figure 6.2a, the aLMW DOC did not contribute to the oxygen consumption, while the aHMW DOC accounted for as much as the bulk DOC (32 ± 6%). Therefore, all the DOC mineralization was due exclusively to the aHMW DOC, a fact that validates the SRC hypothesis (Benner and Amon, 2015) using the shallow overturning cell of

the MedSea as an *in situ* incubator. Note that this result is valid for the bulk DOC but does not necessarily apply to the myriads of individual compounds that constitute this pool. Furthermore, considering the intercepts of the three regression equations (being all significant, $p < 0.001$; Table 6.1), we can estimate the DOC concentration at the time of water mass formation (when AOU should be null).

Table 6.1: Linear regressions (model II) between DOC and FDOM indices (y–variable) and apparent oxygen utilization (x–variable) obtained from bulk DOM and apparent HMW (aHMW) and LMW (aLMW) fractions from samples collected at the salinity maximum (LIW). n = 9, m = slope, b = intercept, SE = Standard error and NS = Non significant. *, **, *** correspond with $p < 0.05$, $p < 0.01$ and $p < 0.001$, respectively. DOM <0.7 µm, aHMW <0.7 µm and >1 kDa and aLMW <1 kDa.

Fraction	y–variable	m ± SE	b ± SE	R^2
DOM	DOC	$-21 \pm 2 \times 10^{-2}$***	63 ± 1***	0.93
aHMW	DOC	$-23 \pm 4 \times 10^{-2}$***	45 ± 2***	0.84
aLMW	DOC	$7 \pm 5 \times 10^{-2}$ NS	19 ± 1***	0.15
DOM	Peak C	$35 \pm 4 \times 10^{-4}$***	0.43 ± 0.02***	0.92
aHMW	Peak C	$18 \pm 3 \times 10^{-4}$***	0.20 ± 0.02***	0.83
aLMW	Peak C	$21 \pm 3 \times 10^{-4}$***	0.23 ± 0.02***	0.84
DOM	Peak C*	$9 \pm 1 \times 10^{-3}$***	0.50 ± 0.04***	0.96
aHMW	Peak C *	$87 \pm 5 \times 10^{-4}$***	0.31 ± 0.03***	0.97
aLMW	Peak C*	$6 \pm 1 \times 10^{-3}$***	1.00 ± 0.05***	0.87
DOM	Peak T	$-10 \pm 4 \times 10^{-3}$*	2.4 ± 0.1***	0.58
aHMW	Peak T	$-6 \pm 1 \times 10^{-3}$*	1.1 ± 0.1***	0.63
aLMW	Peak T	$-4 \pm 1 \times 10^{-3}$***	1.29 ± 0.04***	0.83
DOM	Peak T*	0.01 ± 0.6 NS	3.2 ± 0.3***	0.00
aHMW	Peak T *	$7 \pm 20 \times 10^{-3}$ NS	2.1 ± 0.1***	0.02
aLMW	Peak T*	$-28 \pm 7 \times 10^{-3}$**	5.7 ± 0.3***	0.73

It results in 63 ± 1 µmol–C L^{-1}, of which 45 ± 2 µmol–C L^{-1} corresponds to aHMW DOC and 19 ± 1 µmol–C L^{-1} to aLMW DOC. If we discount a 25% due to molecules smaller than 1 kDa that are present in the aHMW fraction, the corrected partition turns to be 39 µmol–C L^{-1} of aHMW DOC and 25 µmol–C L^{-1} of aLMW DOC. The DOC concentration at the formation time for the bulk DOC is comparable with the previously reported value for the LIW (67 ± 1 µmol–C L^{-1}; Santinelli et al., 2010). The evolution of the percentage of aHMW DOM (%aHMW, on a carbon basis) with the AOU along the LIW transit from its formation site (Figure 6.2b) shows a significant inverse relationship ($R^2 = 0.58$, $p < 0.05$). This relationship is independent of considering (black circles in Figure 6.2b) or not (white circles in Figure 6.2b) the 25% of LMW molecules contained in the aHMW DOM fraction. The slopes of both linear regressions are not significantly different. This observation supports the view that aHMW molecules are preferentially consumed in the intermediate waters of the MedSea simultaneously to water mass ageing, and therefore large DOM would be more bioreactive than the smaller

counterpart. It also corroborates that, although our size fractionation system does not allow obtaining a 100% pure aHMW DOM fraction, our conclusions are not influenced by this fact. Moreover, our findings are in agreement with the size–age–composition relationships of DOM reported in recent studies (Walker et al., 2011, 2016a, 2016b).

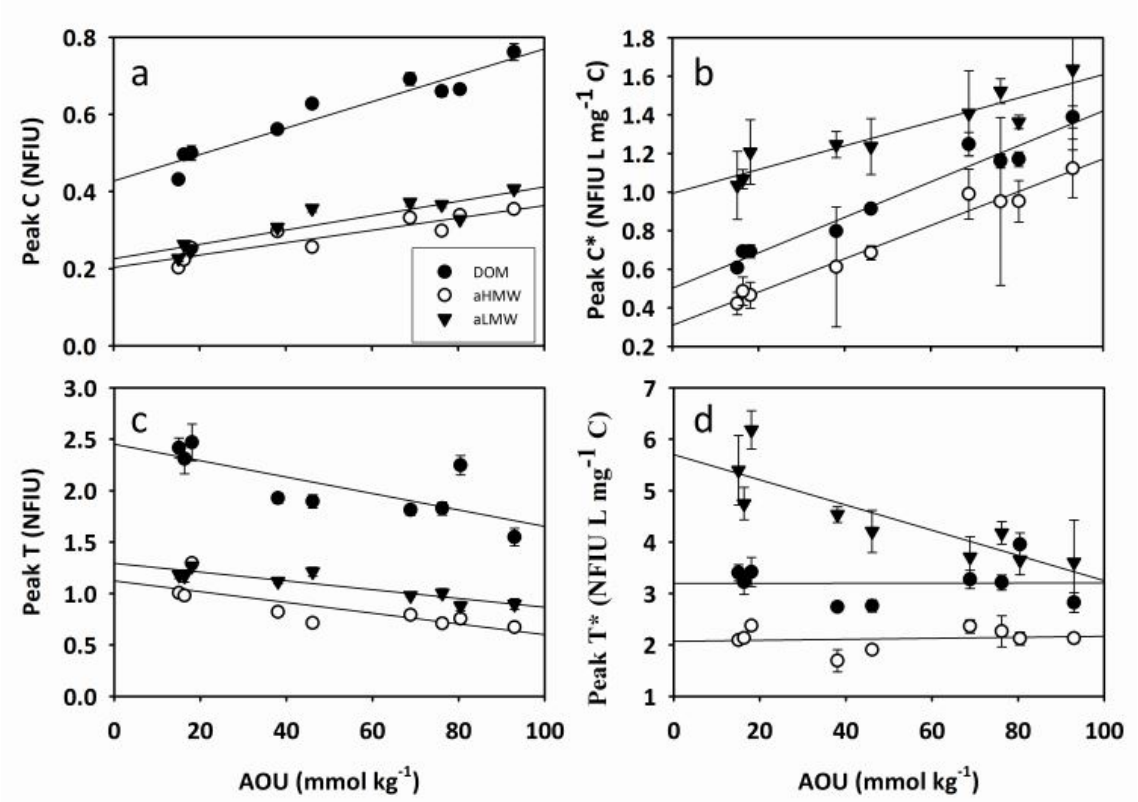

Figure 6.3: *DOM size–fractionation with apparent oxygen utilization on a fluorescence basis. DOM (solid black circles), aHMW (open circles) and aLMW (solid black triangles) represent the bulk DOM, the apparent high molecular weight fraction and the apparent low molecular weight fractions, respectively, of samples collected along the core–of–flow of the Levantine Intermediate Water. (A) Humic–like fluorescence (peak C), (B) humic–like fluorescence per carbon unit (peak C*), (C) protein–like fluorescence (peak T) and (D) protein–like fluorescence per carbon unit (peak T*) with respect to apparent oxygen utilization (AOU). Error bars represent standard errors.*

It could be argued that the DOC–AOU relationship (Figure 6.2a) is distorted by the sinking flux of biogenic particulate organic carbon (POC). However, in the ultra–oligotrophic eastern basin, where the core–of–flow of the LIW is shallower (200–300 m), the vertical flux of POC is minor compared with the injection of DOC in the water mass formation area of the LIW (Santinelli, 2015; Guyennon et al., 2015). In the western basin, although the vertical flux of POC is higher than in the eastern basin, the amount reaching the core–of–flow of the LIW at 350–400 m presents high turnover rates. As POC consists mainly on the labile products of synthesis and early degradation of plankton (Sarmiento and Gruber, 2006), the POC reaching the intermediate waters will be degraded in time scales of hours to weeks (Sempéré et al.,

2000). Therefore, the observed DOC–AOU relationship along the core–of–flow of the LIW would be essentially driven by the consumption of semi–refractory HMW DOC than of labile sinking POC.

3.2 Testing the microbial carbon pump hypothesis

There is little information on the size distribution of coloured DOM (CDOM) in ocean waters (Osburn et al., 2014; Gao and Guéguen, 2017; Xu and Guo, 2017). Here we observed that the aLMW fraction hosts more humic– and protein–like fluorescence intensity per carbon unit than the aHMW DOM fraction (Figure 6.3b, d). Particularly, for the protein–like fluorescence (peak T) the contribution is higher in the less aged waters (low AOU), while for the humic–like fluorescence (peak C) the two DOM fractions presented a significant increase with AOU (Figure 6.3a–b). This is indicative of the production of humic–like fluorescence per unit of carbon in parallel to the general trend of DOC and aHMW DOC consumption. All together, these observations support the MCP hypothesis, which postulates that refractory DOM is produced during the mineralization of bioavailable organic matter, either dissolved or in suspended and sinking particles (Jiao et al., 2010). Specifically, the generation rate of humic–like substances was 30% higher in the HMW DOC than in the LMW DOC (Table 6.1; Figure 6.3b) due to DOC dynamics: aHMW DOC was consumed while LMW DOC remained constant. On the other hand, peak T exhibited a significant decrease in both DOM fractions with AOU (Figure 6.3c), indicative of the utilization of this type of compounds during mineralization processes. This finding suggests that small organic compounds related to protein–like molecules were also degraded when intermediate waters aged. Changes of peak T in the LMW fraction were not reflected in the bulk DOC due to the lower sensitivity of the DOC analytical technique compared with fluorescence spectroscopy. Therefore, the LMW fraction also contains some bioreactive molecules although the bulk fraction is essentially refractory. For the aHMW DOC and the bulk DOC we observed that the rate of protein–like substances consumption was equal to the rate of DOC consumption (as the horizontal lines in Figure 6.3d suggest). These results indicate that the overall behaviour of the bulk DOC pool does not necessarily match the specific response of particular compounds or compound groups as the fluorophores studied here, and they also reconcile the two hypothesis studied in this work, the SCR and the MCP.

It can be argued that the longitudinal changes observed in the DOC and FDOM of the different size fractions could partially be due to mixing of intermediate waters (LIW and EIW) with other water masses instead of ageing. However, water mass mixing would reinforce our hypothesis since EIW in the western basin is the oldest water mass. Then, if EIW is mixing with

the surrounding water masses, which are younger than EIW, the longitudinal changes in DOC and its partition in aLMW and aHMW compounds should be more evident than those really observed.

4 Conclusions

We provide *in situ* support for the SRC hypothesis, out of the artefacts of microbial incubation experiments. Our results are neither distorted by alterations in the structural continuum of DOM during size–fractionation previous to *in vitro* experiments nor by subsequent "bottle effects" during incubations. Fractionation by ultrafiltration before *in vitro* degradation experiments breaks down the DOM structural continuum and, therefore, could not be the most appropriate approach for studying the DOM size–reactivity. In addition, we have demonstrated that DOM decomposition accounted for 30 ± 3% of the oxygen utilization at the shallow overturning circulation cell of the MedSea. The unique DOM fraction responsible for this oxygen consumption was the aHMW fraction, suggesting that larger molecules are more bioreactive than the smaller counterpart. Further, in parallel to the aHMW consumption, we observed fluorescence humic–like substances accumulation in both fractions (aHMW and aLMW) and a fluorescence of protein–like substances decline in the aLMW fraction supporting the MCP model. Although our study is based on a relatively small and shallow overturning cell, we believe that our results could be extrapolated to the global ocean. To confirm this, it would be necessary to perform similar studies in the main water mass formation areas of the world ocean.

Chapter 7
General discussion

General discussion

Given that chapters 2 to 6 of this PhD thesis contain their own discussion, the aim of this section is to deal with some controversial issues, either methodological or conceptual, that have emerged when writing those chapters. In addition, this general discussion intends to be transversal, i.e. all the questions presented below involve more than one of the chapters included in this PhD thesis.

1 What is the removal rate of the DOM in the Mediterranean Sea?

To determine the removal rate of DOM from a certain water parcel, for example a water mass or basin, it is necessary to estimate the transit time. Unfortunately, there is a lack of consensus in the literature about how to derive or estimate this parameter (see Table 7.1). In fact, the first obstacle is the diverse and confuse terminology used by physical oceanographer and marine biogeochemists. Recurrently used terms include ventilation time, transient time, residence time, transport time, turnover time, transfer time, apparent travel time, tracer age and renewal time. To avoid misunderstandings regarding the terminology, firstly it is important to remember that renewal time is used to refer to water masses, however removal, turnover or residence time is used to refer to substances (i.e. organic matter, inorganic nutrients, etc.). Table 7.1 summarizes the definitions of these terms.

Table 7. 1: Summary of the main terms for referring time scales on water masses and substances.

Term	Definition
Water mass age or ventilation time	Time elapsed since a water parcel left the mixed layer (Roether et al., 1998; Schneider et al., 2014)
Transient /Transit time	Time used by a water mass to travel a certain distance.
Residence time	Ratio between the total amount of a substance in a water parcel and the flux (amount of the substance per unit time) that enters or leaves the parcel
Renewal time	Ratio between the total volume of a water parcel and the water flow (volume per time unit) that enters or leaves the parcel
Turnover time	Ratio between the total amount of a substance in a water parcel and the net rate at which it is produced or consumed within that volume
Travel/transport/transfer time	Time elapsed from the formation site until the study area (Roether et al., 1998; Schneider et al., 2014)
Apparent tracer age	Time passed since the concentration of the interior tracer was equal to the surface concentration, considered in equilibrium with the atmosphere (Schneider et al., 2014)

In chapter 4 and 6 we paid especial attention to the Levantine Intermediate water (LIW) as it is the only water mass intercepted along the entire Mediterranean Sea (MedSea). Roether et al. (1998) reported a transit time of 8 years from the formation area of the LIW to the Sicily Strait based on transient tracer data. Later, Gačić et al. (2013), based on salinity anomalies, reported a transient time of 10–13 years. More recently, Schneider et al. (2014) obtained a transit time from the formation area up to the Ionian Sea of about 22 years. Schneider et al. (2014) also reported a mean age for the LIW in the Alboran Sea of about 70 years. Furthermore, Stöven and Tanhua (2014) arrived to a mean age of 25 years for the LIW in the western part of the Levantine basin and of 15 years in the Ionian Sea (see their Table 4). To sum up, different mean ages/transit times were reported depending on the tracers used (CFC's, SF6, Tritium/Helium) and/or the method of estimation.

Powley et al. (2016) have calculated what they called "residence" times (although "renewal" time would be a more appropriate term) for all the water masses of the MedSea using a box model. They reported renewal times (tR) of 8.7 and 7.0 years for the intermediate layer of the eastern and western basins, respectively. Using this box model approach, tR for the intermediate waters of the whole MedSea would be about 13 years (see blue box below). It is important to keep in mind that the renewal time is the time over which 100 x (1 – 1/e) % of the volume of the study volume is renewed (Hansell, 2013). Therefore this means that in 13 years 63% of the intermediate waters of the entire MedSea are renewed, in 26 years 86% are renewed [=100·(1 – $1/e^2$)%], in 39 years 95% are renewed [=100·(1 – $1/e^3$)%], and so on. Knowledge of the renewal time allows us to estimate the DOC removal rate (R) using the equation:

$$R = \frac{DOC_i - DOC_f}{t_R} \qquad (7.1)$$

Where DOC_i and DOC_f are the initial (in the formation area) and final (in the Strait of Gibraltar) concentrations of dissolved organic carbon (DOC). In the blue box below it is explained how equation (7.1) is derived. From our data, we observed a decrease of 12 µM of DOC in the LIW from its formation area (DOC = 57 µM) up to the Strait of Gibraltar (DOC = 45 µM). Therefore, a removal rate of 0.92 µmol C L^{-1} yr^{-1} is obtained. Hansell et al. (2012) reported a DOC removal rate of 2.2 µmol C kg^{-1} yr^{-1} for the LIW after Santinelli et al. (2010). Note that the latter is higher because it was an estimate for the eastern MedSea including the Tyrrhenian Sea whereas our DOC removal rate includes the whole MedSea.

Alike, we calculated the removal rates of fluorescent dissolved organic matter (FDOM) in the intermediate waters. For peak T (protein–like substances) we observed a decline in

fluorescence intensity from the formation site (8.0 x 10^{-3} RU) to Gibraltar Strait (4.8 x 10^{-3} RU) resulting in a removal rate of 2.5 x 10^{-4} RU yr^{-1} using equation (7.1). Conversely, for peak C (humic–like substances) we observed an increase of the fluorescence intensity from 5.0 x 10^{-3} to 7.6 x 10^{-3} RU. Therefore, using equation (7.1) again, we obtained a net production rate of 2.0 x 10^{-4} RU yr^{-1} of humic–like substances along the route of the intermediate waters.

Once the removal (for DOC and peak–T) or net production (for peak –C) rates of these substances have been obtained (Table 7.2), we have calculated the corresponding turnover times with the equation:

$$\text{Turnover} = \frac{\widehat{DOC}}{R} \qquad (7.2)$$

Where $\widehat{DOC}$ is the mean concentration of DOC in the intermediate water and R is the removal rate calculated with equation (7.1). Equivalent equations can be written for peak–T and peak–C. See the blue box below for further explanations. The resulting turnover time of DOC (Table 7.2) was 4–fold the renewal time of the intermediate waters. Humic–like substances also showed turnover times longer than the renewal time of the water mass and also longer than the turnover time of the protein–like substances due to the higher bio–reactivity of the later (Table 7.2).

Table 7.2: Mean DOC concentration in µM C, humic–like and protein–like fluorescence intensity in Raman units (RU), removal rates of DOC and FDOM in RU per year and turnover times in years for the global ocean (taken from Catalá et al., 2015b) and for the intermediate waters along the salinity maxima of the MedSea (this PhD thesis). * taken from Hansell et al., 2009. Note that for protein–like peaks in the global ocean is referred to peak B and for the MedSea to peak T.

	Global Ocean	MedSea
Mean values		
DOC		50.2
Peak C	12.2 x 10^{-3}	6.6 x 10^{-3}
Peak M	9.2 x 10^{-3}	8.3 x 10^{-3}
Peak B/T	4.9 x 10^{-3}	6.1 x 10^{-3}
Removal rate		
DOC		–0.92
Peak C	2.8 x 10^{-5}	20 x 10^{-5}
Peak M	1.5 x 10^{-5}	21 x 10^{-5}
Peak B/T	–1.3 x 10^{-5}	–25 x 10^{-5}
Turnover time		
DOC	370*	55
Peak C	435	33
Peak M	610	40
Peak B/T	379	24

Catalá et al. (2015) have reported net removal/production rates of fluorescent DOM for the global ocean an order of magnitude lower than those in the MedSea, despite fluorescence intensities were of the same order (Table 7.2). Therefore, in the MedSea the removal processes occur faster than in the global ocean. Furthermore, turnover times were much shorter in the MedSea than in the global ocean, in accordance with the renewal time of the water masses involved in each case, 370 years for the global ocean (Catalá et al., 2016) and 13 years for the intermediate waters of the MedSea. In both cases the removal rate of peak M was higher than peak C (Table 7.2), suggesting a slower processing of the marine humic–like substances in the ocean.

Intermediate waters renewal time calculation

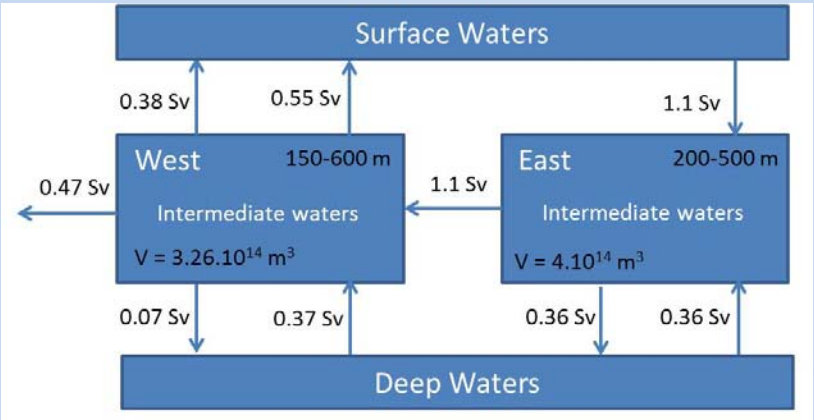

Simplified scheme representing surface, intermediate and deep waters of the MedSea. Inputs and outputs of the intermediate waters are included. Flows in Sv (10^6 m^3/s) from Powley et al., 2016.

The renewal time of the intermediate waters can be calculated as: $tR = \frac{V}{q}$ (7.3)

Where V is the total volume of the intermediate waters (East + West = 7.26 x 10^{14} m^3) and q is the total volume entering the intermediate water (1.83 Sv). The resulting renewal time for the intermediate waters of the MedSea is about 13 years.

DOC removal rate calculation

The mass balance of DOC in the intermediate water s of the MedSea can be expressed as:

$$\frac{d(DOC\,.\,V)}{dt} = \left(DOC_i - DOC_f\right) q - R \qquad (7.4)$$

Where DOC is the average concentration of DOC in the intermediate waters, DOC_i is the DOC concentration at the formation site of the LIW, DOC_f is the DOC concentration at the Strait of Gibraltar, V is the total volume, q is the volume entering the intermediate waters, and R is the DOC removal rate.

Rearranging equation (7.4): $\frac{dDOC}{dt} = \left(DOC_i - DOC_f\right).\frac{q}{V} - R$ (7.5)

Assuming that DOC is in steady state: $\frac{dDOC}{dt} = 0$ (7.6)

Substituting equation (7.6) in (7.5): $\left(DOC_i - DOC_f\right)\frac{q}{V} - R = 0$ (7.7)

Rearranging equation (7.7) $\mathrm{R} = (DOC_i - DOC_f).\frac{\mathrm{q}}{\mathrm{V}}$ (7.8)

Finally, considering equation 7.3, the DOC removal rate (equation 7.1) can be expressed as:

$$R = \frac{DOC_i - DOC_f}{tR}$$

In summary, to obtain accurate DOM removal rates, it is essential to estimated correctly the renewal times of the water masses involved.

2 What is the main driver of the AOU distribution in the intermediate layers of the MedSea?

It is well–recognized that, at the global ocean scale, the export flux of biogenic organic carbon from the epipelagic layer to the ocean interior is mainly due to sinking POC (80%), with DOC playing a secondary role (20%) (Ridgwell and Arndt, 2015). However, in the MedSea, as in other ocean oligotrophic regions, the contribution of DOC to the carbon export is higher, even surpassing that of sinking POC (Copin–Montégut and Avril, 1993; Carlson et al., 1994; Avril, 2002; Santinelli et al., 2013; Guyennon et al., 2015; Santinelli, 2015). DOC is exported to the ocean interior by two main processes: i) winter convective mixing of the DOC accumulated above the seasonal thermocline; and ii) downward transport during water masses formation, particularly during short scale violent storms within the ocean (Salat et al., 2010). In addition, biological mediated processes, as zooplankton diel vertical migration, have been reported as an important mechanism of total carbon export (POC + DOC) from the surface to the intermediate layers (Steinberg et al., 2008; Isla et al., 2015). The importance of winter mixing was first established by Carlson et al. (1994) in the Sargasso Sea. Out of the water mass formation areas, the thickness of the winter mixed layer is <150 m. Therefore, the epipelagic DOC found below 150 m is transported there either at the water mass formation sites or via solubilisation of sinking POC. Specifically, for the intermediate layer of the MedSea (200–500 m), the water mass injecting DOC in the Mediterranean Sea is the Levantine Intermediate Water (LIW).

In chapter 2 we estimated the contribution of DOC to the oxygen demand of the meso– and bathypelagic Mediterranean Sea regardless of water mass mixing. In the eastern basin, DOC was responsible for 66 ± 10% of the oxygen demand and in the western basin the contribution was reduced to just 24 ± 4%. This marked difference is related to the ultra–oligotrophy and higher DOC accumulation in the surface mixed layer of the eastern as compared with the western basin together with DOC in the eastern basin being less degraded than in the western basin (chapter 4). In chapter 6, we have followed the core–of–flow of the LIW, which is centred between 200 and 300 m in the eastern basin. Given that the sinking POC flux is weak compared with the injection of DOC during the formation of LIW (below 100 m DOC represents the 90% of the organic carbon annual flux, red values in box below) and that the water mass flows below 150 m, it is reasonable to assume that the DOC contribution to the oxygen consumption in the intermediate and deep layers are not going to be particularly affected either by the sinking POC flux or by the winter convective mixing of DOC.

In the western basin the picture changes and sinking POC was the main responsible for the oxygen consumption, despite being less exported than DOC (box below). In this basin the POC export below 100 m is higher (7.0 Mt C yr^{-1}) than in the eastern basin (2.6 Mt C yr^{-1}). We applied Martin's (1987) equation (see box in the next page) to test if our calculation of the DOC concentration attributed to the AOU was affected by this fact. We estimated that only 25% (1.75 Mt C yr^{-1}) of the sinking POC flux at 100 m reaches the core depth of the EIW in the western basin (400 m). In addition, these materials, with sinking rates ranging from 5 to more 200 m d^{-1} (Patara et al., 2009; Lee et al., 2009), present very low residence times, days to weeks, in the intermediate waters. Furthermore, Sempéré et al. (2000) estimated that the degradation rates of POC collected from a sediment trap at 200 m varied between 0.05 and 3.93 d^{-1}. This is consistent with the overall idea that sinking POC consists mainly on the labile products of synthesis and early degradation of plankton (Sarmiento and Gruber, 2006). In summary, the POC reaching 400 m will be quickly consumed. On the contrary, the DOC decay rate estimated in the first section of chapter 7.1 (0.92 µmol C L^{-1} yr^{-1}) and the time–scale for that decay (13 yr) indicate that the DOC pool removed along the core–of–flow of the LIW and EIW was in between the semi–labile (lifetime of 1.5 yr) and semi–refractory (lifetime of 20 yr) categories defined by Hansell (2013). So, the turnover times and removal processes of sinking POC and DOC are decoupled. In this sense, although it is true that the longitudinal gradient of AOU is mainly controlled by the sinking POC flux in the western basin, POC removal occurs at a completely different time–scale than DOC removal and, therefore, the "main picture" of the DOC–AOU relationship cannot be explained by the vertical flux of the labile POC but by the progressive removal of semi–refractory DOC.

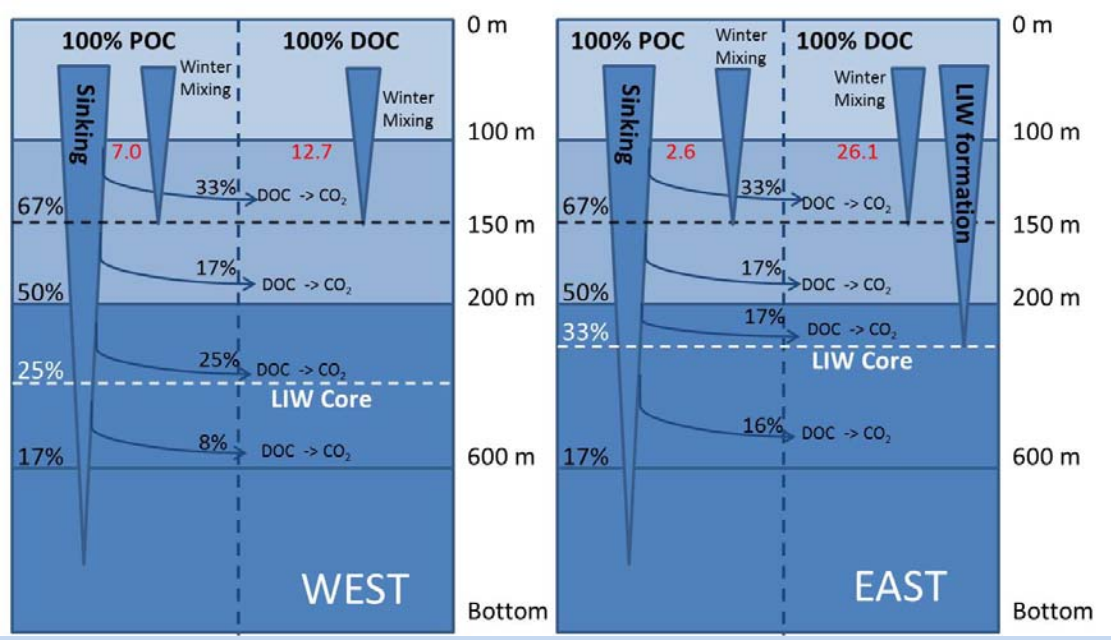

Scheme of DOC and POC export in the western (left panel) and eastern basin (right panel). Note that in the eastern basin an important input of DOC occurs during LIW formation, which does not exist in the western basin. Red values represent the annual flux of organic carbon export below 100 m in Mt C yr^{-1}. Fluxes taken from Guyennon et al. (2015).

POC export calculation

To calculate the POC flux to the intermediate layer of the MedSea we applied the equation proposed by Martin et al. (1987):

$$F(z) = F_0 \left(\frac{z}{z_0}\right)^{-b} \qquad (1)$$

where F (z) is the POC flux at depth (z), F_0 is the export flux at z_0 (usually the base of the euphotic zone, about 100 m) and b is the fitting parameter that modulates the POC flux decay with depth (b =1; Gogou et al., 2014).

Considering F_0 as the 100% of the POC produced in the epipelagic layer, the POC flux from 100 m reaching the core–of–flow of the LIW (300 m) and EIW (400 m) in the eastern and western basins, respectively, can be calculated:

$$F(400) = 100 \left(\frac{400}{100}\right)^{-1} = 25\%$$

$$F(300) = 100 \left(\frac{300}{100}\right)^{-1} = 33\%$$

Note that the 67% of the POC exported at 100 m reach 150 m, therefore by difference 33% has been degraded, through the biological carbon pump, and converted into DOM, which in turn go back to CO_2.

3 Which fluorescence units should we use?

Along the literature there is a lack of consensus regarding fluorescence intensity units as discussed previously by Catalá (2015) and Aparicio (2016). There are three general ways to normalize arbitrary fluorescence intensities: i) Raman units (RU) normalization: normalizes fluorescence intensities to the integrated area under the curve of the Raman peak of a MQ sample, measured the same day, at excitation (Ex) of 350 nm and emission (Em) between 365 to 430 nm, following the trapezoidal rule of integration (Lawaetz and Stedmon, 2009; Murphy et al., 2010); ii) quinine sulphate normalization (QSU in ppb): standarizes by dividing the fluorescence units of any Ex/Em wavelength pair by the QSU fluorescence intensity at Ex/Em 340–350/440–450 nm; and iii) the normalized fluorescence intensity units (NFIU): which comprises the measurement of the quinine sulphate fluorescence intensity at the same Ex/Em wavelengths of the peak of interest. All normalization procedures present pros and cons and can be more suitable depending on the specific circumstances of each study. While RU normalization was proposed as a universal normalization (Lawaetz and Stedmon, 2009), and was widely used in the last years (Jørgensen et al., 2011; Catalá, 2015; Aparicio, 2015; Yamashita et al., 2017) it was recently suggested that the Raman peak can change its location depending on the instrument, the lamp signal intensity and the time of use (Aparicio, 2015), preventing comparisons between works. On the other hand, QSU standardization needs a calibration of the spectrofluorometer against a sulphuric acid quinine sulphate solution, which implies the use of chemicals. The calibration curve obtained with the fluorescence measurements at an Ex/Em 350 nm/ 450 nm, provides a reliable information about possible signal drifts. In addition, a calibration curve procedure, favours the reproducibility of this analysis and thus makes feasible the comparison of data among different studies performed elsewhere (Yamashita and Tanoue, 2003; Aparicio, 2016). Nevertheless, this normalization is based on the fluorescence properties of peak C, and therefore it is not appropriate for the amino acid and protein region where quinine sulphate does not fluoresce. To overcome this limitation, a much appropriate alternative was proposed by Nieto–Cid et al. (2005) which standarized FDOM intensities against two standard solutions, a sulphuric acid quinine sulphate for humic–like substances and a tryptophan solution for protein–like compounds. Then, the fluorescence intensity is calibrated at the pair wavelengths where the peaks of interest fluoresce, making measurements more reliable, reproducible and comparable with other studies. In this PhD thesis we used both RU (chapter 2) and NFIU (chapter 5 and 6). In chapter 2 we run PARAFAC analysis for finding new fluorophores and we show the basin–wide fluorescence of dissolved organic matter (FDOM) distribution. In this case we decided to use

RU as in previous global FDOM distributions (Jørgensen et al., 2011, Catalá et al., 2015b) to make easier the comparisons. However, in chapter 5 and 6 we aim to answer to specific questions by means of fluorescence intensity peak peaking measurements which were calibrated with quinine sulphate and tryptophan solutions at the same Ex/Em wavelengths of the peak of interest is measured allowing us to express the fluorescence intensities in NFIU which are more correct, precise and also allow for direct comparisons with other studies.

4 What are the advantages and disadvantages of using classical fluorescence peaks or PARAFAC modelling?

The first attempts to use fluorescence data to characterize the bulk DOM was by means of the peak picking method. This is a quantitative procedure that records peak intensities within pre–defined regions of interest (Coble, 1996). Later parallel factor analysis (PARAFAC) has been used to decompose EEMs into components (Stedmon and Bro, 2008), as in chapters 3 and 5. Aside from PARAFAC, other statistical approaches have been applied to EEMs, such as principal components analysis (PCA) or, more recently, self–organizing maps (SOM) (Bieroza et al., 2011, 2012; Ejarque–Gonzalez and Butturini, 2014). SOM is an unsupervised artificial neural network algorithm that explores patterns and combined with correlation analysis identifies individual fluorescence components in large EEMs data sets. SOM clusterizes and reduces the dimensionality of EEMs without any assumption about data structure including outliers which are naturally integrated in the analysis (Bieroza et al., 2012). In this PhD thesis we used both PARAFAC modelling and classical fluorescence peak picking depending on the purpose. PARAFAC modelling was used with the main aim of identifying potential new fluorophores in the MedSea and peak picking for quantifying fluorescence intensities and inferring DOM biogeochemical cycling processes.

Peak picking at selected wavelengths presents the following advantages compared to PARAFAC:

1) It is less time consuming.
2) Samples are less exposed to the short wave UV radiation of the spectrofluorometer and, then, they are less prone to undergo photodegradation.
3) Repeated fluorescence measurements of each peak can be obtained without expending a lot of time making the analysis more robust and reproducible (Korak et al., 2014).
4) Results are more easily comparable with other studies because of the measurement at fixed wavelengths.

The main disadvantage of this methodology is that it is useless for finding new fluorophores or to detect deviations in the Ex/Em wavelength of the peaks among different data sets.

On the other hand, the major advantage of PARAFAC modelling is that it decomposes each sample into a group of components that are independent among them, so it constitutes an excellent tool for finding new fluorophores. In addition, in this PhD thesis, the PARAFAC components obtained from the HOTMIX samples correlated pretty well with the classical peaks defined by Coble (1996) and Stedmon et al. (2003). The results are summarized in Figure 7.1, where every PARAFAC component was correlated with the corresponding classical peak/peaks: C1, C2, C3 and C4 were correlated with peak C, peak M, peak T and peak E, respectively.

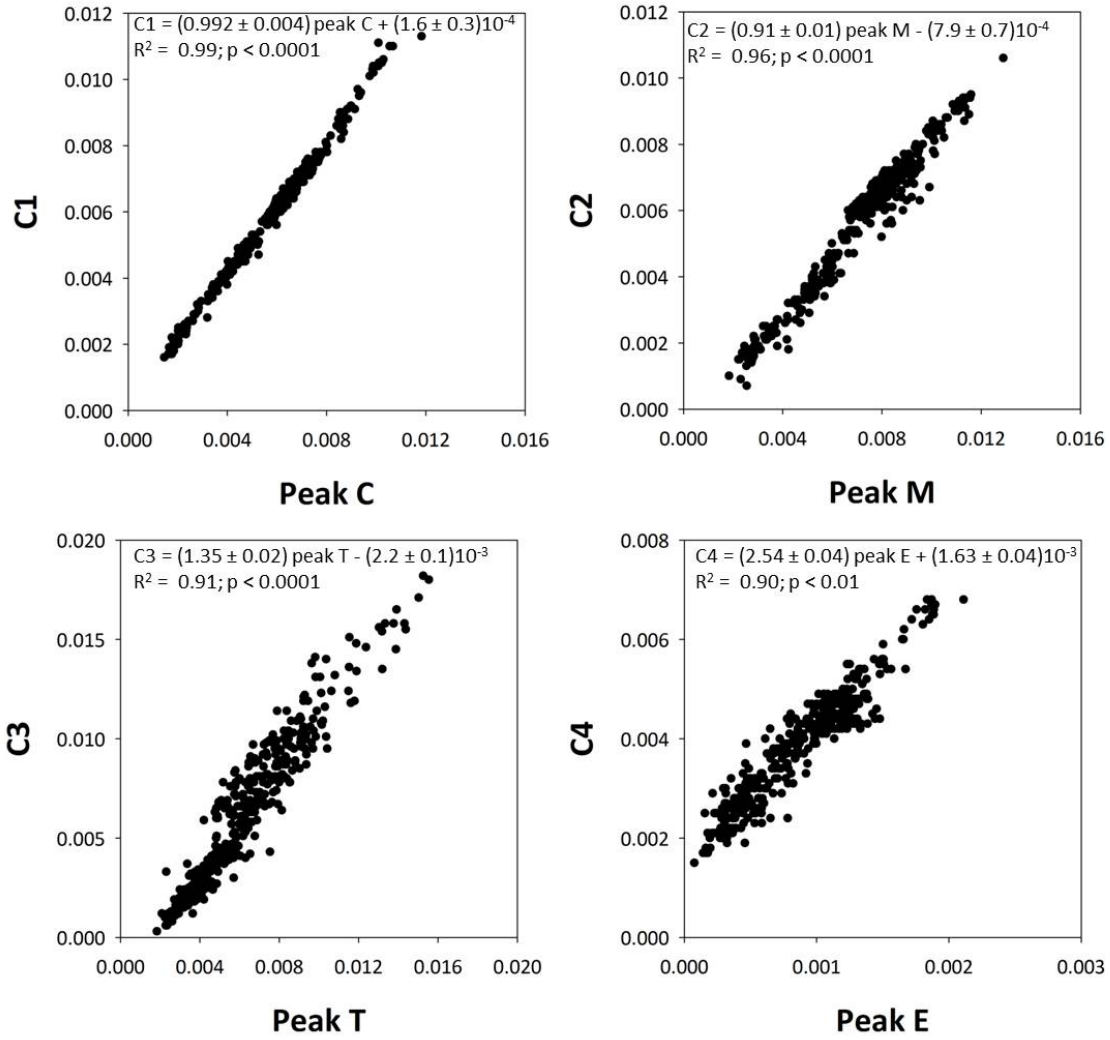

Figure 7.1: *Relationships between the classical peaks C, M, T and E and the forth components obtained by the PARAFAC analysis in chapter 3.Fluorescence in Raman units.*

The origin intercept and slope of the linear regression for C1–peak C (Figure 7.1a) and C2–peak M are close to zero and one, respectively, and R^2 is > 0.96 indicating that peaks C and M are very good proxies to the humic–like PARAFAC components C1 and C2. For C3 and C4, R^2 is high (> 0.90), but the origin intercept departs from zero and the slope from one. For the case of C3, this component is a mixture of peaks T (tryptophan) and B (tyrosine) (chapter 3 in page 101) whereas peak T represent only the fluorescence due to tryptophan. In the case of C4, this component is characterised by two maxima, one at Ex/Em 270 nm/510 nm and the second at Ex/Em 420 nm/510 nm (Figure 3.2 in page 101). The shorter wavelength peak is characterised by higher intensity than the second. Whereas the intensity of component C4 is referred to the shorter wavelength peak, peak E was defined at the longer wavelength peak.

PARAFAC modelling presents the following disadvantages:

1) PARAFAC assumes that all species absorb and emit light independently of each other. This model does not account for potential electronic interactions between chromophores that could lead to altered emission properties by charge transfer interaction (Sharpless and Blough, 2014). This is especially important to humic–like substances fluorescing in the visible range where red–shift of the emission maxima with increasing excitation wavelength, together with the monotonically–decreasing fluorescence quantum yields occurs. In addition, fluorescence of protein–like components have been reported to be quenched by the humic–like components (Wang et al., 2015).
2) As any statistical method, it can be applied only to large data set of samples.
3) Comparisons with other PARAFAC models are not precise, since sometimes fluorescence spectra of components identified in different studies did not overlap exactly and vary in their peak positions. To help on this issue, it has been developed the online tool OpenFluor, to compare the components obtained by a given PARAFAC model with every single PARAFAC model existing in the database, providing component equivalences (www.openfluor.org, Murphy et al., 2014). We should keep in mind that as discussed by Aparicio (2016) the equivalent PARAFAC components could not necessarily correspond to the same fluorophores or compounds despite presenting very similar spectra.

5 What type of isolation technique is more suitable for the molecular characterisation of marine DOM?

The isolation techniques commonly used for marine DOM concentration are solid phase extraction (SPE) and ultrafiltration (UF). The former is the technique of choice in chapter 4 for DOM isolation and desalting prior to molecular level characterization by high resolution Fourier–Transform Ion Cyclotron Resonance Spectrometry (FT–ICR–MS). Conversely, the latter is more suitable for studying DOM size fractions and it was used in chapter 6 for testing the size–reactivity continuum hypothesis.

UF techniques use membranes with a cut–off of, usually, 1 KDa for providing a fraction of high molecular weight (HMW, >1 KDa, retentate) and a fraction of low molecular weight (LMW, <1 KDa, filtrate or permeate). There are different types of tangential ultrafiltration methodologies, among them, the most used are: i) cross–flow ultrafiltration devices provided with membrane coils (Benner et al., 1992; Guo et al., 1996, 2000) used to process large–volume samples (10s to 1000s of litres) and ii) high–performance stirred UF cells operated with membrane filters (Simjouw et al., 2005) that processes low–volume samples (generally up to 5 litres). The UF methodology used will depend on the objective of the study, HMW isolation *versus* %HMW quantification. The first one consists on isolating as much HMW–DOC as possible for elemental, molecular and isotopic characterization from large volumes of seawater, regardless of its specific recovery percentage (Benner et al., 1992, Guo et al., 1996). This classical ultrafiltration mode needs additional desalting and freeze–dry steps, which reduce the recovery of the HMW fraction obtained to 10–30%. The second one is used in order to quantify the %HMW through measurements of time–series of permeate samples and the use of the ultrafiltration permeate model without paying attention to the retentate samples. The %HMW is calculated by difference and the reported values are between 35% and 55% (Guo et al., 1996, 2000; Guo and Santschi, 2007; Cai and Guo, 2009).

A pivotal factor to define the UF approach is the concentration factor (CF), i.e. the ratio between the sample volume and the retentate volume. For isolation, tangential ultrafiltration uses larger CF that implies larger time of ultrafiltration (several hours to days), resulting in a purer HMW fraction and also in an increase of the permeate concentration as concentration gradients increase in the retentate reservoir. The reason for this increase of the permeate concentration with the CF is still under debate. It could be due to either the permeation of LMW molecules or the breakthrough of HMW molecules (Guo et al., 2000). Evidences based on the use of standard macromolecules with known molecular weights and molecular probes

demonstrated that the increase of the permeate concentration with increasing CF was due to the permeation of LMW molecules rather that permeation of HMW molecules, which occurs only for those molecules with molecular weight close to the membrane cut–off (Guo et al., 2000; Guo and Santschi, 2007). On the contrary, when using lower CF, which is the usual when operating with stirring cells, it takes less time of processing (a few hours) and results in a pure LMW fraction, while the HMW fraction still contains a portion of LMW molecules. For the case of the samples processed in chapter 6, all of the HMW molecules will be inside the cell but mixed with up to 25% of the LMW molecules due to the low concentration factor used, CF = 4. The remaining 75% of the LMW molecules will pass to the elutriate fraction. Therefore, whereas the LMW fraction contains only LMW molecules, the HMW fraction contains a major proportion of HMW molecules and a minor proportion of LMW molecules. A higher CF would allow obtaining a purer HMW fraction because higher CF will minimize the retention of LWM molecules (Guo et al., 2000). For example, if the CF were 10, the HMW fraction could contain a maximum of 5% of LMW molecules, but the ultrafiltration time would increase.

In summary, in this PhD thesis we have used the up–to–date available DOM isolation techniques more suitable for the aim of each chapter allowing to obtain answers to the specific questions proposed in each chapter.

6 How representative of the bulk DOM is the SPE–DOM obtained by using PPL cartridges?

The performance of DOM–SPE implies specific extraction and elution conditions (pH = 2 and the use of methanol for elution). Such conditions can change the molecular composition of the original DOM through reactions, e.g. pH–dependent dissociation of high molecular weight (HMW) molecules into smaller ones (Li et al., 2017). This molecular dissociation would partly explain the apparent low molecular weight (MW) of the SPE–DOM analysed by FT–ICR–MS found in chapter 4.

As marine DOM comprises a complex mixture of compounds with a wide diversity in elemental composition, molecular weight, structure, reactivity, polarity and, thus, in their physico–chemical properties, no available resin will be able to recover quantitatively the DOM pool. For marine samples PPL cartridges (non–polar) showed the highest recovery and presented minimal extreme (too strong or too weak) DOM–sorbent interactions (Dittmar et al., 2008; Green et al., 2013; Raeke et al., 2016) and were the resins of choice for isolating the

DOM of the samples used in this thesis. On the contrary, polar or ion exchange resins showed the lowest marine DOM recovery (Li et al., 2017).

Further questions that need to be answered regarding SPE are: what type of molecules or compound groups are preferentially retained by the PPL cartridge? Are all those molecules recovered with methanol during the elution step? Is the methanol producing an overestimation of the DOC extraction efficiencies? Are PPL cartridges undergoing leaching processes?

SPE–DOM recoveries are very different regarding the type of sorbent used for the isolation (Dittmar et al., 2008; Li and Minor, 2015; Li et al., 2017). Moreover, significantly different DOC recoveries were found between freshwater and seawater samples. While freshwater samples DOC recoveries ranged from 61% to 82% (Perminova et al., 2014; Li et al., 2017), for marine samples ranged from 38% to 68% when PPL cartridges were used (Dittmar et al., 2008; Li et al., 2017). In chapter 4 we have reported an extraction efficiency of our MedSea samples of 47.3 ± 3.9%. Previous studies have associated this lower recovery to the average higher molecular size and higher polarity of the marine SPE–DOM compared to terrestrial SPE–DOM (Dittmar et al., 2008; Koch et al., 2005; Osterholz et al., 2016).

We sorted the samples used in this thesis by depth layers (chapter 4) and found that deep chlorophyll maximum (DCM) samples presented significantly lower DOC recoveries (Figure 7.2). It could be related with the less efficient elution reported for HMW compounds (Chen et al., 2016; Raeke et al., 2016). It is in good agreement since DOM in upper layers is considered, on average, hosting higher proportion of HMW compounds, such us polysaccharides, proteins and amino–sugars, which have been reported to be recovered less efficiently during PPL extraction (Chen et al., 2016).

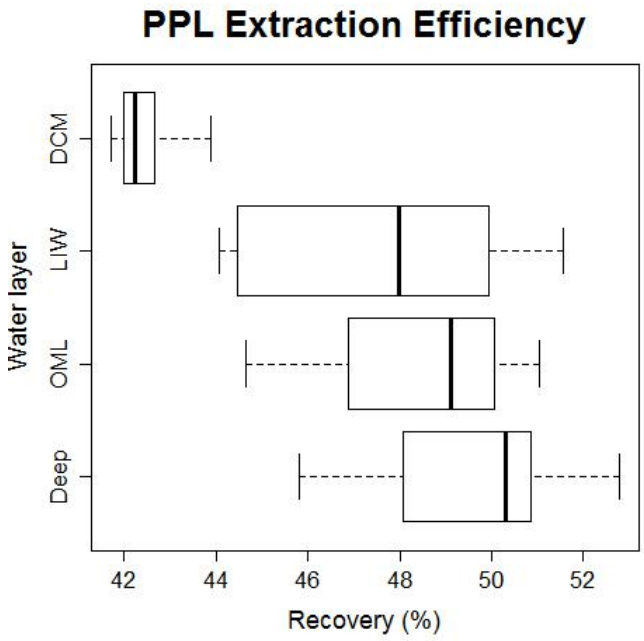

Figure 7. 2: *Box plot of the solid phase extraction efficiency using PPL cartridges and sorting the samples by depth layers. DCM (deep chlorophyll maximum), LIW (Levantine Intermediate Water), OML (oxygen minimum layer), Deep (samples collected below 1000 m).*

The coloured and fluorescent DOM (CDOM and FDOM) fractions also presented different extraction efficiencies between sorbent and sample types. While CDOM was scarcely recovered by PPL in river samples, marine samples presented a higher recovery of this fraction (Chen et al., 2016). Further, Li and Minor (2015) reported even higher CDOM recoveries relative to DOC recoveries for Lake Superior samples using C18 and SDB–XS (poly styrenedivinylbenzene copolymer) disks, suggesting a preferential retention of CDOM compounds. We tested the size dependence on the extraction efficiency of a seawater sample collected in the Mediterranean overflow at 241 m (Strait of Gibraltar) by passing through PPL cartridges the whole DOM (seawater filtered by GF/F), high molecular weight fraction and low molecular weight fractions (ultrafiltrated seawater with a 1KDa cut–off filter). The DOC recoveries were 59.6, 59.7 and 52.4% for the whole DOM, HMW and LMW, respectively. Thus, slightly lower recovery was found for the LMW fraction. We also tested the recovery of the CDOM and FDOM fractions using absorbance and fluorescence spectroscopy and we found that 83% of the carbon–specific Naeperian absorption coefficient at 254 nm (a254*; proxy for conjugated carbon double bonds) was extracted by PPL, suggesting a preferential extraction of the aromatic compounds. This recovery was higher to that found by Chen et al. (2016) in a marine surface sample collected off the south coast of the Korean peninsula (37.5%). More than 65% of the humic–like intensity was extracted using PPLs. However protein–like compounds were worst extracted, accounting for 48% of the original intensity. Note that

although these results are from just one sample, so they are not conclusive, they are in concordance with the findings from Chen et al. (2016) who reported higher recovery for humic–like than for the protein–like compounds. Chen et al. (2016) also proposed as an alternative reason for the apparent loss of FDOM in the SPE extracts conformation changes or charge transfer complexes DOM.

PPL extracts are enriched in rather oxygenated (high O/C ratio) and more unsaturated compounds (low H/C ratio) (Li et al., 2017; Raeke et al., 2016). Raeke et al. (2016) tested a set of 18 model compounds of a wide elemental compositional range to assess the extraction efficiency. As a result, very polar and small molecules, e.g. gallic acid or glutaric acid, were poorly extracted in freshwater using PPL cartridges, which is also in accordance to the results reported by Chen et al. (2016). Further, Raeke et al. (2016) found evidences for an incomplete elution of a fraction of apparent high molecular weight (HMW) in freshwaters rather than incomplete extraction. Sleighter and Hatcher (2008) compared the molecular composition of a whole water swamp sample with its respective C18 extract finding that the later missed mainly tannines and aliphatic amines/amides molecules.

On the other hand, DOC foreign to the sample could be added to the SPE extracts from residual amounts of methanol used during the elution step (Raeke et al., 2016) or resin leaching (Li et al., 2017) overestimating the SPE extraction efficiencies. Residual amounts of methanol after solvent evaporation is not detected by bulk DOC measurements, it would be necessary to use size–exclusion chromatography coupled to organic carbon detection to quantify the potential DOC contamination associated to the methanol as Raeke et al. (2016) performed for freshwater. These authors have reported SPE extraction efficiency overestimation by 1–60%. Leaching processes will produce increased apparent DOC recovery and lead to contamination peaks in the mass spectra of DOM extracts. Hydrocarbon–rich molecules leaching will produce higher average H/C and lower O/C ratios than the DOM alone. PPL cartridges have not shown leaching behaviour (Dittmar et al., 2008, Li et al., 2017). On the contrary, polar resins are prone to undergo leaching (Li et al., 2017).

Despite the limitations of SPE using PPLs, it has been chosen for the DOM isolation in this PhD thesis because, up to date, this methodology has provided the highest recovery, can isolate both polar and non polar DOM compounds, presents a good reproducibility and is easy to handle, especially in the field. In addition, this SPE–DOM provides a good representation of the original sample. In figure 4.2 (page 140) the distribution of SPE–DOC was parallel to the distribution of bulk DOM. Further, the molar C/N ratio of the SPE PPL extracts (21 ± 2 on

average) was comparable to that of the bulk DOM (17 ± 3 on average) (Dittmar et al., 2008). Moreover, SPE PPL extracts offer a similar mass spectrum to that of the bulk DOM sample, (Raeke et al., 2016). For all these reasons SPE using PPLs is very suitable for DOM isolation and subsequent molecular characterization by high–resolution mass spectrometry or NMR.

7 What is FT–ICR–MS really measuring?

Relevant side questions here would be: are all the DOM molecules extracted by SPE analyzed by FT–ICR–MS? Why the average molecular weight calculated from the FT–ICR–MS data is so low when compared with the bulk DOM? Are all molecules single charged?

The FT–ICR–MS analytical window is firstly limited by the SPE extraction efficiency, as discussed in the previous section, and secondly by the ionization efficiency technique. The widely used ionization technique for marine samples is the electrospray ionization (ESI) in negative mode. ESI is a “soft” ionization technique that generates ions in the mass range of 10 < m/z < 3000 without producing fragmentation of the molecules, thus molecules remains almost intact. Further, ESI only ionizes polar compounds (Kujawinski et al., 2002; Mopper et al., 2007; D’Andrilli et al., 2010). As ESI is a selective technique not all the molecules isolated by SPE will be ionized or present the same ionization efficiency (Reemtsma et al., 2008). For instance, hydrocarbons are not ionized by ESI (Kujawinski, 2002), saccharides presented low ionization efficiency (Raeke et al., 2016) and HMW molecules are less sensitively detected than LMW compounds (These and Reemtsma, 2003). However, carboxylic acids are preferentially ionized relative to nitrogen–containing compounds. This is in agreement with what we reported in chapter 4 being CRAM the second more abundant molecular group in our samples analyzed by ESI FT–ICR–MS.

FT–ICR–MS data of SPE–DOM provides lower molecular weight values compared to those reported for the bulk DOM sample (Koch et al., 2005; Hertkorn et al., 2013; Osterholz et al., 2014; Hansman et al., 2015; Chen et al., 2016). This could be explained by three main reasons: i) PPL extraction prior FT–ICR–MS analysis leads to a preferential loss of the biopolymer fraction of DOM (Chen et al., 2016), ii) the ESI FT–ICR–MS preferentially ionizes relatively small molecules, as well as compounds above 1000 amu are hardly visible as intact ions (These and Reemtsma, 2003; Mopper et al., 2007) and iii) the potential disaggregation of larger molecules stabilized by weak forces, non–covalently bonded complexes or associations during the electrospray ionization. The latter is in agreement with the hypothesis that HMW DOM, humic acids and colloidal natural organic matter are non–covalent aggregations of

smaller molecules (Mopper et al., 2007). Part of this decrease on SPE–DOM MW can be directly associated to the previous concentration step by SPE procedures, as suggested by Chen et al. (2016) results. These authors observed a decline in the MW from 1255 to 736 Da analyzing marine samples by size exclusion chromatography coupled to organic carbon detector (SEC–OCD) prior and after PPL extraction. They also reported a preferential loss of the biopolymer fraction (>10 KDa; polysaccharides, proteins and amino sugars) and the LMW fraction (MW < 350 Da; acids, alcohols, aldehydes, ketones, amino acids and sugars).

The charge of a compound detected by ESI–FT–ICR–MS can be determined by examining its isotopic distribution in the mass spectra. The first isotope peak (e. g. one ^{13}C instead of all ^{12}C) always occurs 1/z amu units after the original compound. In chapter 4, all the detected mass peaks are single charged based on isotopologues analysis ^{12}C–^{13}C.

Although FT–ICR–MS analysis provides unprecedented insights into the DOM molecular characterization, a lot of information cannot be interpreted yet. More than 400.000 peaks are detected in a mass spectrum, however we were able to assign molecular formula only to 3689 peaks (chapter 4).

It is noteworthy that in literature there is not a consensus about FT–ICR–MS data treatment. For instance, there are works that uses no normalized data (Hertkorn et al., 2013), normalizes using the sum of all detected peaks (Osterholz et al., 2014), sum of all peaks with intensities higher than 5 x noise (this PhD thesis), assigns 100% of the intensity to the base peak (Koch et al., 2014), or chose the 50 molecules with higher intensities (Schmidt et al., 2017). A consensus about FT–ICR–MS data would be desirable for comparison purposes.

8 Can CDOM and FDOM parameters reconcile with molecular features?

Optical and molecular measurements span different DOM fractions. While optical parameters only provide information about the coloured fraction of DOM, molecular level analysis refer to the solid extractable and ionizable DOM as it was discussed above.

In chapter 2 we have reported the absorption coefficients $a254$ and $a325$. The former is a proxy to the abundance of conjugated carbon double bonds that correlates with the concentration of DOC, and the latter is a proxy to the abundance of aromatic carbon double bonds (both directly proportional). Moreover, the spectral slope $S_{275–295}$ and the spectral slope ratio SR have been presented as proxies to the average molecular weight of the coloured fraction of DOM (inversely proportional). In chapter 3 we have identified the presence of well–

defined bio–refractory humic– and bio–labile protein–like fluorescence peaks or components and have calculated standard fluorescence indices such as BIX, HIX and QY(340), which have been traditionally used in freshwater aquatic systems but are much less common in marine systems in general and the open ocean in particular. BIX is suggested as a proxy to recently produced DOM from biological activity, however HIX and QY(340) are indicative of the presence of refractory material formed by diagenetic processes. Finally, in chapter 4 we have reported the abundance of compounds classes, such as the highly unsaturated compounds and the unsaturated aliphatic compounds, which has been suggested as proxies to bio–refractory and bio–labile compounds, respectively. We also reported DBE, AI_{mod} and Ideg, which are indicative of unsaturation, aromaticity and degraded DOM, respectively (directly correlated).

In Table 7.2 we summarize the agreements and disagreements between the information provided by the optical and molecular parameters reported in chapters 2, 3 and 4. Maximum values of *a*254 (chapter 2) and protein–like fluorescence intensity and BIX (chapter 3) have been recorded in the epipelagic layer, which is in good agreement with the highest values of unsaturated aliphatic compounds and lower values of average molecular weight and Ideg found in chapter 4. $S_{275–295}$ (chapter 2) presented the highest values at the surface layer, which is in accordance with the lowest average molecular weights found in chapter 4. On the contrary, the absorption parameter indicating aromaticity (*a*325) presented higher values at the surface and lower at depth that is in contrast with the molecular parameters indicating aromaticity (DBE and AI_{mod}; chapter 4), which were lower at surface and higher at depth. This is related to the counterintuitive behaviour of *a*325 in the MedSea suggesting consumption instead of production of aromatic compounds contrary to what happen in the global ocean, as discussed in chapter 3. HIX and QY(340), also indicative of aromaticity, presented lower values at the surface and higher at depth in agreement with the patterns found in chapter 4 for DBE and AI_{mod}. However, when only focused on the LIW an increase of *a*325 was observed in chapter 2 from East to West what is in accordance with the increase of peak M, peak E, HIX and QY(340) in chapter 3 and with the increase of AI_{mod}, DBE, highly unsaturated compounds and Ideg in chapter 4.

Focusing again on the LIW, in chapter 2 a decline of *a*254 westwards (from the formation site to the Gibraltar Strait) disagrees with the increase on DBE reported in chapter 4. This is likely due to the different DOM fractions considered by the optical and molecular techniques and/or to the different initial DOM in both basins. While the eastern basin is ultra–oligotrophic where DOM is accumulated because of the decoupling between DOM production and consumption, the western basin is less oligotrophic presenting higher primary production

and heterotrophic activity that could lead to structurally different initial DOM. In addition, the decline in $S_{275–295}$ observed in chapter 2 is in good agreement with the increase of average MW observed in chapter 4.

In summary, while some optical and molecular parameters are in perfect agreement, others face due to the different analytical window of both approaches.

Table 7.2: Summary of the optical and molecular parameters used as proxies of DOM chemical characteristics. Agreement or disagreement between the trends of optical and molecular parameters are also indicated. α and β represent a direct and inverse relationship, respectively. MW = molecular weight, *a*254 = absorption coefficient at 254 nm, *a325* = absorption coefficient at 325 nm, HIX = humification index, BIX = biological index, QY(340) = quantum yield at 340 nm, DBE = double bond equivalent, AI_{mod} = aromaticity index modified, Ideg = degradation index, UA = unsaturated aliphatic compounds and HU = highly unsaturated compounds.

Proxy	Conjugation	Aromaticity	Degradation	MW	Bio–labile	Bio–refractory
Optical parameter	*a*254 (α)	*a325*(α)	HIX, QY(340) (α)	$S_{275–295}$, SR (β)	BIX(α)	HIX, QY(340) (α)
Molecular parameter	DBE(α)	AI_{mod}, DBE (α)	Ideg(α)	MW(α)	UA(α)	HU(α)
Agreement	No	No	Yes	Yes	Yes	Yes

9 Can we infer molecular data from fluorescent measurements?

Firstly, in chapter 3 we have shown the dynamics and patterns of the fluorescent DOM in the whole MedSea, secondly in chapter 4 we have reported the DOM molecular features and finally in chapter 5 we have demonstrated that the DOM optical and molecular properties are intimately related. In addition, taking advantage of these relationships we established multiple linear regressions (Table 5.4; page 174) to estimate molecular indices from optical indices in the MedSea, which are more time demanding and costly to obtain.

These multiple regression models were fitted using the 29 samples for which we have peak C* and peak T* measurements from a Perkin–Elmer LS55 spectrometer and molecular parameters from FT–ICR–MS analyses (Table 5.4; page 174). The resulting regression equations can be employed to estimate the molecular parameters of the 331 samples collected in the MedSea during the cruise HOTMIX 2014 for the determination of peak C* and peak T* fluorescence intensities. Since the latter were performed with a JY–Horiba Spex Fluoromax–4 spectrofluorometer, the measurements of the 29 samples determined with both spectrofluorometers were used to intercalibrate both instruments ($R^2 = 0.88$, $p < 0.0001$ for peak C and $R^2 = 0.77$, $p < 0.0001$ for peak T). Using θ, peak C* and peak T* we were then able to estimate some molecular indices (DBE, Ideg, unsaturated aliphatic compounds and CRAM)

and build up detailed maps of their distribution for the whole MedSea. The model goodness is confirmed in Figure 7.3, where we compared the results from the regression models and the measured values using linear regressions. Note that these relationships do not imply a direct causation but the existence of a common cause or causes of variation between optical and molecular indices. The model goodness is also confirmed in Figure 7.4 where colored dots represent measured values for the molecular parameters.

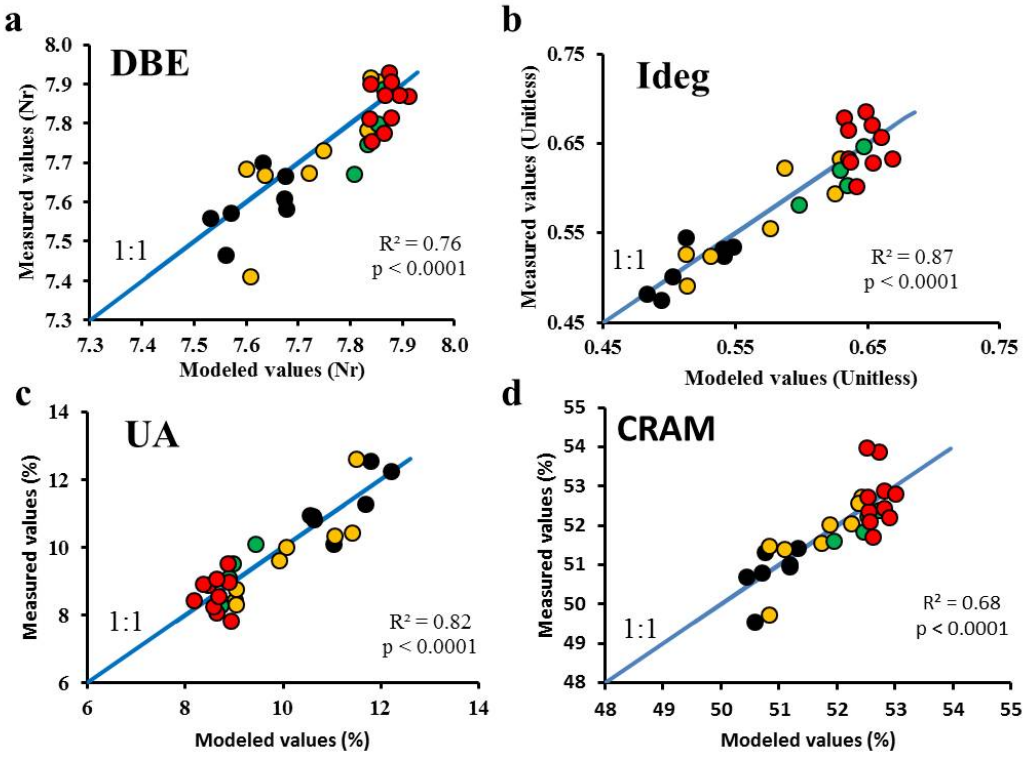

Figure 7.3: *Comparison of modeled and measured molecular DOM properties. The modeled values were calculated using the multiple linear regression models and the measured values were obtained from the FT–ICR–MS analysis for (a) double bond equivalent (DBE), (b) degradation index (Ideg), (c) unsaturated aliphatic compounds and (d) carboxyl–rich alicyclic molecules (CRAM). Colored dots represent samples collected at different layers, deep chlorophyll maximum (black), Levantine intermediate water (yellow), oxygen minimum layer (green) and deep waters (red). Note that there is a random deviation from the 1:1 line (blue line). For the CRAM regression (plot d) red dots with higher measured values correspond with samples collected at station 1 and the black and yellow dots, with lower measured values, correspond with samples collected at station 7 and 1, respectively.*

These results indicate that the calculated models work well for the MedSea ($R^2 > 0.68$, $p < 0.0001$) and reliable detailed spatial molecular information from FDOM measurements can be gained.

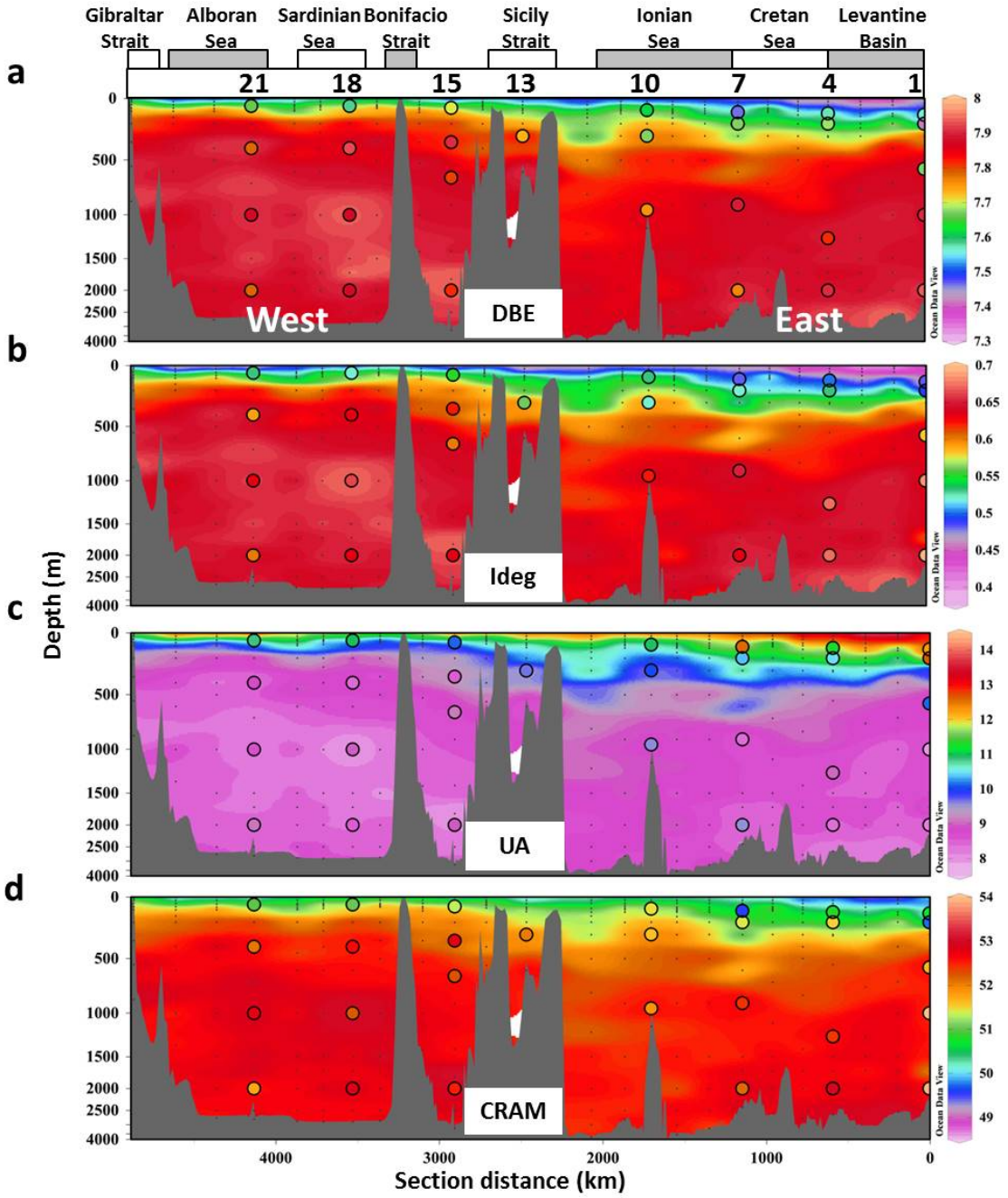

***Figure 7.4**: Distributions of the estimated molecular parameters. (a) double bond equivalent (DBE) in number, (b) degradation index (Ideg) unitless, (c) unsaturated aliphatic compounds (UA) in % and (d) carboxyl–rich alicyclic molecules (CRAM) in % for the whole Mediterranean Sea determined from fluorescence measurements. Colored dots represent molecular parameters calculated by FT–ICR–MS analysis. Figure created using Ocean Data View (version 4.7.8, R. Schlitzer, 2016. http://odv.awi.de).*

Regarding these distributions (Figure 7.4), the upper layer of the eastern basin showed SPE–DOM with lower DBE, degradation state and CRAM than the western basin. However, it presented more abundance of unsaturated aliphatic compounds. Note that for the CRAM distribution (Figure 7.4d) the mismatches in the samples collected at station 1 (200, 1000 and

2000 m) and station 7 (110 m) were due to the fact that in the scatter plot (Figure 7.3d) the points exhibited a stronger divergence from the linear regression line.

Although differences between measured and modeled values of %CRAM in these samples were apparent, the other molecular parameters (Ideg, AImod, DBE) did not show such differences. To check if these samples could lead to a different result in the model, we discarded these points to obtain a new model and new estimated values. Comparing the results from the two models, the new one presented slightly lower values in some deep regions but the estimated values patterns were not different than in the former one. For this reason we decided to keep these samples into the model.

In summary, we have established, for the first time, a useful tool to exploit optical measurements as a proxy to estimate molecular parameters in open ocean waters.

10 Is there a "master variable" for marine DOM characterization in the MedSea?

A common key variable along almost all chapters of this PhD thesis is the apparent oxygen utilization (AOU). AOU represents the cumulative oxygen consumption from the formation area to the study section and it is considered as a good proxy for ageing and net community respiration (community respiration minus the autotrophic oxygen production).

In chapter 2 AOU helped us to reflect the differential ageing of the 19 water masses intercepted during the HOTMIX cruise. In addition, in chapters 2 and 3 AOU was one of the key variables explaining the basin–scale distribution of DOC and DOM optical characteristics (CDOM and FDOM) in surface waters. While in chapter 2 AOU was the variable that most explained the DOC and $a254$ variability in the epipelagic layer, in chapter 3 explained the variability of humic–like peak M fluorescence, HIX and QY(340). Further, for the meso– and bathypelagic layers AOU was included as a biogeochemical parameter into the multiple regression models to generate a mixing–biogeochemical model of DOC, CDOM and FDOM. AOU improved the explained variance for all variables except peak E and allowed to discern the variability associated to the local mineralization processes to that associated to the water mass mixing and basin–scale mineralization.

In chapter 4 AOU was used as an environmental variable in the PCoA and it was plotted close to molecular parameters related with degraded DOM. Moreover, the correlation between AOU and degradation index (Ideg) suggested a degradation ratio per oxygen consumption unit faster in the MedSea than in the Atlantic Ocean.

In chapter 6 AOU allowed us to test and corroborate the size reactivity continuum (SRC) and the microbial carbon pump (MCP) models in the field. Further, AOU was used to estimate the contribution of DOC in the oxygen consumption and reveal which size fraction accounts more for this consumption. In addition we found an increase of humic–like and a decrease of protein–like fluorescence intensity with AOU for all DOM size fractions.

Chapter 8
General Conclusions

General conclusions

1) Basin–wide variability of dissolved organic carbon (DOC), absorption coefficient of coloured dissolved organic matter (CDOM) at 254 nm (a254), marine humic–like fluorescence (peak M) and fluorescence indices (biological index (BIX), humification index (HIX) and fluorescence quantum yield (QY(340)) in the Mediterranean Sea is mainly explained by cumulative net community respiration (AOU) in the epipelagic Mediterranean Sea. On the contrary, the variability of the absorption coefficient of CDOM at 325 nm (a325), protein–like (peak T) and soil fulvic acids (peak E) fluorescence are mainly dictated by potential temperature for the former and by prokaryote heterotrophic abundance, for the two later.

2) Basin–wide distributions of DOC, CDOM and fluorescent DOM (FDOM) in the meso– and bathypelagic layers of the Mediterranean Sea are driven by water mass mixing and basin–scale mineralization processes. Considering eastern and western basin separately, the former is more influenced by water mass mixing processes which are linked to its ultra–oligotrophy.

3) Local DOC mineralization processes contribute to 66 ± 10% of the oxygen demand in the eastern basin and to only 24 ± 4% in the western basin of the Mediterranean Sea.

4) The molecular composition of DOM in the Mediterranean Sea is controlled mainly by the origin of the water mass and DOM mineralization using AOU as a canonical variable. Mediterranean Sea outflow showed different DOM molecular composition compared with the surface Atlantic inflow.

5) A link between DOM optical and molecular properties has been found, for the first time in ocean water, corroborating previous results previously obtained in coastal, estuarine and freshwater.

6) Following the microbial degradation of DOM along the salinity maximum, characteristic of the intermediate waters of the Mediterranean Sea, and applying for the first time an *in situ* approach, we demonstrated that the larger fraction of DOM (HMW DOM) was exclusively responsible for the oxygen consumption in intermediate waters, validating the size–reactivity continuum hypothesis in the field.

7) The renewal time of the intermediate waters of the Mediterranean Sea is 13 years and the removal rate of DOC in those waters is 0.99 μM yr^{-1}.

8) Along this PhD thesis we have found evidences for the validity of the size–reactivity–continuum and microbial carbon pump hypotheses through the results obtained from CDOM, FDOM, molecular level and DOM size–fractionation analysis.

References

Adloff, F., Somot, S., Sevault, F., Jordà, G., Aznar, R., Déqué, M., Herrmann, M., Marcos, M., Dubois, C., Padorno, E., Alvarez–Fanjul, E., Gomis, D., 2015. Mediterranean Sea response to climate change in an ensemble of twenty first century scenarios. Clim. Dyn. 45, 2775–2802. doi: 10.1007/s00382–015–2507–3.

Aluwihare, L.I., Meador, T.B., 2008. Chemical composition of marine dissolved organic nitrogen, in: Capone, D.G., Bronk, D.A., Mulholland, M.R., Carpenter, E.J. (Eds.), Nitrogen in the Marine Environment. Academic Press, pp. 95–140.

Aluwihare, L.I., Repeta, D.J., Chen, R.F., 1997. A major biopolymeric component to dissolved organic carbon in surface sea water. Nature 387, 166. doi: 10.1038/387166a0.

Aluwihare, L.I., Repeta, D.J., Pantoja, S., Johnson, C.G., 2005. Two Chemically Distinct Pools of Organic Nitrogen Accumulate in the Ocean. Science 308, 1007 LP–1010. doi: 10.1126/science.1108925.

Álvarez–Salgado, X.A., Nieto–Cid, M., Álvarez, M., Pérez, F.F., Morin, P., Mercier, H., 2013. New insights on the mineralization of dissolved organic matter in central, intermediate, and deep water masses of the northeast North Atlantic. Limnol. Oceanogr. 58, 681–696. doi: 10.4319/lo.2013.58.2.0681.

Álvarez, M., Brea, S., Mercier, H., Álvarez–Salgado, X.A., 2014. Mineralization of biogenic materials in the water masses of the South Atlantic Ocean. I: Assessment and results of an optimum multiparameter analysis. Prog. Oceanogr. 123, 1–23. doi: 10.1016/j.pocean.2013.12.007.

Amon, R.M.W., Benner, R., 1996. Bacterial utilization of different size classes of dissolved organic matter. Limnol. Oceanogr. 41, 41–51. doi: 10.4319/lo.1996.41.1.0041.

Amon, R.M.W., Benner, R., 1994. Rapid cycling of high–molecular–weight dissolved organic matter in the ocean. Nature 369, 549. doi: 10.1038/369549a0.

Anderson, L.A., 1995. On the hydrogen and oxygen content of marine phytoplankton. Deep Sea Res. Part I Oceanogr. Res. Pap. 42, 1675–1680. doi: 10.1016/0967–0637(95)00072–E.

Anderson, L.A., Sarmiento, J.L., 1994. Redfield ratios of remineralization determined by nutrient data analysis. Global Biogeochem. Cycles 8, 65–80. doi: 10.1029/93GB03318.

Andrew, A.A., Del Vecchio, R., Subramaniam, A., Blough, N. V., 2013. Chromophoric dissolved organic matter (CDOM) in the Equatorial Atlantic Ocean: Optical properties and their relation to CDOM structure and source. Mar. Chem. 148, 33–43. doi: 10.1016/j.marchem.2012.11.001.

Andrie, C., Merlivat, L., 1988. Tritium in the western Mediterranean Sea during 1981 Phycemed cruise. Deep Sea Res. Part A. Oceanogr. Res. Pap. 35, 247–267. doi: 10.1016/0198–0149(88)90039–8.

Antia, N.J., Harrison, P.J., Oliveira, L., 1991. The role of dissolved organic nitrogen in phytoplankton nutrition, cell biology and ecology. Phycologia 30, 1–89. doi: 10.2216/i0031–8884–30–1–1.1.

Aparicio, F.L., 2016. Tracing the dynamics of dissolved organic matter in marine systems exposed to natural and experimental perturbations. PhD Thesis, Universitat Politècnica de Catalunya.

Aparicio, F.L., Nieto–Cid, M., Borrull, E., Calvo, E., Pelejero, C., Sala, M.M., Pinhassi, J., Gasol, J.M., Marrasé, C., 2016. Eutrophication and acidification: Do they induce changes in the dissolved organic matter dynamics in the coastal Mediterranean Sea? Sci. Total Environ. 563–564, 179–189. doi: 10.1016/j.scitotenv.2016.04.108.

Aparicio, F.L., Nieto–Cid, M., Borrull, E., Romero, E., Stedmon, C.A., Sala, M.M., Gasol, J.M., Ríos, A.F., Marrasé, C., 2015. Microbially–mediated fluorescent organic matter transformations in the deep ocean. Do the chemical precursors matter? Front. Mar. Sci. 2, 106. doi: 10.3389/fmars.2015.00106.

Aparicio, F.L., Nieto–Cid, M., Calvo, E., Pelejero, C., López–Sanz, À., Pascual, J., Salat, J., Sánchez–Pérez, E.D., La Fuente, P. De, Gasol, J.M., Marrasé, C., 2017. Wind–induced changes in the dynamics of fluorescent organic matter in the coastal NW Mediterranean. Sci. Total Environ. 609, 1001–1012. doi: 10.1016/j.scitotenv.2017.07.170.

Arakawa, N., Aluwihare, L.I., Simpson, A.J., Soong, R., Stephens, B.M., Lane–Coplen, D., 2017. Carotenoids are the likely precursor of a significant fraction of marine dissolved organic matter. Sci. Adv. 3, e1602976. doi: 10.1126/sciadv.1602976.

Arístegui, J., Duarte, C.M., Agustí, S., Doval, M., Álvarez–Salgado, X.A., Hansell, D.A., 2002. Oceanography: Dissolved organic carbon support of respiration in the dark ocean. Science 298, 1967. doi: 10.1126/science.1076746.

Arrieta, J.M., Mayol, E., Hansman, R.L., Herndl, G.J., Dittmar, T., Duarte, C.M., 2015. Ocean chemistry: Dilution limits dissolved organic carbon utilization in the deep ocean. Science. 348, 331–333. doi: 10.1126/science.1258955.

Arrigo, K.R., Brown, C.W., 1996. Impact of chromophoric dissolved organic matter on UV inhibition of primary productivity in the sea. Mar. Ecol. Prog. Ser. 140, 207–216. doi: 10.3354/meps140207.

Artegiani, A., Gacic, M., Michelato, A., Kovacevic, V., Russo, A., Paschini, E., Scarazzato, P., Smircic, A., 1993. The Adriatic Sea hydrography and circulation in spring and autumn (1985–1987). Deep Sea Res. Part II: Top. Stud. Oceanogr. 40, 1143–1180. doi: 10.1016/0967–0645(93)90065–U.

Astraldi, M., Balopoulos, S., Candela, J., Font, J., Gacic, M., Gasparini, G., Manca, B., Theocharis, A., Tintoré, J., 1999. The role of straits and channels in understanding the characteristics of Mediterranean circulation. Progr. Oceanogr. 44, 65–108. doi: 10.1016/S0079–6611(99)00021–X.

Astraldi, M., Conversano, F., Civitarese, G., Gasparini, G.P., Ribera d'Alcalà, M., Vetrano, A., 2002. Water mass properties and chemical signatures in the central Mediterranean region. J. Mar. Syst. 33–34, 155–177. doi: 10.1016/S0924–7963(02)00057–X.

Bauer, J.E., 2002. Chapter 8 – Carbon Isotopic Composition of DOM, in: Hansell, D.A., Carlson, C.A. (Eds.), Biogeochemistry of Marine Dissolved Organic Matter. Academic Press, San Diego, pp. 405–453. doi: 10.1016/B978–012323841–2/50010–5.

Beaupré, S.R., 2015. Chapter 6 – The Carbon Isotopic Composition of Marine DOC, in: Hansell, D.A., Carlson, C.A. (Eds.), Biogeochemistry of Marine Dissolved Organic Matter. Academic Press, San Diego, pp. 335–368. doi: 10.1016/B978–0–12–405940–5.00006–6.

Beaupré, S.R., Druffel, E.R.M., 2012. Photochemical reactivity of ancient marine dissolved organic carbon. Geophys. Res. Lett. 39, L18602. doi: 10.1029/2012GL052974.

Belkin, I.M., 2009. Rapid warming of Large Marine Ecosystems. Prog. Oceanogr. 81, 207–213. doi: 10.1016/j.pocean.2009.04.011.

Benner, R., 2002. Chapter 3 – Chemical Composition and Reactivity, in: Hansell, D.A., Carlson, C.A. (Eds.), Biogeochemistry of Marine Dissolved Organic Matter. Academic Press, San Diego, pp. 59–90. doi: 10.1016/B978–012323841–2/50005–1.

Benner, R., Amon, R.M.W., 2015. The size–reactivity continuum of major bioelements in the ocean. Ann. Rev. Mar. Sci. 7, 185–205. doi: 10.1146/annurev–marine–010213–135126.

Benner, R., Biddanda, B., 1998. Photochemical transformations of surface and deep marine dissolved organic matter: Effects on bacterial growth. Limnol. Oceanogr. 43, 1373–1378. doi: 10.4319/lo.1998.43.6.1373.

Benner, R., Biddanda, B., Black, B., McCarthy, M., 1997. Abundance, size distribution, and stable carbon and nitrogen isotopic compositions of marine organic matter isolated by tangential–flow ultrafiltration. Mar. Chem. 57, 243–263. doi: 10.1016/S0304–4203(97)00013–3.

Benner, R., Kaiser, K., 2003. Abundance of amino sugars and peptidoglycan in marine particulate and dissolved organic matter. Limnol. Oceanogr. 48, 118–128. doi: 10.4319/lo.2003.48.1.0118.

Benner, R., Pakulski, J.D., McCarthy, M., Hedges, J.I., Hatcher, P.G., 1992. Bulk chemical characteristics of dissolved organic matter in the ocean. Science. 255, 1561–1564. doi: 10.1126/science.255.5051.1561.

Bergamasco, A., Malanotte–Rizzoli, P., 2010. The circulation of the Mediterranean Sea: a historical review of experimental investigations. Adv. Oceanogr. Limnol. 1, 11–28. doi: 10.1080/19475721.2010.491656.

Berman, T., Bronk, D.A., 2003. Dissolved organic nitrogen: a dynamic participant in aquatic ecosystems. Aquat. Microb. Ecol. 31, 279–305. doi: 10.3354/ame031279.

Bensi, M., Rubino, A., Cardin, V., Hainbucher, D., Mancero–Mosquera, I., 2013. Structure and variability of the abyssal water masses in the Ionian Sea in the period 2003–2010. J. Geophys. Res. Ocean. 118, 931–943. doi: 10.1029/2012JC008178.

Béthoux, J.P., Morin, P., Chaumery, C., Connan, O., Gentili, B., Ruiz–Pino, D., 1998. Nutrients in the Mediterranean Sea, mass balance and statistical analysis of concentrations with respect to environmental change. Mar. Chem. 63, 155–169. doi: 10.1016/S0304–4203(98)00059–0.

Bethoux, J.P., Tailliez, D., 1994. Deep–Water in the Western Mediterranean Sea, Yearly Climatic Signature and Enigmatic Spreading, in: Malanotte–Rizzoli, P., Robinson, A.R. (Eds.), Ocean Processes in Climate Dynamics: Global and Mediterranean Examples. Springer Netherlands, Dordrecht, pp. 355–369. doi: 10.1007/978–94–011–0870–6_15.

Bianchi, T.S., Osburn, C., Shields, M.R., Yvon–Lewis, S., Young, J., Guo, L., Zhou, Z., 2014. Deepwater Horizon oil in Gulf of Mexico waters after 2 years: transformation into the dissolved organic matter pool. Environ. Sci. Technol. 48, 9288–97. doi: 10.1021/es501547b.

Biddanda, B., Benner, R., 1997. Carbon, nitrogen, and carbohydrate fluxes during the production of particulate and dissolved organic matter by marine phytoplankton. Limnol.

Oceanogr. 42, 506–518. doi: 10.4319/lo.1997.42.3.0506.

Bieroza, M., Baker, A., Bridgeman, J., 2012. Exploratory analysis of excitation–emission matrix fluorescence spectra with self–organizing maps—A tutorial. Educ. Chem. Eng. 7, e22–e31. doi: 10.1016/j.ece.2011.10.002.

Bieroza, M., Baker, A., Bridgeman, J., 2011. Classification and calibration of organic matter fluorescence data with multiway analysis methods and artificial neural networks: an operational tool for improved drinking water treatment. Environmetrics 22, 256–270. doi: 10.1002/env.1045.

Bracchini, L., Dattilo, A.M., Hull, V., Loiselle, S.A., Nannicini, L., Picchi, M.P., Ricci, M., Santinelli, C., Seritti, A., Tognazzi, A., Rossi, C., 2010. Spatial and seasonal changes in optical properties of autochthonous and allochthonous chromophoric dissolved organic matter in a stratified mountain lake. Photochem. Photobiol. Sci. 9, 304–314. doi: 10.1007/s00027–010–0150–y.

Bray, J.R., Curtis, J.T., 1957. An ordination of the upland forest communities of southern Wisconsin. Ecol. Monogr. 27, 326–349. doi: 10.2307/1942268.

Bricaud, A., Babin, M., Claustre, H., Ras, J., Tièche, F., 2010. Light absorption properties and absorption budget of Southeast Pacific waters. J. Geophys. Res. Ocean. 115, C08009. doi: 10.1029/2009JC005517.

Bricaud, A., Ciotti, A.M., Gentili, B., 2012. Spatial–temporal variations in phytoplankton size and colored detrital matter absorption at global and regional scales, as derived from twelve years of SeaWiFS data (1998–2009). Global Biogeochem. Cycles 26, GB1010. doi: 10.1029/2010GB003952.

Bro, R., 1997. PARAFAC. Tutorial and applications. Chemom. Intell. Lab. Syst. 38, 149–171. doi: 10.1016/S0169–7439(97)00032–4.

Broecker, W.S., 1974. “NO”, a conservative water–mass tracer. Earth Planet. Sci. Lett. 23, 100–107. doi: 10.1016/0012–821X(74)90036–3.

Bronk, D.A., 2002. Chapter 5 – Dynamics of DON, in: Hansell, D.A., Carlson, C.A. (Eds.), Biogeochemistry of Marine Dissolved Organic Matter. Academic Press, San Diego, pp. 153–247. doi: 10.1016/B978–012323841–2/50007–5.

Bronk, D.A., Glibert, P.M., Ward, B.B., 1994. Nitrogen uptake, dissolved organic nitrogen release, and new production. Science 265, 1843–1846. doi: 10.1126/science.265.5180.1843.

Cai, Y., Guo, L., 2009. Abundance and variation of colloidal organic phosphorus in riverine, estuarine, and coastal waters in the northern Gulf of Mexico. Limnol. Oceanogr. 54, 1393–1402. doi: 10.4319/lo.2009.54.4.1393.

Cardin, V., Bensi, M., Pacciaroni, M., 2011. Variability of water mass properties in the last two decades in the South Adriatic Sea with emphasis on the period 2006–2009. Cont. Shelf Res. 31, 951–965. doi: 10.1016/j.csr.2011.03.002.

Cardin, V., Civitarese, G., Hainbucher, D., Bensi, M., Rubino, A., 2015. Thermohaline properties in the Eastern Mediterranean in the last three decades: Is the basin returning to the pre–EMT situation? Ocean Sci. 11, 53–66. doi: 10.5194/os–11–53–2015.

Carlson, C.A., 2002. Chapter 4 – Production and Removal Processes, in: Hansell, D.A., Carlson, C.A. (Eds.), Biogeochemistry of Marine Dissolved Organic Matter. Academic Press, San Diego, pp. 91–151. doi: 10.1016/B978–012323841–2/50006–3.

Carlson, C.A., Ducklow, H.W., Michaels, A.F., 1994. Annual flux of dissolved organic carbon from the euphotic zone in the northwestern Sargasso Sea. Nature 371, 405–408. doi: 10.1038/371405a0.

Carlson, C.A., Hansell, D.A., 2015. Chapter 3 – DOM Sources, Sinks, Reactivity, and Budgets, in: Hansell, D.A., Carlson, C.A. (Eds.), Biogeochemistry of Marine Dissolved Organic Matter. Academic Press, San Diego, pp. 65–126. doi: 10.1016/B978–0–12–405940–5.00003–0.

Carlson, C.A., Hansell, D.A., Nelson, N.B., Siegel, D.A., Smethie, W.M., Khatiwala, S., Meyers, M.M., Halewood, E., 2010. Dissolved organic carbon export and subsequent remineralization in the mesopelagic and bathypelagic realms of the North Atlantic basin. Deep. Res. Part II Top. Stud. Oceanogr. 57, 1433–1445. doi: 10.1016/j.dsr2.2010.02.013.

Carr, M.–E., Friedrichs, M.A.M., Schmeltz, M., Noguchi Aita, M., Antoine, D., Arrigo, K.R., Asanuma, I., Aumont, O., Barber, R., Behrenfeld, M., Bidigare, R., Buitenhuis, E.T., Campbell, J., Ciotti, A., Dierssen, H., Dowell, M., Dunne, J., Esaias, W., Gentili, B., Gregg, W., Groom, S., Hoepffner, N., Ishizaka, J., Kameda, T., Le Quéré, C., Lohrenz, S., Marra, J., Mélin, F., Moore, K., Morel, A., Reddy, T.E., Ryan, J., Scardi, M., Smyth, T., Turpie, K., Tilstone, G., Waters, K., Yamanaka, Y., 2006. A comparison of global estimates of marine primary production from ocean color. Deep Sea Res. Part II Top. Stud. Oceanogr. 53, 741–770. doi: 10.1016/j.dsr2.2006.01.028.

Catalá, T.S., 2015. Insights in the microbial carbon pump in the global ocean with spectroscopic techniques. PhD Thesis, Universidad de Granada.

Catalá, T.S., Álvarez–Salgado, X.A., Otero, J., Iuculano, F., Companys, B., Horstkotte, B., Romera–Castillo, C., Nieto–Cid, M., Latasa, M., Morán, X.A.G., Gasol, J.M., Marrasé, C., Stedmon, C.A., Reche, I., 2016. Drivers of fluorescent dissolved organic matter in the global epipelagic ocean. Limnol. Oceanogr. 61, 1101–1119. doi: 10.1002/lno.10281.

Catalá, T.S., Reche, I., Álvarez, M., Khatiwala, S., Guallart, E.F., Benítez–Barrios, V.M., Fuentes–Lema, A., Romera–Castillo, C., Nieto–Cid, M., Pelejero, C., Fraile–Nuez, E., Ortega–Retuerta, E., Marrasé, C., Álvarez–Salgado, X.A., 2015a. Water mass age and aging driving chromophoric dissolved organic matter in the dark global ocean. Global Biogeochem. Cycles 29, 917–934. doi: 10.1002/2014GB005048.

Catalá, T.S., Reche, I., Fuentes–Lema, A., Romera–Castillo, C., Nieto–Cid, M., Ortega–Retuerta, E., Calvo, E., Álvarez, M., Marrasé, C., Stedmon, C.A., Álvarez–Salgado, X.A., 2015b. Turnover time of fluorescent dissolved organic matter in the dark global ocean. Nat. Commun. 6, 5986. doi: 10.1038/ncomms6986.

Chavez, F.P., Messié, M., Pennington, J.T., 2010. Marine Primary Production in Relation to Climate Variability and Change. Ann. Rev. Mar. Sci. 3, 227–260. doi: 10.1146/annurev.marine.010908.163917.

Chen, C.–S., Anaya, J.M., Chen, E.Y.–T., Farr, E., Chin, W.–C., 2015. Ocean Warming–Acidification Synergism Undermines Dissolved Organic Matter Assembly. PLoS One 10, e0118300. doi: 10.1371/journal.pone.0118300.

Chen, H., Stubbins, A., Perdue, E.M., Green, N.W., Helms, J.R., Mopper, K., Hatcher, P.G., 2014.

Ultrahigh resolution mass spectrometric differentiation of dissolved organic matter isolated by coupled reverse osmosis–electrodialysis from various major oceanic water masses. Mar. Chem. 164, 48–59. doi: 10.1016/j.marchem.2014.06.002.

Chen, M., Kim, S., Park, J.–E., Jung, H.–J., Hur, J., 2016. Structural and compositional changes of dissolved organic matter upon solid–phase extraction tracked by multiple analytical tools. Anal. Bioanal. Chem. 408, 6249–6258. doi: 10.1007/s00216–016–9728–0.

Chen, R.F., 1967. Fluorescence Quantum Yields of Tryptophan and Tyrosine. Anal. Lett. 1, 35–42. doi: 10.1080/00032716708051097.

Church, J.A., Clark, P.U., Cazenave, A., Gregory, J.M., Jevrejeva, S., Levermann, A., Merrifield, M.A., Milne, G.A., Nerem, R.S., Nunn, P.D., Payne, A.J., Pfeffer, W.T., Stammer, D., Unnikrishnan, A.S., 2013. Sea Level Change, in: Stocker, T.F., Qin, D., Plattner, G.–K., Tignor, M., Allen, S.K., Boschung, J., Nauels, A., Xia, Y., Bex, V., Midgley, P.M. (Eds.), Climate Change 2013: The Physical Science Basis. Contribution of Working Group I to the Fifth Assessment Report of the Intergovernmental Panel on Climate Change. Cambridge University Press, Cambridge.

Church, M.J., Ducklow, H.W., Karl, D.M., 2002. Multiyear increases in dissolved organic matter inventories at Station ALOHA in the North Pacific Subtropical Gyre. Limnol. Oceanogr. 47, 1–10. doi: 10.4319/lo.2002.47.1.0001.

Clark, L.L., Ingall, E.D., Benner, R., 1998. Marine phosphorus is selectively remineralized. Nature 393, 426. doi: 10.1038/30881.

Coble, P.G., 2007. Marine Optical Biogeochemistry: The Chemistry of Ocean Color. Chem. Rev. 107, 402–418. doi: 10.1021/cr050350+.

Coble, P.G., 1996. Characterization of marine and terrestrial DOM in seawater using excitation–emission matrix spectroscopy. Mar. Chem. 51, 325–346. doi: 10.1016/0304–4203(95)00062–3.

Coble, P.G., Green, S.A., Blough, N. V, Gagosian, R.B., 1990. Characterization of dissolved organic matter in the Black Sea by fluorescence spectroscopy. Nature 348, 432. doi: 10.0.4.14/348432a0.

Coble, P.G., Lead, J., Baker, A., Reynolds, D.M., Spencer, R.G.M., 2014. Aquatic Organic Matter Fluorescence, Cambridge Environmental Chemistry Series. Cambridge University Press, Cambridge. doi: 10.1017/CBO9781139045452.

Cory, R.M., McKnight, D.M., 2005. Fluorescence Spectroscopy Reveals Ubiquitous Presence of Oxidized and Reduced Quinones in Dissolved Organic Matter. Environ. Sci. Technol. 39, 8142–8149. doi: 10.1021/es0506962.

Covert, J.S., Moran, M.A., 2001. Molecular characterization of estuarine bacterial communities that use high– and low–molecular weight fractions of dissolved organic carbon. Aquat. Microb. Ecol. 25, 127–139. doi: 10.3354/ame025127.

Cruzado, A., 1985. Chemistry of Mediterranean waters., in: Margalef, R. (Ed.), The Western Mediterranean. Pergamon Press, pp. 126–147.

Cuss, C.W., Guéguen, C., 2015. Relationships between molecular weight and fluorescence properties for size–fractionated dissolved organic matter from fresh and aged sources. Water Res. 68, 487–497. doi: 10.1016/j.watres.2014.10.013.

Cyr, F., Tedetti, M., Besson, F., Beguery, L., Doglioli, A.M., Petrenko, A.A., Goutx, M., 2017. A new glider–compatible optical sensor for dissolved organic matter measurements: Test case from the NW Mediterranean sea. Front. Mar. Sci. 4. doi: 10.3389/fmars.2017.00089.

D'Andrilli, J., Dittmar, T., Koch, B.P., Purcell, J.M., Marshall, A.G., Cooper, W.T., 2010. Comprehensive characterization of marine dissolved organic matter by fourier transform ion cyclotron resonance mass spectrometry with electrospray and atmospheric pressure photoionization. Rapid Commun. Mass Spectrom. 24, 643–650. doi: 10.1002/rcm.4421.

Dachs, J., Calleja, M.L., Duarte, C.M., del Vento, S., Turpin, B., Polidori, A., Herndl, G.J., Agustí, S., 2005. High atmosphere–ocean exchange of organic carbon in the NE subtropical Atlantic. Geophys. Res. Lett. 32, L21807. doi: 10.1029/2005GL023799.

Dahlén, J., Bertilsson, S., Pettersson, C., 1996. Effects of uv–a irradiation on dissolved organic matter in humic surface waters. Environ. Int. 22, 501–506. doi: 10.1016/0160–4120(96)00038–4.

Dainard, P.G., Guéguen, C., 2013. Distribution of PARAFAC modeled CDOM components in the North Pacific Ocean, Bering, Chukchi and Beaufort Seas. Mar. Chem. 157, 216–223. doi: 10.1016/j.marchem.2013.10.007.

De La Rocha, C.L., 2006. The Biological Pump, in: Holland, H.D., Turekian, K.K. (Eds.), Treatise on Geochemistry. Pergamon Press, Oxford, pp. 1–29. doi: 10.1016/B0–08–043751–6/06107–7.

Dickson, R.R., Brown, J., 1994. The production of North Atlantic Deep Water: sources, rates, and pathways. J. Geophys. Res. 99, 12 319–12 341. doi: 10.1029/94JC00530.

Dittmar, T., 2015. Chapter 7 – Reasons Behind the Long–Term Stability of Dissolved Organic Matter, in: Hansell, D.A., Carlson, C.A. (Eds.), Biogeochemistry of Marine Dissolved Organic Matter. pp. 369–388. doi: 10.1016/B978–0–12–405940–5.00007–8.

Dittmar, T., Koch, B., Hertkorn, N., Kattner, G., 2008. A simple and efficient method for the solid–phase extraction of dissolved organic matter (SPE–DOM) from seawater. Limnol. Oceanogr. Methods 6, 230–235. doi: 10.4319/lom.2008.6.230.

Dittmar, T., Paeng, J., 2009. A heat–induced molecular signature in marine dissolved organic matter. Nat. Geosci. 2, 175–179. doi: 10.1038/ngeo440.

Dittmar, T., Stubbins, A., 2014. Dissolved organic matter in aquatic systems, in: Holland, H., Turekian, K. (Eds.), Treatise of Geochemistry. Elsevier, pp. 125–156. doi: 10.1016/B978–0–08–095975–7.01010–X.

Dunne, J.P., Sarmiento, J.L., Gnanadesikan, A., 2007. A synthesis of global particle export from the surface ocean and cycling through the ocean interior and on the seafloor. Global Biogeochem. Cycles 21, GB4006. doi: 10.1029/2006GB002907.

Ejarque–Gonzalez, E., Butturini, A., 2014. Self–organising maps and correlation analysis as a tool to explore patterns in excitation–emission matrix data sets and to discriminate dissolved organic matter fluorescence components. PLoS One 9, e99618. doi: 10.1371/journal.pone.0099618.

Emelianov, M., Font, J., Turiel, A., Mullot, C., Solé, J., Poulain, P.M., Julià, A., Vitrià, M.R., 2006. Transformation of levantine intermediate water tracked by MEDARGO floats in the Western Mediterranean. Ocean Sci. 2, 281–290. doi: 10.5194/os–2–281–2006.

Endres, S., Galgani, L., Riebesell, U., Schulz, K.–G., Engel, A., 2014. Stimulated Bacterial Growth under Elevated pCO2: Results from an Off–Shore Mesocosm Study. PLoS One 9, e99228. doi: 10.1371/journal.pone.0099228.

Engel, A., Piontek, J., Grossart, H.–P., Riebesell, U., Schulz, K.G., Sperling, M., 2014. Impact of CO2 enrichment on organic matter dynamics during nutrient induced coastal phytoplankton blooms. J. Plankton Res. 36, 641–657. doi: 10.1093/plankt/fbt125.

Engelhaupt, E., Bianchi, T.S., Wetzel, R.G., Tarr, M.A., 2003. Photochemical Transformations and Bacterial Utilization of High–Molecular–Weight Dissolved Organic Carbon in a Southern Louisiana Tidal Stream (Bayou Trepagnier). Biogeochemistry 62, 39–58. doi: 10.2307/1469872.

Fellman, J.B., Hood, E., Spencer, R.G.M., 2010. Fluorescence spectroscopy opens new windows into dissolved organic matter dynamics in freshwater ecosystems: A review. Limnol. Oceanogr. 55, 2452–2462. doi: 10.4319/lo.2010.55.6.2452.

Fichot, C.G., Benner, R., 2011. A novel method to estimate DOC concentrations from CDOM absorption coefficients in coastal waters. Geophys. Res. Lett. 38, L03610. doi: 10.1029/2010GL046152.

Fichot, C.G., Sathyendranath, S., Miller, W.L., 2008. SeaUV and SeaUVC: Algorithms for the retrieval of UV/Visible diffuse attenuation coefficients from ocean color. Remote Sens. Environ. 112, 1584–1602. doi: 10.1016/j.rse.2007.08.009.

Flerus, R., Lechtenfeld, O.J., Koch, B.P., McCallister, S.L., Schmitt–Kopplin, P., Benner, R., Kaiser, K., Kattner, G., 2012. A molecular perspective on the ageing of marine dissolved organic matter. Biogeosciences 9, 1935–1955. doi: 10.5194/bg–9–1935–2012.

Fukuzaki, K., Imai, I., Fukushima, K., Ishii, K.–I., Sawayama, S., Yoshioka, T., 2014. Fluorescent characteristics of dissolved organic matter produced by bloom–forming coastal phytoplankton. J. Plankton Res. 36, 685–694. doi: 10.1093/plankt/fbu015.

Gačić, M., Schroeder, K., Civitarese, G., Cosoli, S., Vetrano, A., Eusebi Borzelli, G.L., 2013. Salinity in the Sicily Channel corroborates the role of the Adriatic–Ionian Bimodal Oscillating System (BiOS) in shaping the decadal variability of the Mediterranean overturning circulation. Ocean Sci. 9, 83–90. doi: 10.5194/os–9–83–2013.

Gao, Z., Guéguen, C., 2017. Size distribution of absorbing and fluorescing DOM in Beaufort Sea, Canada Basin. Deep Sea Res. Part I Oceanogr. Res. Pap. 121, 30–37. doi: 10.1016/j.dsr.2016.12.014.

Gascard, J.C., 1978. Mediterranean deep water formation; baroclinic instability and oceanic eddies. Oceanol. Acta 1, 315–330.

Gasparini, G.P., Ortona, A., Budillon, G., Astraldi, M., Sansone, E., 2005. The effect of the Eastern Mediterranean Transient on the hydrographic characteristics in the Strait of Sicily and in the Tyrrhenian Sea. Deep Sea Res. Part I: Oceanogr. Res. Pap. 52, 915–935. doi: 10.1016/j.dsr.2005.01.001.

Giorgi, F., 2006. Climate change hot–spots. Geophys. Res. Lett. 33, L08707. doi: 10.1029/2006GL025734.

Gogou, A., Sanchez–Vidal, A., Durrieu De Madron, X., Stavrakakis, S., Calafat, A.M., Stabholz, M., Psarra, S., Canals, M., Heussner, S., Stavrakaki, I., Papathanassiou, E., 2014. Carbon

flux to the deep in three open sites of the Southern European Seas (SES). J. Mar. Syst. 129, 224–233. doi: 10.1016/j.jmarsys.2013.05.013.

Gonnelli, M., Galletti, Y., Marchetti, E., Mercadante, L., Retelletti Brogi, S., Ribotti, A., Sorgente, R., Vestri, S., Santinelli, C., 2016. Dissolved organic matter dynamics in surface waters affected by oil spill pollution: Results from the Serious Game exercise. Deep. Res. Part II Top. Stud. Oceanogr. 133, 88–99. doi: 10.1016/j.dsr2.2016.05.027.

Gonsior, M., Hertkorn, N., Conte, M.H., Cooper, W.J., Bastviken, D., Druffel, E., Schmitt–Kopplin, P., 2014. Photochemical production of polyols arising from significant photo–transformation of dissolved organic matter in the oligotrophic surface ocean. Mar. Chem. 163, 10–18. doi: 10.1016/j.marchem.2014.04.002.

Gonsior, M., Peake, B.M., Cooper, W.T., Podgorski, D.C.C., D'Andrilli, J., Dittmar, T., Cooper, W.J., 2011. Characterization of dissolved organic matter across the Subtropical Convergence off the South Island, New Zealand. Mar. Chem. 123, 99–110. doi: 10.1016/j.marchem.2010.10.004.

Gonsior, M., Schmitt–Kopplin, P., Bastviken, D., 2013. Depth–dependent molecular composition and photo–reactivity of dissolved organic matter in a boreal lake under winter and summer conditions. Biogeosciences 10, 6945–6956. doi: 10.5194/bg–10–6945–2013.

Goto, S., Tada, Y., Suzuki, K., Yamashita, Y., 2017. Production and Reutilization of Fluorescent Dissolved Organic Matter by a Marine Bacterial Strain, Alteromonas macleodii. Front. Microbiol. 8, 507. doi: 10.3389/fmicb.2017.00507.

Grasshoff, K., Kremling, K., Ehrhardt, M., 1999. Determination of nutrients. In: L. Brügmann, L., Kremling, K. (Eds.). Methods of Seawater Analysis. WILEY–VCH Verlag GmbH, pp. 159–228.

Green, N.W., Perdue, E.M., Aiken, G.R., Butler, K.D., Chen, H., Dittmar, T., Niggemann, J., Stubbins, A., 2014. An intercomparison of three methods for the large–scale isolation of oceanic dissolved organic matter. Mar. Chem. 161, 14–19. doi: 10.1016/j.marchem.2014.01.012.

Green, S.A., Blough, N. V, 1994. Optical absorption and fluorescence properties of chromophoric dissolved organic matter in natural waters. Limnol. Oceanogr. 39, 1903–1916. doi: 10.4319/lo.1994.39.8.1903.

Gueguen, C., Kowalczuk, P., 2014. Colored Dissolved Organic Matter in Frontal Zones, in: Belking, I.M. (Eds.), Chemical Oceanography of Frontal Zones, Handbook of Environmental Chemistry. Springer, Berlin. doi: 10.1007/698_2013_244.

Guo, L., Santschi, P.H., 1996. A critical evaluation of the cross–flow ultrafiltration technique for sampling colloidal organic carbon in seawater. Mar. Chem. 55, 113–127. doi: 10.1016/S0304–4203(96)00051–5.

Guo, L., Santschi, P.H., Cifuentes, L.A., Trumbore, S.E., Southon, J., 1996. Cycling of high–molecular–weight dissolved organic matter in the Middle Atlantic Bight as revealed by carbon isotopic (13C and 14C) signatures. Limnol. Oceanogr. 41. doi: 10.4319/lo.1996.41.6.1242.

Guo, L., Santschi, P.H., Warnken, K.W., 1995. Dynamics of dissolved organic carbon (DOC) in oceanic environments. Limnol. Oceanogr. 40, 1392–1403. doi: 10.4319/lo.1995.40.8.1392

Guo, L., Wen, L.–S., Tang, D., Santschi, P.H., 2000. Re–examination of cross–flow ultrafiltration for sampling aquatic colloids: Evidence from molecular probes. Mar. Chem. 69, 75–90. doi: 10.1016/S0304–4203(99)00097–3.

Gutiérrez–Rodríguez, A., Latasa, M., Estrada, M., Vidal, M., Marrasé, C., 2010. Carbon fluxes through major phytoplankton groups during the spring bloom and post–bloom in the Northwestern Mediterranean Sea. Deep Sea Res. Part I Oceanogr. Res. Pap. 57, 486–500. doi:10.1016/j.dsr.2009.12.013.

Guyennon, A., Baklouti, M., Diaz, F., Palmieri, J., Beuvier, J., Lebaupin–Brossier, C., Arsouze, T., Béranger, K., Dutay, J.–C., Moutin, T., 2015. New insights into the organic carbon export in the Mediterranean Sea from 3–D modeling. Biogeosciences 12, 7025–7046. doi: 10.5194/bg–12–7025–2015.

Hainbucher, D., Rubino, A., Cardin, V., Tanhua, T., Schroeder, K., Bensi, M., 2014. Hydrographic situation during cruise M84/3 and P414 (spring 2011) in the Mediterranean Sea. Ocean Sci. 10, 669–682. doi: 10.5194/os–10–669–2014.

Hainbucher, D., Rubino, A., Klein, B., 2006. Water mass characteristics in the deep layers of the western Ionian Basin observed during May 2003. Geophys. Res. Lett. 33, L05608. doi: 10.1029/2005GL025318.

Hansell, D.A., 2013. Recalcitrant dissolved organic carbon fractions. Ann. Rev. Mar. Sci. 5, 421–445. doi: 10.1146/annurev–marine–120710–100757.

Hansell, D.A., 2009. Dissolved organic carbon in the carbon cycle of the Indian Ocean, Geophys. Monogr. Ser. 185, 217–230. doi: 10.1029/2007GM000684.

Hansell, D.A., Carlson, C.A., Repeta, D.J., Schlitzer, R., 2009. Dissolved organic matter in the ocean a controversy stimulates new insights. Oceanography 22, 202–211. doi: 10.5670/oceanog.2009.109.

Hansell, D.A., Carlson, C.A., Schlitzer, R., 2012. Net removal of major marine dissolved organic carbon fractions in the subsurface ocean. Global Biogeochem. Cycles 26, GB1016. doi: 10.1029/2011GB004069.

Hansman, R.L., Dittmar, T., Herndl, G.J., 2015. Conservation of dissolved organic matter molecular composition during mixing of the deep water masses of the northeast Atlantic Ocean. Mar. Chem. 177, 288–297. doi: 10.1016/j.marchem.2015.06.001.

Hassoun, A.E.R., Guglielmi, V., Gemayel, E., Goyet, C., Abboud–Abi Saab, M., Giani, M., Ziveri, P., Ingrosso, G., Touratier, F., 2015. Is the Mediterranean Sea Circulation in a Steady State?, J. Water Resour. and Ocean Scie. 4, 6–17. doi: 10.11648/j.wros.20150401.12.

Hawkes, J.A., Hansen, C.T., Goldhammer, T., Bach, W., Dittmar, T., 2016. Molecular alteration of marine dissolved organic matter under experimental hydrothermal conditions. Geochim. Cosmochim. Acta 175, 68–85. doi: 10.1016/j.gca.2015.11.025.

Helm, K.P., Bindoff, N.L., Church, J.A., 2011. Observed decreases in oxygen content of the global ocean. Geophys. Res. Lett. 38, L23602. doi: 10.1029/2011GL049513.

Helms, J.R., Mao, J., Chen, H., Perdue, E.M., Green, N.W., Hatcher, P.G., Mopper, K., Stubbins, A., 2015. Spectroscopic characterization of oceanic dissolved organic matter isolated by reverse osmosis coupled with electrodialysis. Mar. Chem. 177, 278–287. doi: 10.1016/j.marchem.2015.07.007.

Helms, J.R., Stubbins, A., Ritchie, J.D., Minor, E.C., Kieber, D.J., Mopper, K., 2008. Absorption spectral slopes and slope ratios as indicators of molecular weight, source, and photobleaching of chromophoric dissolved organic matter. Limnol. Oceanogr. 53, 955–969. doi: 10.4319/lo.2008.53.3.0955.

Hertkorn, N., Benner, R., Frommberger, M., Schmitt–Kopplin, P., Witt, M., Kaiser, K., Kettrup, A., Hedges, J.I., 2006. Characterization of a major refractory component of marine dissolved organic matter. Geochim. Cosmochim. Acta 70, 2990–3010. doi: 10.1016/j.gca.2006.03.021.

Hertkorn, N., Frommberger, M., Witt, M., Koch, B.P., Schmitt–Kopplin, P., Perdue, E.M., 2008. Natural organic matter and the event horizon of mass spectrometry. Anal. Chem. 80, 8908–8919. doi: 10.1021/ac800464g.

Hertkorn, N., Harir, M., Cawley, K.M., Schmitt–Kopplin, P., Jaffé, R., 2016. Molecular characterization of dissolved organic matter from subtropical wetlands: a comparative study through the analysis of optical properties, NMR and FTICR/MS. Biogeosciences 13, 2257–2277. doi: 10.5194/bg–13–2257–2016.

Hertkorn, N., Harir, M., Koch, B.P., Michalke, B., Schmitt–Kopplin, P., 2013. High–field NMR spectroscopy and FTICR mass spectrometry: Powerful discovery tools for the molecular level characterization of marine dissolved organic matter. Biogeosciences 10, 1583–1624. doi: 10.5194/bg–10–1583–2013.

Herzsprung, P., von Tümpling, W., Hertkorn, N., Harir, M., Büttner, O., Bravidor, J., Friese, K., Schmitt–Kopplin, P., 2012. Variations of DOM quality in inflows of a drinking water reservoir: Linking of van Krevelen diagrams with EEMF spectra by rank correlation. Environ. Sci. Technol. 46, 5511–5518. doi: 10.1021/es300345c.

Hirose, K., 2007. Metal–organic matter interaction: ecological roles of ligands in oceanic DOM. Appl. Geochemistry 22, 1636–1645. doi: 10.1016/j.apgeochem.2007.03.042.

Holm–Hansen, O., Lorenzen, C.J., Holmes, R.W., Strickland, J.D.H., 1965. Fluorometric determination of chlorophyll. J. du Cons. 30, 3–15. doi: 10.1093/ icesjms/30.1.3.

Hopkinson Jr., C.S., Vallino, J.J., 2005. Efficient export of carbon to the deep ocean through dissolved organic matter. Nature 433, 142–145. doi: 10.1038/nature03191.

Houpert, L., Durrieu de Madron, X., Testor, P., Bosse, A., D'Ortenzio, F., Bouin, M.–N., Dausse, D., Le Goff, H., Kunesch, S., Labaste, M., Coppola, L., Mortier, L., Raimbault, P., 2016. Observations of open–ocean deep convection in the northwestern Mediterranean Sea: Seasonal and interannual variability of mixing and deep water masses for the 2007–2013 Period. J. Geophys. Res. Ocean. 121, 8139–8171. doi: 10.1002/2016JC011857.

Huertas, I.E., Ríos, A.F., García–Lafuente, J., Navarro, G., Makaoui, A., Snchez–Romn, A., Rodriguez–Galvez, S., Orbi, A., Ruíz, J., Pérez, F.F., 2012. Atlantic forcing of the Mediterranean oligotrophy. Global Biogeochem. Cycles 26. doi: 10.1029/2011GB004167.

Huguet, A., Vacher, L., Relexans, S., Saubusse, S., Froidefond, J.M., Parlanti, E., 2009. Properties of fluorescent dissolved organic matter in the Gironde Estuary. Org. Geochem. 40, 706–719. doi: 10.1016/j.orggeochem.2009.03.002.

Isla, A., Scharek, R., Latasa, M., 2015. Zooplankton diel vertical migration and contribution to deep active carbon flux in the NW Mediterranean. J. Mar. Syst. 143, 86–97. doi: 10.1016/j.jmarsys.2014.10.017.

Jannasch, H.W., 1994. The microbial turnover of carbon in the deep–sea environment. Glob. Planet. Change 9, 289–295. doi: 10.1016/0921–8181(94)90022–1.

Jiao, N., Herndl, G.J., Hansell, D.A., Benner, R., Kattner, G., Wilhelm, S.W., Kirchman, D.L., Weinbauer, M.G., Luo, T., Chen, F., Azam, F., 2010. Microbial production of recalcitrant dissolved organic matter: Long–term carbon storage in the global ocean. Nat. Rev. Microbiol. 8, 593–599. doi: 10.1038/nrmicro2386.

Jones, V., Meador, T.B., Gogou, A., Migon, C., Penkman, K.E.H., Collins, M.J., Repeta, D.J., 2013. Characterisation and dynamics of dissolved organic matter in the Northwestern Mediterranean Sea. Prog. Oceanogr. 119, 78–89. doi: 10.1016/j.pocean.2013.06.007.

Jørgensen, L., Stedmon, C.A., Kragh, T., Markager, S., Middelboe, M., Søndergaard, M., 2011. Global trends in the fluorescence characteristics and distribution of marine dissolved organic matter. Mar. Chem. 126, 139–148. doi: 10.1016/j.marchem.2011.05.002.

Jørgensen, L., Stedmon, C.A., Granskog, M.A., Middelboe, M., 2014. Tracing the long-term microbial production of recalcitrant fluorescent dissolved organic matter in seawater. Geophys. Res. Lett. 41, 2481–2488. doi: 10.1002/2014GL059428.

Jullion, L., Jacquet, S.H.M., Tanhua, T., 2017. Untangling biogeochemical processes from the impact of ocean circulation: First insight on the Mediterranean dissolved barium dynamics. Global Biogeochem. Cycles 31, 1256–1270. doi: 10.1002/2016GB005489.

Kaiser, K., Benner, R., 2012. Organic matter transformations in the upper mesopelagic zone of the North Pacific: Chemical composition and linkages to microbial community structure. J. Geophys. Res. Ocean. 117, C01023. doi: 10.1029/2011JC007141.

Kaiser, K., Benner, R., 2009. Biochemical composition and size distribution of organic matter at the Pacific and Atlantic time–series stations. Mar. Chem. 113, 63–77. doi: 10.1016/j.marchem.2008.12.004.

Kalle, K., 1949. Fluoreszenz und Gelstoff in Bottnischen und Finnischen Meerbusen, Dtsch. Hydrogr. Z. 2, 117–124.

Karl, D.M., Björkman, K.M., 2015. Chapter 5 – Dynamics of Dissolved Organic Phosphorus, in: Hansell, D.A., Carlson, C.A. (Eds.), Biogeochemistry of Marine Dissolved Organic Matter. Academic Press, San Diego, pp. 233–334. doi: 10.1016/B978–0–12–405940–5.00005–4.

Kattner, G., Simon, M., Koch, B.P., 2011. Molecular Characterization of Dissolved Organic Matter and Constraints for Prokaryotic Utilization, in: Jiao, N., Azam, F., Sanders, S. (Eds.), Microbial Carbon Pump in the Ocean. American Association for the Advancement of Science, Washington, United States, Washington, pp. 60–61.

Keeling, R.F., Körtzinger, A., Gruber, N., 2010. Ocean Deoxygenation in a Warming World. Ann. Rev. Mar. Sci. 2, 199–229. doi: 10.1146/annurev.marine.010908.163855.

Kellerman, A.M., Kothawala, D.N., Dittmar, T., Tranvik, L.J., 2015. Persistence of dissolved organic matter in lakes related to its molecular characteristics. Nat. Geosci. 8, 454–459. doi: 10.1038/NGEO2440.

Khodse, V.B., Bhosle, N.B., 2011. Bacterial utilization of size–fractionated dissolved organic matter. Aquat. Microb. Ecol. 64, 299–309. doi: 10.3354/ame01529.

Kieber, R.J., Hydro, L.H., Seaton, P.J., 1997. Photooxidation of triglycerides and fatty acids in

seawater: Implication toward the formation of marine humic substances. Limnol. Oceanogr. 42, 1454–1462. doi: 10.4319/lo.1997.42.6.1454.

Kim, H.–C., Lee, K., 2009. Significant contribution of dissolved organic matter to seawater alkalinity. Geophys. Res. Lett. 36, L20603. doi: 10.1029/2009GL040271.

Kim, S., Kramer, R.W., Hatcher, P.G., 2003. Graphical Method for Analysis of Ultrahigh–Resolution Broadband Mass Spectra of Natural Organic Matter, the Van Krevelen Diagram. Anal. Chem. 75, 5336–5344. doi: 10.1021/ac034415p.

Kinsey, J.D., Corradino, G., Ziervogel, K., Schnetzer, A., Osburn, C.L., 2018. Formation of Chromophoric Dissolved Organic Matter by Bacterial Degradation of Phytoplankton–Derived Aggregates. Front. Mar. Sci. 4, 430. doi: 10.3389/fmars.2017.00430.

Klein, B., Roether, W., Manca, B.B., Bregant, D., Beitzel, V., Kovacevic, V., Luchetta, A., 1999. The large deep water transient in the Eastern Mediterranean. Deep Sea Res. Part I: Oceanogr. Res.Pap. 46, 371–414. doi: 10.1016/S0967–0637(98)00075–2.

Koch, B.P., Dittmar, T., 2006. From mass to structure: An aromaticity index for high–resolution mass data of natural organic matter. Rapid Commun. Mass Spectrom. 20, 926–932. doi: 10.1002/rcm.2386.

Koch, B.P., Dittmar, T., 2016. Erratum: From mass to structure: An aromaticity index for high–resolution mass data of natural organic matter (Rapid Communications in Mass Spectrometry (2006) 20 (926–932) doi: 10.1002/rcm.2386). Rapid Commun. Mass Spectrom. 30, 250. doi: 10.1002/rcm.7433.

Koch, B.P., Kattner, G., Witt, M., Passow, U., 2014. Molecular insights into the microbial formation of marine dissolved organic matter: Recalcitrant or labile? Biogeosciences 11, 4173–4190. doi: 10.5194/bg–11–4173–2014.

Koch, B.P., Witt, M., Engbrodt, R., Dittmar, T., Kattner, G., 2005. Molecular formulae of marine and terrigenous dissolved organic matter detected by electrospray ionization Fourier transform ion cyclotron resonance mass spectrometry. Geochim. Cosmochim. Acta 69, 3299–3308. doi: 10.1016/j.gca.2005.02.027.

Kolowith, L.C., Ingall, E.D., Benner, R., 2001. Composition and cycling of marine organic phosphorus. Limnol. Oceanogr. 46, 309–320. doi: 10.4319/lo.2001.46.2.0309.

Koprivnjak, J.F., Pfromm, P.H., Ingall, E., Vetter, T.A., Schmitt–Kopplin, P., Hertkorn, N., Frommberger, M., Knicker, H., Perdue, E.M., 2009. Chemical and spectroscopic characterization of marine dissolved organic matter isolated using coupled reverse osmosis–electrodialysis. Geochim. Cosmochim. Acta 73, 4215–4231. doi: 10.1016/j.gca.2009.04.010.

Kouassi, A.M., Zika, R.G., 1992. Light-induced destruction of the absorbance property of dissolved organic matter in seawater. Toxicol. Environ. Chem. 35, 195–211. doi: 10.1080/02772249209357816.

Kovačević, V., Manca, B.B., Ursella, L., Schroeder, K., Cozzi, S., Burca, M., Mauri, E., Gerin, R., Notarstefano, G., Deponte, D., 2012. Water mass properties and dynamic conditions of the Eastern Mediterranean in June 2007. Prog. Oceanogr. 104, 59–79. doi: 10.1016/j.pocean.2012.05.006.

Kowalczuk, P., Tilstone, G.H., Zabłocka, M., Röttgers, R., Thomas, R., 2013. Composition of

dissolved organic matter along an Atlantic Meridional Transect from fluorescence spectroscopy and Parallel Factor Analysis. Mar. Chem. 157, 170–184. doi: 10.1016/j.marchem.2013.10.004.

Kramer, G.D., Herndl, G.J., 2004. Photo– and bioreactivity of chromophoric dissolved organic matter produced by marine bacterioplankton. Aquat. Microb. Ecol. 36, 239–246. doi: 10.3354/ame036239.

Kujawinski, E.B., 2002. Electrospray ionization Fourier transform ion cyclotron resonance mass spectrometry (ESI FT–ICR MS): Characterization of complex environmental mixtures. Environ. Forensics 3, 207–216. doi: 10.1006/enfo.2002.0109.

Lam, B., Simpson, A.J., 2008. Direct 1H NMR spectroscopy of dissolved organic matter in natural waters. Analyst 133, 263–269. doi: 10.1039/b713457f.

Langdon, C., 2010. Determination of dissolved oxygen in seawater by Winkler titration using the amperometric technique. Go–sh. repeat Hydrogr. Man. a Collect. Expert reports Guidel. Ed. by BM Sloyan C.Sabine, IOC/IOCCP, Paris.

Laruelle, G.G., Roubeix, V., Sferratore, A., Brodherr, B., Ciuffa, D., Conley, D.J., Dürr, H.H., Garnier, J., Lancelot, C., Le Thi Phuong, Q., Meunier, J.–D., Meybeck, M., Michalopoulos, P., Moriceau, B., Ní Longphuirt, S., Loucaides, S., Papush, L., Presti, M., Ragueneau, O., Regnier, P., Saccone, L., Slomp, C.P., Spiteri, C., Van Cappellen, P., 2009. Anthropogenic perturbations of the silicon cycle at the global scale: Key role of the land–ocean transition. Global Biogeochem. Cycles 23, GB4031. doi: 10.1029/2008GB003267.

Lascaratos, A., 1993. Estimation of deep and intermediate water mass formation rates in the Mediterranean Sea. Deep. Res. Part II 40, 1327–1332. doi: 10.1016/0967–0645(93)90072–U.

Lascaratos, A., Roether, W., Nittis K., Klein, B., 1999. Recent changes in deep water formation and spreading in the eastern Mediterranean Sea: a review. Progr. Oceanogr. 44, 5–36. doi: 10.1016/S0079–6611(99)00019–1.

Latasa, M., Morán, X.A.G., Scharek, R., Estrada, M., 2005. Estimating the carbon flux through main phytoplankton groups in the northwestern Mediterranean. Limnol. Oceanogr. 50, 1447–1458. doi: 10.4319/lo.2005.50.5.1447.

Lavonen, E.E., Kothawala, D.N., Tranvik, L.J., Gonsior, M., Schmitt–Kopplin, P., Köhler, S.J., 2015. Tracking changes in the optical properties and molecular composition of dissolved organic matter during drinking water production. Water Res. 85, 286–294. doi: 10.1016/j.watres.2015.08.024.

Lawaetz, A.J., Stedmon, C.A., 2009. Fluorescence intensity calibration using the Raman scatter peak of water. Appl. Spectrosc. 63, 936–940. doi: 10.1366/000370209788964548.

Lechtenfeld, O.J., Kattner, G., Flerus, R., McCallister, S.L., Schmitt–Kopplin, P., Koch, B.P., 2014. Molecular transformation and degradation of refractory dissolved organic matter in the Atlantic and Southern Ocean. Geochim. Cosmochim. Acta 126, 321–337. doi: 10.1016/j.gca.2013.11.009.

Lee, C., Peterson, M.L., Wakeham, S.G., Armstrong, R.A., Miquel, J.C., Fowler, S.W., Hirschberg, D., Beck, A., Xue, J., 2009. Particulate organic matter and ballast fluxes measured using time–series and settling velocity sediment traps in the northwestern Mediterranean Sea. Deep Sea Res. Part II Top. Stud. Oceanogr. 56, 1420–1436. doi:

10.1016/j.dsr2.2008.11.029.

Lermusiaux, P.F.J., Robinson, A.R., 2001. Features of dominant mesoscale variability, circulation patterns and dynamics in the strait of sicily. Deep Sea Res. Part I: Oceanogr. Res. Pap. 48, 1953–1997. doi: 10.1016/S0967–0637(00)00114–X.

Letscher, R.T., Hansell, D.A., Carlson, C.A., Lumpkin, R., Knapp, A.N., 2013. Dissolved organic nitrogen in the global surface ocean: Distribution and fate. Global Biogeochem. Cycles 27, 143–153. doi: 10.1029/2012GB004449.

Letscher, R.T., Moore, J.K., Teng, Y.–C., Primeau, F., 2015. Variable C : N : P stoichiometry of dissolved organic matter cycling in the Community Earth System Model. Biogeosciences 12, 209–221. doi: 10.5194/bg–12–209–2015.

Li, H., Minor, E.C., 2015. Dissolved organic matter in Lake Superior: insights into the effects of extraction methods on chemical composition. Environ. Sci. Process. Impacts 17, 1829–1840. doi: 10.1039/C5EM00199D.

Li, Y., Harir, M., Uhl, J., Kanawati, B., Lucio, M., Smirnov, K.S., Koch, B.P., Schmitt–Kopplin, P., Hertkorn, N., 2017. How representative are dissolved organic matter (DOM) extracts? A comprehensive study of sorbent selectivity for DOM isolation. Water Res. 116, 316–323. doi: 10.1016/j.watres.2017.03.038.

Loginova, A.N., Thomsen, S., Engel, A., 2016. Chromophoric and fluorescent dissolved organic matter in and above the oxygen minimum zone off Peru. J. Geophys. Res. Ocean. 121, 7973–7990. doi: 10.1002/2016JC011906.

Loh, A.N., Bauer, J.E., Druffel, E.R.M., 2004. Variable ageing and storage of dissolved organic components in the open ocean. Nature 430, 877–881. doi: 10.1038/nature02780.

Lønborg, C., Álvarez–Salgado, X.A., 2014. Tracing dissolved organic matter cycling in the eastern boundary of the temperate North Atlantic using absorption and fluorescence spectroscopy. Deep. Res. Part I Oceanogr. Res. Pap. 85, 35–46. doi: 10.1016/j.dsr.2013.11.002.

Lønborg, C., Álvarez–Salgado, X.A., 2012. Recycling versus export of bioavailable dissolved organic matter in the coastal ocean and efficiency of the continental shelf pump. Global Biogeochem. Cycles 26, GB3018. doi: 10.1029/2012GB004353.

Lønborg, C., Álvarez–Salgado, X.A., Davidson, K., Martínez–García, S., Teira, E., 2010a. Assessing the microbial bioavailability and degradation rate constants of dissolved organic matter by fluorescence spectroscopy in the coastal upwelling system of the Ría de Vigo. Mar. Chem. 119, 121–129. doi: 10.1016/j.marchem.2010.02.001.

Lønborg, C., Álvarez–Salgado, X.A., Davidson, K., Miller, A.E.J., 2009. Production of bioavailable and refractory dissolved organic matter by coastal heterotrophic microbial populations. Estuar. Coast. Shelf Sci. 82, 682–688. doi: 10.1016/j.ecss.2009.02.026.

Lønborg, C., Álvarez–Salgado, X.A., Duggan, S., Carreira, C., 2017. Organic matter bioavailability in tropical coastal waters: The Great Barrier Reef. Limnol. Oceanogr. doi: 10.1002/lno.10717.

Longhurst, A., 2007. Ecological Geography of the Sea, Second edition. Academic Press, London.

López-Jurado, J., Gonzalez-Pola, C., Velez-Belchi, P., 2005. Observation of an abrupt disruption

of the long-term warming trend at the Balearic Sea, western Mediterranean Sea, in summer 2005. Geophys. Res. Lett. 32, L24606. doi: 1029/2005GL024430.

Luna, G.M., Bianchelli, S., Decembrini, F., De Domenico, E., Danovaro, R., Dell'Anno, A., 2012. The dark portion of the Mediterranean Sea is a bioreactor of organic matter cycling. Global Biogeochem. Cycles 26, GB2017. doi: 10.1029/2011GB004168.

Manca, B. B., Budillon, G., Scarazzato, P., Ursella, L., 2003. Evolution of dynamics in the Eastern Mediterranean affecting water mass structures and properties in the Ionian and Adriatic Seas. J. Geophys. Res.108, 1–19. doi: 10.1029/2002JC001664.

Manca, B., Ibello, V., Pacciaroni, M., Scarazzato, P., Giorgetti, A., 2006. Ventilation of deep waters in the Adriatic and Ionian Seas following changes in thermohaline circulation of the Eastern Mediterranean, Climate Research 31, 239–256. doi: 10.3354/cr031239.

Mannino, A., Russ, M.E., Hooker, S.B., 2008. Algorithm development and validation for satellite–derived distributions of DOC and CDOM in the U.S. Middle Atlantic Bight. J. Geophys. Res. Ocean. 113, C07051. doi: 10.1029/2007JC004493.

Manzella, G.M.R., La Violette, P.E., 1990. The seasonal variation of water mass content in the western Mediterranean and its relationship with the inflows through the straits of Gibraltar and Sicily. J. Geophys. Res. 95, 1623. doi: 10.1029/JC095iC02p01623.

Marbà, N., Jorda, G., Agusti, S., Girard, C., Duarte, C.M., 2015. Footprints of climate change on Mediterranean Sea biota. Front. Mar. Sci. 2, 56. doi: 10.3389/fmars.2015.00056.

Martin, J.H., Knauer, G., Karl, D.M., Broenkow, W.W., 1987. VERTEX: carbon cycling in the northeast Pacific. Deep–Sea Res. 34, 267–285. doi: 10.1016/0198–0149(87)90086–0.

Maugendre, L., Gattuso, J.–P., Poulton, A.J., Dellisanti, W., Gaubert, M., Guieu, C., Gazeau, F., 2017. No detectable effect of ocean acidification on plankton metabolism in the NW oligotrophic Mediterranean Sea: Results from two mesocosm studies. Estuar. Coast. Shelf Sci. 186, 89–99. doi: 10.1016/j.ecss.2015.03.009.

McCarthy, M., Hedges, J., Benner, R., 1996. Major biochemical composition of dissolved high molecular weight organic matter in seawater. Mar. Chem. 55, 281–297. doi: 10.1016/S0304–4203(96)00041–2.

McCarthy, M., Pratum, T., Hedges, J., Benner, R., 1997. Chemical composition of dissolved organic nitrogen in the ocean. Nature 390, 150. doi: 10.1038/36535.

McCarthy, M.D., Bronk, D.A., 2008. Analytical methods for the study of nitrogen, in: Capone, D.G., Bronk, D.A., Mulholland, M.R., Carpenter, E.J. (Eds.), Nitrogen in the Marine Environment. Academic Press, pp. 1219–1276.

McKnight, D.M., Boyer, E.W., Westerhoff, P.K., Doran, P.T., Kulbe, T., Andersen, D.T., 2001. Spectrofluorometric characterization of dissolved organic matter for indication of precursor organic material and aromaticity. Limnol. Oceanogr. 46, 38–48. doi: 10.4319/lo.2001.46.1.0038.

Meador, T.B., Gogou, A., Spyres, G., Herndl, G.J., Krasakopoulou, E., Psarra, S., Yokokawa, T., De Corte, D., Zervakis, V., Repeta, D.J., 2010. Biogeochemical relationships between ultrafiltered dissolved organic matter and picoplankton activity in the Eastern Mediterranean Sea. Deep sea Res. II 57, 1460–1477. doi: 10.1016/j.dsr2.2010.02.015.

Medeiros, P.M., Seidel, M., Powers, L.C., Dittmar, T., Hansell, D.A., Miller, W.L., 2015. Dissolved organic matter composition and photochemical transformations in the northern North Pacific Ocean. Geophys. Res. Lett. 42, 863–870. doi: 10.1002/2014GL062663.

MEDOC group, 1970. Observation of Formation of Deep Water in the Mediterranean Sea, 1969. Nature 227, 1037–1040. doi: 10.1038/2271037a0.

Millot, C., 2013. Levantine Intermediate Water characteristics: An astounding general misunderstanding | Las características de LIW: Un malentendido asombroso. Sci. Mar. 77, 217–232. doi: 10.3989/scimar.03518.13A.

Millot, C., 1999. Circulation in the Western Mediterranean Sea. J. Mar. Syst. 20, 423–442. doi: 10.1016/S0924–7963(98)00078–5.

Minor, E.C., Swenson, M.M., Mattson, B.M., Oyler, A.R., 2014. Structural characterization of dissolved organic matter: a review of current techniques for isolation and analysis. Environ. Sci. Process. Impacts 16, 2064–2079. doi: 10.1039/C4EM00062E.

Mladenov, N., Sommaruga, R., Morales–Baquero, M., Laurion, I., Camarero, L., Diéguez, M., Camacho, A., Delgado Huertas, A., Torres, O., Chen, Z., Felip, M., Reche, I., 2011. Dust inputs and bacteria influence dissolved organic matter in clear alpine lakes. Nat. Comms., 2:405. doi: 10.1038/ncomms1411.

Moore, R.H., Ingall, E.D., Sorooshian, A., Nenes, A., 2008. Molar mass, surface tension, and droplet growth kinetics of marine organics from measurements of CCN activity. Geophys. Res. Lett. 35, L07801. doi: 10.1029/2008GL033350.

Mopper, K., Kieber, D.J., 2002. Chapter 9 – Photochemistry and the Cycling of Carbon, Sulfur, Nitrogen and Phosphorus, in: Hansell, D.A., Carlson, C.A. (Eds.), Biogeochemistry of Marine Dissolved Organic Matter. Academic Press, San Diego, pp. 455–507. doi: 10.1016/B978–012323841–2/50011–7.

Mopper, K., Kieber, D.J., Stubbins, A., 2015. Chapter 8 – Marine Photochemistry of Organic Matter: Processes and Impacts, in: Hansell, D.A., Carlson, C.A. (Eds.), Biogeochemistry of Marine Dissolved Organic Matter. Academic Press, San Diego, pp. 389–450. doi: 10.1016/B978–0–12–405940–5.00008–X.

Mopper, K., Stubbins, A., Ritchie, J.D., Bialk, H.M., Hatcher, P.G., 2007. Advanced instrumental approaches for characterization of marine dissolved organic matter: Extraction techniques, mass spectrometry, and nuclear magnetic resonance spectroscopy. Chem. Rev. 107, 419–442. doi: 10.1021/cr050359b.

Moran, M.A., Kujawinski, E.B., Stubbins, A., Fatland, R., Aluwihare, L.I., Buchan, A., Crump, B.C., Dorrestein, P.C., Dyhrman, S.T., Hess, N.J., Howe, B., Longnecker, K., Medeiros, P.M., Niggemann, J., Obernosterer, I., Repeta, D.J., Waldbauer, J.R., 2016. Deciphering ocean carbon in a changing world. Proc. Natl. Acad. Sci. 113. doi: 10.1073/pnas.1514645113.

Moran, M.A., Sheldon, W.M., Zepp, R.G., 2000. Carbon loss and optical property changes during long–term photochemical and biological degradation of estuarine dissolved organic matter. Limnol. Oceanogr. 45, 1254–1264. doi: 10.4319/lo.2000.45.6.1254.

Moran, M.A., Zepp, R.G., 1997. Role of photoreactions in the formation of biologically labile compounds from dissolved organic matter. Limnol. Oceanogr. 42, 1307–1316. doi: 10.4319/lo.1997.42.6.1307.

Moutin, T., Raimbault, P., 2002. Primary production, carbon export and nutrients availability in western and eastern Mediterranean Sea in early summer 1996 (MINOS cruise). J. Mar. Syst. 33–34, 273–288. doi: 10.1016/S0924–7963(02)00062–3.

Murphy, K.R., Butler, K.D., Spencer, R.G.M., Stedmon, C.A., Boehme, J.R., Aiken, G.R., 2010. Measurement of dissolved organic matter fluorescence in aquatic environments: An interlaboratory comparison. Environ. Sci. Technol. 44, 9405–9412. doi: 10.1021/es102362t.

Murphy, K.R., Stedmon, C.A., Wenig, P., Bro, R., 2014. OpenFluor– an online spectral library of auto–fluorescence by organic compounds in the environment. Anal. Methods 6, 658. doi: 10.1039/c3ay41935e.

Murphy, K.R.K.R., Stedmon, C.A., Graeber, D., Bro, R., 2013. Fluorescence spectroscopy and multi–way techniques. PARAFAC. Anal. Methods 5, 6557–6566. doi: 10.1039/c3ay41160e.

Nagata, T., 2008. Organic matter–bacteria interactions in seawaters, in: Kirchman, D.L. (Ed.), Microbial Ecology of the Oceans. Wiley, New Jersey, pp. 207–241.

Nelson, N.B., Carlson, C.A., Steinberg, D.K., 2004. Production of chromophoric dissolved organic matter by Sargasso Sea microbes. Mar. Chem. 89, 273–287. doi: 10.1016/j.marchem.2004.02.017.

Nelson, N.B., Gauglitz, J.M., 2016. Optical Signatures of Dissolved Organic Matter Transformation in the Global Ocean. Front. Mar. Sci. 2, 118. doi: 10.3389/fmars.2015.00118.

Nelson, N.B., Siegel, D.A., 2013. The global distribution and dynamics of chromophoric dissolved organic matter. Ann. Rev. Mar. Sci. 5, 447–476. doi: 10.1146/annurev–marine–120710–100751.

Nelson, N.B., Siegel, D.A., 2002. Chapter 11 – Chromophoric DOM in the Open Ocean, in: Hansell, D.A., Carlson, C.A. (Eds.), Biogeochemistry of Marine Dissolved Organic Matter. Academic Press, San Diego, p. 547–578. doi: 10.1016/B978–012323841–2/50013–0.

Nelson, N.B., Siegel, D.A., Carlson, C.A., Swan, C., Smethie, W.M., Khatiwala, S., 2007. Hydrography of chromophoric dissolved organic matter in the North Atlantic. Deep Sea Res. Part I Oceanogr. Res. Pap. 54, 710–731. doi: 10.1016/j.dsr.2007.02.006.

Nelson, N.B., Siegel, D.A., Carlson, C.A., Swan, C.M., 2010. Tracing global biogeochemical cycles and meridional overturning circulation using chromophoric dissolved organic matter. Geophys. Res. Lett. 37, L03610. doi: 10.1029/2009GL042325.

Nelson, N.B., Siegel, D.A., Michaels, A.F., 1998. Seasonal dynamics of colored dissolved material in the Sargasso Sea. Deep Sea Res. Part I Oceanogr. Res. Pap. 45, 931–957. doi: 10.1016/S0967–0637(97)00106–4.

Nielsen, J. N., 1912. Hydrography of the Mediterranean and adjacent waters. Rep. Dan. Oceanogr. Exp. Medit. 1, 77–192.

Nieto–Cid, M., Álvarez–Salgado, X.A., Gago, J., Pérez, F.F., 2005. DOM fluorescence, a tracer for biogeochemical processes in a coastal upwelling system (NW Iberian Peninsula). Mar. Ecol. Prog. Ser. 297, 33–50. doi: 10.3354/meps297033.

Nieto–Cid, M., Álvarez–Salgado, X.A., Pérez, F.F., 2006. Microbial and photochemical reactivity of fluorescent dissolved organic matter in a coastal upwelling system. Limnol. Oceanogr. 51, 1391–1400. doi: 10.4319/lo.2006.51.3.1391.

Ogawa, H., Amagai, Y., Koike, I., Kaiser, K., Benner, R., 2001. Production of refractory dissolved organic matter by bacteria. Science. 292, 917–920. doi: 10.1126/science.1057627

Oksanen, J., Blanchet, F.G., Kindt, R., Legendre, P., Minchin, P.R., O'Hara, R.B., Simpson, G.L., Solymos, P., Stevens, M.H.H., Wagner, H., 2016. vegan: Community Ecology Package. R package version 2.3–5.

Organelli, E., Bricaud, A., Antoine, D., Matsuoka, A., 2014. Seasonal dynamics of light absorption by chromophoric dissolved organic matter (CDOM) in the NW Mediterranean Sea (BOUSSOLE site). Deep Sea Res. Part I Oceanogr. Res. Pap. 91, 72–85. doi: 10.1016/j.dsr.2014.05.003.

Ortega–Retuerta, E., Reche, I., Pulido–Villena, E., Agustí, S., Duarte, C.M., 2010a. Distribution and photoreactivity of chromophoric dissolved organic matter in the Antarctic Peninsula (Southern Ocean). Mar. Chem. 118, 129–139. doi: 10.1016/j.marchem.2009.11.008.

Ortega–Retuerta, E., Siegel, D.A., Nelson, N.B., Duarte, C.M., Reche, I., 2010b. Observations of chromophoric dissolved and detrital organic matter distribution using remote sensing in the Southern Ocean: Validation, dynamics and regulation. J. Mar. Syst. 82, 295–303. doi: 10.1016/j.jmarsys.2010.06.004.

Osburn, C.L., Bianchi, T.S., 2016. Editorial: Linking optical and chemical properties of dissolved organic matter in natural waters. Front. Mar. Sci. 3:223. doi: 10.3389/fmars.2016.00223.

Osburn, C.L., Del Vecchio, R., Boyd, T.J., 2014. Physicochemical effects on dissolved organic matter fluorescence in natural waters, in: Coble, P., Lead, J., Baker, A., Reynolds, D.M., Spencer, R.G.M. (Eds.), Aquatic Organic Matter Fluorescence, Cambridge Environmental Chemistry Series. Cambridge University Press, New York, pp. 233–277. doi: 10.1017/CBO9781139045452.012.

Osterholz, H., Dittmar, T., Niggemann, J., 2014. Molecular evidence for rapid dissolved organic matter turnover in Arctic fjords. Mar. Chem. 160, 1–10. doi: 10.1016/j.marchem.2014.01.002.

Osterholz, H., Niggemann, J., Giebel, H.–A., Simon, M., Dittmar, T., 2015. Inefficient microbial production of refractory dissolved organic matter in the ocean. Nat. Commun. 6, 7422. doi: 10.10381ncomms8422.

Özturgut, E., 1976. The Source and Spreading of the Levantine Intermediate Water in the Eastern Mediterranean, Saclant ASW Research Center Memorandum Sm–92. La Spezia, Italy 45.

Panagiotopoulos, C., Sempéré, R., 2005. Analytical methods for the determination of sugars in marine samples: A historical perspective and future directions. Limnol. Oceanogr. Methods 3, 419–454. doi: 10.4319/lom.2005.3.419.

Para, J., Coble, P.G., Charrière, B., Tedetti, M., Fontana, C., Sempéré, R., 2010. Fluorescence and absorption properties of chromophoric dissolved organic matter (CDOM) in coastal surface waters of the northwestern Mediterranean Sea, influence of the Rhône River. Biogeosciences 7, 4083–4103. doi: 10.5194/bg–7–4083–2010.

Patara, L., Pinardi, N., Corselli, C., Malinverno, E., Tonani, M., Santoleri, R., Masina, S., 2009. Particle fluxes in the deep Eastern Mediterranean basins: the role of ocean vertical velocities. Biogeosciences 6, 333–348. doi: 10.5194/bg–6–333–2009.

Paul, A.J., Bach, L.T., Schulz, K.–G., Boxhammer, T., Czerny, J., Achterberg, E.P., Hellemann, D., Trense, Y., Nausch, M., Sswat, M., Riebesell, U., 2015. Effect of elevated CO2 on organic matter pools and fluxes in a summer Baltic Sea plankton community. Biogeosciences 12, 6181–6203. doi: 10.5194/bg–12–6181–2015.

Perez, F.F., Mouriño, C., Fraga, F., Rios, A.F., 1993. Displacement of water masses and remineralization rates off the Iberian Peninsula by nutrient anomalies. J. Mar. Res. 51, 869–892. doi: 10.1357/0022240933223891.

Pérez, G.L., Galí, M., Royer, S.–J., Sarmento, H., Gasol, J.M., Marrasé, C., Simó, R., 2016. Bio–optical characterization of offshore NW Mediterranean waters: CDOM contribution to the absorption budget and diffuse attenuation of downwelling irradiance. Deep Sea Res. Part I Oceanogr. Res. Pap. 114, 111–127. doi: 10.1016/j.dsr.2016.05.011.

Pitta, E., Zeri, C., Tzortziou, M., Mousdis, G., Scoullos, M., 2017. Seasonal variations in dissolved organic matter composition using absorbance and fluorescence spectroscopy in the Dardanelles Straits – North Aegean Sea mixing zone. Cont. Shelf Res. 149, 82–95. doi: 10.1016/j.csr.2016.07.013.

Poole, R., Tomczak, M., 1999. Optimum multiparameter analysis of the water mass structure in the Atlantic Ocean thermocline. Deep Sea Res. Part I Oceanogr. Res. Pap. 46, 1895–1921. doi: 10.1016/S0967–0637(99)00025–4.

Powley, H.R., Krom, M.D., Van Cappellen, P., 2016. Circulation and oxygen cycling in the Mediterranean Sea: Sensitivity to future climate change. J. Geophys. Res. Ocean. 121, 8230–8247. doi: 10.1002/2016JC012224.

Puig, P., Madron, X.D. de, Salat, J., Schroeder, K., Martín, J., Karageorgis, A.P., Palanques, A., Roullier, F., Lopez–Jurado, J.L., Emelianov, M., Moutin, T., Houpert, L., 2013. Thick bottom nepheloid layers in the western Mediterranean generated by deep dense shelf water cascading. Prog. Oceanogr. 111, 1–23. doi: 10.1016/j.pocean.2012.10.003.

Pujo–Pay, M., Conan, P., 2003. Seasonal variability and export of dissolved organic nitrogen in the northwestern Mediterranean Sea. J. Geophys. Res. Ocean. 108, 3188 doi: 10.1029/2000JC000368.

Pujo–Pay, M., Conan, P., Oriol, L., Cornet–Barthaux, V., Falco, C., Ghiglione, J.F., Goyet, C., Moutin, T., Prieur, L., 2011. Integrated survey of elemental stoichiometry (C, N, P) from the western to eastern Mediterranean Sea. Biogeosciences. 8, 883–899. doi: 10.5194/bg–8–883–2011.

Raeke, J., Lechtenfeld, O.J., Wagner, M., Herzsprung, P., Reemtsma, T., 2016. Selectivity of solid phase extraction of freshwater dissolved organic matter and its effect on ultrahigh resolution mass spectra. Environ. Sci. Process. Impacts 18, 918–927. doi: 10.1039/C6EM00200E.

Redfield, A.C., Ketchum, B.H., and Richards, F.A., 1963. The influence of organisms on the composition of seawater, in: Hill, M.N. (Ed.), The Sea. Wiley Interscience, Hoboken, N.J., New York, pp. 26–77.

Reemtsma, T., These, A., Linscheid, M., Leenheer, J., Spitzy, A., 2008. Molecular and Structural

Characterization of Dissolved Organic Matter from the Deep Ocean by FTICR–MS, Including Hydrophilic Nitrogenous Organic Molecules. Environ. Sci. Technol. 42, 1430–1437. doi: 10.1021/es7021413.

Repeta, D.J., 2015. Chapter 2 – Chemical Characterization and Cycling of Dissolved Organic Matter, in: Hansell, D.A., Carlson, C.A. (Eds.), Biogeochemistry of Marine Dissolved Organic Matter. pp. 21–63. doi: 10.1016/B978–0–12–405940–5.00002–9.

Repeta, D.J., Ferrón, S., Sosa, O.A., Johnson, C.G., Repeta, L.D., Acker, M., DeLong, E.F., Karl, D.M., 2016. Marine methane paradox explained by bacterial degradation of dissolved organic matter. Nat. Geosci. 9, 884. doi: 10.1038/NGEO2837.

Repeta, D.J., Hansell, D.A., Carlson, C.A., 2015. Chapter 2 – Chemical characterization and cycling of dissolved organic matter, in: Hansell, D.A., Carlson, C.A. (Eds.), Biogeochemistry of Marine Dissolved Organic Matter. Academic Press, Waltham MA, USA, pp. 22–65.

Reygondeau, G., Guieu, C., Benedetti, F., Irisson, J.–O., Ayata, S.–D., Gasparini, S., Koubbi, P., 2017. Biogeochemical regions of the Mediterranean Sea: An objective multidimensional and multivariate environmental approach. Prog. Oceanogr. 151, 138–148. doi: 10.1016/J.POCEAN.2016.11.001.

Rhein, M., Rintoul, S.R., Aoki, S., Campos, E., Chambers, D., Feely, R.A., Gulev, S., Johnson, G.C., Josey, S.A., Kostianoy, A., Mauritzen, C., Roemmich, D., Talley, L.D., Wang, F., 2013. Observations: Ocean, in: Stocker, T.F., Qin, D., Plattner, G.–K., Tignor, M., Allen, S.K., Boschung, J., Nauels, A., Xia, Y., Bex, V., Midgley, P.M. (Eds.), Climate Change 2013: The Physical Science Basis. Contribution of Working Group I to the Fifth Assessment Report of the Intergovernmental Panel on Climate Change. Cambridge University Press, Cambridge.

Ridgwell, A., Arndt, S., 2015. Chapter 1 – Why Dissolved Organics Matter: DOC in Ancient Oceans and Past Climate Change, in: Hansell, D.A., Carlson, C.A. (Eds.), Biogeochemistry of Marine Dissolved Organic Matter. pp. 1–20. doi: 10.1016/B978–0–12–405940–5.00001–7.

Robinson, A.R., Leslie, W.G., Theocharis, A., Lascaratos, A., 2001. Mediterranean sea circulation. Encycl. Ocean Sci. 1689–1705. doi: 10.1006/rwos.2001.0376.

Roether, W., Klein, B., Beitzel, V., Manca, B.B., 1998. Property distributions and transient–tracer ages in Levantine Intermediate Water in the Eastern Mediterranean. J. Mar. Syst. 18, 71–87. doi: 10.1016/S0924–7963(98)00006–2.

Roether, W., Klein, B., Manca, B., Theocharis, A., Kioroglou, S., 2007. Transient Eastern Mediterranean deep waters in response to the massive dense–water output of the Aegean Sea in the 1990s. Limnol. Oceanogr. 74, 540–571. doi: 10.1016/j.pocean.2007.03.001.

Roether, W., Manca, B.B., Klein, B., Bregant, D., Georgopoulos, D., Beitzel, V., Kovacevic, V., Luchetta, A., 1996. Recent changes in eastern Mediterranean deep waters. Science . 271, 333–335. doi: 10.1126/science.271.5247.333.

Romera–Castillo, C., Álvarez–Salgado, X.A., Galí, M., Gasol, J.M., Marrasé, C., 2013. Combined effect of light exposure and microbial activity on distinct dissolved organic matter pools. A seasonal field study in an oligotrophic coastal system (Blanes Bay, NW Mediterranean). Mar. Chem. 148, 44–51. doi: 10.1016/j.marchem.2012.10.004.

Romera–Castillo, C., Jaffé, R., 2015. Free radical scavenging (antioxidant activity) of natural

dissolved organic matter. Mar. Chem. 177, 668–676. doi: 10.1016/j.marchem.2015.10.008.

Romera–Castillo, C., Letscher, R.T., Hansell, D.A., 2016. New nutrients exert fundamental control on dissolved organic carbon accumulation in the surface Atlantic Ocean. Proc. Natl. Acad. Sci. U. S. A. 113. doi: 10.1073/pnas.1605344113.

Romera–Castillo, C., Nieto–Cid, M., Castro, C.G., Marrasé, C., Largier, J., Barton, E.D., Álvarez–Salgado, X.A., 2011a. Fluorescence: Absorption coefficient ratio – Tracing photochemical and microbial degradation processes affecting coloured dissolved organic matter in a coastal system. Mar. Chem. 125, 26–38. doi: 10.1016/j.marchem.2011.02.001.

Romera–Castillo, C., Sarmento, H., Alvarez–Salgado, X.A., Gasol, J.M., Marrasé, C., 2011b. Net production and consumption of fluorescent colored dissolved organic matter by natural bacterial assemblages growing on marine phytoplankton exudates. Appl. Environ. Microbiol. 77, 7490–7498. doi: 10.1128/AEM.00200–11.

Romera–Castillo, C., Sarmento, H., Álvarez–Salgado, X.A., Gasol, J.M., Marrasé, C., 2010. Production of chromophoric dissolved organic matter by marine phytoplankton 55, 446–454. doi: 10.4319/lo.2010.55.1.0446.

Rubino, A., Hainbucher, D., 2007. A large abrupt change in the abyssal water masses of the eastern Mediterranean. Geophys. Res. Lett. 34, L23607. doi: 10.1029/2007GL031737.

Rossel, P.E., Vähätalo, A.V., Witt, M., Dittmar, T., 2013. Molecular composition of dissolved organic matter from a wetland plant (Juncus effusus) after photochemical and microbial decomposition (1.25 yr): Common features with deep sea dissolved organic matter. Org. Geochem. 60, 62–71. doi: 10.1016/j.orggeochem.2013.04.013.

Salat, J., Font, J., 1987. Water mass structure near and offshore the catalan coast during the winters of 1982 and 1983. Ann. Geophy. 5B, 49–54.

Salat, J., Puig, P., Latasa, M., 2010. Violent storms within the Sea: Dense water formation episodes in the NW Mediterranean. Adv. Geosci. 26, 53–59. doi: 10.5194/adgeo–26–53–2010.

Sannigrahi, P., Ingall, E.D., Benner, R., 2005. Cycling of dissolved and particulate organic matter at station Aloha: Insights from 13C NMR spectroscopy coupled with elemental, isotopic and molecular analyses. Deep Sea Res. Part I Oceanogr. Res. Pap. 52, 1429–1444. doi: 10.1016/j.dsr.2005.04.001.

Santinelli, C., 2015. Chapter 13 – DOC in the Mediterranean Sea, in: Hansell, D.A., Carlson, C.A. (Eds.), Biogeochemistry of Marine Dissolved Organic Matter. Academic Press, San Diego, pp. 579–608. doi: 10.1016/B978–0–12–405940–5.00013–3.

Santinelli, C., Follett, C., Retelletti Brogi, S., Xu, L., Repeta, D., 2015. Carbon isotope measurements reveal unexpected cycling of dissolved organic matter in the deep Mediterranean Sea. Mar. Chem. 177, 267–277. doi: 10.1016/j.marchem.2015.06.018.

Santinelli, C., Hansell, D.A., Ribera d'Alcalà, M., 2013. Influence of stratification on marine dissolved organic carbon (DOC) dynamics: The Mediterranean Sea case. Prog. Oceanogr. 119, 68–77. doi: 10.1016/j.pocean.2013.06.001.

Santinelli, C., Ibello, V., Lavezza, R., Civitarese, G., Seritti, A., 2012a. New insights into C, N and P stoichiometry in the Mediterranean Sea: The Adriatic Sea case. Cont. Shelf Res. 44, 83–

93. doi: 10.5194/bg–12–7025–2015.

Santinelli, C., Nannicini, L., Seritti, A., 2010. DOC dynamics in the meso and bathypelagic layers of the Mediterranean Sea. Deep. Res. Part II Top. Stud. Oceanogr. 57, 1446–1459. doi: 10.1016/jdsr2.2010.02.014.

Santinelli, C., Sempéré, R., Van Wambeke, F., Charriere, B., Seritti, A., 2012b. Organic carbon dynamics in the Mediterranean Sea: An integrated study. Global Biogeochem. Cycles 26, GB4004. doi: 10.1029/2011GB004151.

Sarmiento, J.L., Gruber, N., 2006. Ocean Biogeochemical Dynamics. Princeton University Press. doi: 10.1063/1.2754608.

Schlitzer, R., 2016. Ocean Data View. http://odv.awi.de.

Schlitzer, R., Roether, W., Oster, H., Junghans, H.–G., Hausmann, M., Johannsen, H., Michelato, A., 1991. Chlorofluoromethane and oxygen in the Eastern Mediterranean. Deep Sea Res. Part A, Oceanogr. Res. Pap. 38, 1531–1551. doi: 10.1016/0198–0149(91)90088–W.

Schmidt, F., Koch, B.P., Goldhammer, T., Elvert, M., Witt, M., Lin, Y.–S., Wendt, J., Zabel, M., Heuer, V.B., Hinrichs, K.–U., 2017. Unraveling signatures of biogeochemical processes and the depositional setting in the molecular composition of pore water DOM across different marine environments. Geochim. Cosmochim. Acta 207, 57–80. doi: 10.1016/j.gca.2017.03.005.

Schneider, A., Tanhua, T., Roether, W., Steinfeldt, R., 2014. Changes in ventilation of the Mediterranean Sea during the past 25 year. Ocean Sci. 10, 1–16. doi: 10.5194/os–10–1–2014.

Schröder, K., Gasparini, G.P., Tangherlini, M., Astraldi, M., 2006. Deep and intermediate water in the western Mediterranean under the influence of the Eastern Mediterranean Transient. Geophys. Res. Lett. 33, L21607. doi: 10.1029/2006GL027121.

Schroeder, K., Chiggiato, J., Bryden, H.L., Borghini, M., Ben Ismail, S., 2016. Abrupt climate shift in the Western Mediterranean Sea. Sci. Rep. 6, 23009. doi: 10.1038/srep23009.

Schroeder, K., Garcìa–Lafuente, J., Josey, S.A., Artale, V., Nardelli, B.B., Carrillo, A., Gačić, M., Gasparini, G.P., Herrmann, M., Lionello, P., Ludwig, W., Millot, C., Özsoy, E., Pisacane, G., Sánchez–Garrido, J.C., Sannino, G., Santoleri, R., Somot, S., Struglia, M., Stanev, E., Taupier–Letage, I., Tsimplis, M.N., Vargas–Yáñez, M., Zervakis, V., Zodiatis, G., 2012. Circulation of the Mediterranean Sea and its variability, in: Lionello, P. (Ed.), The Climate of the Mediterranean Region. Elsevier, pp. 187–256. doi: 10.1016/B978–0–12–416042–2.00003–3.

Seidel, M., Beck, M., Riedel, T., Waska, H., Suryaputra, I.G.N.A., Schnetger, B., Niggemann, J., Simon, M., Dittmar, T., 2014. Biogeochemistry of dissolved organic matter in an anoxic intertidal creek bank. Geochim. Cosmochim. Acta 140, 418–434. doi: 10.1016/j.gca.2014.05.038.

Seidel, M., Yager, P.L., Ward, N.D., Carpenter, E.J., Gomes, H.R., Krusche, A. V, Richey, J.E., Dittmar, T., Medeiros, P.M., 2015. Molecular–level changes of dissolved organic matter along the Amazon River–to–ocean continuum. Mar. Chem. 177, 218–231. doi: 10.1016/j.marchem.2015.06.019.

Sempéré, R., Para, J., Tedetti, M., Charrière, B., Mallet, M., 2015. Variability of Solar Radiation

and CDOM in Surface Coastal Waters of the Northwestern Mediterranean Sea. Photochem. Photobiol. 91, 851–861. doi: 10.1111/php.12434.

Sempéré, R., Yoro, S., Van Wambeke, F., Charrière, B., 2000. Microbial decomposition of large organic particles in the northwestern Mediterranean Sea:an experimental approach. Mar. Ecol. Prog. Ser. 198, 61–72. doi: 10.3354/meps198061.

Sharpless, C.M., Blough, N. V., 2014. The importance of charge–transfer interactions in determining chromophoric dissolved organic matter (CDOM) optical and photochemical properties. Environ. Sci. Process. Impacts 16, 654–671. doi: 10.1039/c3em00573a.

Siegel, D.A., Maritorena, S., Nelson, N.B., Hansell, D.A., Lorenzi–Kayser, M., 2002. Global distribution and dynamics of colored dissolved and detrital organic materials. J. Geophys. Res. C Ocean. 107, 3228. doi: 10.1029/2001JC000965.

Simjouw, J.–P., Minor, E.C., Mopper, K., 2005. Isolation and characterization of estuarine dissolved organic matter: Comparison of ultrafiltration and C18 solid–phase extraction techniques. Mar. Chem. 96, 219–235. doi: 10.1016/J.MARCHEM.2005.01.003.

Simpson, A.J., McNally, D.J., Simpson, M.J., 2011. NMR spectroscopy in environmental research: From molecular interactions to global processes. Prog. Nucl. Magn. Reson. Spectrosc. 58, 97–175. doi: 10.1016/j.pnmrs.2010.09.001.

Sipler, R.E., Bronk, D.A., 2015. Chapter 4 – Dynamics of Dissolved Organic Nitrogen, in Hansell, D.A., Carlson, C.A. (Eds.), Biogeochemistry of Marine Dissolved Organic Matter. Academic Press, San Diego, pp. 127–232. doi: 10.1016/B978–0–12–405940–5.00004–2.

Skliris, N., 2014. Past, Present and Future Patterns of the Thermohaline Circulation and Characteristic Water Masses of the Mediterranean Sea, in: Gofredo, S., Dubinsky, Z. (Eds.), The Mediterranean Sea. Its History and Present Challenges. Springer, pp. 29–48. doi: 10.1007/978–94–007–6704–1.

Skliris, N., Sofianos, S., Gkanasos, A., Mantziafou, A., Vervatis, V., Axaopoulos, P., Lascaratos, A., 2012. Decadal scale variability of sea surface temperature in the Mediterranean Sea in relation to atmospheric variability. Ocean Dyn. 62, 13–30. doi: 10.1007/s10236–011–0493–5.

Sleighter, R.L., Hatcher, P.G., 2008. Molecular characterization of dissolved organic matter (DOM) along a river to ocean transect of the lower Chesapeake Bay by ultrahigh resolution electrospray ionization Fourier transform ion cyclotron resonance mass spectrometry. Mar. Chem. 110, 140–152. doi: 10.1016/j.marchem.2008.04.008.

Sparnocchia, S., Gasparini, G., Astraldi, M., Borghini, M., Pistek, P., 1999. Dynamics and mixing of the Eastern Mediterranean outflow in the Tyrrhenian basin. J. Mar. Syst. 20, 301–317. doi: 10.1016/S0924–7963(98)00088–8.

Sparnocchia, S., Pietro Gasparini, G., Schroeder, K., Borghini, M., 2011. Oceanographic conditions in the NEMO region during the KM3NeT project (April 2006–May 2009). Nucl. Instrum. Methods Phys. Res., Sect. A 626–627, S87–S90. doi: 10.1016/j.nima.2010.06.231.

Stedmon, C.A., Cory R. M., 2014. Biological Origins and Fate of Fluorescent Dissolved Organic Matter in Aquatic Environments, in: Coble, P.G., Lead, J., Baker, A., Reynolds, P.M., Spencer, R.G.M. (Eds.), Aquatic Organic Matter Fluorescence. Cambridge University Press, pp. 278–299.

Stedmon, C.A., Markager, S., 2005. Tracing the production and degradation of autochthonous fractions of dissolved organic matter by fluorescence analysis. Limnol. Oceanogr. 50, 686–697. doi: 10.4319/lo.2005.50.2.0686.

Stedmon, C.A., Markager, S., Bro, R., 2003. Tracing dissolved organic matter in aquatic environments using a new approach to fluorescence spectroscopy. Mar. Chem. 82, 239–254. doi: 10.1016/S0304–4203(03)00072–0.

Stedmon, C.A., Nelson, N.B., 2015. Chapter 10 – The Optical Properties of DOM in the Ocean, in: Hansell, D.A., Carlson, C.A. (Eds.), Biogeochemistry of Marine Dissolved Organic Matter. Elsevier, pp. 481–508. doi: 10.1016/B978–0–12–405940–5.00010–8.

Stedmon, C.A., Bro, R., 2008. Characterizing dissolved organic matter fluorescence with parallel factor analysis: A tutorial. Limnol. Oceanogr. Methods 6, 572–579. doi: 10.4319/lom.2008.6.572.

Steinberg, D.K., Van Mooy, B.A.S., Buesseler, K.O., Boyd, P.W., Kobari, T., Karl, D.M., 2008. Bacterial vs. zooplankton control of sinking particle flux in the ocean's twilight zone. Limnol. Oceanogr. 53, 1327–1338. doi: 10.4319/lo.2008.53.4.1327.

Stenson, A.C., Marshall, A.G., Cooper, W.T., 2003. Exact Masses and Chemical Formulas of Individual Suwannee River Fulvic Acids from Ultrahigh Resolution Electrospray Ionization Fourier Transform Ion Cyclotron Resonance Mass Spectra. Anal. Chem. 75, 1275–1284. doi: 10.1021/ac026106p.

Stöven, T., Tanhua, T., 2014. Ventilation of the Mediterranean Sea constrained by multiple transient tracer measurements. Ocean Sci. 10, 439–457. doi: 10.5194/os–10–439–2014.

Stubbins, A., Dittmar, T., 2015. Illuminating the deep: Molecular signatures of photochemical alteration of dissolved organic matter from North Atlantic Deep Water. Mar. Chem. 177, 318–324. doi: 10.1016/j.marchem.2015.06.020.

Stubbins, A., Lapierre, J.–F., Berggren, M., Prairie, Y.T., Dittmar, T., Del Giorgio, P.A., 2014. What's in an EEM? Molecular signatures associated with dissolved organic fluorescence in boreal Canada. Environ. Sci. Technol. 48, 10598–10606. doi: 10.1021/es502086e.

Stubbins, A., Spencer, R.G.M., Chen, H., Hatcher, P.G., Mopper, K., Hernes, P.J., Mwamba, V.L., Mangangu, A.M., Wabakanghanzi, J.N., Six, J., 2010. Illuminated darkness: Molecular signatures of Congo River dissolved organic matter and its photochemical alteration as revealed by ultrahigh precision mass spectrometry. Limnol. Oceanogr. 55, 1467–1477. doi: 10.1016/j.marchem.2015.06.020.

Stuiver, M., Quay, P.D., Ostlund, H.G., 1983. Abyssal water carbon–14 distribution and the age of the world oceans. Science 219, 849–851. doi: 10.1126/science.219.4586.849.

Tanhua, T., Hainbucher, D., Schroeder, K., Cardin, V., Álvarez, M., Civitarese, G., 2013. The Mediterranean Sea system: A review and an introduction to the special issue. Ocean Sci. 9, 789–803. doi: 10.5194/os–9–789–2013.

Theocharis, A., Georgopoulos, D., Lascaratos, A., Nittis, K., 1993. Water masses and circulation in the central region of the Eastern Mediterranean: Eastern Ionian, South Aegean and Northwest Levantine, 1986–1987. Deep Sea Res.Part II 40, 1121–1142. doi: 10.1016/0967–0645(93)90064–T.

Theocharis, A., Nittis, K., Kontoyiannis, H., Papageorgiou, E., Balopoulos, E., 1999. Climatic

changes in the Aegean Sea influence the eastern Mediterranean thermohaline circulation (1986–1997). Geophys. Res. Lett. 26, 1617–1620. doi: 10.1029/1999GL900320.

These, A., Reemtsma, T., 2003. Limitations of Electrospray Ionization of Fulvic and Humic Acids as Visible from Size Exclusion Chromatography with Organic Carbon and Mass Spectrometric Detection. Anal. Chem. 75, 6275–6281. doi: 10.1021/ac034399w.

Thingstad, T.F., Hagström, A., Rassoulzadegan, F., 1997. Accumulation of degradable DOC in surface waters: Is it caused by a malfunctioning microbial loop? Limnol. Oceanogr. 42, 398–404. doi: 10.4319/lo.1997.42.2.0398.

Timko, S.A., Maydanov, A., Pittelli, S.L., Conte, M.H., Cooper, W.J., Koch, B.P., Schmitt–Kopplin, P., Gonsior, M., 2015. Depth–dependent photodegradation of marine dissolved organic matter. Front. Mar. Sci. 2, 1–13. doi: 10.3389/fmars.2015.00066.

Tomczak, M., 1999. Some historical, theoretical and applied aspects of quantitative water mass analysis, J. Mar. Res. 57, 275–303. doi: 10.1357/002224099321618227.

Torres–Valdés, S., Roussenov, V.M., Sanders, R., Reynolds, S., Pan, X., Mather, R., Landolfi, A., Wolff, G.A., Achterberg, E.P., Williams, R.G., 2009. Distribution of dissolved organic nutrients and their effect on export production over the Atlantic Ocean. Global Biogeochem. Cycles 23, GB4019. doi: 10.1029/2008GB003389.

Tsimplis, M.N., Zervakis, V., Josey, S.A., Peneva, E.L., Struglia, M. V, Stanev, E. V, Theocharis, A., Lionello, P., Malanotte–Rizzoli, P., Artale, V., Tragou, E., Oguz, T., 2006. Chapter 4 Changes in the oceanography of the Mediterranean Sea and their link to climate variability, in: Lionello, P., Malannote–Rizzoli, P, Boscolo, R. (Eds.), Mediterranean Climate Variability. Elsevier, pp. 227–282. doi: 10.1016/S1571–9197(06)80007–8.

UNESCO, 1985. The International System of Units (SI) in oceanography. UNESCO Tech. Paper. Marine Science 45, 1–124.

UNESCO, 1986. Progress on oceanographic tables and standards 1983–1986. Work and recommendations of UNESCO/SCOR/ICES/IAPSO joint panel UNESCO. Tech. Pap. Marine Science 50, 1–59.

Velaoras, D., Krokos, G., Nittis, K., Theocharis, A., 2014. Dense intermediate water outflow from the Cretan Sea: A salinity driven, recurrent phenomenon, connected to thermohaline circulation changes. J. Geophys. Res. Ocean. 119, 4797–4820. doi: 10.1002/2014JC009937.

Vetter, T.A., Perdue, E.M., Ingall, E., Koprivnjak, J.–F., Pfromm, P.H., 2007. Combining reverse osmosis and electrodialysis for more complete recovery of dissolved organic matter from seawater. Sep. Purif. Technol. 56, 383–387. doi: 10.1016/j.seppur.2007.04.012.

Vilibić, I., Orlić, M., 2002. Adriatic water masses, their rates of formation and transport through the Otranto Strait. Deep Sea Res. Part I: Oceanogr. Res. Pap. 49, 1321–1340. doi: 10.1016/S0967–0637(02)00028–6.

Wagner, S., Jaffé, R., Cawley, K., Dittmar, T., Stubbins, A., 2015a. Associations between the molecular and optical properties of dissolved organic matter in the Florida Everglades, a model coastal wetland system. Front. Chem. 3, 66. doi: 10.3389/fchem.2015.00066.

Walker, B.D., Beaupré, S.R., Guilderson, T.P., Druffel, E.R.M., McCarthy, M.D., 2011. Large–volume ultrafiltration for the study of radiocarbon signatures and size vs. age

relationships in marine dissolved organic matter. Geochim. Cosmochim. Acta 75, 5187–5202. doi: 10.1016/j.gca.2011.06.015.

Walker, B.D., Beaupré, S.R., Guilderson, T.P., McCarthy, M.D., Druffel, E.R.M., 2016a. Pacific carbon cycling constrained by organic matter size, age and composition relationships. Nat. Geosci. 9, 888–891. doi: 10.1038/NGEO2830.

Walker, B.D., Primeau, F.W., Beaupré, S.R., Guilderson, T.P., Druffel, E.R.M., McCarthy, M.D., 2016b. Linked changes in marine dissolved organic carbon molecular size and radiocarbon age. Geophys. Res. Lett. 43, 10385–10393. doi: 10.1002/2016GL070359.

Wang, Z., Cao, J., Meng, F., 2015. Interactions between protein–like and humic–like components in dissolved organic matter revealed by fluorescence quenching. Water Res. 68, 404–413. doi: 10.1016/j.watres.2014.10.024.

Weishaar, J.L., Aiken, G.R., Bergamaschi, B.A., Fram, M.S., Fujii, R., Mopper, K., 2003. Evaluation of specific ultraviolet absorbance as an indicator of the chemical composition and reactivity of dissolved organic carbon. Environ. Sci. Technol. 37, 4702–4708. doi: 10.1021/es030360x.

Wilson, H.F., Xenopoulos, M.A., 2009. Effects of agricultural land use on the composition of fluvial dissolved organic matter. Nat. Geosci. 2, 37–41. doi: 10.1038/ngeo391.

Wood, S.N., 2006. Generalized additive models : an introduction with R. Chapman & Hall/CRC, London.

Wu, P., Haines, K., Pinardi, N., 2000. Toward an understanding of deep–water renewal in the Eastern Mediterranean. J. Phys. Oceanogr. 30, 443–458. doi: 10.1175/1520–0485(2000)030<0443:TAUODW>2.0.CO;2.

Wünsch, U.J., Murphy, K.R., Stedmon, C.A., 2015. Fluorescence quantum yields of natural organic matter and organic compounds: Implications for the fluorescence–based interpretation of organic matter composition. Front. Mar. Sci. 2, 98 doi: 10.3389/fmars.2015.00098.

Wüst, G., 1961. On the vertical circulation of the Mediterranean Sea. J. Geophys. Res. 66, 3261–3271. doi: 10.1029/JZ066i010p03261.

Xing, X., Claustre, H., Wang, H., Poteau, A., D`Ortenzio, F., 2014. Seasonal dynamics in colored dissolved organic matter in the Mediterranean Sea: Patterns and drivers. Deep Sea Res. Part I Oceanogr. Res. Pap. 83, 93–101. doi: 10.1016/j.dsr.2013.09.008.

Xing, X., Morel, A., Claustre, H., D'Ortenzio, F., Poteau, A., 2012. Combined processing and mutual interpretation of radiometry and fluorometry from autonomous profiling Bio–Argo floats: 2. Colored dissolved organic matter absorption retrieval. J. Geophys. Res. Ocean. 117, C04022. doi: 10.1029/2011JC007632.

Xu, H., Guo, L., 2017. Molecular size–dependent abundance and composition of dissolved organic matter in river, lake and sea waters. Water Res. 117, 115–126. doi: 10.1016/j.watres.2017.04.006.

Yamashita, Y., Cory, R.M.M., Nishioka, J., Kuma, K., Tanoue, E., Jaffé, R., 2010. Fluorescence characteristics of dissolved organic matter in the deep waters of the Okhotsk Sea and the northwestern North Pacific Ocean. Deep. Res. Part II Top. Stud. Oceanogr. 57, 1478–1485. doi: 10.1016/j.dsr2.2010.02.016.

Yamashita, Y., Hashihama, F., Saito, H., Fukuda, H., Ogawa, H., 2017. Factors controlling the geographical distribution of fluorescent dissolved organic matter in the surface waters of the Pacific Ocean. Limnol. Oceanogr. 62, 2360–2374. doi: 10.1002/lno.10570.

Yamashita, Y., Jaffé, R., Maie, N., Tanoue, E., 2008. Assessing the dynamics of dissolved organic matter (DOM) in coastal environments by excitation emission matrix fluorescence and parallel factor analysis (EEM-PARAFAC). Limnol. Oceanogr. 53, 1900–1908. doi: 10.4319/lo.2008.53.5–1900.

Yamashita, Y., Tanoue, E., 2009. Basin scale distribution of chromophoric dissolved organic matter in the Pacific Ocean. Limnol. Oceanogr. 54, 598–609. doi: 10.4319/lo.2009.54.2.0598.

Yamashita, Y., Tanoue, E., 2008. Production of bio–refractory fluorescent dissolved organic matter in the ocean interior. Nat. Geosci. 1, 579–582. doi: 10.1038/ngeo279.

Yamashita, Y., Tanoue, E., 2003. Chemical characterization of protein–like fluorophores in DOM in relation to aromatic amino acids. Mar. Chem. 82, 255–271. doi: 10.1016/S0304–4203(03)00073–2.

Zark, M., Broda, N.K., Hornick, T., Grossart, H.–P., Riebesell, U., Dittmar, T., 2017. Ocean Acidification Experiments in Large–Scale Mesocosms Reveal Similar Dynamics of Dissolved Organic Matter Production and Biotransformation. Front. Mar. Sci. 4, 271. doi: 10.3389/fmars.2017.00271.

Zark, M., Riebesell, U., Dittmar, T., 2015. Effects of ocean acidification on marine dissolved organic matter are not detectable over the succession of phytoplankton blooms. Sci. Adv. 1, e1500531. doi: 10.1126/sciadv.1500531.

Zepp, R.G., Erickson III, D.J., Paul, N.D., Sulzberger, B., 2011. Effects of solar UV radiation and climate change on biogeochemical cycling: interactions and feedbacks. Photochem. Photobiol. Sci. 10, 261–279. doi: 10.1039/C0PP90037K.

Zeri, C., Beşiktepe, T., Giannakourou, A., Krasakopoulou, E., Tzortziou, M., Tsoliakos, D., Pavlidou, A., Mousdis, G., Pitta, E., Scoullos, M., Papathanassiou, E., 2014. Chemical properties and fluorescence of DOM in relation to biodegradation in the interconnected Marmara–North Aegean Seas during August 2008. J. Mar. Syst. 135, 124–136. doi: 10.1016/j.jmarsys.2013.11.019.

Zhao, W., Lv, L., Miao, H., 2013. Tracing the Variability of Dissolved Organic Matter Fluorescence in the East China Sea in the Red Tide Season with use of Excitation–emission Matrix Spectroscopy and Parallel Factor Analysis. Mar. Sci. Res. Dev. 4, 144. doi: 10.4172/2155–9910.1000144.

Zhao, Z., Gonsior, M., Luek, J., Timko, S., Ianiri, H., Hertkorn, N., Schmitt–Kopplin, P., Fang, X., Zeng, Q., Jiao, N., Chen, F., 2017. Picocyanobacteria and deep–ocean fluorescent dissolved organic matter share similar optical properties. Nat. Commun. 8, 15284. doi: 10.0.4.14/ncomms15284.

Ziolkowski, L.A., Druffel, E.R.M., 2010. Aged black carbon identified in marine dissolved organic carbon. Geophys. Res. Lett. 37, L16601. doi: 10.1029/2010GL043963.

Zsolnay, A., Baigar, E., Jimenez, M., Steinweg, B., Saccomandi, F., 1999. Differentiating with fluorescence spectroscopy the sources of dissolved organic matter in soils subjected to drying. Chemosphere 38, 45–50. doi: 10.1016/S0045–6535(98)00166–0.

Annex

LIMNOLOGY
and
OCEANOGRAPHY

ASLO

Limnol. Oceanogr. 62, 2017, 2699–2712

doi: 10.1002/lno.10600

Molecular composition of dissolved organic matter in the Mediterranean Sea

Alba María Martínez-Pérez,[1]* **Helena Osterholz**,[2] **Mar Nieto-Cid**,[1] **Marta Álvarez**,[3] **Thorsten Dittmar**,[2] **Xosé Antón Álvarez-Salgado**[1]

[1]Consejo Superior de Investigaciones Científicas – Instituto de Investigacións Mariñas (CSIC–IIM), Vigo, Spain
[2]Research Group for Marine Geochemistry, Institute for Chemistry and Biology of the Marine Environment (ICBM), Carl von Ossietzky University, Oldenburg, Germany
[3]Instituto Español de Oceanografía (IEO), Centro Oceanográfico de A Coruña, A Coruña, Spain

Abstract

The molecular composition of marine dissolved organic matter (DOM) is still poorly understood, particularly in the Mediterranean Sea. In this work, DOM from the open Mediterranean Sea and the adjacent Northeast Atlantic Ocean was isolated by solid-phase extraction (SPE-DOM) and molecularly characterized using Fourier-transform ion cyclotron resonance mass spectrometry. We assessed the gradual reworking of the SPE-DOM transported by the shallow overturning circulation of the Mediterranean Sea by following the increase in molecular weight (+20 Da), oxygenation (+5%), degradation index (Ideg +22%), and the proportional decrease of unsaturated aliphatic compounds (+34%) along the Levantine Intermediate Water. This reworked SPE-DOM that leaves the Mediterranean Sea through the Strait of Gibraltar strongly contrasts with the fresh material transported by the inflow of Atlantic water (Ideg −25%). In the deep eastern and western overturning cells, the molecular composition of the deep waters varied according to their area and/or time of formation. SPE-DOM of the waters formed in the Aegean Sea during the Eastern Mediterranean Transient (EMT) was more processed than the DOM in pre-EMT waters formed in the Adriatic Sea (molecular weight and the proportion of unsaturated aliphatic compounds were increased by 5 Da and 9%, respectively). Furthermore, pre-EMT waters contain more reworked SPE-DOM (Ideg +7%) than post-EMT waters formed also in the Adriatic Sea. In summary, our study shows that the Mediterranean Sea constitutes a laboratory basin where degradation processes and diagenetic transformations of DOM can be observed on close spatial and temporal scales.

Marine dissolved organic matter (DOM) is one of the largest and least understood reservoirs of reduced carbon on the Earth's surface (Hedges 1992; Hansell 2002). At 662 Pg C, DOM represents 96% of the total organic carbon in the oceans (Hansell et al. 2009). It is produced mainly in the epipelagic layer (0–150 m depth) as a result of phytoplankton photosynthesis and subsequent food web interactions (Carlson 2002). Most of this recently produced DOM is quickly respired to CO_2. However, a small fraction of this material escapes rapid mineralization, accumulating in the upper layers for eventual export to the dark ocean (> 150 m depth) by convective overturning and vertical mixing (Hansell et al. 2009).

To achieve a better understanding of the fate of DOM in the dark ocean, identifying the molecular composition and structure of this material is essential. Previous studies applying ^{1}H nuclear magnetic resonance (NMR), amino acid, and neutral sugar analysis of ultrafiltered DOM (UDOM) revealed that carbohydrates are main constituents of this material at the sea surface of the Mediterranean Sea (Jones et al. 2013). This pool decreases with depth indicating DOM biodegradation. In addition, a strong correlation between amino acid concentration, apparent oxygen utilization (AOU), and picoplankton activity has been observed (Meador et al. 2010; Jones et al. 2013).

Tangential-flow ultrafiltration with a 0.5–1 kDa cut-off is able to isolate up to 30% of marine DOM (Benner et al. 1992; Amon and Benner 1996; Benner et al. 1997). Solid-phase extraction (SPE) using styrene divinyl benzene polymer (PPL) cartridges has more recently been introduced as an efficient method for isolating more than 60% of marine

*Correspondence: albam@iim.csic.es

Additional Supporting Information may be found in the online version of this article.

DOM (Dittmar et al. 2008; Green et al. 2014). The salt-free extracts are accessible by modern, nontargeted ultrahigh-resolution analytical techniques such as Fourier-transform ion cyclotron resonance mass spectrometry (FT-ICR-MS) for a comprehensive characterization. Nowadays, FT-ICR-MS is a widely used technique to distinguish thousands of molecular formulae constituting the DOM pool. Previous studies on the molecular composition of DOM by FT-ICR-MS showed molecular level differences between terrestrial and marine DOM (Koch et al. 2005), open ocean and coastal DOM (Koprivnjak et al. 2009) as well as surface and deep water DOM in the North Pacific (Medeiros et al. 2015) and North Atlantic (Hansman et al. 2015) oceans. Furthermore, the effect of degradation on the molecular composition of DOM was investigated along the eastern Atlantic and Southern Oceans combining FT-ICR-MS with radiocarbon analysis (Flerus et al. 2012; Lechtenfeld et al. 2014). Hertkorn et al. (2006) combined multidimensional NMR with FT-ICR-MS on UDOM, reporting carboxylic-rich alicyclic molecules (CRAM) as a likely major component of the DOM (8% of the whole DOM pool). More studies exist on the molecular characterization of open ocean DOM by FT-ICR-MS (Hertkorn et al. 2006; Chen et al. 2014; Hansman et al. 2015; Medeiros et al. 2015), but DOM composition in the enclosed Mediterranean Sea has not been studied in this detail yet.

The Mediterranean Sea is considered a concentration basin (evaporation > precipitation + runoff) characterized by low nutrient concentrations. This is due to the imbalance between the bottom outflow of nutrient-rich Mediterranean Water and the surface inflow of nutrient-poor Atlantic water (AW) at the Strait of Gibraltar (Huertas et al. 2012). High oxygen concentrations in the deep layers are a consequence of the recent formation of the Mediterranean deep waters (Cruzado 1985). Relatively small in size, the Mediterranean Sea has been used as a test basin for general ocean circulation studies (Béthoux et al. 1998; Bergamasco and Malanotte-Rizzoli 2010). The time scale of the Mediterranean Sea meridional overturning circulation is about 50–80 yr (Pinardi and Masetti 2000), compared to about 350 yr for the world ocean (Laruelle et al. 2009).

During the HOTMIX cruise (April–May 2014), we collected samples at selected depths along a longitudinal transect from the Levantine Sea to the Northeast Atlantic Ocean to characterize the molecular composition of solid-phase extractable DOM (SPE-DOM) through the water column via FT-ICR-MS. The specific objectives of our study are to (1) determine the overall molecular composition of the SPE-DOM in the Mediterranean Sea; (2) compare the molecular composition between the inflow of Atlantic surface water entering the Mediterranean Sea and the overflow of Mediterranean water into the Atlantic Ocean; and (3) explore the main drivers controlling the DOM transformations through changes in the molecular characteristics of SPE-DOM in relation to the "oceanographic model system" of the Mediterranean Sea.

Materials and methods

Study site

The Mediterranean Sea is a semi-enclosed basin opened to the Atlantic Ocean through the Strait of Gibraltar. It is constituted by two basins of similar size, western and eastern, connected via the Strait of Sicily. The main water masses observed in the Mediterranean Sea are the AW in the epipelagic layer, the Levantine Intermediate Water (LIW) in the mesopelagic layer, and the Eastern (EMDW) and Western (WMDW) Mediterranean Deep waters in the bathypelagic layer. The Atlantic inflow enters the Strait of Gibraltar as a surface current of salinity (S) about 36.5, being slightly modified through evaporation and mixing with the outflowing Mediterranean waters, leading to the modified Atlantic water, which moves toward the East through a shallow and open thermohaline cell that spans the two basins and leads to the formation of intermediate waters in the eastern basin (Tsimplis et al. 2006; Bergamasco and Malanotte-Rizzoli 2010). These intermediate waters are formed by convection in the south of Rhodes (LIW) and in the Aegean Sea (Cretan intermediate water) and are found along the whole Mediterranean Sea between 200–500 m depth (Roether et al. 1998; Tsimplis et al. 2006). They present the maximum salinity of the Mediterranean water masses and outflow at the Strait of Gibraltar (Emelianov et al. 2006). The EMDW is formed in the Ionian Sea when water from the Southern Adriatic Sea plunges down through the Strait of Otranto and sinks to depths > 3000 m. Then, it flows eastward and occupies the water column below the LIW in the eastern Mediterranean basin presenting potential temperatures > 13.3°C and salinities > 38.66 (Wu et al. 2000). For a short period of time, during the Eastern Mediterranean Transient (EMT) in the middle 1990s, the main deep-water formation area was the Aegean Sea due to an abrupt shift in the climate and hydrography in this area, providing a warmer, more saline and denser deep water mass than the previously existing EMDW of Adriatic origin (Roether et al. 1996; Lascaratos et al. 1999; Klein et al. 2003). Hence, pre- and post-EMT varieties of EMDW of Adriatic origin coexists in the bathypelagic layer of the eastern basin. On the other basin, the WMDW is formed in winter in the Gulf of Lions (Gascard 1978) and occupies the water column below the LIW in the western Mediterranean basin with temperatures between 12.75°C and 12.80°C and salinities between 38.44 and 38.46 (Millot 1999). During the winter of 2004–2005, a strong convection event in the Gulf of Lions (Western Mediterranean Transition) led to the formation of a new WMDW variety, saltier and slightly warmer than previously (salinity of 38.47–38.50 and temperature of 12.87–12.90°C compared to 38.41–38.47 and 12.75–12.92°C; López-Jurado et al. 2005; Beuvier et al.

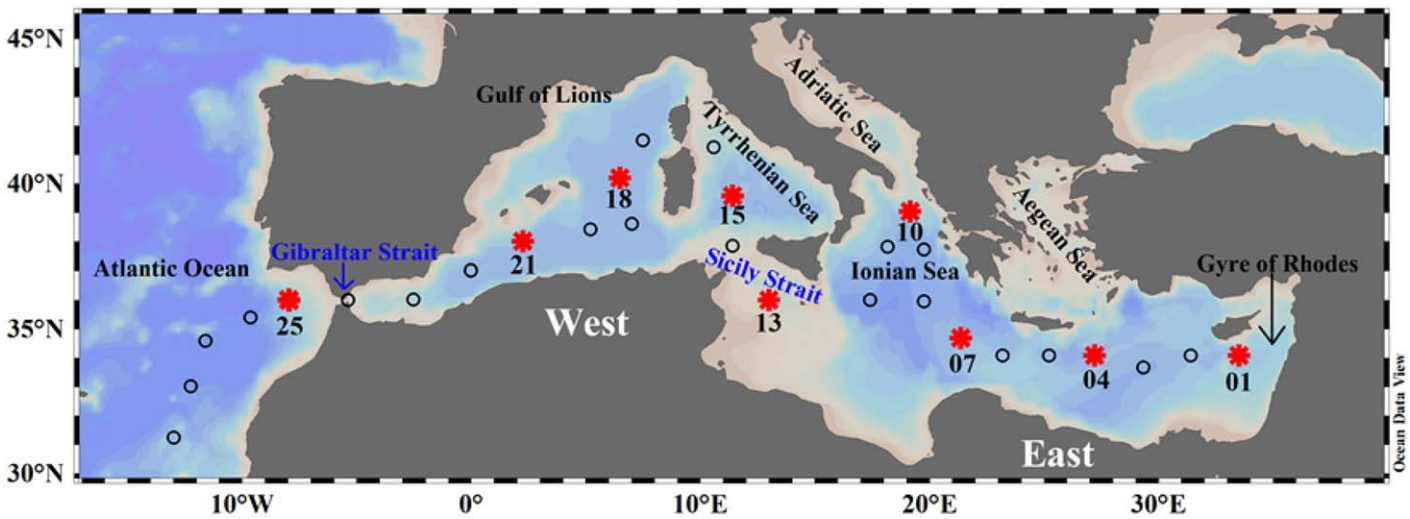

Fig. 1. Study area and sampling stations. The circles depict all cruise stations and asterisks represent the stations where samples were taken for molecular characterization of the DOM. Figure created using ODV software (Schlitzer 2016).

2012; Schroeder et al. 2016). Therefore, in the bathypelagic layer of the western Mediterranean, different varieties of WMDW coexist as well.

Sampling and determination of core parameters

Water samples were collected during the trans-Mediterranean cruise HOTMIX aboard R/V *Sarmiento de Gamboa* in spring 2014 (Heraklion, Crete, 27 April—Las Palmas, Canary Islands, 29 May). The transect consisted of 24 stations crossing the Mediterranean Sea from the Levantine Basin to the Strait of Gibraltar and 5 stations in the adjacent Northeast Atlantic Ocean (Fig. 1). At each station, full-depth continuous conductivity-temperature-depth (SBE 911 plus CTD probe), dissolved oxygen (DO; SBE-43 oxygen sensor) and chlorophyll fluorescence (SeaPoint fluorometer) profiles were recorded. Water samples were collected to analyze salinity, DO, and chlorophyll *a* (Chl *a*) to calibrate the sensors for conductivity, DO, and fluorescence, respectively. Conductivity measurements were converted into practical salinity scale values (UNESCO 1985). Samples for salinity were measured with a Guildline Portasal salinometer Model 8410A. Chl *a* concentration was determined in seawater samples (500 mL) filtered through Whatman GF/F filters and stored frozen until analysis. Pigments were extracted in cold acetone (90% v/v) for 24 h and analyzed by means of a 10 AU Turner Designs bench fluorometer, previously calibrated with pure Chl *a* (Sigma Aldrich), according to Holm-Hansen et al. (1965). DO was determined following the Winkler potentiometric method modified after Langdon (2010). The AOU ($AOU = O_{2sat} - O_2$) was calculated using the algorithm proposed by Benson and Krause (UNESCO 1986) for oxygen saturation (O_{2sat}). Potential temperature (θ) was calculated using TEOS-10 (UNESCO 2010).

Collection of SPE-DOM samples

At nine stations (red asterisks in Fig. 1) water samples were collected for the solid phase extraction of DOM (SPE-DOM) to perform FT-ICR-MS analysis. Four to five depths were sampled depending on the bathymetry of the stations (Fig. 2), except for the site at the Strait of Sicily (Sta. 13) where only LIW was sampled due to its shallowness. The deep chlorophyll maximum (DCM) was sampled according to the maximum fluorescence intensity, the LIW was sampled at the absolute maximum of the salinity profile at each station, the oxygen minimum layer (OML) was established on basis of the absolute minimum of the DO profile, and the deep waters were sampled according to the salinity and temperature characteristic of the bathypelagic zone of the eastern and western Mediterranean basins (Fig. 2).

The sampling strategy was restricted by time constraints during the cruise, which limited the number of collected samples, especially in the bathypelagic layer where different varieties of deep waters were found. Unfortunately, we were not able to sample any station in the Ionian Sea, so we missed the youngest variety of the EMDW. Note that although the hydrographic properties of the OML sample at Sta. 4 are reported in Supporting Information Table S1, this sample was rejected from the FT-ICR-MS analysis due to a contamination problem.

Water samples were collected in 5-liter acid-cleaned polycarbonate carboys, and then stored in the dark at 13°C until filtration within 5 h. Filtration was performed through precombusted (450°C, 4 h) Whatman GF/F filters in an acid-clean all-glass filtration system under positive pressure with low flow of high purity N_2. Two-liters aliquots of the filtrate were collected in acid-cleaned polytetrafluoroethylene (PTFE) bottles for SPE-DOM. Approximately 10 mL of the filtrate

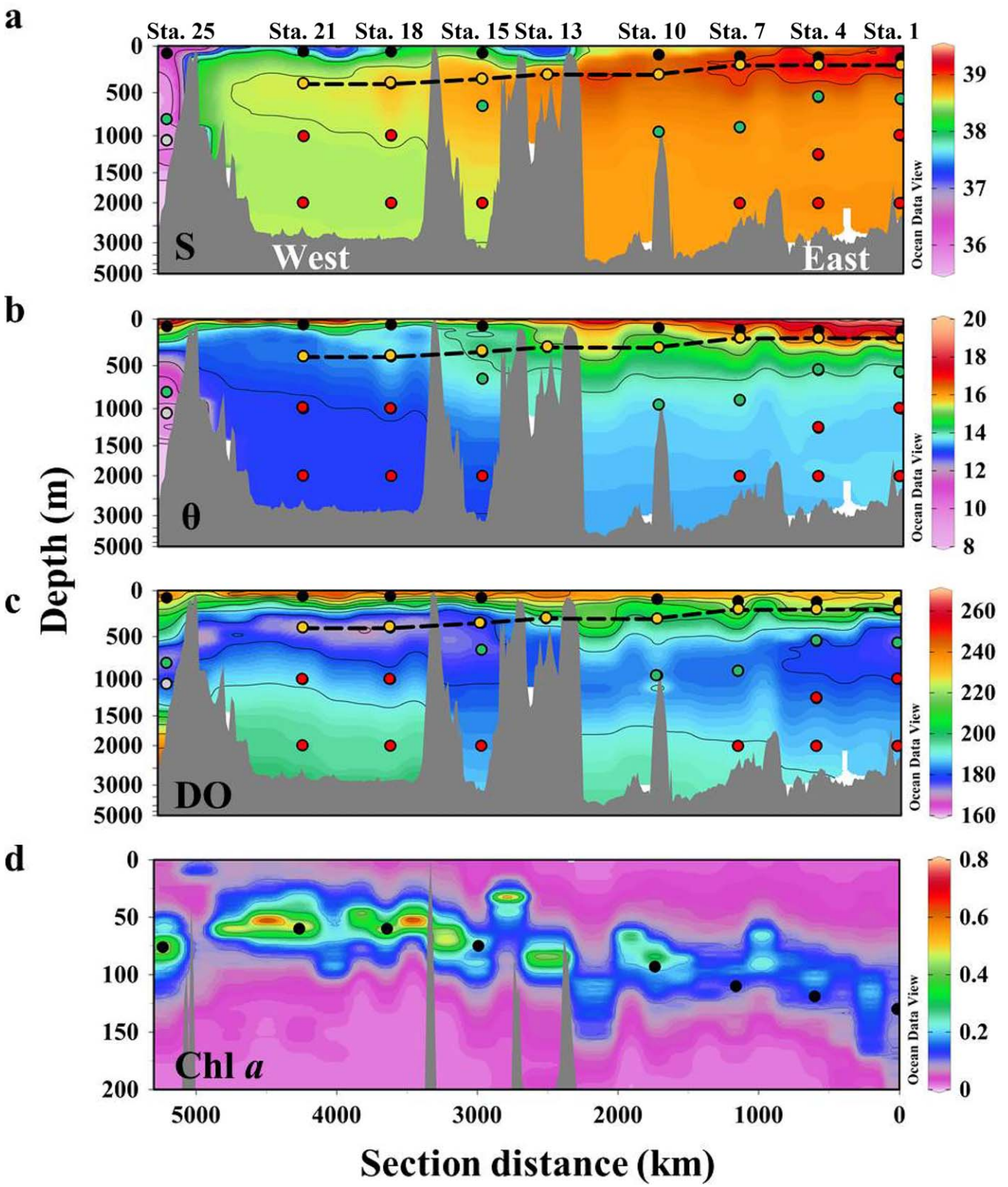

Fig. 2. Distribution of (**a**) salinity (S), (**b**) potential temperature (θ) in °C, (**c**) DO in μmol kg^{-1}, and (**d**) fluorescence of Chl *a* in mg m^{-3} obtained from the sensors attached to the rosette sampler along the Mediterranean Sea. Black, yellow, green, and red dots represent samples taken in the epipelagic layer (DCM), LIW, OML, and deep waters, respectively. The dashed black line represents the route of the LIW along the transect. Note that the depth is displayed on a nonlinear scale. Values from all stations were used to show these distributions. Figure created using ODV software (Schlitzer 2016).

were collected for initial DOC determination in precombusted (450°C, 12 h) glass ampoules. These samples were acidified with H_3PO_4 (85%, p.a., Merck) to pH < 2, the ampoules were fire-sealed and stored in the dark at 4°C until analysis in the base laboratory. DOC concentrations were measured with a Shimadzu TOC-V organic carbon analyzer by high temperature catalytic oxidation. The system was calibrated daily with potassium hydrogen phthalate (99.95–100.05%, p.a., Merck). The precision of the equipment was ± 1 μmol L^{-1}. The accuracy was successfully tested daily with the DOC reference materials provided by D. A. Hansell (University of Miami, U.S.A.).

For SPE-DOM isolation, the filtered sea water sample (2 L) was acidified to pH 2 with HCl (37%, p.a., Merck) and the DOM was extracted on board with commercially available modified styrene divinyl benzene polymer cartridges (PPL, Agilent) as described in Dittmar et al. (2008). After extraction, cartridges were rinsed with acidified ultrapure water (pH 2, HCl 37%, p.a., Merck) to remove remaining salts and frozen at −20°C. Once in the base lab, the cartridges were dried by flushing with high purity N_2 and eluted with 6 mL of methanol (high pressure liquid chromatography (HPLC)-grade, Sigma-Aldrich). Extracts were stored in amber vials at −20°C. DOC concentrations in the extracts were measured after complete evaporation of an aliquot and re-dissolution in ultrapure water. The extraction efficiency is the ratio of SPE-DOC to initial DOC concentrations. The mean extraction efficiency was 47.3% ± 3.9% on a carbon basis. Some of the epipelagic water samples showed slightly lower extraction efficiencies, likely due to the fact that PPL cartridges do not efficiently elute/retain the larger molecules (Chen et al. 2016; Raeke et al. 2016), which can be a significant fraction of DOM in the surface mixed layer.

FT-ICR-MS analysis

SPE-DOM methanol extracts were diluted with ultrapure water and methanol (MS grade) to yield a DOC concentration of 15 mg C L^{-1} and a methanol-to-water ratio of 1 : 1 (v/v). Duplicates of each sample were prepared for analysis by ultrahigh-resolution mass spectrometry using a Solarix FT-ICR-MS (Bruker Daltonik GmbH) connected to a 15 Tesla superconducting magnet (Bruker Biospin). Samples were infused at a flow rate of 120 μL h^{-1} into the electrospray ionization source (ESI; Apollo II ion source, Bruker Daltonik GmbH) with the capillary voltage set to 4 kV in negative mode. Ions were accumulated in the hexapole for 0.3 s prior to transfer into the ICR cell. Data acquisition was done in broadband mode with a scanning range of 150–2000 Da. For each mass spectrum, 500 scans were accumulated. The spectra were mass calibrated (linear) using the Bruker Daltonics Data Analysis software package with an internal calibration list consisting of 51 known $C_xH_yO_z$ molecular formulae over the mass range of the samples. With this calibration procedure, a mass error of < 0.1 ppm was achieved. SPE-DOM from the North Equatorial Pacific Intermediate Water (NEqPIW) collected at a depth of 670 m at the Natural Energy Laboratory of Hawaii Authority (NELHA) in Kona, Hawaii (Green et al. 2014) was used as an internal reference sample to assess instrument variability over time (Osterholz et al. 2014; Hansman et al. 2015). Molecular formulae were assigned to peaks considering a maximum mass error of 0.5 ppm and in the mass range between 150 Da and 850 Da by applying the following restrictions: $^{12}C^{1}_{1-130}H_{1-200}$ $O^{14}_{1-50}N_{0-4}S_{0-2}P_{0-2}$ as described in Seidel et al. (2014). Only compounds with a signal-to-noise (S/N) ratio of 4 and higher were used for further analysis. Moreover, compounds present in less than 20% of samples with a maximum S/N less than 20 were removed, as well as the molecules containing the following heteroatom combinations: NSP, N_2S, N_3S, N_4S, N_2P, N_3P, N_4P, NS_2, N_2S_2, N_3S_2, N_4S_2, and S_2P as these are less likely to occur in nature and, furthermore, to be more conservative in assigning molecular formulae to a given *m/z*. The FT-ICR-MS signal intensity of each identified molecular formula was normalized to the sum of all molecular formula intensities with S/N higher than 5 in each sample. We assumed that the inorganic (and organic) matrix is approximately the same for all the samples, so the intensity of each molecular mass is only affected by its concentration. Further, Seidel et al. (2015) incrementally mixed Amazon DOM with open Atlantic Ocean DOM showing that the response signal of ESI-FT-ICR-MS was linear to the mixing ratio. Therefore, we interpret the FT-ICR-MS data semi-quantitatively (Seidel et al. 2015; Hawkes et al. 2016). The analytical window of the FT-ICR-MS was restricted by both the SPE method and electrospray ionization efficiency. The SPE method, using PPL cartridges, allows to concentrate from the most apolar DOM species through to highly polar molecules, but not the smallest polar molecules (i.e., short chain organic acids and free amino acids) and colloidal aggregates (Chen et al. 2016; Hawkes et al. 2016; Raeke et al. 2016). ESI is a low-fragmentation technique that preferentially ionizes polar functional groups (Kujawinski 2002), therefore carbohydrates are likely less efficiently ionized by ESI than organic acids as it was suggested by Stubbins et al. (2010).

The aromaticity and the degree of unsaturation of a compound were assessed based on its molecular formula and were expressed as the modified aromaticity index ($AI_{mod} = [1 + C - {}^1/_2O - S - {}^1/_2H - {}^1/_2N - {}^1/_2P]/[C - {}^1/_2O - S - N - P]$) and double bond equivalents ($DBE = 1 + {}^1/_2[2C - H + N + P]$), respectively (Koch and Dittmar 2006, 2016). Higher AI and DBE are indicative of higher presence of aromatic or even condensed aromatic molecules (Koch and Dittmar 2006), which have been suggested to be resistant to biodegradation (Stubbins et al. 2010; Rossel et al. 2013). The degradation index (Ideg) was calculated using the formula proposed by Flerus et al. (2012) ranging between 0 and 1. It is used as a simple proxy to assess the relative degradation state of the SPE-DOM, and Flerus et al. (2012) suggested that a

higher Ideg points toward a more reworked DOM. The intensity-weighted averages of molecular weight, number of elemental atoms (C, H, O), number of heteroatoms (N, S, P), molar ratios (H/C, O/C, and C/N), AI_{mod}, and DBE were calculated for each sample by taking into account the FT-ICR-MS signal intensity of each assigned molecular formula. We sorted the assigned formulae into groups of formulae containing the following atoms: CHO, CHON, CHOS, CHOP, CHONS, and CHOSP. In addition, we assigned the identified molecular formula to compound groups based on established molar ratios, AI_{mod}, DBE and heteroatoms contents (Seidel et al. 2014). The compound groups used in this work were: (1) polyphenols ($0.5 < AI_{mod} < 0.666$) which are highly aromatic compounds, (2) highly unsaturated compounds ($AI_{mod} < 0.5$, $H/C < 1.5$, and $O/C < 0.9$), (3) unsaturated aliphatic ($1.5 < H/C < 2$, $O/C < 0.9$, and $N = 0$), and (4) carboxyl-rich alicyclic molecules (CRAM, $0.3 < DBE/C < 0.68$, $0.2 < DBE/H < 0.95$, and $0.77 < DBE/O < 1.75$) as described by Hertkorn et al. (2006). These parameters are summarized in Supporting Information Table S4. Note that 94% of the molecular formulae assigned to CRAM were also classified as highly unsaturated compounds. As this grouping includes a mixture of structural isomers and does not imply the presence of a structural entity in the sample (Seidel et al. 2014), we emphasize that this categorization is not unambiguous and alternative structures may exist for a given molecular formula. However, this classification is a useful tool to identify likely structures behind an identified molecular formula. All molecular parameters of each sample were calculated as averages of the duplicates.

Statistical analysis

Bray–Curtis dissimilarity matrices (Bray and Curtis 1957) were computed based on relative signal average intensities. Principal coordinates analysis (PCoA) was then used for graphical representation of the DOM variability on the first two major axes of compositional change. Environmental and calculated parameters were correlated to the PCoA factors and graphed accordingly (Pearson's product moment correlation). The analyses were performed in R (version 3.1.1, R Development Core Team 2012, [http://cran.r-project.org/]) and using the package vegan (Oksanen et al. 2016).

Multiple linear regressions were performed using R. Moreover, the Student's *t*-test was used for determining the significant differences between sample means (Supporting Information Table S3).

Results

Hydrography and bulk dissolved organic carbon background

Discrete sampling depths were chosen on basis of the vertical profiles of S, θ, DO, and Chl *a* (Fig. 2). The DCM (black dots in Fig. 2) was deeper in the eastern than in the western basin (Supporting Information Table S1), showing higher DO and Chl *a* in the western basin. Regarding the LIW, the salinity maximum (yellow dots in Fig. 2) was found between 200 m and 300 m in the eastern basin, accompanied by a relative maximum of θ and DO. In the western basin, the salinity maximum was located deeper (between 350 m and 400 m) concurring with a relative maximum of θ and a minimum of DO. In general, the S, θ, and DO along the core of the LIW were lower in the western than in the eastern basin (Supporting Information Table S1; Fig. 2a–c). The OML (green dots in Fig. 2a–c) was found at 744 ± 211 m ($n = 4$) in the eastern basin. It coincided with the depth of the LIW in the western basin. Regarding the bathypelagic layer (red dots in Fig. 2), the eastern basin was dominated by the EMDW, which was saltier and warmer than the analogous waters in the western basin, dominated by the WMDW. DO values were similar in both basins.

DOC concentrations (Supporting Information Fig. S1 and Supporting Information Table S1) showed the maximum values of the sampling depths at the DCM (> 60 μmol L^{-1}), decreasing to a minimum of 43–44 μmol L^{-1} in the deep waters. In the epipelagic layer, an inverse relationship between Chl *a* and DOC concentration was observed (Fig. 1d and Supporting Information Fig. S1a). It is remarkable that in the LIW the DOC decreased significantly from 60.2 ± 0.9 μmol L^{-1} in the easternmost station (Sta. 1) to 47.4 ± 0.7 μmol L^{-1} in the western basin (Sta. 18) (Supporting Information Fig. S1). Conversely, in the deep waters the distribution of the DOC did not reveal any significant gradient between the western and eastern basins. Our DOC concentrations confirmed the published vertical profile in both basins (Pujo-Pay et al. 2011; Santinelli 2015 and references therein). Atlantic samples showed similar DOC concentrations as the Mediterranean Sea samples (Supporting Information Fig. S1).

Mediterranean SPE-DOM molecular signatures

The distribution of the concentration of solid phase extracted DOC (SPE-DOC) was parallel to the concentration of the bulk DOC (Supporting Information Fig. S1) although carbon extraction efficiency was $47.3\% \pm 3.9\%$. SPE-DOC therefore constitutes a good proxy of the bulk DOC.

A total of 6057 resolved molecular masses of singly charged compounds were detected in the FT-ICR-MS spectra of the 32 SPE-DOM samples analyzed from the Mediterranean Sea and Northeast Atlantic Ocean, covering a mass range of 154–817 Da. We identified 3689 molecular formulae in the mass range of 157–736 Da, not considering ^{13}C isotopologues. The most abundant type of formulae was CHO, followed by CHON, CHOS, CHOP, CHONS, and finally CHOSP (Supporting Information Table S3).

The NEqPIW sample repeatedly analyzed as a reference sample to control the instrument variation over time also let us compare the molecular composition of the SPE-DOM in the Mediterranean Sea with one of the oldest water masses of the world ocean: NEqPIW (Supporting Information Table S3). As expected, we observe that the Mediterranean Sea

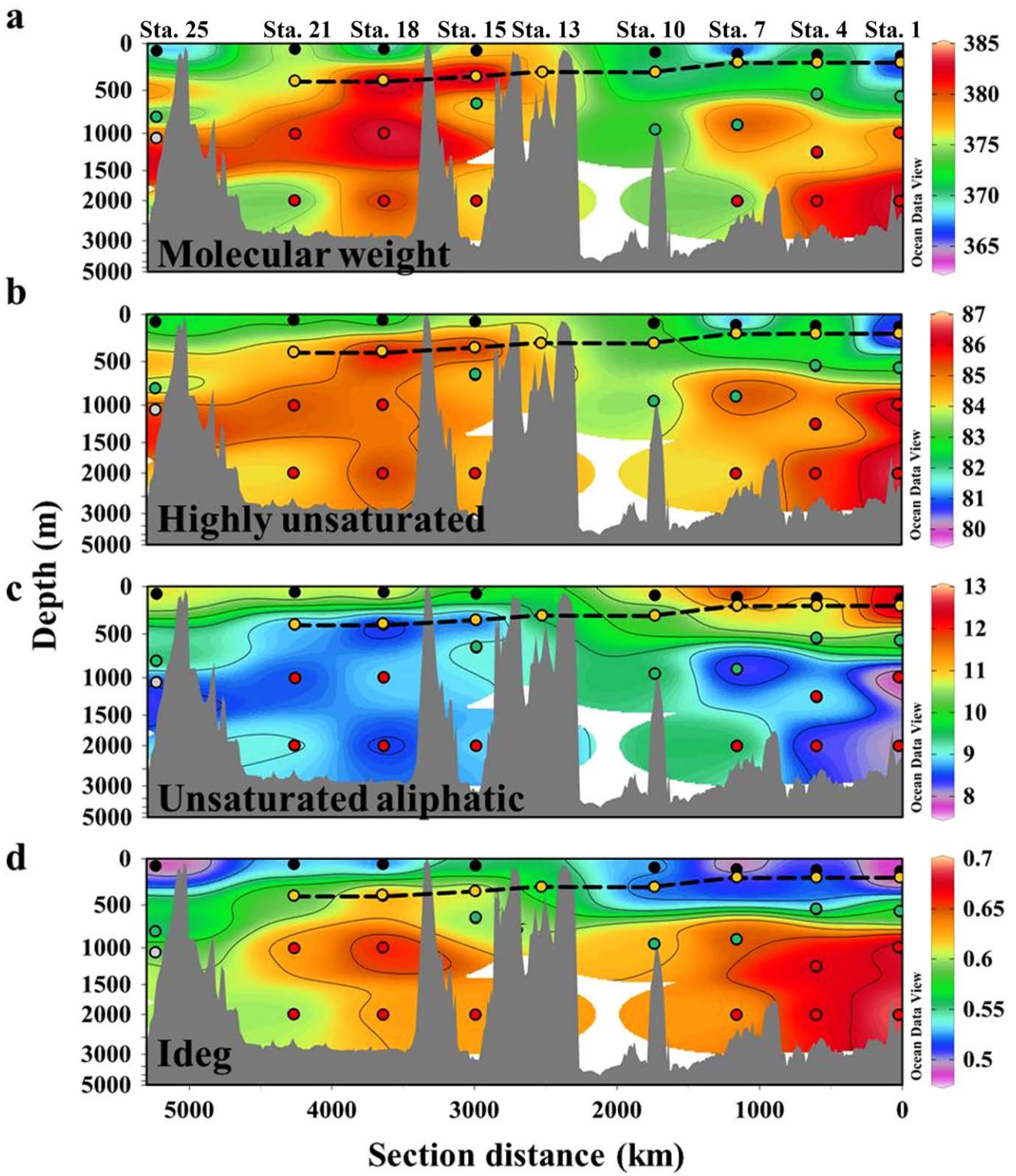

Fig. 3. Distributions of (**a**) molecular weight in Dalton, (**b**) highly unsaturated compounds in %, (**c**) unsaturated aliphatic compounds in %, and (**d**) Ideg (range between 0 and 1, unitless) using averages of duplicates in the Mediterranean Sea and Northeast Atlantic Ocean. The dashed black line represents the route of the LIW along the transect. Note that the depth is displayed on a nonlinear scale. Figure created using ODV software (Schlitzer 2016).

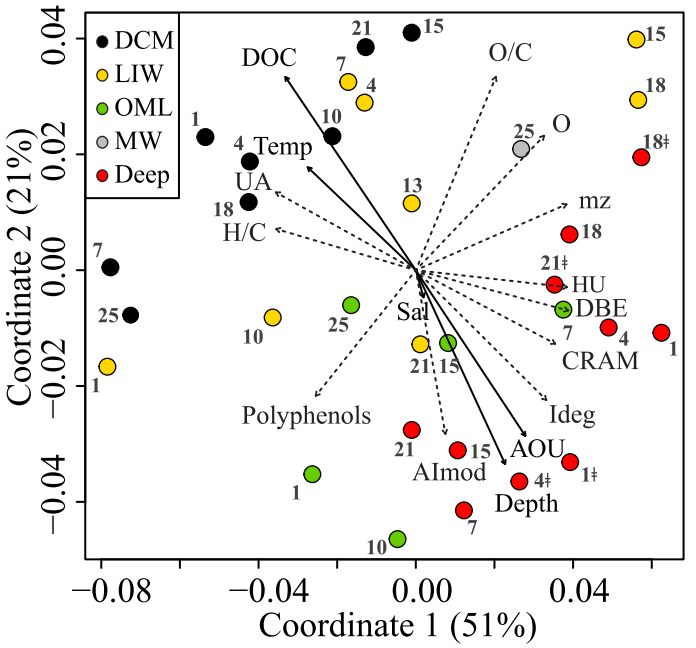

Fig. 4. PCoA of all detected molecular formulae and their normalized FT-ICR-MS signal intensities (averages of duplicates), based on Bray-Curtis dissimilarity of all samples, color coded by waters dominating in each layer. Environmental and calculated parameters fitted to the PCoA factors are shown with black bold and dashed arrows, respectively. HU, highly unsaturated compounds; Sal, Salinity; Temp, Temperature; UA, unsaturated aliphatic compounds. The symbol ǂ represents samples collected at 1000 m.

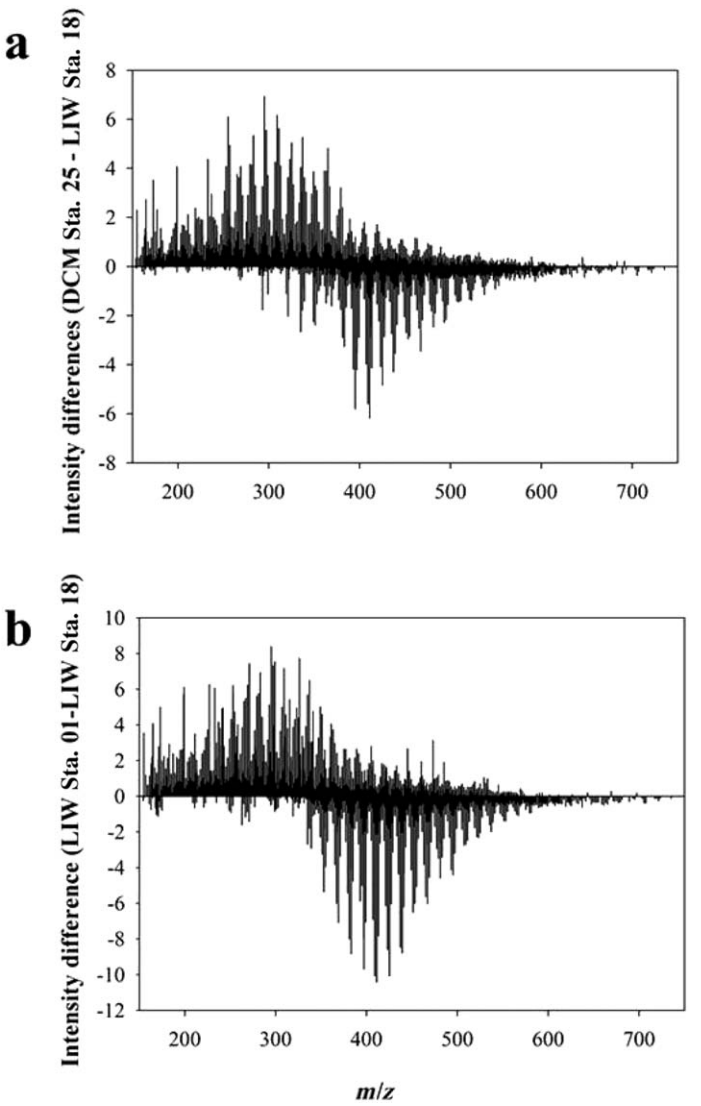

Fig. 5. Differences of FT-ICR-MS normalized signal intensities of SPE-DOM along a molecular mass scale (*m/z*) between (**a**) the inflow of AW collected at the DCM in Sta. 25 and the overflow of Mediterranean water represented by the LIW at Sta. 18, (**b**) LIW collected at Sta. 01 (near formation site) and LIW at Sta. 18 in the western basin. Positive differences correspond to higher relative intensities of DCM at Sta. 25 and LIW at Sta. 01 DOM, while negative differences correspond to higher relative intensities in the LIW Sta. 18 DOM, respectively, for (**a**) and (**b**) panels. The weighted average molecular mass of these differential spectra was calculated taking into account absolute peak heights of positive and negative peaks.

contains significantly less reworked DOM (lower molecular weight, O/C, DBE, and Ideg) than the NEqPIW.

The AW entering the Mediterranean Sea through the Strait of Gibraltar (represented by the DCM sample at Sta. 25; black dot in Fig. 3) exhibited a significantly different molecular composition than the overflow of Mediterranean water (represented by the LIW at Sta. 18; yellow dot in Fig. 3). Specifically, the SPE-DOM found in the AW inflow displayed lower molecular weight, O/C ratio, DBE, Ideg, CRAM, and highly unsaturated compounds contribution, as well as a higher proportion of unsaturated aliphatic compounds and an increased H/C ratio (Fig. 3 and Supporting Information Table S2). A PCoA to link molecular composition to environmental parameters that includes all samples (Fig. 4) also reveals the molecular dissimilarity between the Atlantic inflow and the Mediterranean overflow. While the Atlantic sample was found in the negative part of both axes, the LIW sample was found in the positive. Note that the first two coordinates of the PCoA comprised 72% of the SPE-DOM molecular variability. The differences between the inflow and outflow at the Strait of Gibraltar were also explored using a differential mass spectrum (Fig. 5a), subtracting the normalized peak intensities of the LIW at Sta. 18 from the normalized peak intensities of the DCM at Sta. 25. Positive differences of intensity showed peaks of higher relative intensities in the Atlantic inflow with an average molecular weight of 349 Da. Negative signals indicated peaks of higher relative intensities in the Mediterranean overflow enriched in compounds of an average molecular weight of 432 Da. Note that LIW at Sta. 18 was chosen to represent the Mediterranean water overflow as LIW at Sta. 21 is influenced by the mixing with WMDW as it is located close to the deep waters in the θ/S diagram (Supporting Information Fig.

S2c) and apart from the LIW at Sta. 15 and 18 in the PCoA (Fig. 4).

To study the DOM degradation along the shallow overturning circulation cell of the Mediterranean Sea, we followed the compositional changes of SPE-DOM collected in the core-of-flow of the LIW. The molecular characteristics of the LIW samples were uneven and the samples were split in the PCoA (Fig. 4): while the eastern basin samples were found in the negative part of the first coordinate, the western basin samples were located in the positive. In addition, a constrained analysis of principal coordinates based on Bray-Curtis dissimilarities revealed significant molecular differences between both basins ($p < 0.05$, $n = 8$). Specifically, as the LIW flowed westward we observed a raise of molecular size (Fig. 3a), O/C ratio, DBE, and AI_{mod}. Moreover, we observed an increase of the Ideg and the proportion of highly unsaturated molecules, as well as a decrease of the proportion of unsaturated aliphatic molecules (Fig. 3b–d and Supporting Information Table S2). Again, these differences were examined in more detail using a differential spectrum (Fig. 5b), subtracting the normalized peak intensities of the LIW at Sta. 18 (western basin, more reworked DOM) from the normalized peak intensities of the LIW at Sta. 1 (eastern basin, fresher DOM). Positive differences of intensity showed peaks with higher relative intensities in the LIW at Sta. 1, where this sample presented an enrichment of molecules with an average molecular weight of 335 Da. Negative signals indicated peaks with higher relative intensities in the LIW at Sta. 18, sample enriched in molecules of an average molecular weight of 427 Da.

Concerning the deep waters, in the eastern basin, samples collected at 2000 m depth at Sta. 1 and 4 (EMT) fell closely together in the PCoA analysis (Fig. 4). However, the samples collected at 1000 m at Sta. 1 and 4 (pre-EMT) and at 2000 m at Sta. 7 (post-EMT) grouped in our ordination and were separated from the EMT samples. Comparing the molecular composition of SPE-DOM in these water masses, the deep water at Sta. 7 showed a less degraded SPE-DOM signature (lower molecular weight, oxygen, DBE, Ideg, highly unsaturated and higher contribution of unsaturated aliphatic compounds; Fig. 3 and Supporting Information Table S2).

Globally, the PCoA revealed a clear separation of the samples by water layers. Along both PCoA axes, less reworked DOM was clearly separated from more degraded DOM. Samples collected at the DCM (recently formed) were characterized by less reworked DOM (higher proportion of unsaturated aliphatic compounds, higher H/C ratio and DOC concentration). Highly unsaturated molecules, likely susceptible to photochemical processes, and photoresistant unsaturated aliphatic molecules comprised the largest fraction of the SPE-DOM (> 90%) in all samples (Supporting Information Table S2). Since abundances are expressed as relative contributions (percentages), the increase of one kind of compounds entails the decrease of the others. Thus, the lower percentage of highly unsaturated compounds in the epipelagic layer (Fig. 3b) could be due to the photochemical removal of this type of molecules in the photic layer.

Discussion

Despite the relatively small size and short residence times of the Mediterranean Sea, a PCoA analysis revealed that the molecular composition of DOM was found to be heterogeneous among basins and water layers. We show that this heterogeneity is mainly caused by three different factors that control the DOM molecular composition in the Mediterranean Sea: water mass origin, biodegradation and photobleaching.

Water mass origin as a driver of SPE-DOM composition

We found that the overall molecular composition of the Mediterranean Sea was significantly less reworked than the NEqPIW (Supporting Information Table S3). This water mass acts a reference for refractory DOM, as it is one of the oldest, least ventilated, water masses of the global ocean (Stuiver et al. 1983; Osterholz et al. 2015). This result demonstrates the noticeable molecular differences between the Mediterranean Sea DOM and the NEqPIW DOM in spite of presenting similar radiocarbon ages as recently reported by Santinelli et al. (2015).

The exchange across the Strait of Gibraltar results in the Atlantic inflow transporting relatively fresh, nutrient-poor (Huertas et al. 2012), and less degraded DOC-rich surface AWs into the Mediterranean Sea. On the other hand, the Mediterranean outflow transports salty, nutrient-rich and reworked DOC-poor intermediate Mediterranean water into the Atlantic. Accordingly, Ideg and DBE of the SPE-DOC in the Mediterranean overflow increased by 25% and 5%, respectively, and the proportion of unsaturated aliphatic compounds decreased by 24% compared to the Atlantic inflow. Given that the AW that enters the Mediterranean Sea is part of the shallow overturning cell of the Mediterranean intermediate waters that constitute the Gibraltar overflow (Schneider et al. 2014), it is expected that the difference in composition is implemented during completion of that overturning circulation within the Mediterranean Sea basin. When the LIW is formed (Sta. 1), the DOM molecular composition is similar to the DOM Atlantic inflow (DCM in Sta. 25) (Sta. 25-black dot and Sta. 1-yellow dot in Fig. 4). However, once the LIW flows in the shallow overturning circulation across the Mediterranean Sea this water mass transports more degraded DOM as will be discussed in the next section.

Deep waters in the eastern basin exhibited significant molecular differences related to their formation site (Aegean vs. Adriatic) or time (pre- vs. post-EMT). Samples collected at 2000 m depth at Sta. 1 and 4 presented more degraded DOM (molecular weight increased by 5 Da, the proportion of polyphenols by 6% and the proportion of unsaturated aliphatic compounds decreased by 9%) than samples collected at 1000 m at the same stations (Figs. 3, 4; Supporting

Information Table S2). These molecular changes were attributed to the fact that samples collected at 2000 m were formed in the Aegean Sea during the EMT (according to their thermohaline properties and oxygen concentrations; Supporting Information Fig. S2d and Supporting Information Table S1; Roether et al. 1996, Lascaratos et al. 1999, Klein et al. 2003). However, samples collected at 1000 m were formed in the Adriatic Sea in the pre-EMT which showed lower S and DO concentration than the deep waters of Aegean origin (Lascaratos et al. 1999; Schneider et al. 2014). These results support the idea that water mass origin drives the DOM molecular composition. Regarding the formation time of these deep waters, it would be plausible that the oldest (pre-EMT) would host most degraded DOM, however, the results show the opposite. It seems that water mass origin has a higher impact on DOM molecular composition than water mass age in the deep waters of the eastern Mediterranean Sea. On the other hand, samples collected at 2000 m at Sta. 7 (post-EMT) presented less degraded DOM (lower molecular weight (−5 Da), Ideg (−7%), DBE (−2%), and an about 9% higher proportion of unsaturated aliphatic compounds) than the sample collected at Sta. 1 at 1000 m (pre-EMT). In this case, although both water masses were formed in the Adriatic Sea, their formation times were different according to their thermohaline properties and DO concentrations (Supporting Information Fig. S2d and Supporting Information Table S1), which lead to dissimilar DOM molecular signatures.

Diagenetic transformations of SPE-DOM through the Mediterranean Sea

The samples taken along the salinity maximum of the LIW show a total decrease in DOC concentration of 15 μmol L^{-1} attributed to prokaryotic degradation within the shallow overturning circulation of the Mediterranean Sea (black dashed line in Figs. 2a–c, 3). A highly significant linear relationship between DOC and AOU was found along the LIW pathway followed during the cruise ($r = -0.96$, $p < 0.001$, $n = 9$). The slope of this linear regression (model II; Sokal and Rohlf 1995) was -0.21 ± 0.02, which, converted into oxygen equivalents using the canonical Redfield $-O_2/C$ ratio of 1.4, translates into 0.30 ± 0.03, i.e., the $30\% \pm 3\%$ of the oxygen consumption was due to the microbial oxidation of DOC. To minimize the effect of water mass mixing on the DOC/AOU relationship, we performed a multiple linear regression of DOC with θ, S, and AOU. Doing this the slope changed to -0.31 ± 0.08, which, converted into oxygen equivalents as above, resulted in a $43\% \pm 11\%$ of the oxygen consumption due to prokaryotic oxidation of DOC. Note that this number is not significantly different from the previously obtained with the simple linear regression. These values are consistent with previous estimates in the Mediterranean Sea by Santinelli et al. (2010, 2012), which ranged from 38% to 53%. Such a result is much higher than the 10–20% found in the dark global ocean (Arístegui et al. 2002). Warmer deep-water temperatures in the Mediterranean Sea (>13°C vs. < 5°C; Dickson and Brown 1994), which stimulate the prokaryotic degradation processes, is the likely reason behind this difference. Microbial oxidation leads to decreasing DOC concentrations along the overturning cell and the remaining DOC is, indeed, more reworked. In this regard, in agreement with Hansman et al. (2015), we found a positive relationship between the Ideg and AOU for all collected samples: Ideg = (0.0019 ± 0.0002) AOU + (0.50 ± 0.01) ($R^2 = 0.71$, $p < 0.0001$). The obtained regression slope suggests that the degradation ratio per oxygen consumption unit is faster in the Mediterranean Sea than in the Atlantic Ocean, given that it is significantly higher ($p < 0.0001$) than the regression slope obtained by Hansman et al. (2015) in the Atlantic Ocean (slope = 0.00073 ± 0.00003, $R^2 = 0.64$, $p < 0.001$). This more efficient degradation could also be related to the above mentioned warmer deep-water temperatures in the Mediterranean Sea. As a consequence, the rate of microbial processes would be about twofold higher in the Mediterranean Sea than in the Atlantic Ocean, according to the Arrhenius law. As for the case of DOC, to assess the role of water mass mixing in this relationship, we performed a multiple linear regression of Ideg with θ, S, and AOU ($R^2 = 0.80$; $p < 0.003$, Ideg/AOU slope = 0.0011 ± 0.0003). Whereas the standard deviation of Ideg ($SD_{Ideg} = 0.065$) retains the variability due to both water mass mixing and biogeochemical processes in the Mediterranean Sea, the standard deviation of the residuals of the multiple linear regression of Ideg with θ and S ($SD_{\Delta Ideg} = 0.035$) retains only the variability due to biogeochemical processes. Therefore, from the ratio of both SD, it can be inferred that 54% of the observed variability of Ideg could be explained by processes not associated to water mass mixing. We could presume that the mixing of LIW, with EMDW in the eastern basin and with WMDW in the western basin, can be partly responsible for the different molecular composition observed in the LIW of Sta. 1 and 18. However, in the western basin, mixing cannot be the only process affecting the LIW, since this water mass with the highest AOU is surrounded by water bodies (the DCM on top and the WMDW underneath) which present lower AOU values (Supporting Information Table S1). Concomitantly, part of the observed changes in the molecular composition of SPE-DOM could be due to the production/consumption of higher/lower molecular weight compounds as the LIW becomes older (more degraded) in its route westward. A parallel increase in molecular weight (Fig. 5b) and oxygenation (5%) and a decrease of the H/C ratio (Supporting Information Table S2) were found to be indicators of degraded organic matter (Flerus et al. 2012; Hertkorn et al. 2013, Chen et al. 2014), in accordance with an increase of the Ideg (22%). A higher DBE and AI_{mod} are indicative of an increasing degree of aromaticity and unsaturation (Koch and Dittmar 2006, 2016). In addition, a higher proportion of highly unsaturated compounds (7%) is also indicative of

reworked DOM, as these compounds are considered refractory and produced during the remineralization processes in the meso- and bathypelagic layers (Seidel et al. 2015). Conversely, unsaturated aliphatic compounds are considered bio-labile molecules, as they comprise a major fraction of phytoplankton exudates (Medeiros et al. 2015). We observed a decrease by 34% of the proportion of unsaturated aliphatic compounds in the LIW along its route westward.

Photodegradation vs. biodegradation in the epipelagic layer

Photochemical processes have been proposed as an abiotic pathway for DOC degradation in the surface ocean (Mopper et al. 2015). The Ideg is used to assess the degradation state of the SPE-DOM. Since photodegradation can produce biolabile aliphatic and peptide-like compounds (Stubbins et al. 2010; Stubbins and Dittmar 2015), we hypothesize that this process could lead to a lower Ideg. We observed an increasing trend of Ideg with depth (Fig. 3d), likely indicating a synergy between an increasing contribution of prokaryote DOM degradation with depth, and the potential photodegradation and new production in the photic layer. However both processes, new production and photodegradation, cannot be deciphered by applying the Ideg. Therefore, we do not find conclusive evidence for the effect of photodegradation in the Mediterranean Sea, probably due to the great depth of the shallowest level that we sampled (DCM). In addition, the cruise was conducted in April–May, i.e., after winter mixing and when solar radiation is not at the summer maximum. Further studies/experiments should be performed to clarify the role of photochemical processing on the DOM composition in the Mediterranean Sea.

Conclusions

Despite the small size and relatively short residence time of the Mediterranean Sea, water mass origin and mineralization processes lead to contrasting molecular composition of SPE-DOM with depth and basin. SPE-DOM in the Mediterranean Sea was remarkably different from the SPE-DOM in the Atlantic Ocean inflow. Considering the shallow overturning cell of the Mediterranean Sea, the evolution of the molecular composition of SPE-DOM from the Levantine basin to the Strait of Gibraltar evidences the transformation of these materials since LIW is formed. As a result, a westward decrease of DOC concentrations and a lower proportion of unsaturated aliphatic compounds are observed, as well as an increase in average molecular weight and enrichment in unsaturation, oxygenation, state of degradation, and highly unsaturated compounds as the SPE-DOM is degraded. We found that the water mass origin and the formation time lead to distinct DOM molecular properties. Thus, pre-EMT deep waters formed in the Adriatic Sea presented less degraded DOM than deep waters formed in the Aegean Sea during the EMT. In addition, different varieties of deep waters formed in the Adriatic Sea (pre- and post-EMT) presented different DOM molecular composition in spite of being formed in the same area. Consequently, the Mediterranean Sea constitutes a suitable model basin for future DOM studies as water bodies of different molecular composition can be observed in closest proximity. Taking advantages of forthcoming hydrographic cruises, it would be worthwhile to study the molecular composition of DOM in the Mediterranean waters at their formation sites and help to complete the picture of DOM molecular composition and turnover in the Mediterranean Sea.

References

Amon, R. M., and R. Benner. 1996. Bacterial utilization of different size classes of dissolved organic matter. Limnol. Oceanogr. **41**: 41–51. doi:10.4319/lo.1996.41.1.0041

Arístegui, J., C. M. Duarte, S. Agustí, M. Doval, X. A. Álvarez–Salgado, and D. A. Hansell. 2002. Oceanography: Dissolved organic carbon support of respiration in the dark ocean. Science **298**: 1967. doi:10.1126/science. 1076746

Benner, R., J. D. Pakulski, M. McCarthy, J. I. Hedges, and P. G. Hatcher. 1992. Bulk chemical characteristics of dissolved organic matter in the ocean. Science **255**: 1561–1564. doi:10.1126/science.255.5051.1561

Benner, R., B. Biddanda, B. Black, and M. McCarthy. 1997. Abundance, size distribution, and stable carbon and nitrogen isotopic compositions of marine organic matter isolated by tangential–flow ultrafiltration. Mar. Chem. **57**: 243–263. doi:10.1016/S0304-4203(97)00013-3

Bergamasco, A., and P. Malanotte–Rizzoli. 2010. The circulation of the Mediterranean Sea: A historical review of experimental investigations. Adv. Oceanogr. Limnol. **1**: 11–28. doi:10.1080/19475721.2010.491656

Béthoux, J. P., P. Morin, C. Chaumery, O. Connan, B. Gentili, and D. Ruiz–Pino. 1998. Nutrients in the Mediterranean Sea, mass balance and statistical analysis of concentrations with respect to environmental change. Mar. Chem. **63**: 155–169. doi:10.1016/S0304-4203(98)00059-0

Beuvier, J., and others. 2012. Spreading of the Western Mediterranean Deep Water after winter 2005: Time scales and deep cyclone transport. J. Geophys. Res. **117**: 1–26. doi: 10.1029/2011JC007679

Bray, J. R., and J. T. Curtis. 1957. An ordination of the upland forest communities of southern Wisconsin. Ecol. Monogr. Ecol. Soc. Am. **27**: 326–349. doi:10.2307/1942268

Carlson, C. A. 2002. Chapter 4 – production and removal processes, p. 91–151. *In* D. A. Hansell and C. A. Carlson [eds.], Biogeochemistry of marine dissolved organic matter. Academic Press.

Chen, H., A. Stubbins, E. M. Perdue, N. W. Green, J. R. Helms, K. Mopper, and P. G. Hatcher. 2014. Ultrahigh resolution mass spectrometric differentiation of dissolved organic matter isolated by coupled reverse osmosis–electrodialysis from

various major oceanic water masses. Mar. Chem. **164**: 48–59. doi:10.1016/j.marchem.2014.06.002

Chen, M., S. Kim, J. E. Park, H. J. Jung, and J. Hur. 2016. Structural and compositional changes of dissolved organic matter upon solid–phase extraction tracked by multiple analytical tools. Anal. Bioanal. Chem. **408**: 6249–6258. doi:10.1007/s00216-016-9728-0

Cruzado, A. 1985. Chemistry of Mediterranean waters, p. 126–147. *In* R. Margalef [eds.], The Western Mediterranean. Pergamon Press.

Dickson, R. R., and J. Brown. 1994. The production of North Atlantic Deep Water: Sources, rates, and pathways. J. Geophys. Res. **99**: 12319–12341. doi:10.1029/94JC00530

Dittmar, T., B. Koch, N. Hertkorn, and G. Kattner. 2008. A simple and efficient method for the solid–phase extraction of dissolved organic matter (SPE–DOM) from seawater. Limnol. Oceanogr.: Methods **6**: 230–235. doi:10.4319/lom.2008.6.230

Emelianov, M., J. Font, A. Turiel, C. Mullot, J. Solé, P. M. Poulain, A. Julià, and M. R. Vitrià. 2006. Transformation of levantine intermediate water tracked by MEDARGO floats in the Western Mediterranean. Ocean Sci. **2**: 281–290. doi:10.5194/os-2-281-2006

Flerus, R., O. J. Lechtenfeld, B. P. Koch, S. L. McCallister, P. Schmitt–Kopplin, R. Benner, K. Kaiser, and G. Kattner. 2012. A molecular perspective on the ageing of marine dissolved organic matter. Biogeosciences **9**: 1935–1955. doi:10.5194/bg-9-1935-2012

Gascard, J. C. 1978. Mediterranean deep water formation baroclinic instability and oceanic eddies. Oceanol. Acta **1**: 315–330.

Green, N. W., E. M. Perdue, G. R. Aiken, K. D. Butler, H. Chen, T. Dittmar, J. Niggemann, and A. Stubbins. 2014. An intercomparison of three methods for the large–scale isolation of oceanic dissolved organic matter. Mar. Chem. **161**: 14–19. doi:10.1016/j.marchem.2014.01.012

Hansell, D. A. 2002. Chapter 15 – DOC in the global ocean carbon cycle, p. 685–715. *In* D. A. Hansell and C. A. Carlson [eds.], Biogeochemistry of marine dissolved organic matter. Academic Press.

Hansell, D. A., C. A. Carlson, D. J. Repeta, and R. Schlitzer. 2009. Dissolved organic matter in the ocean a controversy stimulates new insights. Oceanography **22**: 202–211. doi:10.5670/oceanog.2009.109

Hansman, R. L., T. Dittmar, and G. J. Herndl. 2015. Conservation of dissolved organic matter molecular composition during mixing of the deep water masses of the northeast Atlantic Ocean. Mar. Chem. **177**: 288–297. doi:10.1016/j.marchem.2015.06.001

Hawkes, J. A., C. T. Hansen, T. Goldhammer, W. Bach, and T. Dittmar. 2016. Molecular alteration of marine dissolved organic matter under experimental hydrothermal conditions. Geochim. Cosmochim. Acta **175**: 68–85. doi:10.1016/j.gca.2015.11.025

Hedges, J. I. 1992. Global biogeochemical cycles: Progress and problems. Mar. Chem. **39**: 67–93. doi:10.1016/0304-4203(92)90096-S

Hertkorn, N., R. Benner, M. Frommberger, P. Schmitt–Kopplin, M. Witt, K. Kaiser, A. Kettrup, and J. I. Hedges. 2006. Characterization of a major refractory component of marine dissolved organic matter. Geochim. Cosmochim. Acta **70**: 2990–3010. doi:10.1016/j.gca.2006.03.021

Hertkorn, N., M. Harir, B. P. Koch, B. Michalke, and P. Schmitt–Kopplin. 2013. High–field NMR spectroscopy and FTICR mass spectrometry: Powerful discovery tools for the molecular level characterization of marine dissolved organic matter. Biogeosciences **10**: 1583–1624. doi:10.5194/bg-10-1583-2013

Holm-Hansen, O., C. J. Lorenzen, R. W. Holmes, and J. D. Strickland. 1965. Fluorometric determination of chlorophyll. J. Cons. Int. Explor. Mer. **30**: 3–15. doi:10.1093/icesjms/30.1.3

Huertas, I. E., and others. 2012. Atlantic forcing of the Mediterranean oligotrophy. Global Biogeochem. Cycles **26**: GB2022. doi:10.1029/2011GB004167

Jones, V., T. B. Meador, A. Gogou, C. Migon, K. E. H. Penkman, M. J. Collins, and D. J. Repeta. 2013. Characterisation and dynamics of dissolved organic matter in the Northwestern Mediterranean Sea. Prog. Oceanogr. **119**: 78–89. doi:10.1016/j.pocean.2013.06.007

Klein, B., and others. 2003. Accelerated oxygen consumption in eastern Mediterranean deep waters following the recent changes in thermohaline circulation. J. Geophys. Res. **108**: 8107. doi:10.1029/2002JC001454

Koch, B. P., M. Witt, R. Engbrodt, T. Dittmar, and G. Kattner. 2005. Molecular formulae of marine and terrigenous dissolved organic matter detected by electrospray ionization Fourier transform ion cyclotron resonance mass spectrometry. Geochim. Cosmochim. Acta **69**: 3299–3308. doi:10.1016/j.gca.2005.02.027

Koch, B. P., and T. Dittmar. 2006. From mass to structure: An aromaticity index for high–resolution mass data of natural organic matter. Rapid Commun. Mass Spectrom. **20**: 926–932. doi:10.1002/rcm.2386

Koch, B. P., and T. Dittmar. 2016. Erratum: From mass to structure: An aromaticity index for high–resolution mass data of natural organic matter. Rapid Commun. Mass Spectrom. **30**: 250. doi:10.1002/rcm.7433 doi:10.1002/rcm.7433

Koprivnjak, J. F., and others. 2009. Chemical and spectroscopic characterization of marine dissolved organic matter isolated using coupled reverse osmosis–electrodialysis. Geochim. Cosmochim. Acta **73**: 4215–4231. doi:10.1016/j.gca.2009.04.010

Kujawinski, E. B. 2002. Electrospray ionization Fourier transform ion cyclotron resonance mass spectrometry (ESI FT–ICR MS): Characterization of complex environmental mixtures. Environ. Forensics **3**: 207–216. doi:10.1080/713848382

Langdon, C. 2010. Determination of dissolved oxygen in seawater by Winkler titration using the amperometric

technique, report N°. 14. *In* B. M. Sloyan and C. Sabine [eds.], GO–SHIP repeat hydrography manual: A collection of expert reports and guidelines. IOC/IOCCP.

Laruelle, G. G., and others. 2009. Anthropogenic perturbations of the silicon cycle at the global scale: Key role of the land–ocean transition. Global Biogeochem. Cycles **23**: GB4031. doi:10.1029/2008GB003267

Lascaratos, A., W. Roether, K. Nittis, and B. Klein. 1999. Recent changes in deep water formation and spreading in the eastern Mediterranean Sea: A review. Prog. Oceanogr. **44**: 5–36. doi:10.1016/S0079-6611(99)00019-1

Lechtenfeld, O. J., G. Kattner, R. Flerus, S. L. McCallister, P. Schmitt–Kopplin, and B. P. Koch. 2014. Molecular transformation and degradation of refractory dissolved organic matter in the Atlantic and Southern Ocean. Geochim. Cosmochim. Acta **126**: 321–337. doi:10.1016/j.gca.2013.11.009

López-Jurado, J.-L., C. González-Pola, and P. Vélez-Belchí. 2005. Observation of an abrupt disruption of the long-term warming trend at the Balearic Sea, western Mediterranean Sea, in summer 2005. Geophys. Res. Lett. **32**: L24606. doi:10.1029/2005GL024430

Meador, T. B., and others. 2010. Biogeochemical relationships between ultrafiltered dissolved organic matter and picoplankton activity in the Eastern Mediterranean Sea. Deep-Sea Res. Part II Top. Stud. Oceanogr. **57**: 1460–1477. doi:10.1016/j.dsr2.2010.02.015

Medeiros, P. M., M. Seidel, L. C. Powers, T. Dittmar, D. A. Hansell, and W. L. Miller. 2015. Dissolved organic matter composition and photochemical transformations in the northern North Pacific Ocean. Geophys. Res. Lett. **42**: 863–870. doi:10.1002/2014GL062663

Millot, C. 1999. Circulation in the Western Mediterranean Sea. J. Mar. Syst. **20**: 423–442. doi:10.1016/S0924-7963(98)00078-5

Mopper, K. D., J. Kieber, and A. Stubbins. 2015. Chapter 8-Marine photochemistry of organic matter: Processes and impacts, p. 389–450. *In* D. A. Hansell and C. A. Carlson [eds.], Biogeochemistry of marine dissolved organic matter. Elsevier.

Oksanen, J., and others. 2016. vegan: Community ecology package. R package version 2.3–5. Available from https://cran.r-project.org/web/packages/vegan/index.html. Accessed May 22, 2017.

Osterholz, H., T. Dittmar, and J. Niggemann. 2014. Molecular evidence for rapid dissolved organic matter turnover in Arctic fjords. Mar. Chem. **160**: 1–10. doi:10.1016/j.marchem.2014.01.002

Osterholz, H., J. Niggemann, H. Giebel, M. Simon, and T. Dittmar. 2015. Inefficient microbial production of refractory dissolved organic matter in the ocean. Nat. Commun. **6**: 7422. doi:10.1038/ncomms8422

Pinardi, N., and E. Masetti. 2000. Variability of the large scale general circulation of the Mediterranean Sea from observations and modelling: A review. Palaeogeogr. Palaeoclimatol. Palaeoecol. **158**: 153–174. doi:10.1016/S0031-0182(00)00048-1

Pujo-Pay, M., and others. 2011. Integrated survey of elemental stoichiometry (C, N, P) from the western to eastern Mediterranean Sea. Biogeosciences **8**: 883–899. doi:10.5194/bg-8-883-2011

Raeke, J., O. J. Lechtenfeld, M. Wagner, P. Herzsprung, and T. Reemtsma. 2016. Selectivity of solid phase extraction of freshwater dissolved organic matter and its effect on ultrahigh resolution mass spectra. Environ. Sci. Process. Impacts. **18**: 918–927. doi:10.1039/c6em00200e

Roether, W., B. B. Manca, B. Klein, D. Bregant, D. Georgopoulos, V. Beitzel, V. Kovacevic, and A. Luchetta. 1996. Recent changes in eastern Mediterranean deep waters. Science **271**: 333–335. doi:10.1126/science.271.5247.333

Roether, W., B. Klein, V. Beitzel, and B. B. Manca. 1998. Property distributions and transient–tracer ages in Levantine Intermediate Water in the Eastern Mediterranean. J. Mar. Syst. **18**: 71–87. doi:10.1016/S0924-7963(98)00006-2

Rossel, P. E., A. V. Vähätalo, M. Witt, and T. Dittmar. 2013. Molecular composition of dissolved organic matter from a wetland plant (Juncus effusus) after photochemical and microbial decomposition (1.25 yr): Common features with deep sea dissolved organic matter. Org. Geochem. **60**: 62–71. doi:10.1016/j.orggeochem.2013.04.013

Santinelli, C. 2015. Chapter 13 – DOC in the Mediterranean Sea, p. 579–608. *In* D. A. Hansell and C. A. Carlson [eds.], Biogeochemistry of marine dissolved organic matter. Elsevier.

Santinelli, C., L. Nannicini, and A. Seritti. 2010. DOC dynamics in the meso and bathypelagic layers of the Mediterranean Sea. Deep-Sea Res. Part II Top. Stud. Oceanogr. **57**: 1446–1459. doi:10.1016/j.dsr2.2010.02.014

Santinelli, C., R. Sempéré, F. Van Wambeke, B. Charriere, and A. Seritti. 2012. Organic carbon dynamics in the Mediterranean Sea: An integrated study. Global Biogeochem. Cycles **26**: GB4004. doi:10.1029/2011GB004151

Santinelli, C., C. Follett, S. Retelletti Brogi, L. Xu, and D. Repeta. 2015. Carbon isotope measurements reveal unexpected cycling of dissolved organic matter in the deep Mediterranean Sea. Mar. Chem. **177**: 267–277. doi:10.1016/j.marchem.2015.06.018

Schlitzer, R. 2016. Ocean data view. http://odv.awi.de. Accessed May 22, 2017.

Schneider, A., T. Tanhua, W. Roether, and R. Steinfeldt. 2014. Changes in ventilation of the Mediterranean Sea during the past 25 year. Ocean Sci. **10**: 1–16. doi:10.5194/os-10-1-2014

Schroeder, K., J. Chiggiato, H. L. Bryden, M. Borghini, and S. B. Ismail. 2016. Abrupt climate shift in the Western Mediterranean Sea. Sci. Rep. **6**: 23009. doi:10.1038/srep23009

Seidel, M., and others. 2014. Biogeochemistry of dissolved organic matter in an anoxic intertidal creek bank. Geochim. Cosmochim. Acta **140**: 418–434. doi:10.1016/j.gca.2014.05.038

Seidel, M., and others. 2015. Molecular–level changes of dissolved organic matter along the Amazon River–to–ocean

continuum. Mar. Chem. **177**: 218–231. doi:10.1016/j.marchem.2015.06.019

Sokal, F. F., and F. J. Rohlf. 1995. Biometry: The principles and practice of statistics in biological research, 3rd ed. W. H. Freeman and Company.

Stubbins, A., and others. 2010. Illuminated darkness: Molecular signatures of Congo River dissolved organic matter and its photochemical alteration as revealed by ultrahigh precision mass spectrometry. Limnol. Oceanogr. **55**: 1467–1477. doi:10.4319/lo.2010.55.4.1467

Stubbins, A., and T. Dittmar. 2015. Illuminating the deep: Molecular signatures of photochemical alteration of dissolved organic matter from North Atlantic Deep Water. Mar. Chem. **177**: 318–324. doi:10.1016/j.marchem.2015.06.020

Stuiver, M., P. D. Quay, and H. G. Ostlund. 1983. Abyssal water carbon–14 distribution and the age of the world oceans. Science **219**: 849–851. doi:10.1126/science.219.4586.849

Tsimplis, M. N., and others. 2006. Chapter 4– changes in the oceanography of the Mediterranean Sea and their link to climate variability, p. 227–282. *In* P. Lionello, P. Malanotte–Rizzoli, and R. Boscolo [eds.], Mediterranean climate variability. Elsevier.

UNESCO. 1985. The International System of Units (SI) in oceanography. UNESCO Tech. Paper. Mar. Sci. **45**: 1–124.

UNESCO. 1986. Progress on oceanographic tables and standards 1983–1986. Work and recommendations of UNESCO/SCOR/ICES/IAPSO joint panel. UNESCO Tech. Pap. Mar. Sci. **50**: 1–59.

UNESCO. 2010. The international thermodynamic equation of seawater: Calculation and use of thermodynamic properties. Intergovernmental Oceanographic Commission, Manuals and Guides No.56, UNESCO/IOC/SCOR/IAPSO (English), p. 196.

Wu, P., K. Haines, and N. Pinardi. 2000. Toward an understanding of deep–water renewal in the Eastern Mediterranean. J. Phys. Oceanogr. **30**: 443–458. doi:10.1175/1520-0485(2000)030<0443:TAUODW>2.0.CO;2

Acknowledgments

The authors are grateful to the Captain, crew, technicians, and scientists aboard the R/V *Sarmiento de Gamboa* for their support during the cruise. We especially thank M. J. Pazó, V. Vieitez, M. Friebe, and I. Ulber for DOC measurements; K. Klaproth for support with FT-ICR-MS analysis; M. Manecki and B. E. Noriega for their help with data processing; and J. Niggemann for valuable discussions. This work was financed by the project HOTMIX (grant CTM2011-30010-C02-01-MAR and 02-MAR) and the project FERMIO (MINECO, CTM2014-57334-JIN), both co-financed with FEDER funds. A.M.M.-P. was funded by a predoctoral fellowship (reference BES-2012-056175) and a short stay fellowship (reference EEBB-I-14-08926) from the Spanish Ministry of Economy and Competitiveness. M. N.-C. was partially supported by the CSIC Program "Junta para la Ampliación de Estudios," co-financed by the ESF (reference JAE DOC 040), co-financed with FEDER funds.

Conflict of Interest

None declared.

Submitted 14 June 2016
Revised 16 February 2017; 27 April 2017
Accepted 05 May 2017

Associate editor: Peter Hernes

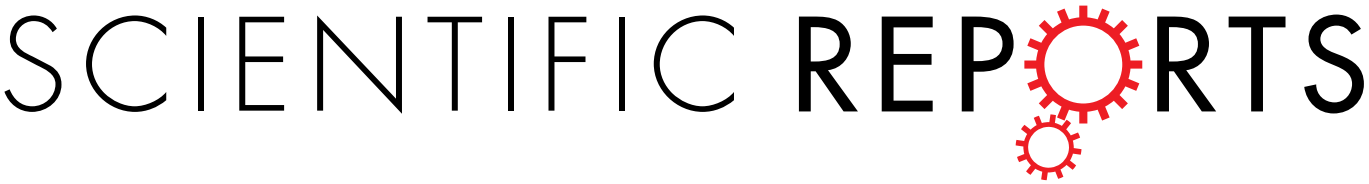

OPEN

Linking optical and molecular signatures of dissolved organic matter in the Mediterranean Sea

Received: 1 February 2017
Accepted: 3 May 2017
Published online: 13 June 2017

Alba María Martínez-Pérez[1], Mar Nieto-Cid[1], Helena Osterholz[2], Teresa S. Catalá[1,2,3], Isabel Reche[3], Thorsten Dittmar[2] & Xosé Antón Álvarez-Salgado[1]

Dissolved organic matter (DOM) plays a key role in global biogeochemical cycles and experiences changes in molecular composition as it undergoes processing. In the semi-closed basins of the oligotrophic Mediterranean Sea, these gradual molecular modifications can be observed in close proximity. In order to extend the spatial resolution of information on DOM molecular composition available from ultrahigh resolution mass spectrometry in this area, we relate this data to optical (fluorescence and absorption spectroscopy) measurements. Covariance between molecular formulae signal intensities and carbon-specific fluorescence intensities was examined by means of Spearman's rank correlations. Fifty two per cent of the assigned molecular formulae were associated with at least one optical parameter, accounting for 70% of the total mass spectrum signal intensity. Furthermore, we obtained significant multiple linear regressions between optical and intensity-weighted molecular indices. The resulting regression equations were used to estimate molecular parameters such as the double bond equivalent, degradation state and occurrence of unsaturated aliphatic compounds from optical measurements. The statistical linkages between DOM molecular and optical properties illustrate that the simple, rapid and cost-efficient optical spectroscopic measurements provide valuable proxy information on the molecular composition of open ocean marine DOM.

Marine dissolved organic matter (DOM) comprises a complex mixture of molecules essentially uncharacterized and present at very low concentrations[1,2]. It is well established that DOM plays a key role in marine biogeochemical cycles: it constitutes the primary source of nutrients and energy for heterotrophic growth[3], regulates the UV and visible light absorption[4], undergoes photochemical processing[5], acts as a trace metal ligand[6] and presents antioxidant activity for minimizing the negative effects of free radicals in aquatic organisms[7] among other services to the marine ecosystems. DOM is mainly produced in the ocean epipelagic layer (0–150 m depth) as a result of phytoplankton photosynthesis and subsequent food web interactions[8]. Most of this recently produced DOM is biologically labile and thus has a short lifetime[9,10]. However, a small fraction of that DOM escapes rapid mineralization because it is originally resistant or it is transformed into resistant materials through abiotic processes or during the microbial processing of bioavailable DOM[11]. This DOM which escapes rapid remineralization accumulates in the surface layer for eventual export to the dark ocean (>150 m depth) by convective overturning and vertical mixing[12,13].

A small fraction of DOM absorbs light in the UV and visible range of the spectrum; it is called colored DOM (CDOM) and it is present in the ocean ubiquitously[4]. Furthermore, a fraction of CDOM emits fluorescence; it is called fluorescent DOM (FDOM) and it is widely used to trace the reactivity, composition[14–17], sources and chemical structure of DOM[18–22]. Fourier Transform Ion Cyclotron Resonance Mass Spectrometry (FT-ICR-MS) is a widely used technique nowadays to distinguish thousands of molecular formulae constituting the DOM pool. Although this technique does not unambiguously reveal the structure of DOM compounds, it offers new possibilities for the characterization of individual formulae or classes of molecules. The linkage between optical and chemical properties of DOM in natural waters is a subject of rising interest among aquatic biogeochemists[23]. Recent studies have combined FT-ICR-MS and optical measurements to better understand the composition of

[1]Consejo Superior de Investigaciones Científicas - Instituto de Investigacións Mariñas (CSIC-IIM), Vigo, Spain. [2]Research Group for Marine Geochemistry, Institute for Chemistry and Biology of the Marine Environment (ICBM), Carl von Ossietzky University, Oldenburg, Germany. [3]Departamento de Ecología and Instituto del Agua, Universidad de Granada, Granada, Spain. Correspondence and requests for materials should be addressed to A.M.M. (email: albam@iim.csic.es)

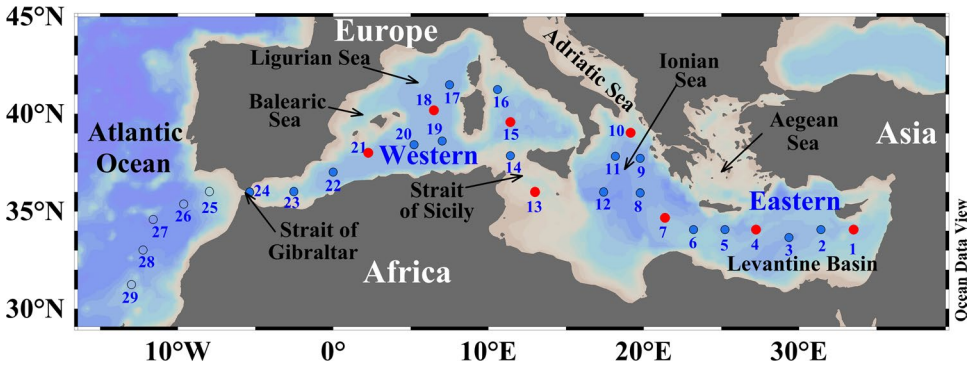

Figure 1. Study area and sampling stations. The circles depict all the cruise stations. Red circles represent the stations where samples were taken for the molecular characterization of DOM. Red and blue circles represent the stations where samples were collected for DOM fluorescence and absorption characterization. Figure created using Ocean Data View (version 4.7.8, R. Schlitzer, 2016. http://odv.awi.de).

DOM in natural waters[24,25] but few of them have directly related optical and molecular signatures[26–31]. These studies, mainly focused on freshwater and coastal systems, have reported significant relationships between optical indices and molecular formulae. However, DOM of terrestrial and marine origin is characterized by contrasting molecular size and composition, as well as absorption and fluorescence spectral properties[4,32]. Therefore, the results obtained in previous studies conducted in freshwater and coastal systems should not be directly generalized to open ocean waters.

In this study, we link the fluorescence and absorption of DOM with the molecular signatures obtained from the FT-ICR-MS data of 29 samples from the open epi–, meso– and bathypelagic waters of the Mediterranean Sea. Our main objective is to determine the covariance between optical and molecular signatures in this low-CDOM ocean system and examine similarities and differences with the relationships found in high-CDOM freshwater and coastal systems. Furthermore, we aim to go a step ahead by establishing semi-quantitative relationships between an assortment of calculated optical and molecular indices. Our final goal is the use of fluorescence and absorption spectroscopy measurements as a proxy for the indices obtained from molecular data, which are more time demanding and costly to obtain. Note that these relationships do not imply a direct causation but the existence of a common cause or causes of variation between optical and molecular indices.

Material and Methods

Sampling strategy. During the trans-Mediterranean cruise HOTMIX (see cruise track in Fig. 1) aboard R/V Sarmiento de Gamboa (Heraklion, Crete, 27 April 2014 – Las Palmas, Canary Islands, 29 May 2014), water samples were collected using a SBE 38 rosette sampler, equipped with 24 (12 L) Niskin bottles. Conductivity, temperature and depth probes (CTD SBE 911 plus) as well as oxygen (SBE-43 oxygen sensor) and fluorescence (SeaPoint fluorometer) sensors were attached to the rosette. Distributions of salinity, potential temperature, dissolved oxygen and chlorophyll *a* are shown in Figure S1. We used these profiles to sample the deep chlorophyll maximum, the salinity maximum, the oxygen minimum layer and the deep waters. For the determination of dissolved organic carbon (DOC), optical properties, and molecular formulae, seawater samples were collected in 5-litres acid-cleaned polycarbonate carboys. Prior to filtration (within 5 hours), samples were stored in the dark at 13 °C and then filtered through precombusted (450 °C, 4 h) Whatman GF/F filters. Two-liter aliquots of the filtrate were collected in acid-cleaned PTFE bottles for solid phase extraction of DOM (SPE-DOM).

Dissolved organic carbon and optical measurements. Aliquots of 10 mL of the filtrate were collected for DOC quantification in precombusted (450 °C, 12 h) glass ampoules. These samples were acidified with H_3PO_4 (85%, p.a., Merck) to pH < 2 and the ampoules were flame sealed and stored in the dark at 4 °C until analysis in the base laboratory. DOC concentration was determined with a Shimadzu TOC-V organic carbon analyzer by high temperature catalytic oxidation (HTCO). Potassium hydrogen phthalate (99.95–100.05%, p.a., Merck) was used to calibrate the system daily. The precision of the equipment was ±1 μmol L^{-1}. The accuracy was checked daily with the DOC reference materials provided by D. A. Hansell (University of Miami, USA).

Absorbance of CDOM was measured on board using a double beam Perkin Elmer lambda 850 spectrophotometer equipped with 10 cm path length quartz cuvettes for sample and reference (ultrapure water, Milli-Q, Millipore Advantage A10). Spectral scans were collected from 250 nm to 750 nm at 1 nm intervals and constant room temperature. The absorbance was converted into Naeperian absorption coefficient (m^{-1})[33]. The carbon-specific absorption coefficient at 254 nm ($a254^*$; L m^{-1} mg^{-1} C) was calculated.

FDOM was determined on board with a Perkin Elmer LS55 luminescence spectrometer. Slit widths were 10 nm for both excitation and emission wavelengths. Measurements were performed at room temperature in a 1 cm quartz fluorescence cell and Milli-Q was used as a reference blank. The spectrofluorometer was tested daily: intensity of the Raman peak was tested with a sealed Milli-Q water cell (Perkin Elmer) while p-terphenyl and tetraphenylbutadiene methacrylate blocks (Starna) were used to check the instrument signal intensity at the excitation-emission wavelengths characteristic of the aromatic amino acids and humic-like substances, respectively. Excitation (Ex)-emission (Em) matrices (EEMs) were generated by combining 22 fluorescence emission

spectra from 300 to 560 nm at excitation wavelengths ranging from 240 to 450 nm at 10 nm intervals. Rayleigh scatter bands were removed mathematically from the EEMs. Parallel factor analysis (PARAFAC) was used to decompose the fluorescence signal of the EEMs into the underlying individual fluorescent components[34]. Data analyses were performed using the DOMFluor 1_7 Toolbox8 and conducted in Matlab R2014B (MathWorks, USA). A four-component model with the most common fluorescent peaks of aquatic environments was obtained (Figure S2), two of them of humic-like nature, compatible with peaks A + C (at Ex/Em < 270–350/470 nm) and M (at Ex/Em 330/402 nm) and two of amino acid-like nature, attributed to tryptophan and tyrosine at Ex/Em 280/374 nm and 270/306 nm, respectively. Model validation was performed by split-half diagnostics and random initialization[35,36].

Given that the PARAFAC components (Figure S2) match the classical fluorescence peak intensities at selected Ex/Em wavelength pairs previously established[37], we decided to use the latter to allow direct comparison with previous studies. The selected Ex/Em wavelengths were 250/435 nm (peak A) due to general humic substances; 340/440 nm (peak C) due to humic substances of terrestrial origin; 320/410 nm (peak M) due to humic substances of marine origin; and 280/350 nm (peak T) and 270/304 nm (peak B) due to protein-like substances. The fluorescence of each peak was determined by subtracting the Milli-Q blank peak height from the sample average peak height. All the samples were normalized using a solution of quinine sulphate dihydrate (≥99.0%, purum for fluorescence, Fluka) and tryptophan (≥99.0%, Fluka) standards in H_2SO_4 0.05 M (95–97%, p.a., Merck) allowing to express fluorescence in Normalized Fluorescence Intensity Units (NFIU)[38]. The fluorescence of each peak was then calculated as the mean of 4 individual measurements, which presented a coefficient of variation of $<6 \pm 2\%$ ($n = 30$) for all the peaks. Carbon-specific fluorescence of humic-like (peaks A*, C* and M*) and protein-like (peak T*) substances were calculated dividing the fluorescence intensity by the DOC concentration (in NFIU L mg^{-1} C). Humic-/protein-like and terrestrial/marine fluorescence ratios (A/T, C/T, M/T and C/M) were also calculated. In addition, we calculated fluorescence-based indices such as the fluorescence (FI)[39], freshness (FrI)[29], biological (BIX)[40] and humification (HIX)[41] indices (see Table 1 for wavelength ranges).

Solid phase extraction and FT-ICR-MS analysis. For SPE-DOM isolation, filtered seawater samples (2 L) were acidified to pH 2 and the DOM was extracted on board using PPL cartridges (Agilent)[42]. After extraction, cartridges were rinsed with acidified ultrapure water to remove remaining salts and frozen at −20 °C. Once in the base lab, the cartridges were dried by flushing with high purity N_2 and eluted with 6 mL of methanol (HPLC-grade, Sigma-Aldrich). SPE-DOM methanol extracts were diluted with ultrapure water and methanol (MS grade) to yield a DOC concentration of 15 mg C L^{-1} and a methanol-to-water ratio of 1:1 (v/v) for analysis by ultrahigh-resolution mass spectrometry using a Solarix FT-ICR-MS (Bruker Daltonik GmbH) connected to a 15 Tesla superconducting magnet (Bruker Biospin). Molecular formulae were assigned to the detected masses[43]. The signal intensity of each identified molecular formula was normalized to the sum of all molecular formula intensities with signal-to-noise ratio (S/N) higher than 5 in each sample, so we can interpret the FT-ICR-MS data semi-quantitatively[44]. The degree of unsaturation of a compound was assessed based on its molecular formula and was expressed as the double bond equivalent (DBE)[45,46] and the degradation index (Ideg) was calculated[47]. The identified molecular formulae were assigned to compound groups based on established molar ratios, modified aromaticity index, DBE and heteroatom contents as described elsewhere[43]. This assignment into molecular compound groups is not an unambiguous method for molecular structure determination, but it provides a useful overview of likely structures behind a given set of molecular formulae. The averages per sample, weighted by relative intensity of the detected masses, of molecular weight (MW), DBE and abundance of compound groups were also calculated. The reproducibility and the detection limit of the FT-ICR-MS method was assessed in previous works[48,49] by performing multiple measurements of the same reference sample. This sample, collected at a depth of 670 m at the Natural Energy Laboratory of Hawaii Authority (NELHA) in Kona, Hawaii[50], was also used as an internal reference sample to assess and correct for instrument variability over time. In our work, the detection limit was established at a fixed signal-to-noise ratio (S/N) higher than 4. In addition, we tested the reproducibility of the peak detection using NELHA sample replicates ($n = 13$) and found a coefficient of variation of $13 \pm 6\%$.

Statistical analyses and graphical tools. Carbon-specific fluorescence peak intensities, fluorescence ratios, *a*254*, FI, FrI, HIX and BIX were correlated with all assigned molecular formulae applying Spearman's rank correlations. Each individual optical parameter was correlated with each individual molecule. Spearman's rank correlation coefficients (r) greater than 0.43 were considered significant at the 99% confidence limit (Student's t-test for a set of 29 samples). Therefore, all molecular formulae correlating with $r > 0.43$ with a given optical index were assigned to that optical index. A similar approach was applied in previous studies[26,27,29]. In addition, multiple linear regression models between molecular parameters and optical indices were calculated using Pearson's regressions. To determine if our sample size allows to detect significant differences we performed a power analysis for $n = 29$. We found that the power was higher than 0.72 for all variables. We therefore assume that the sample size $n = 29$ is appropriate to detect significant differences. To validate our models we performed a cross validation exercise. We used 80% of the samples to obtain the models and then validated them with the remaining 20% of the samples. The subsets to obtain and validate the models were chosen randomly and repeated 1000 times. Then, we calculated the error of the estimation for the 1000 runs and obtained mean errors. All the statistical analyses were performed in R[51] (version 3.1.1, 2014-07-10, http://cran.r-project.org/). Figure 1 was created using the Ocean Data View (ODV) software[52], Fig. 2 was created using Sigma plot (version 11.0), Fig. 3 was produced using the R (version 3.1.1, 2014-07-10), Fig. 4 was created using the ODV software and Fig. 5 was produced using Microsoft Excel 2010.

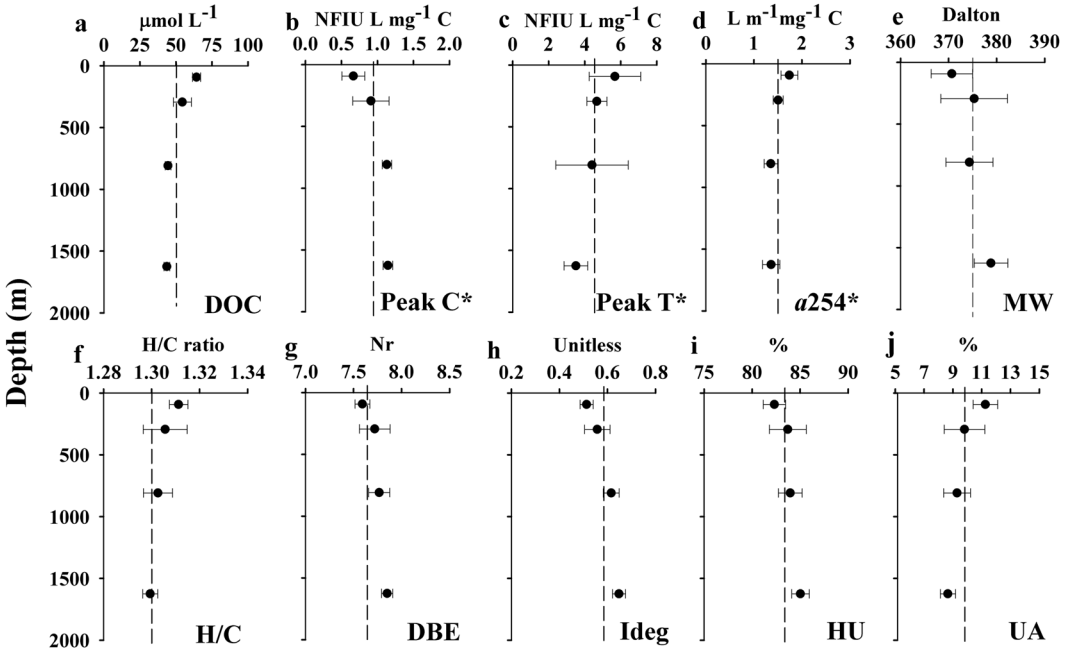

Figure 2. Vertical profiles of DOC, optical and molecular parameters averaged by water layer (**a**) DOC, (**b**) carbon-specific fluorescence intensity of humic-like substances (peak C*), (**c**) carbon-specific fluorescence intensity of protein-like substances (peak T*), (**d**) carbon-specific absorption coefficient at 254 nm (*a*254*), (**e**) average molecular weight (MW), (**f**) H/C ratio, (**g**) double bond equivalent (DBE), (**h**) degradation index (Ideg), (**i**) relative abundance of the highly unsaturated (HU) and (**j**) relative abundance of unsaturated aliphatic (UA) compounds. Error bars are standard deviation and the dashed lines represent the mean value for each variable. Figure created using the software Sigma plot (version 11.0).

Results and Discussion

Carbon stock and optical characterization of DOM in the Mediterranean Sea. DOC concentrations of the collected samples showed the characteristic exponential decay profile with depth found in the open ocean. Considering the sampling depths, maximum concentrations higher than 60 µmol C L^{-1} were observed at the deep chlorophyll maximum (DCM) and minimum concentrations of about 42 µmol C L^{-1} were found in the deep waters (Fig. 2a). These results are in agreement with previous studies in the Mediterranean Sea[53,54]. The vertical distribution of the C-specific fluorescence of humic-like substances (peak C*) increased with depth although leveling off from about 750 m to the bottom (Fig. 2b). The increase of peak C* with depth was likely caused by the production of humic-like materials during microbial respiration processes in meso- and bathypelagic layers[16,55–57] and its accumulation due to the refractory nature (centennial turnover times) of this material[17,58]. The peak C* minimum at the DCM can also be attributed to the vulnerability of humic-like substances to photobleaching in the upper mixed layer[15,59]. Conversely, the vertical profile of the carbon-specific fluorescence of protein-like substances (peak T*) was opposite to peak C* (Fig. 2c). The maximum value for peak T* at the sampling depths was found at the DCM and attributed to the accumulation of semi-labile materials, such as amino acids from phytoplankton exudation, cell autolysis and microzooplankton grazing[60,61]. In addition, those substances are much less vulnerable to photodegradation than humic-like substances[62], which leads to their accumulation in this layer. The observed decrease of peak T* with depth likely resulted from the bio-labile nature of these compounds, as it was suggested in a previous study[63], who found a strong relationship between protein-like fluorescence and biodegradable DOC. In our study, the peak T* profile was also similar to the DOC profile, showing a similar pattern to other ocean areas[14]. This finding indicates that peak T* at the DCM accumulates at a higher rate than the bulk DOM and it would be consumed faster in the deep ocean. The carbon-specific absorption coefficient at 254 nm (*a*254*), used as an aromaticity index[18], showed a decreasing profile with depth, although it remained constant from about 750 m to the bottom (Fig. 2d), similar to the DOC and peak T* profiles (Fig. 2a,c).

The FI reveals information about DOM origin, terrestrial versus microbial[64], and ranged between 1.8 and 2.2. This result indicates that FDOM in the Mediterranean Sea presented a predominantly microbial origin[21]. FrI and BIX, both indicators of recent biological activity[29,40], ranged between 0.8 and 1.0. HIX, a proxy to the DOM humification degree, ranged between 0.9 and 7.6. The values of these indices are indicative of weak humic character and important recent autochthonous sources of DOM[40]. FI, FrI and BIX showed a vertical profile similar to *a*254*, DOC and peak T*. However HIX was, as expected, more similar to the profile of peak C*.

Molecular level DOM characterization in the Med Sea. A total of 6057 resolved molecular masses of singly charged compounds were detected in the FT-ICR-MS spectra covering a mass range of 154–817 Da. We assigned 3689 molecular formulae in the mass range of 157–736 Da, not considering ^{13}C isotopologues. The vertical profile of the molecular parameters calculated from the mass spectra (Fig. 2e–j) showed that DOM

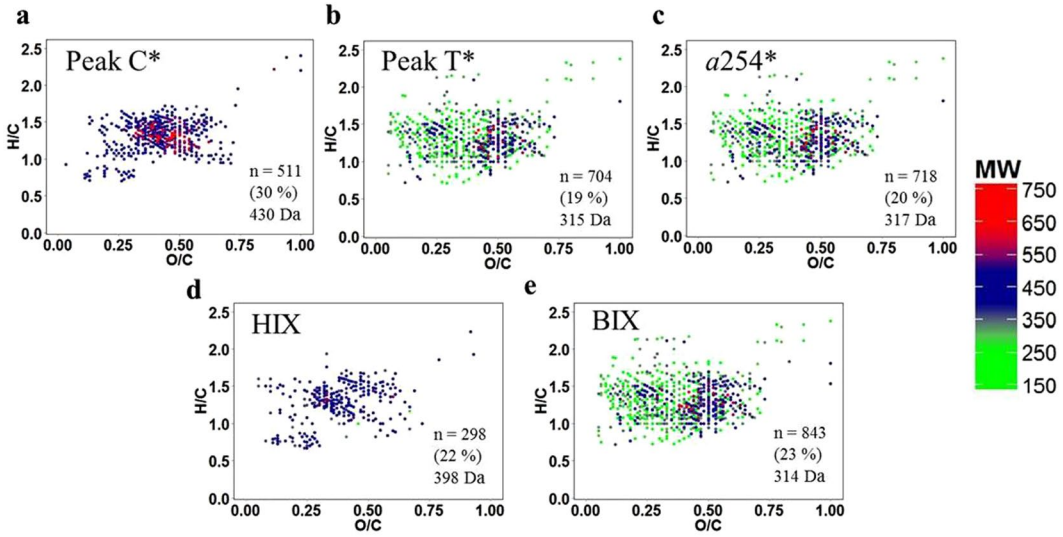

Figure 3. Van Krevelen diagrams. Molecular formulae positively correlated with (**a**) peak C*, (**b**) peak T*, (**c**) a254*, (**d**) HIX and (**e**) BIX. Color scale represents the molecular weight. In the right-bottom corner of each panel is summarized the number of molecular formulae correlating, the percentage of peak intensity and the average molecular weight. Figure created using R software (version 3.1.1, 2014-07-10, http://cran.r-project.org/).

compounds were more unsaturated and of higher molecular weight with depth. As it has been suggested, the MW increases from recent to aged material[47]. In addition, lower H/C and higher O/C ratios have been observed as indicators of reworked organic matter[47,65]. The downwards increasing profiles of DBE, degradation index and the abundance of highly unsaturated compounds together with the decrease in unsaturated aliphatic compounds and H/C ratio indicated an increase of the unsaturation degree with depth. These results are in agreement with previous studies[47,66]. Highly unsaturated compounds increased with depth as they are likely produced during the remineralization processes in the meso- and bathypelagic layers. On the contrary, maximum proportions of unsaturated aliphatic compounds were found at the DCM as they comprise a major fraction of phytoplankton exudates[66]. These compounds are then presumably consumed throughout the water column due to their bioavailability. The most abundant group of molecules, in terms of number of formulae, was represented by the highly unsaturated compounds ($70.4 \pm 0.6\%$), followed by unsaturated aliphatics ($13.7 \pm 0.7\%$), polyphenols ($11.8 \pm 0.2\%$), peptides ($2.5 \pm 0.1\%$), saturated fatty acids with heteroatoms ($0.78 \pm 0.05\%$) and sugars with heteroatoms ($0.6 \pm 0.1\%$). Carboxyl-rich alicyclic molecules (CRAM)[67] accounted for $21.9 \pm 0.6\%$ of the total number of molecular formulae. Note that 94% of the molecular formulae assigned to CRAM were also classified as highly unsaturated compounds. All assigned molecular formulae were represented in a van Krevelen diagram (Figure S3) grouped by compound classes.

Linking optical and molecular properties of SPE-DOM. We explored the covariability of each one of the 3689 molecular formulae identified from the FT-ICR-MS analysis with the C-specific fluorescence intensities, fluorescence indices and absorption coefficients described in the Material and Methods section by means of Spearman's rank correlations (99% confidence limit). Our statistical analysis indicated that 52% of the 3689 assigned molecular formulae were correlated, either positively or negatively, with one or more optical parameter. These molecular formulae accounted for 70% of the mass spectrum peak intensities. Considering only the positive correlations ($r > 0.43$), 46% of the molecular formulae (65% of the spectra signal intensity) correlated with one or more optical parameter (Table 1). These percentages were slightly higher than those found in Canadian boreal rivers[27], but lower than in the Florida Everglades[29]. Note that the number of molecular formulae not correlating (NC) with any optical parameter was different for the positive and negative correlations (Tables 1 and S1, respectively). This is due to the fact that a molecular formulae that correlated positively with one or more optical parameters but did not correlate negatively with any optical parameter will count in the no correlation group in Table S1 (negative correlations) but not in Table 1 (positive correlations). The majority of the formulae correlated significantly with more than one optical parameter (Table S2). These results indicate that fluorescence and absorption measurements covary with a substantial fraction of the SPE-DOM and not only with the minor fraction of fluorescent molecular formulae. Note that the fractions of DOM captured by both techniques are different, and both techniques have specific analytical windows. For optical measurements only the colored/fluorescent pools of DOM are considered. Furthermore, FDOM can be affected by quenching processes, which depend on the sample matrix[68]. FT-ICR-MS analysis, on the other hand, provides information on the solid-phase extractable and ionizable fraction. In this regard, SPE-DOM comprises a wide range of the most apolar DOM molecules to highly polar molecules, but not the smallest ionic molecules (i.e. short chain organic acids and free amino acids) and colloidal aggregates[69]. ESI is a soft ionization technique that preferentially ionizes polar functional groups that renders DOM molecules their water solubility[70].

	All	NC	Peak A*	Peak C*	Peak M*	Peak T*	A/T	C/T	M/T	C/M	*a*254*	FI	FrI	BIX	HIX
Nr total formulae	3689 (100)	1995 (35)	408 (27)	511 (30)	432 (25)	704 (19)	396 (27)	447 (29)	429 (28)	72 (2)	718 (20)	441 (12)	825 (22)	843 (23)	298 (22)
MW (Da)	375	366	426	430	433	315	420	421	422	350	317	289	313	314	398
Nr formulae with N	1456 (100)	756 (52)	135 (10)	156 (10)	133 (8)	328 (24)	140 (11)	161 (12)	153 (11)	35 (4)	324 (24)	222 (16)	389 (28)	390 (29)	112 (12)
Black Carbon (Nr)	8 (100)	3 (23)	0 (0)	0 (0)	0 (0)	3 (45)	0 (0)	0 (0)	0 (0)	0 (0)	2 (32)	3 (47)	4 (62)	0 (0)	3 (0)
Polyphenols (Nr)	433 (100)	220 (47)	32 (16)	36 (16)	30 (11)	93 (13)	35 (17)	39 (18)	37 (18)	7 (2)	93 (14)	74 (12)	124 (19)	121 (19)	46 (23)
Highly unsaturated (Nr)	2594 (100)	1460 (35)	293 (29)	279 (32)	317 (27)	448 (17)	288 (29)	316 (32)	305 (31)	56 (2)	454 (18)	271 (11)	509 (20)	523 (21)	193 (22)
Unsaturated aliphatic (Nr)	507 (100)	238 (30)	73 (29)	83 (30)	75 (28)	122 (23)	70 (27)	76 (28)	73 (27)	5 (4)	133 (24)	74 (15)	144 (26)	152 (28)	51 (23)
Saturated fatty acids (Nr)	28 (100)	10 (11)	0 (0)	1 (1)	0 (0)	13 (62)	0 (0)	0 (0)	0 (0)	0 (0)	13 (62)	7 (38)	16 (66)	17 (88)	0 (0)
Sugars (Nr)	30 (100)	20 (32)	3 (35)	3 (35)	3 (35)	2 (8)	4 (23)	6 (52)	6 (52)	0 (0)	2 (8)	2 (8)	3 (11)	3 (11)	2 (18)
Peptides (Nr)	89 (100)	44 (33)	7 (15)	9 (17)	7 (15)	23 (30)	7 (15)	10 (17)	8 (16)	4 (4)	21 (29)	10 (9)	25 (42)	24 (42)	6 (6)

Table 1. Positive correlations between the total assigned molecular formulae as well as the different type of molecular groups and the optical parameters; carbon-specific fluorescence intensity in NFIU L mg^{-1} C of general humic-like substances (peak A*), terrestrial humic-like substances (peak C*), marine humic-like substances (peak M*), protein-like substances (peak T*), fluorescence ratios (peak A/T, C/T and M/T ratios), carbon-specific absorption coefficient at 254 nm (*a*254*; L m^{-1} mg^{-1} C), fluorescence index (FI) calculated as the ratio of emission at 470 and 520 nm at excitation wavelength 370 nm, freshness index (FrI) calculated as the ratio between 380 and the maximum intensity between 420 and 435 nm at 310 emission wavelength, biological index (BIX) determined as the ratio of emission at 380 and 430 nm at 310 nm of excitation wavelength and the humification index (HIX) calculated as the ratio between the integrated emission spectra between 435 and 480 and 300–345 nm at 260 nm of excitation wavelength. NC = no correlation. MW = intensity-weighted average molecular weight, Nr = number. Numbers in parentheses correspond to the signal intensity percentage from the spectra.

A statistical linkage between molecular formulae and optical properties does not necessarily imply that compounds with a given molecular formula contain fluorophores or chromophores, but it indicates similar biogeochemical behavior in an aquatic system[28].

The number of positive correlations ($r > 0.43$) between the molecular formulae and humic-like compounds and fluorescence ratios (peak A/T, C/T and M/T) were fewer compared to the negative correlations ($r < -0.43$), however they accounted for higher relative spectrum intensities (Tables 1 and S1). On the contrary, the number of molecules positively correlated with peak T*, *a*254*, FrI and BIX was much higher than the number of negative correlations but they accounted for relatively lower spectrum intensities. Plotting the significant correlations into Van Krevelen diagrams (Fig. 3), where the color scale represents the molecular weight of each formula, we can distinguish the molecular families associated with each optical parameter. For the range of materials isolated with our SPE methodology, which excludes free amino acids and colloidal aggregates (see above), we observed that peak C* correlated positively with higher average MW formulae and peak T* correlated with lower average MW formulae. *a*254* and BIX correlated positively with formulae similarly to peak T* whereas HIX was related to peak C* (Fig. 3). Van Krevelen diagrams representing the negative correlations for the same variables (Figure S4) showed the opposite trend, peak C* and HIX correlated with lower average MW molecules and peak T*, *a*254* and BIX were related to higher average MW molecules.

We also studied the correlations between different groups of molecules and the optical indices (Table 1). We observed that about 59% of the spectrum intensity assigned to polyphenols correlated with one or more optical parameter. These compounds were negatively correlated with peak M*, fluorescence ratios A/T, C/T and M/T and BIX and positively with peak T*, *a*254* and HIX. These findings are in agreement with the fact that some polyphenols fluoresce in an area relatively close to the protein-like substances region[58,71]. Furthermore, it was suggested that hydrocarbons are detected in the peak T* region[27].

About 70% of the mass spectrum intensity of highly unsaturated compounds, the most abundant group in our samples (Figure S5a), correlated both positively and negatively with all the optical parameters (Tables 1 and S1). The unsaturated aliphatic compounds were the group that accounted the most to the correlations with the optical properties (about 75% of their mass spectrum intensity). Almost the same percentage of these compounds correlated positively and negatively with peaks A*, C*, M* and the fluorescence ratios A/T, C/T and M/T (Tables 1 and S1). However, the positive correlations were greater compared with the negative for peak T*, likely due to the labile nature of these compounds as it was suggested in previous studies[15,22,63], and for some of the fluorescence indices (FI, FrI and BIX) which are proxies for recent biologic activity.

The saturated fatty acids correlated only negatively with peak A*, C* and M*, the ratios A/T, C/T and M/T and HIX and positively with peak T*, *a*254*, FI, FrI and BIX. Similarly, peptides correlated negatively with peak

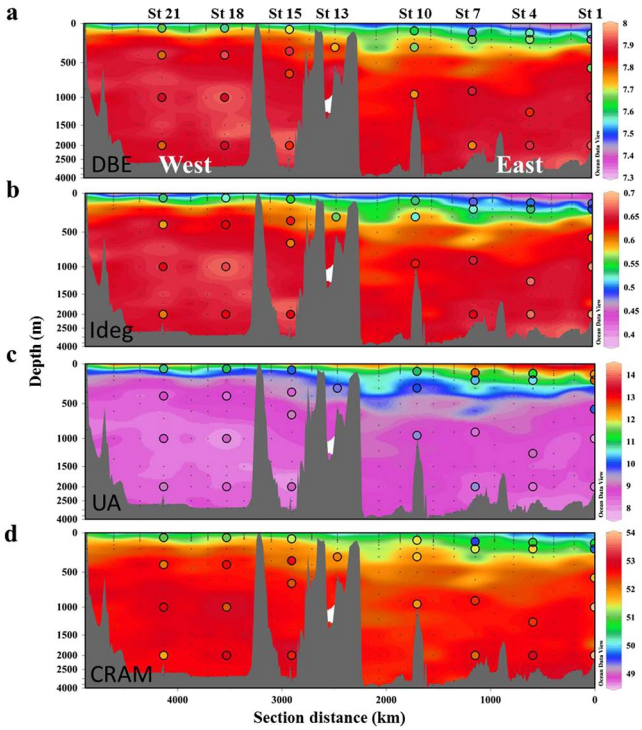

Figure 4. Distributions of the estimated molecular parameters. (**a**) double bond equivalent (DBE) in number, (**b**) degradation index (Ideg) unitless, (**c**) unsaturated aliphatic compounds (UA) in % and (**d**) carboxyl-rich alicyclic molecules (CRAM) in % for the whole Mediterranean Sea determined from fluorescence measurements. Colored dots represent molecular parameters calculated by FT-ICR-MS analysis. Figure created using Ocean Data View (version 4.7.8, R. Schlitzer, 2016. http://odv.awi.de).

	Peak C*	Peak T*	θ	Intercept	SEE	R^2	p- value
DBE	0.32 (0.12); *beta* = 0.55	−0.02 (0.01); *beta* = −0.22	−0.02 (0.02); *beta* = −0.24	7.89 (0.47)	1.0	0.73	<0.0001
Ideg	0.13 (0.03); *beta* = 0.50	−0.016 (0.003); *beta* = −0.30	−0.0015 (0.006); *beta* = −0.31	0.75 (0.11)	4.6	0.85	<0.0001
UA	−2.5 (0.9); *beta* = −0.44	0.23 (0.07); *beta* = 0.22	0.39 (0.18); *beta* = 0.39	5.5 (3.4)	6.7	0.80	<0.0001
CRAM	1.8 (0.7); *beta* = 0.43	−0.24 (0.05); *beta* = −0.30	−0.21 (0.15); *beta* = −0.27	54.2 (2.7)	1.1	0.65	<0.0001

Table 2. Mean values (standard deviation) of the coefficients of the multiple linear regressions (Pearson) for n = 1000 between the intensity-weighted average molecular parameters from FT-ICR-MS analysis of the SPE-DOM (DBE = double bond equivalent[46], Ideg = degradation index[47], unsaturated aliphatic compounds (UA) and CRAM = carboxyl rich alicyclic molecules)[67] and potential temperature and the optical properties of the DOM (carbon-specific fluorescence intensity of the humic-like compounds (peak C*) and the protein-like compounds (peak T*) in NFIU L mg^{-1} C. *beta* = Normalized regression coefficients, SEE = standard error of estimate in %.

A*, C*, M*, the ratios A/T, C/T, M/T and HIX, but only positively with peak T* and *a*254*. These results are in agreement with the fact that saturated fatty acids are presumably bioavailable molecules[72].

The distribution of all the molecules positively correlated with peak C* and peak T* are graphically shown in Figure S5b and c. Compared with the mean compound group distribution of SPE-DOM in the Mediterranean Sea (Figure S5a), molecules correlating with peak C* were enriched in highly unsaturated compounds and impoverished in polyphenols. Conversely, molecules correlating with peak T* were enriched in unsaturated aliphatic molecules but impoverished in highly unsaturated molecules. In addition, peak T* showed an enrichment in polyphenols compared to peak C*.

Inferring DOM molecular indices from optical properties. Once we have verified the existence of significant correlations between DOM molecular formulae and optical properties, we propose using multiple linear regressions to estimate molecular indices from optical indices. First, a correlation matrix including salinity (S), potential temperature (θ), peak C*, peak T* and a254* was obtained (data not shown) to check for covariance between these variables. On basis of this analysis, Peak C* and peak T* along with θ were chosen for performing the multiple regressions. These regression models were fitted using the 29 samples for which we have peak C* and peak T* measurements together with FT-ICR-MS molecular parameters. The cross validation exercise of the

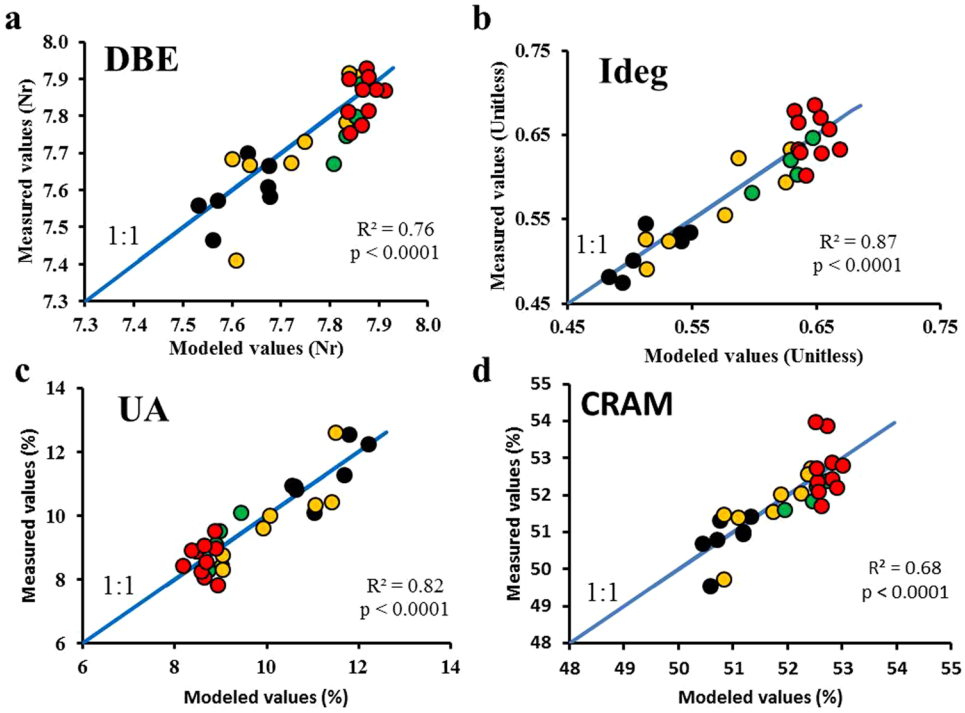

Figure 5. Comparison of modeled and measured molecular DOM properties. The modeled values were calculated using the multiple linear regression models and the measured values were obtained from the FT-ICR-MS analysis for (**a**) double bond equivalent (DBE), (**b**) degradation index (Ideg), (**c**) unsaturated aliphatic compounds and (**d**) carboxyl-rich alicyclic molecules (CRAM). Colored dots represent samples collected at different layers, deep chlorophyll maximum (black), Levantine intermediate water (yellow), oxygen minimum layer (green) and deep waters (red). Note that there is a random deviation from the 1:1 line (blue line). For the CRAM regression (plot **d**) red dots with higher measured values correspond with samples collected at station 1 and the black and yellow dots, with lower measured values, correspond with samples collected at station 7 and 1, respectively.

multiple regression of each molecular index with peak C*, peak T* and θ (see Materials and Methods) yielded estimated mean errors of 1, 5, 7 and 1% for DBE, Ideg, UA and CRAM, respectively. Therefore, the models were able to estimate molecular parameters from optical indices with a relatively low error. Then, we calculated the mean and standard deviation of the regression coefficients obtained after the 1000 times that each regression model was run to perform the cross validation exercise. These mean regression coefficients (Table 2) were not significantly different from the regression coefficients obtained with the individual multiple linear regressions of the molecular indices with peak C*, peak T* and θ for the 29 samples. The regression coefficients showed that peak C* was positively correlated with DBE, Ideg and CRAM, but negatively with unsaturated aliphatic compounds. Opposite results were obtained with peak T*. Regarding the normalized regression coefficients (beta), they were higher for peak C* than for peak T* for all the regressions (Table 2). The relative weight of peak T* increases when modeling Ideg and CRAM.

The mean regression coefficients in Table 2 were then used to estimate the molecular parameters of the 400 samples collected during the cruise for the determination of peak C* and peak T* (Fig. 4). Since the latter were performed with a JY-Horiba Spex Fluoromax-4 spectrofluorometer, the measurements of the 29 samples determined with both spectrofluorometers were used to intercalibrate both instruments ($R^2 = 0.88$, $p < 0.0001$ for peak C and $R^2 = 0.77$, $p < 0.0001$ for peak T). Using θ, peak C* and peak T* we were then able to estimate molecular indices (DBE, Ideg, unsaturated aliphatic compounds and CRAM) and build up detailed maps of their distribution for the whole Mediterranean Sea. The model goodness is confirmed by the low mean error of the estimates from the cross validation exercise, by Fig. 4 where colored dots represent measured values for the molecular parameters, and by Fig. 5 where we compared the measured and modeled values using linear regressions. These results indicate that the multiple regression models work well for the Mediterranean Sea ($R^2 > 0.65$, $p < 0.0001$) and reliable detailed spatial molecular information from FDOM measurements can be gained. Regarding these distributions (Fig. 4), the upper layer in the eastern basin showed SPE-DOM with lower DBE, degradation state and CRAM than the western basin but presented more abundance of unsaturated aliphatic compounds. Note that for the CRAM distribution (Fig. 4d) the mismatches in the samples collected at station 1 (200, 1000 and 2000 m) and station 7 (110 m) were due to the fact that in the scatter plot (Fig. 5d) the points exhibited a stronger divergence from the linear regression line. Although differences between measured and modeled values of % CRAM in these samples were apparent, the other molecular parameters (i.e. Ideg, AImod, and DBE) did not show such differences. To check if these samples could lead to a different result in the model, we discarded these samples as outliers to obtain a new model and new estimated values. Comparing the two model results (Figure S6), the new

model presented slightly lower values in some deep regions but the patterns were not different than in the former model. For this reason we decided to keep these samples in the model.

Overall, in this work we have shown that optical and molecular properties correlated significantly in the Mediterranean Sea. In detail, we have observed relationships between different SPE-DOM groups of molecules and specific DOM fluorescence or absorption parameters. Furthermore, we have established, for the first time, empirical multiple regression models to estimate molecular parameters from optical measurements in open ocean waters.

References

1. Benner, R. Chemical composition and reactivity in *Biogeochemistry of Marine Dissolved Organic Matter* (eds Hansell, D. A. & Carlson, C. A.) 59–90 (Academic Press, 2002).
2. Repeta, D. J., Hansell, D. A. & Carlson, C. A. Chemical characterization and cycling of dissolved organic matter in *Biogeochemistry of Marine Dissolved Organic Matter* (eds Hansell, D. A. & Carlson, C. A.) 22–65 (Academic Press, Waltham MA, USA, 2015).
3. Cuss, C. W. & Guéguen, C. Relationships between molecular weight and fluorescence properties for size-fractionated dissolved organic matter from fresh and aged sources. *Water Res.* **68**, 487–497 (2015).
4. Nelson, N. B. & Siegel, D. A. The global distribution and dynamics of chromophoric dissolved organic matter. *Ann. Rev. Mar. Sci.* **5**, 447–476 (2013).
5. Mopper, K. & Kieber, D. J. Photochemistry and the cycling of carbon, sulfur, nitrogen and phosphorous in *Biogeochemistry of Marine Dissolved Organic Matter* (eds Hansell, D. A. & Carlson, C. A.) 455–507 (Academic Press, 2002).
6. Hirose, K. Metal–organic matter interaction: ecological roles of ligands in oceanic DOM. *Appl. Geochemistry* **22**, 1636–1645 (2007).
7. Romera-Castillo, C. & Jaffé, R. Free radical scavenging (antioxidant activity) of natural dissolved organic matter. *Mar. Chem.* **177**, 668–676 (2015).
8. Carlson, C. A. Production and removal processes in *Biogeochemistry of Marine Dissolved Organic Matter* (eds Hansell, D. A. & Carlson, C. A.) 91–151 (Academic Press, 2002).
9. Hansell, D. A., Carlson, C. A., Repeta, D. J. & Schlitzer, R. Dissolved organic matter in the ocean a controversy stimulates new insights. *Oceanography* **22**, 202–211 (2009).
10. Hansell, D. A. Recalcitrant dissolved organic carbon fractions. *Ann. Rev. Mar. Sci.* **5**, 421–445 (2013).
11. Jiao, N. *et al*. Microbial production of recalcitrant dissolved organic matter: long-term carbon storage in the global ocean. *Nature reviews. Microbiology* **8**, 593–9 (2010).
12. Carlson, C. A., Ducklow, H. W. & Michaels, A. F. Annual flux of dissolved organic carbon from the euphotic zone in the northwestern Sargasso Sea. *Nature* **371**, 405–408 (1994).
13. Thingstad, T. F., Hagström, A. & Rassoulzadegan, F. Accumulation of degradable DOC in surface waters: Is it caused by a malfunctioning microbial loop? *Limnol. Oceanogr.* **42**, 398–404 (1997).
14. Jørgensen, L. *et al*. Global trends in the fluorescence characteristics and distribution of marine dissolved organic matter. *Mar. Chem.* **126**, 139–148 (2011).
15. Nieto-Cid, M., Álvarez-Salgado, X. A. & Pérez, F. F. Microbial and photochemical reactivity of fluorescent dissolved organic matter in a coastal upwelling system. *Limnol. Oceanogr.* **51**, 1391–1400 (2006).
16. Yamashita, Y. *et al*. Fluorescence characteristics of dissolved organic matter in the deep waters of the Okhotsk Sea and the northwestern North Pacific Ocean. *Deep. Res. Part II Top. Stud. Oceanogr.* **57**, 1478–1485 (2010).
17. Catalá, T. S. *et al*. Turnover time of fluorescent dissolved organic matter in the dark global ocean. *Nat. Commun.* **6**, 5986 (2015).
18. Weishaar, J. L. *et al*. Evaluation of specific ultraviolet absorbance as an indicator of the chemical composition and reactivity of dissolved organic carbon. *Environ. Sci. Technol.* **37**, 4702–4708 (2003).
19. Yamashita, Y. & Tanoue, E. Chemical characterization of protein-like fluorophores in DOM in relation to aromatic amino acids. *Mar. Chem.* **82**, 255–271 (2003).
20. Helms, J. R. *et al*. Absorption spectral slopes and slope ratios as indicators of molecular weight, source, and photobleaching of chromophoric dissolved organic matter. *Limnol. Oceanogr.* **53**, 955–969 (2008).
21. Fellman, J. B., Hood, E. & Spencer, R. G. M. Fluorescence spectroscopy opens new windows into dissolved organic matter dynamics in freshwater ecosystems: A review. *Limnol. Oceanogr.* **55**, 2452–2462 (2010).
22. Romera-Castillo, C., Sarmento, H., Alvarez-Salgado, X. A., Gasol, J. M. & Marrasé, C. Net production and consumption of fluorescent colored dissolved organic matter by natural bacterial assemblages growing on marine phytoplankton exudates. *Appl. Environ. Microbiol.* **77**, 7490–7498 (2011).
23. Osburn, C. L. & Bianchi, T. S. Editorial: Linking optical and chemical properties of dissolved organic matter in natural waters. *Front. Mar. Sci.* **3**, 223 (2016).
24. Gonsior, M., Schmitt-Kopplin, P. & Bastviken, D. Depth-dependent molecular composition and photo-reactivity of dissolved organic matter in a boreal lake under winter and summer conditions. *Biogeosciences* **10**, 6945–6956 (2013).
25. Gonsior, M. *et al*. Characterization of dissolved organic matter across the Subtropical Convergence off the South Island, New Zealand. *Mar. Chem.* **123**, 99–110 (2011).
26. Herzsprung, P. *et al*. Variations of DOM quality in inflows of a drinking water reservoir: Linking of van Krevelen diagrams with EEMF spectra by rank correlation. *Environ. Sci. Technol.* **46**, 5511–5518 (2012).
27. Stubbins, A. *et al*. What's in an EEM? Molecular signatures associated with dissolved organic fluorescence in boreal Canada. *Environ. Sci. Technol.* **48** (2014).
28. Kellerman, A. M., Kothawala, D. N., Dittmar, T. & Tranvik, L. J. Persistence of dissolved organic matter in lakes related to its molecular characteristics. *Nat. Geosci.* **8**, 454–459 (2015).
29. Wagner, S., Jaffé, R., Cawley, K., Dittmar, T. & Stubbins, A. Associations between the molecular and optical properties of dissolved organic matter in the Florida Everglades, a model coastal wetland system. *Front. Chem.* **3** (2015).
30. Lavonen, E. E. *et al*. Tracking changes in the optical properties and molecular composition of dissolved organic matter during drinking water production. *Water Res.* **85**, 286–294 (2015).
31. Timko, S. A. *et al*. Depth-dependent photodegradation of marine dissolved organic matter. *Front. Mar. Sci.* **2**, 1–13 (2015).
32. Osburn, C. L., Del Vecchio, R. & Boyd, T. J. Physicochemical effects on dissolved organic matter fluorescence in natural waters in *Aquatic Organic Matter Fluorescence* (eds Coble, P. G., Lead, J., Baker, A., Reynolds, D. M. & Spencer, R. G. M.) 233–277 (Cambridge University Press, 2014).
33. Green, S. A. & Blough, N. V. Optical absorption and fluorescence properties of chromophoric dissolved organic matter in natural waters. *Limnol. Oceanogr.* **39**, 1903–1916 (1994).
34. Bro, R. PARAFAC. Tutorial and applications. *Chemom. Intell. Lab. Syst.* **38**, 149–171 (1997).
35. Murphy, K. R., Stedmon, C. A., Graeber, D. & Bro, R. Fluorescence spectroscopy and multi-way techniques. PARAFAC. *Anal. Methods* **5**, 6557–6566 (2013).
36. Stedmon, C. A. & Bro, R. Characterizing dissolved organic matter fluorescence with parallel factor analysis: A tutorial. *Limnol. Oceanogr. Methods* **6**, 572–579 (2008).

37. Coble, P. G. Characterization of marine and terrestrial DOM in seawater using excitation-emission matrix spectroscopy. *Mar. Chem.* **51**, 325–346 (1996).
38. Nieto-Cid, M., Álvarez-Salgado, X. A., Gago, J. & Pérez, F. F. DOM fluorescence, a tracer for biogeochemical processes in a coastal upwelling system (NW Iberian Peninsula). *Mar. Ecol. Prog. Ser.* **297**, 33–50 (2005).
39. Cory, R. M. & McKnight, D. M. Fluorescence Spectroscopy Reveals Ubiquitous Presence of Oxidized and Reduced Quinones in Dissolved Organic Matter. *Environ. Sci. Technol.* **39**, 8142–8149 (2005).
40. Huguet, A. *et al*. Properties of fluorescent dissolved organic matter in the Gironde Estuary. *Org. Geochem.* **40**, 706–719 (2009).
41. Zsolnay, A., Baigar, E., Jimenez, M., Steinweg, B. & Saccomandi, F. Differentiating with fluorescence spectroscopy the sources of dissolved organic matter in soils subjected to drying. *Chemosphere* **38**, 45–50 (1999).
42. Dittmar, T., Koch, B., Hertkorn, N. & Kattner, G. A simple and efficient method for the solid-phase extraction of dissolved organic matter (SPE-DOM) from seawater. *Limnol. Oceanogr. Methods* **6**, 230–235 (2008).
43. Seidel, M. *et al*. Biogeochemistry of dissolved organic matter in an anoxic intertidal creek bank. *Geochim. Cosmochim. Acta* **140**, 418–434 (2014).
44. Seidel, M. *et al*. Molecular-level changes of dissolved organic matter along the Amazon River-to-ocean continuum. *Mar. Chem.* **177**, 218–231 (2015).
45. Koch, B. P. & Dittmar, T. Erratum: From mass to structure: An aromaticity index for high-resolution mass data of natural organic matter (Rapid Communications in Mass Spectrometry (2006) 20 (926–932). *Rapid Commun. Mass Spectrom.* **30**, 250 doi:10.1002/rcm.2386) (2016).
46. Koch, B. P. & Dittmar, T. From mass to structure: An aromaticity index for high-resolution mass data of natural organic matter. *Rapid Commun. Mass Spectrom.* **20**, 926–932 (2006).
47. Flerus, R. *et al*. A molecular perspective on the ageing of marine dissolved organic matter. *Biogeosciences* **9**, 1935–1955 (2012).
48. Riedel, T. & Dittmar, T. A method detection limit for the analysis of natural organic matter via fourier transform ion cyclotron resonance mass spectrometry. *Anal. Chem.* **86**, 8376–8382 (2014).
49. Hawkes, J. A., Dittmar, T., Patriarca, C., Tranvik, L. & Bergquist, J. Evaluation of the Orbitrap Mass Spectrometer for the Molecular Fingerprinting Analysis of Natural Dissolved Organic Matter. *Anal. Chem.* **88**, 7698–7704 (2016).
50. Green, N. W. *et al*. An intercomparison of three methods for the large-scale isolation of oceanic dissolved organic matter. *Mar. Chem.* **161**, 14–19 (2014).
51. R Core Team. R: A languaje and environment for statistical computing. R foundation for Statistical Computing, Vienna, Austria. URL http://www.R-project.org/ (2013).
52. Schlitzer, R. Ocean Data View. Alfred Wegener Institute, Bremerhaven, Germany. URL http://www.odv.awi.de/ (2016).
53. Pujo-Pay, M. *et al*. Integrated survey of elemental stoichiometry (C, N, P) from the western to eastern Mediterranean Sea. *Biogeosciences* **8**, 883–899 (2011).
54. Santinelli, C. DOC in the Mediterranean Sea in *Biogeochemistry of marine dissolved organic matter* (eds Hansell, D. A. & Carlson, C. A.) 579–608 (Academic Press, 2015).
55. Meador, T. B. *et al*. Biogeochemical relationships between ultrafiltered dissolved organic matter and picoplankton activity in the Eastern Mediterranean Sea. *Deep sea Res. II* **57**, 1460–1477 (2010).
56. Santinelli, C., Nannicini, L. & Seritti, A. DOC dynamics in the meso and bathypelagic layers of the Mediterranean Sea. *Deep-Sea Research Part II: Topical Studies in Oceanography* **57**, 1446–1459 (2010).
57. Dainard, P. G. & Guéguen, C. Distribution of PARAFAC modeled CDOM components in the North Pacific Ocean, Bering, Chukchi and Beaufort Seas. *Mar. Chem.* **157**, 216–223 (2013).
58. Yamashita, Y., Jaffé, R., Maie, N. & Tanoue, E. Assessing the dynamics of dissolved organic matter (DOM) in coastal environments by excitation emission matrix fluorescence and parallel factor analysis (EEM-PARAFAC). *Limnol. Oceanogr.* **53**, 1900–1908 (2008).
59. Catalá, T. S. *et al*. Drivers of fluorescent dissolved organic matter in the global epipelagic ocean. *Limnol. Oceanogr.* **61**, 1101–1119 (2016).
60. Biddanda, B. & Benner, R. Carbon, nitrogen, and carbohydrate fluxes during the production of particulate and dissolved organic matter by marine phytoplankton. *Limnol. Oceanogr.* **42**, 506–518 (1997).
61. Nagata, T. Organic matter-bacteria interactions in seawaters in *Microbial ecology of the oceans* (ed. Kirchman, D. L.) 207–241 (Wiley, 2008).
62. Stedmon, C. A. & Cory R. M. Biological origins and ffate of fluorescent dissolved organic matter in aquatic environments in *Aquatic Organic Matter Fluorescence* (eds Coble, P. G., Lead, J., Baker, A., Reynolds, P. M. & Spencer, R. G. M.) 278–299 (Cambridge University Press, 2014).
63. Lønborg, C., Álvarez-Salgado, X. A., Davidson, K., Martínez-García, S. & Teira, E. Assessing the microbial bioavailability and degradation rate constants of dissolved organic matter by fluorescence spectroscopy in the coastal upwelling system of the Ría de Vigo. *Mar. Chem.* **119**, 121–129 (2010).
64. McKnight, D. M. *et al*. Spectrofluorometric characterization of dissolved organic matter for indication of precursor organic material and aromaticity. *Limnol. Oceanogr.* **46**, 38–48 (2001).
65. Chen, H. *et al*. Ultrahigh resolution mass spectrometric differentiation of dissolved organic matter isolated by coupled reverse osmosis-electrodialysis from various major oceanic water masses. *Mar. Chem.* **164**, 48–59 (2014).
66. Medeiros, P. M. *et al*. Dissolved organic matter composition and photochemical transformations in the northern North Pacific Ocean. *Geophys. Res. Lett.* **42**, 863–870 (2015).
67. Hertkorn, N. *et al*. Characterization of a major refractory component of marine dissolved organic matter. *Geochim. Cosmochim. Acta* **70**, 2990–3010 (2006).
68. Hawkes, J. A., Hansen, C. T., Goldhammer, T., Bach, W. & Dittmar, T. Molecular alteration of marine dissolved organic matter under experimental hydrothermal conditions. *Geochim. Cosmochim. Acta* **175**, 68–85 (2016).
69. Kujawinski, E. B. Electrospray ionization Fourier transform ion cyclotron resonance mass spectrometry (ESI FT-ICR MS): Characterization of complex environmental mixtures. *Environ. Forensics* **3**, 207–216 (2002).
70. Sharpless, C. M. & Blough, N. V. The importance of charge-transfer interactions in determining chromophoric dissolved organic matter (CDOM) optical and photochemical properties. *Environ. Sci. Process. Impacts* **16**, 654–671 (2014).
71. Bianchi, T. S. *et al*. Deepwater Horizon oil in Gulf of Mexico waters after 2 years: transformation into the dissolved organic matter pool. *Environ. Sci. Technol.* **48**, 9288–97 (2014).
72. Kieber, R. J., Hydro, L. H. & Seaton, P. J. Photooxidation of triglycerides and fatty acids in seawater: Implication toward the formation of marine humic substances. *Limnol. Oceanogr.* **42**, 1454–1462 (1997).

Acknowledgements

The data used for this study are available from the authors on request. The authors are grateful to the Captain, crew, technicians and scientists aboard the R/V Sarmiento de Gamboa, led by chief scientist J. Arístegui, for their support during the cruise. We specially thank to M.J. Pazó, V. Vieitez, M. Friebe and I. Ulber for DOC measurements, K. Klaproth for support with the FT-ICR-MS analysis, M. Manecki and B.E. Noriega for their help with data processing, I. Fuentes for helping with R and J. Niggemann for valuable discussion. This work

was funded by the project HOTMIX (grant number CTM2011-30010-C02-MAR) and the project FERMIO (MINECO, CTM2014-57334-JIN), both co-financed with FEDER funds. A.M.M.-P. was funded by a predoctoral fellowship (reference BES-2012-056175) and a short stay fellowship (reference EEBB-I-14-08926) from the Spanish Ministry of Economy and Competitiveness. M.N.-C. was supported by the CSIC Program "Junta para la Ampliación de Estudios" co-financed by the ESF (reference JAE DOC 040) and the project FERMIO (MINECO, CTM2014-57334-JIN). T.S.C. was supported by a postdoctoral contract jointly financed by the project CGL2014-52362R of the Spanish Ministry of Economy and Competitiveness and FEDER funds and the University of Granada, and by a predoctoral fellowship (reference AP2009-2138) from the Ministerio de Educación, Cultura y Deporte.

Author Contributions

A.M.M.-P., M.N.-C. and X.A.A.-S. designed research. A.M.M.-P., M.N.-C., T.S.C. participated in the field work. A.M.M.-P., H.O., and T.D. participated in the mass spectrometry analyses, processing and interpretation. T.S.C. executed PARAFAC modelling. A.M.M.-P., M.N.-C., H.O., T.S.C., I.R., T.D. and X.A.A.-S. contributed to the discussion of the results presented in the manuscript. A.M.M.-P. wrote the first draft manuscript, which was complemented by significant contributions of all co-authors.

Additional Information

Supplementary information accompanies this paper at doi:10.1038/s41598-017-03735-4

Competing Interests: The authors declare that they have no competing interests.

Publisher's note: Springer Nature remains neutral with regard to jurisdictional claims in published maps and institutional affiliations.

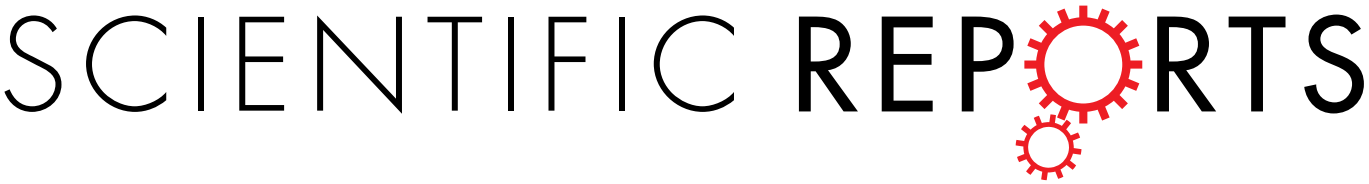

OPEN

Deep-ocean dissolved organic matter reactivity along the Mediterranean Sea: does size matter?

Received: 3 April 2017
Accepted: 6 June 2017
Published online: 18 July 2017

Alba María Martínez-Pérez[1], Xosé Antón Álvarez-Salgado[1], Javier Arístegui[2] & Mar Nieto-Cid[1]

Despite of the major role ascribed to marine dissolved organic matter (DOM) in the global carbon cycle, the reactivity of this pool in the dark ocean is still poorly understood. Present hypotheses, posed within the size-reactivity continuum (SRC) and the microbial carbon pump (MCP) conceptual frameworks, need further empirical support. Here, we provide field evidence of the soundness of the SRC model. We sampled the high salinity core-of-flow of the Levantine Intermediate Water along its westward route through the entire Mediterranean Sea. At selected sites, DOM was size-fractionated in apparent high (aHMW) and low (aLMW) molecular weight fractions using an efficient ultrafiltration cell. A percentage decline of the aHMW DOM from 68–76% to 40–55% was observed from the Levantine Sea to the Strait of Gibraltar in parallel with increasing apparent oxygen utilization (AOU). DOM mineralization accounted for 30 ± 3% of the AOU, being the aHMW fraction solely responsible for this consumption, verifying the SRC model in the field. We also demonstrate that, in parallel to this aHMW DOM consumption, fluorescent humic-like substances accumulate in both fractions and protein-like substances decline in the aLMW fraction, thus indicating that not only size matters and providing field support to the MCP model.

Most of the 662 Pg C of dissolved organic matter (DOM) accumulated in the oceans is resistant to microbial degradation and, therefore, stored for hundreds to thousands of years[1,2]. The mechanisms behind this long-term storage of carbon are still poorly understood[3]. The microbial carbon pump (MCP) concept has emerged in recent years as one of the most plausible mechanisms to explain this storage. Within the MCP framework, refractory DOM is originated as a by-product of the microbial mineralization of bioavailable organic matter[4,5].

Closely related with the MCP concept is the size-reactivity continuum (SRC) hypothesis to explain marine DOM reactivity[6]. According to this assumption, initially based on microbial degradation experiments[7,8], changes in the bioavailability of DOM would be explained by varying proportions of more labile high molecular weight (HMW) DOM compared with slower degrading low molecular weight (LMW) DOM. Earlier works showing patterns, compositions and concentrations of major DOM biochemical compounds (carbohydrates and amino acids) in the ocean provided independent validation of the relative reactivity of different size classes of organic matter[9–11]. Posterior field studies supported the SRC hypothesis as they found higher $\Delta^{14}C$ values in the HMW DOC fraction compared to the LMW DOC fraction[12,13]. Lastly, it has been recently reported a significant dissolved organic matter size-age-composition relationship that is also consistent with the SRC model[14–16]. These studies suggest microbial degradation as the primary source of recalcitrant DOM to the deep ocean, in agreement with the MCP conceptual model. Nevertheless, other works based on bacterial degradation experiments have found discrepancies with the SRC model[17,18], as they observed that LMW DOM is biologically more reactive than HMW DOM.

Focusing only on the colored fraction of DOM (CDOM) a different picture may arise, facing the SRC hypothesis. It is well established that fluorescence spectroscopy measurements at specific wavelength pairs are due to

[1]Consejo Superior de Investigaciones Científicas - Instituto de Investigacións Mariñas (CSIC-IIM), Vigo, Spain. [2]Instituto de Oceanografía y Cambio Global (IOCAG), Universidad de Las Palmas de Gran Canaria, 35017, Las Palmas de Gran, Canaria, Spain. Correspondence and requests for materials should be addressed to A.M.M.-P. (email: albam@iim.csic.es)

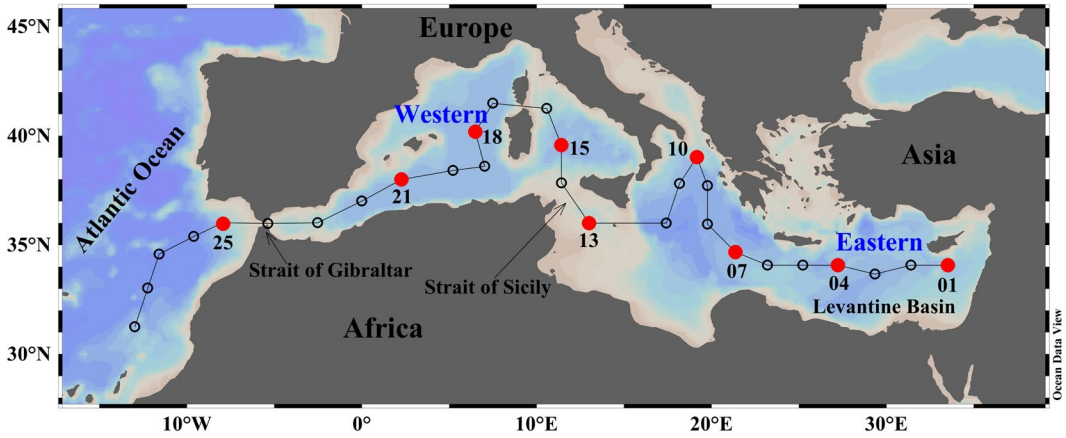

Figure 1. Map of the study area and sampling stations during the HOTMIX cruise. Open circles indicate all stations sampled during the cruise and solid red circles represent the stations where samples for DOM size-fractionation were taken. Figure created using Ocean Data View (Schlitzer, R., Ocean Data View, odv.awi.de, 2017).

refractory humic-like substances and to bioavailable protein-like compounds[19,20]. Microbial cultures have demonstrated consumption of the protein-like and production of the humic-like DOM in a daily to yearly basis[21–23]. The generation of humic-like substances implies the formation of structurally complex molecules that, apparently, challenges the SRC postulates.

Here, we assess the validity of the SRC model *in situ*, by following the course of two size fractions of DOM along the shallow overturning circulation cell of the Mediterranean Sea[24,25]. We chose this region because its high temperatures boost biogeochemical rates, resulting in shorter spatial and time scales, acting as a natural laboratory to explore processes happening at a global extent. The shallow branch of the Mediterranean overturning circulation drives the Levantine intermediate water (LIW), which is formed by convection in the northern part of the Levantine basin. LIW is found along the whole Mediterranean Sea between 200 m depth in the eastern and 500 m depth in the western basin, displaying the maximum salinity of all Mediterranean water masses[26]. According to the SRC hypothesis, the LIW in the Levantine basin (close to its formation site) should transport a higher concentration of DOM with a higher average molecular weight. This DOM would be progressively consumed within the overturning cell in such a way that the LIW leaving the Strait of Gibraltar would transport less DOM with a lower average molecular weight. Regarding the optical properties of DOM, at the formation site we would expect enrichment in bioavailable protein-like substances and depletion in refractory humic-like compounds. Conversely, as the LIW displaces westwards, the proportions of protein- and humic-like substances should reverse.

Results and Discussion

Nine stations were occupied along the Mediterranean Sea (Fig. 1)[27] for DOM sampling at different depths covering the whole water column. The deep chlorophyll maximum (DCM), Levantine Intermediate Water (LIW) and the Eastern (EMDW) and Western Mediterranean Deep Water (WMDW) levels were sampled (for more details see Methods; Fig. S1). These DOM samples were size-fractionated using a 1 kDa cut-off membrane (Millipore, PLAC 150 mm), and the dissolved organic carbon (DOC) and fluorescence intensity (FDOM) of all fractions were determined (see Methods). On a carbon basis, the mass balance for the size-fractionation process presented an error lower than 10% for all the samples. The high recovery of our low-volume ultrafiltration cell (50–80%) was mainly due to the low concentration factor (CF) of just 4 used in this study. This cell allowed us to separate the size fractions in less than 5 hours in such a way that several samples can be processed within the same day (see Methods). On the contrary, standard ultrafiltration methodologies for large sample volumes, isolate about 30–55% of the marine DOM[28,29], applying CFs ranging from about 12 to about 500, depending on the purpose of the ultrafiltration (%HMW quantification[28,30] *versus* isolation[13]). Ultrafiltration using higher CFs is more time consuming, which is not compatible with our oceanographic approach. Given that our separation method is not comparable with the classical approaches in using ultrafiltration methods, we refer hereinafter to the fraction <1 kDa as apparent LMW DOM (aLMW DOM) and the fraction >1 kDa as apparent HMW DOM (aHMW DOM). Furthermore, due to the ultrafiltration system and the CF used in this study, our aHMW fraction may include up to 25% of low molecular weight molecules (see Methods).

Testing the size-reactivity continuum hypothesis. DOC and the carbon-specific fluorescence of humic-like (peak C*) and protein-like (peak T*) substances for the different sampling depths are represented against the apparent oxygen utilisation (AOU; see Methods) in Fig. S2. DCM or deep water samples showed narrow AOU variations through the cruise track (mean $\pm$ SD; 4.5 ± 3.1 and 64.4 ± 5.2 µmol kg^{-1}, respectively; blue rectangle boxes in Fig. S2). Recently ventilated DCM waters presented very low AOU values, whereas aged deep waters exhibited significantly higher values. Instead, samples collected at the intermediate salinity maximum layer displayed a wide AOU range (mean $\pm$ SD; 50.2 ± 30.3 µmol kg^{-1}; red rectangle boxes in Fig. S2) revealing an

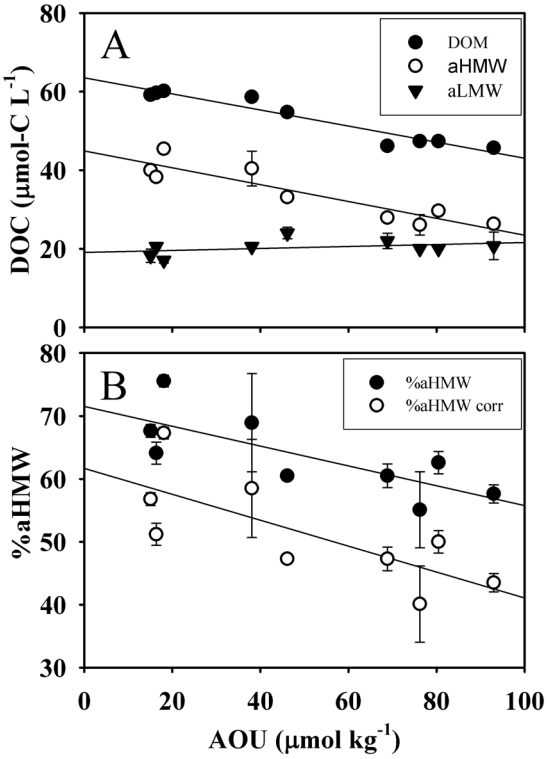

Figure 2. DOM size-fractionation with apparent oxygen utilization on a carbon basis. (**A**) size-fractionated DOC where DOM (solid black circles), aHMW (open circles) and aLMW (solid black triangles) represent the bulk DOC, the apparent high molecular weight fraction and the apparent low molecular weight fraction, respectively. (**B**) aHMW percentage (solid black circles) and corrected aHMW percentage (open circles) with respect to apparent oxygen utilization (AOU) of samples collected along the core-of-flow of the Levantine Intermediate Water. Error bars represent standard errors.

increasing trend from the Levantine basin (water mass formation area) to the Strait of Gibraltar (Figs S1 and S2). For the sake of the interest of our study, we focused on samples with the highest proportion of LIW, which is the single water mass crossing the entire Mediterranean Sea. This allowed us to observe changes in DOM size-fractionation, as this intermediate water was ageing along their westward route from the Levantine basin to the Atlantic Ocean[25].

The DOM size-fractionation at the LIW level is illustrated in more detail in Figs 2 and 3. A significant decrease of DOC with increasing AOU was detected for the bulk DOM and the aHMW fraction (Fig. 2A), revealing that larger organic compounds are preferably consumed during mineralization processes. However, the aLMW DOC concentration showed a slight increase with AOU, although it was not significant. Note that although up to 25% of the aHMW fraction corresponds with low molecular weight molecules, the changes observed cannot be due to this smaller DOM since, as observed in Fig. 2A, the LMW fraction did not undergo any decay with AOU. Thus, we can infer that larger molecules are more bioreactive. Taking into account the slopes of the linear regressions (Fig. 2A, Table 1) and converting them into carbon equivalents using the canonical Redfield -O_2/C ratio of 1.4[31] we obtained that 30 ± 3% of the oxygen utilization at the LIW was due to the DOM decomposition. This result is in agreement with the value reported for the intermediate and deep waters of the Eastern Mediterranean Sea (27 ± 18%)[32], but slightly lower than the 38% reported for the LIW[33]. Our values are higher than those found in the global ocean (10–20%)[34] and highlight the relevance of the DOC pool for oxygen consumption in the mesopelagic layers of the Mediterranean Sea. In addition, the partition of DOC into aHMW and aLMW allowed to establish, for the first time, the contribution of each apparent fraction to the overall mineralization. As observed in Fig. 2A, the aLMW DOC did not contribute to the oxygen consumption, while the aHMW DOC accounted for as much as the bulk DOC (32 ± 6%). Therefore, all the DOC mineralization was due exclusively to the aHMW DOC, a fact that validates the SRC hypothesis[6] using the shallow overturning cell of the Mediterranean Sea as an *in situ* incubator. Note that this result is valid for the bulk DOC but does not necessarily apply to the myriads of individual compounds that constitute this pool. Furthermore, considering the intercepts of the three regression equations (being all significant, $p < 0.001$; Table 1), we can estimate the DOC concentration at the time of water mass formation (when AOU should be null). It results in 63 ± 1 µmol-C L^{-1}, of which 45 ± 2 µmol-C L^{-1} corresponds to aHMW DOC and 19 ± 1 µmol-C L^{-1} to aLMW DOC. If we discount a 25% due to molecules smaller than 1 kDa that are present in the aHMW fraction, the corrected partition turns to be 39 µmol-C L^{-1} of aHMW DOC and 25 µmol-C L^{-1} of aLMW DOC. The DOC concentration at the formation time for the bulk DOC is comparable with the previously reported value for the LIW (67 ± 1 µmol-C L^{-1})[33]. The evolution of the percentage of aHMW DOM (%aHMW, on a carbon basis) with the AOU along the LIW transit from its

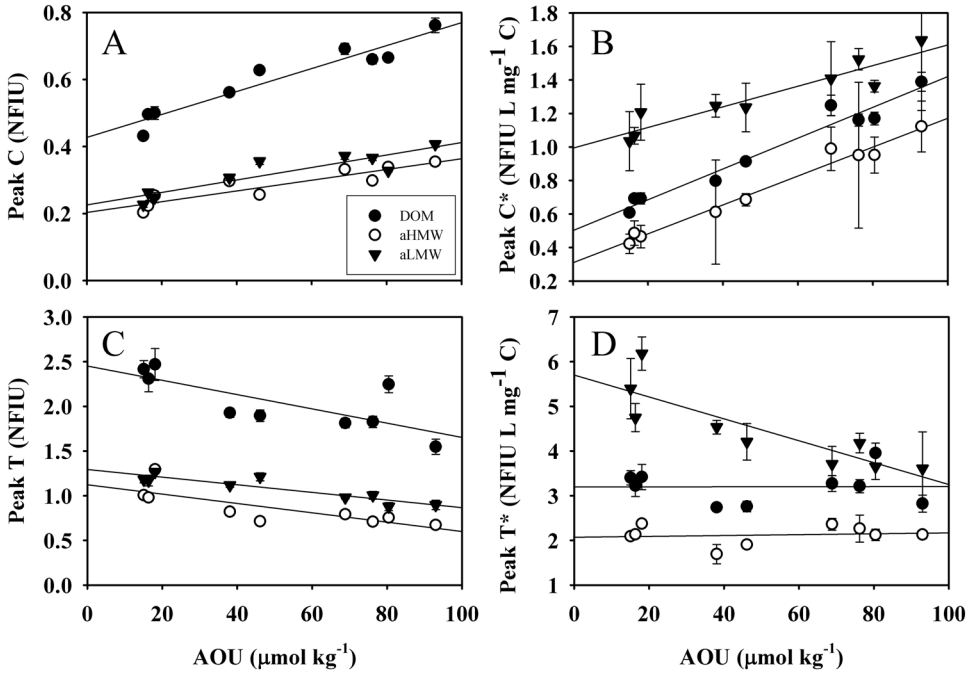

Figure 3. DOM size-fractionation with apparent oxygen utilization on a fluorescence basis. DOM (solid black circles), aHMW (open circles) and aLMW (solid black triangles) represent the bulk DOM, the apparent high molecular weight fraction and the apparent low molecular weight fractions, respectively, of samples collected along the core-of-flow of the Levantine Intermediate Water. (**A**) Humic-like fluorescence (peak C), (**B**) humic-like fluorescence per carbon unit (peak C*), (**C**) protein-like fluorescence (peak T) and (**D**) protein-like fluorescence per carbon unit (peak T*) with respect to apparent oxygen utilization (AOU). Error bars represent standard errors.

Fraction	y-variable	m ± SE	b ± SE	R^2
DOM	DOC	$-21 \pm 2 \times 10^{-2}$***	63 ± 1***	0.93
aHMW	DOC	$-23 \pm 4 \times 10^{-2}$***	45 ± 2***	0.84
aLMW	DOC	$7 \pm 5 \times 10^{-2}$NS	19 ± 1***	0.15
DOM	Peak C	$35 \pm 4 \times 10^{-4}$***	0.43 ± 0.02***	0.92
aHMW	Peak C	$18 \pm 3 \times 10^{-4}$***	0.20 ± 0.02***	0.83
aLMW	Peak C	$21 \pm 3 \times 10^{-4}$***	0.23 ± 0.02***	0.84
DOM	Peak C*	$9 \pm 1 \times 10^{-3}$***	0.50 ± 0.04***	0.96
aHMW	Peak C *	$87 \pm 5 \times 10^{-4}$***	0.31 ± 0.03***	0.97
aLMW	Peak C*	$6 \pm 1 \times 10^{-3}$***	1.00 ± 0.05***	0.87
DOM	Peak T	$-10 \pm 4 \times 10^{-3}$*	2.4 ± 0.1***	0.58
aHMW	Peak T	$-6 \pm 1 \times 10^{-3}$*	1.1 ± 0.1***	0.63
aLMW	Peak T	$-4 \pm 1 \times 10^{-3}$***	1.29 ± 0.04***	0.83
DOM	Peak T*	0.01 ± 0.6^{NS}	3.2 ± 0.3***	0.00
aHMW	Peak T *	$7 \pm 20 \times 10^{-3}$ NS	2.1 ± 0.1***	0.02
aLMW	Peak T*	$-28 \pm 7 \times 10^{-3}$**	5.7 ± 0.3***	0.73

Table 1. Linear regressions (model II) between DOC and FDOM indices (y-variable) and apparent oxygen utilization (x-variable) obtained from bulk DOM and apparent HMW (aHMW) and LMW (aLMW) fractions from samples collected at the salinity maximum (LIW). n = 9, m = slope, b = intercept, SE = Standard error and NS = Non significant. *, **, *** correspond with $p < 0.05$, $p < 0.01$ and $p < 0.001$, respectively. DOM <0.7 µm, aHMW <0.7 µm and >1 kDa and aLMW <1 kDa.

formation site (Fig. 2B) shows a significant inverse relationship ($r^2 = 0.58$, $p < 0.05$). This relationship is independent of considering (black circles in Fig. 2B) or not (white circles in Fig. 2B) the 25% of LMW molecules contained in the aHMW DOM fraction. The slopes of both linear regressions are not significantly different. This observation supports the view that aHMW molecules are preferentially consumed in the intermediate waters of the Mediterranean Sea simultaneously to water mass ageing, and therefore large DOM would be more bioreactive than the smaller counterpart. It also corroborates that, although our size fractionation system does not allow

obtaining a 100% pure aHMW DOM fraction, our conclusions are not influenced by this fact. Moreover, our findings are in agreement with the size-age-composition relationships of DOM reported in recent studies[14–16].

Taking into account that the renewal time of the LIW in the entire Mediterranean Sea is about 13 years[35] and that DOC decreases by 18 µmol-C L^{-1} from the formation area of the LIW (DOC = 63 µmol L^{-1}) to the Strait of Gibraltar (DOC = 45 µmol L^{-1}), a DOC removal rate of 1.38 µmol-C L^{-1} yr^{-1} is obtained. This rate is lower than the previously reported rate of 2.2 µmol-C kg^{-1} yr^{-1} [36, 37] because the latter was an estimate for the eastern Mediterranean Sea including the Tyrrhenian Sea, whereas our DOC removal rate includes the whole Mediterranean Sea. The calculated DOC removal rate and its corresponding lifetime indicate that the aHMW DOC consumed along the core-of-flow of the LIW is a mixture of semi-labile (lifetime, 1.5 years) and semi-refractory (lifetime, 20 years) DOC according to Hansell's classification[38].

It could be argued that the DOC-AOU relationship (Fig. 2A) is distorted by the sinking flux of biogenic particulate organic carbon (POC). However, in the ultra-oligotrophic eastern basin, where the core-of-flow of the LIW is shallower (200–300 m), the vertical flux of POC is minor compared with the injection of DOC in the water mass formation area of the LIW[39, 40]. In the western basin, although the vertical flux of POC is dominant, the amount reaching the core-of-flow of the LIW at 350–400 m presents high turnover rates. As POC consists mainly on the labile products of synthesis and early degradation of plankton[41], the POC reaching the intermediate waters will be degraded in time scales of hours to weeks[42]. Therefore, the observed DOC-AOU relationship along the core-of-flow of the LIW would be essentially driven by the consumption of semi-refractory HMW DOC than of labile sinking POC.

Testing the microbial carbon pump hypothesis. There is little information on the size distribution of coloured DOM (CDOM) in ocean waters[43–45]. Here we observed that the aLMW fraction hosts more humic- and protein-like fluorescence intensity per carbon unit than the aHMW DOM fraction (Fig. 3B,D). Particularly, for the protein-like fluorescence (peak T) the contribution is higher in the less aged waters (low AOU), while for the humic-like fluorescence (peak C) the two DOM fractions presented a significant increase with AOU (Fig. 3A,B). This is indicative of the production of humic-like fluorescence per unit of carbon in parallel to the general trend of DOC and aHMW DOC consumption. All together, these observations support the MCP hypothesis, which postulates that refractory DOM is produced during the mineralization of bioavailable organic matter, either dissolved or in suspended and sinking particles[5]. Specifically, the generation rate of humic-like substances was 30% higher in the HMW DOC than in the LMW DOC (Table 1; Fig. 3B) due to DOC dynamics: aHMW DOC was consumed while LMW DOC remained constant. On the other hand, peak T exhibited a significant decrease in both DOM fractions with AOU (Fig. 3C), indicative of the utilization of this type of compounds during mineralization processes. This finding suggests that small organic compounds related to protein-like molecules were also degraded when intermediate waters aged. Changes of peak T in the LMW fraction were not reflected in the bulk DOC due to the lower sensitivity of the DOC analytical technique compared with fluorescence spectroscopy. Therefore, the LMW fraction also contains some bioreactive molecules although the bulk fraction is essentially refractory. For the aHMW DOC and the bulk DOC we observed that the rate of protein-like substances consumption was equal to the rate of DOC consumption (as the horizontal lines in Fig. 3D suggest). These results indicate that the overall behaviour of the bulk DOC pool does not necessarily match the specific response of particular compounds or compound groups as the fluorophores studied here, and reconcile the two hypothesis studied in this work, the SCR and the MCP.

It can be argued that the longitudinal changes observed in the DOC and FDOM of the different size fractions could partially be due to mixing of LIW with other water masses instead of ageing. However, water mass mixing would reinforce our hypothesis since LIW in the western basin is the oldest water mass of the whole Mediterranean Sea. Then, if LIW is mixing with the surrounding water masses, which are younger than LIW, the longitudinal changes in DOC and its partition in aLMW and aHMW compounds should be more evident than those really observed.

In summary, we provide *in situ* support for the SRC hypothesis, out of the artefacts of microbial incubation experiments. Our results are neither distorted by alterations in the structural continuum of DOM during size-fractionation previous to *in vitro* experiments nor by subsequent "bottle effects" during incubations. Fractionation by ultrafiltration before *in vitro* degradation experiments breaks down the DOM structural continuum and, therefore, could not be the most appropriate approach for studying the DOM size-reactivity. Although our study is based on a relatively small and shallow overturning cell, we believe that our results can be extrapolated to the global ocean. To confirm this, it would be necessary to perform similar studies in the main water mass formation areas of the world ocean.

Methods

Study area and sampling. The main water masses observed in the Mediterranean Sea are the Atlantic water (AW) in the epipelagic layer, the LIW in the mesopelagic layer and the Eastern (EMDW) and Western (WMDW) Mediterranean Deep waters in the bathypelagic layer. The Atlantic inflow enters the Strait of Gibraltar as a surface current of salinity about 36.5, being slightly modified through mixing with the outflowing Mediterranean waters. This Modified Atlantic Water (MAW) moves towards the East as part of an overturning cell that involves the whole Mediterranean Sea and leads to the formation of intermediate waters in the eastern basin[24, 25, 46].

Water samples were collected at nine stations (solid red circles in Fig. 1) during the trans-Mediterranean cruise HOTMIX aboard the R/V Sarmiento de Gamboa in the spring of 2014 (Heraklion, Crete, 27th April – Las Palmas, Canary Islands, 29th May). At each station, full-depth continuous conductivity-temperature-depth (SBE 911 plus CTD probe), dissolved oxygen (SBE-43 oxygen sensor) and chlorophyll fluorescence (SeaPoint fluorometer) profiles were recorded. These probes were attached to a rosette sampler (SBE 38) equipped with 24 Niskin bottles of 12 litres. The temperature and pressure sensors were calibrated at the Sea Bird laboratory before the

cruise. Water samples were collected to analyse salinity (S), dissolved oxygen (DO) and chlorophyll *a* (Chl *a*), data used to calibrate the sensors for conductivity, DO and fluorescence, respectively. Conductivity measurements were converted into practical salinity scale values[47]. Samples for salinity were collected and stored in 250 mL type II glass and measured with a Guildline Portasal salinometer Model 8410A. Chl *a* concentration was determined in seawater samples (500 mL) filtered through Whatman GF/F filters and stored frozen until analysis. Pigments were extracted in cold acetone (90% v/v) for 24 h and analysed by means of a 10 AU Turner Designs bench fluorometer, previously calibrated with pure Chl *a* (Sigma Aldrich)[48]. Dissolved oxygen samples were taken in pyrex "iodine titration" flasks with flared necks and ground glass stoppers, with a nominal volume of about 115 mL. Dissolved oxygen was determined following the modified Winkler potentiometric method[49]. The apparent oxygen utilization, ($AOU = O_2sat - O_2$) was calculated using a algorithm for the oxygen saturation[50], O_2sat. Four to five depths were sampled depending on the bathymetry of the stations, except for the station at the Strait of Sicily (stn 13) where only LIW was sampled due to its shallowness. Deep chlorophyll maximum (DCM) samples were distinguish according to the maximum fluorescence intensity, the LIW was sampled at the absolute maximum of the salinity profile of each station, the oxygen minimum layer (OML) was established on basis of the absolute minimum of the dissolved oxygen profile, and the deep waters were sampled according to the salinity and temperature characteristic of the bathypelagic zone of the eastern and western Mediterranean basins (Fig. S1).

DOM size-fractionation. DOM water samples were collected in 5-litres acid-cleaned polycarbonate carboys and stored in the dark at 13 °C until filtration within 5 hours. Filtration was performed through precombusted (450 °C, 4 h) Whatman GF/F filters in an acid-clean all-glass filtration system under positive pressure with low flow of high purity N_2. Two-litre aliquots of the filtrate were collected in acid-cleaned PTFE bottles for DOM size-fractionation using an ultrafiltration cell (Millipore, 2000) equipped with a cut-off membrane of 1000 Da (Millipore, PLAC 150 mm). A pressure of 55 psi, using high purity N_2, was maintained during the fractionation splitting the DOM into an apparent high molecular weight (aHMW, >1000 Da; 0.5 L) and an apparent low molecular weight (aLMW, <1000 Da; 1.5 L) fractions. The ultrafiltration cell was cleaned between samples by passing 0.3 L of NaOH through the membrane filter, followed by three rinses with 1 L of MQ water. The efficiency of the ultrafiltration cell (>90%) was checked using a solution of vitamin B12 (1355 Da; Sigma, 50 mg L^{-1}). For large-volume ultrafiltration systems, previous works[29,51] reported lower efficiency rates (about 80%) using the same solution of vitamin B12. This fact was due to the general decrease of the retention rate with increasing concentration factors (CF). In our case, the CF (sample volume/retentate volume) was 4. We used a low CF for two main reasons: i) the ultrafiltration time increased with higher CF, so we keep it low in order to processes a significant number of samples, and ii) to ensure a pure aLMW fraction, which is much less studied compared to the aHMW fraction. Note that due to this CF and the ultrafiltration cell system used in this study, up to 25% of the aHMW fraction may correspond with low molecular weight molecules. In this system the sample is not recirculated, but it is being forced to a continuous and vigorous stirring inside the ultrafiltration cell. Then, the bulk DOM and aLMW fraction are pure treatments, but the aHMW fraction presents all the high molecular weight molecules (100%) plus a portion of the low molecular weight molecules (up to 25% of the aHMW fraction) due to the retention of aLMW-DOM during ultrafiltration. Taking into account that the %aHMW ranged between 76 to 55% and that in our ultrafiltration system the retentate was 0.5 L and the permeate 1.5 L, applying a simple system of 2 linear equations with 2 unknowns, the lower molecular weight molecules in the aHMW fraction varied between 8 and 15%, respectively.

Dissolved organic carbon (DOC) and fluorescence spectroscopy (FDOM). Approximately 100 mL of the DOM filtrate, and the HMW and LMW fractions were collected for DOC and FDOM analyses. Aliquots of 10 mL were collected in precombusted (450 °C, 12 h) glass ampoules for DOC determination. These samples were acidified with H_3PO_4 (85%, p.a., Merck) to pH < 2 and the ampoules were heat-sealed and stored in the dark at 4 °C until analysis in the base laboratory. DOC concentrations were measured using a Shimadzu TOC-V organic carbon analyser following a high temperature catalytic oxidation (HTCO) method. The system was calibrated daily with potassium hydrogen phthalate (99.95–100.05%, p.a., Merck). The precision of the equipment was ± 1 μmol L^{-1}. The accuracy was successfully tested daily with the DOC reference materials provided by D. A. Hansell (University of Miami, USA). FDOM was determined on board with a Perkin Elmer LS55 luminescence spectrometer. Slit widths were 10.0 nm for both excitation and emission wavelengths. Measurements were performed at constant room temperature (25 °C) in a 1 cm quartz fluorescence cell and Milli-Q water was used as a reference blank. The spectrofluorometer was tested daily: the intensity of the Raman peak was evaluated using a sealed Milli-Q water cell (Perkin Elmer) while p-terphenyl and tetraphenylbutadiene methacrylate blocks (Starna) were employed to check the instrument signal intensity at the excitation-emission wavelengths characteristic of the aromatic amino acids and humic-like substances, respectively. Measurements were performed at the classical fluorescence peaks[18], selecting Ex/Em wavelengths of 340/440 nm (peak C), due to humic substances of terrestrial origin, and 280/350 nm (peak T), due to protein-like substances. The fluorescence of each peak was determined by subtracting the Milli-Q blank peak height from the sample average peak height. All the samples were normalized using a solution of quinine sulphate dihydrate (≥99.0%, purum for fluorescence, Fluka) and tryptophan (≥99.0%, Fluka) standards in H_2SO_4 0.05 M (95–97%, p.a., Merck) allowing to express fluorescence in normalized fluorescence intensity units (NFIU[52]).

References

1. Hansell, D. A., Carlson, C. A., Repeta, D. J. & Schlitzer, R. Dissolved organic matter in the ocean a controversy stimulates new insights. *Oceanography* **22**, 202–211 (2009).
2. Hansell, D. A. Recalcitrant dissolved organic carbon fractions. *Ann. Rev. Mar. Sci* **5**, 421–445 (2013).
3. Dittmar, T. *In Biogeochemistry of Marine Dissolved Organic* Matter (eds Hansell, D. A. & Carlson, C. A.) 369–388 (Academic Press, 2015).

4. Ogawa, H., Amagai, Y., Koike, I., Kaiser, K. & Benner, R. Production of refractory dissolved organic matter by bacteria. *Science* **22**, 917–920 (2001).
5. Jiao, N. *et al*. Microbial production of recalcitrant dissolved organic matter: long-term carbon storage in the global ocean. *Nature reviews. Microbiology* **8**, 593–9 (2010).
6. Benner, R. & Amon, R. M. W. The size-reactivity continuum of major bioelements in the ocean. *Ann. Rev. Mar. Sci* **7**, 185–205 (2015).
7. Amon, R. M. W. & Benner, R. Rapid cycling of high-molecular-weight dissolved organic matter in the ocean. *Nature* **369**, 549–552 (1994).
8. Amon, R. M. W. & Benner, R. Bacterial utilization of different size classes of dissolved organic matter. *Limnol. Oceanogr.* **41**, 41–51 (1996).
9. Benner, R., Pakulski, J. D., McCarthy, M., Hedges, J. I. & Hatcher, P. G. Bulk chemical characteristics of dissolved organic matter in the ocean. *Science* **255**, 1561–1564 (1992).
10. McCarthy, P. & Hedges, T. J. & Benner, R. Chemical composition of dissolved organic nitrogen in the ocean. *Nature* **390**, 150–154 (1997).
11. Aluwihare, L., Repeta, D. J. & Chen, R. F. A major biopolymeric component to dissolved organic carbon in surface sea water. *Nature* **387**, 166–169 (1997).
12. Loh, A. N., Bauer, J. E. & Druffel, E. R. M. Variable ageing and storage of dissolved organic components in the open ocean. *Nature* **430**, 877–881 (2004).
13. Guo, L. D., Santschi, P. H., Cifuentes, L. A., Trumbore, S. E. & Southon, J. Cycling of high-molecular-weight dissolved organic matter in the Middle Atlantic Bight as revealed by carbon isotopic (C-13 and C-14) signatures. *Limnol. Oceanog* **41**(6), 1242–1252 (1996).
14. Walker, B. D., Beaupré, S. R., Guilderson, T. P., Druffel, E. R. M. & McCarthy, M. D. Large-volume ultrafiltration for the study of radiocarbon signatures and size vs. age relationships in marine dissolved organic matter. *Geochim. Cosmochim. Acta* **75**, 5187–5202 (2011).
15. Walker, B. D. *et al*. Linked changes in marine dissolved organic carbon molecular size and radiocarbon age. *Geophys. Res. Lett.* **43**, 10385–10393 (2016).
16. Walker, B. D., Beaupré, S. R., Guilderson, T. P., McCarthy, M. D. & Druffel, E. R. M. Pacific carbon cycling constrained by organic matter size, age and composition relationships. *Nat. Geosci.* **9**, 888–891 (2016).
17. Covert, J. S. & Moran, M. A. Molecular characterization of estuarine bacterial communities that use high- and low-molecular weight fractions of dissolved organic carbon. *Aquat. Microb. Ecol.* **25**, 127–139 (2001).
18. Khodse, V. B. & Bhosle, N. B. Bacterial utilization of size-fractionated dissolved organic matter. *Aquat. Microb. Ecol.* **64**, 299–309 (2011).
19. Coble, P. G. Characterization of marine and terrestrial DOM in seawater using excitation-emission matrix spectroscopy. *Mar. Chem.* **51**, 325–346 (1996).
20. Stedmon, C. A. & Nelson, N. B. In *Biogeochemistry of Marine Dissolved Organic* Matter (eds Hansell, D. A. & Carlson, C. A.) 481–508 (Academic Press, 2015).
21. Nieto-Cid, M., Álvarez-Salgado, X. A. & Pérez, F. F. Microbial and photochemical reactivity of fluorescent dissolved organic matter in a coastal upwelling system. *Limnol. Oceanogr.* **51**, 1391–1400 (2006).
22. Lønborg, C., Álvarez-Salgado, X. A., Martínez-García, S., Miller, A. E. J. & Teira, E. Stoichiometry of dissolved organic matter and the kinetics of its microbial degradation in a coastal upwelling system. *Aquat. Microb. Ecol.* **58**, 117–126 (2010).
23. Jørgensen, L. *et al*. Global trends in the fluorescence characteristics and distribution of marine dissolved organic matter. *Mar. Chem.* **126**, 139–148 (2011).
24. Bergamasco, A. & Malanotte-Rizzoli, P. The circulation of the Mediterranean Sea: a historical review of experimental investigations. *Adv. Oceanogr. Limnol* **1**, 11–28 (2010).
25. Tsimplis, M. N. *et al*. Chapter 4 Changes in the oceanography of the Mediterranean Sea and their link to climate variability. *Developments in Earth and Environmental Sciences* **4**, 227–282 (2006).
26. Emelianov, M. *et al*. Transformation of levantine intermediate water tracked by MEDARGO floats in the Western Mediterranean. *Ocean Sci.* **2**, 281–290 (2006).
27. Schlitzer, R. Ocean Data View (2017). http://odv.awi.de.
28. Guo, L., Santschi, P. H. & Warnken, K. W. Dynamics of dissolved organic carbon (DOC) in oceanic environments. *Limnol. Oceanogr.* **40**, 1392–1403 (1995).
29. Guo, L. & Santschi, P. H. A critical evaluation of the cross-flow ultrafiltration technique for sampling colloidal organic carbon in seawater. *Mar. Chem.* **55**, 113–127 (1996).
30. Cai, Y. & Guo, L. Abundance and variation of colloidal organic phosphorus in riverine, estuarine, and coastal waters in the northern Gulf of Mexico. *Limnol. Oceanogr.* **54**(4), 1393–1402 (2009).
31. Redfield, A. C., Ketchum, B. H. & Richards, F. A. In *The* Sea (ed. Hill, M. N.) **2**, 26–77 (Wiley Interscience, Hoboken, N. J., 1963).
32. Meador, T. B. *et al*. Biogeochemical relationships between ultrafiltered dissolved organic matter and picoplankton activity in the Eastern Mediterranean Sea. *Deep sea Res. II* **57**, 1460–1477 (2010).
33. Santinelli, C., Nannicini, L. & Seritti, A. DOC dynamics in the meso and bathypelagic layers of the Mediterranean Sea. *Deep-Sea Research Part II: Topical Studies in Oceanography* **57**, 1446–1459 (2010).
34. Arístegui, J. *et al*. Oceanography: Dissolved organic carbon support of respiration in the dark ocean. *Science* **298**, 1967 (2002).
35. Powley, H. R., Krom, M. D. & Van Cappellen, P. Circulation and oxygen cycling in the Mediterranean Sea: Sensitivity to future climate change. *J. Geophys. Res. Ocean* **121**, 8230–8247 (2016).
36. Hansell, D. A., Carlson, C. A. & Schlitzer, R. Net removal of major marine dissolved organic carbon fractions in the subsurface ocean. *Global Biogeochem. Cycles* **26**(1), GB1016 (2012).
37. Santinelli, C., Hansell, D. A. & Ribera d'Alcalà, M. Influence of stratification on marine dissolved organic carbon (DOC) dynamics: The Mediterranean Sea case. *Prog. Oceanogr.* **119**, 68–77 (2013).
38. Hansell, D. A. Recalcitrant dissolved organic carbon fractions. *Ann. Rev. Mar. Sci* **5**, 421–445 (2013).
39. Guyennon, A. *et al*. New insights into the organic carbon export in the Mediterranean Sea from 3-D modeling. *Biogeosciences* **12**, 7025–7046 (2015).
40. Santinelli, C. In *Biogeochemistry of marine dissolved organic matter* (eds Hansell, D. A. & Carlson, C. A.) 579–608 (Academic Press, 2015).
41. Sarmiento, J. L. & Gruber, N. In *Ocean biogeochemical dynamics* 173-226 (Princeton University Press, 2006).
42. Sempéré, R., Yoro, S., Van Wambeke, F. & Charrière, B. Microbial decomposition of large organic particles in the northwestern Mediterranean Sea:an experimental approach. *Mar. Ecol. Prog. Ser.* **198**, 61–72 (2000).
43. Osburn, C. L., Del Vecchio, R., & Boyd, T. J. In *Aquatic Organic* Matter Fluorescence (eds Coble, P. G., Lead, J., Baker, A., Reynolds, D. M. & Spencer, R. G. M.) 233-277 (NewYork, Cambridge University Press, 2014).
44. Gao, Z. & Guéguen, C. Size distribution of absorbing and fluorescing DOM in Beaufort Sea, Canada Basin. *Deep Sea Res. Part I Oceanogr. Res. Pap* **121**, 30–37 (2017).
45. Xu, H. & Guo, L. Molecular size-dependent abundance and composition of dissolved organic matter in river, lake and sea waters. *Water Res* **117**, 115–126 (2017).
46. Tanhua, T. *et al*. The Mediterranean Sea system: A review and an introduction to the special issue. *Ocean Science* **9**, 789–803 (2013).

47. UNESCO. The International System of Units (SI) in oceanography. *UNESCO Tech Paper Mar Sci* **45**, 1–124 (1985).
48. Holm-Hansen, O., Lorenzen, C. J., Holmes, R. W. & Strickland, J. D. H. Fluorometric determination of chlorophyll. *J. du Cons* **30**, 3–15 (1965).
49. Langdon, C. Determination of dissolved oxygen in seawater by Winkler titration using the amperometric technique. *Go-sh. repeat Hydrogr. Man. a Collect. Expert reports* Guidel. Ed. by *BM Sloyan C.Sabine*, *IOC/IOCCP*, *Paris* (2010).
50. Benson, B. & Krause, J. The concentration and isotopic fractionation of oxygen dissolved in freshwater and seawater in equilibrium with the atmosphere. *Limnol. Oceanogr.* **29**(3), 620–632 (1984).
51. Guo, L., Wen, L.-S., Tang, D. & Santschi, P. H. Re-examination of cross-flow ultrafiltration for sampling aquatic colloids: Evidence from molecular probes. *Mar. Chem.* **69**, 75–90 (2000).
52. Nieto-Cid, M., Álvarez-Salgado, X. A., Gago, J. & Pérez, F. F. DOM fluorescence, a tracer for biogeochemical processes in a coastal upwelling system (NW Iberian Peninsula). *Mar. Ecol. Prog. Ser.* **297**, 33–50 (2005).

Acknowledgements

The authors are grateful to the Captain, crew, technicians and scientists aboard the R/V Sarmiento de Gamboa for their support during the cruise. We specially thank to M.J. Pazó and V. Vieitez for DOC and nutrient measurements, H. Sanleón-Bartolomé and M. Álvarez for dissolved oxygen measurements and M. Emelianov for salinity measurements and CTD data processing. This work was funded by the project HOTMIX (grant number CTM2011–30010-C02 01-MAR and 02-MAR) and the project FERMIO (MINECO, CTM2014-57334-JIN), both co-financed with FEDER funds. A.M.M.-P. was funded by a predoctoral fellowship (reference BES-2012-056175) from the Spanish Ministry of Economy, Industry and Competitiveness and the project MODMED from CSIC (PIE, 201730E020). M.N.-C. was partially supported by the CSIC Program "Junta para la Ampliación de Estudios" co-financed by the ESF (reference JAE DOC 040).

Author Contributions

A.M.M.-P., X.A.A.-S. and M.N.-C. designed the research. All authors contributed to the field work and performed the data processing and interpretation. A.M.M.-P and M.N.-C. wrote the first draft of the manuscript, which was complemented by significant contributions and discussions of all co-authors.

Additional Information

Supplementary information accompanies this paper at doi:10.1038/s41598-017-05941-6

Competing Interests: The authors declare that they have no competing interests.

Publisher's note: Springer Nature remains neutral with regard to jurisdictional claims in published maps and institutional affiliations.